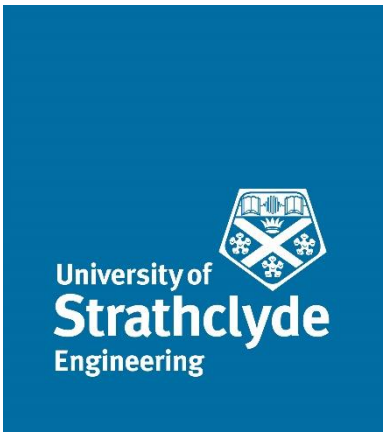

Fatigue Design Criteria for Austenitic Stainless Steels Based on Simplified Elastic-Plastic Analysis

A thesis submitted to the University of Strathclyde for the degree of Doctor of Philosophy in the Department of Mechanical and Aerospace Engineering

July 2020

David Macarthur Clarkson

Supervisor: Professor Donald Mackenzie

Declaration of Author's Rights

This thesis is the result of the author's original research. It has been composed by the author and has not been previously submitted for examination which has led to the award of a degree.

David M. Clarkson

31 July 2020

Abstract

Pressure-retaining components of civil light-water reactor (LWR) plants are susceptible to low-cycle fatigue damage throughout their operational life. In the UK civil nuclear industry, the assurance of such components against fatigue failure has traditionally been achieved by satisfying the elastic design-by-analysis (DBA) criteria outlined in Section III of the American Society of Mechanical Engineers (ASME) Boiler and Pressure Vessel Code (BPVC). The demonstration of a fatigue usage factor of unity against an S-N fatigue design curve forms the basis for establishing acceptable designs. The ASME III procedure is deterministic, and it is presumed that uncertainties are accounted for by conservatism arising from the largely unquantified margins imposed by the original Code authors, and accumulated from the use of pessimistic input variables and methodological assumptions in the assessment. Whilst this conservatism was tolerable in the past, the emergent industry understanding of the deleterious effect of the LWR coolant environment on fatigue life and its strong dependence on strain rate and temperature for austenitic stainless steels has spawned additional regulatory requirements to incorporate LWR environmental effects into traditional Code fatigue assessments. Consequently, the application of extant assessment methods, now exacerbated by environmental fatigue penalty factors, can pose difficulties in satisfying Code requirements for some critical components, potentially introducing unnecessary design constraints and an additional in-service inspection burden.

It is well understood that the current ASME III procedure for fatigue evaluation neglects several key variables, is often very conservative and provides an unquantified design margin, and thus does not provide a consistent measure of component risk. The desire for longer plant design life and the potential for civil plants to adopt flexible modes of operation has increased the urgency to develop a more accurate fatigue evaluation procedure, recognising that the traditional design margins, and indeed the acceptance criterion itself, may not be fit for purpose when considering modern plant performance requirements and economic constraints. Accordingly, several actions have been initiated as part of the ‘ASME 2025 Nuclear Code’ initiative to modernise the existing fatigue design rules. This includes future code development to adopt a

risk-informed design methodology based on probabilistic methods with target reliability as an acceptance criterion for fatigue. To this end, ASME has commenced development of a new plant system design standard for establishing plant system and component reliability targets. In the UK, probabilistic methods for fatigue assessment are also gaining traction within industry, and are currently under consideration by the Department for Business, Energy and Industrial Strategy (BEIS) and the Technical Advisory Group on the Structural Integrity of High Integrity Plant (TAGSI) in anticipation of their future application in nuclear plant safety cases. Adopting a risk-informed design methodology will require improved accuracy of predicting fatigue crack initiation, which in pressure vessels is strongly influenced by the plastic strain range experienced on the component surface. ASME III prescribes simplified elastic-plastic analysis procedures wherein the plastic strain range may be estimated from elastic analysis using a plasticity correction factor (K_e). However, the existing approach is recognised to be very conservative, especially for ductile materials such as austenitic stainless steels.

The aim of this work is to investigate these conservatisms and develop alternative approaches for simplified elastic-plastic fatigue analysis of austenitic stainless steel components with improved accuracy and practicality, suitable for future application to probabilistic fatigue initiation analysis. Extant K_e methods prescribed within various nuclear and non-nuclear codes and standards are reviewed to understand their relative advantages and limitations. A framework is proposed for calculating the actual plasticity correction factor (K_e^{FEA}) implied by detailed elastic-plastic analysis. A large number of elastic-plastic finite element analyses are performed for a range of case studies considering plant representative components and loading conditions. The performance of the various code K_e factors are evaluated and compared. Two alternative approaches – the *Global Plasticity Correction Factor* (F_g) and *Stress-Modified Neuber* (SMN) methods – are proposed and validated against the compiled K_e^{FEA} results. Both approaches are shown to be fully compatible with existing methods for assessing environmentally assisted fatigue. Through a benchmark problem, the proposed methods are demonstrated to give a more appropriate evaluation of fatigue usage, enabling significant improvements in component design life.

Acknowledgements

First and foremost, I would like to thank my supervisor Prof. Donald Mackenzie for his time, support, and valuable technical discussions throughout this project. I would also like to thank my examination committee, Mr. Keith Wright, Prof. David Nash and Dr. Athanasios Toumpis for their useful input and advice.

I would like to thank Rolls-Royce for providing the funding to complete this work. Special thanks are extended to Mr. Chris Bell for providing me the opportunity to undertake this project and for his invaluable guidance and mentorship. I would also like to acknowledge my colleagues and friends within the Rolls-Royce Small Modular Reactor programme, especially my peers Abeer, Amritpal, Declan, Ed, Joe and Paul, who were also undertaking sponsored research projects. I wish them every success in future.

Finally, I would like to thank my family for their enduring love and support throughout this process.

Table of Contents

Table of Tables

Table of Figures

Nomenclature

Organisations and Governing Bodies

AFCEN	Association Française pour les règles de Conception, de construction et de surveillance en exploitation des matériels des Chaudières Electro Nucléaires (French Association for Design, Construction and In-service Inspection Rules for Nuclear Island Components)
ANL	Argonne National Laboratory
ASME	American Society of Mechanical Engineers
ASTM	American Society for Testing and Materials
BEIS	Department for Business, Energy and Industrial Strategy (BEIS)
BNCS	ASME Board on Nuclear Codes and Standards
BPVC	Boiler and Pressure Vessel Code
CORDEL WG	Cooperation in Reactor Design Evaluation and Licensing Working Group (a WNA Working Group)
EPRI	Electric Power Research Institute
JSME	Japan Society of Mechanical Engineers
MCSTF	Mechanical Codes & Standards Task Force (a CORDEL Task Force)
MITI	Ministry of International Trade and Industry (Japan)
NRC	United States Nuclear Regulatory Commission
PNAEG	PNAE-G-7-002-86: Rules of Strength Calculation for Equipment and Pipelines of Nuclear Power Plants (Russia)
RR	Rolls-Royce
TAGSI	UK Technical Advisory Group on the Structural Integrity of High Integrity Plant
TENPES	Thermal and Nuclear Power Engineering Society (Japan)
WGDM	ASME Working Group on Design Methodology
WGEFEM	ASME Working Group on Environmental Fatigue Evaluation Methods
WGFS	ASME Working Group on Fatigue Strength
WRC	Welding Research Council
WNA	World Nuclear Association

Technical Abbreviations

BFC	Best-fit curve
BPVC	Boiler & Pressure Vessel Code
C&S	Codes & Standards
CC	Code Case
CUF	Cumulative usage factor
DBA	Design-by-analysis
DFC	Design fatigue curve
EPP	Elastic perfectly-plastic
EVP	Extreme value pairing
F	Peak stress
FE(A)	Finite element (analysis)
FSRF	Fatigue strength reduction factor
HTC	Convective heat transfer coefficient
LWR	Light-water reactor
MRA	Modified rate approach
NLKH	Non-linear kinematic hardening
P	Primary stress
PRA	Probabilistic risk assessment
PTP	Peak-to-peak
Q	Secondary stress
RF	Shakedown reserve factor
R-O	Ramberg-Osgood
SCL	Stress classification line
SMN	Stress-modified Neuber correction
SNW	Strain-life weighted method
SRL	Stress redistribution locus
SS	Stainless steel
SSC	Stress-strain curve

Variables, Constants

A	R5 V2/3 cyclic Ramberg-Osgood coefficient
A, B, C	Parameters in the Generalised Langer model
A_0	Parameter in JSME and EN-13445 K_e equations
A_1, A_2, A_3	Parameters in AD 2000-Merkblatt K_e equations
B_1	Parameter in JSME K_e equation
C	Chaboche hardening parameter
F_{en}	Environmental fatigue penalty factor
$F_{en,eff}$	Effective environmental fatigue penalty factor
E_a	Elastic modulus of analysis
E_c	Reference elastic modulus of DFC
E_s	Secant modulus
E_T	Tangent modulus
F_e	Proposed sectional plasticity correction factor
F_g	Proposed global plasticity correction factor
F_{lt}	Local thermal correction factor in RR F_u method
F_n	Sectional plastic correction factor in RR F_u method
F_p	Proposed surface plasticity correction factor
F_u	RR unified correction factor
K	Monotonic Ramberg-Osgood coefficient; Parameter in JSME K_e equation
K^c	Cyclic Ramberg-Osgood coefficient
K_1, K_2	Parameters in ASME VIII-2, Annex 5-C K_e equation
K_e	Fatigue plasticity correction factor (strain concentration factor)
$K_{e,A0}$	JSME MITI Notification 501 correction factor
$K_{e,eq}$	Equivalent K_e factor
K_e^{EN}	EN-13445 Annex 18 K_e factor
K_e^{FEA}	K_e determined by elastic-plastic FEA
K_e^{JSME}	JSME PVB 3315.1 K_e factor

$K_e^{JSME\ CC}$	JSME NC-CC-005 K_e factor
K_e^{MB}	AD 2000-Merkblatt K_e factor
$K_e^{N\text{-}779}$	CC N-779 K_e factor
K_e^{PNAEG}	PNAE-G-7-002-86 K_e factor
K_e^{R}	Ranganath's K_e factor
K_e^{ther}	RCC-M B-3234.6 thermal plastic correction factor
$K_e^{VIII\text{-}2}$	ASME VIII-2, Section 5.5.3 K_e factor
$K_e^{XIII\text{-}3450}$	ASME III, Appendix XIII-3450 K_e factor
K_e^{5C}	ASME VIII-2, Annex 5-C K_e factor
K_n	Neuber notch plasticity correction factor
$K_n^{N\text{-}779}$	CC N-779 notch factor
K_n^{R}	Ranganath notch factor
K_{np}^{5C}	ASME VIII-2, Annex 5-C notch plasticity adjustment factor
K_{nl}^{5C}	ASME VIII-2, Annex 5-C non-local plastic strain redistribution factor
K_{th}^{R}	Ranganath Poisson's ratio correction factor
K_v	Poisson's ratio correction factor
K_v^{EN}	EN-13445 Annex 18 Poisson's ratio correction factor
K_v^{MB}	AD 2000-Merkblatt Poisson's ratio correction factor
$K_v^{N\text{-}779}$	CC N-779 Poisson's ratio correction factor
K_v^{5C}	ASME VIII-2, Annex 5-C Poisson's ratio correction factor
K_T	Elastic stress concentration factor
K_σ	Stress redistribution factor
N_{exp}	Cycles to failure determined experimentally
N_f	Predicted number of cycles to failure; number of allowable cycles.
N_f^{FEA}	Allowable cycles from elastic-plastic FEA
$N_f^{N\text{-}779}$	Allowable cycles from CC N-779
$N_f^{Ranganath}$	Allowable cycles from Ranganath's method
$N_f^{XIII\text{-}3450}$	Allowable cycles from ASME III, Appendix XIII-3450
N_T	Transition life

$2N_f$	Number of reversals to failure
O'	Transformed dissolved oxygen concentration
P_i	Internal pressure
R	Parameter in Ranganath's K_e^R equation for $3S_m < S_n \leq 3mS_m$
R^*	Parameter in Ranganath's K_e^R equation for $S_n > 3mS_m$
S_a	Alternating stress amplitude
S_{alt}	Alternating stress intensity
S_m	Design stress intensity
S_n	Primary-plus-secondary stress intensity range
$S_{n,tb}$	Thermal bending stress intensity range
$S_{n,tm}$	Thermal membrane stress intensity range
$S_{n\text{-}tb}$	Primary-plus-secondary less thermal bending stress intensity range
S_p	Primary-plus-secondary-plus-peak (total) stress intensity range
$S_{p,lt}$	Local thermal stress intensity range
S_p^{mech}	Total mechanical stress intensity range
S_p^{ther}	Total thermal stress intensity range
ΔT	Temperature change
T'	Transformed temperature
U	Cumulative usage factor
U_{en}	Environmentally-corrected cumulative usage factor
b	Fatigue strength exponent
c	Fatigue ductility exponent
d	Heat penetration depth
dp	Equivalent plastic strain increment
e	Element thickness
m	Material parameter in ASME III K_e equation
n	Monotonic Ramberg-Osgood exponent; strain hardening parameter in ASME III K_e equation; number of expected cycles

n^c	Cyclic Ramberg-Osgood exponent
q	Elastic follow-up factor for global plasticity
q_p	Elastic follow-up factor for local plasticity
r	Radius
Δt	Time increment
w	SNW weighting factor
α	Coefficient of thermal expansion
α_i	Chaboche i^{th} backstress tensor
α_{NLK}	Chaboche total (superimposed) backstress tensor
β	R5 V2/3 cyclic Ramberg-Osgood exponent
γ	Engineering shear strain; Chaboche relaxation parameter
δ	Displacement
ε	Total strain
$\dot{\varepsilon}'$	Transformed strain rate
ε_f	True fracture ductility
$\varepsilon_f^{'}$	Fatigue ductility coefficient
$\Delta\varepsilon$	Total strain range
$\Delta\varepsilon_{EOSR}$	Effective octahedral (von Mises) shear strain range
$\Delta\varepsilon_{ESSR}$	Effective shear (Tresca) strain range
$\Delta\varepsilon_{ETSR}$	Equivalent total strain range (von Mises)
$\Delta\varepsilon_{MPT}$	Numerically maximum principal total strain range
κ	SMN modification factor, thermal diffusivity
ν, ν^*	Poisson's ratio (assuming elastic or plastic behaviour)
ρ	Mass density, notch root radius of curvature
σ	Stress
$\Delta\sigma$	Stress range
σ_e	Fatigue endurance limit
σ_f	True fracture stress

σ_f'	Fatigue strength coefficient
σ_I	Tresca stress intensity
σ_m	Mean stress
σ_R	Rankine stress intensity
σ_u	Ultimate tensile strength
σ_{VM}	von Mises stress intensity
σ_y	Monotonic yield strength
σ_y^c	Cyclic yield strength
ϕ	Parameter in modified Navarro algorithm

Subscripts, Superscripts

a	Alternating; amplitude
b	Bending
e	Elastic
ep	Elastic-plastic
eq	Equivalent
f	Failure; allowable
FEA	Elastic-plastic FEA
m	Membrane
os	Offset
p	Plastic
u	Ultimate tensile strength
y	Yield
x, y, z	Local Cartesian coordinates (radial, longitudinal, circumferential)
r, z, θ	Cylindrical coordinates (radial, longitudinal, circumferential)
1, 2, 3	Principal components

1. Introduction

In the design of many structures and components, fatigue must be considered as a potential failure mechanism. The fatigue strength of common materials such as structural steels can be established through mechanical testing under a constant load amplitude. Using this knowledge, fatigue assessment procedures can be used to predict the behaviour of a material under its intended operating conditions, thereby assuring against fatigue failure. In the nuclear industry, such procedures are generally prescriptive and embodied within internationally recognised codes and standards (C&S). These usually incorporate large design factors and can be quite conservative. This can introduce constraints on the design and/or operation of the plant and introduce an additional inspection/maintenance burden. However, the operational loads experienced by most structures is not reflective of test conditions, and consequently the material behaviour can be very different. This is especially true of nuclear power plant pressure vessels, which experience complex, variable amplitude loading. Furthermore, plastic action persists throughout the life of such vessels, which can be difficult to predict. One possible route to capture this behaviour accurately is to perform full-scale mock-up tests under actual operating conditions. Whilst the structural response of a component can be reliably measured experimentally in this way, performing such tests is often precluded, owing to time and budget constraints. Accordingly, the validation of assessment procedures must often rely on results obtained from detailed finite element analysis (FEA).

In order to optimise the fatigue performance of pressure vessel components, accurate prediction of the elastic-plastic response under various loading conditions is required. However, simulation of elastic-plastic material behaviour can be complicated, and is typically expensive and time-consuming. Furthermore, some C&S provide little guidance on implementing such an approach. A practical and reliable method to predict elastic-plastic strains based on knowledge of the purely elastic behaviour of a structure is therefore invaluable to the component designer and stress analyst.

1.1. Background

Austenitic stainless steels are used in many engineering applications, from automotive and aerospace components to pressure vessels and piping utilised in conventional and

nuclear power plants. In the latter case, they are utilised heavily within the primary circuit of Light-Water Reactor (LWR) plants, including both Pressurised Water Reactor (PWR) and Boiler Water Reactor (BWR) plants. In modern PWR designs, reactor coolant primary pipework is usually fabricated from austenitic stainless steels owing to its high ductility and corrosion resistance. Pressure-retaining components of PWRs can be susceptible to fatigue throughout their operational life, owing mainly to fluctuations in pressure and temperature. Transient variations in the reactor coolant temperature may arise due to changes in the power state of the plant. For thick-walled components, sharp thermal gradients can develop, resulting in high surface stresses. When these variations occur frequently, surface micro cracks may initiate. If left to grow over time, the micro crack network may develop into a single dominant crack, which can propagate through-wall, resulting in leakage. Lack of accessibility can often make it difficult to inspect and monitor certain components. Accordingly, the fatigue assessment methods adopted in nuclear industry C&S must provide confidence that a component will not suffer a fatigue failure within its intended design life.

1.2. ASME BPVC Section III

In the UK civil nuclear industry, the assurance of pressure vessels and piping components against fatigue is achieved by satisfying the elastic design-by-analysis (DBA) requirements outlined in Section III of the ASME Boiler and Pressure Vessel (BPVC) Code [1], herein referred to as *'ASME III*' or *'the Code'*. ASME III, Appendix XIII-3520 provides a systematic procedure to evaluate fatigue at a single location in a vessel based on stress ranges obtained from elastic finite element (FE) analysis. By artificially associating these fictitious stresses to the actual strains experienced by a component, the prediction of fatigue life is made possible. Where necessary, simplified elastic-plastic penalty factors, referred to widely as *Plasticity Correction Factors (PCFs),* are applied in order to account for non-linear material behaviour, so enabling an estimation of elastic-plastic strains. This is known as *Simplified Elastic-Plastic Analysis*.

A review of the published literature (Section 2) highlights that austenitic stainless steels in particular possess exceptional fatigue properties, especially in the low-cycle regime where plasticity is prevalent. Existing Code methods do not build on a complete

understanding of fatigue behaviour in the presence of plasticity however, and consequently, tend to be very conservative, especially for austenitic stainless steel components. This can result in unnecessarily pessimistic predictions of component fatigue life, leading to difficulties in satisfying Code requirements. Accordingly, there is currently a strong industry need to develop more accurate and reliable PCFs for fatigue design of austenitic stainless steel components.

The objective of this thesis is to develop alternative approaches to improve the simplified elastic-plastic fatigue analysis of austenitic stainless steel components. To achieve this, existing approaches within ASME III and other recognised C&S were reviewed. Due consideration was paid to developing the most appropriate methodological framework for deriving PCFs directly from elastic-plastic FE models. It is hoped that some of the outcomes of this work will prove helpful to improving the existing rules for simplified elastic-plastic analysis prescribed within ASME III.

1.3. Thesis Structure

Chapter 2 provides a fundamental overview of fatigue in austenitic stainless steels, considering the strain-life framework, cyclic stress-strain behaviour, mean stress effects, and cumulative damage. Chapter 3 discusses the procedures for fatigue analysis adopted by ASME III. The elastic DBA framework is introduced along with the basic methodology and assumptions for FE-based fatigue adopted within this thesis. The need for modernised fatigue rules, including more accurate simplified elastic-plastic analysis criteria, is briefly discussed in the current industry context. Chapter 4 examines existing approaches for simplified elastic-plastic analysis of austenitic stainless steels based on elastic DBA, prescribed within ASME III and various other internationally recognised nuclear and non-nuclear C&S. In Chapter 5, a framework is developed for determination of realistic PCFs from elastic-plastic FE models. Consideration is given to the choice of cyclic plasticity model and multiaxial strain measure. Chapter 6 describes the FE models of PWR plant representative components selected as part of an FE analysis campaign for determination of FE-derived PCFs. In Chapter 7, the results obtained from the FE models described in Chapter 6 are discussed in detail. The performance of the Code PCFs determined based on the elastic DBA is evaluated by comparison with those determined directly from

elastic-plastic analysis. The advantages and shortcomings of each method are discussed, along with further recommendations. Chapter 8 presents the work performed to develop and validate two alternative plasticity correction methods for austenitic stainless steels. The potential improvements achievable from both methods is demonstrated for a representative plant component case study. Chapter 9 summarises the main conclusions that have been drawn from this work. Finally, Chapter 10 provides some recommendations for further work to enhance existing industry knowledge in this important area.

2. Overview of Fatigue

2.1. Basic Concepts

2.1.1. Mechanistic Interpretation of Fatigue

Fatigue is a process by which a crack can form and grow under repeated application of variable loads. Fatigue cracks normally initiate on the surface of a component, where stresses tend to be highest. This process is referred to as *crack initiation*. If such cracks are permitted to grow undetected, they can significantly reduce the load carrying capacity of the component. This process is referred to as *crack growth* or *crack propagation*. Eventually, once the crack reaches a critical size, the component may fracture. An example of this is to be found in the failure by fatigue of the fuselage of the de Havilland Comet aircraft in the 1950s, which resulted in the deaths of 147 people [2]. Thus, fatigue is a multi-stage (Figure 1) form of damage of which the consequences can be catastrophic.

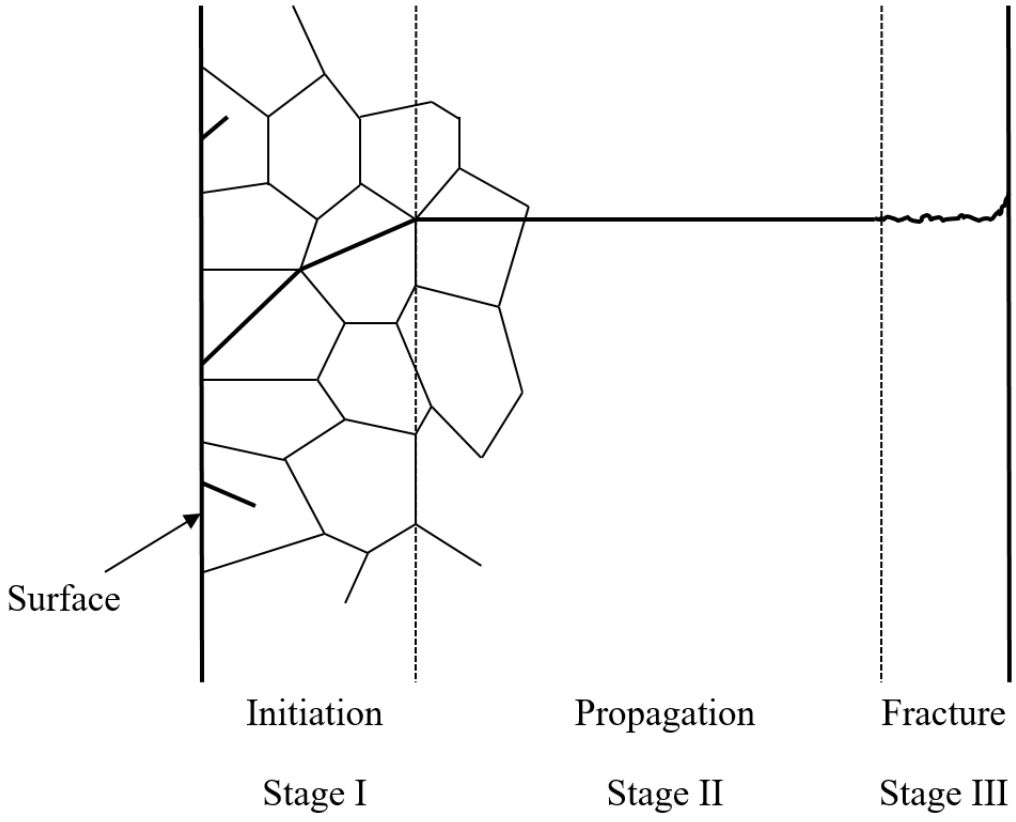

Figure 1. Progression of fatigue failure.

Fatigue damage is irreversible and accumulates as a material absorbs ever-greater amounts of macroscopic deformation energy under repeated loading. Therefore, irreversible deformation or *plasticity* is a necessary condition for fatigue to occur. This macroscopic energy is consumed in the form of microscopic plastic strains within the microstructure of the material. These plastic strains break the molecular bonds within the metal and contribute to damage. Over time, this highly localised plastic cycling leads to the formation of *persistent slip bands* (PSBs) along crystallographic slip planes within the grains of the metal. These slip bands are visible on the metal surface as intrusions and extrusions. Shear micro-crack nucleation then occurs along these slip planes or at grain boundaries due to the additional stress concentration caused by the interaction of PSBs and grain boundaries. These micro cracks can then coalesce to form a single dominant crack.

Once initiated, a fatigue crack tends initially to propagate along planes of maximum shear, oriented at 45° to the applied load. This is known as *short crack growth* or *Stage I crack propagation*. The crack propagates until it is decelerated by a microstructural barrier, such as a grain boundary or inclusion, which cannot accommodate the original crack growth direction. The direction of growth then alternates between shear planes, leading to the characteristic 'zig-zag' appearance on microscopic examination. As the crack grows longer, slip starts to develop along other planes near the crack tip, which produces a shift in the crack orientation such that it propagates perpendicular to the direction of applied load. This process is known as *long crack growth* or *Stage II crack propagation*. A defining characteristic of Stage II crack growth is the formation of ripples or *striations* on the surface of the metal, as the crack advances in a stable manner. Finally, upon reaching a critical length, the crack rapidly propagates in an unstable manner, resulting in final fracture. This is *Stage III* crack propagation.

2.1.2. Fatigue Design Philosophy

Today, two distinct fatigue design philosophies have seen widespread adoption by different industries, *Safe Life Design* and *Damage Tolerant Design*.

The objective of *Safe Life Design* is to design a component in such a way that crack initiation can be assumed precluded within its intended service life. This approach is commonly adopted for situations where regular inspection of a component is not

possible, or where the consequences of fatigue failure would be catastrophic. This often involves the use of large design factors and conservative assumptions relating to material strength and service loading. This approach is most common in the design of pressure equipment, especially those intended for nuclear power plant facilities.

Damage Tolerant Design is concerned with designing structures and components such that they are resistant to fatigue, but does not preclude crack initiation entirely. Structural integrity is instead demonstrated by ensuring that when fatigue cracking occurs in-service, the component can continue to operate normally without failure until the damage can be detected. This approach therefore places a higher emphasis on effective inspection and maintenance to ensure the continued operability of components. Where necessary, fracture mechanics methods may be adopted to estimate critical crack depths and inspection intervals. This approach has been widely adopted within the aerospace and automotive industries.

In the UK civil nuclear industry, fatigue crack initiation has generally been regarded as unacceptable in the design of pressure vessel components. Put differently, if crack initiation is predicted to occur in the design stage, the component is considered to have 'failed'. However, what constitutes a 'fatigue failure' remains an important outstanding question, with many ASME experts divided on whether the fatigue design rules prescribed in Section III are intended to preclude crack initiation or through-wall leakage. To prevent initiation of surface fatigue cracking is increasingly being viewed as unrealistic and instead the aim should be to prevent the development of structurally significant cracks that can threaten component functionality. A review of the ASME Section III fatigue design basis (Section 3) and other recent industry developments highlights a number of important arguments to suggest that total life prediction to through-wall leakage, provided it maintains sufficient design margin, is consistent with the intent of the Code authors. Since leakage due to fatigue involves crack incubation, initiation, and propagation phases, design against initiation can be excessively conservative, especially for ductile components that are tolerant of a significant propagation phase.

For ductile metallic components of LWR plants, which are often subjected to repeated plastic action, Stage II growth tends to occupy the majority of fatigue life. This has

recently led to the emergence of modern assessment methods, sometimes termed *Total Life Approaches*, which aim to characterise each stage of the fatigue process within a systematic procedure to achieve more accurate and representative assessments of components. In this approach, the total fatigue life is separated out into the number of load repetitions to initiate a mechanically small crack considering Stage I nucleation and growth, followed by the number of subsequent repetitions for Stage II crack growth to achieve a failure criterion defined by the designer *a priori* (e.g. through-wall leakage). In this way, a greater emphasis is placed on the much longer Stage II portion of fatigue life, which can be predicted more reliably using fracture mechanics-based crack growth analysis. Furthermore, the application of a total life assessment approach using probabilistic methods introduces the potential for a risk-informed, performance-based acceptance criterion to be adopted for fatigue design. If a probabilistic model of the input variables is adopted, for example using the Monte Carlo method, a quantified margin can then be applied to the predicted total life to leakage, where margin here is expressed as a probability of the component to acceptably perform its intended function or *reliability*. Therefore, there is a need to determine an optimum or *target reliability* to define acceptable fatigue performance, reflecting both the risk and consequences of failure.

In 2018, ASME Nuclear Codes and Standards organisations initiated the "2025 Nuclear Code" initiative [3]. The purpose of the initiative is to modernise all aspects of the existing Code rules to enable designers and operators to take advantage of the many modern design and fabrication methods available today. Important objectives include the development of modernised fatigue analysis rules and incorporation of probabilistic and risk-informed methods with target reliability as an acceptance criterion for fatigue. To achieve this, ASME has also commenced development of a new Plant System Design standard for establishing plant system and component reliability targets by incorporating risk insights derived from a probabilistic risk assessment (PRA). This represents a fundamental shift in fatigue design philosophy for which total life assessment methods have the potential to reap the greatest benefit in future.

However, total life approaches are not yet developed enough to be of practical use in routine fatigue design. The use of a total life assessment based on probabilistic

methods will require improved accuracy of fatigue initiation predictions; the development of alternative simplified elastic-plastic analysis methods for austenitic stainless steels with greater accuracy and practicality will be crucial for generating surrogate models needed for probabilistic fatigue initiation analysis in combination with crack growth analysis for a total life assessment. A review of the technical literature (Section 4) highlights a number of existing approaches proposed as alternatives to the current ASME III simplified elastic-plastic analysis procedure, many of which have been incorporated within other recognised C&S. However, these approaches have some disadvantages, such as inconsistency, over-conservatism or being impractical to apply. Therefore, the focus of this thesis is methods for predicting fatigue crack initiation that can overcome these outstanding limitations.

2.2. Fatigue Behaviour of Austenitic Stainless Steels

This section introduces the fundamental factors pertaining to fatigue life prediction of metallic components in nuclear power plant service. As austenitic stainless steels are a prime focus of this thesis, a general review of the fatigue behaviour of these alloys is undertaken. First, it is necessary to introduce and clarify a number of technical terminologies.

The term ‘cycle’ refers to the situation where the stress or strain in a component varies from an initial state, to a maximum extent, to a minimum extent, and then returns to the initial state (Figure 2). One-half of the cycle load range is known as the *amplitude* or *alternating load*. The average of the maximum and minimum cycle loads is known as the *mean* load. In cycles where the maximum and minimum loads are equal and opposite, the mean load is zero and is known as a *fully reversed* cycle. Figure 2 illustrates an example of constant amplitude sinusoidal loading where each successive cycle possesses the same load amplitude.

The objective of a fatigue damage model is to predict the number of cycles, at a specific load range, that a component can withstand before crack initiation or ‘failure’ is presumed to occur. The term *damage* is commonly defined as the number of cycles expected to occur divided by the number of cycles predicted to cause failure (n/N_f). The efficacy of fatigue damage models has historically been established based on their ability to correlate experimentally observed fatigue lives of small-scale polished

specimens subjected to uniaxial membrane stress- or strain-cycling. In the initiation phase, damage relates to microscopic phenomena including dislocation motion, slip, micro crack formation, and so forth, which can be difficult to correlate with macroscopic measurements in absence of a highly controlled laboratory environment. Indeed, the definition of 'crack initiation' is itself subjective, and the boundary delineating short- and long-crack growth phases is not easily defined. Modern codes of practice relating to fatigue endurance testing of uniform gage specimens such as ASTM E446 [4] and E606 [5] do not give a prescriptive definition of fatigue failure, but instead give various options. One option is to define failure as the number of cycles required to produce total separation or fracture of the specimen. In most modern studies, it is common practice to define the fatigue life as the number of cycles required for the tensile stress to drop 25% from its peak value. Such a load drop corresponds approximately to a 3mm-deep crack in the gage. Consequently, the fatigue life N_f represents the number of cycles to initiate a crack of 3mm depth in a specimen and has become an arbitrary benchmark for which to assess the predictive capability of fatigue damage models. By the principle of similitude, this definition of damage can then be related to real components; that is, the formation of a 3mm-deep crack in a specimen is presumed to equate to the formation of an equivalent crack in a large component or structure.

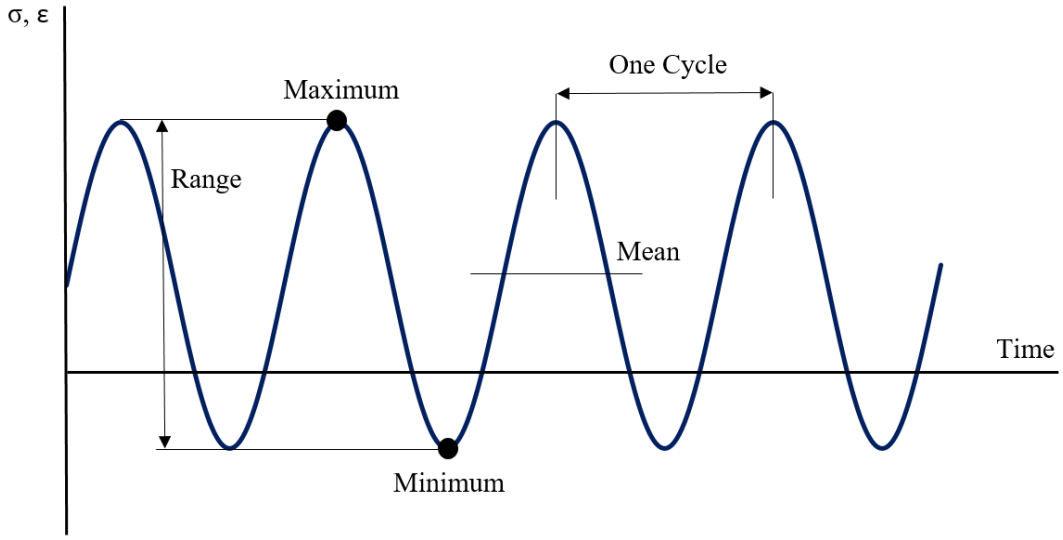

Figure 2. Description of fatigue loading

2.2.1. Classical Uniaxial Strain-Life (ε-N) Framework

The most basic form of fatigue concerns an alternating, fully reversed, uniaxial stress such as that applied to cylindrical specimens in standard load-controlled fatigue testing procedures [4]. This is commonly employed to determine an empirical relation between alternating stress and life, formalised by a stress-life (S-N) curve. Under these conditions, the induced strains are predominantly elastic, with plasticity being largely undetectable on a macroscopic scale. A large number of cycles, normally greater than 10^4, is therefore required to nucleate and grow a crack to induce fracture of the specimen. This behaviour is referred to as *high-cycle fatigue*. The relationship between alternating stress and cycles to failure is commonly represented in the exponential form originally proposed by Basquin [6]:

$$\sigma_a = \sigma_f'\left(2N_f\right)^b \tag{1}$$

where σ_a is the alternating stress, σ_f' is the fatigue strength coefficient, b is the fatigue strength exponent, and $2N_f$ is the number of *reversals* (or *half-cycles*) to failure. On the other hand, where specimen failure occurs within a smaller number of cycles, this is referred to as *low-cycle fatigue*. In this situation, it is recognised that fatigue life is dictated not by stress, but instead by plastic strain which is now dominant compared to the elastic strain. Therefore, to establish an empirical relationship for low-cycle fatigue, *strain-controlled* testing is instead performed where applied strain is the controlled variable [5]. Coffin [7] and Manson [8] found that for a wide variety of metals, the following relationship holds:

$$\varepsilon_a^p = \varepsilon_f'\left(2N_f\right)^c \tag{2}$$

where ε_a^p is the plastic strain amplitude, ε_f' is the fatigue ductility coefficient, and c is the fatigue ductility exponent. The denomination of σ_f' and ε_f' can be somewhat misleading since *fatigue ductility* is also a form of *fatigue strength*, and therefore both parameters aim to quantify a material's resistance to fatigue failure. To clarify, these parameters respectively characterise the ability of material to resist fatigue under predominantly elastic and plastic deformations, respectively. By superposition of Eq. (1) and (2), the relationship between total strain amplitude and cycles to failure is best represented by the so-called Coffin-Manson relation [9], traditionally written as:

$$\varepsilon_a = \varepsilon_a^e + \varepsilon_a^p = \frac{\sigma_f'}{E}(2N_f)^b + \varepsilon_f'(2N_f)^c \quad (3)$$

where ε_a^e is the elastic strain amplitude implied by Eq. (1) and E is the Young's modulus. It is straightforward to visualise the Coffin-Manson relation by examining the logarithmic transformations of Eq. (1) and (2) in graphical form (Figure 3). Both equations show a log-linear relationship. The coefficients of Eq. (1) and (2) represent the intercept, which quantifies respectively the stress amplitude and plastic strain amplitude that correspond to failure in a single reversal (i.e. when $2N_f = 1$). The exponents of Eq. (1) and (2) represents the slope of the lines in log-log space, which describes the rate of change of fatigue life with respect to stress amplitude and plastic strain amplitude, respectively. The elastic strain amplitude is negligible for low-cycle, and the Coffin-Manson curve approximates its plastic part in that region. On the other hand, high-cycle fatigue is associated with predominantly elastic strains and the Coffin-Manson curve approximates its elastic part in this region.

In the Coffin-Manson framework, cyclic plasticity effects are assumed negligible in the case where $N_f > N_T$, where N_T is known as the *transition life* where the contribution of elastic and plastic strains to the total strain amplitude are approximately equal, $\varepsilon_a^e = \varepsilon_a^p$. The concept of a transition life is useful as a rule-of-thumb to demarcate the boundary between low- and high-cycle fatigue regimes for different materials. In situations where $N_f >> N_T$, this corresponds to high-cycle fatigue, and the stress-based Basquin relation (Eq. (1)) is expected to give reasonable fatigue life predictions. On the other hand, in situations where $N_f < N_T$, this corresponds to the low-cycle fatigue and a relation based on strain such as Coffin-Manson (Eq. (3)) must be used to obtain reliable life estimates. The transition life can be calculated directly by setting $\varepsilon_a^e = \varepsilon_a^p$ and solving Eq. (3):

$$\varepsilon_a^e = \varepsilon_a^p \rightarrow \frac{\sigma_f'}{E}(2N_T)^b = \varepsilon_f'(2N_T)^c \rightarrow N_T = \frac{1}{2}\left(\frac{\sigma_f'}{E\varepsilon_f'}\right)^{1/(c-b)} \quad (4)$$

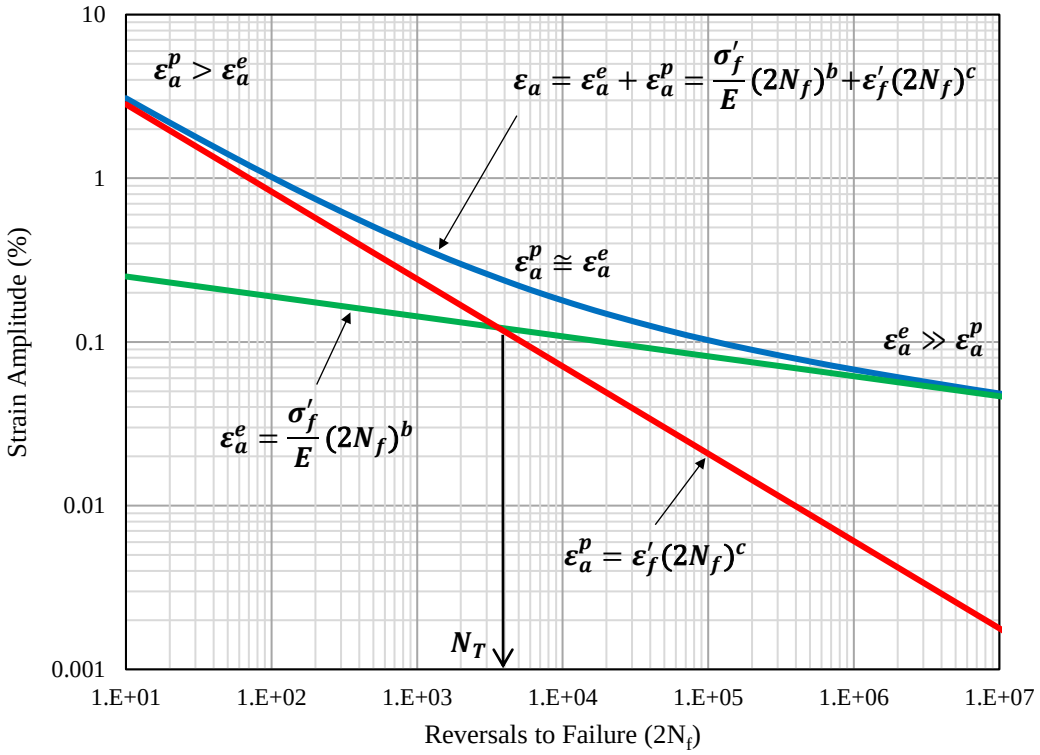

Figure 3. Illustration of Coffin-Manson relation for typical structural alloys.

A number of other functions have been proposed to express the fatigue strain or stress amplitude versus cycles to failure. Another useful model is that proposed by Langer [10], expressed in the form

$$\varepsilon_a = A\left(N_f\right)^{-B} + C \tag{5}$$

where A, B, and C are the parameters of the model. The parameter A represents the strain amplitude corresponding to failure within a single cycle, $N_f = 1$, whilst B represents the rate of change of fatigue life with respect to total strain amplitude. The parameter C represents the endurance limit of the material, defined as the stress or strain level below which a test specimen can be cycled indefinitely without exhibiting fatigue failure. For structural steels, there exists a well-known empirical relationship between the endurance limit, σ_e, and the ultimate tensile strength, σ_u. Bannantine et al [11] noted that for steels with tensile strengths below 1400 MPa, the endurance limit may be approximated as one-half of the ultimate tensile strength. Published in 1958, the U.S. Navy Structural Design Basis for PWR Reactor Pressure Vessels [12] also provides guidance for estimating the endurance limit based on tensile strength; under

these guidelines, σ_e is approximately 0.45 times σ_u for austenitic stainless steels. An important advantage of the Langer model is that it is formulated in terms of total strain amplitude only, thereby obviating the need to partition the elastic and plastic parts. As the vast majority of experimental data reported in the technical literature tends to report only the total strain and cycles to failure, the Langer model is highly favoured for characterising fatigue behaviour, especially within the nuclear industry.

As low-cycle fatigue lives are related to the plastic strains, it follows that those materials with high ductility will exhibit the highest resistance in these conditions. For this reason, austenitic stainless steels are highly favoured for power plant applications due to their exceptional low-cycle fatigue performance across a wide range of service temperatures. A sample of fully reversed strain-life data compiled from various tests published in [13]–[32] conducted on a range of austenitic stainless steel alloys at room temperature in air is shown in Figure 4. The elastic reserve of austenitic stainless steels is generally limited to between 0.1 and 0.15%, and therefore they exhibit a very high transition life, around 10^5-10^6 cycles. It can be seen then fully reversed lifetimes of 10^4 and above are typical for strain amplitudes less than 0.5%. Furthermore, fully reversed lifetimes less than 10^3 are not typical for strain amplitudes less than 1%. The plastic strain amplitude that controls crack initiation in these alloys therefore tends to be very large, sometimes over ten times the elastic strain amplitude. The following generalised Langer best-fit model has been found to capture reasonably the fatigue behaviour of a wide range of austenitic stainless steel grades at room temperature

$$\varepsilon_a(\%) = 24.54 \cdot \left(N_f\right)^{-0.486} + C(\sigma_u) \tag{6}$$

where the constant C varies linearly as a function of σ_u with a slope of $\approx 2.433e^{-4}$ (%). Considering the average value of E at room temperature is 195 GPa, this corresponds roughly to an endurance limit equal to 0.474, which is close to the values proposed by the estimation guidelines in [11], [12]. This means that the endurance strain, ε_e, for austenitic stainless steels can typically vary between 0.12 - 0.23% depending on tensile strength. Thus, even in the very high-cycle regime, the strain amplitude for austenitic stainless steels is rarely ever fully elastic and the effects of plasticity are still very important. It is for this reason that its fatigue behaviour can only be reliably ascertained from strain-controlled testing.

$$\frac{\sigma_e}{\sigma_u} = \frac{195e^3 \cdot 2.433e^{-4}}{100} = 0.474 \quad (7)$$

The fatigue strength of austenitic stainless steels generally exhibits some degradation at elevated temperatures. A sample of fully reversed strain-life data compiled from tests published in [19], [24], [32]–[43] conducted on austenitic stainless steel alloys in the temperature range of 150°C-816°C in air are shown in Figure 5. In the temperature range of 150-300°C, Solomon et al [36] observed a modest reduction in fatigue life of Type 304L SS at strain amplitudes of 0.3%, but a slight increase in fatigue life at strain amplitudes of 0.5%. Other studies in the temperature range 288-350°C conducted by Le Pecheur [32], Reicherter [19], Chopra [24], Baglion [33], Huin [34], and Miura et al [35] imply only a modest reduction, if any, in low-cycle fatigue performance compared to room temperature. However, the reduction in the fatigue endurance limit is more pronounced. At yet higher temperatures, fatigue performance is more adversely affected due to reduction in cyclic strength and chromium carbide precipitation at grain boundaries. Stabilised grades including Nb- and Ti-doped Types 347 and 348 are resistant to the latter degradation mechanism and possess somewhat superior fatigue endurance at higher service temperatures. For temperatures between 600-816°C, austenitic stainless steels can experience up to an order of magnitude reduction in fatigue life for strain amplitudes exceeding 0.3%. Generally, the fatigue performance of austenitic stainless steels for temperatures between 21°C and 430°C can be adequately described by Eq. (6) which is based on room temperature test data, by using the value of σ_u at the prevailing temperature. Both the room temperature and 150-430°C data fall within the same -2σ/-3σ scatter bands on predicted life (Figure 6). For temperatures exceeding 430°C, the fatigue lives fall within another scatter band and require separate treatment. The implications of this are twofold. Firstly, from room temperature up to the range experienced in LWRs under normal operation, usually between 288-325°C, the fatigue behaviour of austenitic stainless steels is only modestly affected. Secondly, the change in fatigue performance implied by differences in alloy composition, heat treatment, and mechanical conditioning is also not particularly significant in this temperature range and enables austenitic stainless steels to be categorised as a representative class of materials, irrespective of these factors.

Since the intent of the strain-life approach is to predict the number of cycles to initiate a fatigue crack, the fact that the strain-life curve follows a power-law relation is of crucial importance. The steeper slope of the strain-life curve in the low-cycle regime is directly related to the mechanistic process of crack nucleation and growth. In the low-cycle fatigue regime, it has been found that crack nucleation and short crack growth (i.e. Stage I) may account for as little as 10% of total fatigue life, compared to 60-70% for high-cycle fatigue [11]. Consequently, even a small change in strain amplitude can dramatically alter the predicted number of cycles to initiation in the low-cycle regime. Thus, accurately predicting the strains experienced by actual structures is fundamental to achieving reliable predictions of fatigue life.

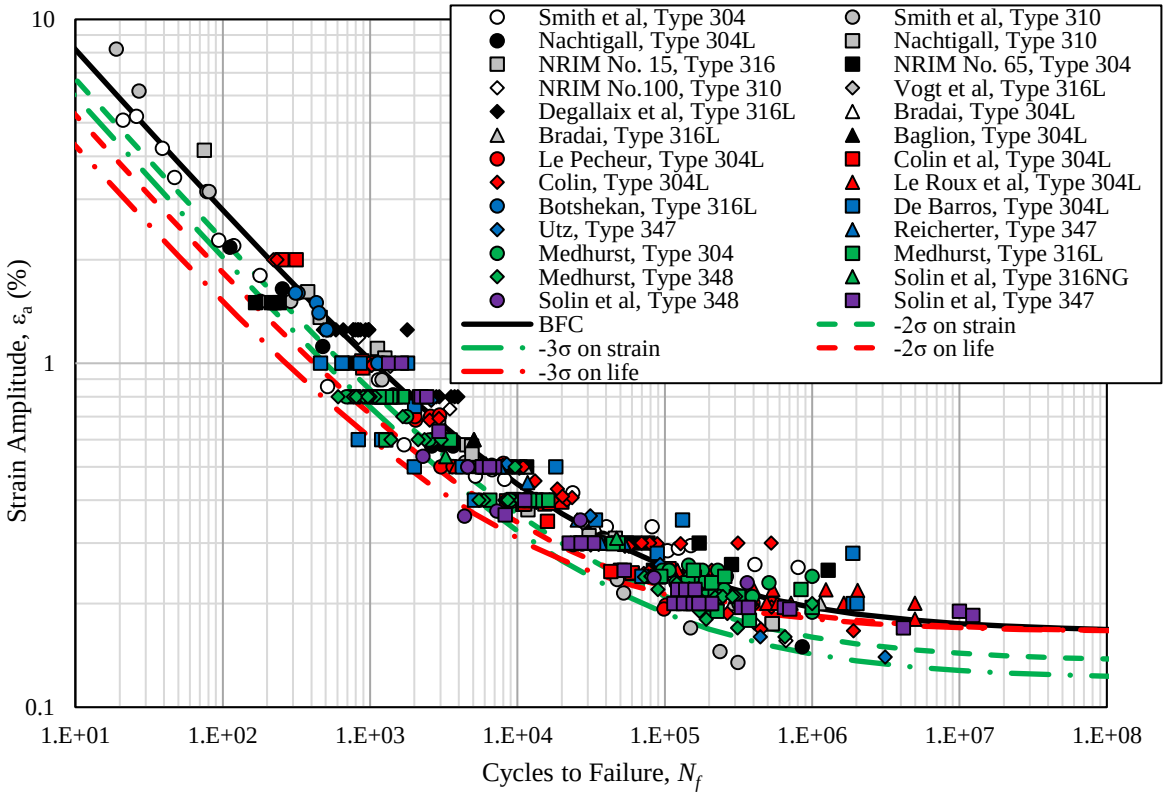

Figure 4. Room temperature strain-life data and Langer best fit curve (BFC) for austenitic stainless steels.

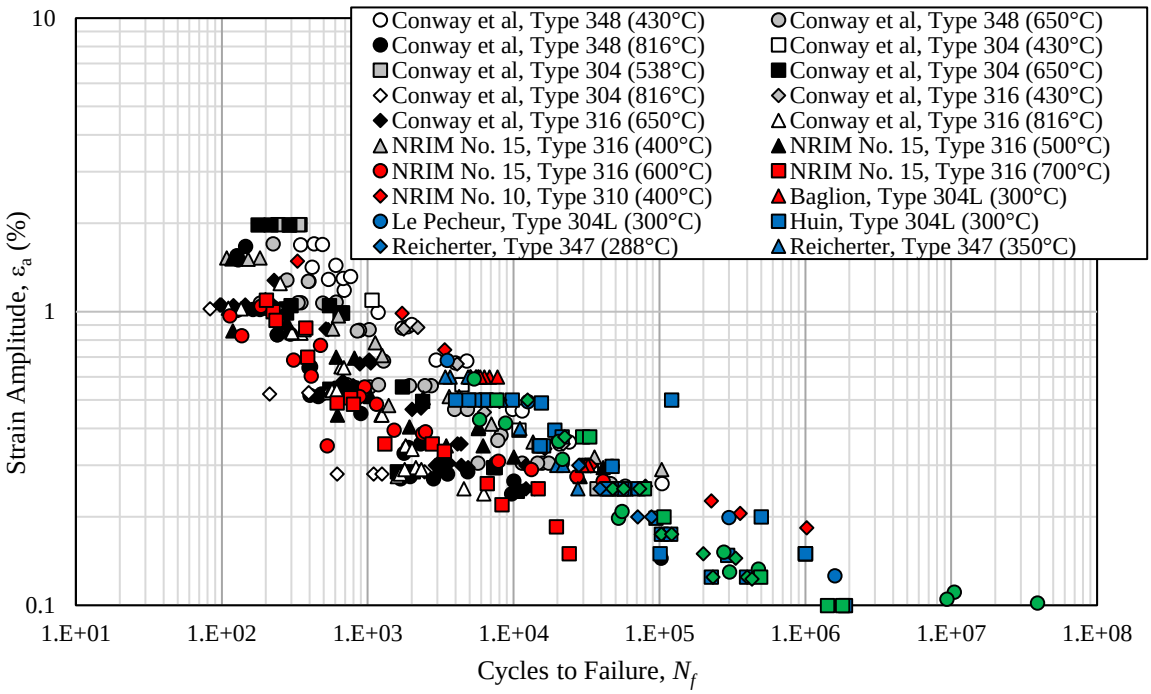

Figure 5. Elevated temperature strain-life data for austenitic stainless steels.

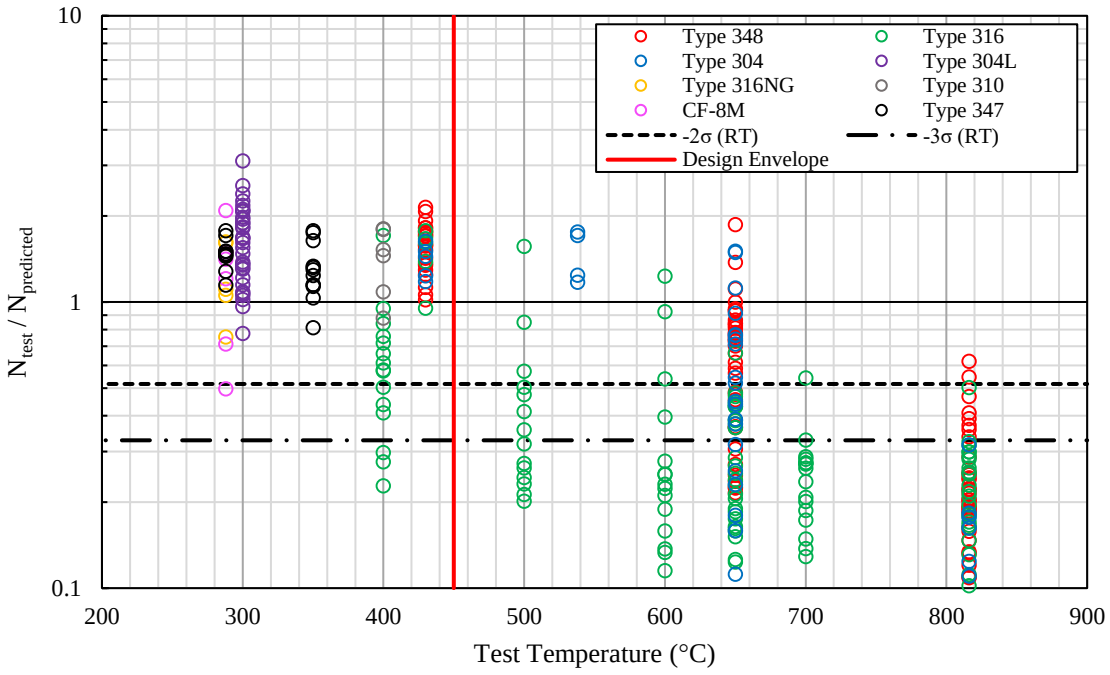

Figure 6. Predicted vs. actual fatigue life based on Generalised Langer Model (Eq. (6)) at elevated temperatures.

2.2.2. Cyclic Stress-Strain Behaviour

Many structural alloys exhibit uniaxial strain hardening behaviour, characterised by a gradual increase in strength caused by progressive plastic deformation. This behaviour is typically modelled using the mathematically simple three-parameter equation proposed by Ramberg and Osgood [44], termed the *Ramberg-Osgood* (R-O) relation (Eq. (8)). Similar to Coffin-Manson, it assumes that any given strain can be decomposed into its elastic and plastic parts, and that while elastic strains follow Hooke's law, the hardening induced by plastic straining is described by a power-law relationship.

$$\varepsilon = \varepsilon^e + \varepsilon^p = \frac{\sigma}{E} + \left(\frac{\sigma}{K}\right)^{\frac{1}{n}} \tag{8}$$

where E is the modulus of elasticity, K is the *hardening coefficient*, and n is the *hardening exponent*. The parameters of Eq. (8) may be obtained from fitting to data obtained from monotonic tensile tests, where K approximates the maximum true stress and n describes the rate of increase of stress with increasing plastic deformation.

The stress-strain behaviour of metals under cyclic loading is often very different to that observed from monotonic testing. This difference in behaviour was first described by Johann Bauschinger, who examined the yield behaviour of several steel bars under tension-compression loading [45]. Bauschinger found that the higher yield value occurred when the bar was unloaded and reloaded in the same direction, whilst the lower occurred when the bar was unloaded and reloaded in the opposite direction. The greater the plasticity in tension, the greater the subsequent reduction in compressive yield strength. This reduction in yield strength upon load reversal is commonly referred to as the *Bauschinger effect* and results in the formation of *hysteresis loops* upon repeated loading and unloading. Unlike their monotonic stress-strain behaviour, metals can be stable, soften, hardening, or exhibit a mixture of softening and hardening under strain-controlled cyclic tests, which presents as an initial monotonic-to-cyclic transient prior to achieving a stable condition. A cyclically stable condition characterised by a closed hysteresis loop (Figure 7) is often achieved quite rapidly, with the initial transient behaviour typically accounting for less than 10% of the fatigue life. The area within a closed hysteresis loop is equal to the energy dissipated during a

cycle. This energy represents the plastic work contributing to the fatigue damage on a microstructural level, and therefore closed hysteresis loops have an important physical meaning. The stress and strain range obtained from stabilised hysteresis loops are used to evaluate fatigue life.

Cyclic stress-strain curves (SSCs) are needed to characterise stress-strain behaviour under fatigue loading, and are usually obtained by joining the tips of several concentric stabilised hysteresis loops, obtained from fully reversed strain-controlled tests of identical specimens at different strain ranges. The monotonic R-O relation (Eq. (8)) may also be adapted to describe the stabilised cyclic stress-strain response via modification to incorporate stress and strain amplitudes:

$$\varepsilon_a = \varepsilon_a^e + \varepsilon_a^p = \frac{\sigma_a}{E} + \left(\frac{\sigma_a}{K^c}\right)^{\frac{1}{n^c}} \tag{9}$$

where K^c is the *cyclic hardening coefficient* and n^c is the *cyclic hardening exponent*. As strain hardening is a plastic process, E remains unaltered. Moreover, Eq. (9) assumes a symmetric cyclic stress-strain response such that the behaviour in tension is the same as that in compression. In other words, the tensile branches of the hysteresis loops corresponding to different strain ranges are found to coincide when their compressive loop tips are superimposed at a common origin. This was behaviour was first described by George Masing and has since been formalised by Eq. (10), sometimes referred to as *Masing's relation*

$$\Delta\varepsilon = \Delta\varepsilon^e + \Delta\varepsilon^p = \frac{\Delta\sigma}{E} + 2 \cdot \left(\frac{\Delta\sigma}{2K^c}\right)^{\frac{1}{n^c}} \tag{10}$$

where $\Delta\sigma$ and $\Delta\varepsilon$ are the stress and total strain range between the hysteresis loop tips.

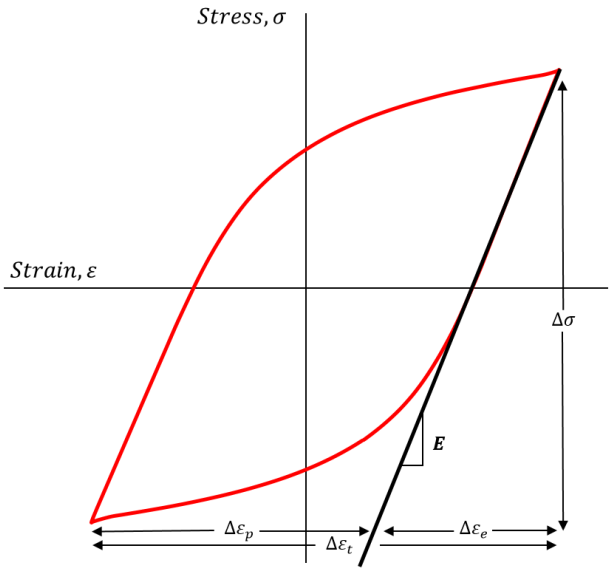

Figure 7. Idealised stress-strain hysteresis loop.

The cyclic stress-strain parameters can often be very different from their monotonic counterparts. This is especially true of austenitic stainless steels, which can cyclically harden such that their yield strength after cyclic stabilisation, termed the *cyclic yield strength*, σ_y^c, can be 150 to 200 percent higher than their *monotonic yield strength*, σ_y. The cyclic yield strength, σ_y^c, is typically defined as the stress amplitude corresponding to a small amount, or 'offset', of plastic strain amplitude, ε_{os}^p. Typically, σ_y^c is defined at 0.2% strain offset, as this can be reliably distinguished in tests.

$$\sigma_y^c = K^c\left(\varepsilon_{os}^p\right)^{n^c} \tag{11}$$

A sample of cyclic strength parameters for room and elevated temperatures of common SS grades compiled from studies published in [13], [20], [25]–[27], [29], [37] is provided in Table 1. n^c determines the cyclic hardening rate, which is generally between two and ten times the monotonic value. n^c can vary from grade-to-grade, and has been found to have a coefficient of variation (COV) of approximately 0.364 at room temperature. K^c on the other hand is related to σ_y^c, which can exhibit greater grade-to-grade variation with a COV of 0.527 at room temperature. The variation of σ_y^c, K^c, and n^c with temperature is shown in Figure 8 and Figure 9. The effect of temperature on cyclic stress-strain behaviour has been found to be relatively small within the range of 21°C and 430°C. Only σ_y^c and K^c experience a modest reduction in this range, whilst n^c remains largely unaffected. Elevated temperatures beyond this

range show a decreasing trend in n^c, thereby further reducing hardening capacity. Cyclic hardening behaviour is also affected by the initial process condition of the material. Medhurst [20] studied the cyclic stress-strain behaviour of Type 304, 316L and 316Ti SS specimens subjected to varying degrees of cold work. Pre-straining was found to increase σ_y^c, but also reduced K^c and n^c compared to virgin material, thereby resulting in a much flatter cyclic SSC.

Concerning LWR plant applications, the following observations are relevant. First, the cyclic hardening capacity appears to suffer only a modest deterioration in the LWR environment (288-325°C) compared to room temperature. In particular, the hardening rate, n^c, is similar to room temperature, whilst K^c is only slightly reduced. Secondly, it is also noteworthy that the initial state of LWR components may dictate their subsequent hardening response under service loading.

Table 1. Sample of cyclic strength parameters for common austenitic stainless steel grades by temperature and material condition.

Alloy Designation	**Temp. (°C)**	**Condition**	**σ_y/σ_y^c**	**K/K^c**	**n/n^c**
SUS 304-HP	23	HR Plate	242/275	484/2872	0.113/0.378
SUS 304-HP	400	HR Plate	156/224	378/2917	0.144/0.413
SUS 304-HP	500	HR Plate	162/254	351/1684	0.124/0.304
SUS 304-HP	600	HR Plate	146/219	336/1162	0.136/0.268
SUS 304-HP	700	HR Plate	146/221	336/996	0.136/0.242
AISI 316L	23	Ann. Plate	273/246	456/1977	0.078/0.335
AISI 316L	23	Ann. Plate	375/298	542/1598	0.059/0.270
AISI 316L	23	Ann. Plate	294/229	438/2827	0.069/0.404
AISI 316L	23	Ann. Plate	400/306	541/1566	0.054/0.263
AISI 316L	23	Ann. Plate	306/260	592/1946	0.109/0.324
AISI 316L	23	Ann. Plate	404/321	670/1746	0.08/0.273
AISI 316L	600	Ann. Plate	156/343	426/1228	0.159/0.205
AISI 316L	600	Ann. Plate	183/315	355/1155	0.109/0.209
AISI 316L	600	Ann. Plate	242/285	415/3302	0.092/0.394
AISI 316L	600	Ann. Plate	306/270	511/5223	0.086/0.477

AISI 304	23	HR & Ann.	745/777	1114/2177	0.063/0.166
AISI 304 ELC	23	HR & Ann.	255/515	578/4118	0.153/0.335
AISI 348	430	HR & Ann. Rod	193/184	-/1698	-/0.327
AISI 348	650	HR & Ann. Rod	152/198	-/716	-/0.185
AISI 348	816	HR & Ann. Rod	114/144	-/336	-/0.125
AISI 304	430	HR & Ann. Rod	172/155	-/3079	-/0.441
AISI 304	650	HR & Ann. Rod	145/166	-/682	-/0.206
AISI 304	816	HR & Ann. Rod	114/125	-/190	-/0.061
AISI 316	430	HR & Ann. Rod	138/204	-/1515	-/0.285
AISI 316	650	HR & Ann. Rod	117/226	-/771	-/0.171
AISI 316	816	HR & Ann. Rod	117/154	-/251	-/0.069
AISI 316	21	HR Plate	257/321	-/2002	-/0.294
AISI 316	400	HR Plate	184/325	-/2207	-/0.308
AISI 316	500	HR Plate	178/393	-/1223	-/0.183
AISI 316	600	HR Plate	164/313	-/986	-/0.185
AISI 316	700	HR Plate	155/193	-/535	-/0.164
AISI 310	21	HR Plate	252/315	-/1278	-/0.226
AISI 310	400	HR Plate	172/296	-/800	-/0.160
AISI 310	600	HR Plate	151/275	-/1392	-/0.261
AISI 310	700	HR Plate	137/203	-/904	-/0.240
AISI 310	800	HR Plate	112/146	-/413	-/0.168
AISI 304	20	Ann. Plate	327/310	-/1564	-/0.260
AISI 304	20	Ann. +5% PS	327/384	-/1307	-/0.197
AISI 304	20	Ann. +10% PS	327/439	-/1264	-/0.170
AISI 304	20	Ann. +15% PS	327/483	-/1262	-/0.155
AISI 316L	20	Ann. Plate	323/343	-/1197	-/0.201

AISI 316L	20	Ann. +5% PS	323/402	-/943	-/0.137
AISI 316L	20	Ann. +10% PS	323/433	-/873	-/0.113
AISI 316L	20	Ann. +15% PS	323/488	-/879	-/0.095
AISI 316Ti	20	Ann. Plate	315/395	-/1011	-/0.151
AISI 316Ti	20	Ann. +5% PS	315/428	-/779	-/0.096
AISI 316Ti	20	Ann. +10% PS	315/453	-/951	-/0.119
AISI 316Ti	20	Ann. +15% PS	315/512	-/874	-/0.086

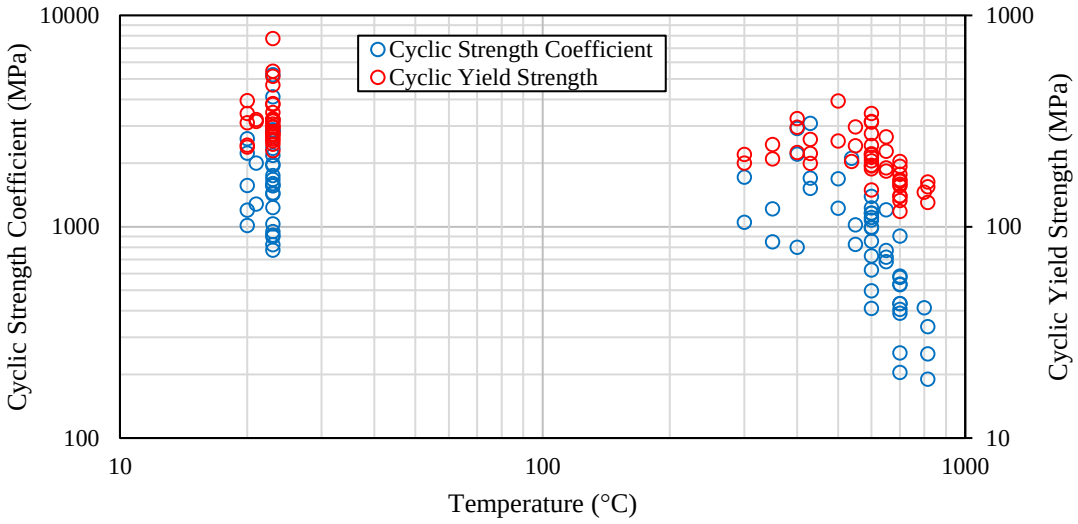

Figure 8. Variation of K^c and $\sigma_y{}^c$ with temperature for austenitic stainless steels.

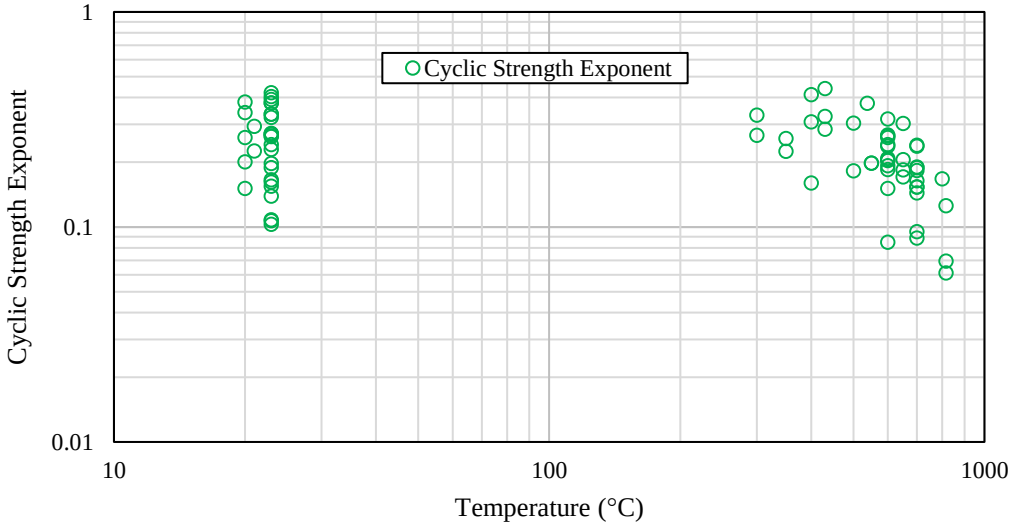

Figure 9. Variation of n^c with temperature for austenitic stainless steels.

2.2.3. Mean Stress Effects

Fatigue crack initiation is dependent on two driving forces. The primary driving force is the applied strain range, which contributes to the cyclic plasticity-induced damage at the microscopic scale. A secondary driving force also exists which is known to affect the rate of short crack growth and is dependent on the maximum stress attained in a cycle, σ_{max}. A number of models have been proposed which aim to quantify the influence of σ_{max} implicitly by considering the mean stress, σ_m. Several stress-based models have been proposed to account for the effects of mean stress, including those of Gerber [46] (Eq. (12)), Soderberg [47] (Eq. (13)), Modified Goodman [48] (Eq. (14)), Morrow [49] (Eq. (15)), Peterson [50] (Eq. (16)), Wellinger-Dietmann [51] (Eq. (17)), and Smith-Watson-Topper (SWT) [52] (Eq. (18)):

$$\sigma_{a,eq} = \frac{\sigma_a}{1 - \left[\frac{\sigma_m}{\sigma_u}\right]^2} \tag{12}$$

$$\sigma_{a,eq} = \frac{\sigma_a \sigma_y}{\sigma_y - \sigma_m} \tag{13}$$

$$\sigma_{a,eq} = \frac{\sigma_a \sigma_u}{\sigma_u - \sigma_m} \tag{14}$$

$$\sigma_{a,eq} = \frac{\sigma_a}{1 - \frac{\sigma_m}{\sigma_f}} \tag{15}$$

$$\sigma_{a,eq} = \frac{7\sigma_a}{8 - \left[1 + \frac{\sigma_m}{\sigma_u}\right]^3} \tag{16}$$

$$\sigma_{a,eq} = \sigma_a \cdot \sqrt{1 - \frac{\sigma_m}{\sigma_u}} \tag{17}$$

$$\sigma_{a,eq} = \sqrt{\sigma_a \sigma_{max}} \quad (18)$$

where $\sigma_{a,eq}$ is the 'equivalent' stress amplitude, σ_a is the stress amplitude, σ_m is the mean stress, σ_y is the yield strength, σ_u is the ultimate tensile strength, and σ_f is the true fracture stress. The concept of these mean stress correction methods is based on the premise that any arbitrary non-reversing cycle characterised by σ_a and σ_m can be transformed into an equivalent fully-reversed cycle characterised by $\sigma_{a,eq}$ only, and whose effect on fatigue damage is equivalent. The calculation of $\sigma_{a,eq}$ can be illustrated using the *Goodman-Haigh diagram* (Figure 10) [48]. The Goodman-Haigh diagram shows the effect of mean stress on the alternating stress required to produce failure. At zero mean stress (R=-1), the required amplitude is $\sigma_a=\sigma_e$, where σ_e is the endurance limit of the material. As the mean stress becomes increasingly tensile, the required alternating stress decreases. $\sigma_{a,eq}$ calculated according to the Goodman and Soderberg approaches decrease linearly, $\sigma_{a,eq}$ by the Gerber, Peterson and Wellinger-Dietmann approaches decrease convexly, whilst σ_{eq} by the SWT approach decreases concavely. It can be seen that both the Goodman and SWT approaches are essentially equal for small mean stresses, but the SWT diverges as the mean stresses exceed one-half yield.

Under the assumption of elastic perfectly-plastic (EPP) material behaviour, if the mean stress increases beyond yield, local redistribution and relaxation is expected to occur and the mean stress would again revert to within the *yield line*. If mean stresses arise due to a dead load, it is possible for mean stresses to be fixed greater than yield, however this would be expected to cause plastic collapse and therefore fatigue would be no longer relevant. In this case, σ_y is the highest value that σ_m can attain which would be expected to affect fatigue life. However, since austenitic stainless steels can exhibit significant cyclic hardening, the use of the monotonic yield strength, σ_y, is potentially non-conservative and therefore inappropriate. Instead, it is the cyclic yield strength, σ_y^c, that is of greatest relevance. Since the fatigue endurance limit of austenitic stainless steels is generally less than the cyclic yield strength, this enables retention of mean stresses under cyclic straining in the high-cycle regime, which can reduce the fatigue life. Therefore, these corrections rely crucially on knowledge of σ_y^c to be applied effectively for alloys that exhibit cyclic hardening. Fortunately, a linear relationship has also been found to exist between the ultimate tensile strength and

cyclic yield strength for austenitic stainless steels (Figure 11). This relationship holds at both room and elevated temperatures, and applies to steels in both the annealed and hot-rolled conditions with σ_u not exceeding 800 MPa. Thus, considering the maximum correction for mean stress effects at $\sigma_m=\sigma_y^c$, the order of conservatism of the approaches is Soderberg < Goodman < SWT < Peterson < Wellinger-Dietmann ≈ Gerber.

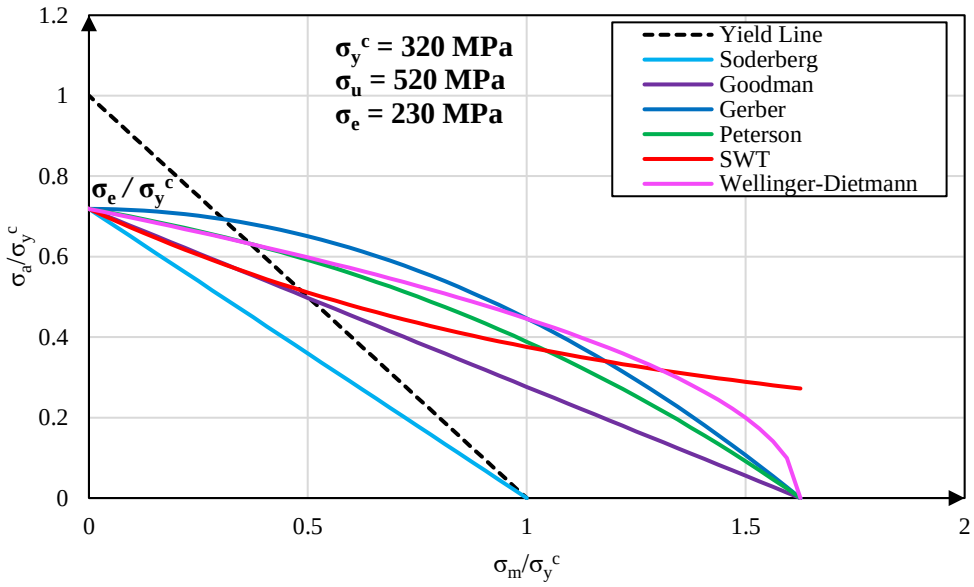

Figure 10. Goodman-Haigh diagram illustrating concept of mean stress correction.

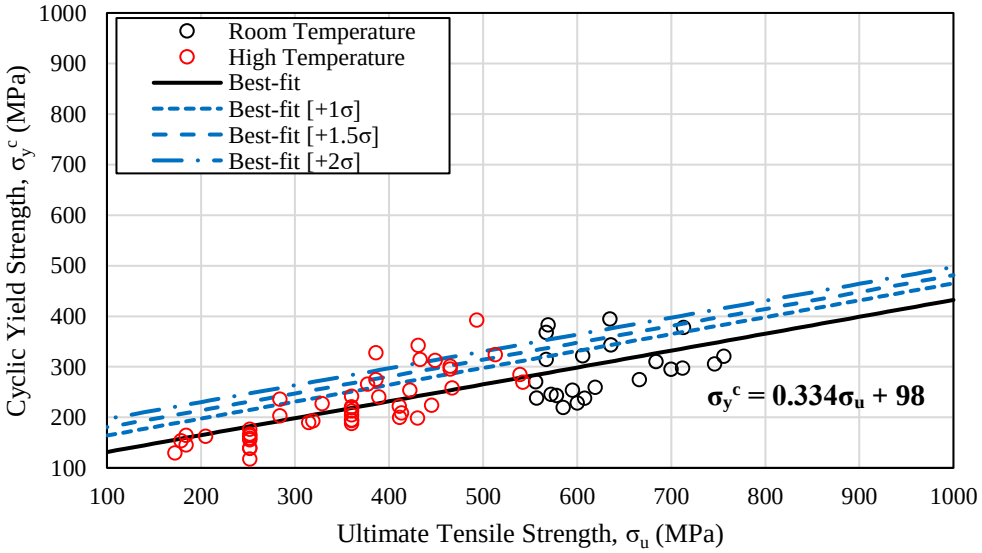

Figure 11. Relation between cyclic yield strength and ultimate tensile strength for austenitic stainless steels.

Mean stress corrections have traditionally been developed based on force-controlled tests, where stress is the controlled variable. A number of these classical models, namely Morrow Elastic (Eq. (19)) Manson-Halford (Eq. (20)) and SWT (Eq. (21)), have since been adapted for use in the strain-life framework by modification of the classical Coffin-Manson relation:

$$\varepsilon_a = \frac{\sigma_f' - \sigma_m}{E}\left(2N_f\right)^b + \varepsilon_f'\left(2N_f\right)^c \tag{19}$$

$$\varepsilon_a = \frac{\sigma_f' - \sigma_m}{E}\left(2N_f\right)^b + \varepsilon_f'\left(\frac{\sigma_f' - \sigma_m}{\sigma_f'}\right)^{c/b}\left(2N_f\right)^c \tag{20}$$

$$\sigma_{max}\varepsilon_a = \frac{\left(\sigma_f'\right)^2}{E}\left(2N_f\right)^{2b} + \sigma_f'\varepsilon_f'\left(2N_f\right)^{b+c} \tag{21}$$

where σ_f', ε_f', b, and c are the Coffin-Manson parameters determined from fully reversed ($\sigma_m = 0$) strain cycling tests. The Morrow Elastic model corrects only the elastic portion of the strain amplitude, which knocks down the Coffin-Manson curve in the high-cycle regime for increasing σ_m. The Manson-Halford model corrects both the elastic and plastic portions of the strain amplitude, though this is likely to be over conservative due to the aforementioned mean stress relaxation effect in cases where $\varepsilon_e^p >> \varepsilon_e^e$. SWT is the only model that is formulated explicitly in terms of the two fatigue-driving forces, ε_a and σ_{max}, and produces a Coffin-Manson type curve relating $\sigma_{max}\varepsilon_a$ to $2N_f$ at any level of mean stress.

Very few studies have examined experimentally the effect of mean stresses on the fatigue behaviour of austenitic stainless steels. Wire et al [53] developed a statistical model to model the effect of mean stress on fatigue life of Type 304 SS at room temperature and 288°C. The model predicted a reduction of 12% in fatigue strength at 10^6 cycles for an applied mean stress of 138 MPa. It was found that large mean stresses could be sustained to half-life in strain-controlled tests when the plastic strains accounted for less than 20% of the total strain. Soo and Chow [54] reported a reduction in fatigue strength of Type 304 SS by 5% at $3\text{x}10^5$ cycles in the case of σ_m = 45 MPa.

Majoine and Tome [55] found that application of a mean stress equal to the alternating stress resulted in a 6% reduction in fatigue strength of Type 347 SS at 10^8 cycles and 316°C. Asada et al [56] investigated the accuracy of mean stress correction approaches using test data from Wire et al [53] and Miura et al [35]. Considering strain-controlled fatigue data for Types 304 and 316NG SS, it was found that the fatigue strength with mean strain was almost the same as that with no mean stress and therefore the difference between the correction methods was not relevant. For the stress-controlled data, the Goodman correction was found to be over-conservative, whilst the SWT and Peterson approaches gave better estimates. This is in general agreement with the consensus amongst other practitioners that the SWT approach correlates most closely with test data for a wide range of steel types. Overall, the effect of mean stresses on the fatigue strength of austenitic stainless steels is concluded to be very modest, and limited only to the very high-cycle regime of 10^6-10^8 cycles.

Several notable interpretations aim to describe the effect of σ_{max} or σ_m at a mechanistic level. One of the most convincing is that proposed by DuQuesnay et al [57], which describes the effect of σ_{max} by dividing the crack initiation phase into two stages. Prior to the initial formation of micro cracks, ductile metals are insensitive to hydrostatic stress, and therefore crack nucleation is solely dependent on ε_a, which promotes dislocation motion. Though it is hypothesised that higher values of σ_m can enhance the growth rate of the dominant micro crack by propping open the crack faces, thereby reducing friction. Examining the growth of micro cracks in uniaxial strain-controlled specimens, DuQuesnay et al found that the cracks remained closed for part of the loading cycle, but the portion of the cycle for which the cracks remained open is greater at higher σ_m. This can also be interpreted in the strain-life framework under the assumption that fatigue damage arises only when the crack is completely open under tension. Under this assumption, damage only occurs in the portion of the hysteresis loop for which the stress exceeds the minimum crack-opening stress (Figure 12):

$$\varepsilon_{a,eff} = \varepsilon_a - \varepsilon_{a,op} \tag{22}$$

where $\varepsilon_{a,eff}$ is the effective strain amplitude which contributes to damage, ε_a is the applied strain amplitude, and $\varepsilon_{a,op}$ is the strain amplitude required to completely open

the crack faces. In most situations, it can be reasonably assumed that $\varepsilon_{a,op}$ is nominally elastic, and may be expressed by

$$\varepsilon_{a,op} = \varepsilon_a - \varepsilon_{a,eff} = \frac{[\sigma_{a,op} - \sigma_{min}]}{E} \tag{23}$$

The crack-opening stress, $\sigma_{a,op}$, which depends on σ_m and controls the effective strain amplitude, $\varepsilon_{a,eff}$, therefore provides a reasonable physical explanation for why mean stresses promote fatigue crack initiation.

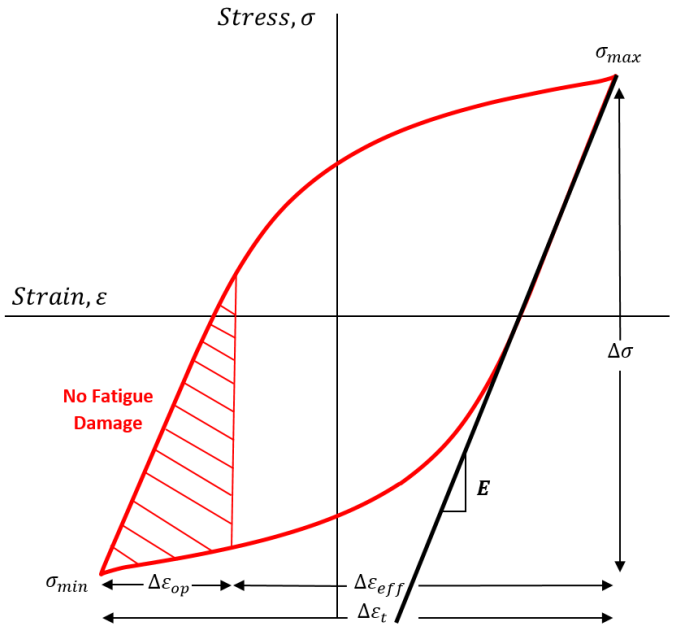

Figure 12. Effective strain range of the hysteresis loop.

2.2.4. Cumulative Damage Under Service Loads

The foregoing models were originally developed based on testing conducted under constant amplitude. In practice however, fatigue is rarely induced by constant amplitude loads, but rather complex variable amplitude service loads, which can often exhibit a high degree of randomness. To assess more realistic variable amplitude loading, the concept of *cumulative damage* has been widely adopted. In this approach, the damage induced by an arbitrary variable amplitude loading history may be reduced to the sum of the individual damages induced by its constituent loading events. This form of relationship was first described by Palmgren in his early investigations into the life prediction of roller bearings [58], which commonly operate under combinations of variable loading and speed. Palmgren stated that:

"…The assumption might be conceivable that for a bearing which has a life of n million revolutions under constant load at a certain rpm (speed), a portion m/n of its durability will have been consumed. If a bearing is exposed to a certain load for a run of m_1 million revolutions where it has a life of n_1 million revolutions, and to a different load for a run of m_2 million revolutions where it will reach a life of n_2 million revolutions, and so on, we will obtain

$$\frac{m_1}{n_1} + \frac{m_2}{n_2} + \frac{m_3}{n_3} + \cdots = 1 \tag{24}$$

Equation (24) was later proposed independently by Miner [59] at Douglas Aircraft, and is now commonly referred to as the *Palmgren-Miner Rule* or *Linear Damage Rule* (LDR). The rule states that the damage caused by many individual loadings are accumulated linearly, and crack initiation is conceded when the total damage is greater than or equal to unity. This is expressed more conveniently by Eq. (25).

$$D = \sum_{i=1}^{k} \frac{n_i}{N_i} \tag{25}$$

where D is the total accumulated damage, k is the total number of loading events, n_i is the number of constant amplitude cycles associated to the i^{th} load range, and N_i is the number of cycles predicted to cause failure under the i^{th} load range.

The LDR implicitly assumes that fatigue damage is independent of the order in which the loadings occur. For loading histories composed of identical loading events, but occurring in a different sequence, the LDR would predict the same damage. This is not true in practice, as load sequence effects been shown experimentally to influence crack initiation and growth [60]. However, oftentimes it is not possible to predict *a priori* the actual sequence in which service loads are likely to occur with a high degree of certainty. This is especially true for components of nuclear power plants, which generally do not have a fixed service cycle and can experience a range of operating transients, often in no particular order. Therefore, despite its shortcomings, the LDR is still widely favoured for its simplicity and practicality, and has seen almost universal adoption within industry codes and standards.

3. ASME Section III Fatigue Design

This section provides an overview of the ASME Section III fatigue assessment methodology, which is the focus of this thesis. First, it is necessary to briefly review its historical development, to provide context and clarify the intent of the original authors of the Code. The concept of *design-by-analysis* and basic ASME III definitions including service load and stress categories are then introduced. The Code requirements for assessing fatigue are reviewed, and the necessary FE stress analysis techniques are examined. The programming methods and engineering assumptions adopted for all elastic fatigue calculations performed in this thesis are also stated. The key limitations of the current Code fatigue rules are highlighted, with a particular emphasis on the treatment of cyclic plasticity effects in austenitic stainless steels. This serves as a starting point for this particular course of study, which aims to develop alternative approaches for predicting cyclic plastic strains with greater accuracy and practicality.

3.1. Historical Background

Prior to the Second World War, most pressure vessels were built to the requirements of either Section I or Section VIII of the ASME BPVC by selecting the appropriate wall thickness such that the maximum stress induced due to sustained internal pressure did not exceed five times the ultimate tensile strength of the material [61]. In other words, most vessels possessed a *design factor* on primary strength of at least five. The determination of such stresses was enabled by rules-based analytical formulae for simple geometries, with the design methodology retrospectively termed the 'Design by Rules' (DBR) approach. Exemptions to this requirement were permitted for some Boilers undergoing regular inspection, allowing for a reduction in the design factor to four. After the United States entered the Second World War, the conservation of raw material became a national priority. Based on the previously good experience with Boilers, the ASME Boiler and Pressure Vessel Committee published Code Case 979, which permitted a reduction in the design factor to four, provided additional requirements were met. These changes were later incorporated into the ASME BPVC following the war.

In the early 1950s, the development of more advanced fuel refining processes for the aerospace and automotive industries necessitated higher design pressures and consequently much thicker pressure vessels. At the time, the fabrication of such vessels to Section VIII requirements was challenging, often requiring manufacturers to invest considerable resource in larger forging presses and radiographic inspection equipment capable of detecting flaws in now much thicker heavy-section welds. This problem was also experienced by the nuclear industry, where design pressures for early nuclear pressure vessels were increasing in a similar fashion. In 1955, a special committee of the ASME BPVC, *Special Committee to Review Code Stress Basis*, was formed to explore the practicality of reducing the design factor further, with an aim to reduce material costs without compromising safety. The special committee decided first to explore requirements specifically for nuclear vessels as their service was limited to either water or steam, and therefore would be more straightforward to address. The subsequent work aimed at the development of a new nuclear code, with the goal of reducing the design factor to three, thereby reducing costs. The special committee evaluated and, where appropriate, modified existing Code criteria addressing design, material selection, fabrication, inspection, and testing requirements to maintain the same standard of safety as Section VIII despite the reduction in design factor. Following review and acceptance of the Special Committee's work, the *ASME BPVC, Section III, Nuclear Vessels*, was published in 1963 by the ASME BPV Committee. In addition, the report entitled *'Criteria of Section III of the ASME Boiler and Pressure Vessel Code for Nuclear Vessels'* [62] was also published and provides an explanation of the technical basis for the new nuclear vessel rules.

The new Section III Code rules were very different to the Section I and VIII rules which existed at the time. The most fundamental conceptual change was the introduction of a new design philosophy termed 'Design-by-Analysis' (DBA) as an alternative to DBR.

3.1.1. Design-By-Analysis

The key premise of DBA was to permit the use of modern stress analysis techniques (pre-dating FEA) to demonstrate acceptability against the major vessel failure modes including plastic collapse, ratchet, fatigue, buckling, etc. An important feature of DBA

is that it relied predominantly on the use of elastically calculated stresses, despite the Code design acceptance criteria being primarily related to elastic-plastic failure modes. Fundamentally, the objective of DBA is to demonstrate that the gross behaviour of a nuclear vessel or piping component should remain elastic under design basis loads. The Code authors recognised however that some allowance for high local stresses contributing to plastic deformation would not necessarily threaten the integrity of the gross structure. Previously, the DBR approach restricted such stresses in a conservative manner, with little allowance even for local yielding. In contrast, the intent in DBA is instead to determine and classify these local stresses into specific categories, each associated with a distinct mode of failure. In this way, more reasonable stress limits could be assigned to local stresses that was not previously possible in DBR.

Alternative provisions for performing plastic DBA were also included in the original 1963 publication of the Code, albeit with relatively scarce detail. At this time, FE stress analysis tools were not yet available to industry, thus plastic DBA saw very limited adoption. Consequently, the vast majority of DBA calculations were initially conducted based on simplified elastic shell discontinuity theory before being adapted for use with FE methods. Since the Code design criteria address plastic failure modes, the elastic DBA criteria are often considerably more conservative than plastic DBA. The intent of plastic DBA is therefore to provide the analyst with an alternative option of satisfying less restrictive rules at the expense of more time-consuming detailed analysis. Often this option is rarely exercised at the outset, but rather as a last resort if it is not possible to achieve design substantiation using elastic DBA. Today, the provisions for DBA are outlined in *Mandatory Appendix XIII – Design Based on Stress Analysis*.

3.1.2. Fatigue Design Basis

One of the most important additions to ASME Section III, compared to Sections I and VIII, was the inclusion of design rules intended to preclude fatigue as a possible mode of failure. The consideration of fatigue as a possible failure mechanism was intended to ensure equivalent reliability of vessel performance to Section VIII, in spite of the reduction in the design factor from four to three [63]. The original intent of the Section

III fatigue rules is that they would apply to new designs rather than for revaluating components already in service. In other words, the rules were intended to evaluate fatigue based on a set of loading events assumed in the design stage, as opposed to the actual operating conditions of the component, which would not be known to the designer *a priori*. These assumed loading events are often referred to as *design transients* and, discussed in 3.2.1, must be categorised according to their severity and expected frequency of occurrence.

The current ASME Section III procedure for fatigue evaluation outlined in ASME III Mandatory Appendix XIII-3520 derives its technical basis from the local strain-life (ε-N) framework discussed in 2.2.1, and was originally developed in the U.S. Naval Nuclear Program in the late 1950s and early 1960s by W.J O'Donnell, B.F. Langer, W.E. Cooper, and J. Farr. The initial proposals of rules to prevent low-cycle fatigue failure were published within the 1958 U.S. Navy report entitled *Tentative Structural Design Basis for Reactor Pressure Vessels and Directly Associated Components* [12], which is widely recognised as the precursor to ASME Section III. Prior to the publication of the 1963 edition of ASME Section III, a very important paper was published by Langer entitled *Design of Pressure Vessels for Low-Cycle Fatigue* [10] which explains comprehensively the background to the fatigue rules subsequently incorporated within ASME Section III.

Based on the earlier work by Coffin and Manson [7], [8], Langer recognised that the pressure vessel designer required a fatigue curve defined in terms of strain amplitude versus cycles to failure, but which contained sufficient design margin to provide confidence that the vessel would not suffer a fatigue failure within its intended design life. A *design fatigue curve* (DFC) could be defined to provide a safe allowable value of strain amplitude for a given number of operating cycles, or conversely, the permissible number of operating cycles for a given value of strain amplitude. Data obtained from small-scale polished specimens tested in air under strain-controlled conditions therefore required the use of *transferability factors* to translate the 'best-fit' or mean fatigue behaviour of the material to construct a DFC which could conservatively account for deleterious effects including data scatter, surface finish, mean stresses, etc., for application to plant components. These *transferability factors* are not *safety factors*, but rather are intended to account for variables which are known

to affect fatigue, but whose effect could not be established quantitatively using technology available at the time. Databases of strain-controlled test data were unfortunately very limited at the time, which precluded Langer from fitting best-fit relations (per Eq. (5)) for different material classes without excessive cost. Instead, the fatigue properties of different materials were approximated based on the following relationship originally proposed by Coffin [7]:

$$c = 2\sqrt{N_f}\varepsilon_a^p \tag{26}$$

where *c* is equal to one-half of the true fracture ductility, ε_f, obtained from a simple tensile test:

$$c = \frac{1}{2}\varepsilon_f = \frac{1}{2} ln \frac{100}{100 - RA} \tag{27}$$

where RA is the percentage reduction in area at fracture.

Substituting Eq. (26) and (27) into Eq. (5), provides the original best-fit fatigue relation underpinning the original ASME Section III Code:

$$\varepsilon_a = \frac{1}{4} ln \frac{100}{100 - RA} N^{-0.5} + \varepsilon_e \tag{28}$$

where ε_e is the endurance strain. Noting that due to Coffin's approximation, the parameter B in Eq. (5) is set fixed at -0.5. In the case of austenitic stainless steels, Langer examined the suitability of Eq. (28) for a range of tests published in studies by [64]–[67], totalling 146 experimental data points. The best-fit curve was obtained by performing linear regression of the logarithms of ε_a vs. N_f, where RA = 72.6% and ε_e = 0.167% were identified as the optimal parameters.

As the Code design allowable values are defined in terms of elastic stresses, in the interest of practicality it was necessary to convert the strain values used in the tests to stresses, which are routinely used in elastic DBA. A reference modulus of elasticity, E_c, was therefore adopted to facilitate the transformation of the test data and best-fit relation. In the original best-fit curve for austenitic stainless steels, E_c was defined as 179 GPa, which corresponds roughly to the value of E at 250°C. It is noteworthy that any value of E_c could have been chosen, so long as it was applied consistently. The original best-fit curve for austenitic stainless steels, defined in terms of stress

amplitude vs. cycles to failure, and obtained by transformation of Eq. (28) is defined as

$$S_a \text{ (MPa)} = \frac{E}{4\sqrt{N_f}} ln \frac{100}{100 - RA} + \sigma_e = 58{,}020 N_f^{-0.5} + 299.9 \qquad (29)$$

where S_a is the alternating stress amplitude, adopting the ASME Code nomenclature. Crucially, S_a is often termed a *pseudo-stress or fictitious stress amplitude* as it is not the actual applied stress in the tests, but is based on the assumption of elastic behaviour and therefore does not represent a real stress when it exceeds the yield strength of the material to which it applies. S_a is adopted for convenience as it has the advantage of being directly compatible to the allowable stresses defined in the Code.

The ASME III best-fit curve is applicable to fully reversed strain cycles, but does not account for the possible deleterious effects of mean stresses. As discussed in 2.2.3, mean stresses have little to no effect on fatigue life in the low-cycle regime. This is due to cyclic yielding which reduces the effective value of mean stress. One difficulty for the designer is determining accurately this effective value of mean stress, accounting for other potential influences, most importantly residual stresses induced by welding, proof tests, and overloads. Thus, Langer suggested in [10] that *"it would be much easier and not unduly conservative to adjust the fatigue curve downward in the high-cycle regime to allow for the maximum possible effect of mean stress"*. ASME III adopts the modified Goodman correction of Eq. (14), with the assumption that the mean stress is equal to the yield strength of the material. Concerning the appropriate value of yield, Langer also recognised that the highest stress amplitude sustainable by the material after initial cycling is the *"yield strength after strain hardening or strain softening"*, or cyclic yield strength, σ_y^c. The stress amplitude corresponding to the maximum possible mean stress correction is therefore equal to:

$$\begin{aligned} S_a' &= S_a \frac{\sigma_u - \sigma_y^c}{\sigma_u - S_a} \; for \; S_a < \sigma_y^c \\ &= S_a \; for \; S_a > \sigma_y^c \end{aligned} \qquad (30)$$

The important implication of this adjustment is that the fatigue designer need only consider the fluctuating part of the stress in an ASME III fatigue assessment, as the effects of tensile static stresses are effectively 'built-in' to the fatigue curve itself.

To construct the DFC, transferability factors of 2 on stress and 20 on life ('*2*&20') were applied separately to the best-fit curve to generate two adjusted fatigue curves. The more conservative of these two factors applied across the entire range of fatigue lives produces the unique DFC. In the low-cycle regime, the factor of 20 on life is dominant, whereas the factor of 2 on stress is dominant in the high-cycle regime. This modification is applied after adjusting for the maximum effect of mean stress. The design factors of 2&20 were based on engineering judgement that recognised unknowns in the service conditions of real components, and thus it was not expected that a vessel should actually operate for twenty times its intended design life. The intention of the DFCs are not to provide an accurate estimate of the actual number of cycles to produce a fatigue failure, but rather to provide a means of establishing acceptable designs. Some further insight into the original 2&20 design factors was provided by Bill Cooper [61], who stated that the factor of 20 on life arose from the product of three sub-factors; a factor of 2.0 to account for data scatter (min. to mean), 2.5 to account for size effects, and 4.0 to account for surface finish and atmosphere. The term 'atmosphere' was intended to reflect the conditions of an industrial environment in comparison with the controlled air environment typical of a laboratory, but was not intended to account for the effects of hot reactor coolant water. Figure 13 shows the Langer best-fit curve and the original 1963 ASME III DFC for austenitic stainless steels alongside the experimental data considered in [10]. The design factors of 2&20 were originally *'checked for appropriateness'* based on cyclic hydrostatic tests performed at the Southwest Research Institute in 1967 [68]. The tests considered 12- and 36-inch diameter vessels fabricated from carbon and low alloy steel. The alternating strain amplitudes from the tests were estimated from strain gauges based on the peak stress. The results of the tests indicated that no crack initiated at any pseudo-stress level below the number of cycles permitted by the DFCs, and through-wall crack penetration was not observed below three times the cycles permitted by the DFCs. A more thorough analysis of pressure vessel tests was presented by Spence and Carlson [69], which included additional test results from the UK, Germany, and Belgium and concluded that the Code DFCs for carbon and low alloy steels provided a lower bound to all the experimental results. It is important to note that room temperature water was used in the cyclic hydrostatic tests reported in [68], and

therefore the vessels are assumed to experience negligible environmental effects on fatigue crack initiation and growth. The tests reported in [69] also used water to pressurise the vessels, with most of the testing conducted between ambient temperature and 70°C. Hence, there is concern that the margin afforded by the Code DFCs under these test conditions is unquantified when extended to plant representative conditions. At the time, no equivalent testing was performed for austenitic materials to examine the appropriateness of the DFC for austenitic stainless steels.

Owing to a lack of data available at the time, the original DFC only extended to 10^6 cycles and therefore did not sufficiently cover the high-cycle regime. In 1977, Jaske and O'Donnell published a paper entitled *Fatigue Design Criteria for Pressure Vessel Alloys* [70] which added a considerable amount of new test data to Langer's original dataset, including new high temperature fatigue data up to 427°C for austenitic stainless steels totalling 246 additional data points, many of which extended into the high-cycle regime. The best-fit curve obtained by Jaske and O'Donnell is given by Eq. (31). Importantly, Jaske and O'Donnell instead adopted a room temperature value of E_c = 195 GPa to facilitate transformation of applied strain amplitude to pseudo-stress amplitude.

$$S_a\ (MPa) = 62{,}610 N_f^{-0.5} + 218 \tag{31}$$

Jaske and O'Donnell proposed a revised DFC applicable to austenitic stainless steels and some Inconels (alloys 600 and 800) which extended to 10^{11} cycles. The DFC recommended in [70] also adopted the maximum modified Goodman correction and design factors of 2&20. In performing the Goodman correction, a cyclic yield strength of 303 MPa was used for σ_y^c and an ultimate strength of 648 MPa was used for σ_u in Eq. (30). These values of σ_y^c and σ_u are based on room temperature data, thereby resulting in a more conservative correction. Whilst the BFC and DFC proposed by Jaske and O'Donnell was acknowledged at the time, it was not formally adopted within the Code. Instead, three separate DFCs for austenitic stainless steels and inconels up to 10^{11} cycles were incorporated into the ASME Section III 1983 Winter Addenda, and denoted separately as Curves A, B, and C. These curves were based on a paper by Manjoine and Tome [55], where Curve C included the maximum effect of mean stress and is essentially identical to the DFC proposed by Jaske and O'Donnell [70].

More recently in 2007, the publication of U.S. Nuclear Regulatory Commission (NRC) Contractor Report NUREG/CR-6909 [71] by the Argonne National Laboratory (ANL) presented an extensive study of fatigue data for austenitic stainless steels in both air and high temperature water environment. A large body of proprietary data was obtained from the U.S. Pressure Vessel Research Council (PVRC) database. NUREG/CR-6909 Revision 1 [72] also considered additional data from the extensive Japanese Nuclear Energy Safety Organisation (JNES) database, though the conclusions of the report remained largely unaltered. The ANL analysis of the austenitic stainless steel data in air also adopted the Langer equation, with the best-fit curve established Eq. (32) for temperatures up to 400°C.

$$S_a\ (MPa) = 70{,}590 N_f^{-0.521} + 218.4 \tag{32}$$

The ANL best-fit curve is somewhat similar to that derived by Jaske and O'Donnell [70], albeit deviating from the $\sqrt{N_f}$ dependence assumed in [10], [70]. The low-cycle fatigue test data used in developing the original ASME Section III fatigue design curve was found to be inconsistent with the much larger ε-N database examined by the ANL. Thus, NUREG/CR-6909 also proposed a revised DFC for austenitic stainless steels that was consistent with the existing database and derived from the ANL model (Eq. (32)). The original factor of 20 on life was determined to be conservative by at least a factor of 1.7 and thus to reduce this conservatism, a revised design factor on life was determined from Monte Carlo analysis. An average value of 9.6 was determined as the appropriate design factor on life that may be used to adjust the ANL model (Eq. (32)) to obtain a DFC for application to plant components. The DFC based on the ANL model was therefore constructed in a manner consistent with the original Code DFC by first correcting for the maximum effect of mean stresses based on the modified Goodman relation, and then adjusting downward the mean-stress-corrected curve by a factor of 2 on stress and 12 on cycles, whichever was most conservative. In performing the Goodman correction, the ANL adopted the same values of σ_y^c and σ_u as Jaske and O'Donnell [70]. The factor of 9.6 was rounded upwards to 12 to provide a little additional conservatism. The resulting DFC based on the ANL model for austenitic stainless steels was subsequently adopted into ASME Section III, Mandatory

Appendix I in 2010, and remains current today. The current Appendix I DFC for austenitic stainless steels is shown in Figure 14.

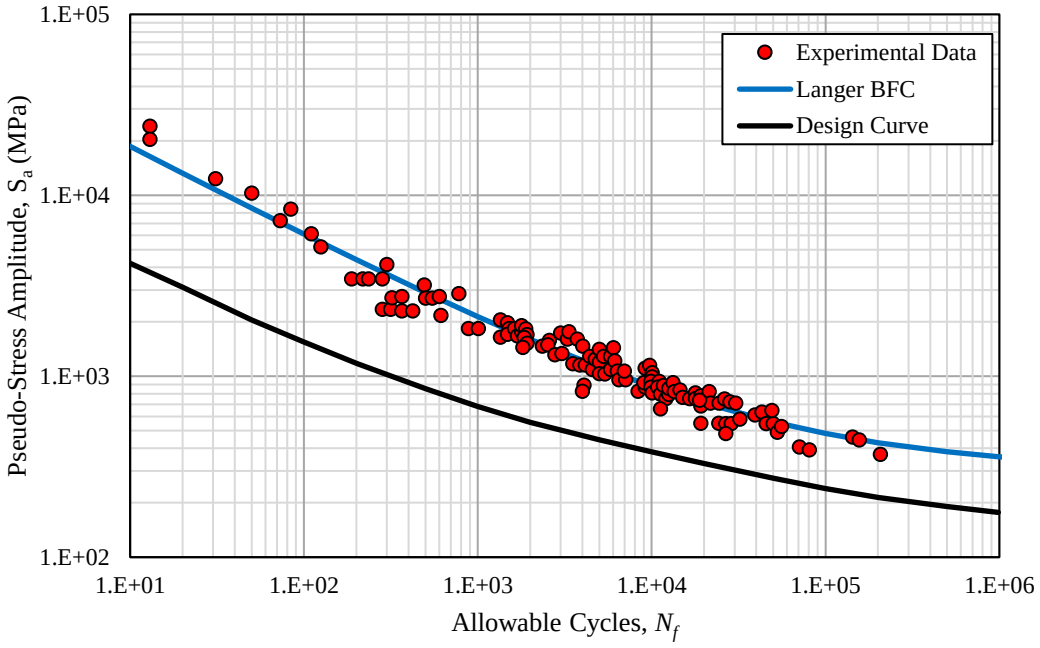

Figure 13. Original Langer BFC and ASME III DFC for austenitic stainless steels.

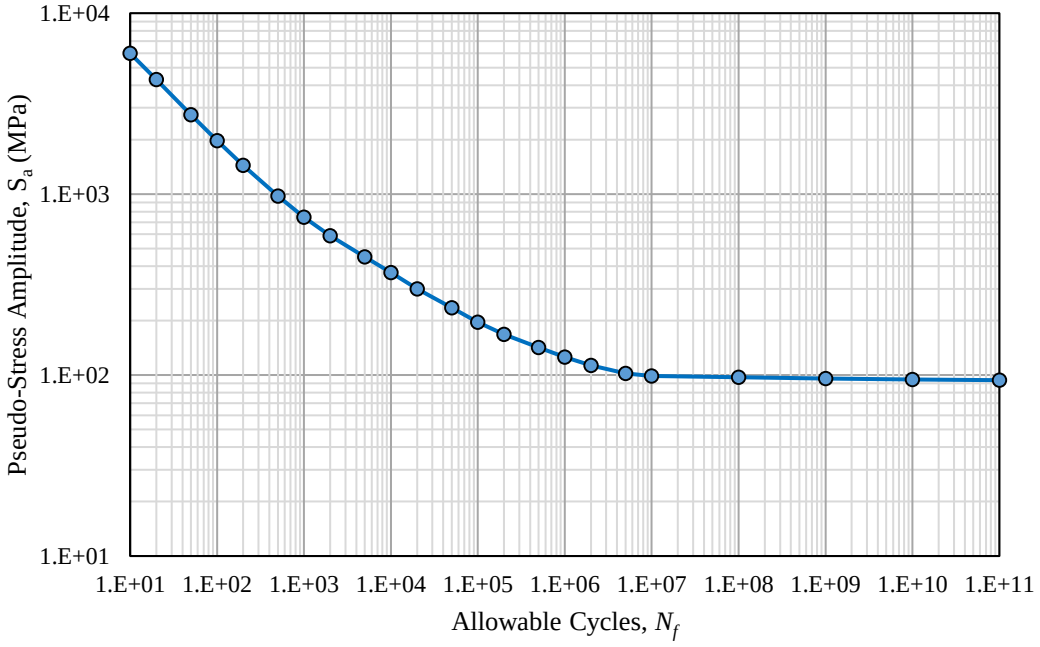

Figure 14. Current ASME III, Mandatory Appendix I DFC.

3.2. Design-By-Analysis Concepts

This section summarises the basic concepts adopted in the ASME III elastic DBA criteria of Mandatory Appendix XIII, namely the definitions of load and stress categories, both of which are crucial to an ASME III fatigue assessment.

3.2.1. Load Categories

As discussed in 3.1.2, the most crucial input to an ASME III fatigue assessment lies in the definition of the design transients assumed to contribute to fatigue damage throughout the intended life of a component. Whilst the assumed design transients can never be expected to represent the actual operational transients to which they relate with certainty, an expectation is that design assumptions should be conservative. Chapter 6, Page 25 (Section III, Subsection NB) of the companion guide to ASME BPVC states the following

"*A rigorous application of the fatigue evaluation was clearly not the intent of the Section III fatigue rules. The major conservatism is that actual plant operational transients have less severity and fewer cycles than design assumptions; therefore the Section III analysis procedures are conservative"*

Design transients are however not equal as far as the consequences of their occurrence to structural integrity are concerned. Accordingly, the Code provides guidance on assigning design transients to specific *load categories*. The applicable load categories are discussed in ASME III Non-Mandatory Appendix B, Subarticle B-2120, *Design*, and are divided into design and service loadings.

Design Loads: B-2122.3 (a) defines the design mechanical loads as equal to or greater than the most severe combination of sustained pressure, temperature, and mechanical loads arising coincidently within events classified as Service Level A.

Service Level A: Loads classified as Service Level A are associated with fluctuations in pressure and temperature that arise due to the regular variations in the power state of the plant. These include operations such as system startup, power transients, load following operations (where applicable), and system shutdown. Due to their regularity, Level A loadings are expected to occur with the highest frequency over the lifetime of the plant, and therefore are very important for fatigue.

Service Level B: Loads classified as Service Level B are those that deviate from the Level A criteria and are likely to occur at a reasonable frequency. Level B loads are associated with abnormal or *upset* plant operation and normally arise due to operator error or electrical malfunctions, but are not sufficient to result in plant outage. Although they have a lower frequency of occurrence, Level B loads are more severe than Level A, and therefore can also pose a significant risk to fatigue.

Service Level C: Service Level C loadings are those that deviate from normal operation with a low probability of occurrence and are sufficient to force a shutdown of the plant. Furthermore, this may necessitate removal of damaged components for inspection and repair. As Level C loadings are anticipated to occur at a low frequency, they are not considered detrimental to fatigue life.

Service Level D: Service Level D conditions are associated with combinations of loadings that are postulated to occur with an extremely low probability of occurrence, and whose consequences are so severe that they threaten the integrity and operability of the plant. These postulated loadings are sometimes termed a *Design Basis Event* (DBE). As with level C, level D transients are not relevant to fatigue.

Test Conditions: This category considers the pressure loading induced by hydrostatic, pneumatic, and leak tests (design pressure multiplied by 1.25). Other types of tests are considered as Service Level B.

An ASME III fatigue assessment must therefore consider all loading events that are classified as Level A or Level B. The Code however does not explicitly define these loadings, but rather it is the responsibility of the equipment owner to designate the appropriate design and service limits for each component within the *transient specification*. Appendix B-2123.1 states the following:

"For Class 1 components… Service Limits A and B are provided in order to evaluate the effect of system operating loads on the fatigue life of the component. For a fatigue analysis the loads applicable to a component should be described in terms of quantities that the designer may use…The variation with respect to time of pressure, temperature, flow rate, etc., as well as the number of times these changes occur in the life of the component, is needed."

It is also necessary to take into account pressure tests in some situations. Appendix XIII-3600 (e) states that:

"Tests, with the exception of the first 10 hydrostatic tests in accordance with NB-6220, the first 10 pneumatic tests in accordance with NB-6320, or any combination of 10 of such tests, shall be considered in the fatigue evaluation of the component."

For convenience, design transients are often further grouped according to their basic characteristics as they relate to the power state of the LWR plant. An example transient specification for a representative civil LWR plant, which provides base-load generating capacity, is shown in Table 2. As shown, a reasonably large number of transients can contribute to fatigue in base-load generating civil LWRs; this is even more significant for components of load-following civil LWRs, which can possess many additional Level A and B transients that are relevant to fatigue. The fatigue analysis of such components are apt to be one of the more time-consuming parts of the design and the required engineering effort to analyse every transient is often not warranted. Thus, a designer may opt to represent multiple lesser transients conservatively within a single *envelope transient* to reduce this work burden. On a per-cycle basis, Level B transients contribute the greatest fatigue damage as they are firmly in the low-cycle regime and induce more severe plastic deformations.

Table 2. Example ASME III Transient Specification (Level A + B)

Transient No.	**Transient Description**	**Number of Cycles**
ASME III Service Level A Transients		
Plant Warmup and Cooldown		
1	Full Plant Warm Up	800
2	Partial Plant Warm Up	800
3	Full Plant Cooldown	800
4	Partial Plant Cooldown	800
Power Transients		
5	Power Increase (5%/min)	850

6	Power Decrease (5%/min)	850
7	Load Regime Variations	25,000
8	Load Regulation	700,000
Steady State		
9	Refuelling	35
10	Reactor Coolant Sampling	3000
11	Chemistry Control	3000
ASME III Service Level B Transients		
12	Loss of Offsite Power	10
13	Turbine Trip	25
14	Reactor Trip (from standby)	20
15	Reactor Trip (from full power)	20
16	Control Rod Release	7
17	Loss of Primary Coolant Flow	5
18	Excessive Feedwater Flow	4
19	Inadvertant Depressurisation	2
20	Partial Loss of SG Feedwater	15

3.2.2. Stress Classification

The basic premise of stress classification is that stresses should be classified according to the consequences of their presence as they relate to relevant failure modes. ASME III, Mandatory Appendix XIII-2600 classifies stresses into three possible categories: primary stresses, secondary stresses, and peak stresses. To perform a fatigue assessment to ASME III, it is required that the stresses in a component be classified as primary or secondary, membrane or bending and peak under the loading conditions described in 3.2.1.

Primary stresses (P) are those direct or shear stresses arising from imposed loads that are necessary to satisfy equilibrium of internal and external forces and moments. The defining characteristic of primary stresses is that they are *unrelenting*, and do not exhibit post-yield redistribution or relaxation. Primary stresses have a large range of effect, acting to deform the entire structure. Consequently, if left unrestricted, primary stresses can lead to excessive plastic deformation in a single application of load. The primary stress is defined in terms of stress resultants and is equal to the algebraic sum of the membrane (P_m) and bending (P_b) components.

Secondary stresses (Q) are those direct or shear stresses arising from self-constraint of the structure and applied thermal loading. The key characteristic of secondary stresses is that they are strain-controlled, since the applied load is balanced by distortion rather than by equilibrium. Local yielding relieves these distortions, allowing the stress to redistribute. For this reason, secondary stresses are often termed *self-limiting*. Secondary stresses are also globally self-equilibrating, though not necessarily locally within a structure or component. Generally, secondary stresses are expected only to cause localised plastic deformations. Secondary stresses include thermal stresses arising from thermal gradients within the structure. One example is a temperature difference across the wall thickness of a vessel, which can induce large through-wall bending stresses. As with primary stresses, secondary stress is also defined in terms of membrane (Q_m) and bending (Q_b) stress resultants. Where these secondary stresses arise due purely to thermal effects, these resultant stresses are often referred simply as *thermal membrane* and *thermal bending* stresses.

Peak stresses (F) are those direct or shear stresses arising because of local discontinuities or local thermal stresses. The defining feature of peak stresses is that they do not contribute to noticeable distortion of the structure. Peak stresses are therefore only of concern with respect to their potential to initiate and propagate fatigue cracks.

To be able to consider the fatigue behaviour of a vessel component, it is important to distinguish between primary and secondary stresses. One means by which this can be achieved is to consider the effect of *elastic follow-up* of the structure in response to applied loading. Elastic follow-up is defined as a measure of the elastic response of a

structure arising due to changes in rigidity under plastic deformation. Many factors can affect the elastic follow-up of a structure, including the geometry, the distance over which a stress acts, and the nature of the stress. Primary stresses do not diminish regardless of the range over which the stress is applied and always serve to enhance local plastic deformations. Primary stresses are therefore considered to produce large elastic follow-up. On the other hand, for stresses acting over a small region, such as local thermal stresses, the effect of elastic follow-up will be small since such local stresses will maintain global equilibrium if removed, allowing for local redistribution and relaxation. Since primary stresses contribute to plastic collapse and secondary stresses do not, the concept of elastic follow-up provides an alternative means by which to define primary and secondary stresses. An example of such a situation is shown by Figure 15 for a hypothetical structure. If the elastic stress in the structure is at point A, in excess of the yield strength, then its true elastic-plastic state, of either B, C, or D, will be dependent on the level of elastic follow-up in the structure. Under pure load control, the stress will run parallel to the strain axis, resulting in infinite deformation with no stress redistribution (A to B). Under pure strain control, the stress can redistribute entirely with no additional increase in strain (A to C). However, in situations where loads are intermediate in character, the structure will deform more than the strain controlled case, but not as much as that observed in pure load control (A to D). The magnitude of elastic follow-up is defined numerically by the slope of the line A-D, often termed the *elastic follow-up factor*, q, and represents the factor by which the elastic follow-up strain, ε_{ep}, exceeds the reduction in elastic strain, ε_e. In this framework, primary stresses have an elastic follow-up factor of infinity, whilst pure secondary stresses have an elastic follow-up factor of unity.

$$q = \frac{\varepsilon_{ep} - \varepsilon_e}{\varepsilon_i - \varepsilon_e} \tag{33}$$

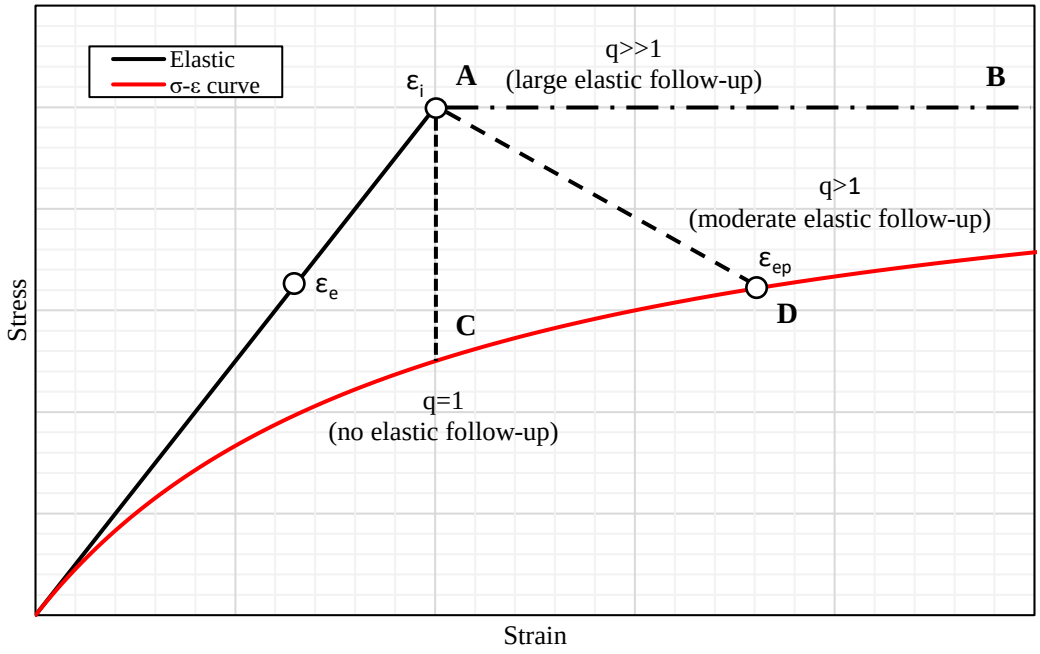

Figure 15. Graphical interpretation of elastic follow-up.

In reality, most secondary stresses in power plant components do not behave per the ideal case of pure strain control, but rather do exhibit some elastic follow-up albeit within a limited capacity. Thus, some stresses that are typically classed as secondary stresses, such as thermal or residual stresses, may exhibit some characteristics of a primary stress such that the secondary stress promotes enhancement of plastic strain following initial yielding.

3.2.3. Theory of Failure

Stresses in pressure vessels are generally multiaxial. Accordingly, the above stress categories of P_m, P_b, Q, and F do not represent single quantities but rather the six unique components, three direct and three shear, of the stress tensor. It is therefore necessary to calculate a single scalar value for comparison with the Code allowable limits. To achieve this ASME III relates the proximity to yielding in a large structure to the proximity to yielding in a simple tensile test by adopting a *strength theory*. In this way, a multiaxial state of stress may be reduced to an equivalent scalar value of stress occurring in a uniaxially stressed specimen. Thus, all references to stress limits within ASME III are actually defined in terms of *uniaxial equivalent stress*.

Prior to the publication of ASME III, Sections I and VIII of the ASME BPVC adopted the maximum principal stress theory of failure, sometimes termed *Rankine theory*. This theory states that yielding occurs when the algebraically largest principal stress exceeds the yield strength of the material, stated more formally by Eq. (34). This reduces simply to the sole component of stress acting in the longitudinal direction in a tensile specimen. In pressure vessels, this reduces to the hoop stress. However, experimental evidence available at the time demonstrated that whilst Rankine theory appeared to provide reasonable failure load estimates for brittle metals such as cast irons, it was not particularly accurate for ductile steels commonly used in pressure vessel fabrication.

$$\sigma_R = \max[\sigma_1, \sigma_2, \sigma_3] = \sigma_y \tag{34}$$

From its 1963 inception, ASME III has adopted the maximum shear stress theory of failure, also known as *Tresca theory*. The maximum shear stress at a point in a vessel is defined as one-half of the algebraic difference between the maximum and minimum of the three principal stresses. Considering the three principal stresses, σ_1, σ_2, σ_3 ordered such that $\sigma_1 > \sigma_2 > \sigma_3$, then the maximum shear stress is equal to ½ (σ_1-σ_3). Tresca theory states that yielding occurs in a structure when the maximum shear stress exceeds the maximum shear stress attained at the yield point in tensile test specimen. Since $\sigma_1 = \sigma_z$, σ_2, $\sigma_3 = 0$, this sets the maximum shear stress to one-half of the yield strength in a tensile specimen. Yielding is therefore conceded in a component when:

$$\frac{1}{2}[\sigma_1 - \sigma_3] = \frac{1}{2}\sigma_y \tag{35}$$

To avoid the unnecessary division by two, the Code authors defined a new quantity termed *'equivalent intensity of combined stress'* or *stress intensity* for short, which could be directly compared with the Code allowable stresses. The Tresca stress intensity, σ_I, is thus defined more formally in Eq. (36) as twice the maximum shear stress, and is equal to the maximum algebraic difference between any two of the three principal stresses, calculated on an elastic basis.

$$\sigma_I = \max[|\sigma_1 - \sigma_2|, |\sigma_2 - \sigma_3|, |\sigma_3 - \sigma_1|] \tag{36}$$

Even in 1963, it was well known that an alternative definition of stress intensity based on *maximum distortion energy theory*, also known as *von Mises theory*, provided superior estimates of yielding in ductile metals compared to Tresca.

$$\sigma_{VM} = \frac{1}{\sqrt{2}} \cdot \sqrt{(\sigma_1 - \sigma_2)^2 + (\sigma_2 - \sigma_3)^2 + (\sigma_3 - \sigma_1)^2} \quad (37)$$

However, the Code authors decided to adopt Tresca theory instead of von Mises. The reasoning for this is elaborated in the original Section III Code Criteria document [62]:

"Most experiments show that the distortion energy theory is even more accurate than the shear theory, but the shear theory was chosen because it is a little more conservative, it is easier to apply, and it offers some advantages in some applications of the fatigue analysis…"

Most engineers at the time did not possess even desktop calculators and so the reasoning for adopting Tresca is understandable from a practical perspective. The other major difference between Tresca and von Mises is that Tresca can be either positive or negative, whilst by definition von Mises is always positive. This makes Tresca more advantageous for fatigue analysis as it takes account of tensile or compressive principal stresses. If von Mises were to be adopted instead, it would be necessary to apply a sign to it. However, as will be shown later in this thesis, both Tresca and von Mises can be applied easily under the same framework using computational methods.

3.2.4. Allowable Stress

It was recognised that a variety of pressure vessel alloys exhibit varying levels of ductility and capacities for strain hardening such that the imposition of allowable limits on stress intensity relative to yield strength alone is not sufficient to account for all possible materials. Thus, in support of using both yield and ultimate tensile strength to establish allowable stresses, Page 9 of the ASME Section III Code criteria [62] states the following:

"In order to prevent unsafe designs in materials with low ductility and in materials with high yield-to-tensile ratios, the Code has always considered both the yield strength and ultimate tensile strength in assigning allowable stresses"

The basic intent is to ensure safe design by restricting the allowable stresses based on the yield strength, whilst still accommodating those materials whose allowable stresses are required to be less than that based on yield strength. Thus, in accordance with ASME III, Appendix XIII-2200, the stress intensity limits are defined in terms of the design stress intensity, S_m, whose values are provided in tabular form within ASME Section II, Part D, Subpart 1, Tables 2A and 2B [73] for ferrous and non-ferrous materials, respectively. The technical bases for establishing design stress intensity values is provided in ASME II, Mandatory Appendix 2. For ferrous materials, S_m is equal to the lesser of one-third of the ultimate tensile strength at temperature, or two-thirds of the yield strength at temperature. A different criterion is specified for austenitic stainless steels owing to their higher strain hardening capacity and ability to resist ratcheting. Page 9 of the ASME Section III Code criteria [62] states that:

"These materials have no well-defined yield point but have strong strain-hardening capabilities so that their yield strength is effectively raised as they are loaded. This means that some permanent deformation during the first loading cycle may occur; however, the basic structural integrity is comparable to that obtained for ferritic materials"

The value of S_m for austenitic materials is dependent on temperature. At room temperature, S_m is equal to two-thirds of the specified minimum yield strength. At higher temperatures, S_m can increase to be as high as 90% of the yield strength at temperature, but never exceeds two-thirds of the room temperature yield strength.

Ferritic

$$S_m = \min \begin{cases} \frac{2}{3}\sigma_y(T) \\ \frac{1}{3}\sigma_u(T) \end{cases} \tag{38}$$

Austenitic

$$S_m = \min \begin{cases} \frac{2}{3}\sigma_y(RT) \\ 0.9\,\sigma_y(T) \end{cases} \quad (39)$$

3.2.5. Design Limits for Cyclic Loading

Under conditions of cyclic loading, ASME Section III recognises that both plastic ratcheting and fatigue pose a risk to the integrity of a vessel component. The repeated application of secondary stresses in the presence of sustained primary stresses may lead to failure by plastic ratcheting, whilst repeated application of cyclic primary, secondary, and peak stresses can promote fatigue failure. To address this, the Code provides stress limits, which, if satisfied, permit both possible modes of failure to be adequately assessed based on elastic stresses only. Crucially, ratchet and fatigue are both considered sequentially; the fatigue assessment by elastic DBA is considered valid only if the ratchet criteria are first satisfied.

3.2.5.1. The $3S_m$ Limit

ASME III, Appendix XIII-3420 imposes the limit that the allowable value of primary-plus-secondary stress intensity range, S_n, shall not exceed three times the design stress intensity, $3S_m$, for any combination of Level A and B service loadings. The $3S_m$ limit assumes no strain hardening.

$$S_n = \Delta(P + Q) \leq 3S_m \quad (40)$$

The above limit is very important in its relation to both ratchet and fatigue, and is referred to herein as the *$3S_m$ limit*. Page 6 of the Section III Code criteria [62] explains the intent of the $3S_m$ limit is to ensure that the range of stress experienced by a vessel component results in a purely elastic response:

"The primary-plus-secondary stress limits are intended to preclude excessive plastic deformation leading to incremental collapse, and to validate the application of elastic analysis when performing the fatigue evaluation"

The rationale behind this limit is two-fold, respectively in its relation to both ratchet and fatigue. Considering the former, so long as S_n remains within the elastic range at every time point and at every location, the vessel will eventually achieve a fully elastic

response after repeated loading has established a favourable pattern of residual stresses. This is known as *elastic shakedown*. The assumption of elastic behaviour is therefore justified since only elastic stresses persist in all load cycles subsequent to shakedown, despite some limited accumulation of plastic deformation in the initial load cycles. The value of S_n can therefore be compared with the $3S_m$ limit to determine the Reserve Factor (RF) on elastic shakedown, where RF > 1.0 satisfies the Appendix XIII-3420 criterion.

$$RF = 3S_m/S_n \tag{41}$$

In the case of fatigue, plastic deformation will generally occur throughout the design life of the vessel. The justification here is that repetitive plastic action generally arises only due to peak stresses acting at local regions, and whose behaviour is controlled by larger regions of the vessel that respond elastically. The most typical example is the peak stress arising at a notch root, where the local material at the notch is controlled by local strains rather than stresses. Whilst the elastic DBA approach necessarily involves the calculation of stresses rather than strains, these stresses actually remain proportional to the actual elastic-plastic strains experienced in reality, where the constant of proportionality is the modulus of elasticity. This recognition is crucially important, as it ensures the stress intensities determined from elastic DBA are directly compatible with the allowable alternating pseudo-stress values adopted by the Code DFCs. Additionally, as far as the Code is concerned, the assumption of elastic behaviour is taken to be applicable in the fatigue assessment if plasticity remains highly localised. The $3S_m$ limit can therefore also be interpreted as a criterion to establish the validity of the assumption of *small-scale yielding* conditions.

The Code does however permit the $3S_m$ limit to be exceeded (RF < 1.0) provided additional requirements for Simplified Elastic-Plastic Analysis outlined in Appendix XIII-3450 are met. These additional checks relate to Thermal Stress Ratchet (Appendix XIII-3430) and the Procedure for Fatigue Evaluation (Appendix XIII-3520). These requirements are discussed briefly next.

3.2.5.2. When $3S_m$ is Exceeded

The limit of $3S_m$ applied to S_n delineates the boundary between loads that when cycled, produce shakedown to elastic action and loads that produce plastic action with

successive load application. Failure to satisfy the $3S_m$ criterion of Eq. (40) generates the potential for two damaging conditions:

a) Progressive distortion (ratcheting) of the structure leading to collapse;
b) Non-conservatism in the elastic based fatigue calculations in that the assumption of small-scale yielding conditions is no longer applicable.

If S_n exceeds $3S_m$, ratcheting is presumed to occur. For hardening materials such as austenitic stainless steels, ratcheting will continue until shakedown occurs, but the amount of ratcheting is unknown and may render the component unserviceable. Appendix XIII-3430 details a simplified elastic procedure for determining whether ratcheting will occur for axisymmetric shell structures. The procedure is based on the theoretical analysis conducted by Miller [74], which considered the response of an open-ended cylinder subjected to a parabolic thermal gradient under the assumption of EPP material behaviour.

To address the possible non-conservatism described in b), a simplified elastic-plastic penalty factor, K_e, must also be used in the Appendix XIII-3520 fatigue assessment.

3.2.5.3. Cumulative Fatigue Usage

ASME III requires that the total stress range arising due to Level A and B transients must satisfy the following criteria,

$$\Delta(P + Q + F) \leq 2S_a \tag{42}$$

where S_a is the alternating stress corresponding to the allowable number of design cycles, N_d, permitted by the Appendix I DFCs. In situations where two or more stress cycles contribute to fatigue, ASME III Appendix XIII-3520 (e) adopts the Palmgren-Miner Rule described in 2.2.4, to determine their cumulative effect. The cumulative fatigue damage, termed the *cumulative usage factor* (CUF), U, for *k* stress cycles is defined by

$$\mathrm{U} = \sum_{i=1}^{k} U_i = \sum_{i}^{k} \frac{n_i}{N_{d,i}} \tag{43}$$

Where U_i is the *partial usage factor* (PUF) for n_i cycles at a stress amplitude $S_{a,i}$, and $N_{d,I}$ is the number of allowable cycles corresponding to $S_{a,i}$ permitted by the Appendix

I DFC. The design is considered acceptable if the cumulative usage factor is calculated to be less than or equal to unity.

$$U \leq 1.0 \tag{44}$$

The meaning of a cumulative usage factor of unity has been a subject of major contention within the ASME Code community, with some ASME experts believing it to correspond to crack initiation whilst others are adamant that it represents through-wall leakage. This is not helped by the fact that the ASME Section III Code criteria document does not explicitly state what is meant by a 'fatigue failure'. Some of this disagreement is attributed to the difference in the treatment of fatigue between Section III and Section XI [75], where the former relates to design and construction of new plants that are assumed defect free before being placed into service, whilst the latter relates only to in-service inspection and operation of existing plants. Section XI permits a fracture mechanics based approach for justification of flaws detected in-service, including fatigue cracks, for a period of continued operation before re-inspection. This has raised the question as to whether the use of a flaw tolerance approach, assuming a postulated flaw present at start of life, and demonstrating equivalent end-of-life margin against through-wall leakage comparable to Section XI requirements, should also be considered acceptable for Section III.

ASME Section III also recognises that experimental methods constitute a reliable means of evaluating the suitability of components for cyclic service. As an alternative to the Mandatory Appendix I DFCs, ASME III Appendix II-1520 permits the justification of components by large scale testing with failure defined per Appendix II-1520 (b) as *"propagation of a crack through the entire thickness, such as would produce a measurable leak in a pressure retaining member"*. The justifiable design life may then be determined as a fraction of the observed experimental life depending on the number of tests performed and the similarity of the test conditions to those expected in service. In accordance with Appendix XIII-1520 (f), the justified design life shall be less than or equal to the minimum experimental life to through-wall leakage divided by a factor of 2.6. The technical basis for the design factor of 2.6 on experimental life to leakage is not stated in the Code criteria document. It has however been tentatively suggested [76] that this factor was adopted as being roughly consistent

with the margin between the cycles permitted by the Code DFCs and minimum cycles needed to cause through-wall crack penetration in the vessel cyclic hydrostatic tests described in [68] (see Section 3.1.2). However, it is unlikely that a factor of 2.6 on life to through-wall leakage would preclude surface crack initiation, especially in the case of a steep strain gradient such as would be experienced at a notch or from thermal shock loading. Therefore, this strongly suggests that the intent of the ASME III fatigue design criteria is to preclude through-wall leakage and rather than crack initiation.

The U.S. Nuclear Regulatory Commission (NRC) have adopted a different stance, stating in NUREG/CR-6909 Rev. 1 [72] that design against a CUF of unity should provide reasonable assurance that fatigue crack initiation will not occur in a component with 95% confidence and 95% probability. This is based on the methodology adopted by the ANL to derive the Appendix I DFCs, which assumes that the formation of a 3mm-deep crack in the gage of small-scale cylindrical specimens based on the 25% load-drop criterion would equate to crack initiation in an actual component. However, it is not clearly stated whether crack initiation in a component is presumed to be of the same 3mm depth observed in a test specimen or different. This acceptance criterion based on crack initiation has been further endorsed in Regulatory Guideline 1.207 [77], though NRC staff do recognise the additional margin that may be present in actual components owing to their typically experiencing a significant through-wall strain gradient as opposed to the membrane loading applied in small-scale test specimens. Importantly, RG 1.207 states, *"Methods to account for this additional margin may be considered by staff on a case-by-case basis, provided sufficient basis and information is provided to the staff to verify that the proposed alternative demonstrates compliance with all applicable NRC regulations"*. This statement is significant as the NRC have recently accepted a Section III Code Case (Record 18-257 [78]) proposed by Steve Gosselin [79] which considers fatigue life and gradient factors to adjust downward the predicted CUF to account for the higher thickness and strain gradient effects associated with actual plant components. Record 18-257 has also received approval from the ASME Board on Nuclear Codes and Standards (BNCS). This represents the first step in the NRC shifting towards accepting that a CUF of unity may be associated with a crack depth greater than 3mm.

3.3. Procedure for Elastic Fatigue Analysis

The elastic DBA methodology defined in ASME III allows for linear superposition of stresses arising from various origins, such as those due to internal pressure, thermal gradients, and seismic effects. For simplicity, stresses in linear elastic fatigue analysis can generally be categorised into two types:

1. Stresses arising due to static loads, including internal pressure, piping moment/torsion, and seismic loads. These are sometimes termed *mechanical stresses*.

2. Stresses which arise due to a non-uniform distribution of temperature in the component. These are termed *thermal stresses*. The thermal stresses evolve based on variations in the axial and radial thermal gradients that exist in the component.

Generally, the contributions of both categories of stresses must be determined independently to enable the stresses to be appropriately classified as primary, secondary, or peak, as described in 3.2.2. This is typically achieved by undertaking separate thermal and structural Finite Element Analysis (FEA) of the different design transients experienced by the component in question. The independent contributions of time-varying mechanical and thermal stresses may then be superimposed to determine the total stresses for fatigue analysis. However, continuum FEA stresses are not directly compatible with the ASME III cyclic stress limits, which are defined in terms of stress resultants. The elastic FEA stresses must first be manipulated or 'post-processed' to obtain the necessary quantities required of the Code. This process is very important and can have a significant impact on the results of 'downstream' fatigue calculations. Following post-processing, a cycle counting method is implemented to identify stress cycles in the transient loading history to enable calculation of CUF.

To the author's knowledge, no commercially available software exists which can perform both the necessary FEA and Code fatigue calculations in a single operation. Thus, all Code fatigue calculations performed throughout this thesis are implemented as working Python routines. Python is a free, open-source programming language that is computationally efficient, highly readable, and widely adopted within the engineering profession [80]. Whilst no Python code is provided in this thesis, the adopted procedures are described in sufficient detail that anyone with programming

experience should be able to implement them without issue. Two add-in modules used throughout this thesis are *numpy* and *scipy* [81], which contain standard libraries of scientific computing algorithms and permit fatigue calculations to be performed with minimal coding effort. Additionally, one of the most popular commercial finite element packages, Abaqus [82], is fully scriptable using Python. This useful feature enables Python algorithms to be easily incorporated into Abaqus as plug-ins or software extensions. Thus, this establishes a direct link between Abaqus, which can be used to perform the FEA to obtain the necessary input data (stress, temperature, etc.) for each transient, and Python routines used to perform the Code fatigue calculations. Abaqus is therefore adopted as the FE software used in this thesis. The specifics of the necessary elastic fatigue calculations and important assumptions adopted throughout this thesis are discussed briefly in the sections that follow.

3.3.1. Consideration of Heat Transfer

In performing the thermal analysis of design transients, it is necessary to specify the thermal boundary conditions. The heat transfer via convection between a contacting fluid and the internal surface of a vessel or pipe is characterised by the *film coefficient* or *heat transfer coefficient* (HTC). The HTC defines the rate of heat transfer across the thin boundary layer formed between the fluid and metal surface. The HTC is a crucial input to any fatigue assessment since it dictates, for a given change in fluid temperature, the strength of the thermal gradient formed within the wall thickness of a component and thus the severity of the thermal stresses experienced on the metal surface. Actual HTCs are quite complex and vary as a function of geometry, fluid pressure and temperature, and local flow rate, and therefore engineering estimates of HTCs are usually employed. The most common approach to obtain HTC values is to use classical handbook solutions for simple geometries. In the majority of cases, the appropriate solution for LWR plants is that of fully developed flow within a hollow cylinder, where the mechanism of heat transfer is considered *forced convection*. The most commonly employed correlation for this situation is that of Dittus-Boelter [83], which gives reasonable values provided the temperature difference between the metal surface and contacting fluid is not too large. Otherwise, more complex correlations such as the Sieder-Tate [84] and Gnielinski [85] equations are likely to yield greater accuracy. In some limited situations where flow is more complex, as in the case of

thermal stratification, the use of CFD to derive HTCs may be necessary; however CFD is computationally expensive and correlations are employed in most cases. The key parameters that define HTCs will normally be included within the component transient specification, and the transient variation of HTCs may be simulated within the thermal analysis. However, in some circumstances it may be more appropriate to adopt an upper-bound constant value for the HTC, for instance where data is unavailable or for the purposes of performing conservative scoping calculations. Once the HTCs are defined, the thermal analysis may be performed for each design transient. The transient temperature distributions from the thermal analyses are then mapped to the structural analysis to generate the thermal stresses relevant to fatigue.

3.3.2. Post-Processing of Finite Element Stresses

The objective of the finite element post-processing operation is to obtain the stress-time history of the necessary stress categories required for fatigue analysis. The six unique components of the Cauchy stress tensor are required. At a minimum, the necessary stresses required are the Primary plus Secondary (linearised) stresses and the Primary plus Secondary plus Peak (total) stresses. These stress histories are later used in the cycle counting procedure to evaluate fatigue usage.

3.3.2.1. Stress Classification Lines (SCLs)

The fatigue usage is evaluated at discrete locations, known as a stress classification line or *SCL*. The SCL represents a straight line spanning the section thickness of a pressure vessel or piping component. The inner and outer points of the SCL are situated on the internal and external surface of the component and it is these points that must be assessed. Generally, fatigue tends to be most severe on the internal surface and thus the interior point of the SCL is of much greater significance.

The orientation of the SCL is very important. Normally, SCLs will be positioned perpendicular to the inner and outer surfaces and therefore normal to the mid-plane through-thickness. However, there are some situations where this is not possible, as it would not capture the location of highest stresses, which are of greatest relevance to fatigue. In these situations, care should be taken to ensure that the SCL is oriented perpendicular to the computed stress contours through-thickness. A good example of

this situation is in crotch region of vessel and piping nozzles, which can often be the fatigue limiting location.

In the assessment of typical components, many SCLs will generally be required to cover the main regions of high stresses, local structural discontinuities, and material discontinuities. If geometric discontinuities are not represented in sufficient detail by the FE model, then application of an appropriate stress concentration factor (SCF) is necessary. Alternatively, some locations may also require the application of a fatigue strength reduction factor (FSRF) to account for local reduction in fatigue strength. Care must be taken in the assessment of material discontinuities in FEA, in particular dissimilar metal welds, since thermal mismatch can induce a sharp discontinuity in the stress field. In this situation, SCLs may be placed either side of the interface but avoiding the singularity. Stress ranges along the length tend to be less sensitive to mesh density and sensible locations for assessment can be determined by plotting the stress variation at the surface across the interface.

The most important function of the SCL is to allow for calculation of stress resultants across the section using continuum FEA stresses. This is the objective of *stress linearisation*, which is discussed next along with some important factors.

3.3.2.2. Linearisation of Stresses

Stress linearisation is one possible methodology adapted for use in FE software, which can be used to extract membrane and bending stress resultants at the SCL locations. Here, the term *Total Stress* is used to refer to the continuum FEA stress and is denoted by σ_{ij}.

Each of the six tensor stress non-linear distributions has an equivalent membrane stress distribution, $\sigma_{ij,m}$, which may be determined from Eq. (45).

$$\sigma_{ij,m} = \frac{1}{\mathrm{t}} \int_0^t \sigma_{ij}(x)\, dx \tag{45}$$

Membrane stress is defined as the average stress along the SCL and by definition is constant through-thickness. Similarly to membrane stress, each of the six tensor stress non-linear distributions has an equivalent 'bending' stress distribution, $\sigma_{ij,b}$, and is determined from

$$\sigma_{ij,b} = \frac{6}{t^2}\int_0^t \sigma_{ij}\left(\frac{t}{2} - x\right)\, dx \tag{46}$$

Bending stress is the part of the stress distribution that varies linearly across the SCL, and has the greatest magnitude on one of the surfaces (or 'outer-fibre'). A key characteristic of the bending stress is that it integrates to net zero force and produces the same net bending moment as the total stress distribution across the SCL. Peak stresses are defined as the difference between the total stress, taking into account any FSRFs or SCFs where necessary, and the sum of the membrane and bending stress contributions.

$$\sigma_{ij,F}(x)\big|_{x=0} = \sigma_{ij}(x)\big|_{x=0} - (\sigma_{ij,m} + \sigma_{ij,b}) \tag{47}$$

$$\sigma_{ij,F}(x)\big|_{x=t} = \sigma_{ij}(x)\big|_{x=t} - (\sigma_{ij,m} - \sigma_{ij,b}) \tag{48}$$

Throughout this thesis, the primary plus secondary stresses (P+Q) are conservatively assumed equal to the sum of the membrane plus bending stresses:

$$\sigma_{ij,P+Q} = \sigma_{ij,m+b} = \sigma_{ij,m} + \sigma_{ij,b} \tag{49}$$

It is crucially important that the stresses be first transformed from the default global coordinate system defined in the FE software, to the local coordinates associated to the SCL under assessment, prior to performing stress linearisation. In this thesis, the following coordinate conventions are used: the local x-direction is parallel to the SCL (radial); the local y-direction is tangential to the SCL (axial), and the local z-direction is in the circumferential plane (meridional/hoop).

The choice of which stress components to linearise can potentially influence the magnitude of the P+Q principal stresses. Welding Research Council (WRC) Bulletin 429 [86] discusses four options for calculation of linearised principal stresses:

1) Membrane plus bending for all six tensor components
2) Membrane plus bending for the direct stress components, membrane only for shear.

3) Membrane plus bending for hoop and axial components, membrane for other components.
4) Membrane plus bending for direct stress components, FE (total) stresses for shear.

Generally, linearisation of all stress components tends to be most prevalent within industry since this is often the default option utilised by FE-based linearisation tools. Out of the options above, only 1 and 3 are relevant for plane unnotched sections in vessels and piping where the SCL is oriented perpendicular to the mid-plane through-thickness; options 2 and 4 will have no impact in this case since shear is negligible. The choice of linearisation method only becomes significant in situations where the radial through-wall stresses are non-negligible, which is generally limited to very thick-walled piping and vessels [87]. In such situations, the radial P+Q stress, $\sigma_{x,P+Q}$, is lower when using Option 3 compared to Option 1 due to neglecting the fictitious bending contribution. The algebraic difference between the principal P+Q stresses is therefore larger for Option 3, resulting in a higher P+Q stress intensity. However, the difference between these two options is minor and the choice of linearisation technique is not of particular issue when it comes to assessing fatigue.

In this thesis, stress linearisation is performed using a custom Python class with the following settings: Newton-Cotes integration (Simpson's Rule) using 200 intermediate points along the SCL; piece-wise linear interpolation between adjacent points; linearisation of all six unique stress components; and no curvature correction. In all cases, stress linearisation is performed at every time-step in the FE stress history to generate a complete history of P+Q stresses. Implementing this approach reproduces exactly the results obtained using the Abaqus built-in linearisation tool with the curvature correction option disabled (Figure 16).

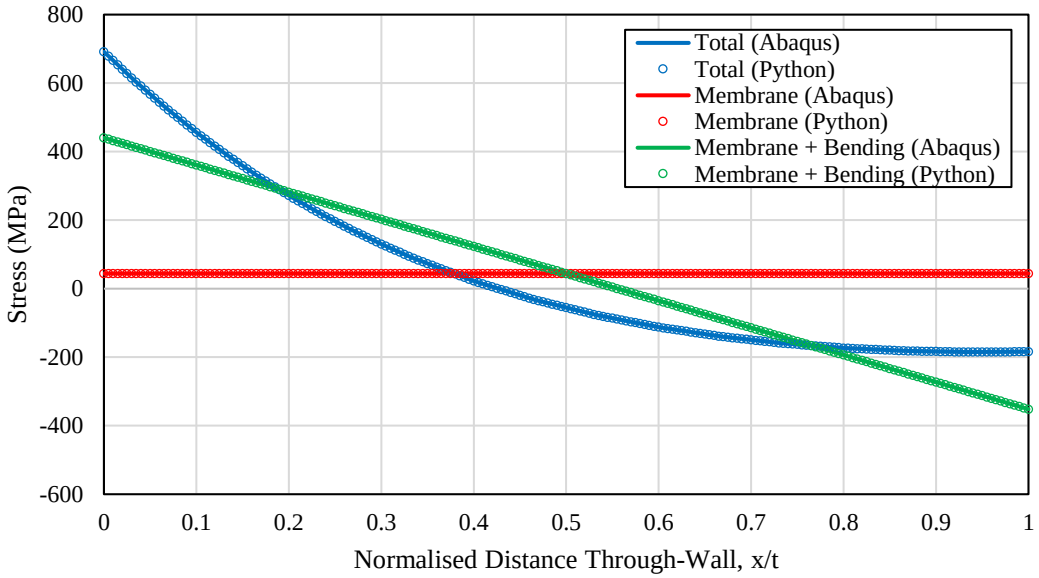

Figure 16. Illustration of Python stress linearisation methodology.

3.3.3. Cycle Counting and Usage Calculation

The objective of cycle counting is to identify the time-points within one or more transient stress-time histories that constitute stress reversals, and to combine these time-points in such a way to produce well-defined stress cycles. The background and best practice recommendations outlined in this section are discussed in the context of an ASME Section III Appendix XIII-3500 fatigue evaluation.

3.3.3.1. Background

Cycle counting forms the first stage of the fatigue analysis outlined in Appendix XIII-3520 *Procedure for Fatigue Analysis*, which states: *"for each condition of cyclic service, determine the stress differences and the alternating stress intensity, S_a, in accordance with XIII-2400"*. The procedure of XIII-2420 involves calculating stress vs. time histories for each transient and choosing a point in time where *"conditions are known to be extreme"*.

ASME III Appendix XIII-1300 (ag) defines a stress cycle as *"a condition in which the alternating stress difference goes from an initial value through an algebraic maximum value and an algebraic minimum value and then returns to the initial value. A single service cycle may involve one or more stress cycles"*. In this statement, the phrase 'service cycle' is interchangeably referred to here as an *event* or *transient*.

Various methodologies for identifying stress cycles have been proposed within the technical literature, for application to both uniaxial and multiaxial stress histories [88]. In most design codes including ASME III, simplified uniaxial cycle counting methods are common, where the identification of stress cycles is performed on the time-history of the uniaxial 'equivalent' stress, that is, either Tresca or von Mises stress intensities. The simplest approach is that of Extreme Value Pairing (EVP), also known as 'Peak-to-Peak' (PTP) counting, and is the methodology adopted within ASME Section III. The procedure involves identifying the relative maxima ('peaks') and minima ('valleys') in the uniaxial stress-time history and pairing each in order of decreasing stress range, eliminating each pair after they are counted. After all pairs are accounted for, the cycle counting procedure is complete. The output of EVP is a list of stress ranges in order of highest-to-lowest, along with the peak and valley time points associated to each range. In the ASME Code fatigue community, a peak-valley pair is also commonly referred to as a *fatigue load pair* and this terminology is adopted herein. An illustration of EVP is provided in Figure 17 and Figure 18. Figure 17 shows an arbitrary uniaxial reversal history, which may be identified from the FEA stress-time history for each of the transients under consideration. Figure 18 illustrates the steps followed by EVP. In this case, the stress history is reordered based on absolute magnitude whilst retaining the sign convention (though this is not a strict requirement of EVP); identifying the relevant stress ranges is then trivial. The highest stress range is identified by the two points marked with circles, the second highest with triangles, the third highest with squares, and so on. This pairing of extreme points in the loading history to produce corresponding ranges continues until no more reversal loci remain. One of the benefits of EVP is that it need not necessarily be applied to an actual loading history obtained in sequence. The order of events does not affect the output obtained from EVP and thus the stress history may be ordered in or out of sequence with that observed under representative plant transient conditions.

In performing a fatigue assessment to ASME III Appendix XIII-3520, the EVP is applied in accordance with ASME III Appendix XIII-2420. The critical time-points across all transients where the stress achieves a peak or valley are directly combined together. In this context, two types of fatigue load pair can arise when applying EVP: *inside pairs*, which consist of a peak and valley from within the same defined transient,

and *outside pairs*, which consist of a peak from one transient and a valley from a separate transient. The alternating stress intensity, S_a, is equal to one-half of the stress range defined by each peak-valley pair. Importantly, the Code requires that S_a be further adjusted for the effects of plasticity and temperature, to obtain a 'corrected' value of alternating stress intensity, S_{alt}. The value of S_{alt} is used to determine the allowable number of cycles on the DFC.

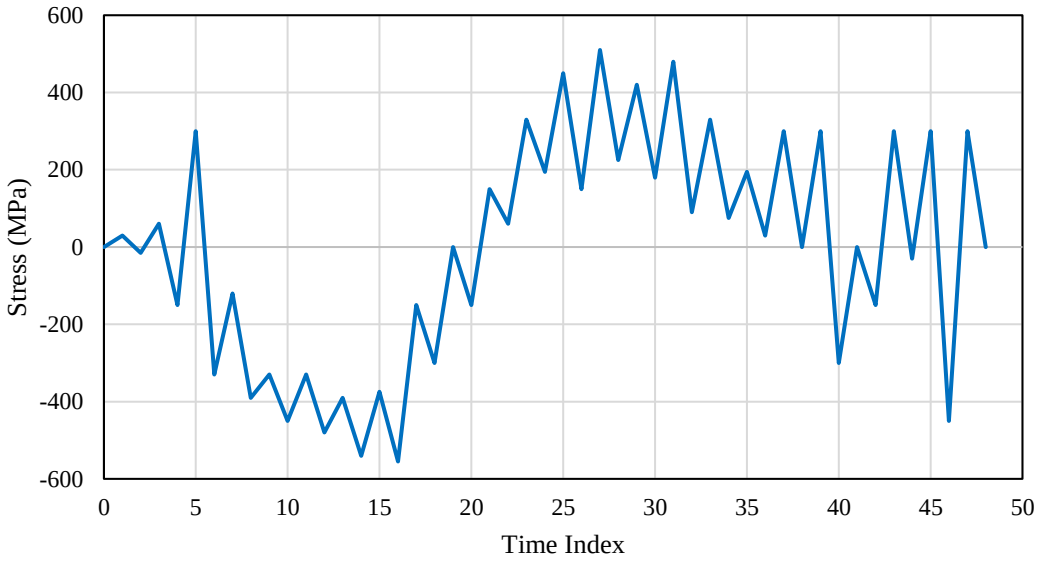

Figure 17. Arbitrary uniaxial reversal history prior to cycle counting using the PTP method.

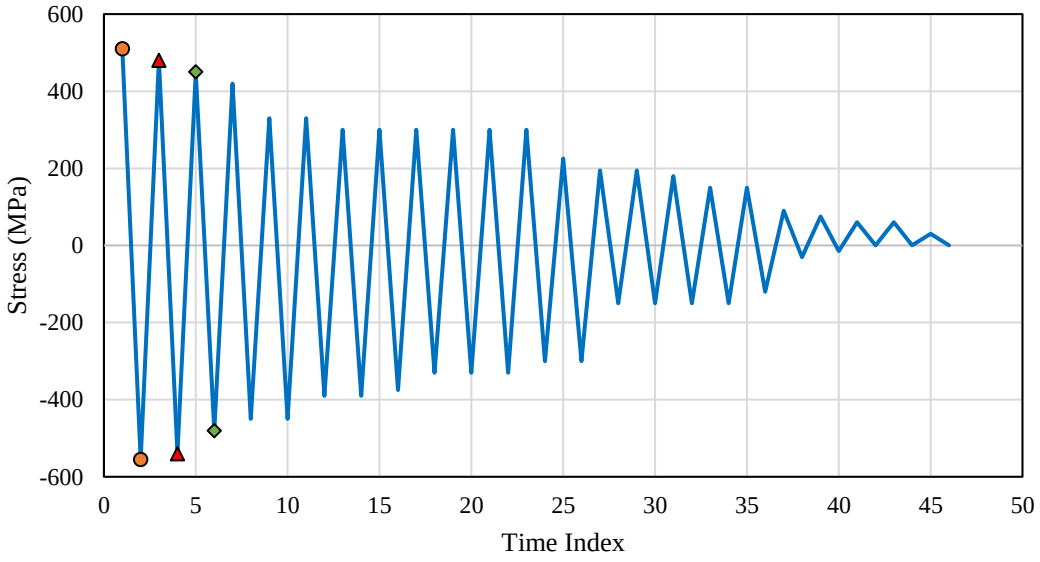

Figure 18. PTP cycle counting applied to reversal history of Figure 17.

3.3.3.2. Alternating Stress Intensity (S_{alt})

The alternating stress intensity, S_{alt}, for each fatigue load pair is calculated per Eq. (50)

$$S_{alt} = \frac{1}{2} K_e S_p \frac{E_c}{E_a} \tag{50}$$

Where the terms S_p, K_e, and E_a are defined below.

S_p

S_p is the primary-plus-secondary-plus-peak (P+Q+F) or *total* stress intensity range. S_p is calculated in the following manner. First, the difference or range of the individual stress components, $\sigma_{ij}^{'}$, is calculated between the time points t_a and t_b, which correspond respectively to the peak and valley of the fatigue load pair.

$$\sigma_{ij}' = {}^{b}\sigma_{ij} - {}^{a}\sigma_{ij}, \qquad for\ i = 1,2,3; j = 1,2,3 \tag{51}$$

From the six component stress differences, the three principal stress differences may be calculated. S_p is equal to the stress intensity range, $\sigma_I^{'}$, calculated by Eq. (36) based on those three principal stress differences, and S_a is one-half this value.

K_e

K_e is a simplified elastic-plastic penalty factor, which accounts for plasticity effects in the elastic fatigue analysis calculations. If the primary-plus-secondary stress intensity range (S_n) exceeds the $3S_m$ limit, K_e must be multiplied to the value of S_a. The K_e factor is determined in accordance with Appendix XIII-3450 (b), and varies as a function of both S_n and S_m, and two material-dependent parameters, *m* and *n*. The Code K_e factor is a major focus of this thesis and is discussed in detail in Chapter 4.

S_n is calculated in the same manner as S_p except based on the P+Q stresses. The allowable stress, S_m, is a function of temperature and is determined for the relevant material in ASME II, Part D, Table 2 (A/B). S_m values that fall between tabulated metal temperatures are calculated by linear interpolation. ASME III Appendix XIII-3420 states that *"when the secondary stress is due to a temperature transient or to restraint of free end displacement, the value of S_m shall be taken as the average of the tabulated S_m values for the highest and lowest temperatures of the metal during the transient. When part or all of the secondary stress is due to a mechanical load, the value of S_m shall be based on the highest metal temperature during the transient".*

Normally, this is interpreted as the average of the S_m values coinciding with the peak and valley of the fatigue load pair. Otherwise, the value of S_m is based on the higher of two metal temperatures, T_a and T_b, calculated respectively at the peak and valley time points, t_a and t_b.

$$S_m = \begin{cases} \frac{1}{2}[S_m(T_a) + S_m(T_b)] \;\; if\ \Delta Q\ is\ thermal\ only \\ S_m(\max[T_a, T_b])\ otherwise \end{cases} \tag{52}$$

E_a/E_c

E_a is the elastic modulus of the analysis. The ratio of the reference modulus of the DFC, E_c, to E_a, E_c/E_a, is used to correct S_{alt} in accordance with ASME III Appendix XIII-3520 (d). This correction allows for transferability between the pseudo-stress values determined from the elastic fatigue analysis and the actual value of alternating strain used to derive the design fatigue curves. Appendix XIII-3520 (d) states the following:

'Multiply S_{alt} (as determined in XIII-2410 or XIII-2420) by the ratio of the modulus of elasticity given on the design fatigue curve to the value of the modulus of elasticity used in the analysis'

What constitutes the 'elastic modulus of the analysis' is not explicitly stated in the Code. Considering that the Code also adopts a temperature-dependent approach for S_m, two options commonly adopted are to use the value of E either at the maximum temperature of cycle or at the average temperature of the cycle. Technically speaking, if the calculation of S_{alt} was instead performed based on elastic pseudo-strain intensities calculated using the instantaneous E value at the peak and valley time points, then this would produce the most physically consistent result. Temperature-dependent values of E are provided in Table M-1 of ASME II, Part D and can be obtained in the same manner as S_m.

$$S_{alt} = \begin{cases} \frac{1}{2} K_e S_p \frac{E_c}{E(max[T_a, T_b])} \ \ (Option\ 1) \\ \frac{1}{2} K_e S_p \frac{E_c}{E(average[T_a, T_b])} \ \ (Option\ 2) \\ \frac{1}{2} K_e E_c \cdot \left[\frac{^m\sigma_I}{^mE} - \frac{^n\sigma_I}{^nE} \right] = \frac{1}{2} K_e E_c \cdot [^m\varepsilon_I - {}^n\varepsilon_I] \ \ (Option\ 3) \end{cases} \quad (53)$$

3.3.3.3. Consideration of Primary-Plus-Secondary Stress

One circumstance that can arise is the possibility of the P+Q stress time history being out-of-phase (lagging) the total stress time history. This is because the P+Q stress is highly dependent on the section thickness, and can have a much slower stress response than that of the total stresses. This can be especially significant for thick-walled components. To illustrate this, consider the case of a pipe of internal radius (r_i) of 350 mm subjected to a sharp thermal shock. Figure 19 shows the total and P+Q hoop stress response for two different wall thicknesses of 30mm and 120mm. As can be seen, for the 30mm pipe thickness, the total and P+Q response vary approximately in-phase. On the other hand, for the 120mm thick pipe, the P+Q stress significantly lags that of the total stress, and only achieves its peak around 200s after the initial thermal shock. Whilst this represents an extreme example, this phenomenon is important and it is not unusual to observe some lag in the P+Q stress in realistic cases.

Consequently, the peak and valley respectively forming S_p and S_n do not normally coincide. This is important since the alternating stress is a function of both K_e and S_p, where K_e is a function of S_n and the design stress intensity, S_m. Performing cycle counting per Appendix XIII-2400 ensures maximisation of S_p, but the Code does not state as an explicit requirement that S_n need also be independently maximised. However, not doing so can have an obvious impact on the calculated value of S_{alt}, and thus it has been generally accepted that some action should be taken in the calculation procedure to account for the phase difference between S_p and S_n. Several approaches have been proposed to achieve this, such as that of Meikle et al [89], Gilman [90], and Costa et al [91]. In this work, the elastic fatigue calculations are performed by identifying separate pairs of peak-valley time points to enable independent maximisation of S_p and S_n for each load pair. This is achieved by scanning the P+Q

stress time history in a user-defined window around the time points that form S_p to determine a conservative value of S_n.

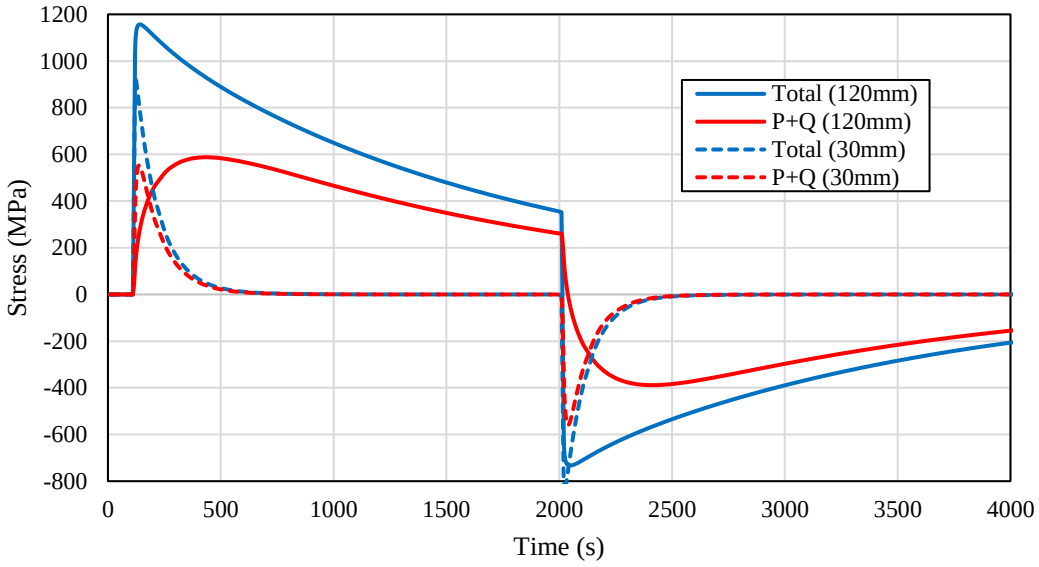

Figure 19. Total and P+Q stress response for simple pipe subjected to thermal shock.

3.4. Industry Need for Modern Fatigue Rules

The current procedure for fatigue evaluation incorporated within Appendix XIII-3520 of ASME Section III has remained largely unchanged since its inception in 1963, and has provided the basis for fatigue design substantiation of Class 1 LWR vessels for nearly a half century. Whilst the rules of Appendix XIII-3520 are straightforward to apply based on elastic stresses, the results can however be very pessimistic. Over the preceding years, this has largely been attributed to the conservatism of the Appendix XIII-3450 K_e factor, which, as will be shown in Chapter 7 of this thesis, can easily result in an overestimate of the strain amplitude (or equivalent pseudo-elastic stress amplitude) by up to a factor of two. This can produce overestimates of the CUF by up to an order of magnitude or more; this is especially the case in the low-cycle regime where the DFC exhibits greater non-linearity. Notwithstanding these conservatisms, the rules of Appendix XIII-3520 have routinely been used to demonstrate acceptable CUF results for pressure vessel and piping components for decades. To date, the vast majority of fatigue failures observed in LWR plants operating worldwide have been

high-cycle fatigue failures associated with loading conditions that were unknown at the time of the original plant designs, such as thermal stratification phenomena and mechanically induced vibrations [92]–[101]. In contrast, there have been virtually no reports of fatigue crack initiation attributed solely to low-cycle fatigue in LWR plants designed to ASME Section III. This is true even of components with a high calculated CUF and confirms the large margin, albeit unquantified, that exists in the Code fatigue analysis rules.

However, as industry looks to the future of nuclear power and some of the new plant designs under development, obtaining a favourable trade-off between plant safety and economic benefits is of paramount importance. Whilst it was possible to demonstrate acceptable CUF based on the original Code fatigue rules, more recently, the industry has struggled to use the same methodology to demonstrate acceptable CUF for new plants with a design life of 60 years. Additionally, there have been proposals for the next generation of LWR plants to adopt flexible modes of operation (or *load following*) to accommodate the variable power demands placed on the grid. The use of LWRs for flexible operation will necessarily involve a greater number of power plant transients, thereby increasing the CUF further. More recently, the emergence of data describing the deleterious effect of the LWR coolant environment on fatigue has spawned additional requirements to demonstrate sufficient margin when environmental effects are included. The combination of the above factors, especially the latter, can result in unacceptable CUF values.

3.4.1. Environmental Fatigue

Gaps in the knowledge existing in the 1960s relating to the DFCs and DBA methods have been further explored as new LWR plant designs have emerged or in-service issues have become known. In recent years, the most significant development has been the recognition that the LWR coolant environment may adversely affect the fatigue performance of reactor structural materials, particularly austenitic stainless steels. The harmful effect of the hot water environment on fatigue crack initiation in small scale polished specimens has been extensively documented in NUREG/CR-6909 Revision 1 [72]. Since the Code DFCs are based on tests conducted in an air environment, they do not explicitly consider this effect, as NB-3121 states: *"It should be noted that the*

tests on which the design fatigue curves (Section III Appendices, Mandatory Appendix I) are based did not include the presence of a corrosive environment which might accelerate fatigue failure". Subsequently, the U.S. NRC published regulatory guideline (RG) 1.207 in 2007 (Rev. 1 [77] as of June 2018), which provides guidance for incorporating the effects of the LWR coolant environment in CUF calculations performed in accordance with ASME III. The deleterious effect of environment is described through an environmental fatigue penalty factor, F_{en}, which is dependent on the material type, strain-rate, temperature, and the dissolved oxygen content of the water in contact with the metal surface. The formulae that describe F_{en} are based upon correlations observed in isothermal tests conducted under constant strain rate (saw-tooth/trapezoidal strain waveforms) and therefore are not representative of the complex loading encountered during plant transients. The ANL defined the F_{en} in NUREG/CR-6909 as the ratio of the component fatigue life in a room temperature air environment to its fatigue life in an LWR environment at operating temperature. Importantly, the existing fatigue data reviewed in [72] for austenitic stainless steels indicated that slow, increasingly tensile strain waveforms were primarily responsible for the environmental reduction in fatigue endurance; no clear environmental fatigue life reduction was observed for compressive-loading cycles. Thus, only tensile portions of a loading cycle are important for consideration of F_{en}. In an Appendix XIII-3520 fatigue assessment, the F_{en} is incorporated within the evaluation by multiplying to the partial usage factor, U_i, obtained for each fatigue load pair, thus obtaining a cumulative usage factor adjusted for environmental effects, U_{en}.

$$U_{en} = \sum_{i=1}^{k} U_i \cdot F_{en,i} = \sum_{i}^{k} \frac{n_i}{N_{d,i}} \cdot F_{en,i} \tag{54}$$

The guidance outlined in RG 1.207 Rev.1 is applicable to new reactor designs submitted for NRC approval, and those operating reactors pursuing license renewal in the United States. The international community has largely followed suit, with many national regulators now imposing similar regulatory requirements.

With the exception of ferritic steels containing a high sulphur content, austenitic stainless steels are the material class most susceptible to environmental reduction of fatigue endurance in the PWR operating environment. Per NUREG/CR-6909 Rev.1

[72], the F_{en} for austenitic stainless steels can vary up to a maximum of 12.8 in the PWR environment, though values between 3.0 and 6.0 are more typical. This can have a dramatic effect on the results of an Appendix XIII-3520 fatigue assessment, potentially increasing the CUF by up to a factor of 10 or more.

It is evident therefore that the superposition of the additional environmental penalty factors with the extant Code fatigue assessment methods and DFCs is unlikely to be acceptable for critical locations, especially when longer design lives are required. However, in-service experience of LWR components has been exemplary with regard to fatigue failure, which has led to issues in analytical justification of the recently introduced F_{en} methodology. Developing an improved understanding of the environmental fatigue behaviour of actual plant components through component features testing under representative loading conditions, compared to the simple specimen testing considered in NUREG/CR-6909 [72], is viewed as fundamental to better quantify margins in the current Code fatigue assessment procedure. Component features testing would also provide additional high-quality experimental data to benchmark potential new assessment methods, such as the Total Life Approach described in Section 2.1.2.

The current fatigue assessment method based on the Appendix I DFCs determines a fatigue initiation life presumed to equate to a 3mm crack depth assuming membrane loading. However, under typical thermal transient loading, through-wall stress distributions in plant components are not membrane stress fields, but rather exhibit a significant strain gradient. Initiated cracks therefore grow into a decaying strain field, and hence the crack growth rate is significantly reduced compared to membrane loading. Thus, the ability to account for through-wall strain gradients up to the presumed 3mm initiation depth is one area where excess conservatism can be significantly reduced. The main advantage of adopting a total life approach is the ability to make initiation life predictions to a much smaller crack depth, such as 250 μm, which is typically taken as a lower bound for the applicability of fracture mechanics methods. This would then enable crack growth methods to determine the number of subsequent cycles, taking into account the strain gradient, R-ratio, crack closure effects, etc., required to achieve a critical crack size or through-wall leak.

Another important advantage of this approach is it can benefit more from the greater industry understanding of environmental effects on crack growth and associated analytical methods (see for example, recent developments by Currie et al [102]), enabling a far more accurate assessment of total life compared to the use of the Code DFCs with F_{en} multipliers.

A representative features testing programme is currently ongoing as an international collaboration activity led by the Electric Power Research Institute (EPRI), co-partnered with Rolls-Royce (RR, UK), Électricité de France (EDF, France), and Naval Nuclear Laboratory (NNL, USA). The five-year programme consists of four phases, beginning in 2018 and expected to conclude in 2022. The test programme considers two sets of plant representative transients on four Type 304L pipe component specimens using a simulated PWR primary water environment. The test loop is currently under construction at Kinectrics in Toronto, with testing expected to commence in 2021. The key objective of this programme is to define factors for fatigue life and fatigue crack growth to permit transference of small-scale specimen data to plant components and to benchmark the test data against the more realistic total life analytical approaches. Despite widespread support by the international community on this matter, representative features testing represents a considerable R&D expense, and is likely to be ongoing for some time before conclusive evidence can be accumulated to further aid development and validation of total life approaches and provide greater confidence to industry.

3.4.2. Strategy for Code Improvements

Whilst the aforementioned efforts to address environmental fatigue are ongoing and will eventually yield significant benefit, the nuclear industry has also collectively begun investigating other areas of improvement to the Code fatigue rules, which might in the meantime provide more immediate relief to designers and operators. Many such areas have been identified within the fatigue action plan published by the ASME Working Group on Environmental Fatigue Evaluation Methods (WGEFEM). The objective of the WGEFEM fatigue action plan was to identify a number of areas that might be updated within the Code to enable a more appropriate evaluation of environmentally assisted fatigue in compliance with regulatory requirements. The

WGEFEM vision is to provide a series of analysis methods of increasing complexity or effort, enabling a designer to benefit from increasing reductions in conservatism. To achieve this, a number of supporting activities have been identified, many of which fall under the responsibility of other ASME working groups. The ASME WGEFEM fatigue action plan has achieved widespread support within the Code community since undergoing initial balloting in 2014.

One of the most important supporting activities identified by the WGEFEM is to investigate improvements to the current Appendix XIII-3450 rules for simplified elastic-plastic analysis. It has been widely acknowledged that the Appendix XIII-3450 K_e factor is a major source of excessive conservativism in an Appendix XIII-3520 fatigue assessment. Some plant designers have adopted detailed calculations based on elastic-plastic FE analysis to address this, though these necessitate considerable computational expense and are subject to additional uncertainties in the assumed cyclic plastic constitutive model. The Code provisions for elastic-plastic fatigue analysis are also extremely limited. Accordingly, the development of more realistic PCFs as an alternative to the Appendix XIII-3450 K_e factor forms Item 18 of the WGEFEM fatigue action plan and falls under the remit of the ASME Working Group on Design Methodology (WGDM) [103]. This highlights the motivation for the following work, which aims to address an important industry need.

4. Determination of K_e by Elastic DBA

In this chapter, the technical basis for the ASME III Appendix XIII-3450 K_e factor is explored to identify limitations to be addressed. Existing alternative approaches proposed based on elastic DBA, including those adopted within other C&S are examined and compared. The methods adopted by each approach to treat plasticity arising due to local thermal and notch effects are interrogated and scrutinised and the limits of applicability of each approach is discussed. These alternative approaches differ considerably in their philosophy and level of complexity, but may be categorised according to their basic requirements. Particular attention is paid to a proposal developed recently by Sam Ranganath, which has recently received approval for publication as an ASME Section III Code Case. Since austenitic stainless steels are the focus of this thesis, the evaluations presented herein are limited to this material class. The accuracy of the elastic DBA K_e methods discussed here is later evaluated in Chapter 7 by comparison with the results obtained from detailed elastic-plastic FEA.

4.1. ASME III Simplified Elastic-Plastic Analysis

4.1.1. Background

To account for the effects of plasticity in an Appendix XIII-3520 fatigue assessment, simplified elastic-plastic correction (penalty) factors, K_e, are provided in Appendix XIII-3450 (formerly Subsection NB-3228.5) for cases where the primary-plus-secondary stress intensity range exceeds the $3S_m$ limit. In such cases, the K_e factors act as a multiplier on the total (including peak) pseudo-elastic stress intensity range, S_p. This accounts for the fact that the strain range calculated under the assumption of elastic behaviour can under-predict the actual elastic-plastic strain range. Thus, the K_e factor is termed a *strain concentration factor*, applied to compensate for strains larger than would otherwise be calculated based on the theory of elasticity.

Langer described the original technical basis for the K_e factor in a lecture entitled *'Design-Stress Basis for Pressure Vessels*' [104], and largely reflects the description provided in the updated ASME Code Criteria document [105] published in 1969 for Sections III and VIII-2. The following quote from Langer describes the circumstances that can arise whereby elastic analysis may under predict the true elastic-plastic strains:

"Strain concentration can occur in any structural member with stress gradients as soon as the loading exceeds the point at which the highest-stressed region becomes plastic. If the plastic zone is highly localized, the surrounding elastic material controls the strain in the plastic material and no strain concentration occurs. When the plastic zone is large enough to become a significant factor in the stress distribution, however, the strains in the plastic zone become larger than those which would be calculated by the theory of elasticity and strain concentration must be considered" B.F. Langer [104]

Langer defined the K_e factor as the actual peak strain divided by the peak strain calculated on the assumption of elastic material behaviour:

$$K_e = \frac{\varepsilon_{ep}}{\varepsilon_e} \tag{55}$$

By assuming that the maximum deflections associated with both ε_e and ε_{ep} are both equal, Langer was able to derive analytical K_e solutions for different materials by analysing two simple configurations:

a) A tapered flat bar subjected to uniaxial tension (Figure 20).
b) A cantilever beam subjected to a vertical displacement at its free end (Figure 21).

For each configuration, Langer assumed a non-linear elastic power law stress-strain relationship:

$$\sigma = K\varepsilon^n \tag{56}$$

where σ is the applied stress, ε is the total strain, *K* is the strain hardening coefficient in units of MPa, and *n* is the dimensionless strain hardening exponent. *n* varies between

zero and unity, with *n=1* corresponding to purely elastic behaviour, whilst *n=0* corresponds to elastic perfectly-plastic behaviour (i.e. for $\varepsilon \rightarrow \infty$, $\sigma = \sigma_y$).

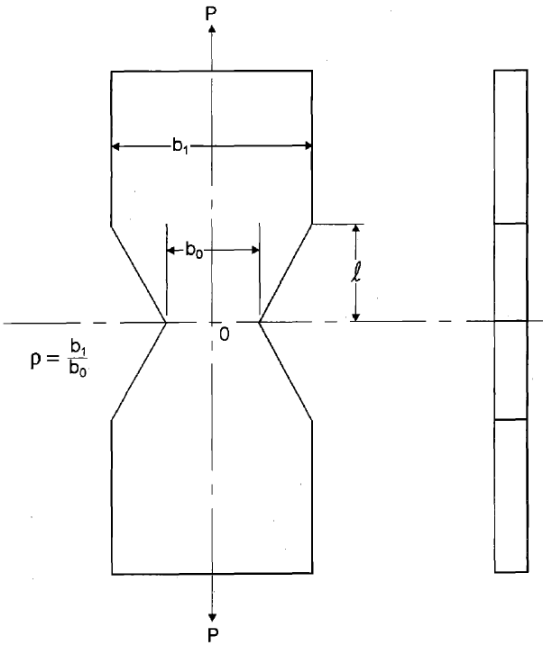

Figure 20. Tapered flat bar loaded in tension considered by Langer [104].

ρ denotes the ratio of the cross-sectional area of the larger section (b_1) to that of the smaller section (b_0), whilst l denotes the vertical length of the tapered region.

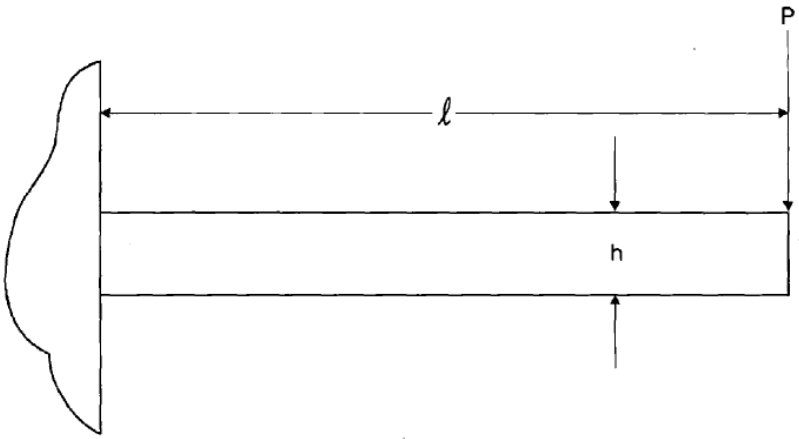

Figure 21. Cantilever beam subjected to an applied end displacement considered by Langer [104].

l and h denote the length and thickness of the beam, respectively.

4.1.2. Tapered Flat Bar Subjected to Uniaxial Tension

Langer examined the case of two tapered flat bars, each considered geometrically identical in the unloaded condition. Bar I is assumed to follow Hooke's Law, whilst bar II follows the non-linear elastic relationship of Eq. (56). Both bars are pulled to the same total elongation, δ. For this configuration, Langer demonstrated (see Appendix A of [104] for full derivation) that the maximum peak strain attained in each bar is calculated as follows:

Bar I (Elastic)

$$\varepsilon_{e,max} = \frac{\delta_{e,max}(b_1 - b_0)}{b_0 l \cdot ln(b_1/b_0)} \tag{57}$$

Bar II (Inelastic)

$$\varepsilon_{ep,max} = \delta_{ep,max}\left(\frac{b_1 - b_0}{l}\right)\left(\frac{1}{b_0 \cdot e^{\frac{1}{n}}}\right)\cdot\left(\frac{1}{n} - 1\right)\left[\frac{1}{\frac{1}{b_0 \cdot e^{(\frac{1}{n}-1)}} - \frac{1}{b_1 \cdot e^{(\frac{1}{n}-1)}}}\right] \tag{58}$$

Where b_0 and b_1 are respectively the cross-sectional areas of the smaller and larger sections of the tapered bar, and *l* is the length of the tapered transition as shown in Figure 20. It should be noted that in the above derivation, the bar is assumed to be of unit thickness in the direction normal to Figure 20.

Thus, K_e represents the ratio of $\varepsilon_{ep,max}$ to $\varepsilon_{e,max}$ under the assumption that the maximum imposed elongation is the same in both cases (i.e. $\delta_{e,max} = \delta_{ep,max}$) and is shown to be a function of the cross-sectional area ratio or 'taper ratio', ρ, between the larger and smaller sections of the tapered bar:

$$K_e = \frac{\varepsilon_{ep,max}}{\varepsilon_{e,max}} = \frac{(\frac{1}{n} - 1)}{1 - \rho^{(1-\frac{1}{n})}} ln(\rho), \qquad where\ \rho = \frac{b_1}{b_0} = taper\ ratio \tag{59}$$

Figure 22 shows the variation in the K_e factor of the tapered bar with strain hardening exponent, *n*, for different cross-sectional area ratios, ρ.

4.1.3. Cantilever Beam Subjected to an Applied Vertical End Displacement

Langer's analytical solution for the cantilever beam is based on the work of Radomski and White [106] and White and Radomski [107], who examined strain concentration in beams with consideration of applied loading conditions and the assumed stress-strain relation. Considering a cantilever beam of rectangular cross-section subjected to an applied vertical displacement at its free end. Assuming Hookean material behaviour, the maximum elastic strain in the beam is calculated from Eq. (60).

$$\varepsilon_{e,max} = \frac{3t\delta_{e,max}}{2l^2} \tag{60}$$

where $\delta_{e,max}$ is the applied displacement at the free end, and *t* and *l* are respectively the beam thickness and beam length. Adopting the non-linear elastic material law described by Eq. (56) results in a linear relation between maximum deflection and maximum inelastic strain. The maximum inelastic strain in the beam is expressed by Eq. (61).

$$\varepsilon_{ep,max} = \frac{t(1+2n)}{2nl^2}\delta_{ep,max} \tag{61}$$

Thus, under the assumption that the maximum deflections are the same for both cases (i.e. $\delta_{e,max} = \delta_{ep,max}$), K_e is defined as the ratio of $\varepsilon_{ep,max}$ to $\varepsilon_{e,max}$:

$$K_e = \frac{\frac{t(1+2n)}{2nl^2}\delta_{ep,max}}{\frac{3t\delta_{e,max}}{2l^2}} = \frac{\left(\frac{1+2n}{n}\right)\delta_{ep,max}}{3\delta_{e,max}} = \frac{1+2n}{3n}, \quad for\ \frac{\delta_{ep,max}}{\delta_{e,max}} = 1 \tag{62}$$

The variation of K_e as a function of strain hardening exponent for the cantilever beam is also included in Figure 22 for comparison with the Tapered Bar analytical solution.

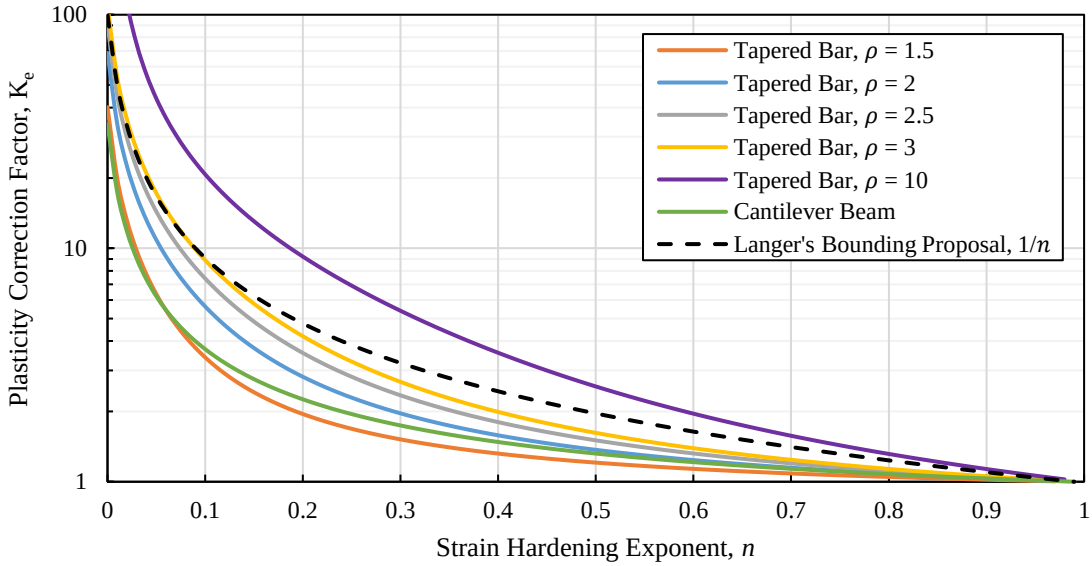

Figure 22. K_e factors derived based on Langer's initial investigations

4.2. Initial ASME III K_e Proposals

Based on the mathematical derivation of K_e factors for the simple configurations, Langer initially proposed a bounding expression for K_e to apply to ASME Code assessments of nuclear pressure vessels. The simple bounding expression of $K_e = 1/n$ was proposed to envelope the predictions for the two configurations, with the exception of the tapered bar in cases where the ratio of cross-sectional areas, ρ, is very large. It is noted that $K_e = 1/n$ was derived from the tapered flat bar solution with a 2/3 reduction in cross-section, which was determined to be realistically bounding for plant components. Though simple, this expression results in a very significant K_e factor for values of $S_n >> 3S_m$. Langer suggested that the $1/n$ approximation was reasonably close to reality [108], though more importantly, he did not clarify the magnitude of the loading required to attain $K_e = 1/n$; specifically, it was not stated explicitly whether $K_e = 1/n$ should be assumed as valid for both $S_n \approx 3S_m$ and $S_n >> 3S_m$. Langer did however state that the load at which $K_e = 1/n$ is reached varies with geometry and material. The full value of $K_e = 1/n$ was arbitrarily set to apply for $S_n \geq 6S_m$, with $K_e = 1.0$ applying for all $S_n \leq 3S_m$. For $3S_m < S_n < 6S_m$, intermediate values of K_e would apply

$$K_e^{Langer} = \begin{cases} 1.0 & if\ S_n \le 3S_m \\ 1.0 + \dfrac{1-n}{n(m-1)}\left(\dfrac{S_n}{3S_m} - 1\right) & if\ 3S_m < S_n < 6S_m \\ \dfrac{1}{n} & if\ S_n \ge 6S_m \end{cases} \quad (63)$$

Langer proposed that the constant parameter *m* be set equal to 2, and provided values for the strain hardening parameter *n* based on material class. Figure 23 shows the original proposed ASME Code K_e factor as a function of S_n/S_m carbon steel, low-alloy steel, austenitic stainless steel, and Ni-Cr-Fe alloys.

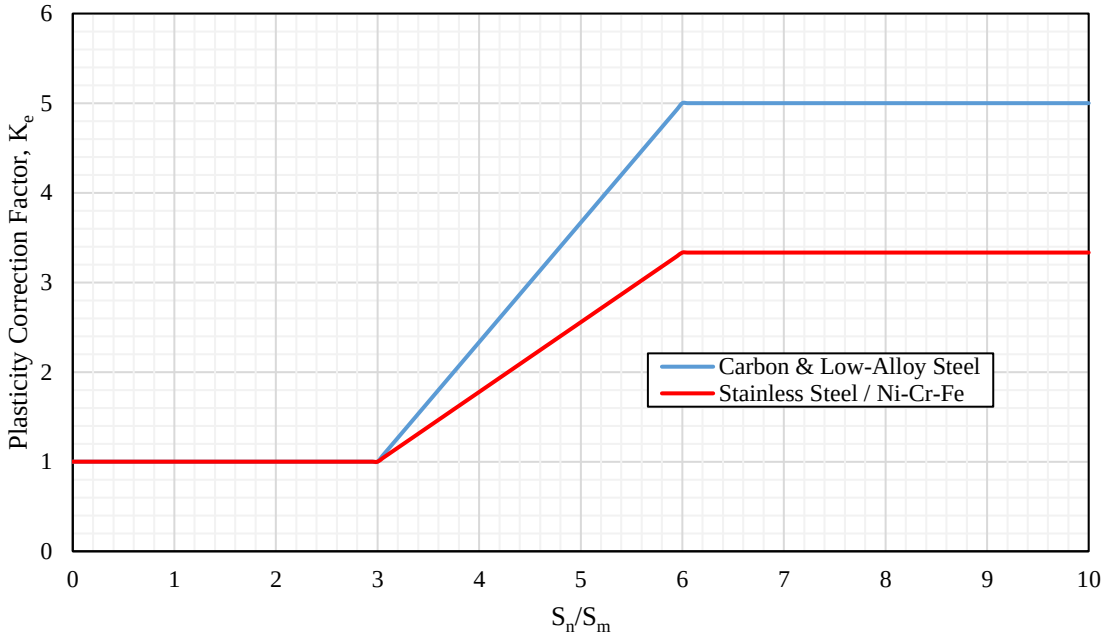

Figure 23. K_e factors from Langer's original proposal

In 1968, Tagart [109] suggested modifications to the value of parameter *m* to be consistent with the B31.7 Rules for Nuclear Power Piping, which were more developed than ASME Section III at the time, and included provisions for *'Simplified Elastic-Plastic Discontinuity Analysis'*. Material-specific values for *m* were proposed for carbon, low-alloy, and austenitic stainless steels. The parameter *m* controls the threshold value of S_n/S_m beyond which the maximum K_e penalty applies. The proposed values of *m* and *n* are shown in Table 3 for each material class. Therefore, for each material, the maximum value of K_e is applicable for $S_n \geq 3mS_m$. This modification proposed by Tagart received approval, and was introduced in the 1971 edition of the

Code, when the vessel and piping rules were published together and the Section III design-by-analysis criteria was revised to include simplified elastic-plastic analysis rules applicable to both NB-3200 vessels (NB-3228.5) and NB-3600 piping components (NB-3653.5). As of April 2020, these rules have remained unchanged since their inception. However, due to editorial changes in 2017, the relevant rules for simplified elastic-plastic analysis of NB-3200 vessels are now provided in Mandatory Appendix XIII-3450 (formerly Subsection NB-3228.5).

4.2.1. ASME Section III, Mandatory Appendix XIII-3450

Two corrections are described in ASME Section III to account for non-linear material behaviour. Surface plasticity effects are accounted for by applying a correction to the local thermal stress intensity range, $S_{p,lt}$, to account for the higher effective Poisson's ratio in the plastic regime; this is described in Appendix XIII-2500 *Application of Elastic Analysis for Stresses Beyond the Yield Strength.* The Code boundary between spatially limited and sectional plasticity is demarcated by the limit of $3S_m$ applied to the range of membrane-plus-bending stress intensity. Where this limit is exceeded, the gross section membrane-plus-bending stress range exhibits plastic cycling, and a correction to account for sectional plasticity is required. In such cases, the provisions of Appendix XIII-3450 apply in lieu of XIII-2500.

One very important perquisite to applying Appendix XIII-3450 is that the range of membrane-plus-bending stress intensity excluding any contribution from thermal bending stresses, $S_{n,tb}$, must remain within the elastic range (i.e. below $3S_m$). This validity criterion is outlined in XIII-3450 (a) and may be represented formulaically by Eq. (64).

$$S_n - S_{n,tb} \leq 3S_m \tag{64}$$

The K_e factor is not intended to accommodate the elastic range being exceeded by primary (i.e. load-controlled) stresses and the above criterion limits its applicability to cases where primary stresses comprise a small portion of the total stress range. The Code authors also recognised that certain types of uniform, far-field thermal stresses could produce high local strains due to elastic follow-up. One example of this behaviour is where a weaker (i.e. lower yield strength) section of pipe exhibits plastic straining whilst the larger section remains essentially elastic. In this case, the weaker

portion is forced to withstand additional straining due to follow-up of the large elastic thermal motions of the larger section, which experiences lower stresses and therefore exhibits higher rigidity. Other examples include local reductions in cross section and mismatch in material rigidity at intersections, which are both relevant to nozzles experiencing expansion stresses from attached piping. Consequently, thermal membrane stresses, $S_{n,tm}$, are implicitly assumed to act as primary stresses and are not subtracted out in Eq. (64). In other words, only $S_{n,tb}$ and $S_{p,lt}$ are permitted to exceed the elastic range of $3S_m$. Any combination of loading which violates this criterion is not permitted by the Code, and simplified elastic-plastic analysis is inapplicable for such cases.

$K_e^{XIII\text{-}3450}$ is calculated per the following equation in XIII-3450 (b):

$$K_e^{XIII-3450} = \begin{cases} 1.0 & if\ S_n \leq 3S_m \\ 1.0 + \dfrac{1-n}{n(m-1)}\left(\dfrac{S_n}{3S_m} - 1\right) & if\ 3S_m < S_n < 3mS_m \\ \dfrac{1}{n} & if\ S_n \geq 3mS_m \end{cases} \quad (65)$$

Both *m* and *n* are provided in Table XIII-3450-1 (shown as Table 3). For austenitic stainless steels, *m* and *n* are 1.7 and 0.3 respectively, and thus the maximum attainable K_e factor of $1/n$ (≈ 3.333) is conceded for S_n/S_m exceeding 5.1.

The Appendix XIII-3450 K_e vs. S_n/S_m correction curves for each material class are shown in Figure 24. As discussed in the previous section, the maximum K_e factor for each material class applies beyond a specific threshold value of S_n/S_m, which is dictated by the tabulated value of *m* provided in Table XIII-3450-1 and shown in Table 3. As shown in Figure 24, the threshold values of S_n/S_m for carbon, low-alloy, and austenitic stainless steel are 9.0, 6.0, and 5.1, respectively. This is an important reason why austenitic stainless steel materials in LWRs tend to be limiting with respect to fatigue usage, despite their DFC being more favourable in the low-cycle regime than other material classes.

Table 3. Material-specific parameters provided in ASME III Appendix XIII-3450 Table-1.

Materials	*m*	*n*	T_{max} (°C)
Carbon steel	3.0	0.2	370
Low alloy steel	2.0	0.2	370
Martensitic stainless steel	2.0	0.2	370
Austenitic stainless steel	**1.7**	**0.3**	**425**
Nickel-chromium-iron	1.7	0.3	425
Nickel-copper	1.7	0.3	425

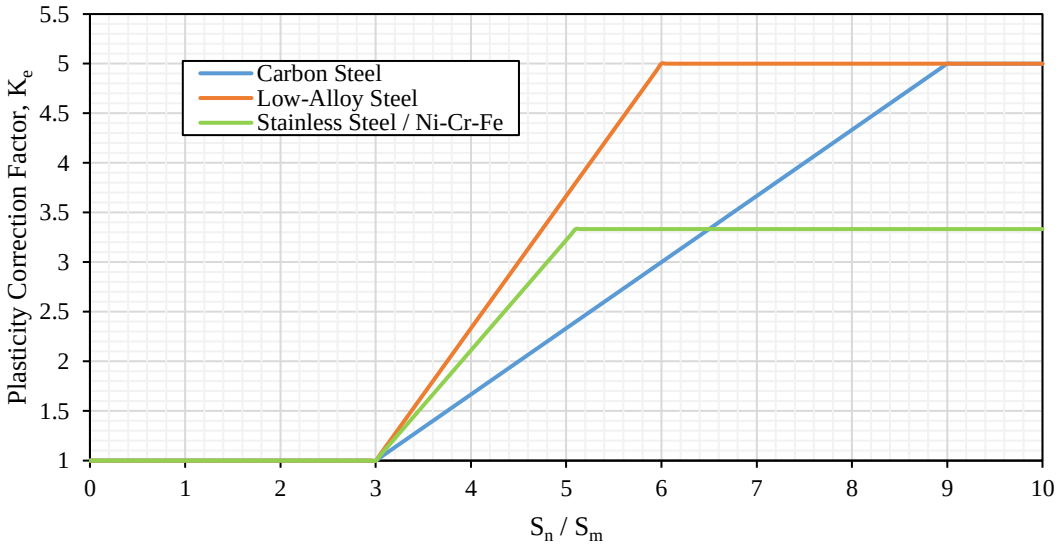

Figure 24. Current K_e factors presented in ASME III, Appendix XIII-3450

Whilst the XIII-3450 K_e factor is straightforward to apply, its bounding nature often results in excessive conservatism in the low-cycle regime. Accordingly, in recent years, considerable industry effort has focused on the development of alternative PCFs, which aim to align more closely the actual elastic-plastic material response at critical locations; some of these alternative proposals have subsequently been adopted within other internationally recognised nuclear design and construction codes.

4.3. Alternative Methods for Simplified Elastic-Plastic Analysis

Due to the excessive conservatism associated with the ASME III Appendix XIII-3450 K_e methodology, a great deal of industry efforts have focused on establishing revised K_e factor expressions to address the following two primary concerns:

i) Reduction in the excessive conservatism of the Appendix XIII-3450 K_e factor, especially for thermal transients.

ii) Provide additional consideration of strain concentration arising at geometric features such as notches, which were not considered in Langer's formulation of the original K_e factor expressions.

A number of important innovations to address these concerns are formalised in Welding Research Council (WRC) Bulletin No. 361 [110]. Most notably, ASME Code Case N-779, which is currently the only code-approved alternative to Appendix XIII-3450, is based partially on the findings outlined in WRC 361.

4.3.1. Welding Research Council Bulletin No. 361

In 1991, the publication of WRC-361: *Improvements on Fatigue Analysis Methods for the Design of Nuclear Components Subjected to the French RCC-M Code* [110] provided the technical basis for proposed improvements to the ASME Code Simplified Elastic-Plastic Analysis procedure. The authors of [110] suggested partitioning S_n to separate the influence of mechanical and thermal loading:

$$S_n = S_n^{mech} + S_n^{ther} \tag{66}$$

where S_n^{mech} represents the portion of S_n arising due to mechanical loading such as pressure and seismic loads, whilst S_n^{ther} represents the portion of S_n arising due to thermal loads. As S_n is itself a linearised quantity, it follows that S_n^{ther} should represent the thermal membrane plus bending contribution to S_n. The authors of WRC-361 suggested that separate K_e factors should apply for S_n^{ther} on the basis that Poisson's ratio effects are not explicitly considered in the ASME Code K_e methodology. They argued that applying a single K_e only on the total value of S_n was excessively conservative and instead proposed a new K_e factor, referred to as K_e^* in WRC-361, constructed as a weighted average of two correction factors, K_e^{ther} applying to thermal

stresses, and K_e^{mech} applying to mechanical stresses. A detailed overview of the approach proposed in WRC-361, which was later modified for adoption within the French RCC-M design code is provided.

4.3.1.1. Consideration of the Effective Poisson's Ratio in Simplified Elastic-Plastic Analysis

Under the assumption of isotropy, the Poisson's ratio of an elastic material ranges between $-1 \leq 0 \leq 0.5$ according to Lame's relation:

$$v = \frac{1}{2} - \frac{E}{6K} \tag{67}$$

where *E* and *K* are the elastic and bulk moduli respectively which must each hold positive values. Most structural steels possess an elastic Poisson's ratio of approximately $\nu = 0.3$. For post-yield deformations associated with zero volume change, the *'effective'* Poisson's ratio, denoted ν^*, increases through the range $0.3 \leq \nu^* \leq 0.5$, and tends asymptotically to $\nu^* = 0.5$ with increasing plastic deformation. This Poisson's ratio effect occurs most commonly for conditions of local thermal ('skin') stresses, which produce a perfectly biaxial state of stress. This state of stress is typical for the internal surface of nuclear pressure vessels and piping components, which are often subjected to sharp thermal transients throughout their operating lifetime.

Considering a step-change thermal shock of magnitude, ΔT, acting on the internal surface of a pipe with thermal expansion coefficient, α, where the stresses expressed in the *z, θ,* and *r* directions represent the axial, hoop, and radial components, respectively. The stress and strain ranges acting on the internal surface of the pipe are described according to Hooke's Law:

$$\begin{aligned} \Delta\sigma_z &= \frac{E}{1-v^2}[\Delta\varepsilon_z + v(\Delta\varepsilon_\theta + \Delta\varepsilon_r)] = \frac{E\alpha\Delta T}{1-v} \\ \Delta\varepsilon_z &= \frac{1}{E}[\Delta\sigma_z - v\Delta\sigma_\theta] = \alpha\Delta T \end{aligned} \tag{68}$$

$$\begin{aligned} \Delta\sigma_\theta &= \frac{E}{1-v^2}[\Delta\varepsilon_\theta + v(\Delta\varepsilon_z + \Delta\varepsilon_r)] = \frac{E\alpha\Delta T}{1-v} \\ \Delta\varepsilon_\theta &= \frac{1}{E}[\Delta\sigma_\theta - v\Delta\sigma_z] = \alpha\Delta T \end{aligned} \tag{69}$$

$$\Delta\sigma_r = 0$$
$$\Delta\varepsilon_r = \frac{1}{E}[-v(\Delta\sigma_z + \Delta\sigma_h)] = \frac{-2v\alpha\Delta T}{1-v} \tag{70}$$

Adopting Tresca theory, the stress and strain intensity ranges are calculated according to Eq. (71).

$$\Delta\sigma_I^e = \frac{E}{1+v}|\Delta\varepsilon_z\ (or\ \Delta\varepsilon_\theta) - \Delta\varepsilon_r| = \frac{E\alpha\Delta T}{1-v}$$
$$\Delta\varepsilon_I^e = \frac{|\Delta\varepsilon_z\ (or\ \Delta\varepsilon_\theta) - \Delta\varepsilon_r|}{1+v} = \frac{\alpha\Delta T}{1-v} \tag{71}$$

Under purely elastic material behaviour, ν is approximately 0.3. However, for conditions where $\Delta\sigma_I^e$ exceeds the elastic range, the Poisson's ratio must be adjusted by equating the volume change under elastic-plastic behaviour to the volume change under purely elastic behaviour. In this manner, a direct comparison can be made between the elastic parameters E and ν their elastic-plastic equivalents, the secant modulus, E_s, and ν^* using the following expression:

$$\frac{\Delta V}{V} = \frac{1-2v^*}{E_s}(\Delta\sigma_1 + \Delta\sigma_2 + \Delta\sigma_3) = \frac{1-2v}{E}(\Delta\sigma_1 + \Delta\sigma_2 + \Delta\sigma_3) \tag{72}$$

and thus,

$$\frac{1-2v^*}{E_s} = \frac{1-2v}{E} \tag{73}$$

After rearranging Eq. (73), one obtains the following expression for the effective Poisson's ratio, ν^*, established by Nadai [111]:

$$v^* = 0.5 - \frac{E}{E_s}(0.5 - v) \tag{74}$$

For very large plastic strains, $E_s \rightarrow 0$ as the SSC approaches a horizontal line, and hence $\nu^* = 0.5 - 0 = 0.5$ for plastic behaviour. Substituting for $\nu^* = 0.5$ into Eq. (75) produces the strain intensity for fully plastic behaviour:

$$\Delta\varepsilon_I^p = \frac{|\Delta\varepsilon_z\ (or\ \Delta\varepsilon_\theta) - \Delta\varepsilon_r|}{1+v^*} = \frac{\alpha\Delta T}{1-v^*} \tag{75}$$

The ratio of the plastically and elastically calculated strain intensity ranges is therefore:

$$\frac{\Delta\varepsilon_I^p}{\Delta\varepsilon_I^e} = \frac{1-v}{1-v^*} \tag{76}$$

Assuming the most conservative bounding value of ν^*, the following ratio is obtained:

$$\frac{\Delta\varepsilon_I^p}{\Delta\varepsilon_I^e} = \frac{0.7}{0.5} = 1.4 \tag{77}$$

This ratio, defined as K_v in WRC-361 and the present work, was proposed to correct the elastically calculated value of $\Delta\sigma_I^e$ to account for the higher value of ν^* when the elastic range is exceeded. The K_v of 1.4 is an upper-bound value that assumes fully plastic material behaviour and an equi-biaxial state of stress, and therefore may not be entirely appropriate in case where only modest plastic straining is present. A more accurate calculation of ν^* requires knowledge of the material cyclic SSC, in order to determine the local value of the secant modulus, E_s. At present, non-linear material properties are not provided in ASME Section III. Thus, for practical purposes, the bounding assumption is very useful in this regard, as it can be easily applied in cases where thermal loading is dominant and can significantly reduce the conservatism associated with the XIII-3450 K_e factor. The following weighted-average K_e factor expression was proposed by the authors of WRC-361 [110]:

$$K_e^* = K_v \frac{S_n^{ther}}{S_n} + K_e \frac{S_n^{mech}}{S_n} \tag{78}$$

where K_v and K_e are the correction factors applied to the thermal and mechanical contributions to S_n, respectively. In the above formulation, the ASME III Appendix XIII-3450 K_e factor is assumed to apply for the mechanical load contribution. The ramification of the proposed expression, is that for purely thermal loading, the maximum value of K_e^* is limited to 1.4, significantly less than the ASME III Appendix XIII-3450 maximum of 3.33 for austenitic stainless steels.

It is noteworthy that the above definition of K_v is derived based on Tresca theory, though WRC-361 also draws attention to the use of the von Mises criterion. Adopting von Mises theory instead for the above example, the strain intensity range is determined by Eq. (79).

$$\begin{aligned} \Delta\varepsilon_{VM} &= \frac{\sqrt{2}}{2(1+\nu^*)}[(\Delta\varepsilon_z - \Delta\varepsilon_\theta)^2 + (\Delta\varepsilon_\theta - \Delta\varepsilon_r)^2 + (\Delta\varepsilon_r - \Delta\varepsilon_z)^2]^{\frac{1}{2}} \\ &= \frac{\sqrt{2}}{2(1+\nu^*)}\frac{1+\nu^*}{1-\nu^*}\alpha\Delta T \end{aligned} \tag{79}$$

Substituting the elastic and plastic values of 0.3 and 0.5 for ν^* in Eq. (79) confirms that the same maximum condition for K_v is also valid for von Mises theory:

$$\frac{\Delta\varepsilon_{VM}^{p}}{\Delta\varepsilon_{VM}^{e}} = \frac{\frac{\sqrt{2}}{3}\cdot\frac{1+0.5}{1-0.5}\cdot\alpha\Delta T}{\frac{\sqrt{2}}{2.6}\cdot\frac{1+0.3}{1-0.3}\cdot\alpha\Delta T} = \frac{\sqrt{2}}{1.01} = 1.4 \tag{80}$$

Moulin and Roche also considered the determination of K_v as a function of the equivalent strain range calculated according to von Mises theory [112], but instead adopts the plastic value of Poisson's ratio in the first term of the Eq. (79) under both elastic and plastic conditions. As shown by Eq. (81), this assumption produces a higher theoretical maximum correction of 1.615, but the definition of ν^* is not consistent between the elastic and elastic-plastic solutions. Nonetheless, the correction derived by Moulin and Roche is still important, since, as will be apparent, it explains the rationale behind other proposals for treatment of thermal-plastic effects, most notably in the French RCC-M Code.

$$\frac{\Delta\varepsilon_{VM}^{p}}{\Delta\varepsilon_{VM}^{e}} = \frac{\frac{\sqrt{2}}{3}\cdot\frac{1+0.5}{1-0.5}\cdot\alpha\Delta T}{\frac{\sqrt{2}}{3}\cdot\frac{1+0.3}{1-0.3}\cdot\alpha\Delta T} = \frac{\sqrt{2}}{0.875} \cong 1.615 \tag{81}$$

The difference between the above definitions of K_v as a function of ν^* is shown by Figure 25. As shown, the K_v proposed by Moulin and Roche becomes increasingly more conservative as $\nu^* \rightarrow 0.5$.

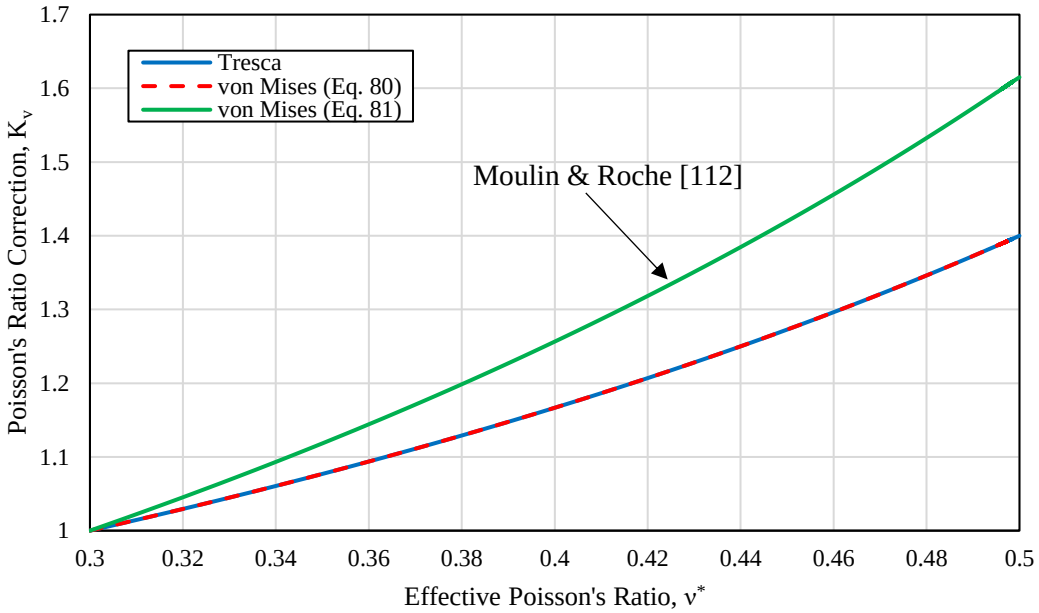

Figure 25. Illustration of K_v as a function of ν^* assuming perfect biaxiality.

4.3.1.2. Proposal of Neuber Analysis for Notch Effects

The original ASME Code K_e factor expressions did not explicitly consider the presence of notches, which may act as regions of local strain concentration. In cases where a notch is present, WRC-361 recommends that notch plasticity be accounted through inclusion of a notch plasticity factor, K_n, determined using Neuber's rule. The authors proposed that the notch plasticity factor should be applied on top of the weighted-average K_e^* factor where appropriate.

K_n is derived by considering Neuber's relation for an arbitrary geometry. Neuber stipulated that the square of the theoretical elastic stress concentration factor is equal to the product of the stress and strain concentration factors, so long as the region of plasticity remains highly localised and well contained by the elastic bulk behaviour of the structure.

$$K_T^2 = K_\sigma K_\varepsilon \tag{82}$$

Where K_σ and K_ε represent the ratio of the local notch stresses and strains to the nominal stresses and strains respectively. Under Hookean material behaviour, $K_\sigma = K_\varepsilon$ and thus $K_\sigma = K_\varepsilon = K_T$. However, for a non-linear material law such as that described by Eq. (56), the strain concentration factor increases beyond its elastic value:

$$K_\varepsilon = \frac{\varepsilon_{notch}}{\varepsilon_{nominal}} = K_T^{\left(\frac{2}{n+1}\right)} \quad (83)$$

K_T is already considered explicitly in an elastic analysis, assuming all structural features are included in the relevant finite element model. Therefore, the degree of additional plastic straining beyond that determined on a purely elastic basis may be calculated by normalising Eq. (83) with respect to K_T:

$$K_n = \frac{K_\varepsilon}{K_T} = \frac{K_T^{\left(\frac{2}{n+1}\right)}}{K_T} = K_T^{\left(\frac{1-n}{1+n}\right)} \quad (84)$$

The authors of WRC-361 recommended that notch plasticity be accounted for in cases where the use of the purely elastic quantity, K_T, would under predict the total strain. K_n is therefore interpreted as a correction factor to account for the additional strain concentration experienced at local discontinuities under conditions of globalised plasticity, over and above that experienced under conditions of local plasticity (i.e. small-scale yielding). However, a notch correction factor is not included in ASME III. Indeed, the ASME III procedure does not include any correction for peak stresses in excess of yield; one exception is for local thermal stresses per Appendix XIII-2500, for $S_n < 3S_m$. Implicit in the ASME III procedure is the assumption that the Appendix XIII-3450 K_e factor is sufficiently conservative to account for the combined effects of sectional and notch plasticity. For implementation in the RCC-M Code, the authors of WRC-361 [110] recommended that K_T be identified numerically from the ratio of S_p/S_n at the discontinuity location. This enables K_T to be easily calculated 'on-the-fly' for fully featured FE models. It should be noted that this ratio is only mechanically significant if the divergence between S_p and S_n is solely due to the presence of the notch. In addition, the authors of WRC-361 [110] recommend that in cases where the S_p/S_n ratio arises due to local (non-linear) thermal stresses only, then the total thermal stresses need only be corrected by K_v, excluding the additional K_n correction.

4.3.2. ASME Code Case N-779

ASME Code Case (CC) N-779 [113], approved in 2009, provides alternative K_e factor expressions that may be used as an alternative to Appendix XIII-3450. The correction methodology underpinning Code Case N-779 was discussed extensively by the ASME Working Group on Design Methodology (WGDM) from early 2007 until the Case

received final approval on January 26th 2009 following several rounds of balloting. The technical justification for Code Case N-779 is based on the work of Stephen A. Adams, further details of which are available from Code Committee correspondences of the WGDM [114]. The expressions are similar to those described in WRC-361, albeit slightly more complex, requiring three additional categories of stress rather than two, the thermal bending stress range, $S_{n,tb}$, the local thermal stress range, $S_{p,lt}$, and the total stress range less the contribution of thermal bending and local thermal stresses, $S_{p\text{-}lt\text{-}tb}$. The plasticity-adjusted alternating stress amplitude according to CC N-779 is calculated per Eq. (85):

$$S_{alt} = \frac{1}{2}\left[K_e^{XIII-3450} S_{p-tb-lt} + K_v^{N-779} S_{p,lt} + K_v^{N-779} K_n^{N-779} S_{n,tb}\right] \qquad (85)$$

where $K_e^{XIII-3450}$ is defined by Eq. (65); K_v^{N-779} is a Poisson's ratio correction factor, defined by Eq. (86), which varies as a function of $S_{n,tb}$ and $S_{p,lt}$:

$$K_v^{N-779} = \begin{cases} 1.0 & if\ S_p \le 3S_m \\ 1.0 + 0.4\ \dfrac{S_p - 3S_m}{S_{n,tb+lt}} & if\ S_p > 3S_m\ and\ S_{p-lt-tb} < 3S_m \\ 1.4 & if\ S_p > 3S_m\ and\ S_{p-lt-tb} \ge 3S_m \end{cases} \qquad (86)$$

K_n^{N-779} is a notch plasticity correction factor defined by Eq. (87):

$$K_n^{N-779} = \begin{cases} 1.0 & if\ S_{p-lt} \le 3S_m \\ 1.0 + \left[\left(\dfrac{S_{p-lt}}{S_n}\right)^{\frac{1-n}{1+n}} - 1\right]\dfrac{S_{p-lt} - 3S_m}{S_{p-lt}} & if\ S_{p-lt} > 3S_m \end{cases} \qquad (87)$$

where $S_{p\text{-}lt}/S_n$ is equal to the numerical stress concentration factor and *n* is the strain-hardening exponent given in Table XIII-3450-1 for the applicable material class. Both K_v^{N-779} and $K_v^{N-779}K_n^{N-779}$ are constrained to remain less than or equal to $K_e^{XIII-3450}$. K_n^{N-779} only applies in cases where the finite element model does not fully describe the actual geometry of the notch region. If the notch feature is fully captured in the model, and is reasonably well meshed, then K_n^{N-779} is equal to unity. It is also clear from the

above formulation that $K_n^{N\text{-}779}$ is equal to unity in absence of peak stresses arising from mechanical loading, since the relation $S_{p\text{-}lt}$ is always equal to S_n in the case of purely thermal loading. The behaviour of $K_v^{N\text{-}779}$ and $K_n^{N\text{-}779}$ are illustrated in Figure 26 and Figure 27, respectively. $K_v^{N\text{-}779}$ tends to a maximum of 1.4 in situations where both S_p and $S_{p\text{-}lt\text{-}tb}$ exceed $3S_m$. This aligns with the theoretical maximum K_v of 1.4 derived in Eq. (77) adopting Tresca theory. In the most pessimistic scenario where $K_v^{N\text{-}779}$ is assumed equal to unity, $K_n^{N\text{-}779}$ tends to a maximum of 2.41 in situations where S_n slightly exceeds the elastic range. It can be seen that CC N-779 retains the original $K_e^{XIII\text{-}3450}$ factor, but applies this only to the mechanical and thermal membrane contributions to S_p. Thus, the CC N-779 expressions are expected to yield much lower corrections for the case of purely thermal loading. In determination of S_{alt} according to Eq. (85), the expectation is that each sub factor be multiplied to the range of the unique components of each stress tensor before forming the stress intensity of the result.

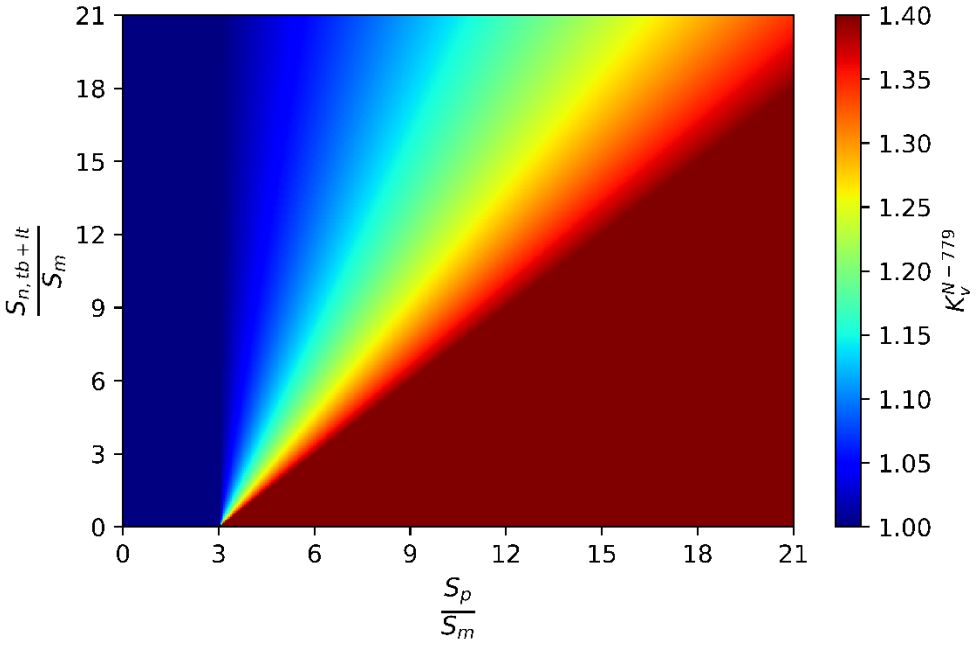

Figure 26. Illustration of Code Case N-779 $K_v^{N\text{-}779}$ factor

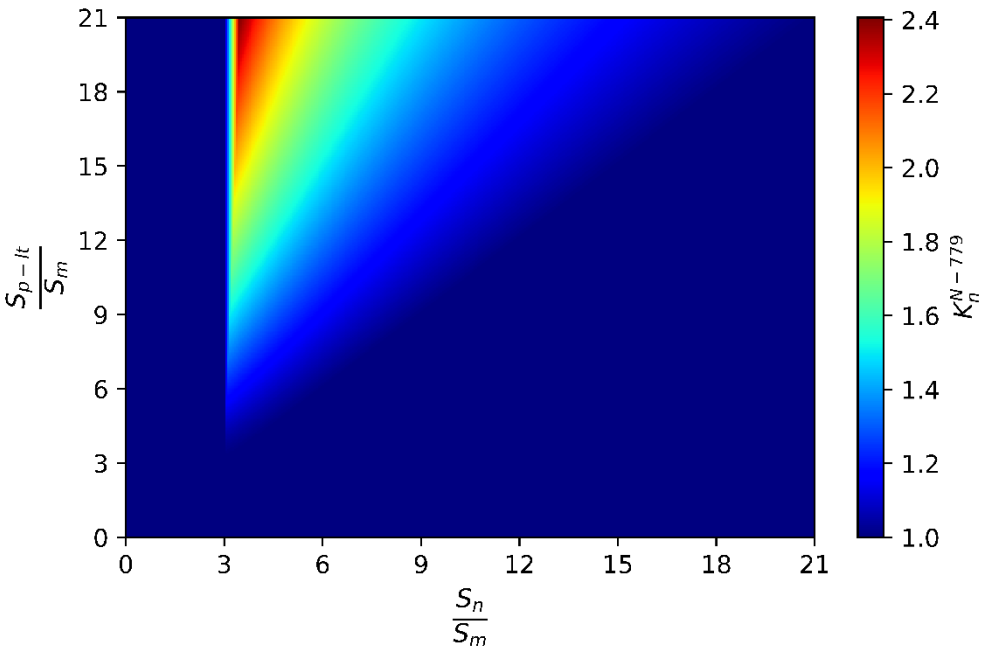

Figure 27. Illustration of Code Case N-779 $K_n^{N\text{-}779}$ factor (assuming $K_v^{N\text{-}779}$ = 1.0).

Whilst CC N-779 has the potential to produce less pessimistic values of S_{alt} compared to Appendix XIII-3450, the equations are rather complicated and necessarily require that stresses arising due to mechanical and thermal loads be obtained separately. This is not necessarily an issue, since this is still a necessary step to satisfy the requirements of Appendix XIII-3450 (a) (per Eq. (64)). Additionally, CC N-779 requires calculation of several stress quantities, e.g. $S_{p\text{-}lt\text{-}tb}$ and S_{lt+tb}, which are not typically reported in standard fatigue tables. This has generally precluded the application of CC N-779 for plant license extension, since it necessitates a costly re-run of prior FE analyses to obtain these missing quantities. Nonetheless, CC N-779 remains the only alternative to Appendix XIII-3450 for application of simplified elastic-plastic fatigue analysis to new plant designs and its potential is explored further in this work for this purpose.

It should also be noted that whilst CC N-779 was granted approval by ASME, the U.S. NRC have taken a different stance more recently by excluding it from the list of approved Code Cases in Regulatory Guide 1.193 [115]. The following quote summarises the NRC position on N-779: *"The NRC finds the new K_e factor analysis method to be complicated to use and prone to misapplication. In addition, there is a lack of experimental verification for the proposed K_n factor to address thermal plastic notch effects. Finally, finite element analysis will not be able to capture surface conditions and imperfections in butt and fillet welds."* RG 1.193 Rev 4, August 2014

4.4. Simplified Elastic-Plastic Analysis in Other Nuclear Design Codes

Since the introduction of simplified elastic-plastic analysis in ASME III Subsection NB-3228.5 (now Appendix XIII-3450), several other nuclear design codes have incorporated their own unique approaches. Many of these approaches originally retained a similar form to ASME III Appendix XIII-3450; however, continuing development of C&S over time has resulted in varying degrees of divergence, based in part on country-specific regulatory requirements. In particular, both the French RCC-M and the Japanese JSME Codes, which originally adopted the basic form of ASME III Appendix XIII-3450, have undergone significant modifications in recent decades and now prescribe different K_e factor expressions.

4.4.1. AFCEN RCC-M (France)

Section B 3234.6 of the French nuclear mechanical design code, *RCC-M: Design and Construction Rules for Mechanical Components of PWR Nuclear Islands* [116], utilises K_e factor expressions that are heavily based on the findings published in WRC-361. However, unlike in WRC-361, both Poisson's ratio and notch effects are only considered implicitly. The alternating stress amplitude is determined from one-half times the sum of the plasticity-corrected mechanical and thermal contributions to the total stress range:

$$S_{alt} = \frac{1}{2} \cdot \left[K_e^{mech} S_p^{mech} + K_e^{ther} S_p^{ther} \right] \tag{88}$$

where K_e^{mech} is the correction applied to the mechanical portion of the total stress range, S_p^{mech}, and is equivalent to the ASME III Appendix XIII-3450 $K_e^{XIII\text{-}3450}$ factor. K_e^{ther} is the correction applied to the thermal portion of the total stress range, S_p^{ther}, and is determined according to Eq. (89) for austenitic stainless steels and inconels:

$$K_e^{ther} = max\left(1.0, \quad 1.86 \left[1 - \frac{1}{1.66 + \frac{S_n}{S_m}} \right] \right) \tag{89}$$

Importantly, the RCC-M K_e^{ther} factor is greater than unity for $S_n/S_m \geq 0.51 S_m$ and therefore applies even where S_n remains within the elastic range. Thus, the RCC-M K_e factor is greater than the ASME Code K_e factor for $S_n \leq 3S_m$ and tends asymptotically

to a value of 1.86 for $S_n >> 3S_m$. Faidy presented a comparison of the RCC-M K_e^{mech} and K_e^{ther} factors for a range of increasing S_n/S_m [117]. Figure 28 shows the RCC-M K_e^{mech} and K_e^{ther} correction curves for austenitic stainless steels and inconels.

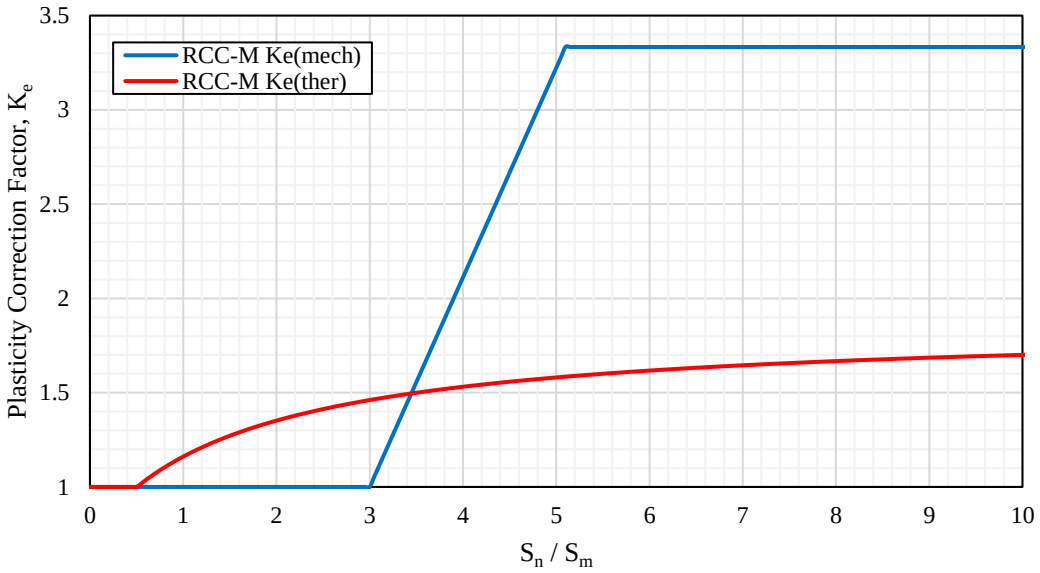

Figure 28. K_e^{mech} and K_e^{ther} prescribed in RCC-M B-3234.6 for austenitic stainless steels.

4.4.2. JSME LWR Structural Design Standard (Japan)

The *Rules on Design and Construction for Nuclear Power Plants, Division 1: Light Water Reactors* [118] published and maintained by the Japan Society of Mechanical Engineers (JSME) initially followed closely the procedure of ASME III Appendix XIII-3450, except where $S_n \approx 3S_m$. It was noted $K_e^{XIII\text{-}3450}$ is not fully conservative in this limited region of modest plasticity, as it does not directly account for peak plastic strain concentration. MITI Notification 501 [119] introduced an additional K_e equation, denoted $K_{e,A0}$, with a material-specific parameter, A_0:

$$K_{e,A_0} = 1.0 + A_0\left(\frac{S_n}{3S_m} - \frac{S_n}{S_p}\right) \; for \; 3S_m < S_n < 3mS_m \tag{90}$$

The factor to be applied to the one-half the alternating stress intensity range, $K_{e,501}$ was defined as the larger of K_e and $K_{e,A0}$ for a given value of S_n. It is shown that this methodology results in $K_{e,A0} > K_e^{XIII\text{-}3450}$ for $S_n \approx 3S_m$.

In recent years, significant changes to the JSME simplified elastic-plastic analysis procedures were introduced by the Committee on Stress Compensated (K_e) Factor (C-

K_e) for Simplified Elastic-Plastic Analysis of the Thermal and Nuclear Power Engineering Society (TENPES) [120]. The revised rules specified in JSME PVB-3315.1 are based on the elastic follow-up model for local plasticity, which was developed initially for experimental Fast-Breeder Reactor (FBR) design [121], and result in less conservative strain concentration factors than ASME III Appendix XIII-3450. The new TENPES K_e factor, denoted K_e', was developed to bound the actual K_e factors obtained for representative LWR components using elastic-plastic FEA:

$$K_e' = 1 + (q - 1)\left(1 - \frac{3S_m}{S_n}\right) \tag{91}$$

where q is the elastic follow-up parameter representing the ratio of the true plastic strain, ε_p, to the strain predicted from elastic analysis, ε_p', as illustrated in Figure 29. q is arbitrarily set to 3.0 in the Japanese FBR Code, on the conservative assumption that purely elastic analysis under predicts the true plastic strain concentration by a factor of three. In deriving K_e', the material was conservatively assumed to be an elastic perfectly-plastic material with yield strength, σ_y set to $1.5S_m$.

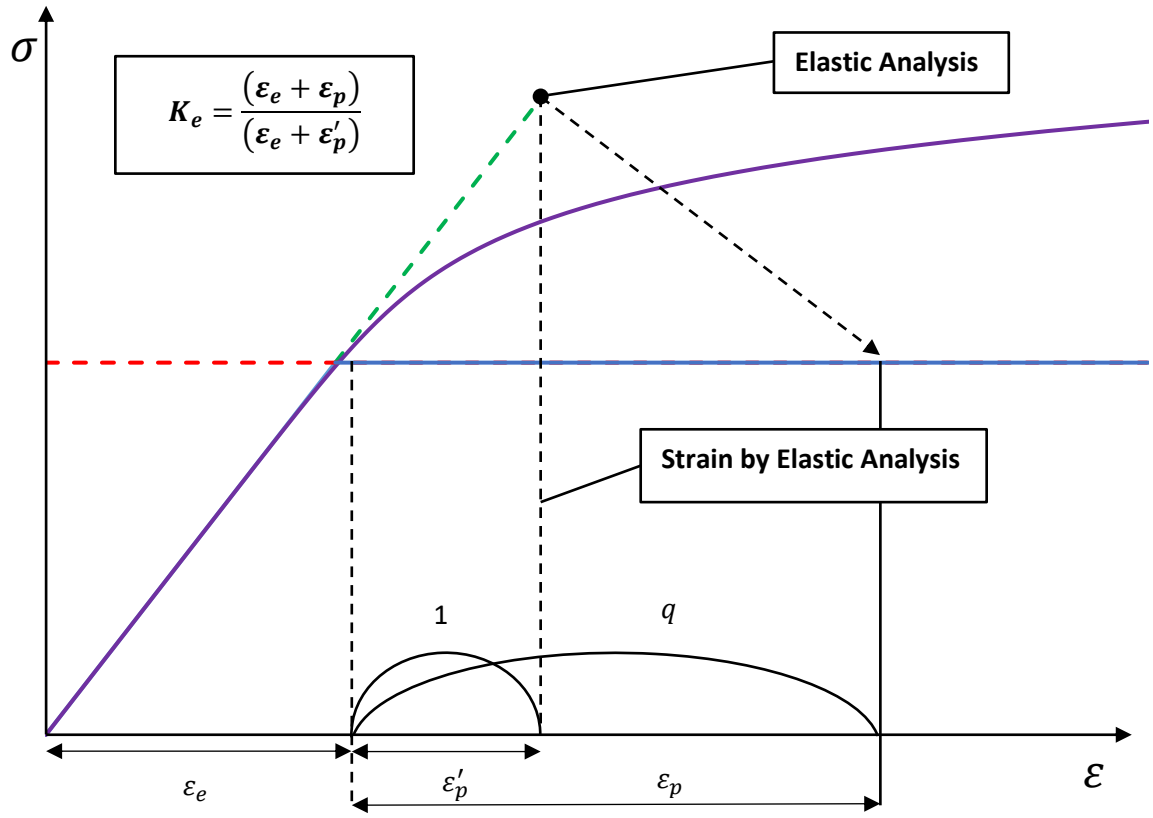

Figure 29. Illustration of the TENPES K_e factor based on the JSME FBR Code elastic follow-up model

The current JSME PVB 3315.1 rules utilise both the new TENPES K_e' and MITI 501 $K_{e,A0}$ in the following manner:

Where there is no intersection of the K_e' and $K_{e,A0}$ equations, a tangent line from the point of the $K_{e,A0}$ curve at $S_n/3S_m = 1$ the K_e' curve should be drawn. $K_{e,A0}$ is designed to account for peak strain concentration at $S_n \approx 3S_m$, and whose magnitude is controlled by a parameter, K, defined as the ratio of S_p to S_n. Thus, for cases of high local stresses (e.g. thermal shock stress, notch stress concentration, etc.), K is higher and hence the $K_{e,A0}$ curve is also more conservative in this region, and will intersect higher up the K_e' curve.

The JSME K_e factor is calculated according to Eq. (92), where material-specific parameters, A_0 and B_0 are defined in Table 4. $K < B_0$ describes the case of intersection of K_e' and $K_{e,A0}$, whilst $K \geq B_0$ describes the case of no intersection of K_e' and $K_{e,A0}$.

$$
\begin{aligned}
K_e^{JSME} &= 1.0 + A_0\left(\frac{S_n}{3S_m} - K\right)\ for\ K < B_0\ and\ \frac{S_n}{3S_m} < C_0 \\
&= 1.0 + (q-1)\left(1 - \frac{3S_m}{S_n}\right) for\ K <\ B_0\ and\ \frac{S_n}{3S_m} \geq\ C_0 \\
&= a\frac{S_n}{3S_m} + A_0\left(1 - \frac{1}{K}\right) + 1 - a\ for\ K \geq B_0\ and\ \frac{S_n}{3S_m} < C_1 \\
&= 1 + (q-1)\left(1 - \frac{3S_m}{S_n}\right) for\ K \geq B_0\ and\ \frac{S_n}{3S_m} \geq C_1
\end{aligned}
$$

where

$$
\begin{aligned}
K &= S_p/S_n \\
C_0 &= \left[\left(q + \frac{A_0}{K} - 1\right) - \sqrt{(q + \frac{A_0}{K} - 1)^2 - 4A_0(q-1)}\right]/2A_0 \\
a &= A_0\left(1 - \frac{1}{K}\right) + (q-1) - 2\sqrt{A_0(1 - \frac{1}{K})(q-1)} \\
C_1 &= \left[(q-1) - \sqrt{A_0(1 - \frac{1}{K})(q-1)}\right]/a
\end{aligned}
\qquad (92)
$$

Table 4. Values of q, A_0, and B_0 used in JSME K_e Factor Expressions

Materials	q	A_0	B_0(*1)
Low Alloy Steel	3.1	1.0	1.25
Martensitic Stainless Steel	3.1	1.0	1.25
Carbon Steel	3.1	0.66	2.59
Austenitic Stainless Steel	**3.1**	**0.7**	**2.15**
Nickel-Chromium-Iron	3.1	0.7	2.15

$(*1)\ B_0 = \dfrac{A_0(q-1) + 2A_0\sqrt{A_0(q-1)}}{4A_0(q-1) - (q-1)^2}$

Technical justification for the above expressions is provided by an extensive elastic-plastic FE analysis programme summarised by Asada and Nakamura [122], with verification for basic LWR component FE models including a cylinder, nozzle, thermal sleeve/safe-end, and support skirts. The elastic follow-up factor for the JSME was determined to bound the relationships of the FE-derived K_e vs. S_n for these FE models, and a value of q = 3.1 was obtained; this is very similar to q = 3.0 utilised in the FBR Code and was considered an appropriately conservative bounding value. Figure 30 shows the comparison of the JSME PVB-3315.1 K_e^{JSME} and ASME III

Appendix XIII-3450 $K_e^{XIII-3450}$ vs. S_n/S_m curves for austenitic stainless steels. Different loading conditions are considered by varying the parameter K. As expected, it is observed that the JSME PVB-3315.1 K_e^{JSME} is generally less conservative than ASME III Appendix XIII-3450, with the exception of the discontinuity induced at $S_n = 3S_m$, and S_n slightly greater than $3S_m$ depending on the magnitude of K.

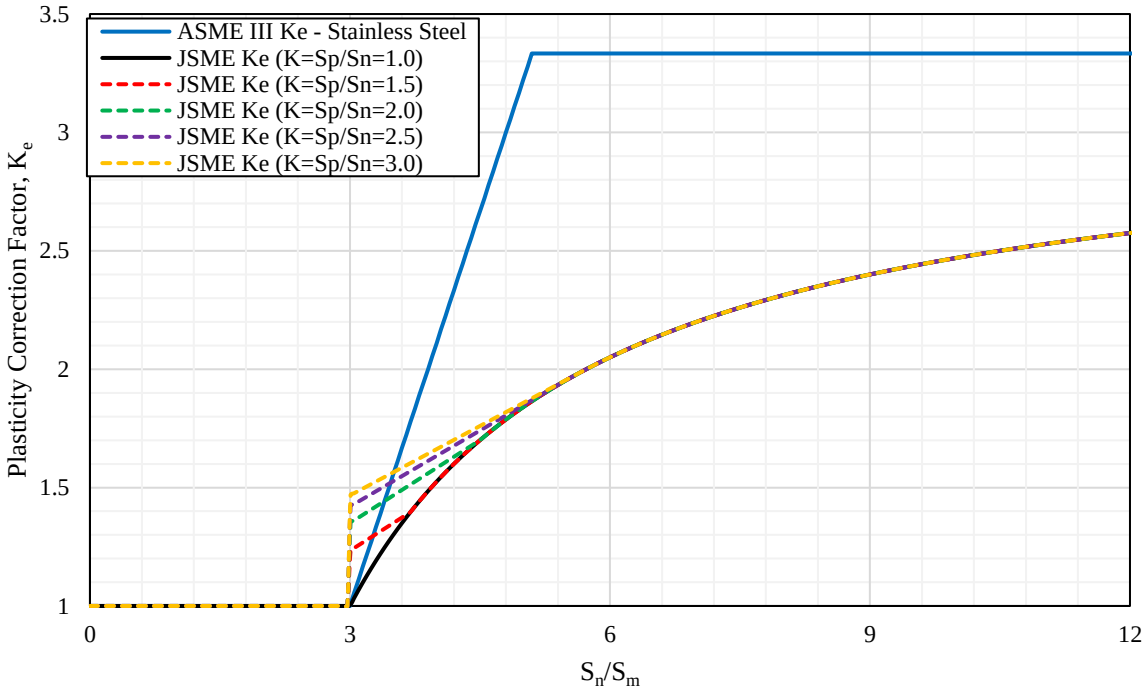

Figure 30. JSME PVB 3315.1 K_e vs S_n/S_m correction curves for austenitic stainless steels

4.4.3. JSME Code Case NC-CC-005 (Japan)

The JSME Code also includes a Code Case entitled NC-CC-005: *Alternative Structural Evaluation Criteria for Class 1 Vessels Based on Elastic-Plastic Finite Element Analysis* [123], which includes expressions for an alternative plasticity correction factor, denoted K_e'' in [123], but referred to as $K_e^{JSME\ CC}$ in this work. The $K_e^{JSME\ CC}$ was also developed by the TENPES committee on Stress Compensated Factor for Simplified Elastic-Plastic Analysis (C-K_e Factor), and is based on the same set of FE models used to derive the JSME PVB-3315.1 K_e^{JSME} factor. $K_e^{JSME\ CC}$ varies as a function of the total stress range, S_p, and can be applied directly on the surface of a component without stress linearisation. The $K_e^{JSME\ CC}$ factor is calculated as follows:

$$K_e^{JSME\ CC} = 1 + (q_p - 1)\left(1 - \frac{1}{S_p/3S_m}\right) \tag{93}$$

where q_p is the elastic follow-up parameter for local plasticity, which is dependent on the ratio of the plastic strain to total strain calculated per the following equation:

$$\begin{aligned} q_p &= (q_1 - q_0)\cdot\left(\frac{\varepsilon_p}{\varepsilon_t}\right) + q_0 = (q_1 - q_0)\cdot\left(\frac{\frac{S_p}{E} - \frac{3S_m}{E}}{\frac{S_p}{E}}\right) + q_0 \\ &= (q_1 - q_0)\cdot\left(1 - \frac{1}{\frac{S_p}{3S_m}}\right) + q_0 \end{aligned} \tag{94}$$

The follow-up sub factors, q_0 and q_1, were selected such that they bound the K_e factors derived from elastic perfectly-plastic FEA for the representative component models discussed in Asada and Nakamura [122]:

$$q_0 = 1.5, q_1 = 4.0 \tag{95}$$

The variation of the $K_e^{JSME\ CC}$ vs. S_n/S_m curve is shown in Figure 31. It is possible for the $K_e^{JSME\ CC}$ to be greater than 1.0 even whilst K_e^{JSME} is equal to 1.0 since K_e^{JSME} assumes that peak strain concentration cannot occur for $S_n < 3S_m$. However, peak strain concentration (i.e. $S_p > 3S_m$) can often occur in such cases in absence of gross section plastic cycling. Therefore, $K_e^{JSME\ CC}$ based on the above values of q_0 and q_1 is very conservative and is always more conservative than K_e^{JSME}. NC-CC-005 recommends that q_p be determined from the actual K_e determined by elastic-plastic analysis, so as to enable derivation of more accurate $K_e^{JSME\ CC}$ expressions for different structures.

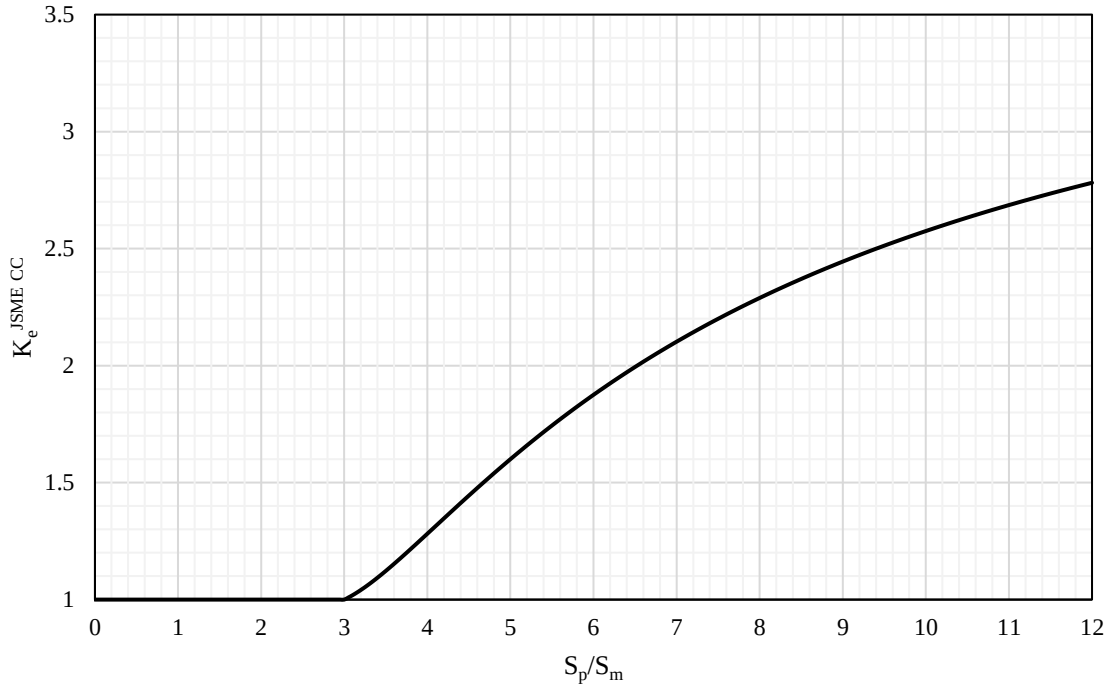

Figure 31.Variation of JSME NC-CC-005 $K_e^{JSME\ CC}$ with S_p / S_m

4.4.4. PNAE G-7-002-86 (Russia)

The Russian Structural Design Standard for Light Water Reactor Plants, PNAE G-7-002-86 [124] (abbreviated PNAEG in this work), contains a unique set of requirements for simplified elastic-plastic fatigue analysis, sharing little similarity to other nuclear codes. Unlike other codes, PNAEG does not directly prescribe a K_e factor, but is instead based on Glinka's approximation of the inelastic strain range [125].

In the *'stress determination procedure'* of PNAEG, if the local stress intensity, σ_L, determined by elastic analysis exceeds the cyclic proportional limit of the material, the stress used in the fatigue analysis, σ_F, to determine the alternating stress amplitude, $\sigma_{aF} = 0.5 \cdot \Delta\sigma_F$, for input to the fatigue curve, is determined per the following formula:

$$\Delta\sigma_F = sign[(\sigma_L)_l - (\sigma_L)_h]\left(2 \cdot R_{pe}^T\right)^{\frac{v-1}{v+1}} \cdot \left\{\frac{1+v}{2}[(\sigma_L)_l - (\sigma_L)_h]^2 + \frac{1-v}{2}\left(2 \cdot R_{pe}^T\right)^2\right\}^{\frac{1}{1+v}} + (\sigma_F)_h \quad (96)$$

where the subscripts l and h denote two points in time where conditions are known to be extreme (with l occurring after h); the *sign()* function is equal to plus-or-minus unity and is used to determine whether l is a maxima ('peak') or minima ('valley') in the stress history; $2R_{pe}^{T}$ is the cyclic yield strength, defined as twice the monotonic proportionality limit stress; ν is the cyclic hardening exponent of the cyclic power-law SSC.

The PNAEG cyclic power-law SSCs are shown in Figure 32 and take the following form:

$$\Delta\sigma = \begin{cases} E^T \cdot \Delta\varepsilon, & if\ \Delta\varepsilon \le 2R_{pe}^T/E^T \\ 2R_{pe}^T \cdot \left(\dfrac{\Delta\varepsilon}{\dfrac{2R_{pe}^T}{E^T}} \right)^{v}, & if\ \Delta\varepsilon > 2R_{pe}^T/E^T \end{cases} \tag{97}$$

$$v = \frac{0.73log_{10}\left[(1 + 1.4 \cdot 10^{-2} \cdot Z^T)\frac{R_m^T}{R_{p,0.2}^T}\right]}{log_{10}\left(\dfrac{2.3log_{10}\dfrac{100}{100 - Z^T}}{2 \cdot 10^{-3} + R_{p,0.2}^T/E^T}\right)} \tag{98}$$

where

$$R_{pe}^T = \left[\frac{R_{p,0.2}^T}{\left(2 \cdot 10^{-3} \cdot E^T + R_{p,0.2}^T\right)^{v}}\right]^{\frac{1}{1-v}} \tag{99}$$

R_m^T = minimum tensile strength at temperature
$R_{p,0.2}^T$ = minimum yield strength at temperature
Z^T = minimum reduction of area (%)
E^T = modulus of elasticity at temperature

The above formulae may be applied provided the following requirement that the absolute magnitude of the range of cyclic surface stress factored by the local stress concentration factor, K_σ, does not exceed four times the cyclic proportional limit stress:

$$\frac{|(\sigma_L)_l - (\sigma_L)_h|}{K_\sigma} \leq 4R_{pe}^T \tag{100}$$

Whilst the PNAEG K_e factor has no explicit definition, an implied K_e factor, denoted K_e^{PNAEG}, can be derived from the quotient of the ranges of the fatigue evaluation stress, $\Delta\sigma_F$, and the local surface stress, $\Delta\sigma_L$.

$$K_e^{PNAEG} = \frac{\Delta\sigma_F}{\Delta\sigma_L} \tag{101}$$

which is equivalent to

$$K_e^{PNAEG} = \left(2 \cdot R_{pe}^T\right)^{\frac{v-1}{v+1}} \cdot \left\{\frac{1+v}{2}[\Delta\sigma_L]^2 + \frac{1-v}{2}\left(2 \cdot R_{pe}^T\right)^2\right\}^{\frac{1}{1+v}} / \Delta\sigma_L \tag{102}$$

The intention of the restriction of $4R_{pe}^T$ on the elastic stress intensity range is not explicitly stated in PNAEG, but the author interprets this to be a restriction against sectional plastic cycling. The PNAEG K_e^{PNAEG} factor is essentially a modified Neuber-type correction, and therefore can only be applied reliably where the global structural response is predominantly elastic. At 300°C, the $4R_{pe}^T$ limit is approximately equal to $4 \cdot 174 = 696$ MPa, which roughly equates to six times the ASME design stress intensity, S_m, at this temperature: $6 \cdot 116 = 696$ MPa. The variation of both parameters remains roughly comparable over a wider range of temperatures. The variation of the K_e^{PNAEG} reformulated in terms of S_n/S_m for different levels of stress concentration factors $K_\sigma = S_p/S_m$ (assuming purely mechanical loading) is shown in Figure 33 along with the associated $6S_m$ limit derived above for stainless steels.

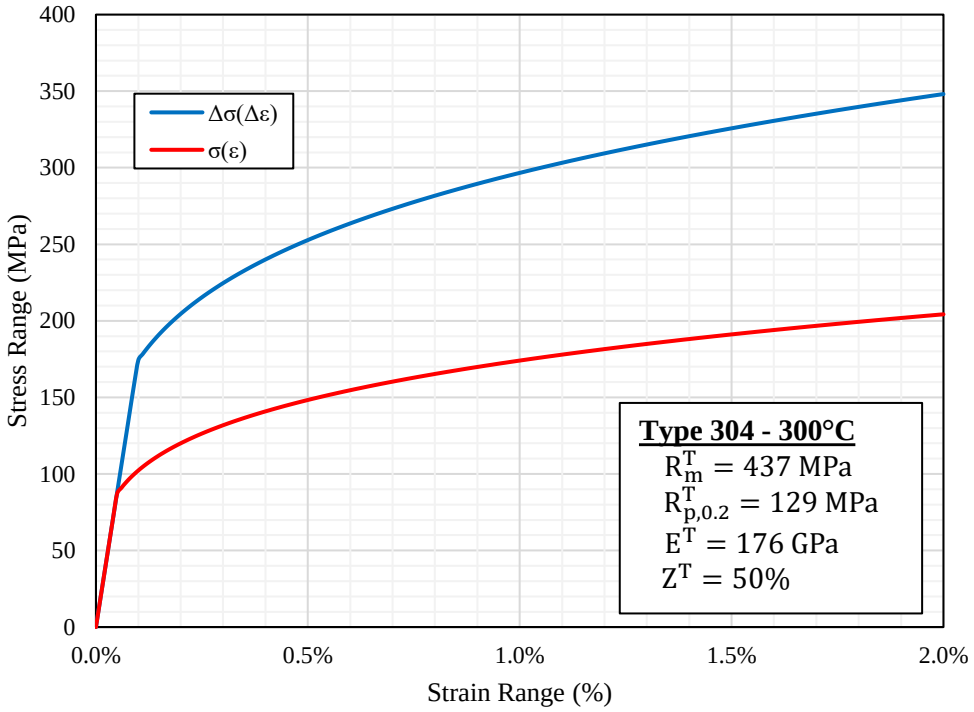

Figure 32. Example elevated temperature static and cyclic SSCs for Type 304 based on PNAEG power-law stress-strain approximation.

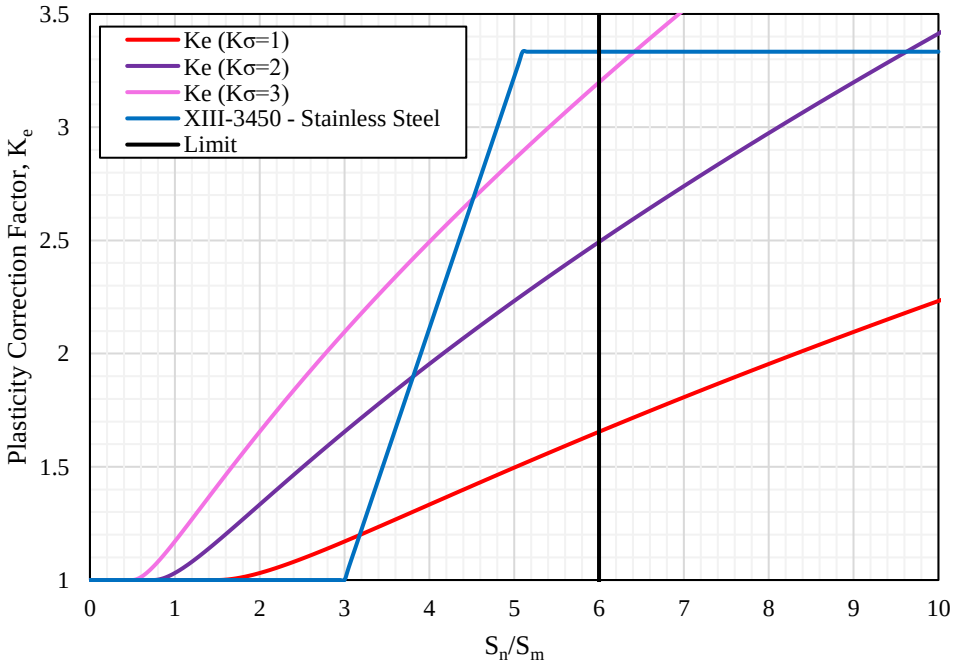

Figure 33. Comparison of ASME III Appendix XIII-3450 K_e and PNAEG K_e for austenitic stainless steels.

4.4.5. R5: Assessment Procedures for the High Temperature Response of Structures (UK)

The UK R5 assessment procedure [126] comprise five volumes for assessing the operating life of components operating in the high temperature creep regime, and have commonly been applied to the integrity assessment of components of the Advanced Gas-Cooled Reactor (AGR). Volumes 2 and 3 relate to the assessment of creep-fatigue crack initiation in defect-free structures, which are considered as a single volume ('V2/3' for reference). V2/3 contains a number of novel procedures, including a generalised methodology for cyclic stress-strain hysteresis loop construction for complex non-isothermal cycles with intermittent creep dwell periods; this methodology is summarised in R5 V2/3 Appendix A7 *Enhancement of Strain Range due to Plasticity and Creep* [127].

The R5 strain enhancement methodology is based on a uniaxial Neuber correction and accounts for both plasticity and creep relaxation by integration of forward creep. The procedure assumes a von Mises yield criterion. Creep is insignificant for LWR plants as their maximum operating temperature is generally restricted to around 325°C. The clauses of A7.3 *Enhancement of Strain Range where Creep is Negligible* are therefore applicable, and the elastically calculated strain range, $\Delta\varepsilon_e$, is enhanced by superposition of two additional terms to give the total strain range, $\Delta\varepsilon_t$:

$$\Delta\varepsilon = \Delta\varepsilon_e + \Delta\varepsilon_p + \Delta\varepsilon_v \tag{103}$$

where $\Delta\varepsilon_p$ is the enhancement due to plasticity, and $\Delta\varepsilon_v$ is the enhancement due to the transition towards constant volume deformation in the plastic regime. The term $\Delta\varepsilon_p$ is estimated for the maximum extension of the linear portion of the cyclic curve, $\Delta\varepsilon_e = \Delta\varepsilon_{e,max}$, by constructing the Neuber hyperbola, shown in Figure 34, which passes through this point:

$$\Delta\sigma\Delta\varepsilon = \Delta\sigma^e\Delta\varepsilon^e \tag{104}$$

The intersection of the Neuber hyperbola with the modified R-O expression of Eq. (105) identifies the plastic strain enhancement, $\Delta\varepsilon_p$:

$$\Delta\varepsilon = \frac{\Delta\sigma}{\bar{E}} + \left(\frac{\Delta\sigma}{A}\right)^{1/\beta} \tag{105}$$

where $\bar{E} = 3E/(2(1+v))$, and A and β are the cyclic R-O parameters provided in R5 V2/3 Section 5.

In R5, the definition of equivalent von Mises strain assumes a plastic value of Poisson's ratio of ν = 0.5, irrespective of whether the material behaviour is elastic or plastic. Therefore, under elastic conditions, the R5 definition of equivalent strain predicts a smaller strain range than that calculated assuming an elastic Poisson's ratio of ν = 0.3. Considering the case of a uniaxial elastic state of stress, σ_1, the elastic von Mises equivalent strain is simply equal to ε_1, whereas the plastic expression used in R5 is equal to $[2(1+\nu)/3]\varepsilon_1$. Thus, the R5 expression is not correct under elastic conditions. This is addressed by substitution of $\bar{E}$ in place of E in the R-O form of Eq. (105). The factor of 3/2(1+ν) is simply the ratio of the numerical factors used in the definitions of von Mises elastic and plastic equivalent strains respectively, and its purpose is to correct the elastic R-O term to be consistent with the R5 definition of equivalent strain.

The enhancement $\Delta\varepsilon_v$ accounts for the increase in the effective Poisson's ratio, ν^*, due to plastic deformation and is estimated in R5 by Eq. (106):

$$\Delta\varepsilon_v = (K_v - 1)\Delta\varepsilon_e \tag{106}$$

where

$$K_v = \frac{(1+v^*)(1-v)}{(1+v)(1-v^*)} \tag{107}$$

and

$$v^* = v\frac{E_s}{\bar{E}} + 0.5\left(1 - \frac{E_s}{\bar{E}}\right) \tag{108}$$

In the R5 methodology, the equivalent strain range is calculated based on the von Mises combination of the strain component ranges between the extreme peak-valley points of the cycle.

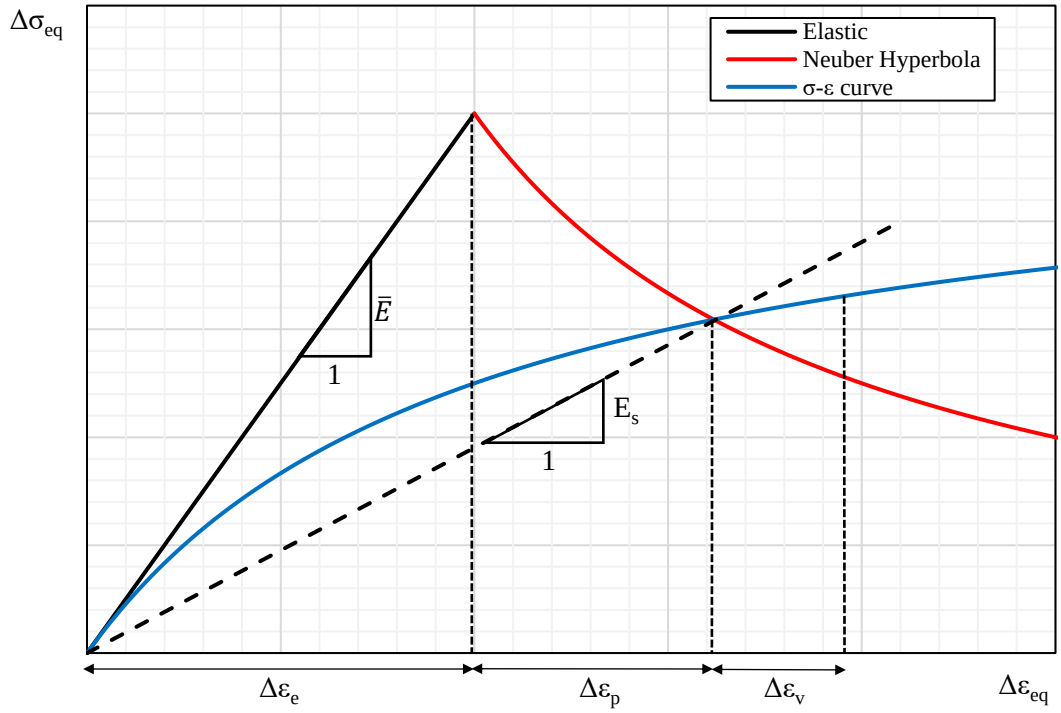

Figure 34. R5 V2/3 Generalised Neuber Methodology for strain enhancement in absence of creep.

4.5. Alternative Methods Proposed By Industry

4.5.1. Ranganath's Method

In 2016, Sam Ranganath of the Electric Power Research Institute (EPRI) proposed a new K_e factor methodology for application to ASME III NB-3200 and NB-3600 assessments of vessel and piping components. Ranganath's approach is similar to that taken in WRC-361, albeit with some important practical modifications, which were outlined in a recent paper presented at the ASME 2017 Pressure Vessels and Piping Conference [128]. Ragnanath's proposed K_e factor, denoted K_e^R in this work, was originally derived based on the weighted-average K_e expression presented in WRC-361:

$$K_e^R = K_{th}^R \frac{S_n^{therm}}{S_n} + K_e \frac{S_n^{mech}}{S_n} \tag{109}$$

The thermal bending stress, $S_{n,tb}$, arising from a linear through-wall temperature gradient, is determined by decomposing S_n:

$$S_{n,tb} = S_n - S_{n-tb} \tag{110}$$

To retain a degree of conservatism, it may then be assumed that any remaining contribution to S_n, including the thermal membrane stress range, $S_{n,tm}$, is classified as arising from mechanical loading, and hence:

$$S_n^{mech} = S_n - S_{n,tb} \tag{111}$$

Thus,

$$K_e^R = K_{th}^R \frac{S_{n,tb}}{S_n} + K_e \frac{S_n - S_{n,tb}}{S_n} \tag{112}$$

The ratio of S_{n-tb} to S_n is defined by a parameter, *R*:

$$R = \frac{S_{n-tb}}{S_n} \tag{113}$$

Therefore,

$$1 - R = 1 - \frac{S_{n-tb}}{S_n} = \frac{S_{n,tb}}{S_n} \tag{114}$$

For fully plastic material behaviour, the Poisson's ratio correction factor, K_{th}^R, has a maximum value of 1.4 based on the assumption of an equi-biaxial state of stress. By setting K_{th}^R conservatively to this maximum value, the following expressions were derived for K_e^R:

$$K_e^R = 1.0 \; for \; S_n \leq 3S_m \tag{115}$$

$$K_e^R = 1.4\frac{S_{n,tb}}{S_n} + K_e \frac{S_n - S_{n,tb}}{S_n} \; for \; 3S_m \leq S_n \leq 3mS_m \tag{116}$$

$$OR$$

$$K_e^R = 1.4(1 - R) + K_e R \; for \; 3S_m \leq S_n \leq 3mS_m \tag{117}$$

To eliminate the step change that results for $S_n = 3S_m$, the authors of [128] proposed the following modification:

$$K_e^R = min\{K_e, 1.4(1 - R) + K_e R\} \; for \; 3S_m < S_n < 3mS_m \tag{118}$$

The maximum value of K_e^R is achieved for $S_n = 3mS_m$ (i.e. $5.1S_m$ for austenitic stainless steels). The Appendix XIII-3450 K_e factor also reaches its maximum value of $1/n$ for $S_n = 3mS_m$. Substituting for $K_e = 1/n$, the following expression is obtained for the maximum K_e^R:

$$K_e^R = \left[1.4 + \left(\frac{1}{n} - 1.4\right)R\right] \; for \; S_n \geq 3mS_m \tag{119}$$

For $3S_m < S_n < 3mS_m$, the value of K_e^R depends on the magnitude of $S_{n\text{-}tb}$. As ASME III Appendix XIII-3450 (a) requires that $S_{n\text{-}tb}$ remains strictly less than $3S_m$ (Eq. (64)), a spectrum of K_e^R may apply between the two limiting conditions of $S_{n\text{-}tb} = 0$ (i.e. S_n is purely thermal bending) and $S_{n\text{-}tb} = 3S_m$.

In their original proposed K_e^R formulation, Ranganath and Palm [128], [129] explicitly rejected the inclusion of a notch factor, K_n^R. This was justified based on the results of elastic-plastic FE analysis performed for a series of component geometries including notches ranging from K_T = 1.6 to 3.0 The K_e^R factor alone was sufficiently conservative to bound the elastic-plastic FE results for these cases. However, based on a parametric study presented by Reinhardt [130], it was noted that the K_e^R factor has the potential to be non-conservative for notch effects combined with significant thermal bending. The proposed K_e^R methodology was presented to the ASME III Code Working Groups on Design Methodology (WGDM) and Fatigue Strength (WGFS) as a draft Code Case (Record 17-225), and the question of whether to include K_n^R was discussed extensively. Generally, the WGDM and WGFS members felt that excluding the notch factor would result in too much reduction in conservatism and therefore Record 17-225 was revised to explicitly include K_n^R [131]. Additionally, in a subsequent revision to the approach, a modified R parameter, R^*, was introduced to be applied in place of R for S_n exceeding $3mS_m$. The final form of K_e^R proposed within Record 17-225 [132] for application to NB-3200 vessels is shown by Eq. (120).

$$K_e^R = \begin{cases} 1.0 \; if \; S_n \leq 3S_m \\ \min[K_e R + 1.4(1-R)K_n^R, K_e] \; if \; 3S_m < S_n \leq 3mS_m \\ \min\left[K_e R^* + 1.4(1-R^*)K_n^R, \frac{1}{n}\right] if \; S_n > 3mS_m \end{cases} \tag{120}$$

where $R^* = \frac{S_{n-tb}}{3mS_m}$ and $K_n^R = K_T^{\frac{1-n}{1+n}}$ as proposed in WRC-361 [110].

Figure 35 shows Ranganath's proposed K_e^R factor vs. S_n/S_m for varying values of R (or $S_{n\text{-}tb}/S_n$) for austenitic stainless steels. As shown, when S_n is composed of pure thermal bending (i.e. R = 0), the maximum penalty factor of $K_e^R = K_{th}^R = 1.4$ is applied to account for Poisson's ratio effects only. Otherwise, the value of K_e^R varies according to the relative contribution of mechanical and thermal membrane stresses to S_n, and eventually becomes equal to the Appendix XIII-3450 K_e factor. As the relative contribution of $S_{n\text{-}tb}$ increases (i.e. R: 0→1), K_e^R increases more sharply and intersects $K_e^{XIII\text{-}3450}$ at a lower threshold value of S_n/S_m. In the situation where S_n is composed entirely of mechanical and/or thermal membrane stresses (i.e. R = 1), K_e^R becomes equivalent to $K_e^{XIII\text{-}3450}$.

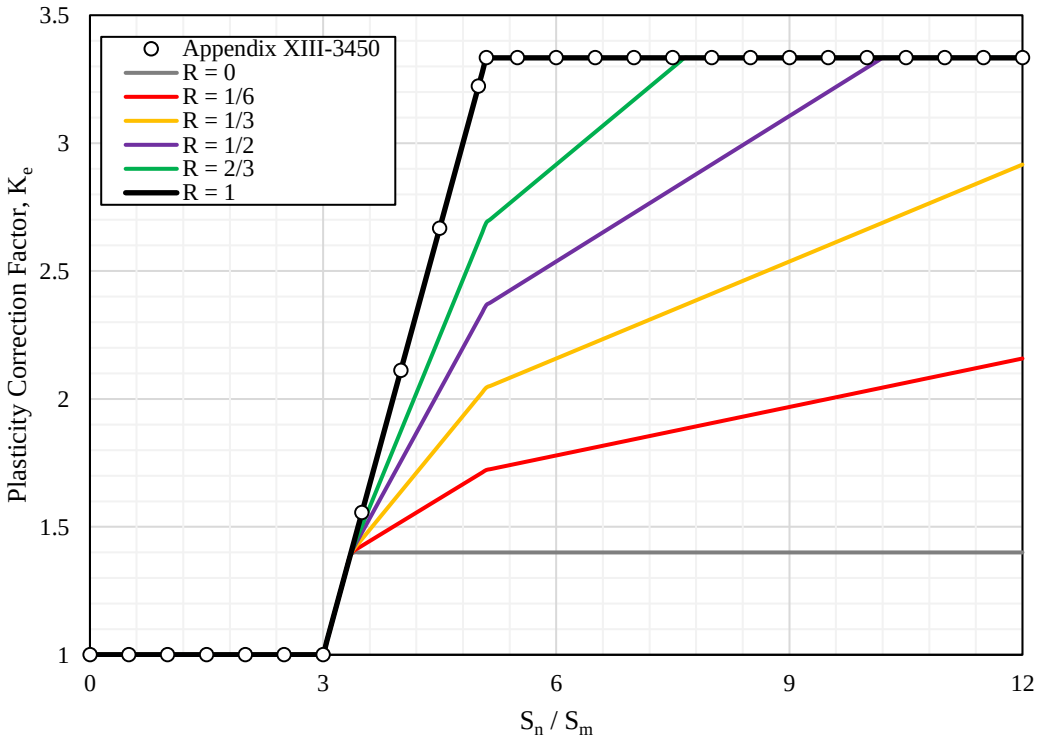

Figure 35. Ranganath's proposed K_e^R factor for austenitic stainless steels as a function of S_n/S_m and R ($S_{n\text{-}tb}/S_n$).

Whilst Record 17-225 provides no explicit guidance on the application of K_n^R, the presentation by Ranganath and Palm at the NRC Public Meeting on Fatigue Research in June 2016 included some early discussion on situations where K_n^R is to be applied.

In the proposal included in the presentation (see [129]), K_n^R was assumed to be constant and equal to unity for $S_n < 3S_m$; in other words, no additional notch strain concentration factor is to be applied over and above K_T in such cases. Where $S_n \geq 3S_m$, K_n^R is assumed to vary linearly from 1.0 at $S_n = 3S_m$ to K_n^R at $S_n \geq 3mS_m$. This may be expressed formulaically by Eq. (121).

$$K_n^R = \begin{cases} 1.0 & if\ S_n \leq 3S_m \\ 1.0 + \dfrac{K_T^{\frac{1-n}{1+n}} - 1}{\dfrac{S_n}{3S_m} - 1} \cdot \dfrac{S_n}{(3S_m)} & if\ 3S_m < S_n \leq 3mS_m \\ K_T^{\frac{1-n}{1+n}} & if\ S_n > 3mS_m \end{cases} \quad (121)$$

It is not known whether this proposed approach is still favoured or whether an outright correction based on the full value of K_n^R is to be applied for any $S_n \geq 3S_m$ at local discontinuities; ultimately, this may be a matter of engineering judgement on the part of the analyst.

As of May 2020, Record 17-225 has received approval from the ASME BNCS and is expected to be published as an ASME Section III Code Case in the near future.

4.5.2. Rolls-Royce: Unified Correction Factor, F_u

Emslie et al of Rolls-Royce presented a comparison of Code K_e factors with results obtained from elastic-plastic finite element analysis for different component geometries [133]: the stepped pipe described by Jones et al [134], a PWR valve, and a PWR nozzle thermal sleeve. Environmental effects were not considered in the study. The results showed that the ASME III XIII-3450 K_e factor produced the lowest number of allowable cycles for thermal cycling, but also has the potential to produce non-conservative fatigue usage predictions for cases where the $S_n \approx 3S_m$. Emslie et al also highlighted a number of practical issues that make application of CC N-779 difficult. In particular, separate FE models must be run in order to evaluate $K_e^{N\text{-}779}$, which can be rather time consuming and potentially increase the probability of calculation errors.

Emslie et al proposed an alternative 'unified' correction factor based on their elastic-plastic FE results. The concept of the unified approach is to account for the effects of both surface and sectional plasticity using a single expression. The ASME III XIII-

3450 K_e factor expressions do not distinguish between surface and sectional plasticity, and consequently there is a discontinuity between surface and sectional plasticity at the $S_n \approx 3S_m$ region. The proposed unified correction factor, F_u, is partially based on the RCC-M K_e^{ther} expression, and is dependent on the local thermal stress range, $S_{p,lt}$, and the linearised stress range, S_n. The authors also argued that the unified correction factor should apply in either case of sectional or surface plasticity. The unified correction factor, F_u, multiplied to the alternating stress amplitude per Eq. (122), is defined as the product of two sub factors, F_{lt} and F_n, expressed by Eqs. (123) and (124), which are intended to address surface and sectional plasticity, respectively. The variation of F_{lt} and F_n as a function of $S_{p,lt}$ and S_n is shown in Figure 36.

$$S_{alt} = S_a F_u = S_a F_{lt}(S_{lt}) F_n(S_n) \tag{122}$$

where

$$F_{lt} = 0.05 + 1.2\left(\frac{S_{p,lt}}{3S_m}\right)^{0.11} \tag{123}$$

$$F_n = \begin{cases} 1 & S_n < 3S_m \\ \left(\frac{S_n}{3S_m}\right)^{0.12} & S_n \geq 3S_m \end{cases} \tag{124}$$

Emslie et al proposed that the local thermal stress, $S_{p,lt}$, should be calculated by linearising the through-wall temperature distribution along the SCL. The linearised temperature, T_{linear}, can then be subtracted from the surface temperature, T_{surf}, to obtain the non-linear portion of the temperature distribution, T_{nl}; this is a purely mathematical concept with T_{nl} possessing the opposite sign to that of T_{surf} and T_{linear}. The local thermal stress is then determined analytically from the following expression:

$$\sigma_{lt} = \frac{E\alpha\left(T_{surf} - T_{linear}\right)}{1 - v} \tag{125}$$

Emslie et al argue that this simplified calculation allows the local thermal stresses to be assessed without having to run a separate thermal stress analysis, adding to the practicality of the F_u factor procedure. However, a separate thermal stress analysis is still required to satisfy the requirement of Appendix XIII-3450 (a), and so the cost savings associated with this procedure are not thought to be altogether that significant. As the empirical formulae underpinning the F_u factor were derived based on thermal

loading applied to plane unnotched specimens, further work may be required to ensure that the F_u factor approach is fit for application to a wider range of geometries and load cases.

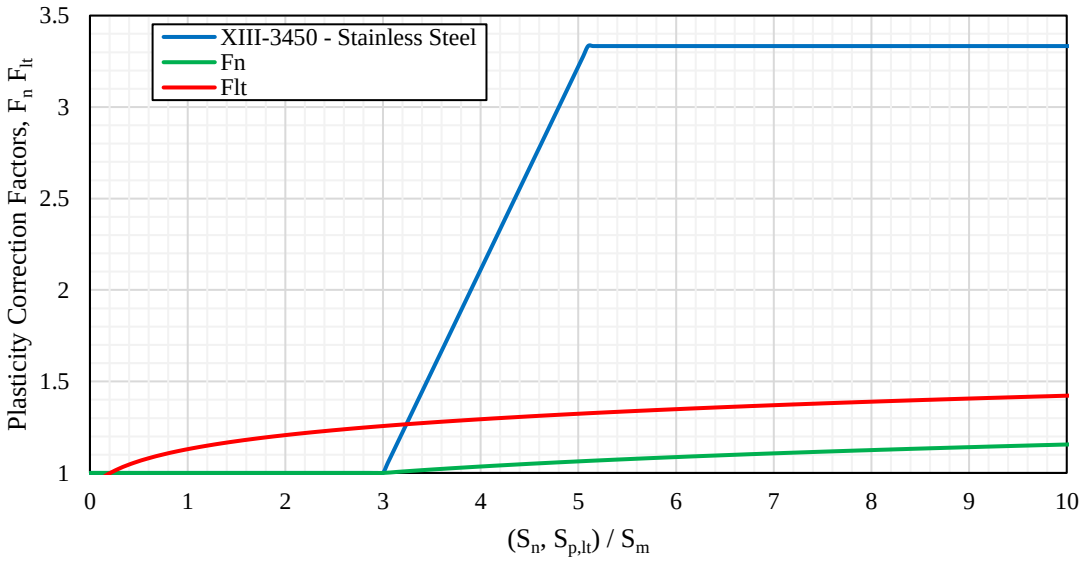

Figure 36. Rolls-Royce proposed F_{lt} and F_n correction factors as a function of ($S_{p,lt}$, S_n)/S_m

4.6. Simplified Elastic-Plastic Analysis in Non-Nuclear Design Codes

Rules for application of simplified elastic-plastic analysis are contained in several non-nuclear design codes. In particular, ASME Section VIII, Division 2 [135] and the European EN-13445 Code [136] contain rules for simplified elastic-plastic analysis that, whilst originally based on ASME Section III, have undergone significant development since their inception. An overview of the simplified elastic-plastic methodologies of both ASME VIII, Division 2 and EN-13445 Annex 18 is provided in this section. Where appropriate, the nomenclature used in these codes has been adapted to be consistent with the terminology adopted in this thesis.

4.6.1. ASME Section VIII, Division 2: Alternative Rules

4.6.1.1. Section 5, Subsection 5.5.3

The ASME Section VIII, Div. 2 elastic fatigue design-by-analysis requirements are outlined in Section 5, Subsection 5.5.3. *Fatigue Assessment – Elastic Stress Analysis and Equivalent Stresses* [135]. A systematic overview of the assessment procedure is

presented in Subarticle 5.5.3.2. In particular, Step 4 requires that the effective alternating stress amplitude, used as input to the fatigue curve for each counted cycle be calculated according to the following expression:

$$S_{alt} = \frac{K_f \cdot K_e^{VIII-2} \cdot S_{p-lt} + K_v^{VIII-2} \cdot S_{p,lt}}{2} \tag{126}$$

where S_p is determined according to the von Mises criterion in ASME VIII, Div. 2.

$$S_p = \frac{1}{\sqrt{2}}\Big[\left(\Delta\sigma_{11,k} - \Delta\sigma_{22,k}\right)^2 + \left(\Delta\sigma_{22,k} - \Delta\sigma_{33,k}\right)^2 + \left(\Delta\sigma_{33,k} - \Delta\sigma_{11,k}\right)^2 + 6\left(\Delta\sigma_{12,k}^2 + \Delta\sigma_{13,k}^2 + \Delta\sigma_{23,k}^2\right)\Big]^{0.5} \tag{127}$$

K_f is a fatigue strength reduction factor introduced to account for any local detail such as a notch or weld, not modelled explicitly, that may act as a local stress raiser. If the local detail has been included in the numerical model, then K_f =1.0.

The Subsection 5.5.3 fatigue penalty factor, denoted K_e^{VIII-2} in this work, is evaluated according to Eq. (128) and is essentially equivalent to ASME III Appendix XIII-3450, with the only difference being that S_n is calculated based on von Mises theory in the former, and Tresca theory in the latter.

$$K_e^{VIII-2} = \begin{cases} 1.0 \;\; for\; S_n \le S_{PS} & if\; S_n \le S_{PS} \\ 1.0 + \dfrac{(1-n)}{n(m-1)}\left(\dfrac{S_n}{S_{PS}} - 1\right) & if\; S_{PS} < S_n < mS_{PS} \\ \dfrac{1}{n} & if\; S_n \ge S_{PS} \end{cases} \tag{128}$$

S_{PS} is the limiting value of S_n beyond which K_e must apply in ASME VIII, Div. 2. In this thesis, S_{PS} is assumed equivalent to $3S_m$.

K_e is multiplied to the von Mises stress intensity range less the contribution of local thermal stresses, $S_{p\text{-}lt}$. Thus, where thermal loading is dominant, the influence of K_e on the resulting magnitude of S_{alt} is greatly diminished.

The Poisson's ratio correction factor, K_v, is evaluated according to the following expression:

$$K_v^{VIII-2} = \left(\frac{1-v}{1-v^*}\right) \tag{129}$$

where ν^* is the effective Poisson's ratio calculated in an equivalent manner to ASME III Appendix XIII-2500.

$$v^* = max\left[0.5 - 0.2\frac{S_y}{S_a}, v\right] \tag{130}$$

K_v is applied only to $S_{p,lt}$, and tends to a maximum value of 1.4 as $\nu^* \rightarrow 0.5$.

The provisions of Subsection 5.5.3 are relatively straightforward to apply, and only extends beyond that of ASME III, Appendix XIII-3450 in so far as allowing local thermal stresses to be addressed separately. Alternatively, it is also permitted that K_e^{VIII-2} can instead be multiplied to S_p only, excluding any consideration of K_v, which is a more conservative option.

4.6.1.2. Section 5, Annex 5-C

Annex 5-C: *Alternative Plasticity Adjustment Factors and Effective Alternating Stress for Elastic Fatigue Analysis* [137] contains alternative procedures for the determination of PCFs for use in a Section 5 Fatigue Assessment. The procedure of Annex 5-C is more detailed than Subsection 5.5.3 and requires calculation of both $S_{n,tb}$ and $S_{p,lt}$. The plasticity-adjusted alternating stress per Annex 5C is determined according to Eq. (131)

$$S_{alt} = \frac{1}{2}\left[K_{nl}^{5C} S_{p-tb-lt} + K_v^{5C} S_{p,lt} + K_v^{5C} K_{np}^{5C} S_{n,tb}\right] \tag{131}$$

where K_{nl}^{5C} is the non-local plastic strain redistribution factor, and is equivalent to the K_e^{VIII-2} expressed by Eq. (128); K_v^{5C} is a Poisson's ratio correction factor defined by Eq. (132), and varies as a function of $S_{p,lt}$ and $S_{n,tb}$:

$$K_v^{5C} = \begin{cases} 1.0 \; if \; S_p \leq S_{PS} \\ 0.6\left[\dfrac{\left(S_p - S_{PS}\right)}{S_{n,lt+tb}}\right] + 1.0 \;\; if \; S_p > S_{PS} \; and \; S_{n,lt+tb} > \left(S_p - S_{PS}\right) \\ 1.6 \;\; if \;\; S_p > S_{PS} \; and \; S_{n,lt+tb} \leq \left(S_p - S_{PS}\right) \end{cases} \tag{132}$$

K_{np}^{5C} is a notch plasticity adjustment factor defined by Eq. (133) to account for local strain concentration due to thermal plastic notch effects:

$$K_{np}^{5C} = \begin{cases} 1.0 & if\ S_{p-lt} \leq S_{PS} \\ min[K_1, K_2] & if\ S_{p-lt} > S_{PS} \end{cases} \quad (133)$$

where

$$K_1 = \left[\left(\frac{S_{p-lt}}{S_n}\right)^{\left(\frac{1-n}{1+n}\right)} - 1.0\right] \cdot \left[\frac{S_{p-lt} - S_{PS}}{S_{p-lt}}\right] + 1.0 \quad (134)$$

$$K_2 = \frac{K_{nl}^{5C}}{K_v^{5C}} \quad (135)$$

If the effect of local stress raising features has been captured sufficiently within the FE model, then a K_{np}^{5C} equal to unity is applicable.

Whilst expressed in a somewhat different manner, the Annex 5-C methodology is very similar to CC N-779, and both approaches are readily comparable. Two key differences are however noteworthy. First, as with Section 5.5.3, Annex 5-C is based on the von Mises theory whilst CC N-779 is based on Tresca theory. The second and more important difference relates to the formulation of the Poisson's ratio correction factor. $K_v^{N\text{-}779}$ tends asymptotically to a maximum of 1.4, which is consistent with the Tresca and von Mises analytical solutions outlined in 4.3.1.1 assuming a consistent definition of ν^*. On the other hand, K_v^{5C} tends asymptotically to a maximum of 1.6, which appears to be more aligned with the solution for K_v proposed by Moulin and Roche (Eq. (83)) [112]. Therefore, Annex 5-C is expected to be more conservative than CC N-779. From a practical perspective, Annex 5-C shares the same limitations as CC N-779 and is difficult to apply reliably without programming methods.

4.6.2. EN-13445 Annex 18

The European standard EN-13445 *"Unfired Pressure Vessels"*, *Part 3* includes a detailed fatigue assessment procedure (denoted the *F-Check*) in Annex 18 [138].

The *F-Check* of EN-13445 differs from the nuclear codified rules considered, since it contains two separate approaches for welded and un-welded assessment locations. The approach for weldments differs considerably from ASME Section III, as it is based on the structural hot spot stress approach [139]. Despite this fundamental difference, the PCFs prescribed for welded and un-welded locations are equivalent. Annex 18

provides expressions for two correction factors, denoted K_e^{EN} and K_v^{EN} in this work. The application of these corrections is dependent on whether the fatigue cycle consists of mechanical, thermal, or combined thermal-mechanical loads. The K_e^{EN} factor applies to the stress range attributed to mechanical loads, S_p^{mech}, and is expressed by Eq. (136):

$$K_e^{EN} = 1 + A_0 \left[\frac{\Delta\sigma_l}{2\sigma_{y,0.2\%}} - 1 \right] \; for \; S_n > 2\sigma_{y,0.2\%} \tag{136}$$

where $\sigma_{y,0.2\%}$ is the 0.2% proof stress, and A_0 is a material-specific parameter which varies as a function of ultimate tensile strength, σ_u. For austenitic stainless steels, A_0 = 0.4 is applicable.

$$A_0 = \begin{cases} 0.5 \; for \; 800 \; MPa \leq \sigma_u \leq 1000 \; MPa \\ 0.4 \; for \; \sigma_u \leq 500 \; MPa \\ 0.4 + \left[\frac{\sigma_u - 500}{3000} \right] \; for \; 500 \; MPa \; \leq \sigma_u < 800 \; MPa \end{cases} \tag{137}$$

K_v^{EN} is the correction applied to the stress range attributed to thermal loads, S_p^{ther}, and expressed by Eq. (138):

$$K_v^{EN} = \frac{0.7}{0.5 + \frac{0.4}{\left[\frac{S_n}{\sigma_{y,0.2\%}} \right]}} \; for \; S_n > 2\sigma_{y,0.2\%} \tag{138}$$

S_{alt} is determined from linear superposition of the mechanical and thermal component stress ranges, accounting for the effects of plasticity and any local stress concentration at the assessment location:

$$S_{alt} = \frac{1}{2} K_T [K_e^{EN} S_n^{mech} + K_v^{EN} S_n^{ther}] \; or \; \frac{1}{2} \left[K_e^{EN} S_p^{mech} + K_v^{EN} S_p^{ther} \right] \tag{139}$$

Overall, the methodology of EN-13445 Annex 18 is quite similar to RCC-M B-3234.6 as it relies on partitioning of S_p and S_n into mechanical and thermal contributions. However, one important difference is that the thermal-plastic correction factor, K_v^{EN}, applies only when S_n exceeds the elastic range of $2R_{p,\,0.2}$, unlike the RCC-M K_e^{ther}, which applies even under elastic conditions.

4.6.3. AD 2000-Merkblatt

The AD 2000-Merkblätter are prepared by seven associations who together form the *"Arbeitsgemeinschaft Druckbehälter"* (AD). The AD 2000-Merkblatt contains safety requirements applicable to the design and construction of conventional power plant pressure vessels entering service in Germany. The structure of AD 2000-Merkblatt is similar to that of EN-13445 since the latter is partially based on the former.

Organised within 'Special Cases', *AD 2000-Merkblatt S2 – Analysis for Cyclic Loading* [140] prescribes rules for detailed fatigue assessment applicable to pressure retaining components fabricated from ferritic and austenitic alloys. Section 6 – *Principal Equivalent Stress Range for Elastic-Plastic Conditions* provides two PCFs, denoted K_e^{MB} and K_v^{MB} in this thesis, which are applicable when S_p exceeds the elastic range of $2\sigma_{y,0.2\%}$. AD 2000-Merkblatt permits the use of either Tresca or von Mises theory for determination of S_p. Section 6.1 describes the case of purely mechanical loading, and requires that S_p be multiplied by K_e^{MB} defined in the range $1.0 \leq S_p/\sigma_{y,0.2\%} \leq 1.5$ by Eq. (140)

$$K_e^{MB} = A_1 \cdot \sqrt{\frac{0.5 \cdot S_p}{\sigma_{y,0,2\%}} - 1} + 1 \tag{140}$$

and in the range $S_p/\sigma_{y,0.2\%} > 1.5$ by Eq. (141).

$$K_e^{MB} = A_2 + A_3 \cdot \frac{0.5 \cdot S_p}{\sigma_{y,0.2\%}} \tag{141}$$

The values of A_1, A_2, and A_3 are dependent on σ_u and are summarised in Table 3. Section 6.2 describes the case of purely thermal loads acting *"through the material thickness"* where S_p is instead multiplied by K_v^{MB}, which is expressed by Eq. (142).

$$K_v^{MB} = \frac{0.7}{0.5 + \frac{0.2}{(0.5 \cdot S_p)/\sigma_{y,0.2\%}}} \tag{142}$$

The K_v^{MB} factor is actually equivalent to K_v^{EN}, but varies as a function of S_p rather than S_n. In the case of local discontinuities, K_e^{MB} is to be applied in place of K_v^{MB} even under purely thermal loading, and is to be used when assessing thermal loads that differ from the above description.

Section 6.3 describes the case of combined thermal-mechanical loading, wherein S_p is multiplied by K_e^{MB} without separating the thermal and mechanical stresses. Thus, AD 2000-Merkblatt S2 adopts a more conservative approach than EN-13445 Annex 18 for combined loading. The variation of K_e^{MB} and K_v^{MB} as a function of $S_a/\sigma_{y,0.2\%}$ is shown by Figure 37. It is noted that AD 2000-Merkblatt S2 methodology does not require stress linearisation, since the above expressions demand only S_p. This is viewed as significant practical advantage compared to EN-13445 Annex 18.

Table 5. Values of material parameters, A_1, A_2, and A_3 in AD 2000-Merkblatt S2

Material Type	A_1	A_2	A_3
Ferritic, $\sigma_u = 800 - 1000\ MPa$	0.518	0.718	0.432
Ferritic, $\sigma_u \leq 500\ MPa$ and Austenitic SS	0.443	0.823	0.327

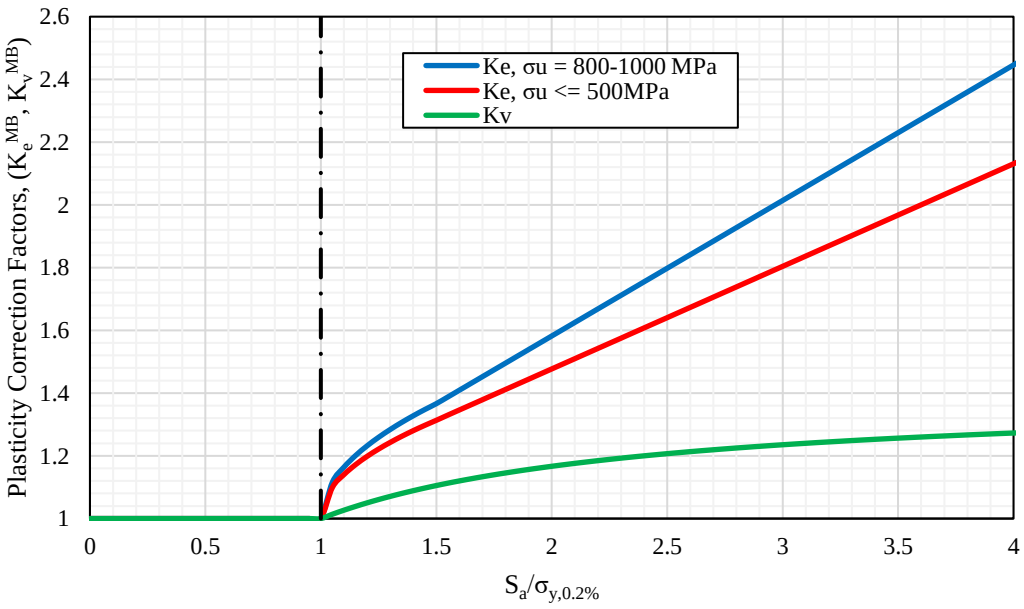

Figure 37. Variation of AD 2000-Merkblatt K_e^{MB} and K_v^{MB} factors as a function of $S_a/\sigma_{y,0.2\%}$

4.7. Discussion

Following its inception in the 1971 Edition of ASME III, the Appendix XIII-3450 K_e factor has remained unchanged. Shortly thereafter, other nuclear C&S such as the French (RCC-M) and Japanese (JSME) codes also introduced simplified elastic-plastic analysis rules that originally preserved the major features of ASME III Appendix XIII-3450. However, it is clear that today there now exist considerable differences in the methodology and technical basis underpinning the various K_e factors adopted for austenitic stainless steels in both nuclear and non-nuclear C&S, which have largely diverged from Langer's original interpretation of K_e.

These alternative implementations fall into three general categories. One involves separating and categorising stresses, and apply a lower penalty to those attributed to thermal loading, which are largely strain-controlled and whose potential for strain concentration is limited. This is the approach proposed by WRC-361 and is adopted by, amongst others, Code Case N-779 and RCC-M B-3234.6. The second approach is to reduce excess conservatism in the K_e factor for all types of loading but ensuring that the correction is still sufficient to bound the strain predicted by elastic-plastic analysis of realistic component geometries subjected to plant representative transients. This is the approach adopted by JSME PVB-3315.1 and NC-CC-005. The third option is to perform a correction of the local strains based on the well-known Neuber and Glinka relations. The Neuber and Glinka approximation schemes are based respectively on the assumption of equivalent complimentary or total strain energy density between the elastic and elastic-plastic solutions, which may only be valid in certain situations. This is the approach adopted by R5 V2/3 and PNAEG. To distinguish the different characteristics of the various code K_e factors based on elastic DBA, each are classified in Table 6 according to their basic requirements.

The accuracy or otherwise of each K_e methodology can only be meaningfully judged by comparing the 'corrected' value of alternating strain predicted by elastic DBA to the actual alternating strain (or pseudo-elastic stress amplitude) determined from elastic-plastic FEA for different structures and loading conditions. This is the subject of Chapter 7 of this thesis. However, existing Code provisions for performing plastic fatigue analysis are outlined in Appendix XIII-3200 but are currently very limited. The

Section III Standards Committee (SC) is currently working towards developing a set of standardised procedures for performing plastic analysis, proposed as *Case 20-153*: *Guidelines for Plastic Analysis in XIII-3200*. However, this activity is ongoing and it is likely to be several years before official Code rules for plastic analysis are available. Therefore, to establish a standard procedure for determination of K_e by elastic-plastic analysis in the following work, it is necessary to review and numerically evaluate the existing proposals within the technical literature to determine the most suitable framework. This is discussed in the next section.

Table 6. Summary of code plasticity correction factors (K_e) based on elastic DBA

✓ = Required ✖ = Not Required

Methodology	Poisson's ratio correction	Notch correction	Stress linearisation	Stress separation	Reference(s)
ASME III XIII-3450	✖	✖	✓	✖	[1]
ASME Code Case N-779	✓	✓	✓	✓	[113], [114]
Ranganath's Method	✓	✓*	✓	✓	[128], [131], [132]
RCC-M	✓	✖	✓	✓	[110], [116]
JSME	✖	✖	✓	✖	[122], [141]
JSME Code Case NC-CC-05	✖	✖	✖	✖	[123], [142]
PNAEG-G7-002-86	✖	✓	✖	✖	[124]
R5 Volume 2/3	✓	✓	✖	✖	[126]
ASME VIII-2, Section 5	✖	✖	✓	✖	[135]
ASME VIII-2, Annex 5C	✓	✓	✓	✓	[137]
EN-13445, Annex 18	✓	✖	✓	✓	[138], [136]
AD 2000-Merkblatt S2	✓	✖	✖	✓	[140]
Rolls-Royce	✓	✖	✓	✓	[133]

*Ranganath's proposal has been revised to include a notch correction factor, K_n^R.

5. Determination of K_e by Plastic DBA

In performing a fatigue assessment by elastic DBA, it is widely acknowledged that the simplified calculation for the strain concentration factor can be very conservative, especially in the case of local plasticity. Therefore, an alternative method is to calculate K_e directly by performing detailed elastic-plastic analysis. This approach compares the strain range calculated from elastic DBA with the total (elastic plus plastic) strain range predicted by elastic-plastic analysis to determine the actual value of K_e. In this way, an upper limit on the effect of global plasticity can be established for a particular structure or set of loading conditions based on the results of elastic-plastic analysis. In particular, ASME Code Case N-779, Part 6 [113] states that:

"An overall elastic-plastic strain concentration factor, K_e', can be determined by elastic-plastic analysis of the component and the load case under consideration. K_e' is defined as the ratio of the numerically maximum principal total strain range from the plastic analysis to that from the elastic analysis. The resulting K_e' can be applied to other load cases with an elastically predicted strain range less than or equal to the elastic stress range of the load case used to derive K_e'"

This approach is advantageous, since it may only be necessary to perform a few analyses to determine some upper-bound K_e factor that could then be used in further calculations; the potential benefits of performing elastic-plastic analysis are therefore more far-reaching in this context.

As an alternative to the procedure of ASME III Appendix XIII-3520, ASME III Appendix XIII-3440 (b) permits the use of plastic fatigue analysis using the cyclic SSC of the material. Cyclic shakedown analysis may then be performed to determine the actual value of alternating strain. The value of S_{alt} for input to the fatigue curve in a plastic analysis is calculated according to Eq. (143):

$$S_{alt} = \frac{1}{2} \cdot \Delta\varepsilon_{eff} \cdot E_c \tag{143}$$

where $\Delta\varepsilon_{eff}$ is the characteristic multiaxial strain range and E_c is the reference Young's modulus of the applicable DFC. Therefore, the actual value of K_e derived from detailed elastic-plastic analysis may be expressed by (144):

$$K_e^{FEA} = \frac{\Delta\varepsilon_{eff}^{ep}}{\Delta\varepsilon_{eff}^{e}} \quad (144)$$

where K_e^{FEA} denotes the PCFs derived from elastic-plastic analysis, whilst $\Delta\varepsilon_{eff}^{ep}$ and $\Delta\varepsilon_{eff}^{e}$ denote the characteristic multiaxial equivalent strain range calculated by elastic and elastic-plastic analysis, respectively.

ASME Section III prescribes neither cyclic SSCs, nor any guidance on the selection of an appropriate cyclic plasticity model for performing elastic-plastic FEA. As implied by Eq. (144), another very important factor is the choice of characteristic strain measure. To enable the reliable calculation of K_e^{FEA} within this work, a framework adopted for performing elastic-plastic fatigue calculations is outlined within this section. First, the appropriate cyclic stress-strain relation is derived based on test data. This is used to calibrate a cyclic plasticity model for implementation within Abaqus. A number of strain measures proposed within the technical literature are introduced and briefly discussed. The performance of each strain measure is evaluated for a benchmark case study on a PWR auxiliary piping nozzle. Based on the findings of this study, the optimal strain measure is justified and adopted for a more extensive FE analysis programme of plant representative components.

5.1. Cyclic Stress-Strain Data

Research laboratories and government institutions have published many of their experimental testing results including fatigue strain vs. life data for austenitic stainless steels. These sources of data, which includes government funded research reports, conference proceedings, journal papers, books, and PhD theses, have been reviewed. The available data in air was compiled, which included around 920 and 800 data points at room temperature and elevated temperature, respectively. This data was used to establish tensile strength dependent strain-life curves with confidence limits presented in Figure 4 to describe austenitic stainless steel fatigue behaviour at temperatures not exceeding 430°C. This same dataset was also examined with the aim of establishing suitable cyclic SSCs for plastic fatigue analysis.

To establish a cyclic stress-strain relationship from test data, it is necessary to isolate the elastic and plastic portions of the strain amplitude applied in the test. This usually requires that the elastic and plastic portions of the strain amplitude be reported

separately. Alternatively, if the stress amplitude is reported at the half-life, then it is also possible to estimate the elastic and plastic strains using the Young's modulus. One fundamental issue is that a large portion of the available test data only reports the applied strain amplitude and the number of cycles to achieve specimen failure, which is normally defined by a 25% reduction in the peak load. For these tests, it is not possible to isolate the elastic and plastic strains as they do not provide the necessary information. This significantly narrowed the scope of applicable data.

5.1.1. NUREG/CR-5704 (Argonne National Laboratory)

Nuclear Regulatory Commission Contractor Report 5704 (NUREG/CR-5704) [24] summarises an experimental testing campaign conducted by the Argonne National Laboratory (ANL) on fatigue of austenitic stainless steels in LWR coolant environments. To supplement the tests conducted in LWR coolant medium, a large number of tests were also conducted in air at room temperature, 288°C, and 350°C. These tests were conducted on types 304, 316, and 316NG as well as two heats of CF-8M castings. Each material received a short solution annealing treatment followed by subsequent water quenching. Fully reversed strain amplitudes up to 1.5% were considered. A symmetric tensile-compressive strain rate of 0.4% was commonly employed for the tests conducted in air, though a small number of tests considered a lower tensile rate of 0.004%.

NUREG/CR-5704 also reports best-fit cyclic SSCs for Types 304, 316, and 316NG SSs in air at room temperature and 288°-430°C. These best-fit SSCs are expressed by a R-O fit, which assumes a Young's modulus of 195 GPa and 176 GPa at room temperature and elevated temperatures, respectively. The cyclic SSCs for Type 304 at room temperature and 288-430°C are expressed by Eqs. (145) and (146), respectively.

$$\varepsilon_a = \frac{\sigma_a}{195000} + \left(\frac{\sigma_a}{4120.76}\right)^{0.457} \quad (RT) \tag{145}$$

$$\varepsilon_a = \frac{\sigma_a}{176000} + \left(\frac{\sigma_a}{2744.84}\right)^{0.433} \quad (288 - 430℃) \tag{146}$$

The NUREG/CR-5704 Type 304 cyclic SSCs are tentatively selected for this work. Their suitability is first briefly evaluated against additional fully reversed strain-

controlled data available from the technical literature. At room temperature, the data published by Smith et al [13], Medhurst [20], NRIM Datasheet No. 65 [28], Keller [38], Bernstein and Loeby [40], and Sandhya et al [42] were considered. In the temperature range of 288-430°C, the available data is limited to that published by Conway et al [37] and Weeks et al [39] for 430°C.

In accordance with Hales et al [143], the confidence limits associated with the cyclic R-O parameters, K^c and n^c, were obtained by non-linear regression analysis of the plastic term in Eqs. (145) and (146) for both the room temperature (RT) and elevated temperature (288-430°C) data sets, respectively. As the NUREG/CR-5704 cyclic SSCs were derived for Type 304 material in the annealed condition, only tests conducted on annealed material were considered in the regression. Concerning tests conducted at room temperature, the data from Smith et al [13] was found to differ considerably from the other sources, the reason for which could not be ascertained; additionally, the data published in NRIM Datasheet No. 65 [28] considered Type 304 material in the hot-rolled condition. Neither of these sources were considered in the regression. In cases where the plastic strain was not directly reported, it was estimated by dividing the stress amplitude at the half-life by the elastic modulus determined from a tensile test, or, where available, from the first ¼ cycle of the cyclic test.

As discussed by Hales et al [143], the 95% confidence limits in both K^c and n^c can show such divergence that both confidence intervals can intersect either side of the mean curve. In reality, n^c tends to show far less variability compared to K^c which is related to the cyclic yield strength of the material. Therefore, the 95% confidence intervals were determined based on K^c alone, whilst retaining the NUREG/CR-5704 best estimate of n^c. Figure 38 and Figure 39 show the NUREG/CR-5704 cyclic SSCs, and the upper and lower 95% confidence limits of the R-O relationship obtained for the room temperature and 288-430°C data, respectively. As shown, the Type 304 best-fit cyclic SSCs proposed in NUREG/CR-5704 represents closely the cyclic behaviour reported in other technical publications.

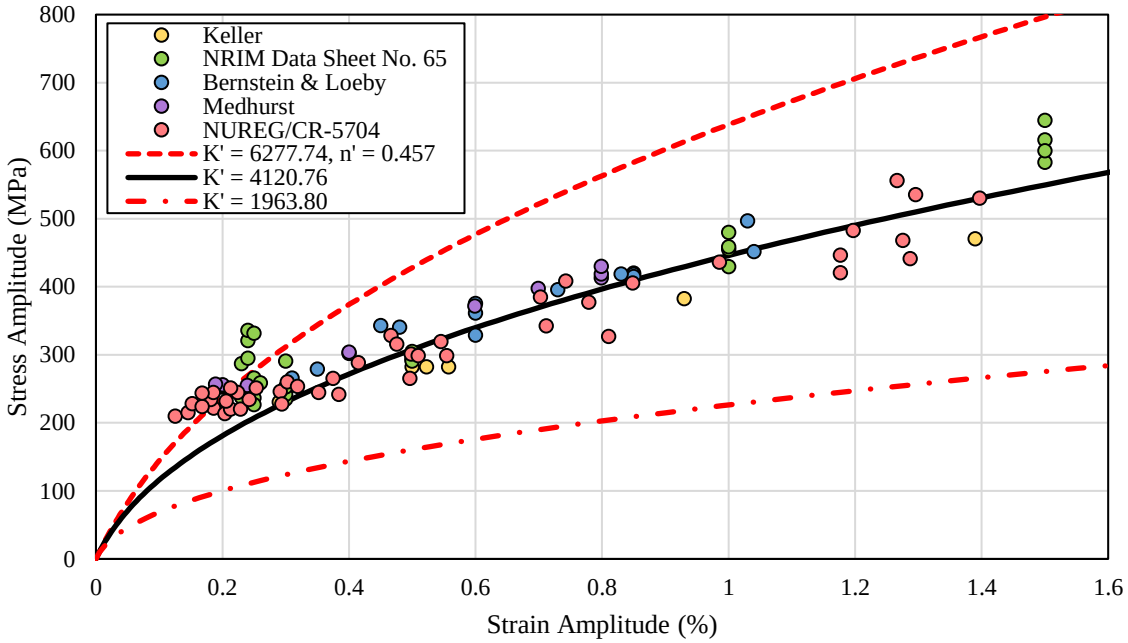

Figure 38. Room temperature NUREG/CR-5704 best fit cyclic SSC for Type 304 with 95% confidence limits.

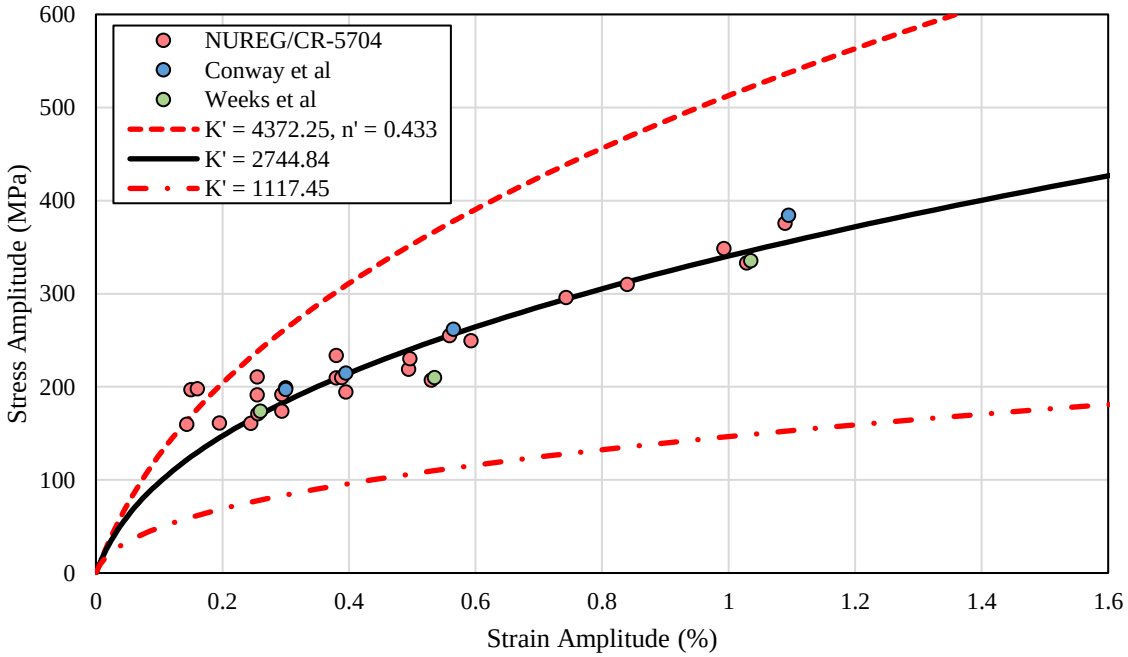

Figure 39. 288-430°C NUREG/CR-5704 best fit cyclic SSC for Type 304 with 95% confidence limits.

5.1.2. Mean vs. Lower Bound

The choice of whether to adopt 5% lower bound or mean cyclic stress-strain properties for elastic-plastic FE analysis can significantly affect the results. In ASME Section II, Part D, the thermal and mechanical properties provided in the lookup tables are nominally mean. In fact, the majority of the input properties to an ASME III fatigue assessment are nominally mean, with the exception of loadings, which have traditionally adopted very pessimistic transient temperature variations and conservative HTCs. This is consistent with Chapter 6, Page 25 of the ASME Section III Companion Guide [144] discussed in 3.2.1, which implies that the main sources of intended conservatism should be focused on the severity of the design transients and their expected frequency of occurrence. It is therefore reasonable to adopt mean cyclic stress-strain properties, as this appears to be more consistent with the overall design philosophy of the Code. It is also judged that the use of lower-bound properties would introduce excessive conservativism into the K_e values obtained from FEA. It is at least more useful to assess the conservatism of the current Code K_e factors compared with the mean elastic-plastic response of the material, as this gives a more accurate indication of inherent design margin.

5.1.3. Comparison with Other Design Codes

Unlike ASME III, other C&S including RCC-MRx and ASME VIII Division 2 do provide cyclic SSCs for application to plastic fatigue analysis. A comparison of the best-fit cyclic SSCs with the cyclic SSCs provided in these design codes is briefly examined here.

In ASME VIII-2, the cyclic SSCs for Type 304 SS are presented in Annex 3D, Table 3.D.2 in the form of cyclic R-O parameters corresponding to different metal temperatures. For intermediate temperatures, interpolation between tabular values is permitted. Table 3D also provides a room temperature cyclic SSC for Type 304 SS in the annealed condition. Little background on the technical basis for the prescribed cyclic SSCs is provided in ASME VIII-2, Annex 3D itself; however, the ASME VIII-2 Criteria and Commentary Report (ASME PTB-1-2014) [145] provides some additional, albeit still quite limited information. Addressing the Annex 3D CSS curves, ASME PTB-1-2014 states that:

"Cyclic stress-strain data is difficult to obtain for the majority of materials in VIII-2, especially as a function of temperature… To address the issue, Baumel and Seeger (Ref. 13 in [145]) *developed a Uniform Material Law for estimating the cyclic stress-strain and strain-life properties for plain carbon and low to medium alloy steels, and for aluminium and titanium alloys…In the fatigue community, it is the recommended method for estimating cyclic stress-strain and strain-life properties when actual data for a specific material is not provided in the form of a correlation or actual data points"* ASME PTB-1-2014, Cyclic Stress-Strain Curve, pp. 29-30.

Concerning Type 304 SS, it is not clear whether the proposed ASME VIII-2 cyclic SSCs have been established from test data, or estimated by correlation. Regardless, Baumel & Seeger's Uniform Material Law [146] is not particularly reliable for estimating the cyclic stress-strain and fatigue properties of austenitic stainless steels, and other estimation techniques such as the Modified Method of Universal Slopes (MMUS) proposed by Muralidharan and Manson [147] have been shown to be superior for these alloys [148].

In the French RCC-MRx Code [149], both room temperature and high temperature cyclic SSCs are provided for austenitic stainless steel Types 304L, 316L, and 316NG in R-O form. The RCC-MRx Code was not available to the author, however the cyclic curves from the 2007 Edition of RCC-MR – the predecessor to RCC-MRx – are provided in Appendix A of the Structural Design Criteria for ITER In-Vessel Components (SDC-IC) [150]. The elevated temperature cyclic SSC is applicable in the temperature range of 300-550°C. Linear interpolation is permitted for intermediate values of temperature between RT and 300°C.

Figure 40 and Figure 41 shows the comparison between the room temperature and 288-430°C NUREG/CR-5704 Type 304 cyclic SSCs with those adopted by the ASME VIII-2 and RCC-MR design codes for strain amplitudes up to 1.5%. The cyclic SSC predicted by the MMUS based on Type 304 tensile properties presented in [151] was also compared. The ASME VIII-2 cyclic SSCs for Type 304 differs considerably in its shape from the other cyclic SSCs, exhibiting a much steeper initial slope and becoming increasingly shallower at higher strain amplitudes; the curves show a much higher degree of saturated hardening, and therefore are much less pessimistic than the other

cyclic SSCs. However, the ASME VIII-2 room temperature cyclic SSC for annealed Type 304 is much similar in shape to the NUREG/CR-5704 cyclic SSC, showing initially greater hardening before the two curves cross at approximately 1% strain amplitude. This is reasonable since the NUREG/CR-5704 best-fit relation was established from tests conducted on specimens obtained in the annealed condition. The RCC-MR cyclic SSCs are also of similar shape to the NUREG/CR-5704 cyclic SSCs, but shows greater saturated hardening at elevated temperature. The MMUS was found to predict cyclic SSCs of very similar shape to those adopted by ASME VIII-2, albeit slightly more pessimistic. It is concluded that a lack of agreement exists between the NUREG/CR-5704 Type 304 cyclic SSCs and those adopted within ASME VIII-2 and RCC-MR. It is difficult to establish the reason for this without further detail on the underlying data used to establish the cyclic R-O parameters provided in these codes. It is also hypothesised that the MMUS – and indeed the estimation scheme used to generate the ASME VIII-2 cyclic SSCs – may be biased towards high-alloy steels that have received prior mechanical treatment; this might partially explain the reduced hardening rate observed for these SSCs compared to the NUREG/CR-5704 best fits. Regardless, based on the foregoing observations, it appears that the use of cyclic SSCs adopted in these design codes may be inappropriate, as they would result in a less conservative value of K_e^{FEA} without reasonable justification. This further justifies the adoption of the NUREG/CR-5704 Type 304 cyclic SSCs for evaluation of K_e^{FEA} in this work.

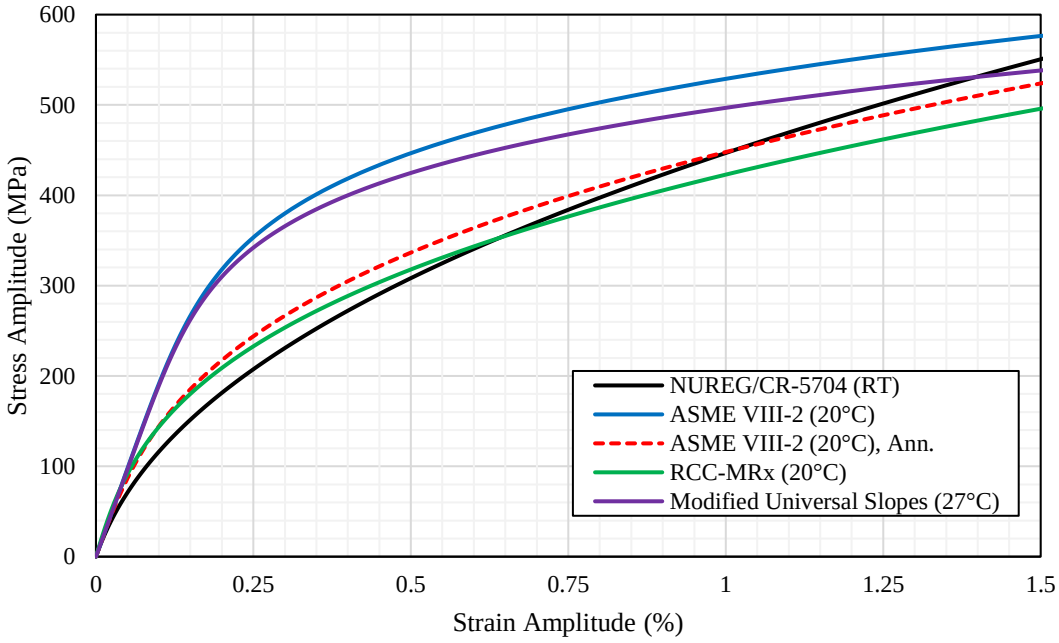

Figure 40. Comparison of NUREG/CR-5704 Type 304 room temperature best fit with other cyclic SSCs.

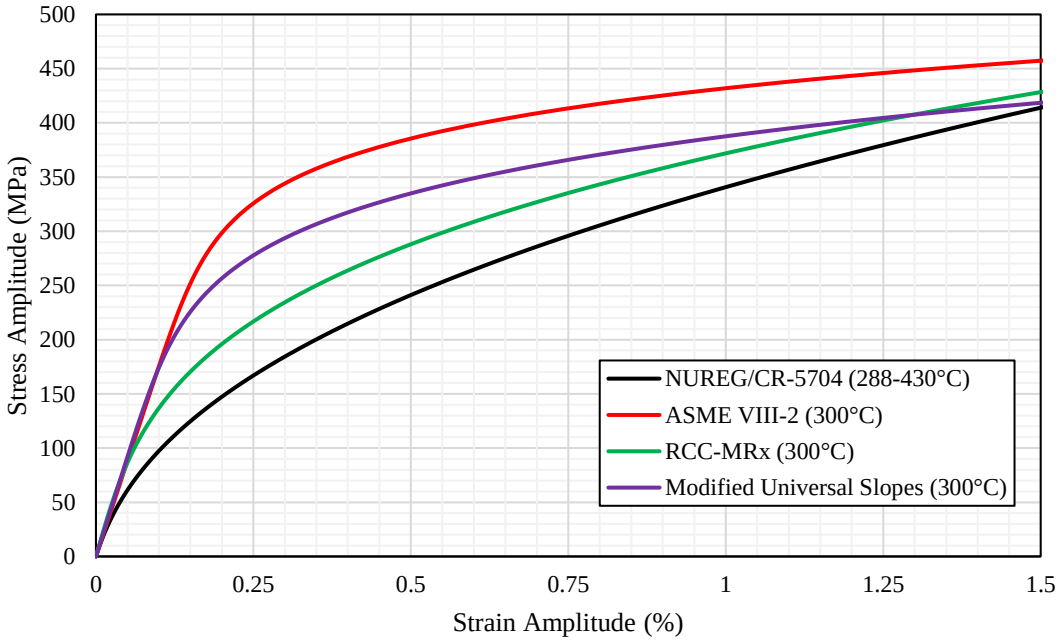

Figure 41. Comparison of NUREG/CR-5704 Type 304 288-430°C best fit with other cyclic SSCs.

5.2. FEA Implementation

5.2.1. Establishing the Stress-Plastic Strain Relation

The R-O form of the cyclic SSC described by Eq. (9) is not typically compatible with commercial finite element software. Most software packages, including Abaqus used throughout this work, require explicit separation of the elastic and elastic-plastic behaviour. The onset of plasticity is described by a cyclic yield stress, σ_y^c, specified by the analyst. However, as Eq. (9) does not define a value of σ_y^c, this must be determined by the analyst. There are a number of methods proposed within the technical literature to determine σ_y^c, which can then be used to derive a suitable stress vs. plastic strain curve for input to FE software. The method used in this work is based on the plastic strain offset approach.

In this approach, an offset of plastic strain amplitude is assumed and is used to position the elastic line. The intersection of this elastic line with the cyclic SSC is then used to define σ_y^c. This is illustrated by Figure 42, where σ_y^c is denoted by the two open circles. For the right-hand circle, the plastic strain amplitude determined by the plastic term of Eq. (9) is equal to the offset value selected by the analyst. The offset strain is calculated by Eq. (147).

$$\varepsilon_{os}^p = \left(\frac{\sigma_y^c}{K^c}\right)^{\frac{1}{n^c}} \tag{147}$$

Conversely, σ_y^c may be determined for an arbitrary offset of plastic strain per Eq. (11). The actual cyclic SSC used in the FE software resembles the two red lines in Figure 42. The first line is the elastic line as is defined by Eq. (148),

$$\varepsilon_a = \frac{\sigma_a}{E} \; for \; \sigma_a \leq \sigma_y^c \tag{148}$$

whilst the second line denotes the plastic portion of the offset cyclic SSC and is defined by Eq. (149).

$$\varepsilon_a = \frac{\sigma_a}{E} + \left(\frac{\sigma_a}{K^c}\right)^{\frac{1}{n^c}} - \varepsilon_{os}^p \; for \; \sigma_a > \sigma_y^c \tag{149}$$

For definition of a plasticity material model, Abaqus requires the relationship between the stress amplitude and plastic strain amplitude, which is defined by Eq. (150).

$$\varepsilon_a^p = \left(\frac{\sigma_a}{K^c}\right)^{\frac{1}{n^c}} - \varepsilon_{os}^p \tag{150}$$

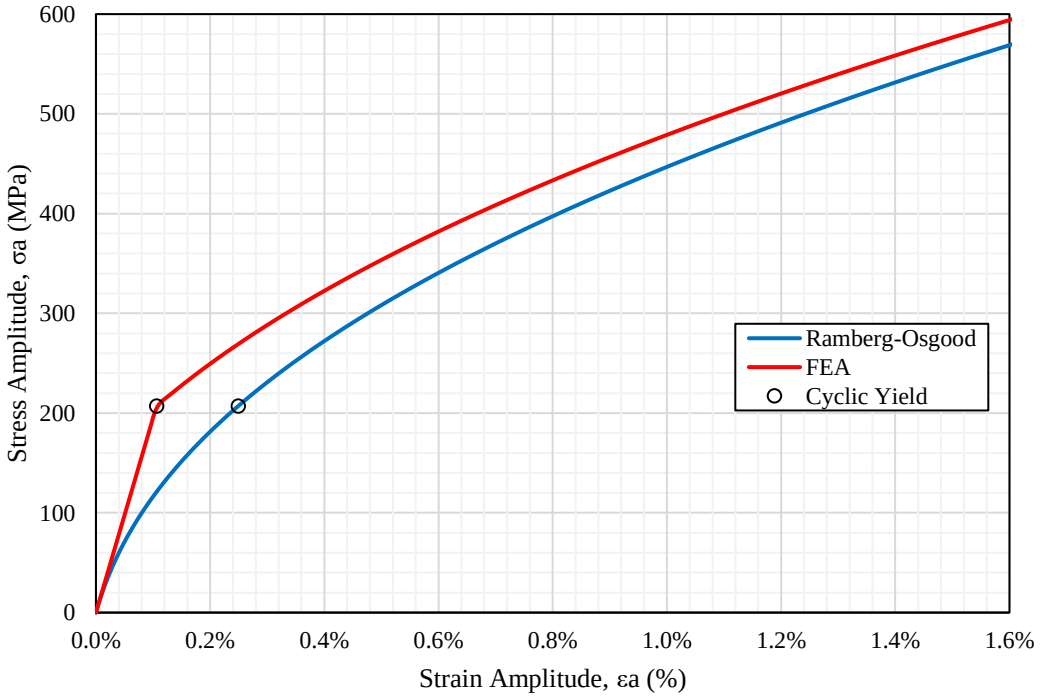

Figure 42. Offset cyclic SSC required for FEA.

It has become common practice to adopt an offset value of 0.2% plastic strain in the above relations, since it can be reliably detected by testing apparatus. However, a different approach is taken in this work wherein rather than specifying a value of ε_{os}^p to establish σ_y^c, the value of σ_y^c is instead specified directly. The rationale for this is based on the Code design philosophy for simplified elastic-plastic analysis. In accordance with Appendix XIII-3450, a K_e factor is not applicable so long as the S_n remains within the elastic range defined by $3S_m$. As far as Appendix XIII-3450 is concerned, peak strain concentration (i.e. localised plasticity) is assumed not to occur for $S_n \leq 3S_m$; essentially, $3S_m$ defines the onset of plasticity according to a strict interpretation of the Code rules. Therefore, if one is to establish a basis for comparison of the current Code K_e factors with more realistic K_e factors established using elastic-plastic FEA, it is important that the onset of plastic behaviour is defined to be consistent with the Code rules. Thus, whilst $3S_m$ denotes the range of elastic behaviour,

$1.5S_m$ therefore denotes the limiting value of stress amplitude beyond which plastic behaviour is presumed to occur. In other words, $1.5S_m$ is recognised as equivalent to σ_y^c and may be substituted into Eqs. (147)-(149).

It is recognised that in ASME III, the value of S_m for austenitic stainless steels is defined as a function of the monotonic yield strength, σ_y, rather than the cyclic yield strength, σ_y^c, which at first glance might be interpreted as excessively conservative. However, on further inspection, S_m and σ_y for Type 304 SS show a significant divergence in behaviour with increasing temperature. Under room temperature conditions, $S_m \approx 2/3\sigma_y$. Interestingly, S_m remains unchanged between room temperature and 150°C. However, beyond 150°C, $S_m \approx 0.9\sigma_y$. At elevated temperatures, $1.5S_m$ is found to be approximately 30-35% higher than σ_y and therefore the Code limit of $3S_m$ does appear to acknowledge the large plastic reserve observed for austenitic stainless steels subjected to cyclic loading. It is noted however that the value of $1.5S_m$ calculated based on σ_y is still significantly lower than average values of cyclic yield strength obtained from test data based on the 0.2% yield-offset criterion. Jaske & O'Donnell [70] report a best-fit room temperature cyclic yield strength value of 303 MPa for Type 304 SS based upon test data taken at the half-life, which is around 38% higher than $1.5S_m$. Nonetheless, $1.5S_m$ was adopted as the definition of cyclic yield stress since it ensures consistency with ASME III and is still reasonably representative of the cyclic stress-strain behaviour despite being somewhat conservative.

The NUREG/CR-5704 Type 304 cyclic SSCs adopted in Eqs. (145) and (146) are applicable to room temperature and temperatures ranging from 288-430°C, respectively. One important issue concerned modelling the transition in cyclic hardening behaviour between room temperature and 288°C, for which cyclic data was not available. As highlighted in Sections 2.2.1 and 2.2.2, the low-cycle fatigue and cyclic plasticity behaviour of austenitic stainless steels show only a modest variation between room temperature and 430°C. However, in absence of reliable test data, it was deemed reasonable to approximate an intermediate cyclic SSC for 150°C conditions. This was done by linear interpolation between the RT and 288-430°C cyclic SSCs. The Cyclic R-O parameters for this intermediate cyclic SSC were determined to be E=185,784 MPa, K^c=3453.34, and n^c=0.4451.

Multiple stress amplitude vs. plastic strain amplitude curves corresponding to RT, 150°C, 288°C, and 430°C were determined in accordance with Eqs. (147)-(150). The value of $\sigma_y^c = 1.5\ S_m$ associated to each curve was established to be 207 MPa for both RT and 150°C, 176.16 MPa for 288°C, and 156.9 MPa for 430°C, based on the tabulated data for Type 304 presented in ASME II, Part D, Table 2A. The corresponding yield-offset values (ε_{os}^p) were calculated by Eq. (147) to be 0.143%, 0.179%, 0.176%, and 0.135%, respectively. The stress amplitude vs. plastic strain amplitude curves are determined according to Eq. (150), and are shown in Figure 43. These curves are then next used to identify the parameters for the Chaboche constitutive model.

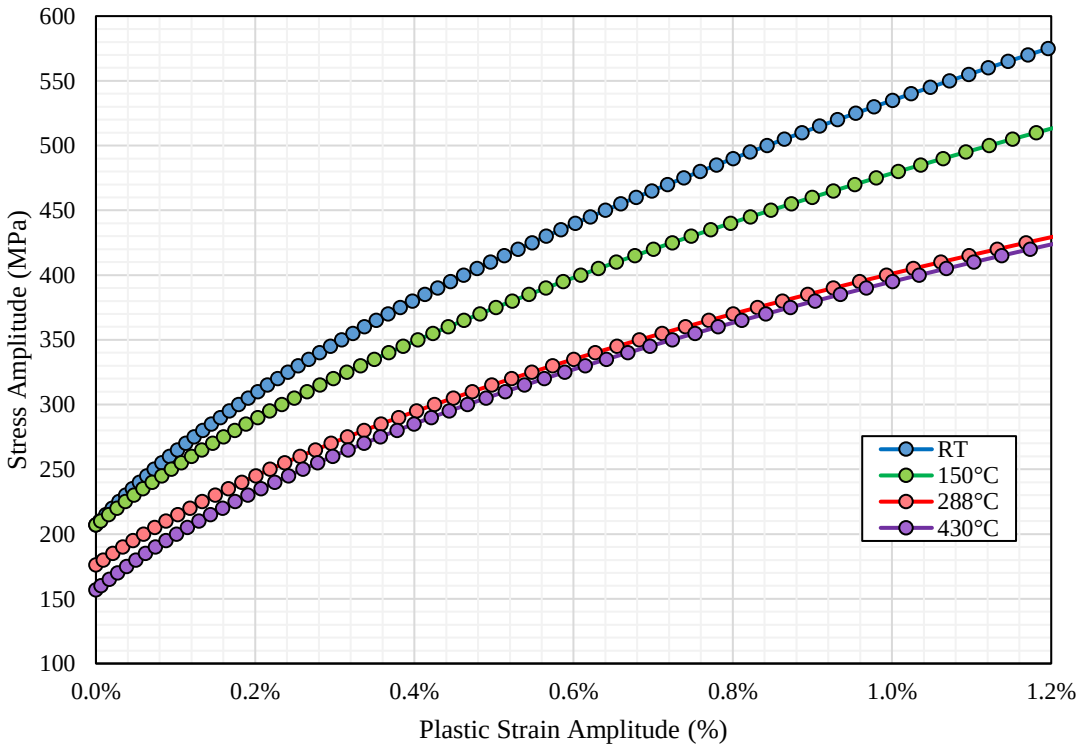

Figure 43. NUREG/CR-5704 Type 304 temperature-dependent stress-plastic strain curves.

5.2.2. Chaboche Plasticity Model Calibration

The rate-independent Chaboche model is presented as a hybrid model incorporating both non-linear kinematic hardening (NLKH) and non-linear isotropic hardening behaviour [152], [153]. Since this work considers only the saturated cyclic SSCs, only the kinematic hardening component is considered here. Kinematic hardening is

represented by superposition of multiple independent backstress tensors, which each behave according to the evolution equations originally proposed by Armstrong & Frederick [154]:

$$\alpha_{NLK} = \sum_{i=1}^{N} \alpha_i \,, \qquad with\ d\alpha = C_i d\varepsilon^p - \gamma_i \alpha_i dp \tag{151}$$

where α_{NLK} is the total superimposed backstress tensor describing the shift of the yield surface in stress space, $d\varepsilon_p$ is the plastic strain increment tensor, and *dp* is the plastic equivalent strain increment according to von Mises theory:

$$dp = \sqrt{\frac{2}{3} d\varepsilon^p \cdot d\varepsilon^p} \tag{152}$$

C and γ are respectively the Chaboche model hardening and relaxation parameters that describe the evolution of the backstress tensor with accumulation of plastic strain. The value of C corresponds to the initial plastic modulus (rate of change of hardening) and the ratio of C/γ represents the strain hardening saturation for increasing amounts of plastic deformation. The non-linear hardening response is introduced by the second term in Eq. (151), which accounts for dynamic recovery [155]. To enable a close match to the cyclic SSCs up to 1.5% strain amplitude, at least 3 independent backstress tensors are usually required [156]. In this work, four backstress terms are considered. The Chaboche model is matched to the cyclic SSCs by relating the backstresses of the Chaboche and R-O models:

$$\sigma_a = \sigma_y^c + \sum_{i=1}^{N} \frac{C_i}{\gamma_i} tanh\left(\gamma_i \varepsilon_a^p\right) \tag{153}$$

where the right-hand term of Eq. (153) is obtained by integrating Eq. (151). The values of C_i and γ_i are acquired by fitting Eq. (153) to the plastic power-law component of the cyclic R-O model:

$$\sigma_a = K^c \left(\varepsilon_a^p\right)^{n^c} \tag{154}$$

This procedure was performed in Python using the *scipy* implementation of the non-linear optimisation algorithm developed by Levenberg and Marquardt [157], [158],

and herein referred to as the Levenberg-Marquardt (LM) algorithm. Initial guesses to C_i and γ_i were chosen such that $C_1>C_2>C_3>C_4$ and $\gamma_1> \gamma_2> \gamma_3 >\gamma_4$. The LM algorithm seeks to minimise the absolute difference between the α_{NLK}-ε_a^p curve and the backstress curve implied by the R-O plasticity model, subject to an arbitrary number of equality and/or inequality constraints. In this case, no inequality constraints were specified, with C_i and γ_i remaining independently unconstrained. However, one equality constraint was defined wherein the value of σ_y^c was constrained to remain equal to $1.5S_m$. This ensures the Chaboche NLKH representation also remains consistent with onset of plastic behaviour defined in ASME III. Applying the above approach, an accurate fit of Eqs. (153) and (154) was achieved. The Chaboche hardening and relaxation parameters are summarised in Table 7 for the NUREG/CR-5704 Type 304 temperature-dependent stress-plastic strain curves shown in Figure 43.

Table 7. Calibrated parameters for NUREG/CR-5704 Chaboche NLKH model

Chaboche Constitutive Model Parameters									
Temp. (°C)	**C_1**	**C_2**	**C_3**	**C_4**	**γ_1**	**γ_2**	**γ_3**	**γ_4**	**σ_y^c**
RT	17449.9	15918.6	14246.9	13738.3	983.8	276.8	85.25	3.10	207
150	12309.1	11235.2	9691.0	14644.8	885.2	274.8	102.8	21.60	207
288	10907.6	9736.1	8039.8	11785.7	899.9	270.5	100.81	21.46	176.16
430	13681.9	11633.9	9218.9	12189.9	1050.0	308.2	108.8	22.20	156.9

For application to elastic-plastic FEA, Abaqus was permitted to use linear interpolation between the temperature-dependent Chaboche models to establish the plastic response. This is reasonable to capture closely the continuous variation in hardening behaviour with temperature. As shown by Figure 44, this linear approximation is also closely representative of the actual variation of $1.5S_m$ with temperature. Whilst it is acknowledged that this produces a slight deviation from the ASME definition of $1.5S_m$

at higher temperatures, most notably between 150°C and 288°C, this was deemed acceptable as a relatively minor compromise.

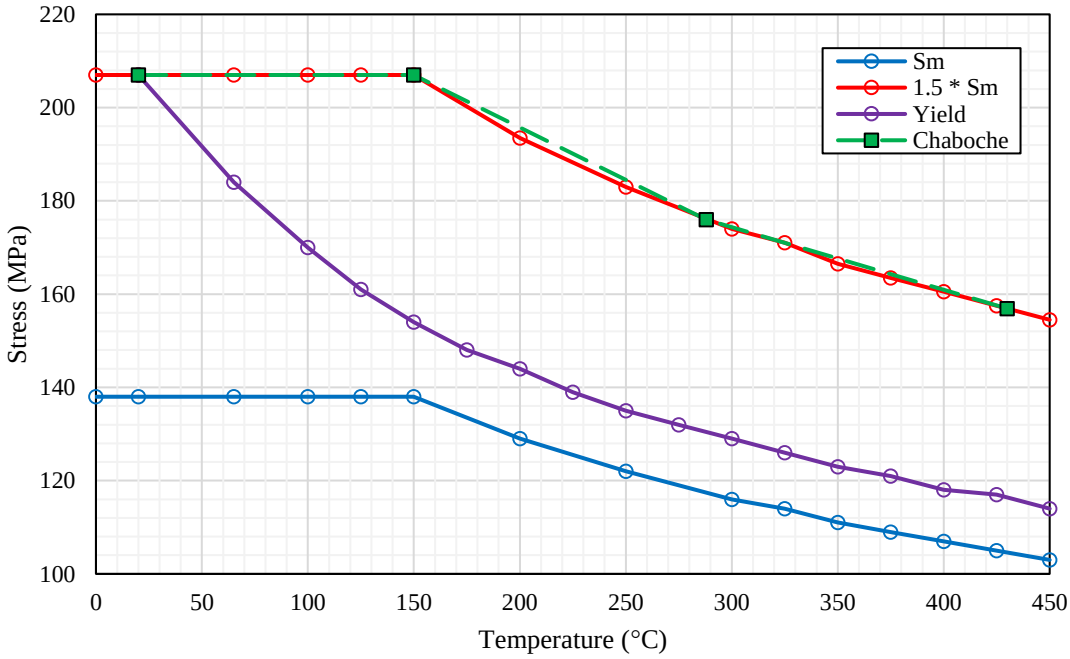

*Figure 44. Comparison of ASME II definition of S_m, 1.5*S_m, and σ_y at temperature for Type 304 with cyclic yield strength, σ_y^c, adopted for the Chaboche NLKH model.*

5.2.3. Verification by Single Element Test

To confirm the suitability of the Chaboche parameters, the temperature-dependent plasticity models were implemented using a single element FEA test in Abaqus. The element was cycled uniaxially through a sequence of linearly increasing and decreasing strain ranges intended to replicate an incremental step-test. Twelve strain levels were considered and the full loading block was repeated six times to achieve hysteresis loop closure. The stress-plastic strain curve fitted by Eq. (153) was then compared to the hysteresis loops predicted by FEA to ensure that it closely approximated the tips of the concentric hysteresis loops established for each strain range. This comparison is shown in Figure 45 and Figure 46 for both the RT and 288°C Chaboche models, respectively. The cyclic SSC fitted by Eq. (153) predicts closely the maximum extent of the stabilised hysteresis loops for both RT and 288°C conditions. The calibrated Chaboche model is therefore confirmed to reproduce the NUREG/CR-5704 cyclic SSCs very well, and is adopted for FEA of plant components.

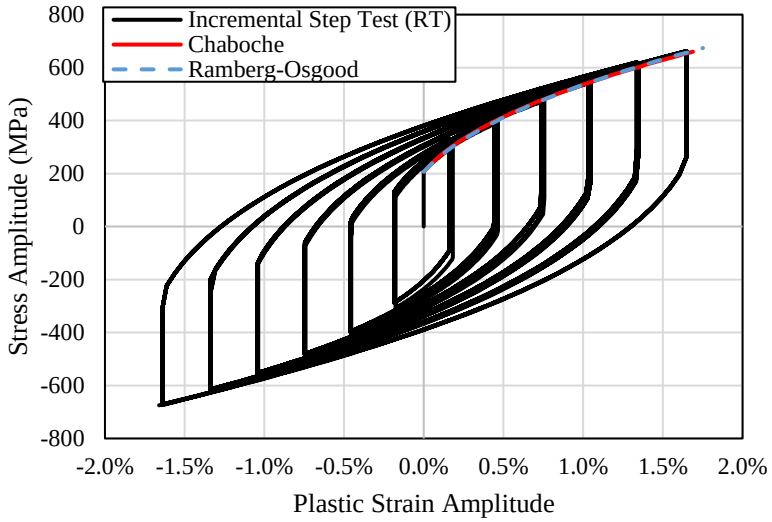

Figure 45. σ_a vs. ε_a^p for single element incremental step test (RT).

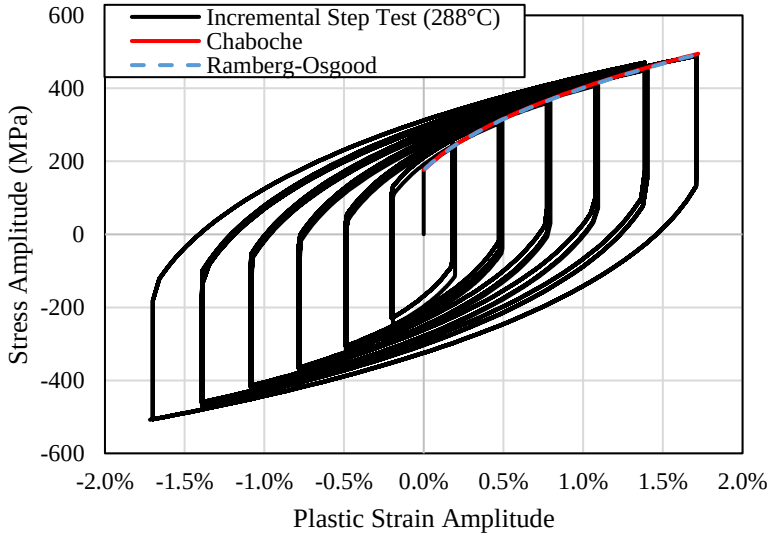

Figure 46. σ_a vs. ε_a^p for single element incremental step test (288°C).

5.3. Strain Measures for Elastic-Plastic FEA

In the textbook *Mechanical Behaviour of Materials*, Dowling [159] categorised plastic fatigue analysis methods into *effective strain* approaches and *critical plane* approaches.

In the effective strain approach, the fatigue life is calculated based on a single equivalent strain value. The intent is to reduce a complex multiaxial state of strain to a scalar value whose effect on fatigue life is equivalent to that of the strain experienced in a uniaxially stressed specimen. This effective strain is calculated based on the

principal strains and therefore is independent of the coordinate system in which the strain components are derived.

The critical plane approach considers a number of candidate planes orientated orthogonally, or at some inclination to the free surface of the component. Both the shear and normal strains are calculated for each candidate plane, and these strain components are used in combination with a critical plane damage model to calculate fatigue damage. The plane experiencing the highest cumulative fatigue damage is termed the 'critical plane' and is taken to be the valid result. A number of different critical plane damage criteria have been proposed for different materials. The Brown-Miller [160], Fatemi-Socie [161], and Smith-Watson-Topper [52] critical plane damage models have emerged as the most popular in industry for application to structural steels. In the case of the Brown-Miller and Fatemi-Socie, these models require additional material parameters, which must be calibrated from multiaxial fatigue test results. Critical plane analysis is more computationally intensive as it involves performing repeated fatigue analyses for multiple candidate planes to determine the plane on which a crack is most likely to initiate. In addition, the damage models used in the critical plane approach tend also to be defined as some variant of the Coffin-Manson relation; this is different to the Langer relation employed in ASME III as it does not include an endurance limit parameter, and therefore a fitting procedure would be required to obtain the correct form. However, one advantage of the critical plane approach is that it yields information about the directionality of the initiated crack, namely the most likely orientation of the crack initiation plane, in addition to the cycles predicted to cause initiation.

In the context of an ASME III fatigue assessment, effective strain approaches are often preferred as they are more practical and are directly compatible with the Appendix I DFCs. This section discusses a number of these candidate strain measures for calculation of K_e by elastic-plastic analysis:

1. Maximum Principal Total Strain Range (MPT).
2. Equivalent Total Strain Range (ETSR)
3. Effective Octahedral Shear Strain Range (EOSR).
4. Maximum Shear Strain Range (ESSR)

In the following discussion, the definition of component shear strains should be noted. Abaqus provides as default output the engineering shear strains, γ_{ij}, which are equal to twice the tensor shear strains. This convention is also adopted here as a matter of convenience.

5.3.1. Numerically Maximum Principal Total (MPT) Strain

ASME III Appendix XIII-3440 (b) states that when a plastic analysis is performed, a cyclic load pair's alternating stress for input to the fatigue curve should be determined by multiplying the *'numerically maximum principal total strain range by one-half the modulus of elasticity at the average temperature of the cycle'*. The MPT strain range was adopted by ASME III from its inception in 1963.

The range of the individual total strain components, $\Delta\varepsilon_{ij}$, are determined from superposition of the ranges of the elastic and plastic component strains:

$$\Delta\varepsilon_{ij} = \Delta\varepsilon_{ij,e} + \Delta\varepsilon_{ij,p} \tag{155}$$

The principal strain ranges are determined based on the ranges of the unique strain components between the extremes of the cycle. Ordering the principal strain ranges in the usual manner such that $\Delta\varepsilon_1$, $\Delta\varepsilon_2$, and $\Delta\varepsilon_3$ are the algebraic maximum, middle, and minimum principal components, the numerically maximum principal total strain is calculated per Eq. (156).

$$\Delta\varepsilon_{MPT} = \max\left(\left|\Delta\varepsilon_{1,e} + \Delta\varepsilon_{1,p}\right|, \left|\Delta\varepsilon_{2,e} + \Delta\varepsilon_{2,p}\right|, \left|\Delta\varepsilon_{3,e} + \Delta\varepsilon_{3,p}\right|\right) \tag{156}$$

Equivalently, in terms of principal total strain ranges:

$$\Delta\varepsilon_{MPT} = max(|\Delta\varepsilon_1|, |\Delta\varepsilon_2|, |\Delta\varepsilon_3|) \tag{157}$$

$\Delta\varepsilon_{MPT}$ correctly reduces to the uniaxial total strain range acting in the direction of applied loading for a uniaxially stressed specimen:

$$\Delta\varepsilon_{MPT} = \Delta\varepsilon_1 = \Delta\varepsilon_z = \Delta\varepsilon_{z,e} + \Delta\varepsilon_{z,p} \tag{158}$$

where $\Delta\varepsilon_z$ acts along the longitudinal axis of the specimen as shown in Figure 47.

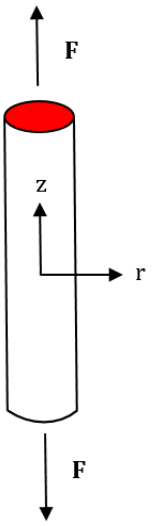

Figure 47. Illustration of specimen under uniaxial state of stress.

That ASME III recommends the use of the MPT strain range for plastic fatigue analysis is somewhat surprising as it is not consistent with the current Tresca-based elastic DBA procedure. Both approaches have been shown to produce very different results for a multiaxial state of stress. Gilman and Ku [162] demonstrated that, even for purely elastic calculations, the value of alternating stress calculated according to Appendix XIII-3440 (b) was 23% less conservative than that calculated based on traditional stress-based Tresca theory for a typical thermal shock transient. The seemingly unintended consequence of this is that a fatigue analysis of a component that remains elastic might result in unacceptable fatigue usage when using the elastic DBA method, but produce acceptable results simply by switching to the current plastic analysis method. In this hypothetical scenario, the difference in the allowable cycles would also be expected to be very significant since even a small reduction in stress amplitude could result in several orders of magnitude increase in predicted life. Clearly, this consistency problem would be desirable to address. Furthermore, in recent discussions of the WGDM and WGFS, the use of the MPT strain measure has been questioned as being potential incorrect when plasticity effects are taken into account. Considering the generalised Hooke's law for a step thermal shock discussed in 4.3.1.1. Under elastic conditions, $\nu = 0.3$, and hence both $\Delta\varepsilon_z$ and $\Delta\varepsilon_\theta$ are equal to $\alpha\Delta T$ and are therefore dominant in absolute terms compared to $\Delta\varepsilon_r$ which is equal to $-0.857\alpha\Delta T$. Under plastic conditions, $\nu = 0.5$ and in this situation, $\Delta\varepsilon_r$ actually becomes the

dominant strain component, being equal to -2αΔT and is therefore twice the absolute magnitude of $\Delta\varepsilon_z$ and $\Delta\varepsilon_\theta$ which remain equal to αΔT. Crucially, the radial strain also has the opposite sign to the hoop and axial strain components. This means that $\Delta\varepsilon_{MPT}$ calculated for this typical situation will be orientated normal to the metal surface, and in the unloaded direction. This was confirmed numerically for a simple cylinder and the solution is illustrated in Figure 48. The dashed lines show the elastic solution and the solid lines show the elastic-plastic solution. The use of the MPT strain range is therefore questionable, as a radially oriented strain range would not be expected to contribute to crack nucleation and subsequent growth. Since crack nucleation in metals normally occurs on planes of maximum shear strain, other effective strain measures based on shear strain are also investigated as suitable alternatives.

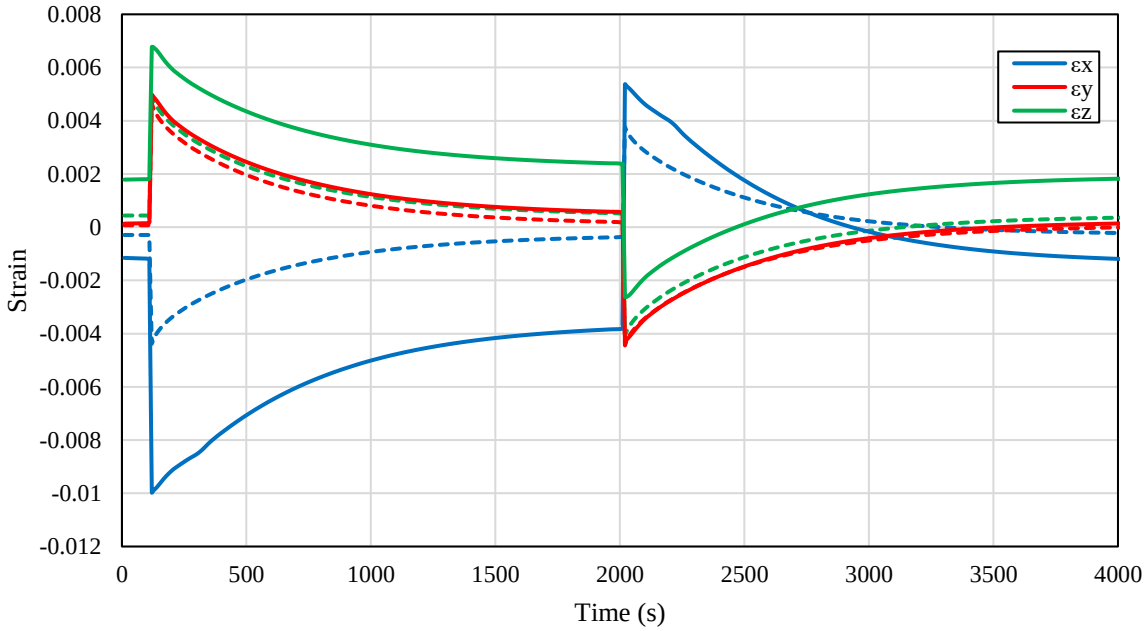

Figure 48. Elastic vs. elastic-plastic strain history for a cylinder under thermal shock.

5.3.2. Equivalent Total Strain Range (ETSR)

The *Equivalent Total Strain Range* (ETSR) is a simplified von Mises based strain measure, which is prescribed in ASME Section III, Division 5 Article NB-T-1413 for the assessment of creep-fatigue damage in high temperature reactor components. The ETSR is defined by Eq. (159),

$$\Delta\varepsilon_{ETSR} = \frac{\sqrt{2}}{2(1+v^*)}\begin{bmatrix}\left(\Delta\varepsilon_x - \Delta\varepsilon_y\right)^2 + \left(\Delta\varepsilon_y - \Delta\varepsilon_z\right)^2 + (\Delta\varepsilon_z - \Delta\varepsilon_x)^2 \\ + 1.5\cdot\left(\Delta\gamma_{xy}{}^2 + \Delta\gamma_{xz}{}^2 + \Delta\gamma_{yz}{}^2\right)\end{bmatrix}^{1/2} \quad (159)$$

where ν^* is either 0.5 or 0.3 depending on whether loading is elastic or plastic. For elastic-plastic conditions, it is normally assumed that elastic strains are small relative to the plastic strains such that the elastic strains can therefore also be treated plastically with $\nu^* = 0.5$. This assumption is adopted herein when calculating $\Delta\varepsilon_{ETSR}$. It should be noted that by adopting this approach, there is a possibility for the ETSR to predict an elastic-plastic strain range below that of the elastic strain range in situations where plasticity effects are mild.

5.3.3. Effective Octahedral Shear Strain Range (EOSR)

The Effective Octahedral Shear Strain Range (EOSR) – or the Effective von Mises Strain Range – was proposed by Dowling [159] for application to proportional multiaxial loading. The EOSR has since been adopted within ASME Section VIII Division 2 Subsection 5.5.3.3 [135]. Unlike the ETSR, the EOSR decomposes the total strain range into its elastic and plastic components as shown by Eq. (160). The elastic stress range is calculated by dividing the von Mises equivalent stress range defined by Eq. (161) by the Young's modulus corresponding to the average load cycle wetted surface temperature. The plastic strain range is calculated as the von Mises combination of the plastic strain range components using Eq. (162).

$$\Delta\varepsilon_{EOSR} = \frac{S_p}{E} + \Delta\varepsilon_{eq}^{p} \quad (160)$$

where

$$S_p = \frac{1}{\sqrt{2}}\begin{bmatrix}\left(\Delta\sigma_x - \Delta\sigma_y\right)^2 + \left(\Delta\sigma_y - \Delta\sigma_z\right)^2 + (\Delta\sigma_z - \Delta\sigma_x)^2 \\ +6\cdot\left(\Delta\tau_{xy}{}^2 + \Delta\tau_{xz}{}^2 + \Delta\tau_{yz}{}^2\right)\end{bmatrix}^{1/2} \quad (161)$$

$$\Delta\varepsilon_{eq}^{p} = \frac{\sqrt{2}}{2(1+v^{*})}\left[\begin{array}{c}\left(\Delta\varepsilon_{x}^{p}-\Delta\varepsilon_{y}^{p}\right)^{2}+\left(\Delta\varepsilon_{y}^{p}-\Delta\varepsilon_{z}^{p}\right)^{2}+\left(\Delta\varepsilon_{z}^{p}-\Delta\varepsilon_{x}^{p}\right)^{2} \\ +1.5\cdot\left(\gamma_{xy}^{p\ 2}+\gamma_{xz}^{p\ 2}+\gamma_{yz}^{p\ 2}\right)\end{array}\right]^{1/2} \quad (162)$$

The calculation of $\Delta\varepsilon_{eq}^{p}$ assumes fully plastic behaviour such that ν^{*} = 0.5. Alternatively, the elastic strain range, $\Delta\varepsilon_{eq}^{e}$, may also be calculated by Eq. (162) by substituting the elastic strain components and ν^{*} = 0.3. This is potentially more accurate since at each cycle extreme, the elastic strains are already computed in FE software based on the Young's modulus at the instantaneous wetted surface temperature. This obviates the need to select some average value of Young's modulus to characterise the entire loading cycle.

5.3.4. Effective Shear Strain Intensity (ESSR)

Recent discussions within the ASME III Working Groups on Design Methodology (WGDM) and Fatigue Strength (WGFS) have focused on addressing the fundamental inconsistency between the elastic DBA approach to fatigue analysis, which uses Tresca theory, and the approach to plastic fatigue analysis, which is instead based on principal strain. The WGDM and WGFS are currently considering an alternative Tresca-based shear strain measure proposed by Damiani [163], as a replacement to the MPT strain range currently prescribed in Appendix XIII-3440 (b). The alternative strain measure, termed the *Effective Shear Strain Intensity* (ESSR) in this work, is defined by Eq. (163),

$$\Delta\varepsilon_{ESSR} = \varepsilon_{r}^{e} + \frac{2}{3}\varepsilon_{r}^{p} \quad (163)$$

where ε_{r}^{e} and ε_{r}^{p} are the elastic and plastic portions of $\Delta\varepsilon_{ESSR}$ determined from the following steps taken directly from the WGDM revised technical guidance document:

1. Considering the following terms from the plastic analysis for the complete cycle.

   Stress components: σ_{11}, σ_{22}, σ_{33}, σ_{12}, σ_{13}, σ_{23}

   Plastic strain components: ε_{11}^{p}, ε_{22}^{p}, ε_{33}^{p}, γ_{12}^{p}, γ_{13}^{p}, γ_{23}^{p},

2. Divide the stress components from the plastic analysis by the modulus of elasticity at the corresponding temperature of the cycle, σ_{11}/E, σ_{22}/E, σ_{33}/E, σ_{12}/E, σ_{13}/E, σ_{23}/E, to generate the elastic strain components.
3. Determine separate algebraic differences, for two unique points in time throughout the cycle, for the elastic strain components calculated in Step 1 and plastic strain components.
4. Calculate separate principal values for the differenced terms determined in Step 2. The elastic principal values are denoted $\varepsilon_1^{e'}$, $\varepsilon_2^{e'}$, $\varepsilon_3^{e'}$. The plastic principal values are $\varepsilon_1^{p'}$, $\varepsilon_2^{p'}$, $\varepsilon_3^{p'}$.
5. The elastic and plastic shear strain range terms are determined by the maximum absolute value of the principal term differences:

$$\varepsilon_r^e = max\left(\left|\varepsilon_1^{e\prime} - \varepsilon_2^{e\prime}\right|, \left|\varepsilon_2^{e\prime} - \varepsilon_3^{e\prime}\right|, \left|\varepsilon_3^{e\prime} - \varepsilon_1^{e\prime}\right|\right)$$

$$\varepsilon_r^p = max\left(\left|\varepsilon_1^{p\prime} - \varepsilon_2^{p\prime}\right|, \left|\varepsilon_2^{p\prime} - \varepsilon_3^{p\prime}\right|, \left|\varepsilon_3^{p\prime} - \varepsilon_1^{p\prime}\right|\right)$$

6. Steps 3 through 5 are determined for all unique points in time throughout the cycle. The extremes of the cycle are identified such that the value of $\Delta\varepsilon_{ESSR}$ is maximised.

The factor of 2/3 in Eq. (163) is to account for the axial and diametral portion of strain that would be present in a uniaxially loaded cylindrical specimen. This ensures that Eq. (163) reduces correctly to Eq. (158) under uniaxial loading. The definition of $\Delta\varepsilon_{ESSR}$ in Damiani's proposal provides a strain corollary to how fatigue is determined for the elastic DBA approach based on stress intensity. From this standpoint, the proposal is attractive as it ensures a consistent basis between the elastic and plastic analysis approaches.

5.3.5. Discussion

Some practical advantages and disadvantages of the candidate strain measures are discussed here.

Reinhardt [164] presented a theoretical comparison of various strain measures using simple instantaneous load cases. The strain measures are normalised relative to a maximum value of one, to enable a simple comparison. The results are shown in Figure 49 for each of the load cases considered by Reinhardt [164]. Note that this example

assumes a fully plastic Poisson's ratio of $\nu = 0.5$ is assumed, and thus the EOSR and ETSR are equivalent. As can be seen, the greatest difference between the strain measures occurs for the case of a pressurised cylinder and that of pure shear, where the ESSR is found to be 13% higher than the ETSR and EOSR strain measures, and 25% higher than the MPT strain measure. This difference between the Tresca and von Mises yield criteria is evident when considering the different distances formed by the intersection of the radial line representing pure shear with the Tresca hexagon and von Mises circle in deviatoric stress space (Figure 50). The maximum theoretical difference between these two strain measures is $2/\sqrt{3}$ (or $\approx 15.5\%$), occurring for the case of pure shear where the Tresca and von Mises yield surfaces show the largest deviation.

One disadvantage of von Mises based strain measures that has been highlighted in the technical literature (see for example Section 7.4.8 of Draper [165]) is that they cannot be directly analysed using cycle counting. This is because the Von Mises equivalent strain is always positive, irrespective of whether the component strains are positive or negative. Some approximate methods have been proposed for converting von Mises equivalent strain histories to make them more amenable to cycle counting, sometimes referred to as *signed von Mises* criteria. This typically involves assigning the sign of the numerically maximum principal strain, or alternatively the sign of the mean normal (hydrostatic) strain, to the von Mises equivalent strain. However, this problem can normally be avoided altogether when implementing the criteria of ASME III Appendix XIII-2420. Using this approach, the von Mises strain history is determined relative to some extreme state, and thus the sign is positive at all times. This amounts to performing the cycle count on the *relative von Mises strain.* Therefore, this is not perceived to be a major disadvantage in this context.

Another important factor concerns the ability of each strain measure to predict closely the fatigue lives observed from multiaxial fatigue testing. Such data sources are relatively scarce within the technical literature, especially for austenitic stainless steels. Itoh et al [166] performed non-proportional low-cycle fatigue tests on Type 304 SS considering 14 different strain paths. The results indicate that for non-proportional loading, the strain path also has an important influence on fatigue life, which cannot be captured by simply considering the two extreme points of the cycle. Another

example is that described by Socie and Marquis [167], where a constant amplitude uniaxial load varies in its direction of application with each cycle. In this case, the equivalent strain remains constant, but the loading will trace out a circular path. This has been shown to produce significantly more damage than if the loading direction were held constant. For this reason, effective strain approaches are generally limited in their applicability to proportional or only modestly non-proportional multiaxial loadings. Fortunately, highly non-proportional loading is relatively rare in fatigue analysis of pressure vessel components. As fatigue crack nucleation usually occurs on the internal surface, this essentially fixes one of the three principal axes. The other two axes can only rotate in the presence of time-varying, out-of-plane shear loading. Out-of-plane shear can only feasibly occur in nozzles because of large torsional loads induced by the motion of an attached piping system. However, even this is rare in practice and is usually a consequence of poor design. The available experimental data is therefore of little practical significance here where calculation of K_e^{FEA} is the chief concern.

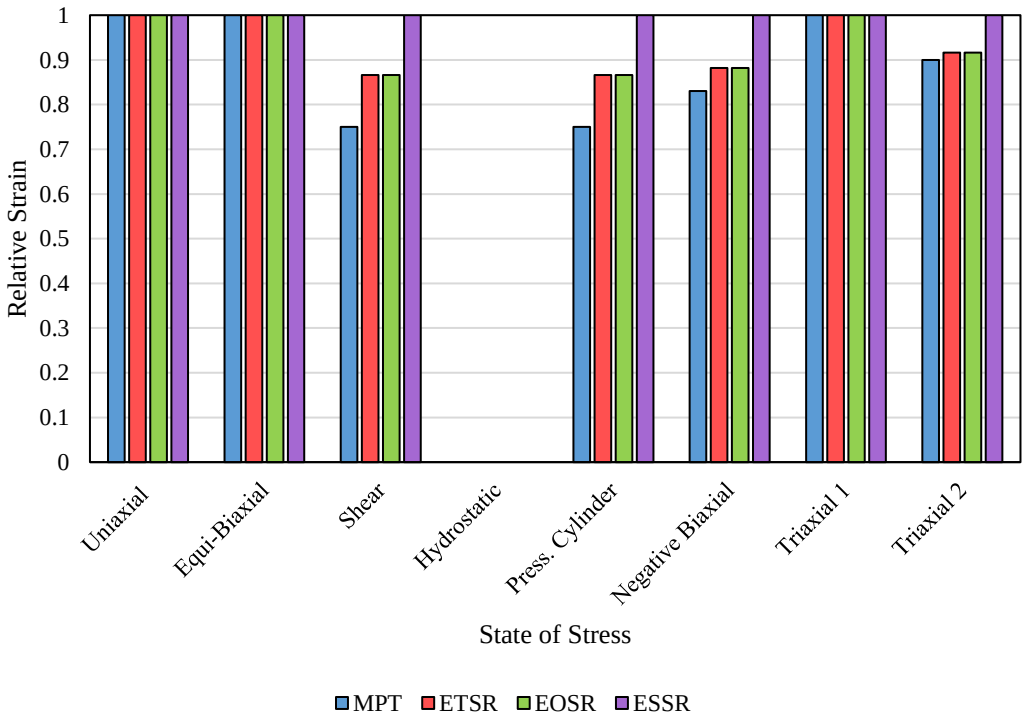

Figure 49. Comparison of strain measures for idealised example case in Reinhardt [164].

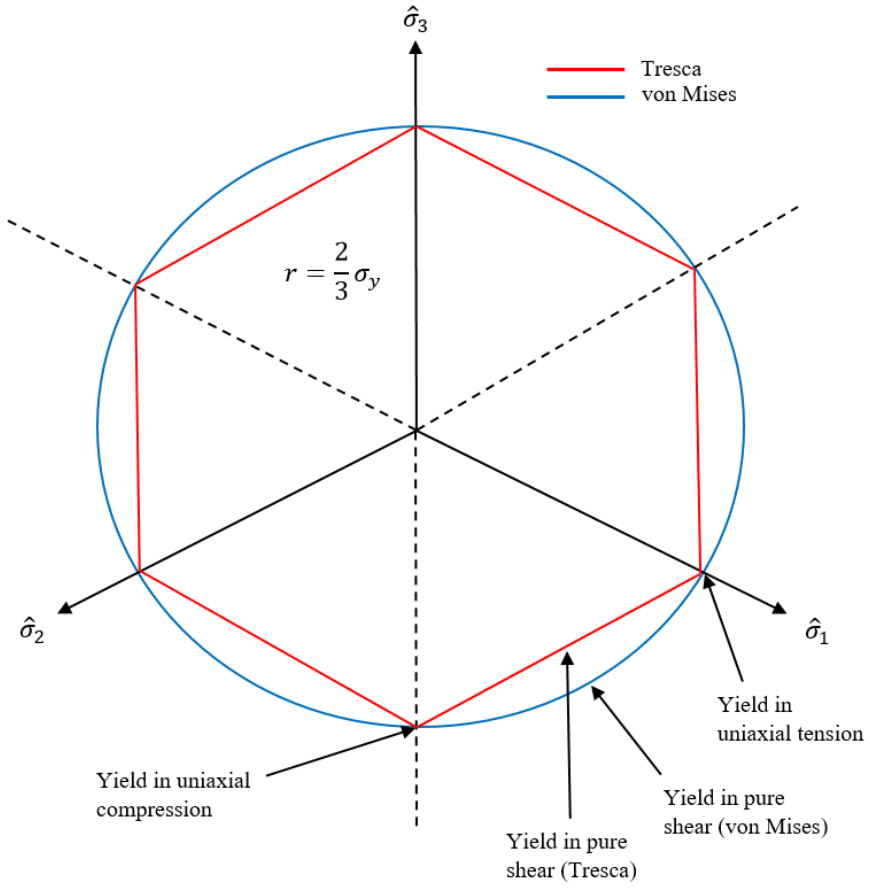

Figure 50. Comparison of Tresca and von Mises yield surfaces in deviatoric stress space.

5.4. Case Study: Fatigue Analysis of a PWR Auxiliary Piping Nozzle

To establish the choice of strain measure best suited for evaluation of K_e^{FEA}, a benchmark problem was established to compare their relative performance considering a fatigue case study of a representative LWR plant component. The aim of this case study is to permit a critical review of each strain measure for a realistic scenario, with consideration of both accuracy and practicality.

5.4.1. Description of Case Study

Class 1 reinforced piping nozzles of PWR plants commonly experience severe cyclic thermal loading, and can encounter some difficulties with fatigue and plastic ratchet assessments. The main coolant line (MCL) nozzle described in Benchmark Problem 2 in Part 2a of the WNA CORDEL Benchmark Report on Non-Linear Analysis Design

Rules [168] was selected as a case study to compare the performance of the different effective strain measures. The assembly is composed of a main reactor coolant run pipe, nozzle forging, and branch pipe. The component geometry and major dimensions are shown in Figure 51.

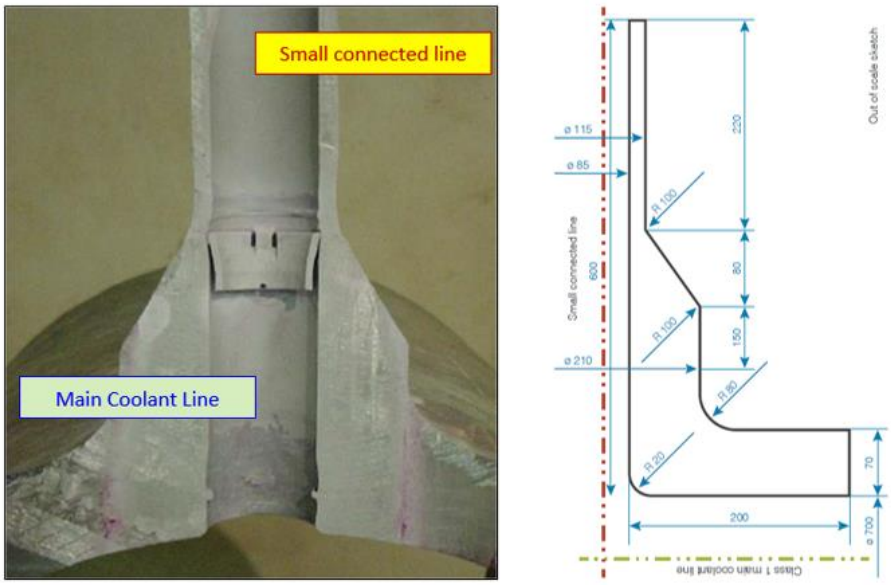

Figure 51. CORDEL MCL nozzle geometry definition from [168]

The main pipe has an outer diameter of 770 mm and a thickness of 70 mm. The branch pipe has an outer diameter of 57.5 mm and a thickness of 15 mm. They are connected by a nozzle forging of maximum outer diameter 210 mm and thickness of 62.5 mm.

A 2D FE model of the MCL nozzle was created in Abaqus [82], whereby an equivalent sphere radius was defined as two times the radius of the MCL run pipe; this was done in an attempt to mimic the pressure stresses that would be expected to arise in a full 3D FE model of the nozzle. The 2D FE model definition is shown by Figure 52. The locations of the stress classification lines (SCLs) defined for fatigue analysis are shown in Figure 53. In total, there are 10 assessment locations, 3 in the branch pipe, 4 in the nozzle reinforcement, 1 spanning the nozzle crotch corner, and two in the MCL run pipe.

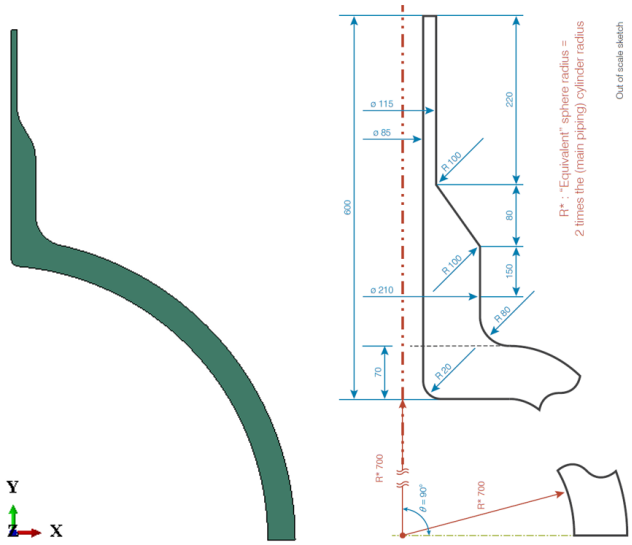

Figure 52. MCL nozzle 2D FE model definition

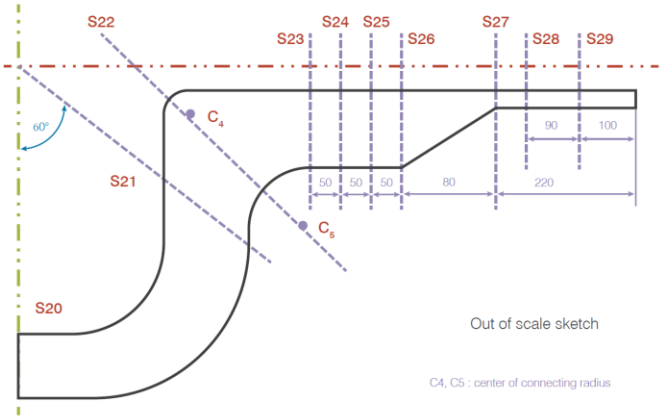

Figure 53. Analysis sections for 2D model.

The loads and boundary conditions for the MCL nozzle are defined in Figure 54. The cross-section of the main run pipe (i.e. the sphere in the 2D model) is constrained to remain fixed in the global y-direction, replacing end pressure load 1. Since internal pressure represents a zero external force resultant acting on the branch pipe, the equivalent load due to the stress induced by internal pressure must be applied as an external load acting in the opposite direction. A closed-end condition was assumed and therefore only the axial stress is relevant. The self-equilibrating end-cap pressure, P_c, or end pressure load 2 in Figure 54, applied to the end of the branch pipe is calculated by Eq. (164)

$$P_c = \frac{(P_i r_i^2)}{(r_o^2 - r_i^2)} \tag{164}$$

where r_i and r_o are the internal and external radii of the branch pipe, respectively. To simulate the displacement of the large attached piping system not modelled, the end of the branch pipe was constrained to expand in-plane. The convective HTC between the internal metal surface and contacting fluid was assumed infinite. All external surfaces were assumed adiabatic.

Two design transients are specified for the MCL nozzle and are shown in Figure 55. The transient specification consists of a 220°C thermal shock under a constant operating pressure of 15.5 MPa (T1), and a 150°C thermal shock combined with a pressure drop (T2). The frequency of occurrence of T1 and T2 are 100 and 800 cycles, respectively.

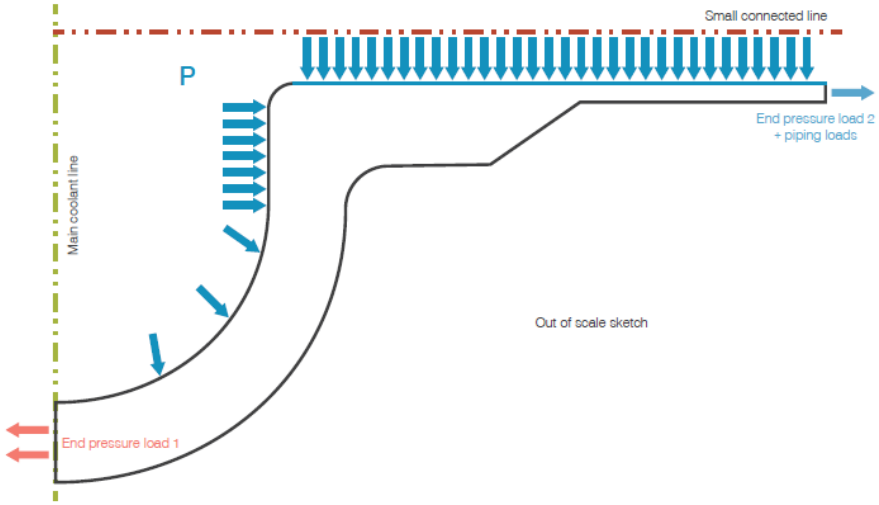

Figure 54. MCL nozzle loads and boundary conditions.

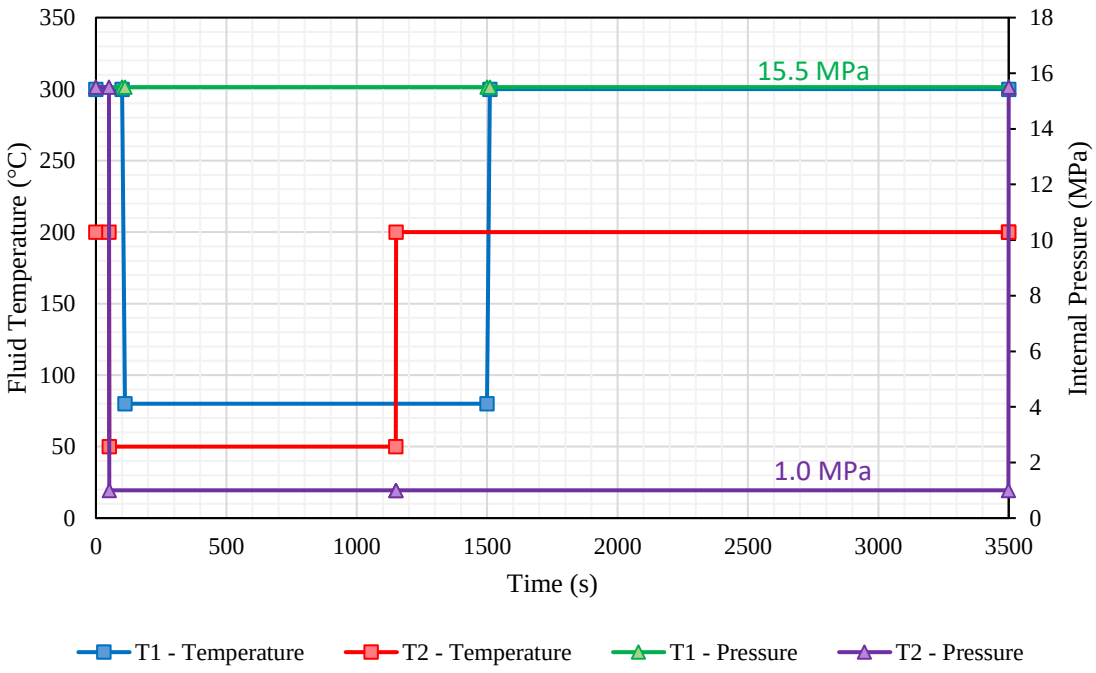

Figure 55. Illustration of design transients T1 and T2.

In this benchmark, the entire assembly is defined to be of SA-312 Type 304 stainless steel material. The thermal and mechanical properties for SA-312 Type 304 were obtained from ASME II Part D, Table 2A [73]. The cyclic plasticity behaviour is described by the NUREG/CR-5704 temperature-dependent Chaboche model defined in Table 7.

Due to the thermal shocks occurring in T1 and T2, a sufficient number of elements must be specified near the internal surface to capture the temperature fields and peak stresses. For T1, the 150°C thermal shock occurs in 1s which is very sharp. A rough estimate of the heat penetration depth in a given time for a simple pipe may be estimated from Eq. (165) knowing only the average thermal diffusivity of the metal:

$$d = \sqrt{3\kappa t} = 3.68\,mm \tag{165}$$

From Eq. (165), d is calculated to be 3.68 mm for a 1s thermal shock. The required element thickness of the first mesh layer can be established more accurately by Eq. (166), assuming a minimum time increment, Δt, of 0.1s.

$$e < \sqrt{\frac{6\lambda\Delta t}{\rho C_p}} = 1.606\ mm \tag{166}$$

For the benchmark problem, a minimum element thickness of 0.5 mm was adopted. In the inner surface, 10 layers from 0.5mm to 5mm were specified as shown by Figure 56. The final mesh contained a total of 3340 8-node quadratic quadrilateral elements of type CAX8R, with 10,395 unique nodal points.

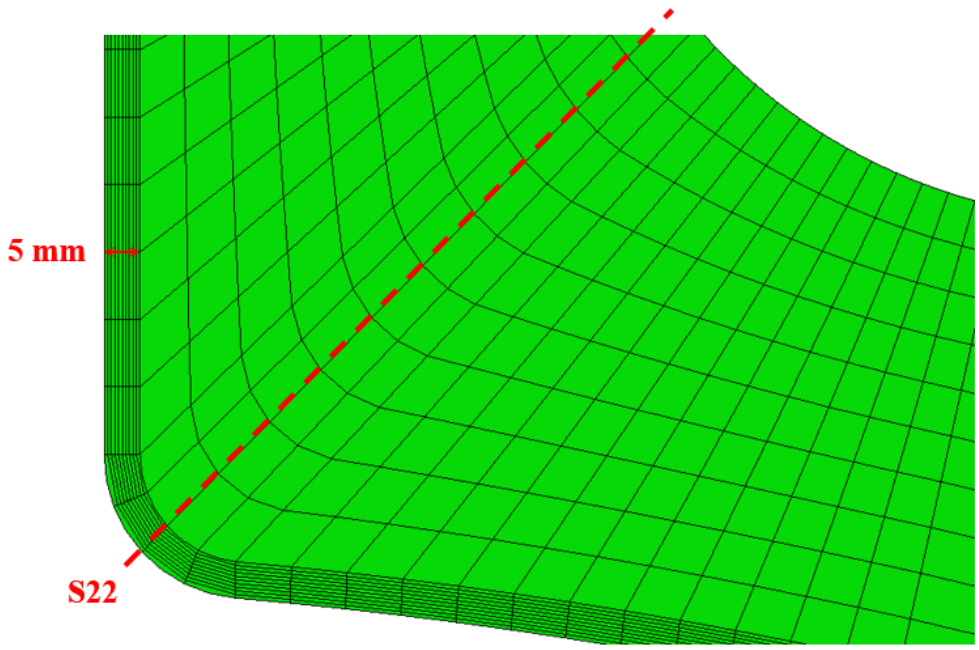

Figure 56. Detail of FE mesh discretisation.

5.4.2. Initial Elastic Fatigue Assessment

The initial elastic fatigue assessment was performed in accordance with the DBA criteria of ASME Section III Appendix XIII-3520 and RCC-M Section B-3234.5. The time-points corresponding to the maximum and minimum stress intensity difference across both transients were identified and cross-combined to determine S_p for each load pair. Due to the nature of the problem specification, only two local cycles (i.e. inside fatigue pairs) were formed for all locations, one within each transient. As a result, the variation in the K_e factors was the only source of difference between the two Code methodologies in this instance. In all cases, the linearised stress history was

scanned within a time-window around the extreme time points that formed S_p, to determine a conservative value of S_n for the purposes of K_e calculation.

Figure 57 and Figure 58 shows the variation in S_p and S_n and the K_e factors calculated at each assessment location, respectively. K_e factors were found to be applicable for most assessment locations since S_n considerably exceeded the $3S_m$ limit. Figure 59 shows the CUF calculated at each assessment location expending all transient repetitions. Usage factors were found to be highest in the nozzle crotch region (S22, S23) and the main coolant line (S20, S21). The trend in CUF is aligned most closely with S_n rather than S_p, and highlights the dominant influence of K_e (which is a function of S_n) on the final results. The RCC-M approach is considerably less conservative than ASME III, with each showing maximum CUFs of 3.87 and 13.76, respectively. The lower CUF calculated by the RCC-M approach is due to its more realistic stainless steel thermal-plastic correction factor, K_e^{ther}. A further reduction in excess conservatism is achievable by elastic-plastic fatigue analysis.

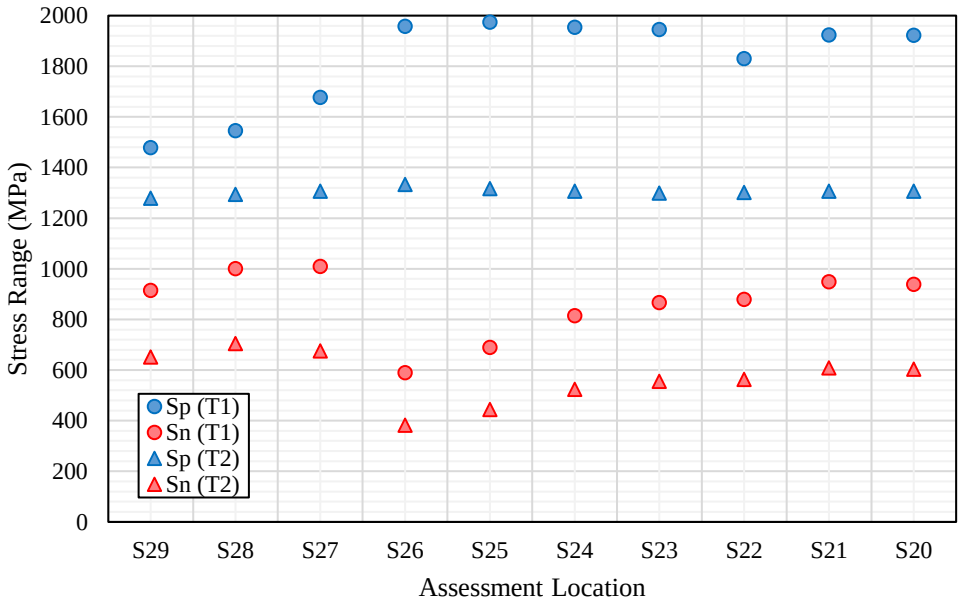

Figure 57. Variation of S_p and S_n from elastic DBA

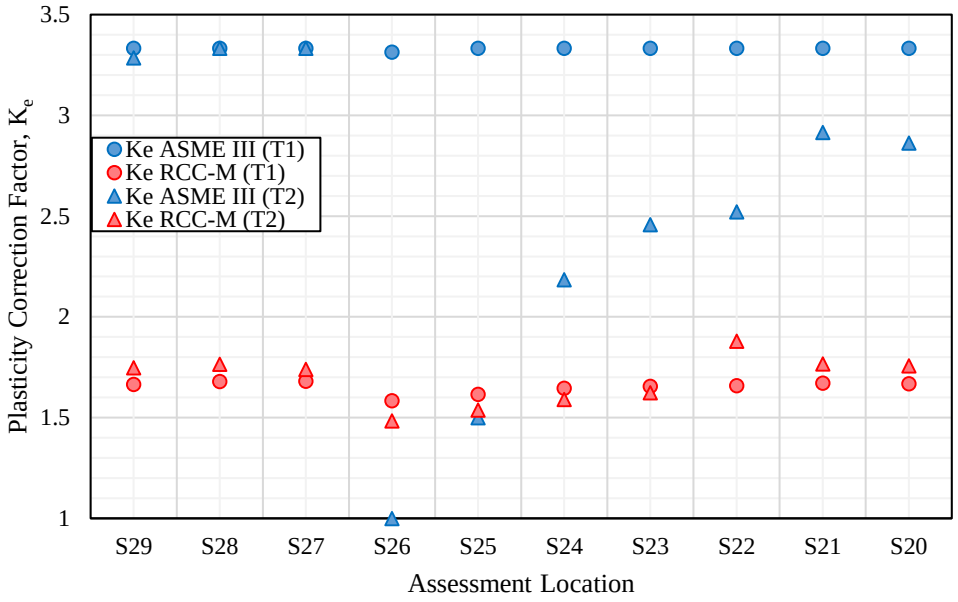

Figure 58. Variation of Code plasticity correction (K_e) factors

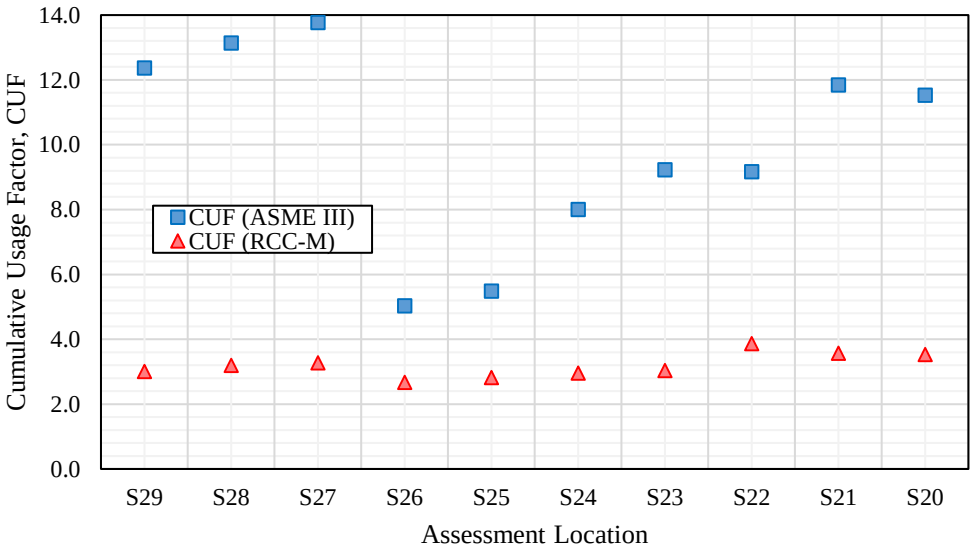

Figure 59. Variation of CUFs calculated by ASME III and RCC-M

5.4.3. Elastic-Plastic Fatigue Assessment

Cycle-by-cycle analysis was performed using the Chaboche 4-term non-linear kinematic hardening (NLKH) model discussed in Section 5.2.2 (as implemented in Abaqus [169]). In order to ensure that the stabilised hysteresis loop was evaluated, the full transient loading cycle was simulated sequentially for 10 repetitions, and the stress and strain range calculated from the final load cycle was taken as the valid result. In this case, there was little variation between subsequent cycles, and plastic shakedown

was observed within the simulation period. One exception was at the nozzle crotch corner for Transient 1, where a small but decreasing ratchet strain was evident. However, the difference in the hysteresis loop tip-to-tip strain range between cycles was found to be negligible, and therefore the final cycle was still evaluated for the purposes of this case study.

Figure 60 and Figure 61 shows the variation in alternating stress calculated by plastic fatigue analysis based on the effective strain measures discussed in 5.3 for T1 and T2, respectively. Significant differences in S_{alt} are observed between the ASME strain measures considered. In particular, the S_{alt} values calculated according to MPT were found to be 10-25% lower than those calculated using the other strain measures.

The ETSR approach was found to produce values of S_{alt} that were between 5-8% lower than EOSR, despite both being based on von Mises strain theory. This is due to the formulation of the ETSR strain measure wherein the elastic strains are assumed to be small relative to the plastic strains such that they can be treated plastically – i.e. assuming an effective Poisson's ratio, $\nu^* = 0.5$. In the case of very large plasticity such that $\nu^* \approx 0.5$, the ETSR will be approximately equal to the EOSR. However, since in most situations ν^* is often some intermediate value between 0.3 and 0.5, the ETSR can deviate somewhat below the 'correct' value calculated based on EOSR.

Concerning the EOSR and ESSR approaches, the difference in the predicted values of S_{alt} was found to be relatively small. This was attributed to the fact that the Tresca and von Mises yield formulations produce similar equivalent strain ranges for an equi-biaxial state of stress typical of thermal shock loading. One exception was the nozzle crotch corner (S22) which exhibits a higher degree of multiaxiality, wherein the ESSR was found to be approximately 11% higher than the EOSR. It is however expected that in most situations, the difference in S_{alt} values calculating using these two strain measures will be within 10%.

The CUFs calculated at each location are also shown in Figure 62 for each effective strain measure considered. The CUFs obtained from the initial fatigue assessment to

ASME III and RCC-M are shown for comparison. The fatigue limiting location by elastic-plastic fatigue analysis is determined to be at location S25, situated within the nozzle reinforcement region. This differs from ASME III and RCC-M, which predict the limiting location to be at the juncture between the nozzle and branch piping (S27) and the nozzle crotch corner (S22), respectively. This is attributed to stress redistribution occurring over the initial transient cycling period prior to shakedown, resulting in unfavourable strain concentration in the nozzle. The CUFs by elastic-plastic fatigue analysis vary considerably depending on the choice of strain measure. The limiting CUF is found to be between a minimum of 0.964 and a maximum of 1.553 when calculated using the MPT and ESSR measures, respectively. The appropriateness of each strain measure for direct evaluation of K_e is further examined and discussed.

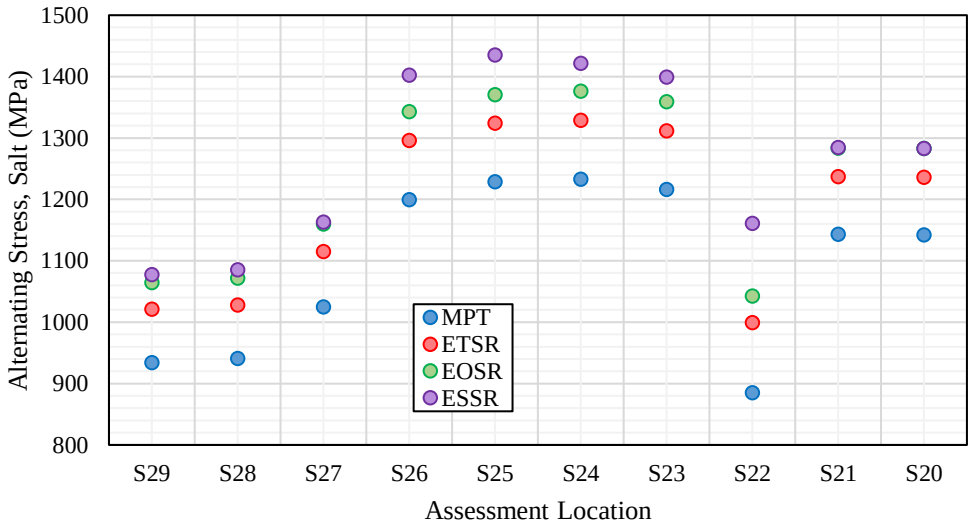

Figure 60. Variation in S_{alt} calculated by plastic analysis for Transient 1

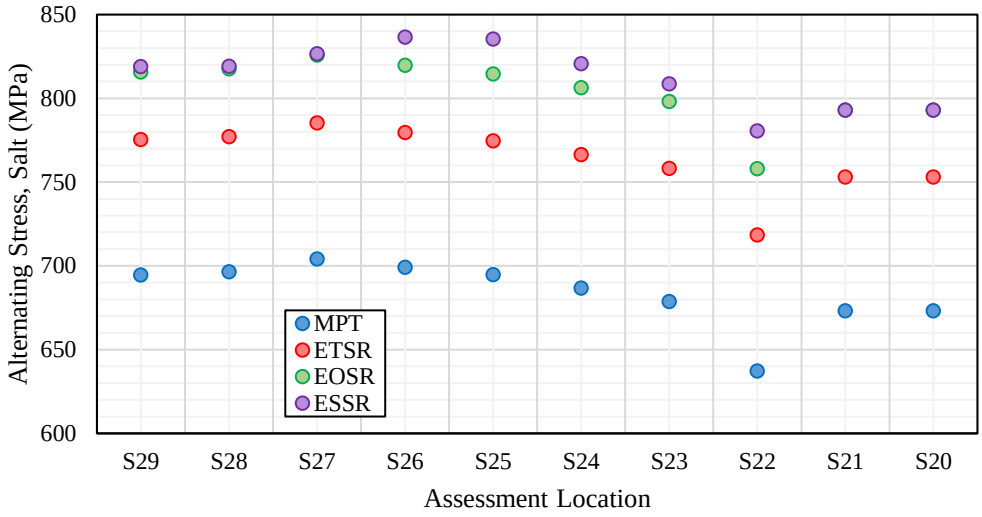

Figure 61. Variation in S_{alt} calculated by plastic analysis for Transient 2

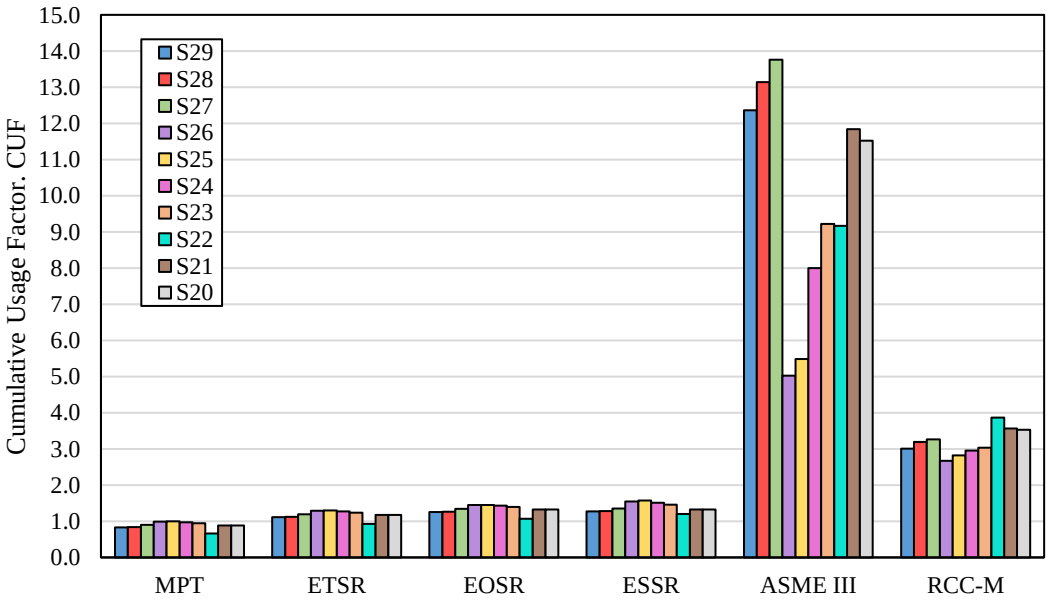

Figure 62. Summary of CUF results calculated at each assessment location.

5.4.4. Direct Evaluation of K_e^{FEA}

For the most damaging situations, the K_e factor calculated according to ASME III Appendix XIII-3450 achieved the maximum possible penalty of 3.33. Therefore, for comparison with the Code rules, more realistic K_e^{FEA} factors were calculated from the elastic-plastic analysis results according to Eq. (144).

To examine more clearly the differences between the ASME strain measures in terms of the calculated K_e^{FEA} factors, it is useful to examine the FE contour plot of K_e^{FEA}.

The K_e^{FEA} contours may be generated by calculating the maximum strain intensity range at each node of the FE model by considering all significant time points within the elastic and elastic-plastic loading histories. The contour plots of K_e^{FEA} determined for the branch piping and nozzle regions using each ASME strain measure are shown in Figure 63 and Figure 64, respectively. To enable greater clarity, the contour plots are restricted to show only $K_e^{FEA} \geq 1.0$; the deep blue contours therefore represent the condition of $K_e^{FEA} \leq 1.0$.

Based on elastic analysis results, it is reasonable to expect strain concentration to occur for regions where S_p exceeds the elastic range; conversely for regions of low stress, usually on outer surface where S_p remains within $3S_m$, stress redistribution means that K_e^{FEA} must go below unity to maintain the overall balance of deformation within the component. This can also be understood from the elastic follow-up concept, whereby the elastic recovery or 'spring-back effect' of the region of higher rigidity (i.e. the elastic core within the wall thickness) enhances the displacement of the lower rigidity region (i.e. the internal surface which suffers loss of constraint), since the total displacement is constant and this results in strain concentration on the inner surface. It is however important also to recognise that K_e^{FEA} is not related to the magnitude of strain intensity itself and so it is not necessarily the case that K_e^{FEA} is maximum on the inner surface. The K_e^{FEA} distributions calculated using the ETSR, ESSR, and EOSR approaches are all generally similar as they are each based on different definitions of shear strain and predict the maximum K_e^{FEA} to occur within the wall thickness. In contrast, the MPT K_e^{FEA} distribution is entirely different and predicts the maximum K_e^{FEA} to occur on the internal surface.

Figure 65 and Figure 66 show the variation in K_e^{FEA} calculated at each assessment location for Transients 1 and 2, respectively. Despite predicting lower values of S_{alt}, the K_e^{FEA} values calculated according to MPT are actually 15-30% higher than those calculated using the other strain measures. The principal directions associated to MPT in the elastic and elastic-plastic evaluations were often found to be different however due to the Poisson's ratio effect described in 5.3.1. For the branch pipe and nozzle regions (S23-S29), the K_e^{FEA} calculated according to MPT was found to be

approximately equal to the ratio of the radial strain range calculated by elastic-plastic analysis to the hoop strain range calculated by elastic analysis. The physical meaning of K_e^{FEA} is therefore unclear in this situation.

Interestingly, the values of K_e^{FEA} calculated based on ESSR and EOSR were found to be very similar, differing by only around 5% at most. This was also the case for the nozzle crotch corner (S22), where the K_e^{FEA} values were almost the same, despite a significant divergence in S_{alt}. Overall, it is clear that even though the Tresca-based ESSR is a more conservative strain measure compared to the von Mises-based EOSR, the K_e^{FEA} calculated based on ESSR is not necessarily higher than the K_e^{FEA} calculated according to EOSR.

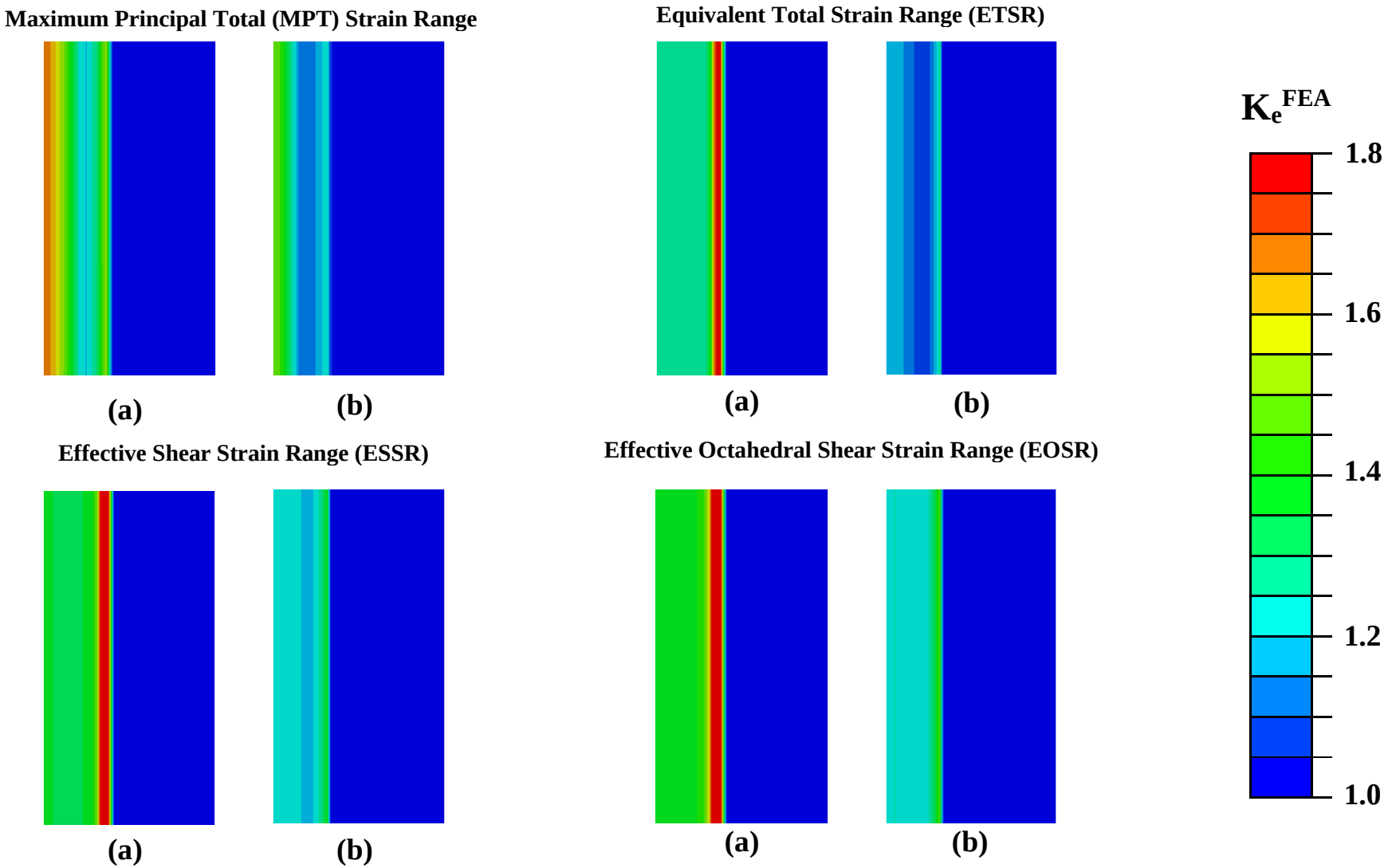

Figure 63. Contour plot of K_e^{FEA} for branch pipe. (a) Transient 1; (b) Transient 2.

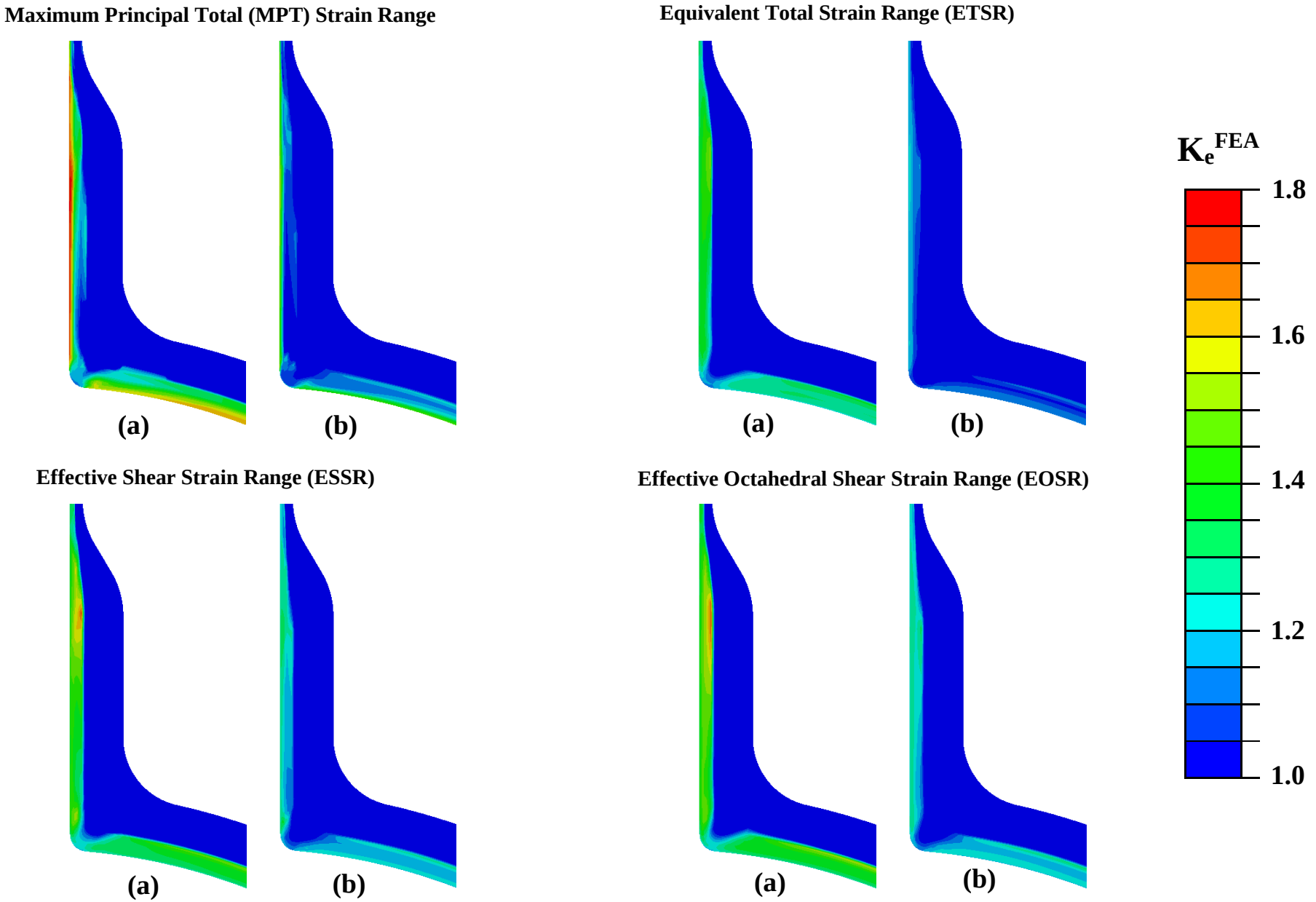

Figure 64. Contour plot of K_e^{FEA} for nozzle region. (a) Transient 1; (b) Transient 2.

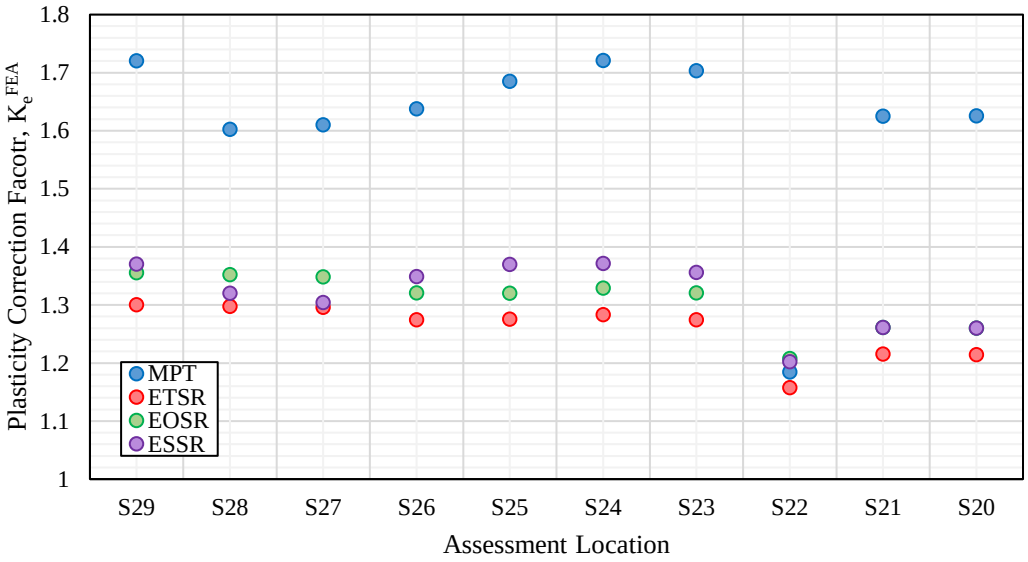

Figure 65. Variation in K_e^{FEA} calculated for Transient 1.

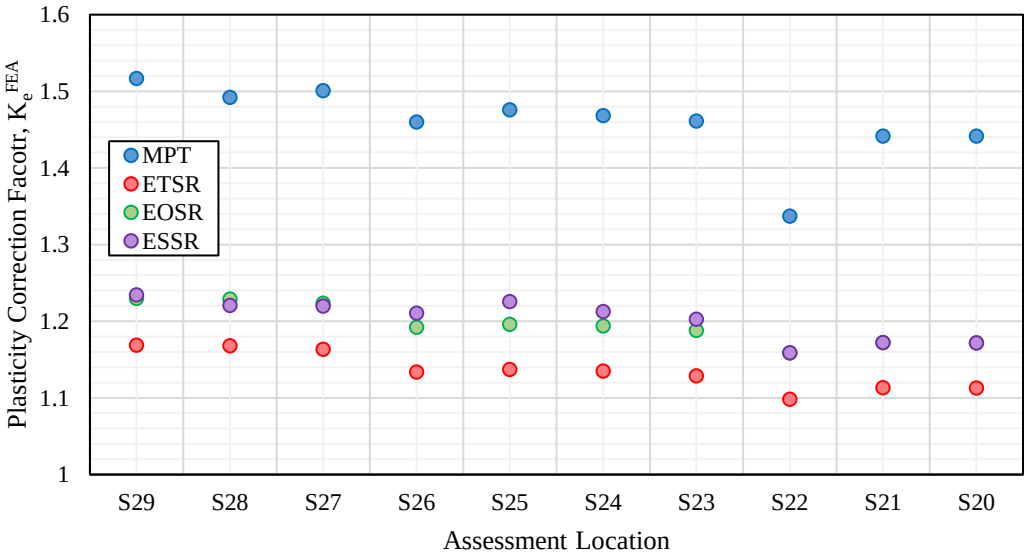

Figure 66. Variation in K_e^{FEA} calculated for Transient 2.

5.4.5. Discussion

The trend behaviour of K_e^{FEA} as a function of S_n/S_m across all assessment locations of the MCL nozzle is examined further here. Figure 67 shows the K_e^{FEA} values and best-fit curves based on the FE results with ASME III and RCC-M included for comparison. The round and triangular markers denote the K_e^{FEA} for T1 and T2, respectively. By visual examination of the elastic-plastic analysis results, it is clear that T1 envelopes

T2 in terms of severity; one would therefore expect to be able to use the K_e^{FEA} values for T1 to assess T2 and other less severe transients in an appropriately conservative manner per CC N-779, Part 6 [113].

However, concerning the MPT this is not strictly true, as evidenced by Figure 68, which shows the percentage difference in the K_e^{FEA} for T1 relative to T2. At the nozzle crotch corner (S22), the value of S_p by elastic analysis for T1 is 40% higher than for T2. However, the K_e^{FEA} calculated by MPT for T1 is actually 12% lower than for T2 at this location. This is believed to be due to the effect of the pressure drop of T2, which partially counter-acts the effect of the thermal shock on the hoop strain range. Since the MPT closely approximates the hoop strain at this location in the elastic analysis, this causes an amplification of K_e^{FEA} despite T2 actually being less damaging. The criterion of CC N-779, Part 6 therefore may not be straightforward to apply for certain locations using the MPT criterion. It is also somewhat counter-intuitive that the least conservative strain measure in terms of predicted fatigue damage should result in the largest PCFs. If the Tresca-based elastic fatigue evaluation were re-run using these K_e^{FEA} corrections, MPT would actually produce the most conservative results. This is evidently incorrect. It is therefore proposed that the EOSR and ESSR should be considered as potential alternatives to the current MPT strain measure prescribed by ASME III XIII-3440 (b).

The K_e^{FEA} values calculated according to EOSR and ESSR are very similar. However, some differences in K_e^{FEA} obtained by both approaches cannot be fully explained by the different definitions of equivalent strain. One possible explanation for this concerns the overall procedure for K_e^{FEA} determination. It is important that a consistent set of rules are used across both the FEA and correction factor derivation, such that the FE derived plastic strains used in the calculation are reliant on the same yield criterion underpinning the chosen effective strain range. Most commercial FEA software use a von Mises plasticity formulation by default, as the corresponding yield surface is smooth and continuously differentiable everywhere. Tresca plasticity is typically not available in commercial FE packages (including ABAQUS) as its yield surface contains singularities (i.e. the corners of the hexagon) which can present numerical stability problems. In this context, use of the EOSR is advantageous since it is guaranteed to be consistent with the von Mises plasticity formulation used in the FEA.

On the other hand, unless a Tresca plasticity formulation is implemented in the FEA (e.g. by using a custom UMAT subroutine), the use of ESSR would not be consistent with the plastic strain calculations performed in the FE software. For this reason, the EOSR is judged the favoured approach in most cases. It should still however be emphasised that in situations involving thermal loading, both yield criteria might still be expected to give fairly similar results, though it could account for some of the differences in the K_e^{FEA} values observed here.

It is however acknowledged that the aforementioned critical plane strain approaches may offer a more accurate estimation of cycles to crack initiation for plant representative thermal transient loading. This is supported by recent work conducted by Leary et al [170] who performed a critical review of four strain measures: the MPT, ETSR, and EOSR measures as described in this work, and a strain energy density based critical plane approach proposed in [171]. To support their comparison, Leary et al considered the experimental data available from thermal fatigue tests conducted on two Type 304 stepped pipe specimens as reported in PVP2004-2748 [134]. In this work, Leary et al adopted the ANL mean fatigue curve (Eq. (32)), which was modified using the methodology proposed by Batten et al [172] to represent initiation of a 250 μm deep crack. Leary et al found that the critical plane approach could predict most accurately the number of experimental cycles to initiate a 250 μm-deep crack in the thickest section of the stepped pipe specimen. Considering mean and lower bound cyclic stress-strain data, the critical plane approach predicted 756 and 1225 cycles to initiate a 250 μm crack, respectively; this compared favourably to the geometric mean (878) and longest life (1408) to initiate a 250 μm deep crack in the test. The MPT, ETSR, and EOSR measures were all found to be pessimistic, underestimating the 250 μm initiation life by up to a factor of four when used in conjunction with lower bound cyclic stress-strain data. Therefore, if elastic-plastic analysis is to be utilised with the sole intent of predicting more accurate initiation lives, then critical plane approaches are likely to be the better option.

Nonetheless, based on the observations noted in this case study, the EOSR is still concluded to be the most practical effective strain measure where determination of K_e^{FEA} by elastic-plastic analysis is the primary concern. Being based on von Mises

theory, it characterises most closely the general plasticity behaviour of structures. It can also be calculated very efficiently, allowing for the rapid generation of K_e^{FEA} contour plots that would otherwise be very time-consuming to produce were a critical plane approach to be adopted instead. The EOSR was therefore adopted for all further detailed FE analyses performed in this thesis, which considered a wide variety of LWR plant representative components.

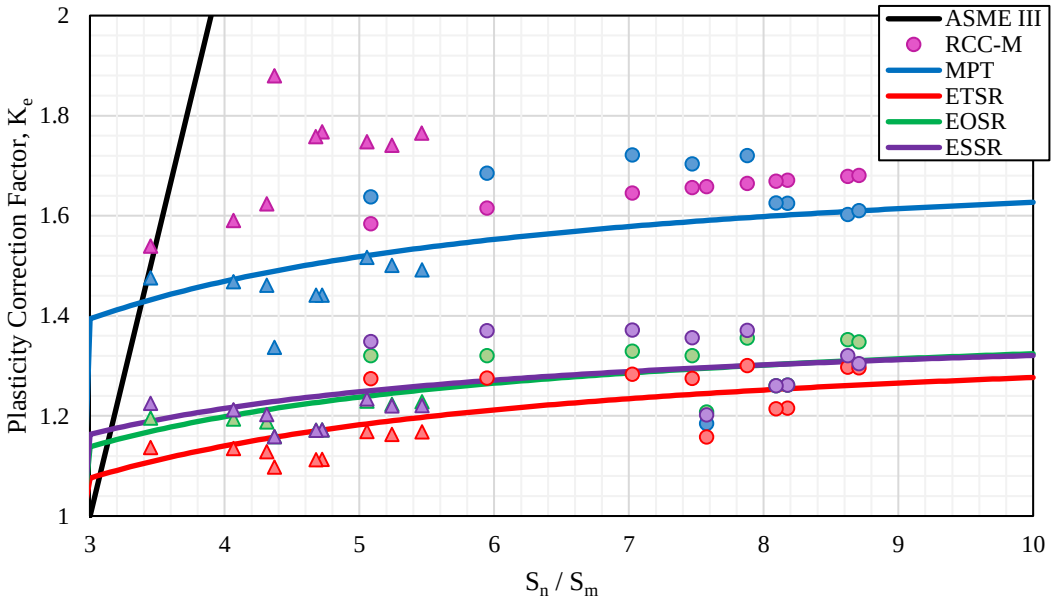

Figure 67. K_e vs. S_n/S_m for MCL nozzle

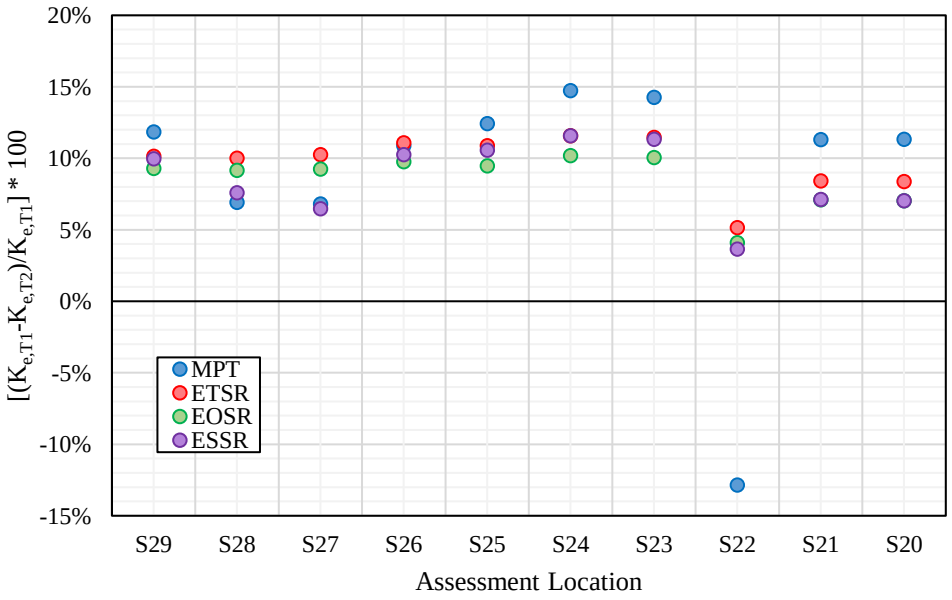

Figure 68. Percentage (%) difference in K_e: T1 vs. T2

6. Description of LWR Plant Representative Finite Element Models

This section presents a description of the finite element modelling programme considering various case studies, which were selected for the detailed assessment of K_e^{FEA} by elastic-plastic analysis. The case studies were selected to be representative of a variety of LWR primary-circuit components, subjected to plant representative thermal transients. The cases studies considered for detailed evaluation are:

1. A thick-walled cylinder subjected to sustained pressure and parabolic thermal gradient [74].
2. The Bettis Stepped Pipe described by Jones et al [134].
3. Three different auxiliary piping nozzle geometries.
    a. The MCL nozzle discussed in 5.4 from Part 2a of the CORDEL Report on Non-Linear Analysis Design Rules [168].
    b. The charging nozzle and safety injection nozzle described in Nitzel et al [173].
4. Tapered nozzle-in-vessel from Kobayashi and Yamada [174].
5. PWR nozzle with attached thermal sleeve from Hartwig [175].
6. Nuclear vessel skirt support (Y-Piece) from Kasahara [176].
7. Thin-walled pipe with an external, circumferential, semi-circular notch.

A description of each case study along with major engineering assumptions is presented below.

6.1. Thick-walled Cylinder

The problem, originally considered by Miller [74], was selected to investigate the influence of sustained pressure acting in combination with cyclic thermal loading on K_e^{FEA}. Figure 69 illustrates the 2D axisymmetric FE model, loading, and boundary conditions adopted for the cylinder considered by Miller. The inner radius of the cylinder is 350 mm with wall thickness of 70 mm. The bottom face of the cylinder is fixed in the axial direction, whilst the top face is constrained to expand in plane.

Miller's theoretical analysis considered a parabolic thermal gradient through-thickness and this was also adopted here. The inner surface temperature of the cylinder was

varied directly assuming an infinite heat transfer coefficient. The outer surface of the cylinder was assumed adiabatic. The analyses considered multiple combinations of sustained pressure and cyclic thermal loading. The cylinder is initially at a temperature of 300°C before experiencing a thermal shock cycle. The ramp time for the down- and up-shock is 10s. The sustained pressure load cases were considered from a minimum of P = 10 MPa up to a maximum of P = 25 MPa with an increment of 1.25 MPa. For each case of sustained pressure, 8 cases of cyclic thermal loading were considered with T_{min} = 21, 50, 100, 150, 175, 200, 225, 250°C. In total, 104 different load combinations were evaluated. In the structural model, a closed-end condition was assumed and the end cap pressure, P_c, applied to the top of the cylinder for each load case was calculated by Eq. (164).

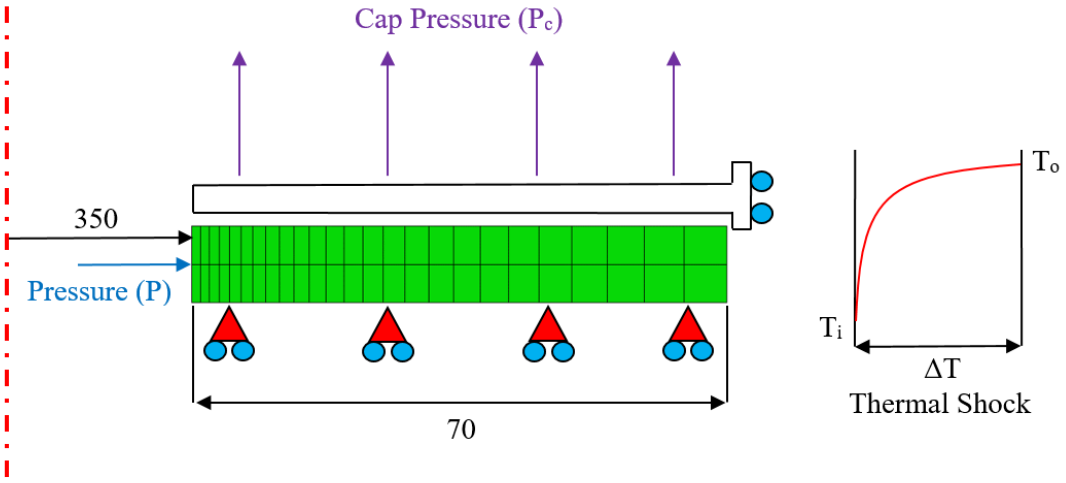

Figure 69. Thick-walled cylinder FE mesh, dimensions, and boundary conditions.

6.2. Bettis Stepped Pipe

Thermal fatigue tests as described in [134] were carried out at Bettis Laboratories (USA) to provide data against which to compare the performance of the Code fatigue methods and DFCs. The thermal fatigue tests of Type 304 stainless steel pipes were conducted by alternately cycling hot and cold water through a pipe of varying thickness. Low dissolved oxygen water was used, consistent with PWR conditions, in order to evaluate environmental effects on fatigue initiation. The pipes were stepped to four different thicknesses (4.55, 8.12, 11.7, and 15.2 mm) to vary the thermal resistance along the length of the pipe.

The pipe was held a constant internal pressure of 17.2 MPa. Flow rates of 2.4 and 3.2 l/s were used for the cold and hot water injections. This flow rate was sufficiently rapid to simulate a near-step change in the bulk fluid temperature in contact with the bore of the pipe. Water temperature was raised rapidly from 38℃ to 343℃ in 3 s, followed by a hold at elevated temperature for 237 s. Subsequently, the water temperature was cooled rapidly back to 38℃ in 3 s followed by a further hold period of 237 s. This process was repeated until crack initiation was detected; crack initiation was defined by nucleation of a 0.254 mm ($1/100^{th}$ of an inch) surface crack. The test conditions equate to an 8-minute continuous transient consisting of a symmetric, fully-reversed, 4 minute hot shock and 4 minute cold-shock combination.

The FE model of the stepped pipe was created in Abaqus to analyse the thermal and pressure loading of the pipes. The FE model utilised 8-node, 2D axisymmetric elements for the analysis. The FE mesh is shown in Figure 70 with major dimensions highlighted. Twenty elements through the thickness of the pipe section with a bias to the inside surface was deemed to be sufficient to accurately capture the through-wall temperature distribution, with the FE model containing a total of 2680 quadratic quadrilateral elements with 8349 unique nodal points. The stress classification lines (SCLs) selected for fatigue assessment are also highlighted in Figure 70, and are located at the mid-point of each stepped pipe section.

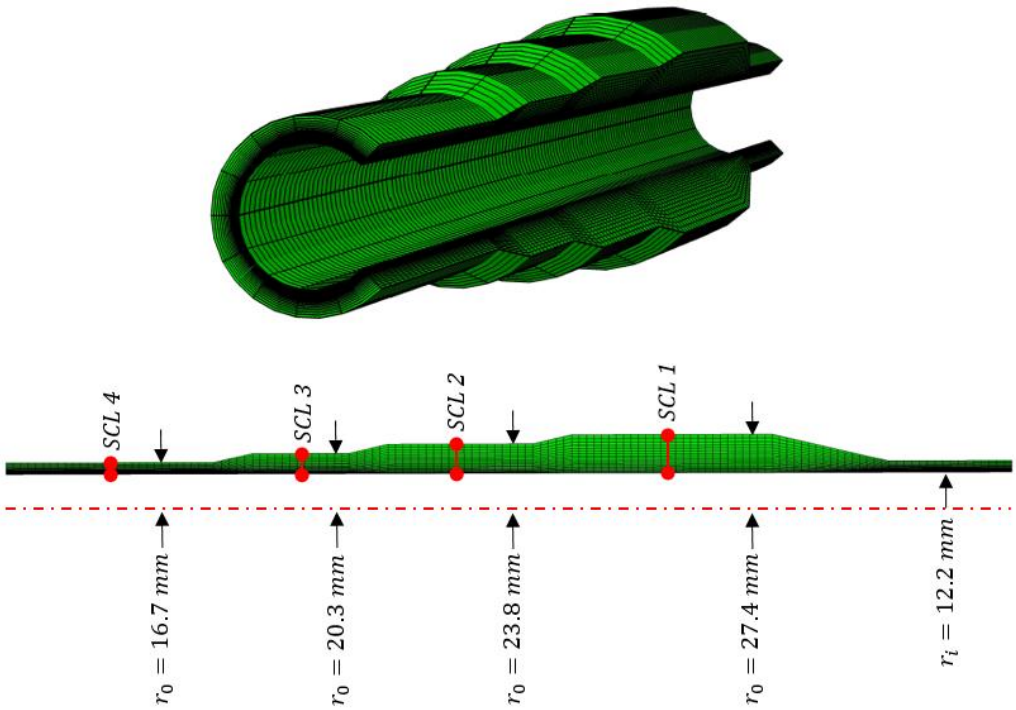

Figure 70. Stepped pipe FE mesh, major dimensions, and SCL locations

In Jones *et al* [134], the fluid temperature contacting the pipe bore was described to vary *"linearly between the upstream and downstream temperature detectors as a function of time"*. In addition, it was noted that *"Since the water flow rate was very high, the film coefficients on the inside of the pipe were determined to be very high (3000 to 5000 BTU/(hr-ft^2-°F)). This essentially drove the inner pipe wall to the fluid temperature"*. Based on these observations, a temperature-dependent HTC was adopted as the most appropriate for the thermal analysis. The variation of the HTC with temperature is shown in Figure 71, with the maximum and minimum water temperatures marked for reference. The outside metal surface was assumed adiabatic. The evolution of the transient temperature fields was captured in sufficient detail by setting the solution control options to ensure that the gauss point temperature increment between successive time-steps did not exceed 2°C. The transient temperature history calculated at the interior (ID) and exterior (OD) points of each SCL are shown in Figure 72. It takes far longer for thermal equilibrium to be established across the thickest pipe section compared to the thinner sections.

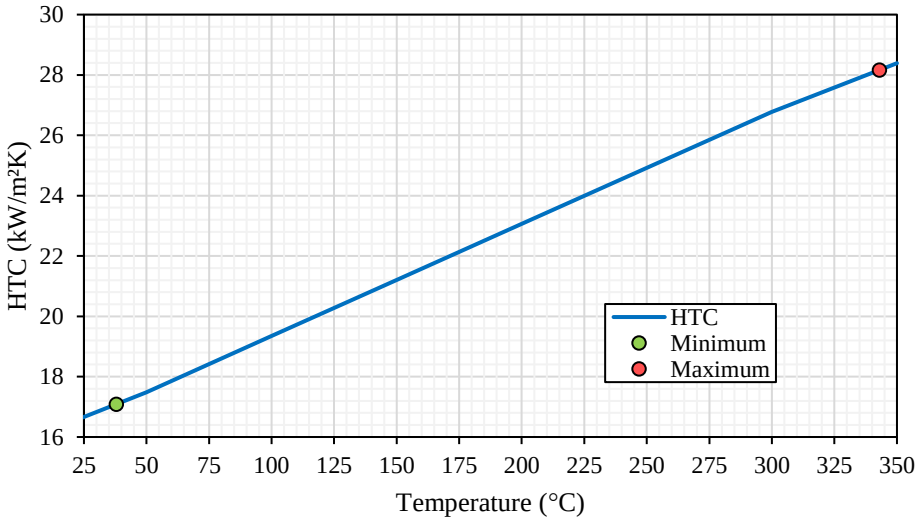

Figure 71. Temperature-dependent HTC used in thermal analysis of the stepped pipe test

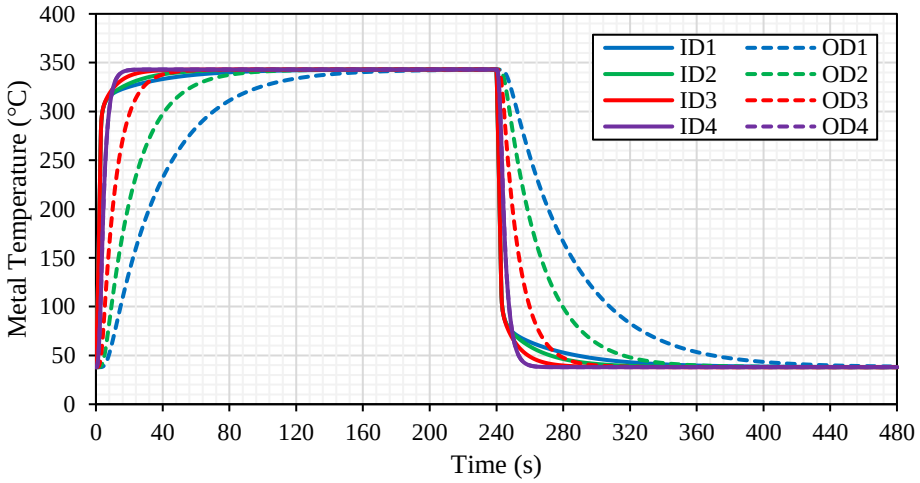

Figure 72. Transient temperature history calculated at each SCL for the test transient.

In Jones et al [134], the structural analysis assumed that pipe loads arose only due to the effects of internal pressure. A closed end condition was therefore assumed and a P_{cap} of 19.343 MPa was calculated per Eq. (164) and applied to one end of the stepped pipe. To constrain the model against rigid body motion, the opposite end of the pipe was constrained to remain fixed in the longitudinal direction. The free end of the pipe was also constrained to expand in-plane. This was achieved by coupling the longitudinal displacements of the nodal points situated on the free end of the pipe.

In addition to the test transient described above, an additional fifty-five arbitrary transients were also analysed for the stepped pipe geometry. This consisted of a range of symmetric and asymmetric thermal shock transients, which considered different HTCs and ramp rates. Fatigue analysis was performed for each transient based on the results output from the elastic and elastic-plastic FE runs; the analysis was limited to consider only the interior assessment points for each SCL since this is where crack initiation was observed in the tests.

6.3. PWR Auxiliary Piping Nozzles

Three nozzle geometries of this type were selected for evaluation. The first is the generic main coolant line nozzle described in Part 3 of the CORDEL Mechanical Codes and Standards Task Force (MCSTF) Report on Non-Linear Analysis Design Rules [168] and which was initially considered in Section 2. This is henceforth referred to as the 'CORDEL nozzle'. Two other auxiliary piping nozzles – the charging and safety injection nozzles – were also selected for evaluation. The charging and safety injection nozzles are attached to segments of the RCS cold leg run pipe, connecting the main line to small bore attached piping. A description of both nozzles and their major dimensions is provided in the U.S. NRC sponsored report published by Nitzel *et al* of the Idaho National Engineering Laboratory (INEL) [173], though the plant to which they belong is anonymised. It is noted that the nozzles described in the CORDEL Benchmark Report [168] and in Nitzel *et al* [173] were respectively fabricated from Type 316L and Type 316 material, but were instead assumed to be Type 304 in the present work to utilise the temperature-dependent NUREG/CR-5704 Type 304 Chaboche model described in 5.2.2. Besides, Type 304 is an equally reasonable grade of austenitic stainless steel used to fabricate piping nozzles.

The FE models of the nozzles were developed in Abaqus [82]. The 2D axisymmetric FE model of the CORDEL nozzle is shown in Figure 73 alongside a quarter symmetric 3D FE model for comparison. The SCL locations selected for the fatigue assessment are also shown in Figure 73. Equivalent SCL locations were also selected for the charging and safety injection nozzles.

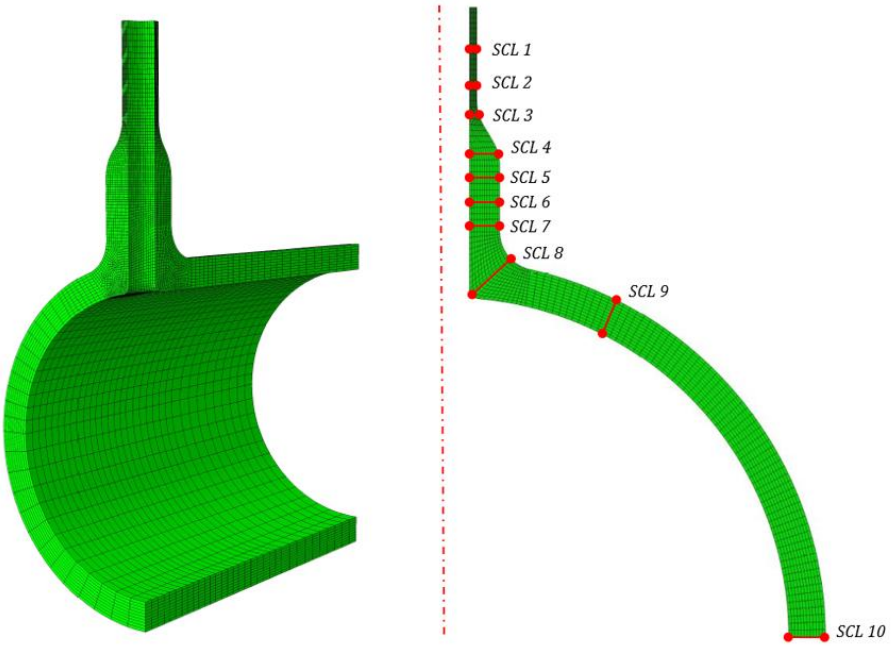

Figure 73. 2D axisymmetric FE model of CORDEL nozzle with SCL locations highlighted.

The design transients selected for evaluation were the same for all three nozzles. The vessel is initially at its steady state operating condition of 15.5 MPa internal pressure, and uniform temperature of 350°C. The RCS coolant water contacting the internal surface of the assembly then undergoes a rapid decrease in temperature lasting 10s. After a further soak period of 1400s, the RCS coolant water temperature recovers rapidly back to its initial temperature of 350°C in 10s, and is followed by further soak out period of 1400s. Thus, a full thermal cycle taking place under constant operating pressure is completed in 3500s. A range of symmetric thermal shock transients were considered by varying the minimum RCS coolant water temperature achieved during the initial cold shock event. The full design transient description is illustrated in Figure 74.

In performing the thermal analysis of the PWR RCS piping nozzles, a constant convective HTC of 22.8 kW/m^2 was adopted for all design transients. This is judged to be somewhat pessimistic compared to the use of the Dittus-Boelter relation [177] with best-estimates of local reactor coolant flow rates. The external metal surface of the nozzles was assumed adiabatic.

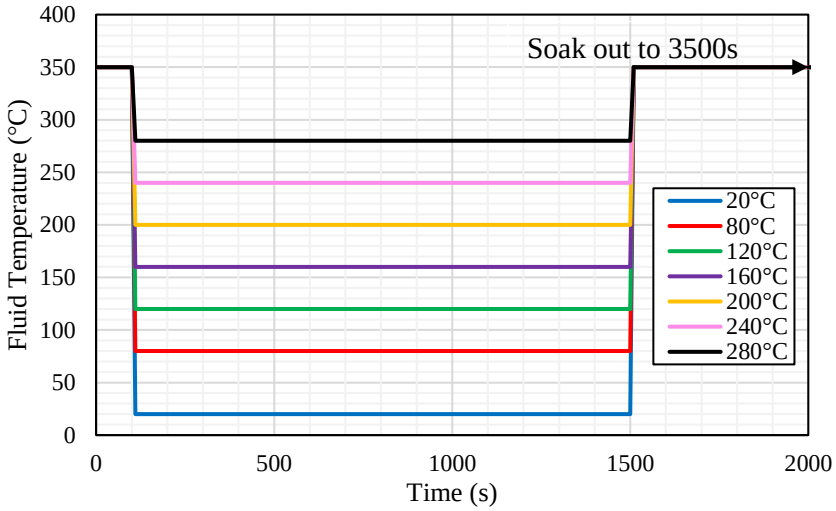

Figure 74. Design thermal transients specified for the PWR RCS piping nozzle analyses.

For the structural model, the bottom face of the shell section was fixed in the Y-direction to constrain the assembly against rigid body motion. A constant pressure of 15.5 MPa was applied to all internal surfaces. A closed-end condition was assumed and an equivalent cap pressure was applied to the end face of the attached piping to satisfy global equilibrium. The cap pressure applied to the end of the branch pipe was calculated using Eq. (164) for each nozzle geometry. To model the response of the attached branch piping system not modelled, a plane end condition was specified for the branch pipe. The nodes lying on the end face of the pipe were constrained to expand in-plane by coupling their displacements along the longitudinal axis of the pipe (aligned with the global Y-axis).

A mesh sensitivity study was initially conducted to establish the level of mesh refinement required to achieve results convergence. Three different mesh sizes were selected for comparison, defined as having 6, 12, and 20 quadratic, quadrilateral elements through-thickness of every continuous section with element bias towards the internal surface. The mesh sensitivity study was conducted for each of the nozzle geometries. It is recognised that the level of mesh refinement could potentially influence both the surface stresses as well as the stress resultants determined from stress linearisation. Therefore, it was appropriate to perform an ASME III Appendix XIII-3520 fatigue scoping assessment using the results obtained for each mesh size and then compare the final calculation results. The scoping calculation was performed

for SCLs 1, 5, 8, and 10 and considered only the most severe design transient attaining a 20°C minimum coolant water temperature. The sensitivity of S_p to mesh density is greater at thicker assessment locations. The results obtained for S_n were essentially the same, and were concluded to be insensitive to the level of mesh refinement. The results of the mesh sensitivity study are summarised in Figure 75 for the CORDEL nozzle. A similar results trend was also observed for the safety injection and charging nozzles. The difference in S_p was limited to 1% between the 12- and 20-element mesh variants. Based on the results, it was decided to adopt 20 elements through-thickness for each of the FE models, since it gave a reasonable payoff between accuracy and computational cost, which was not significantly greater than when using 12 elements through-thickness.

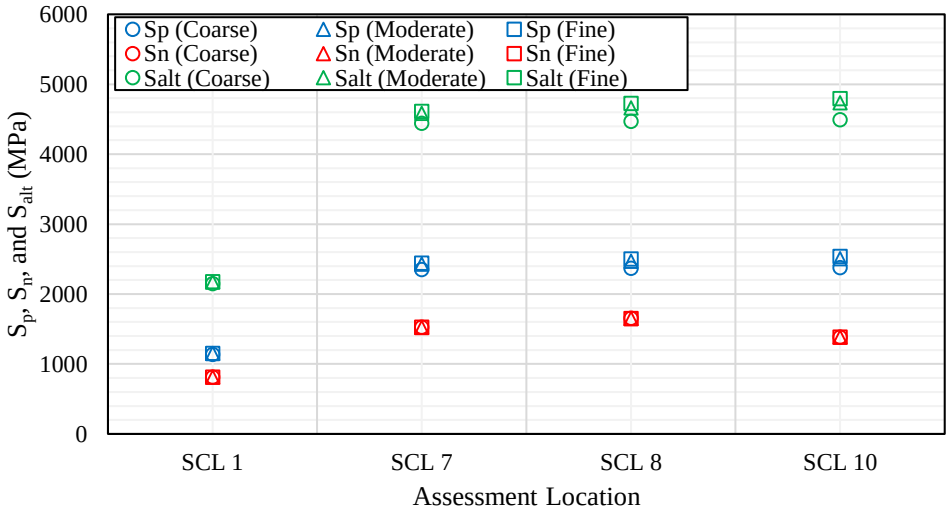

Figure 75. Summary of results obtained from mesh sensitivity study of CORDEL nozzle.

6.4. Tapered Reactor Nozzle-In-Vessel

This case study considers a large tapered nozzle attached to the end of a thick-walled reactor vessel. The tapered transition between the nozzle reinforcement and attached RCS piping presents a local discontinuity. When hot/cold fluid flows into the reactor vessel, an inhomogeneous thermal stress distribution may arise due to large axial variation in thermal resistance. This can produce spatially varying plastic deformations and strain concentration at the discontinuity region. The following case study is similar to that described by Kobayashi and Yamada [174], and adopts an identical nozzle

geometry. The geometry of the nozzle is shown in Figure 76, along with major dimensions.

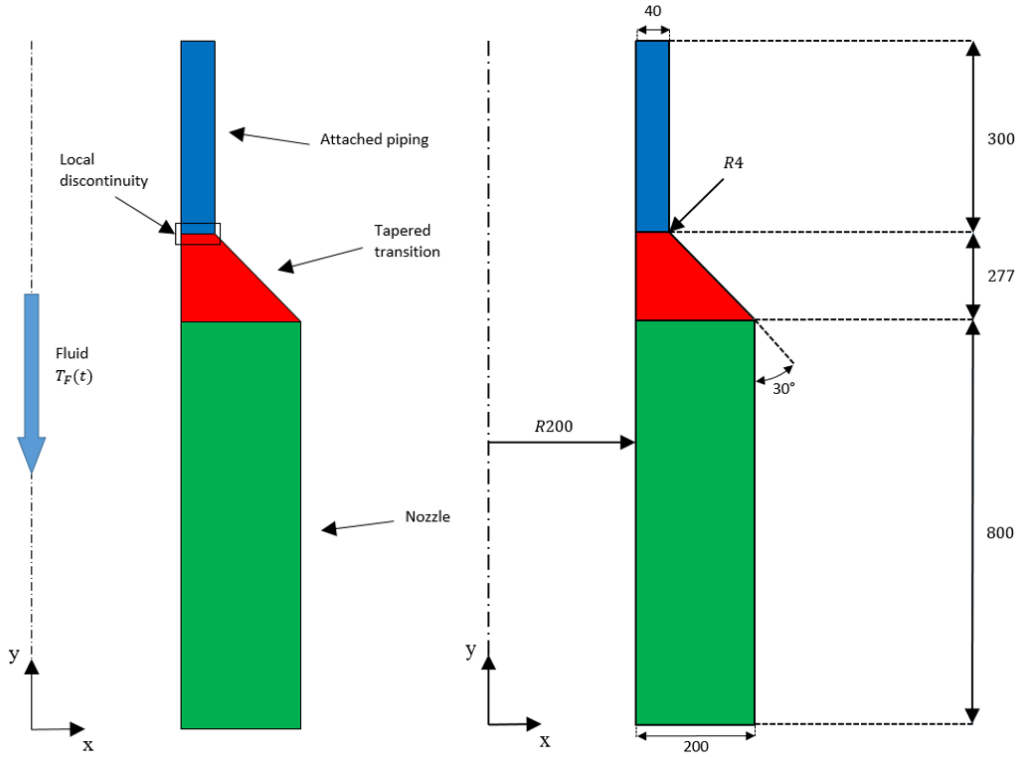

Figure 76. Description of tapered vessel nozzle geometry and major dimensions.

The design thermal transients considered for this study are symmetric thermal shock transients, similar to those considered for the PWR RCS piping nozzles, and shown by Figure 77. It is acknowledged that for this type of component, the design transients considered here are very pessimistic. Normally, coolant heat-up and cool-down rates are carefully controlled during plant start-up and shutdown sequences to ensure that any thermal stresses developed in the RPV shell and nozzle forgings are kept to a minimum. However, of primary concern here is an understanding of the mechanism of strain concentration in similar vessels such that a general conclusion can be drawn that remains applicable when assessing a wider range of thermal shock type transients in fatigue design. With this in mind, it appeared most appropriate to consider a most pessimistic condition, expected to occur very infrequently. In performing the thermal analysis of the tapered nozzle, a convective HTC of 22.8 kW/m^{2}K was specified for the internal surface. All other surfaces of the nozzle were assumed adiabatic.

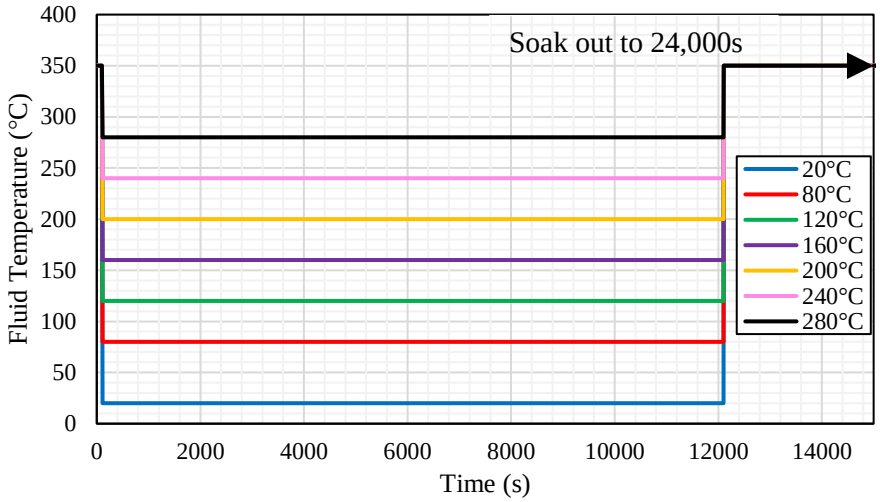

Figure 77. Description of design thermal transients specified for tapered nozzle-in-vessel FE analyses.

For the structural model, the bottom face of the nozzle was fixed in the global Y-direction to constrain the assembly against rigid body motion. A constant pressure of 15.5 MPa was applied to all internal surfaces. A closed-end condition was assumed and the end cap pressure, P_c, calculated to be 35.23 MPa by Eq. (164), was applied to the end face of the attached piping. The nodes lying on the end face of the pipe were constrained to expand in-plane by coupling their displacements along the longitudinal axis of the pipe (aligned with the global Y-axis).

The finite element mesh adopted for the tapered nozzle is shown by Figure 78. The mesh contained 1236 quadrilateral, quadratic elements with 3939 unique nodal points. The mesh was carefully refined at the discontinuity induced by the nozzle-to-pipe juncture. The high thermal resistance of the nozzle leads to the formation of very large radial thermal gradient during the thermal shock. Additionally, the large difference in thickness between the nozzle and attached piping results in development of an axial thermal gradient as heat penetrates through the thickness of the pipe at a faster rate than the nozzle. This mismatch in thermal behaviour is known to promote elastic follow-up, and its effect on K_e^{FEA}, particularly at the juncture (SCL 3) is of significant interest in this case study.

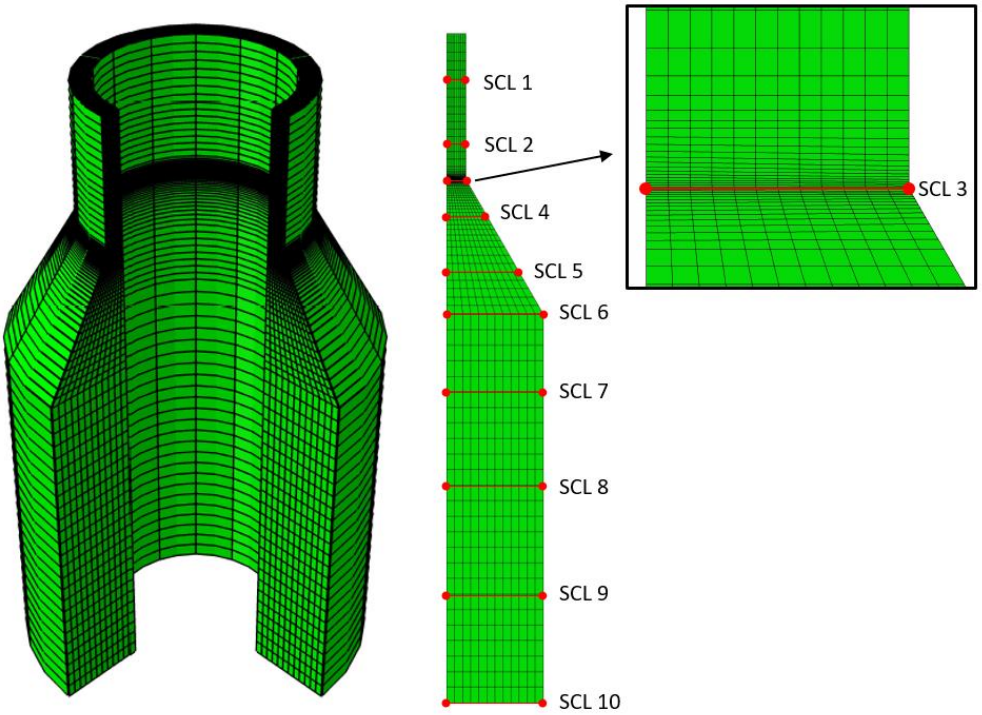

Figure 78. 2D axisymmetric FE mesh of tapered nozzle-in-vessel with SCL locations highlighted.

6.5. PWR Nozzle with Attached Thermal Sleeve

This case study considers a PWR vessel nozzle with an attached thermal sleeve. The purpose of the thermal sleeve is to soak the high cyclic thermal stresses experienced by these nozzles, mitigating potential fatigue damage in the more susceptible nozzle crotch region. The following case study is that described in Hübel's Simplified Theory of Plastic Zones textbook [175], and is based on a simplified version of the original nozzle design specification provided by AREVA NP GmbH; the geometry of the nozzle is as described in Hübel [175] and is shown in Figure 79. The major dimensions of the nozzle are detailed in Figure 79. The FE model of the nozzle is shown in Figure 80 with the relevant SCL locations highlighted.

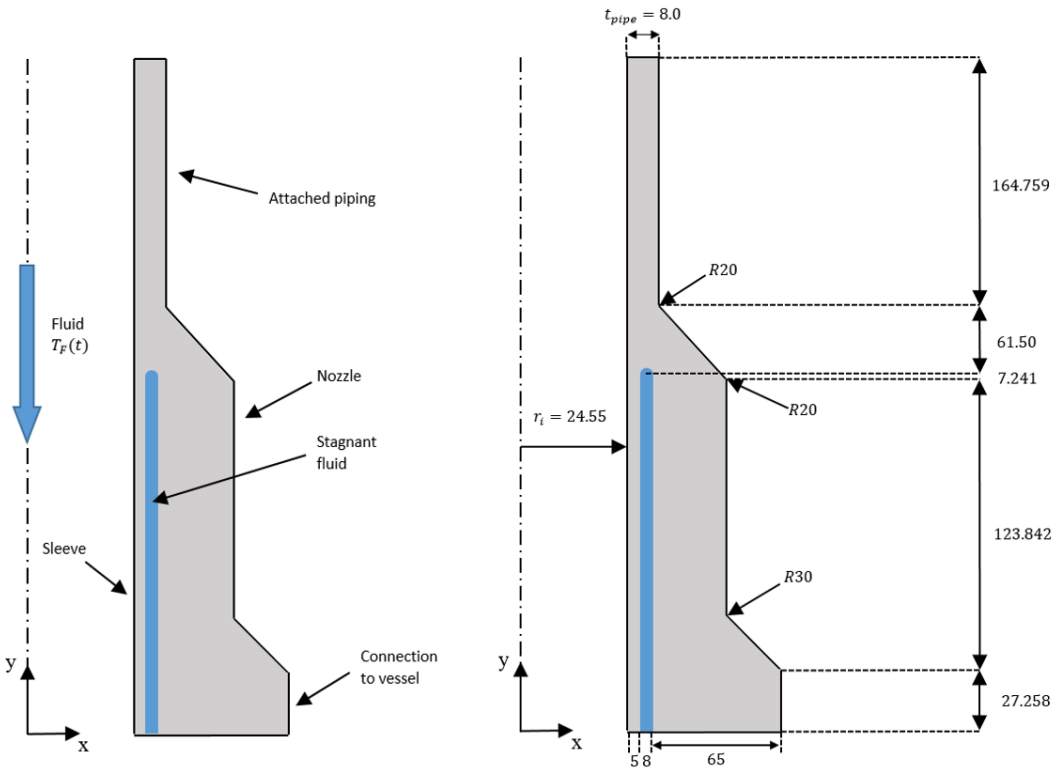

Figure 79. Geometry and major dimensions of PWR nozzle with thermal sleeve from Hübel [175]

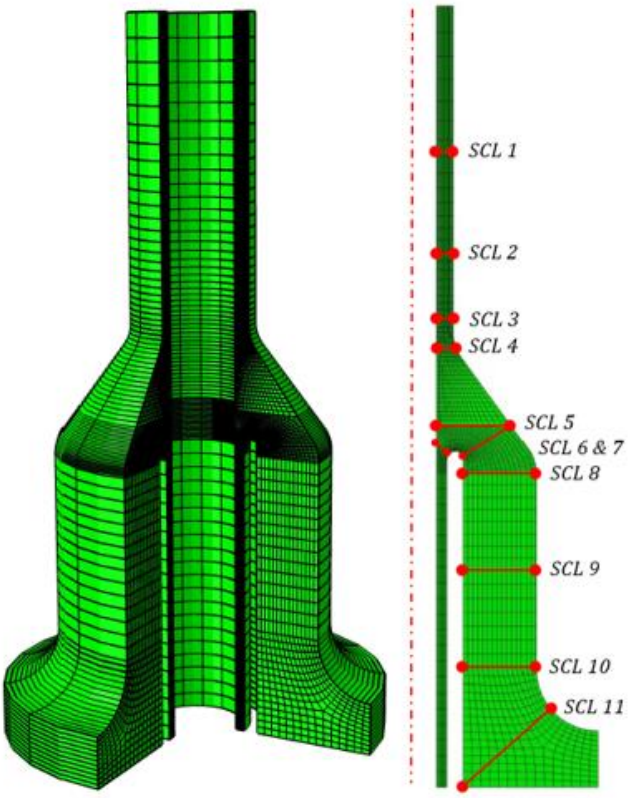

Figure 80. FE model of PWR nozzle with thermal sleeve.

The design transient considered in this case study is an asymmetric thermal transient equivalent to that described in Hübel [175]. The entire assembly is initially at a uniform operating temperature of 350°C. The loading event consists of a thermal down-ramp characterised by an injection of cold fluid through the nozzle, while the larger connected vessel remains at 350°C. Following a short holding time, a faster up-ramp returns the fluid temperature back to its initial temperature of 350°C, completing the thermal cycle. In Hübel [175], the minimum fluid temperature was taken to be 50°C, but for this case study a range of different minimum fluid temperatures were considered such that results could be obtained for thermal shocks of varying severity. A full description of the design transients considered is shown in Figure 81.

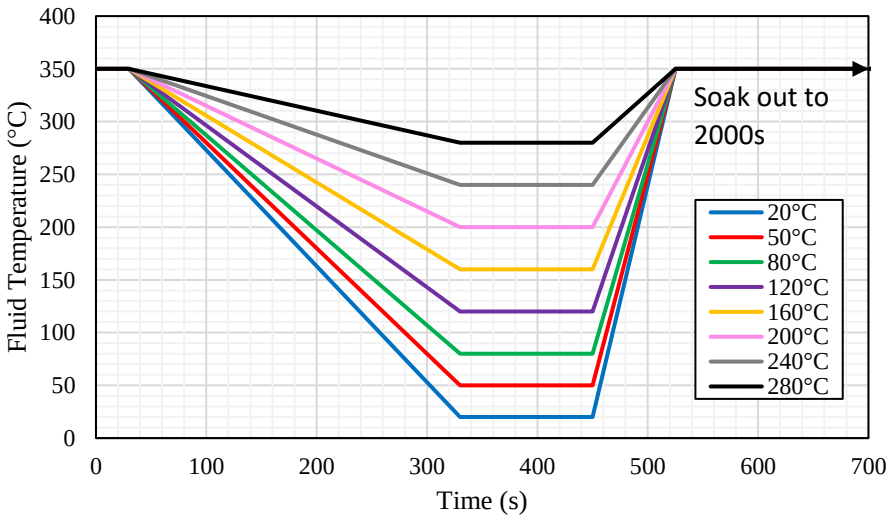

Figure 81. Description of design thermal transients considered for PWR nozzle thermal sleeve.

The heat transfer problem for this case study differs from that of the previous nozzles since the large vessel to which the nozzle is attached maintains an elevated temperature whilst the nozzle experiences a sharp decrease in temperature. Due to conduction, both radial and axial temperature gradients are likely to occur, with the latter arising as the thermal shock progresses. The thermal sleeve possesses a low thermal resistance due to its minimal section thickness thereby minimising thermal stresses. Consistent with Hübel [175], a constant HTC of 30 kW/m^{2}K is specified for the internal surface of the pipe and sleeve attachment. A region of stagnant fluid also exists behind the sleeve, which serves to damp the transfer of heat via convection to the nozzle internal surface. This region of stagnant fluid was included in the thermal FE model as if it were of

solid material, but with modified thermal properties, which aimed to mimic the effect of reduced convection. The density, thermal conductivity, and specific heat associated to the stagnant fluid region were of values 800 kg/m^3, 9 W/mK, and 5000 J/kgK, and assumed temperature-independent. A fixed temperature condition of 350°C was applied to the bottom connection to the larger vessel not modelled. All other external surfaces of the assembly are assumed adiabatic.

The FE mesh for the structural model does not include the elements that were previously associated to the stagnant fluid region in the thermal model. As this region is a fluid, it does not experience stress in the conventional sense, and was used solely to solve for the transient temperature fields throughout the metallic assembly. The bottom of the connection to the vessel was fixed in the global Y-axis to constrain the assembly against rigid body motion. The sleeve was however left unconstrained and free to experience vertical displacement. As in Hübel [175], internal pressure was neglected for this case study since the compact nature of the nozzle largely precludes any potential ratchet mechanism arising due to primary stresses. The pipe was constrained to expand in-plane by coupling the vertical displacements of all nodal points lying on the end face of the pipe.

The transient temperature distributions calculated corresponding to the end of the cold shock (330s) and the end of the hot shock (525s) are shown in Figure 82. Radial and axial thermal gradient are clearly shown to be significant for this structure. Figure 83 shows the magnified thermo-elastic structural displacements calculated corresponding to the initial condition, end of the cold fluid injection (330s), and the end of the recovery to steady state (525s). The presence of the large axial gradient in Figure 83 produces elevated membrane and bending action in the axial and circumferential planes. This is especially significant at the thermal sleeve attachment juncture.

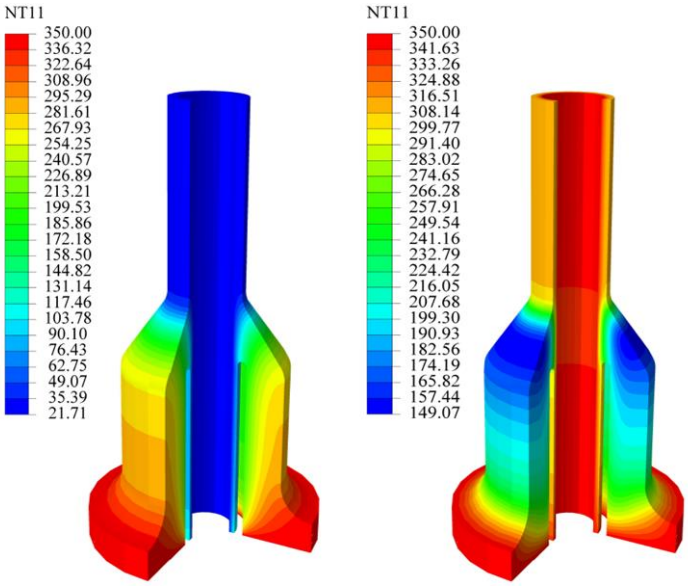

Figure 82. Temperature distributions calculated for most severe design transient.

Left at end of initial cold shock period (330s), right at end of recovery to steady state operating condition (525s).

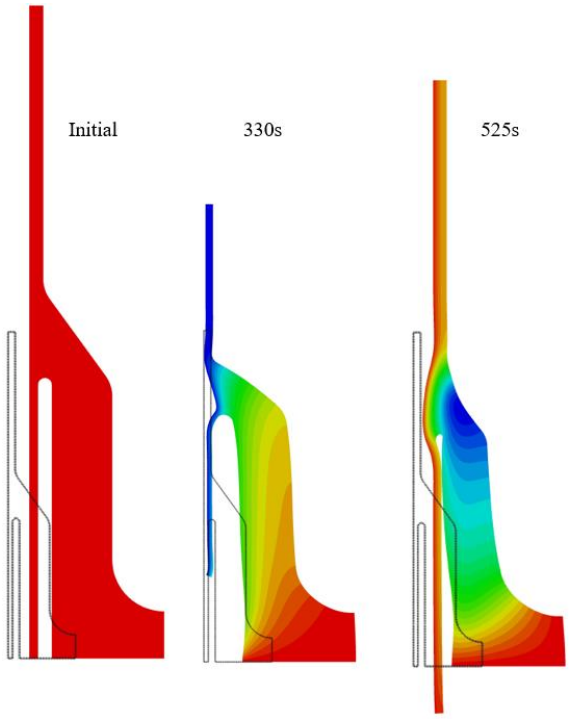

Figure 83. Displacements calculated at key time points during design transient.

Contours refer to the temperatures. Displacements are magnified by a factor of 60.

Figure 84 shows a contour plot of maximum $S_p/3S_m$ calculated at every node in the FE model for the most severe design transient. The maximum value of 3.14 is situated on the inner surface slightly above the notch imposed by the thermal sleeve attachment at

point B. Other regions of potentially high strain concentration include the notch itself, point C, and the internal and external surface of the nozzle-to-pipe juncture, points A (I) and A (O). Of additional concern is the sectional plasticity (implied by $S_p/3S_m$ > 1.0) observed within the sleeve thickness near the attachment point, which may pose problems in satisfying the prerequisite requirements of ASME III Appendix XIII-3450 (a). Accordingly, SCLs 4-7 shown in Figure 80 were positioned to capture these locations of interest.

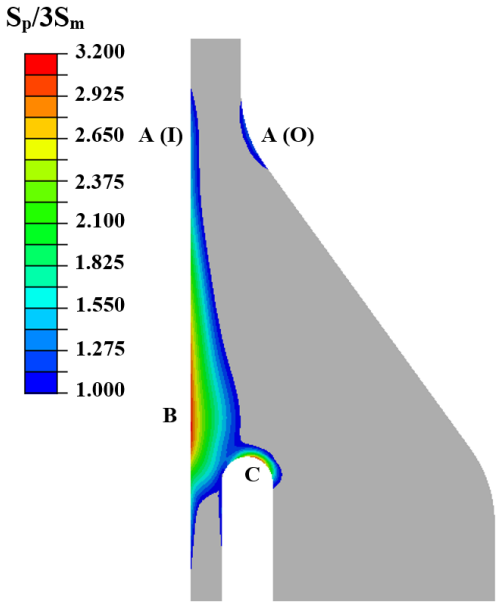

Figure 84. Distribution of $S_p/3S_m$ for most severe design transient.

6.6. Nuclear Vessel Skirt Support

One of the most common methods used to support large vertical vessels including LWR RPVs is by means of a branched cylindrical shell called a *skirt*. Skirts are often lap-, fillet-, or butt-welded to the lower head region of the vessel. The use of a skirt rather than other alternatives (e.g. legs, saddles, rings, etc.) is desirable as it minimises local stresses at the attachment point. Skirts are particularly attractive for large, heavy vessels such as RPVs, as they are able to transfer the vessel dead load uniformly across their entire circumference. Generally, for nuclear power plant applications, cylindrical skirts are preferred as their fabrication cost is lower than conical skirts. A skirt-type geometry was considered for this case study. The geometry is the axisymmetric Y-piece structure under thermal loading considered by Kasahara [176]. The finite

element model of the Y-piece is shown in Figure 85 with major dimensions highlighted.

The fatigue critical location is at the attachment point between the skirt and the vessel. This region can experience high discontinuity stresses due to the geometry. In addition, it can experience very high secondary thermal stresses when the vessel undergoes a warmup or cooldown transient. This mainly occurs due to the time lag by heat conduction and heat transfer between the skirt and the air gap. Generally, the thinner the skirt, the better able it is to adjust to the temperature of the vessel and thus minimise thermal stresses developing. Adopting a 'hot box' design whereby the susceptible region maintains a uniform temperature, or insulating the internal and external surfaces of the skirt are also common practices that can minimise stresses. Nonetheless, skirt supports are still an area of design concern and are susceptible to fatigue. Unlike primary coolant pipework and nozzle attachments, which are generally more susceptible to fatigue induced by Service Level B transients, vessel support structures can still be susceptible to fatigue under Service Level A transients, which occur more frequently.

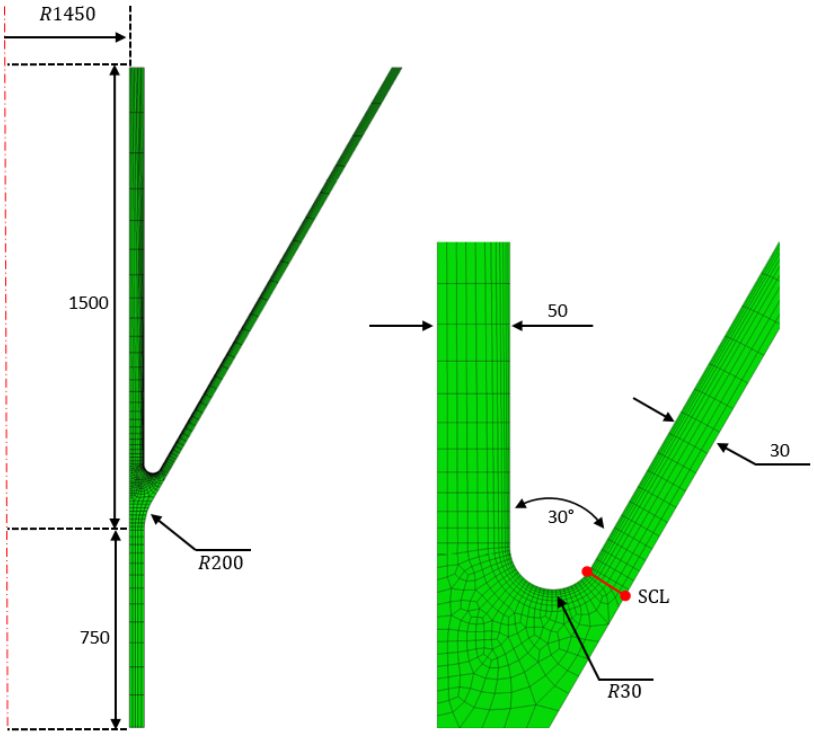

Figure 85. FE model and major dimensions of Y-piece structure [176].

Dimensions are provided in mm.

This case study considers strain concentration at the vessel-to-skirt juncture undergoing a sequential warm-up and cool-down cycle, which was considered as a single design transient. The temperature of the assembly is initially uniform at 50°C. The loading conditions were assumed quasi-static by warming the inner surface of the cylinder up to a maximum temperature, whilst the skirt edge was maintained at 50°C. The severity of the design transient was considered by varying the maximum temperature attained by the vessel internal surface, as this directly controls the strength of the thermal gradient experienced at the skirt juncture. Multiple design transients were considered based on maximum vessel temperatures ranging from 100°C to 450°C, and are illustrated by Figure 86.

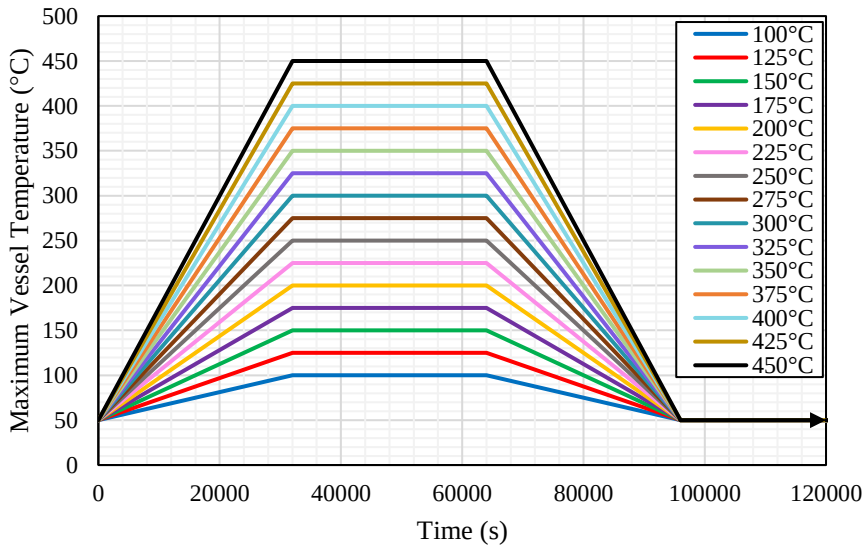

Figure 86. Design thermal transients considered for Y-piece structure.

In the thermal analysis model, an infinite convective HTC was assumed for the internal surface of the vessel. Since the analysis is quasi-static, this assumption results in the most pessimistic steady-state temperature distribution in the assembly. In the structural model, an encastre condition was specified for the base of the skirt attachment, which constrains the assembly against rigid body motion. The vessel was also constrained to expand in-plane by coupling the longitudinal (global Y) displacements of the nodal points situated on the bottom face of the axisymmetric vessel. Internal pressure was not considered in this case study.

A mesh sensitivity study was conducted to investigate the influence of mesh density on convergence in the stress response at the skirt-to-nozzle juncture. Two candidate

meshes shown in Figure 87 were considered. An Appendix XIII-3520 fatigue scoping calculation was performed for both meshes considering the most severe design transient. The difference in results obtained between the two mesh sizes was not significant. The difference in S_p for both meshes was found to be within 1%, whilst S_n was approximately equal. The finer mesh was adopted nevertheless, as the increase in computational cost was minimal. The displacement of the assembly calculated at the end of the warm-up phase is shown in Figure 88. As the vessel expands longitudinally, the skirt attachment region is also displaced vertically, resulting in high secondary bending stresses and superimposed peak stresses due to the notch. Additionally, a large axial thermal gradient exists between the vessel and skirt, which promotes thermal membrane stress along the length of the skirt.

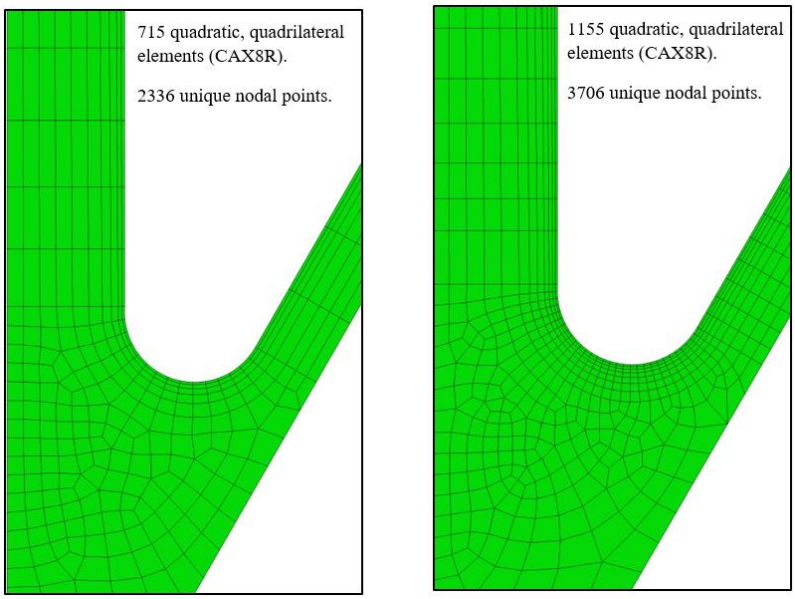

Figure 87. Illustration of mesh size considered in sensitivity study and summary statistics.

Figure 89 shows the contours of maximum $S_p/3S_m$ calculated at the skirt juncture for the most severe design transient. The effect of the notch is clearly pronounced, though the maximum $S_p/3S_m$ does not occur at the notch root, but tends towards the location where the thermal gradient existing between the vessel and skirt is maximised. This conclusion is supported by Figure 88, and accordingly the SCL was positioned at this location.

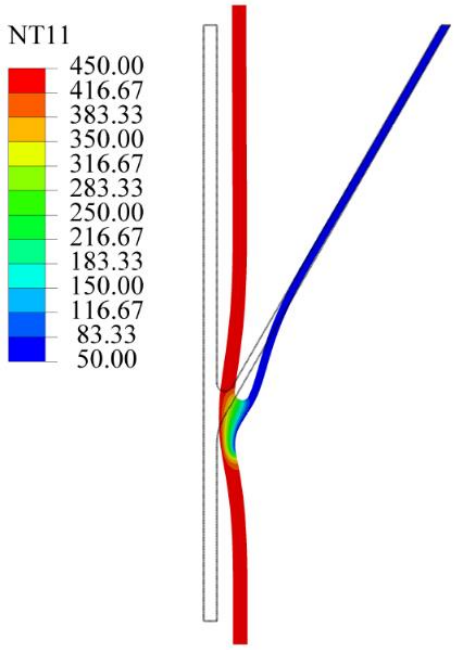

Figure 88. Displacement (10x magnification) of Y-piece at end of warm-up phase.

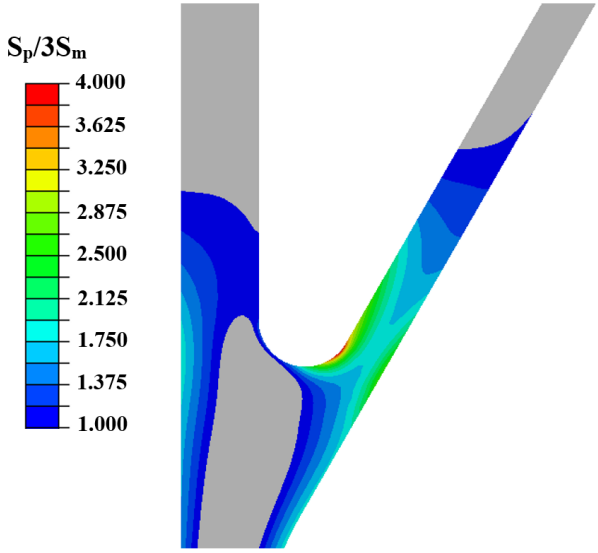

Figure 89. Contours of $S_p/3S_m$ for most severe design transient.

6.7. Notched Thin-Walled Cylinder

To investigate strain concentration under thermal loading in presence of a local discontinuity, a series of FE studies on a thin-walled cylinder with various fully circumferential, semi-circular notches were conducted. The geometry of the cylinder was based on the paper by Fujioka [178], and is illustrated in Figure 90 with major dimensions highlighted. Five semi-circular notches were considered possessing different notch root radii of curvature, ρ, equal to 5, 2.5, 1.25, 0.625, and 0.3125 mm.

By varying ρ, different values of K_T can be derived at the notch root, where K_T may be calculated from the ratio S_p/S_n. Higher values of ρ give lower values of K_T, but the notch now accounts for a greater proportion of the section thickness, which can have a larger effect on the gross plastic behaviour of the cylinder. This case considers three types of thermal loading conditions for the notched cylinder, which are also illustrated in Figure 90: a) an axial temperature gradient varying linearly along the longitudinal axis of the cylinder, b) a radial thermal gradient varying linearly through the thickness of the cylinder, with zero variation in the axial direction, and c) a parabolic thermal gradient through the thickness of the cylinder due to a transient thermal shock. Individual thermal and structural FE models were created for each notch geometry considered, with all sharing common boundary conditions.

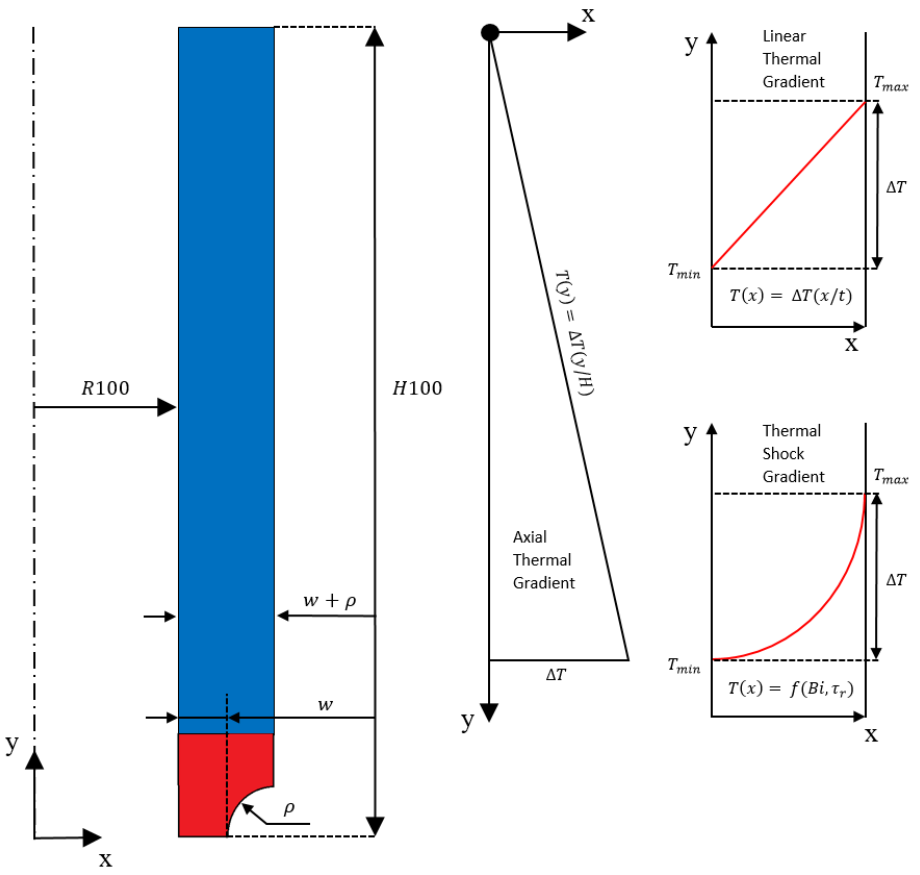

Figure 90. Geometry and dimensions of notched cylinder with different thermal loading conditions.

In the thermal analyses, the initial temperature of the cylinder is assumed uniform at 20°C. Time-varying thermal boundary conditions were applied directly assuming an infinite HTC. In the case of the linear axial thermal gradient, the temperature of the

unnotched end of the FE model was fixed at 20°C, whilst the temperature of the notched end was ramped up to a maximum temperature, T_{max}, before returning to the initial temperature of 20°C. For the linear radial thermal gradient, the internal surface of the cylinder was fixed at 20°C, whilst the temperature of the external surface including the notch face was allowed to vary. Both cases were analysed assuming quasi-steady-state conditions. The case of the parabolic thermal (shock) gradient is non-steady and was therefore analysed as a transient heat transfer problem. The external surface of the cylinder, including the notch face, was ramped up to the maximum temperature, T_{max}, in a time of 10s. The temperature of the external surface was then held constant at T_{max} for 1000s, until thermal equilibrium was established in the cylinder. Finally, the temperature of the external surface was returned back to the initial temperature of 20°C in 10s, completing a single symmetric thermal cycle. In the structural analyses, the bottom face of the cylinder was constrained to remain fixed in the global Y-direction (i.e. along the longitudinal axis of the cylinder). The free end of the cylinder was constrained to expand in-plane.

Both the thermal and structural FE models utilised identical meshes of quadratic, quadrilateral elements, which were refined with element bias along the notch face towards the notch root to ensure that the maximum stress was accurately captured. A mesh sensitivity study was initially conducted for the case of $\rho = 5$ mm, by performing an Appendix XIII-3520 scoping calculation for two candidate meshes. The first mesh contained 343 elements and 1132 nodes at the notch whilst the latter contained 2566 elements and 801 nodes. Both showed less than 0.3% difference in S_p and no difference in S_n. Figure 91 shows the final FE meshes adopted for each of the notch geometries considered in this case study.

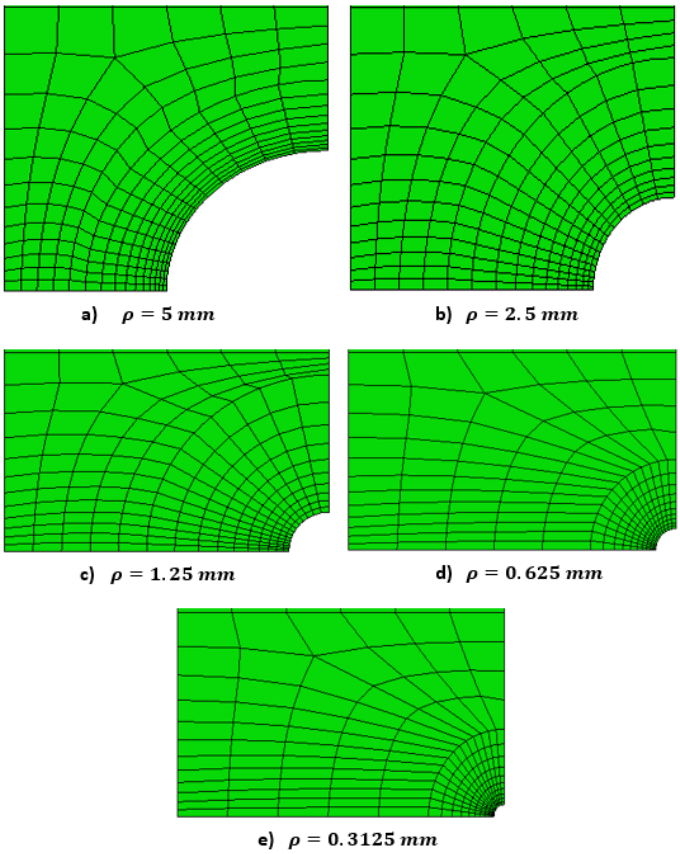

Figure 91. FE meshes adopted for notched cylinder models.

7. Results of Finite Element Case Studies

This section presents the results of the elastic-plastic analyses and discusses some notable observations for each of the FE case studies investigated. The resultant strain amplitudes (or pseudo-stress amplitudes) determined according to the EOSR criterion and the various code K_e methodologies based on elastic DBA have been determined for each FE model. These have been used to estimate the number of allowable cycles at each assessment location in order to evaluate and compare the conservativism in the code K_e factors for a variety of structures and loading conditions.

The results obtained for each FE model are first discussed. ASME Section III is the focus of this thesis, and accordingly a detailed performance comparison is afforded to Appendix XIII-3450, CC N-779, and Ranganath's method for each assessment location to clarify their advantages and limitations. A general performance comparison of the ASME III K_e factors and K_e factors from other codes relative to the FE-derived K_e^{FEA} is then presented. The code K_e methods that produce the most consistently accurate results are identified and discussed. Additionally, a number of recommendations are made to improve the existing methods.

As highlighted in Section 3.3.3.3, S_n has the potential to be out-of-phase with S_p. Thus, to ensure that the maximum value of K_e is captured for the code methods that depend only on S_n, K_e was calculated based on the extremes of S_n. Similarly, for the code methods that depend only on S_p, K_e was calculated based on the extremes of S_p. To enable a direct comparison between code K_e methods that involve more than a single correction factor, and which depend on multiple different stress ranges, an equivalent correction factor, $K_{e,eq}$, must be determined. The purpose of $K_{e,eq}$ is to reduce the combined effect of multiple PCFs to a single value whose effect on S_{alt} is equivalent, and it serves as the basis of comparison for all plasticity correction methods outlined in this section. $K_{e,eq}$ is calculated according to Eq. (167).

$$K_{e,eq} = \frac{2 \cdot S_{alt}}{S_p} \cdot \frac{E_a}{E_c} \tag{167}$$

In the case of complex K_e factors such as CC N-779 for example, the stress tensor ranges corresponding to maximum S_n were input to Eq. (85)-(87), and subsequently

an equivalent $K_{e,eq}$ value was determined from Eq. (167). Then, S_{alt} is recalculated using this calculated $K_{e,eq}$ and the maximum value of S_p; this final value of S_{alt} is used to determine the allowable cycles on the Appendix I DFC. In all cases, the values of S_m and E_a used in the elastic fatigue analyses were calculated based on the maximum temperature of the fatigue load pair. The calculated code K_e factors therefore represent the most conservative possible value. Further calculations have been performed using less pessimistic values of S_m permitted by Appendix XIII-3420 for comparison, but are not presented in this work. The choice of S_m is however acknowledged as an important factor and is discussed further in Section 8.1.

7.1. Thick-walled Cylinder

The results obtained for the thick-walled cylinder considered by Miller [74] are examined in this section for each combination of sustained pressure and cyclic thermal loading. The compiled results obtained for the thick-walled cylinder is shown in Figure 92. The number of allowable cycles calculated using the Appendix I DFC is shown in Figure 92 (a). For the most severe design transient, elastic-plastic FEA permits 145 cycles compared to only 18 cycles permitted by the Appendix XIII-3450. CC N-779 and Ranganath's method permit 125 and 91 cycles, respectively. The contour plot of K_e^{FEA} in the cylinder is shown in Figure 93 for the case of 15 MPa internal pressure. As can be seen, strain concentration on the surface of the cylinder is relatively small, and does not increase significantly with severity of thermal shock. Whilst the magnitude of sustained pressure loading is often crucially important when considering ratchet behaviour, it was found to have a negligible impact on the degree of strain concentration experienced on the internal surface of the cylinder. This is confirmed in Figure 92 (c) which shows that K_e^{FEA} is essentially independent of the magnitude of sustained internal pressure and depends only on the severity of the thermal cycling. This contrasts with the results reported by Asada and Nakamura [122], who found that, for a given level of cyclic thermal loading, K_e^{FEA} may increase as function of the primary membrane stress. However, the results of [122] were based on simplified monotonic analysis of K_e^{FEA} using an elastic perfectly-plastic (EPP) material model, and therefore do not accurately reflect the true behaviour of the material under cyclic loading. The maximum K_e^{FEA} of 1.293 was calculated for the cylinder FE model, which is very modest compared to the value of 3.33 predicted by $K_e^{XIII\text{-}3450}$. Based on

the analytical solution for K_v considering a cylinder subjected to a thermal shock (Section 4.3.1.1), it is expected that K_e^{FEA} will tend asymptotically to a maximum of 1.4 as ν^* approaches its maximum value of 0.5. This appears broadly consistent with the trend observed in Figure 92 (c).

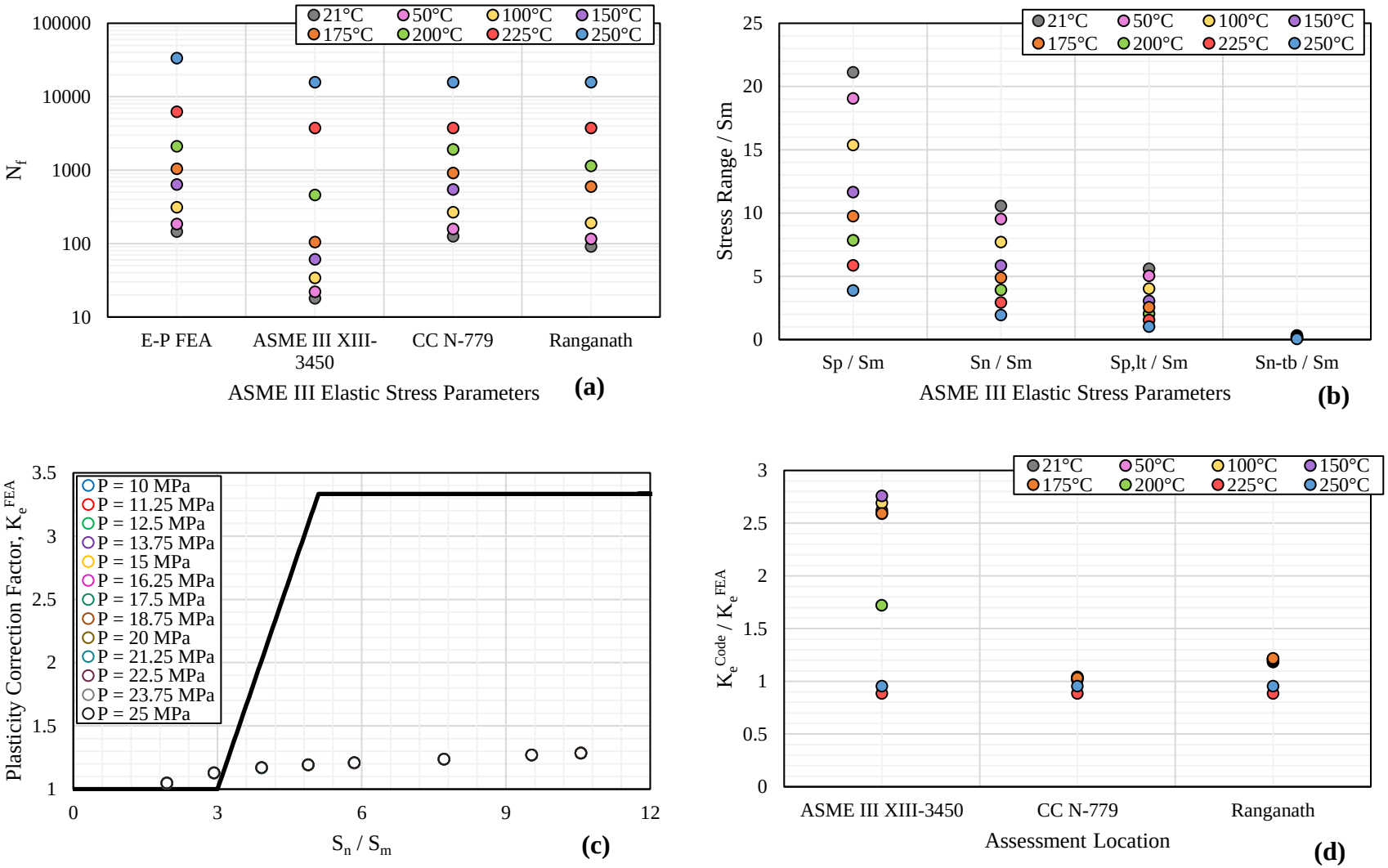

Figure 92. Summary of results obtained for thick-walled cylinder FE model.

(a) Allowable cycles, N_f; (b) ASME III elastic stress parameters; (c) K_e^{FEA} vs. S_n/S_m; (d) Performance of ASME III K_e factors

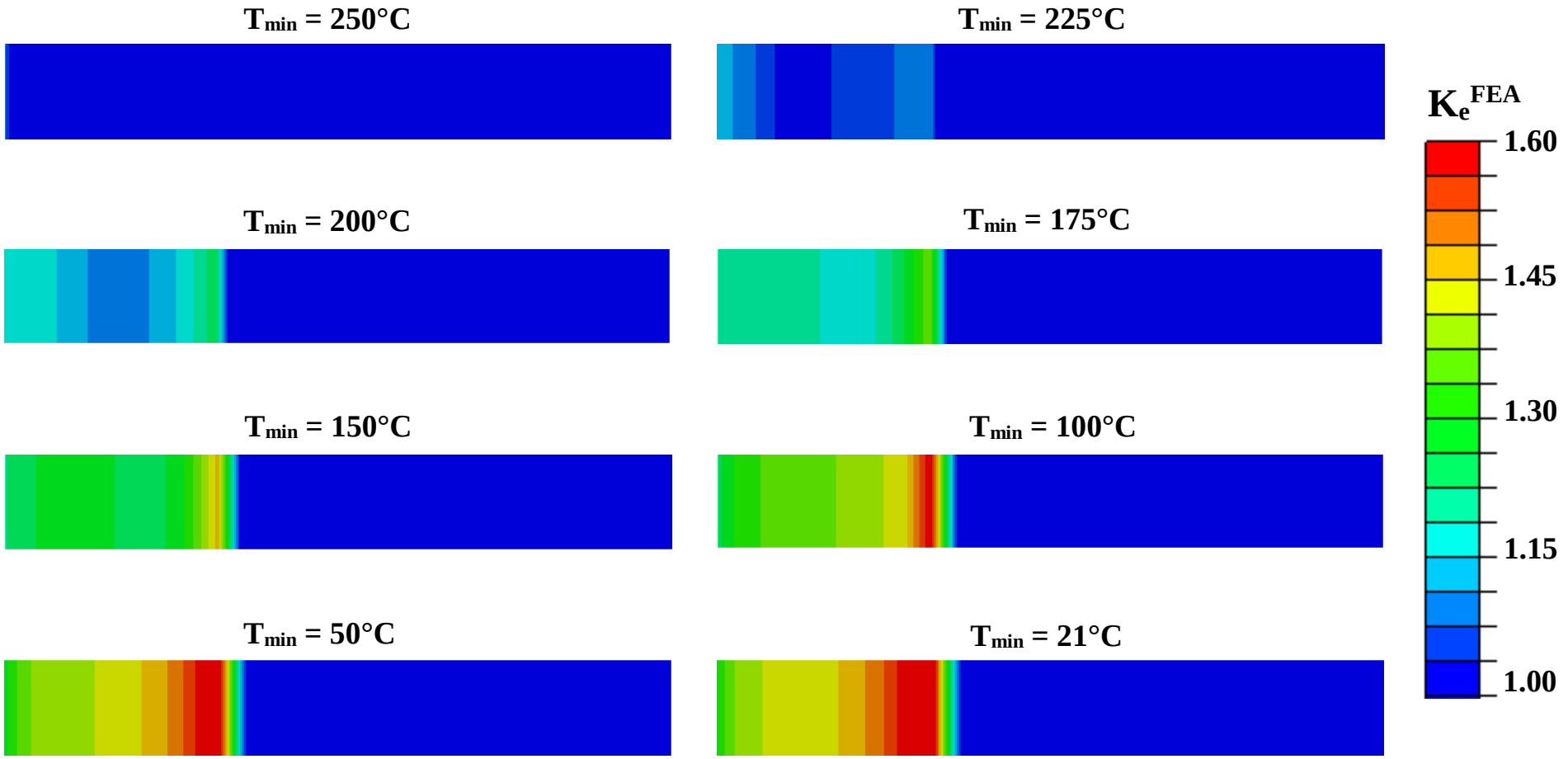

Figure 93. Contour plots of $K_e^{FEA} \geq 1.0$ for Thick-walled Cylinder FE model.

7.2. Bettis Stepped Pipe

For the stepped pipe tests described in [134], the earliest initiation of a 0.254mm crack was estimated to occur after 365 cycles of the test transient. The arithmetic average of all measured defects initiating during the tests was estimated to occur after approximately 1,000 cycles. The authors further explain that crack initiation was defined as initiation of a 0.254 mm deep crack as it was found that whilst many cracks initiated early into the tests (< 50 cycles), many did not propagate further through-thickness after exceeding the influence of the high thermal skin stresses. Jones et al estimated the number of cycles to crack initiation by metallographic examination and counting the fatigue striations backward from the final crack size observed at test termination. The crack growth cycles estimated from the striation count were subtracted from the total cycles to determine the cycles to initiation. Cracks were found only in the two thickest sections due to their experiencing significantly higher cyclic thermal stresses. The elastic-plastic fatigue analysis of the test transient was conducted for every element nodal point in the FE model. A unique set of results for each node was determined by averaging the results obtained at each element node. Table 1 shows a comparison of the allowable cycles calculated using each methodology for the thickest section of the stepped pipe. As can be seen, the current ASME III Appendix XIII-3450 K_e factor permits only 25 cycles using the Appendix I DFC, absent of any consideration of environmental effects. This is less than 20% of the cycles that are permitted by elastic-plastic FE analysis utilising the NUREG/CR-5704 CSS curves.

Table 8. Allowable cycles calculated for 15.2 mm stepped pipe section

Plasticity Correction Method	N_f
Elastic-Plastic FE Analysis	143
ASME III Appendix XIII-3450	25
ASME III Code Case N-779	178
ASME III Code Case N-779 (Modified)	168
Ranganath's Method	80
ASME VIII-2 Section 5.5.3	25
ASME VIII-2 Annex 5C	139
RCC-M	101
JSME	47
JSME NC-CC-005	28
EN-13445 Annex 18	189
AD 2000-Merkblatt S2	170
PNAEG	27
R5 (Neuber)	41
R5 (K_v)	158
Rolls-Royce (F_u)	104

Figure 94 compares the number of cycles to initiation predicted by the ASME III plasticity correction methods with the observed cycles required to achieve a 0.254 mm defect depth in the test. This comparison considered nine cracks detected in the 15.2 mm section and two cracks detected in the 11.7 mm section. It can be seen that all of the approaches considered for calculating the effective strain range produced very conservative estimates of the number of cycles to initiation. These pessimistic results obtained for the stepped pipe are largely due to excessive conservatism in the Code K_e factors. As shown, without even considering environmental effects, detailed elastic-plastic FE analysis predicted only 143 cycles of the test transient to cause crack initiation in the thickest section, which is less than 40% of the lower-bound cycles to initiation observed in the test. Considering the thickest section of the stepped pipe possesses a predicted F_{en} of approximately 3.08 based on the current NUREG/CR-6909 Rev. 1 [72] F_{en} correlations for austenitic stainless steel, this would imply a 3 mm initiation life of 143 / 3.08 ≈ 46 cycles using elastic-plastic FEA in combination with the Appendix I DFC.

It should be noted that the crack initiation criterion of 0.254mm employed by Jones et al [134] in the tests is inconsistent with the Appendix I DFCs, which are based on the number of cycles required to initiate a 3mm deep crack in a uniaxial test specimen. However, whilst the number of cycles to initiate a 0.254mm crack was used to define

‘failure’, it is noteworthy that the two pipe sections were removed after 708 and 2008 cycles, with Jones et al noting the presence of extensive surface cracking in both the 15.2 mm and 11.7 mm sections. The specimen removed from the rig at 708 cycles was the one that possessed only two defects in the thickest section selected for striation counting and were judged to be 0.254 mm deep after 365 and 458 cycles of the test transient, respectively. Importantly, Jones et al state that most of the cracks were at least 0.1 inch (2.54 mm) deep or deeper when the tests were terminated. Indeed, from examination of the pipe specimens in Figure 6 of PVP2004-2748 [134], the thickest 15.2 mm section of the pipe subjected to 2008 experimental cycles (top picture) appears to possess many defects of 2.54 mm or deeper. This suggests that, even when utilising detailed elastic-plastic FEA, the allowable cycles to initiate a 3mm-deep crack according to the Code DFC is extremely pessimistic compared to the range of 0.254mm-deep initiation lives estimated experimentally for the stepped pipe, let alone the number of further test transient cycles required to produce a 3mm-deep crack.

It is also important to recognise that type of loading considered in the stepped pipe tests is fundamentally different to the loading experienced in conventional strain-controlled fatigue tests. The DFCs were derived based on polished, small-scale uniaxial specimens experiencing a constant membrane strain in the gage. In these tests, the crack growth rate accelerates as the crack grows due to the increase in the crack driving force. However, in the stepped pipe tests, Jones et al noted that the crack growth rate decreased sharply and crack arrest was observed in many cases due to the very steep, decaying strain gradient through-thickness. It is assumed that, irrespective of the worst-case crack depth observed at test termination, if the tests were continued then cracks would not be expected to penetrate through-wall for a very large number of additional cycles due to the reasons noted above. Since the intent of the ASME III fatigue criteria is arguably to protect against through-wall leakage rather than crack initiation (see discussion in Section 3.2.5.3), an even greater level of conservatism is implied under the assumption that a CUF equal to unity equates to through-wall leak in an actual plant component. It is evident therefore that the Appendix XIII-3520 procedure is not well suited to assessing fatigue induced by thermal shock loading due to the excessive margin afforded by the K_e factor, DFCs, and additional F_{en} penalty factors.

These observations further emphasise the need to adopt alternative assessment procedures that consider the growth of mechanically short cracks in plant components under realistic loading conditions. Some important work in this area has been performed recently, which considered the stepped pipe experiment as a benchmark example. Mann et al performed a reanalysis of the stepped pipe tests based on the total life approach [179], considering the thickest section of the stepped pipe specimen. In this work, Mann et al utilised a best-fit strain-life curve corresponding to a 250 μm crack depth, developed based on a striation counting study considering crack growth behaviour from 250 μm to 3 mm in small-scale fatigue specimens tested in air and LWR environments. This work found that a 0.254mm crack would be present after approximately 233 cycles, slightly under-predicting the minimum 365 experimental cycles to generate a 0.254 mm crack, as estimated from striation counting in the original analysis by Jones et al. However, subsequent crack growth analysis suggested that to develop a crack of 3mm depth would require 629 further cycles, or 862 cycles in total. Other work conducted by Leary et al ([170], previously discussed in Section 5.4.5) aimed to correlate elastic-plastic FE fatigue life predictions with the experimentally observed 0.254mm initiation lives reported in the stepped pipe tests. In this work, for the 9 defects considered in the original tests, the geometric mean life for the observed 0.254mm defects was evaluated as 878 cycles; an additional 627 cycles were estimated to grow from 0.254mm to 3mm crack depth based on the crack growth rate data presented in Mann et al [179]. This represents an estimated geometric mean 3mm initiation life of 1543 cycles, which is overall much more consistent with the experimental observations reported in [134].

More recent work presented by Wright et al [180] considered a probabilistic total life assessment of the stepped pipe tests, with a target reliability of 10^{-5} against avoidance of leakage (where leakage was defined as a crack depth of 80% through-wall) adopted as an acceptance criterion. The probabilistic analysis results suggested that extant Code deterministic methods would limit cyclic operation to a life of 33 cycles when environmental effects are considered which would equate to a quantified target reliability of less than 10^{-6}. Using a total life approach the best-estimate cycles to leakage was found to be approximately 25,000 cycles, whilst approximately 10,000 cycles were permissible with quantified margin equivalent to a 10^{-5} target reliability.

Therefore, considering the total life to loss of functionality would permit an increase in the Code deterministic life by a factor of 250 and still achieve a target reliability of 10^{-5} against avoidance of leakage for the stepped pipe.

With this in mind, the comparison of the Code K_e factors with K_e^{FEA} is further justified as an important step in reconciling the Code prediction methods with observed component behaviour. A further step is to utilise this improved understanding of elastic-plastic component behaviour to support the initiation stage of a total life assessment.

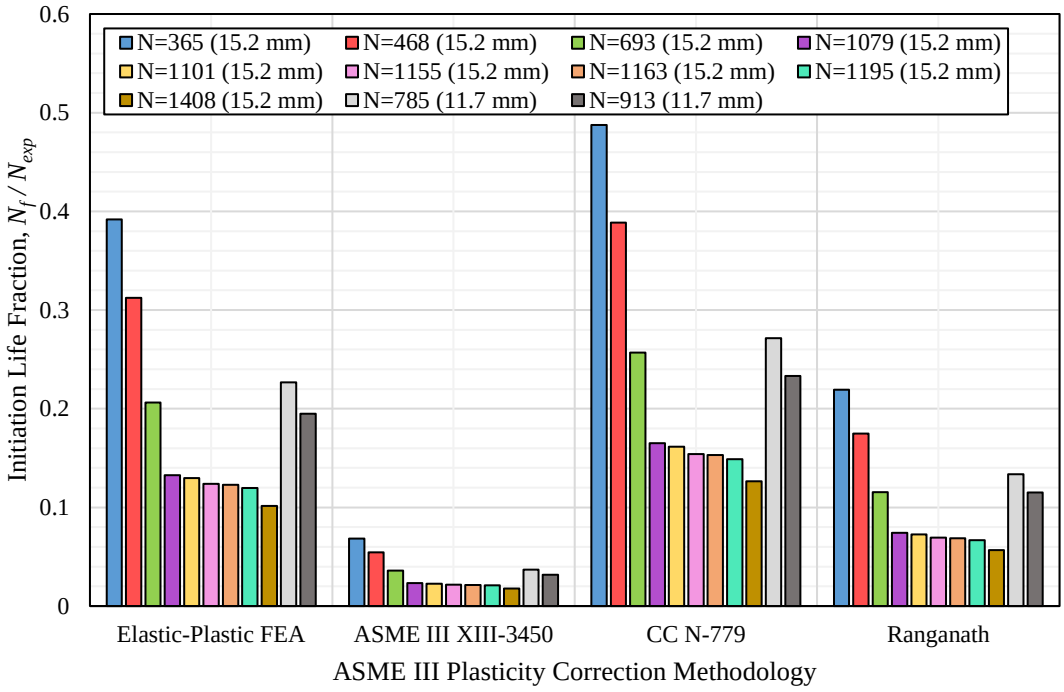

Figure 94. Comparison of N_f and N_{exp} at which 0.254 mm deep cracks were observed in the stepped pipe.

The K_e^{FEA} factors for the stepped pipe were calculated for both the test transient and the arbitrary thermal shock transients. The contour plot of K_e^{FEA} was calculated for the entire FE model, as shown in Figure 95, for a selection of transient load cases. The results were then extracted on the internal surface situated at the mid-point of each stepped pipe section. The ASME III elastic stress parameters determined for selected transients is shown in Figure 96, and the performance of the ASME III K_e factors for these transients is summarised in Figure 97. The K_e^{FEA} calculated for the stepped pipe is relatively modest, tending to a maximum of 1.511 obtained at the thickest section

for the test transient. The trend in K_e^{FEA} vs. S_n/S_m for the stepped pipe is somewhat higher than that of the thick-walled cylinder despite being of similar geometry. This is likely due to the higher elastic follow-up exhibited by a series of inter-connected pipe segments of varying rigidity compared to a single uniform pipe. As shown by Figure 97 (b), $K_e^{XIII-3450}$ was found to be conservative by a factor of 2.0x to 2.6x for the majority of transients considered. In contrast, CC N-779 was found to predict K_e^{FEA} quite closely, though had the potential to be slightly non-conservative; in particular, CC N-779 was found to under predict K_e^{FEA} at the thickest section by 14% for the test transient as shown by Figure 97 (c). Ranganath's method was generally found to produce results that were conservative between a factor of 1.1x and 1.3x, as shown by Figure 97 (d).

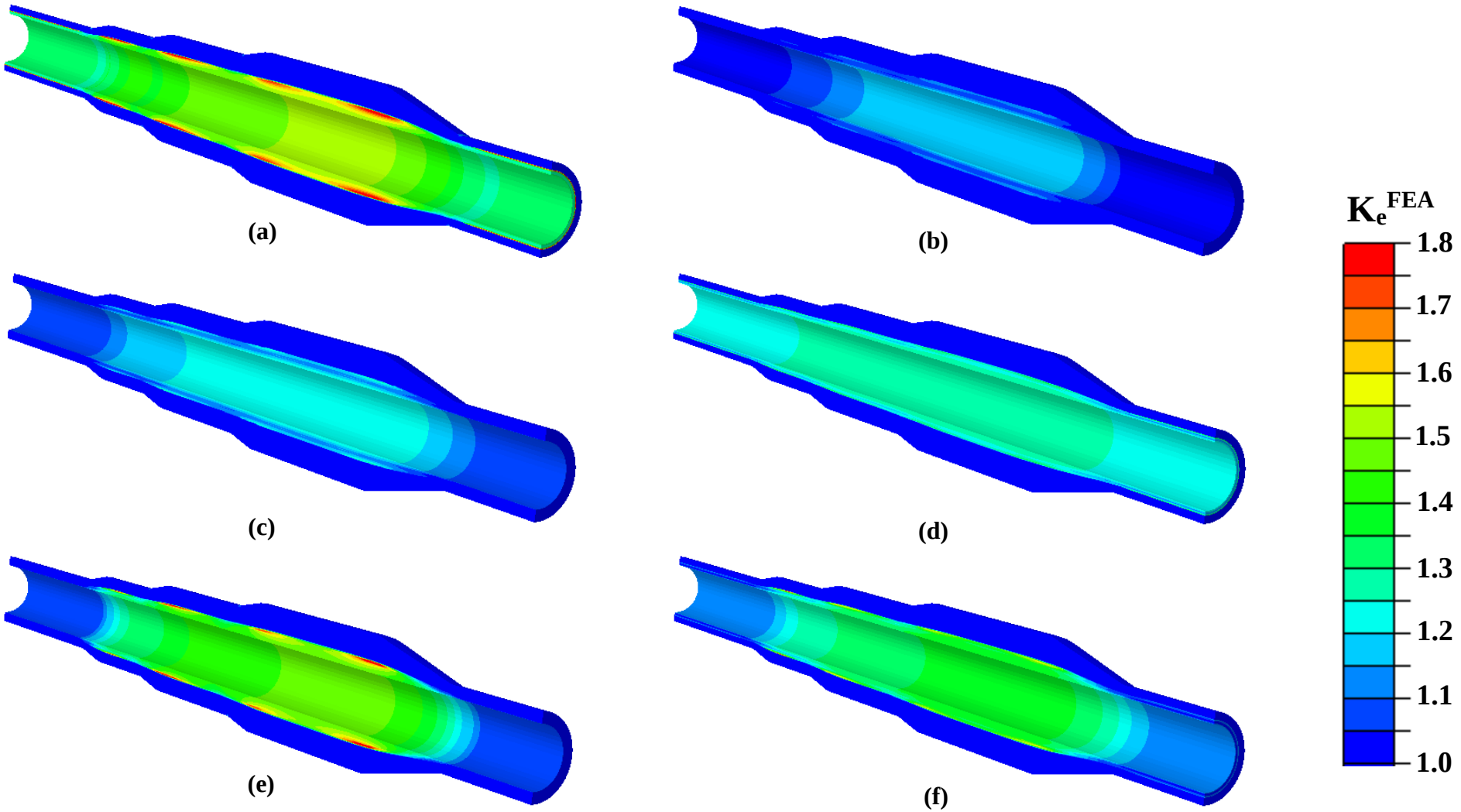

Figure 95. Contour plots of $K_e \geq 1.0$ for stepped pipe FE model.

(a) Test transient; (b) Transient 2; (c) Transient 6; (d) Transient 11; (e) Transient 24; (f) Transient 40.

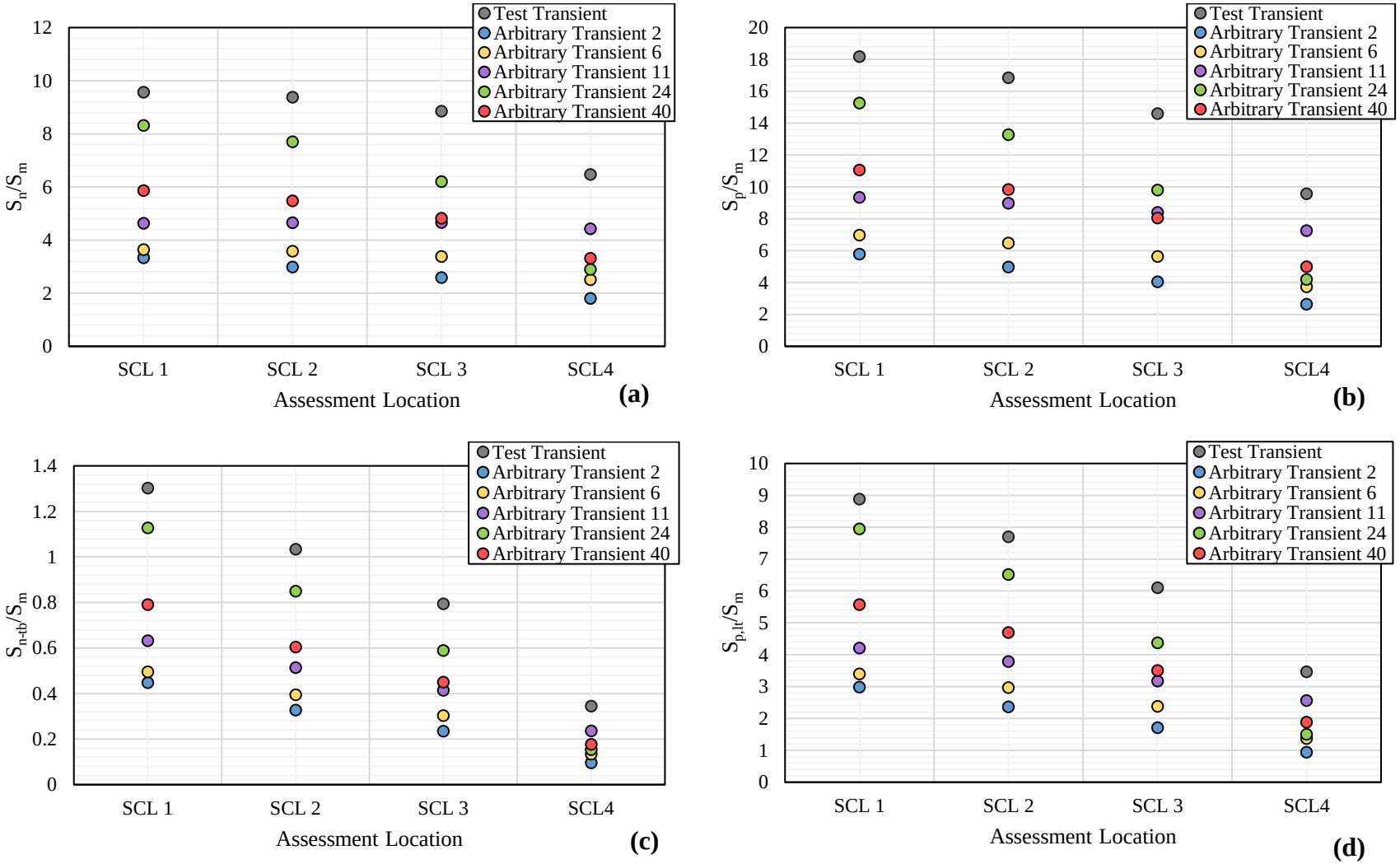

Figure 96. ASME III elastic stress parameters calculated for stepped pipe.

(a) S_n/S_m (b) S_p/S_m (c) $S_{n\text{-}tb}/S_m$ (d) $S_{p,lt}/S_m$

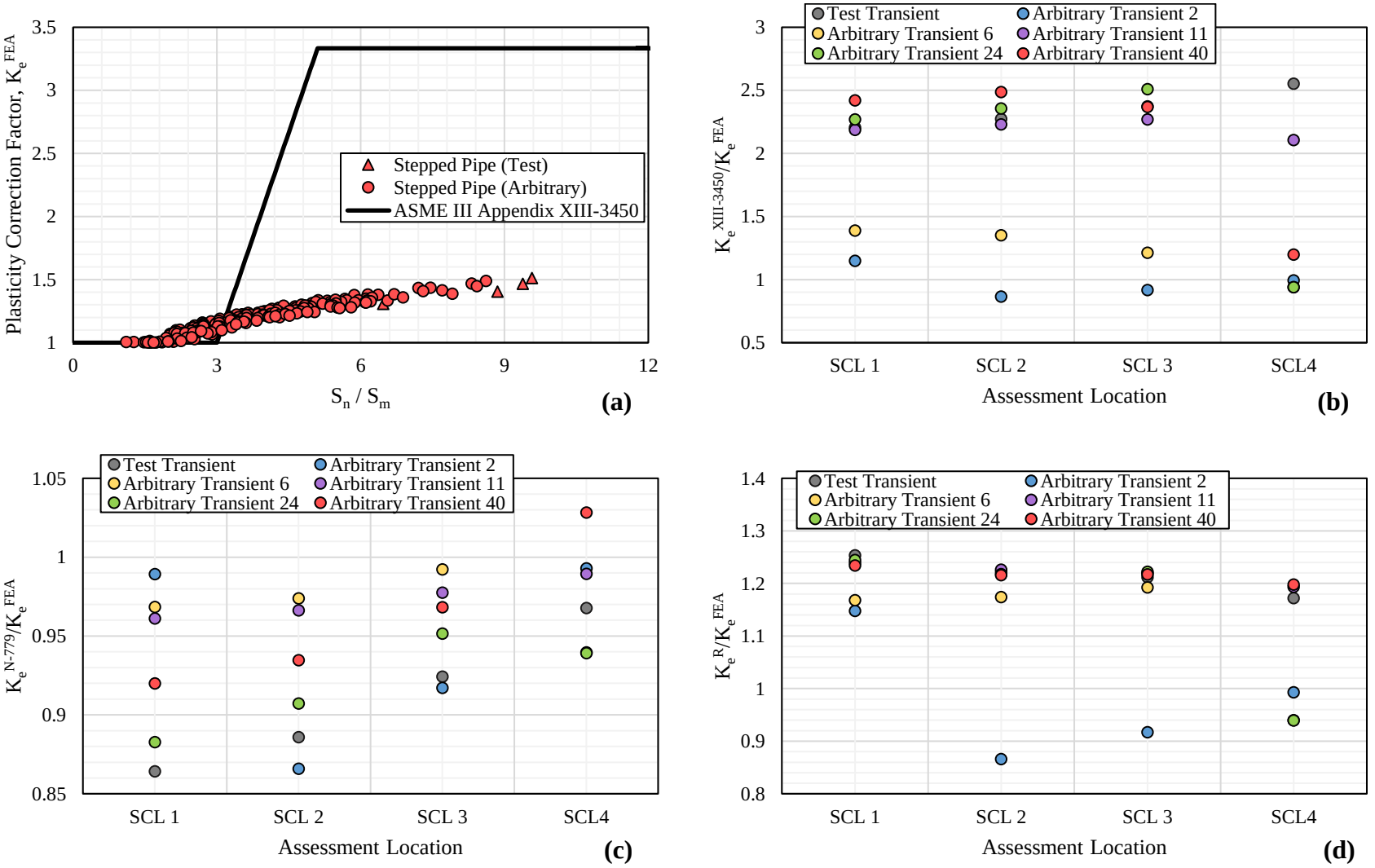

Figure 97. Performance of ASME III K_e factors for stepped pipe.

(a) K_e^{FEA} vs. S_n/S_m (b) Appendix XIII-3450 vs. E-P FEA ($K_e^{XIII-3450}/K_e^{FEA}$) (c) CC N-779 vs. E-P FEA (K_e^{N-779}/K_e^{FEA}) (d) Ranganath's method vs. E-P FEA (K_e^{R}/K_e^{FEA})

7.3. PWR Auxiliary Piping Nozzles

The results obtained for the PWR RCS nozzles are presented and compared in this section. For the sake of brevity, only the CORDEL MCL nozzle results are examined here in detail, though a similar trend was observed for all three components.

The number of allowable cycles calculated at each assessment location using the Appendix I DFC are shown in Figure 98. In Figure 98 (a), the results of the elastic-plastic fatigue analysis revealed the critical location to be SCL 6, situated in the nozzle, which can be seen to permits only 91 cycles of the most severe design transient. This contrasts with the branch pipe (SCL 2) and nozzle crotch corner (SCL 8), which permit 200 and 196 cycles, respectively. ASME III Appendix XIII-3450 also indicates the critical location to be at SCL 6, but permits only 16 cycles as indicated by Figure 98 (b), which is less than 20% of that permitted by elastic-plastic FEA. On the other hand, in Figure 98 (c), CC N-779 predicted the maximum damage to occur in the nozzle crotch corner at SCL 8, allowing for 108 cycles. ASME CC N-779 was generally found to give slighter higher allowable cycles compared with elastic-plastic FEA in the nozzle region, but also permitted a lower number of cycles at the crotch corner and branch piping. In Figure 98 (d), Ranganath's method actually predicted the worst fatigue damage to occur at SCL 3, situated at the tapered transition between the nozzle and the adjoining branch pipe, allowing for only 39 cycles at this location. This is less than one-quarter of the corresponding 162 cycles permitted by elastic-plastic FEA. The allowable cycles predicted by Ranganath's method were lower than that predicted by elastic-plastic FEA at all locations, but much less pessimistic than Appendix XIII-3450.

Figure 99 show the contour plots of K_e^{FEA} determined for the critical nozzle region. The contour plots are restricted to show only the regions of strain concentration (i.e. $K_e^{FEA} \geq 1.0$) for clarity. As shown by Figure 99 the nozzle region exhibits the greatest strain concentration on the internal surface of the reinforcement region, and weakest strain concentration in the crotch corner. As the severity of the transient loading increases, the tapered transition of the nozzle-to-pipe juncture also exhibits strain concentration on the outside surface due to its acting as a mild notch. The internal surface of the branch pipe however shows lower strain concentration compared to the

nozzle, as its lower thermal resistance dampens the thermal stress experienced on the internal surface.

A common trend for all three nozzles is that the highest PCFs occur in the nozzle, whilst the lowest occur in the attached branch piping. This is largely attributed to the higher thermal resistance of the nozzle due to its greater thickness, resulting in more severe thermal stresses in this region. The nozzle crotch corner was also found to exhibit much lower strain concentration compared with other locations, as it is dominated by peak stress whose effect on K_e^{FEA} is concluded to be minor. However, in the case of the charging nozzle a higher K_e^{FEA} is observed in the nozzle compared to the safety injection nozzle, despite it being comparatively thinner. In this case, the nozzle has much lower rigidity compared to the main coolant line piping, and elastic follow-up is therefore of greater significance. Figure 100 shows the variation in the ASME III elastic stress parameters calculated for the CORDEL MCL nozzle. The performance of the ASME III K_e factors were evaluated at each assessment location and the results are highlighted in Figure 101.

As shown by Figure 101 (b), $K_e^{XIII-3450}$ was overall found to be conservative by a factor of 2.2x to 2.9x across all assessment locations for the most severe transients. For the least severe transients, with minimum attained fluid temperatures of 280°C and 240°C, $K_e^{XIII-3450}$ was found to be slightly non-conservative. This is expected since from Figure 100 (a) it is clear that S_n did not always exceed $3S_m$ for these transients, and thus $K_e^{XIII-3450}$ need not apply.

It was observed that CC N-779 exhibited a reduction in performance for the PWR nozzle FE models, and was found to be non-conservative by up to 20%. The results shown in Figure 101 (c) indicate that CC N-779 shows reasonably good predictive capability for the branch and main coolant line piping. However, it significantly under predicts the elastic-plastic strain range in the nozzle reinforcement region, and appears increasingly non-conservative as the severity of the thermal shock increases. As the mesh contains sufficient refinement at local discontinuities, the CC N-779 K_n factor is equal to unity and only the K_e^{N-779} and K_v^{N-779} factors are applicable. In this case, K_e^{N-779} multiplies only the thermal membrane stress range (i.e. $S_{p-lt-tb}$ or S_{n-tb}), but as shown by Figure 100 (c), S_{n-tb} represents only a small fraction of S_n, with the highest

contributions of $S_{n\text{-}tb}$ observed for SCLs 3 and 8. Accordingly, $K_e^{N\text{-}779}$ is highest at these two locations but are still slightly non-conservative for the most severe design transient. On the other hand, for SCLs 4-7 situated in the nozzle, the CC N-779 correction is largely attributed to $K_v^{N\text{-}779}$, but $K_v^{N\text{-}779}$ is not high enough to predict conservatively the elastic-plastic strain range in this region. Whilst $K_v^{N\text{-}779}$ tends to a maximum correction of 1.4, the actual K_e^{FEA} could realistically be up to 1.6 in this region. The explanation for this is believed to be due to elastic follow-up from the much longer adjoining branch piping, which experiences comparatively less stress. CC N-779 $K_v^{N\text{-}779}$ therefore may not be adequate in this situation.

As with CC N-779, the performance of Ranganath's method was also found to vary significantly between assessment locations. However, as shown by Figure 101 (d), K_e^R was found to be conservative in all cases where S_n exceeded $3S_m$, whilst showing a generally increasing trend in conservatism for $S_n >> 3S_m$. The variation in K_e^R is attributed mainly to the relative contribution of $S_{n\text{-}tb}$ to S_n, represented by the parameter, R in Eq. (113), which dictates the weighting applied to the more conservative $K_e^{XIII\text{-}3450}$ when calculating K_e^R. Accordingly, the conservatism of K_e^R was generally found to vary directly with R, and this explains why Ranganath's method predicts the minimum N_f to occur at SCL 3, which differs from that predicted by elastic-plastic FEA. Overall, it can be concluded that K_e^R compares favourably with K_e^{FEA} for the PWR RCS nozzles, though due to the nature of its formulation, has the potential to predict an altogether different fatigue limiting location from that implied by elastic-plastic FEA. This was not a problem in this case, since it still predicted conservative values of N_f for all locations, though merits further examination for other FE models.

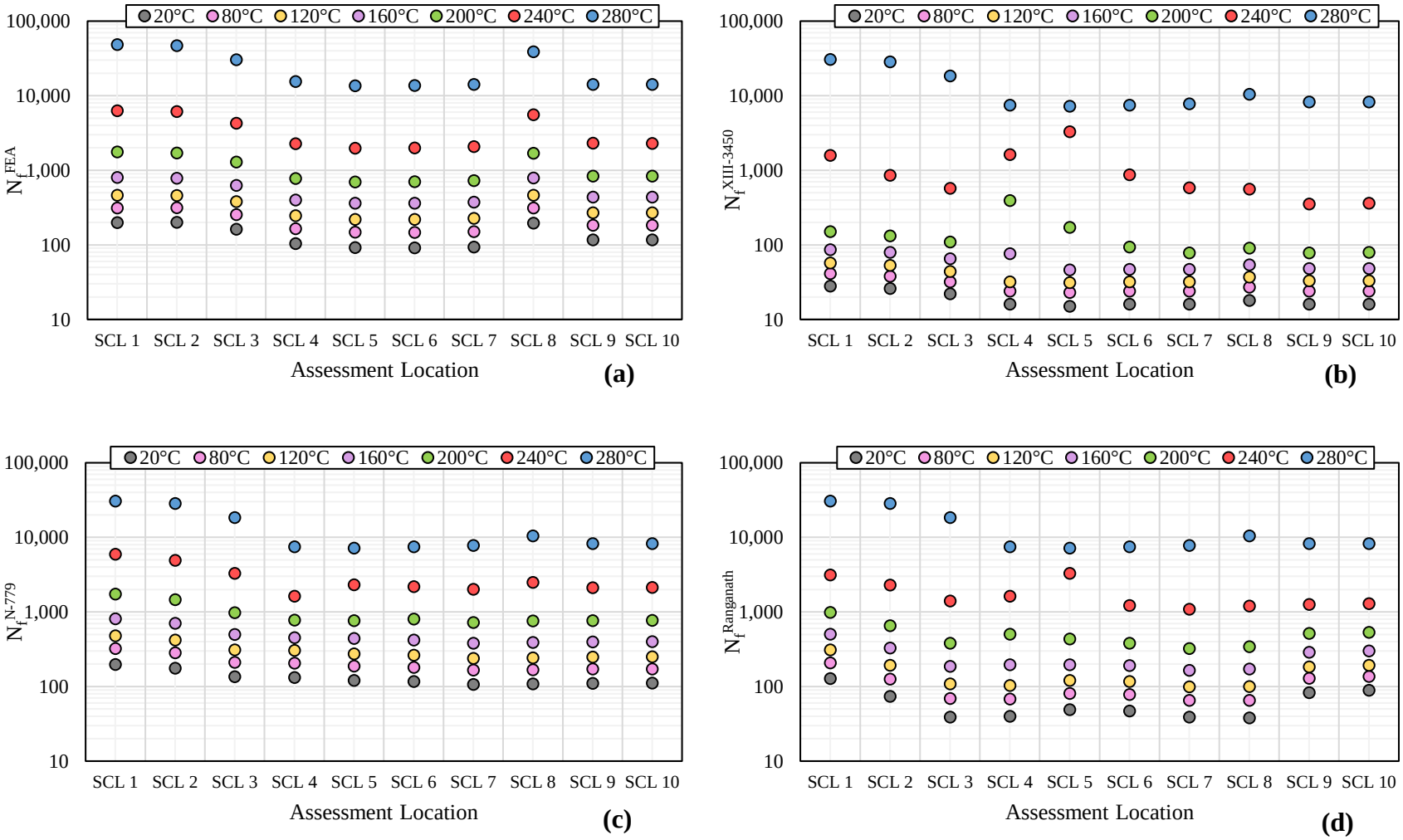

Figure 98. Allowable cycles, N_f, for CORDEL MCL nozzle.

(a) Elastic-plastic FEA; (b) Appendix XIII-3450; (c) CC N-779; (d) Ranganath's method

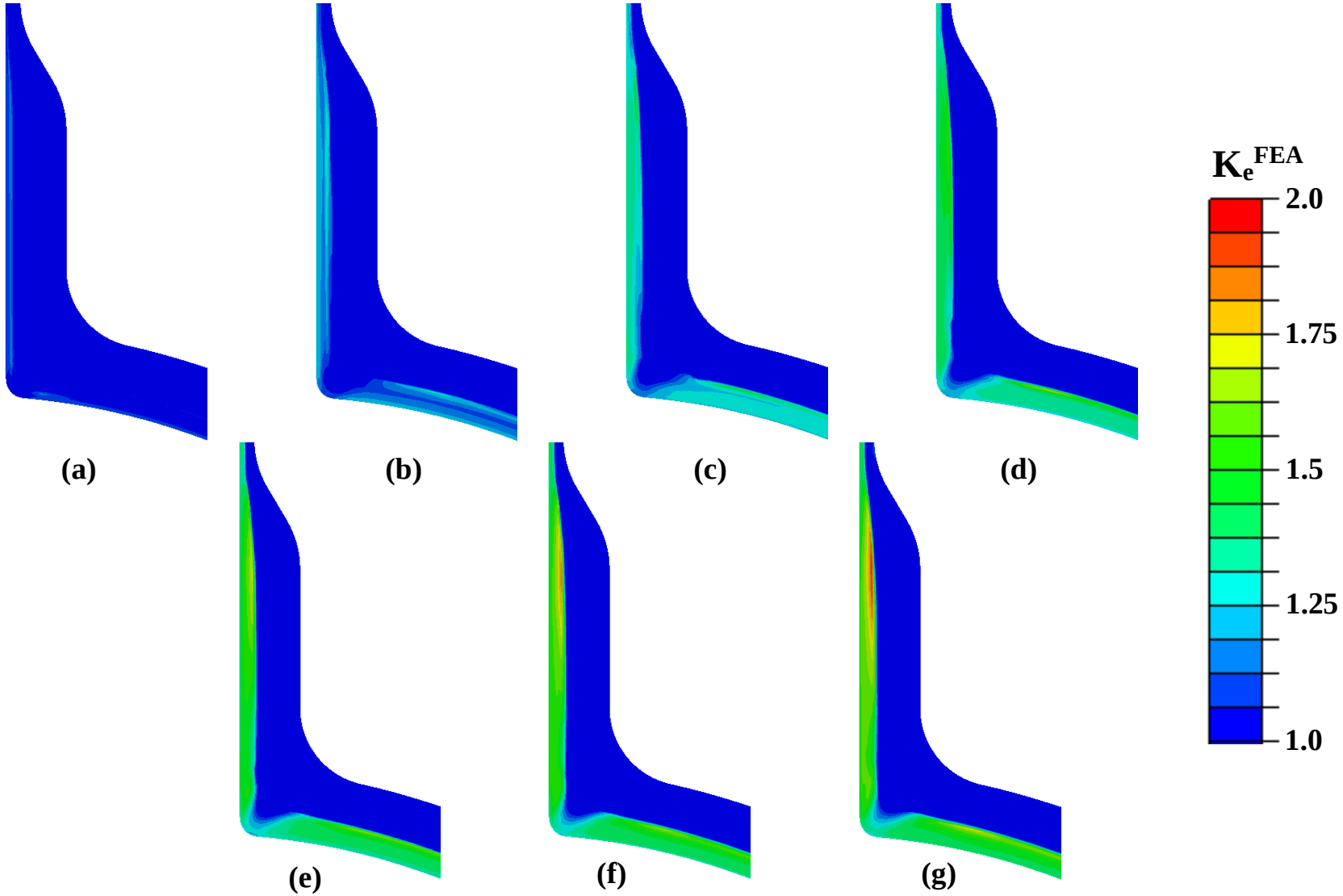

Figure 99. Contour plots of $K_e^{FEA} \geq 1.0$ for CORDEL MCL nozzle by design transient minimum fluid temperature.

(a) 280°C; (b) 240°C; (c) 200°C; (d) 160°C; (e) 120°C; (f) 80°C; (g) 20°C

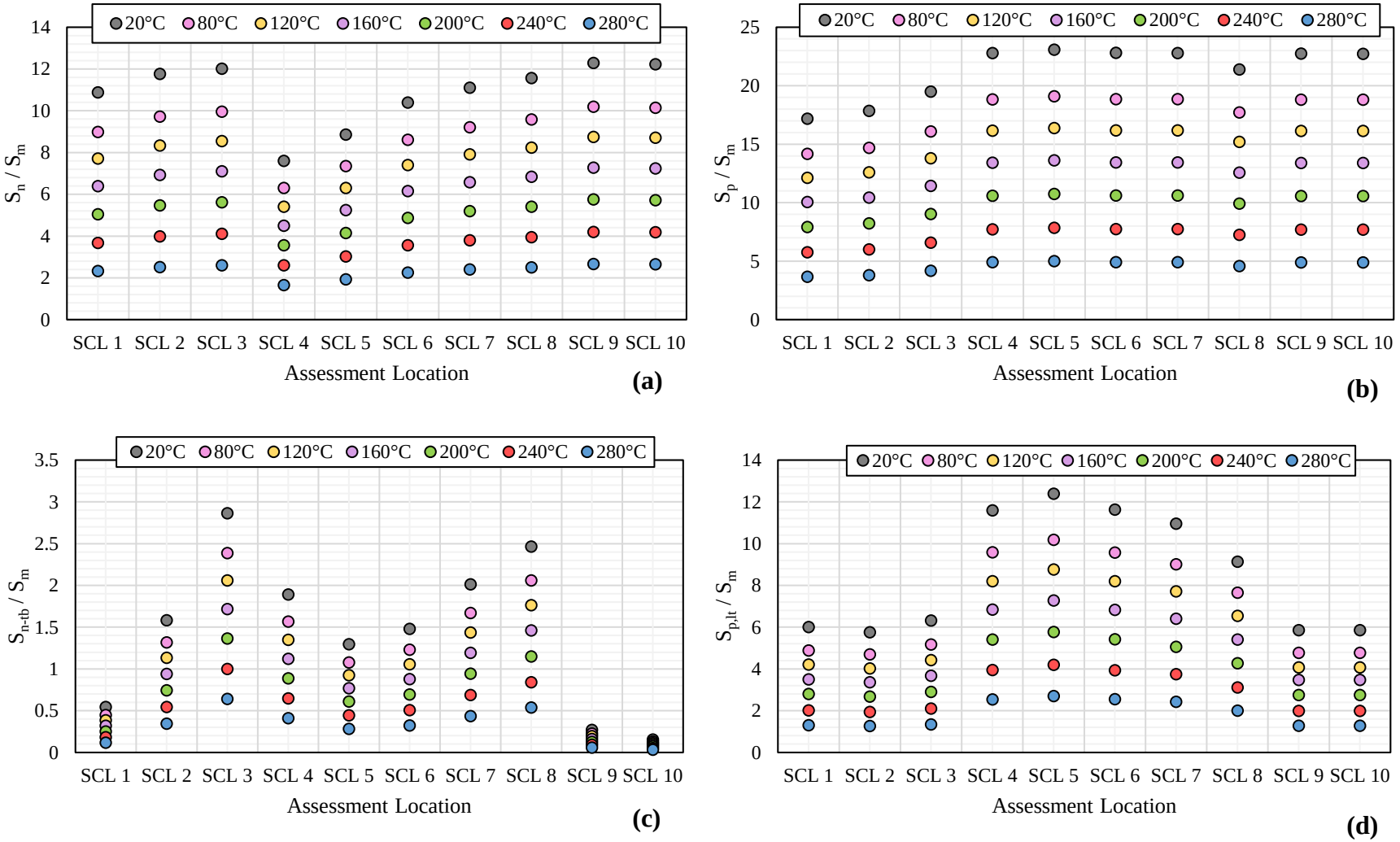

Figure 100. ASME III elastic stress parameters calculated for CORDEL nozzle.

(a) S_n/S_m (b) S_p/S_m (c) $S_{n\text{-}tb}/S_m$ (d) $S_{p,lt}/S_m$

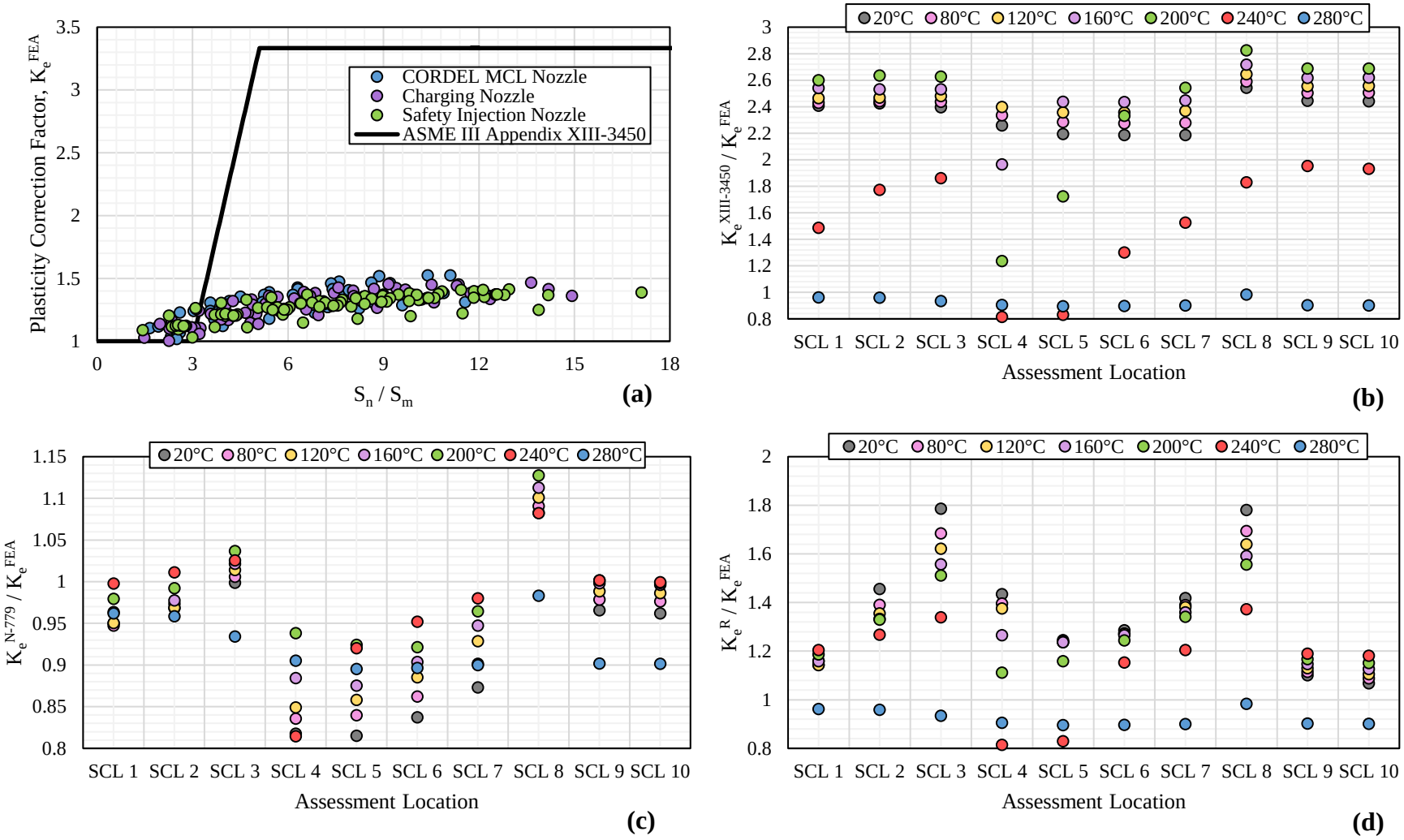

Figure 101. Performance of ASME III K_e factors for CORDEL MCL nozzle.

(a) K_e^{FEA} vs. S_n/S_m (b) Appendix XIII-3450 vs. E-P FEA ($K_e^{XIII-3450}/K_e^{FEA}$) (c) CC N-779 vs. E-P FEA (K_e^{N-779}/K_e^{FEA}) (d) Ranganath's method vs. E-P FEA (K_e^{R}/K_e^{FEA})

7.4. Tapered Nozzle-In-Vessel

This section presents the results obtained from fatigue analysis of the Tapered Vessel-In-Nozzle FE model.

The number of allowable cycles calculate at each assessment location using the Appendix I DFC is shown in Figure 102. As shown by Figure 102 (a), the critical location determined by elastic-plastic fatigue analysis was found to be SCL 8 situated at the mid-length of the nozzle, which permits only 100 cycles of the most severe design transient. Fatigue damage was found to be slightly less severe in the attached piping. Additionally, the nozzle-to-pipe juncture (SCL 3) permits 109 cycles, which is less pessimistic than for the nozzle. In Figure 102 (b), the N_f calculated according to ASME III Appendix XIII-3450 are only 12-15% of those cycles predicted by elastic-plastic FEA. In contrast, the N_f calculated according to CC N-779 shown in Figure 102 (c) were more closely aligned with that of elastic-plastic FEA. However, the fatigue limiting location was predicted to be at SCL 3, which only permits 76 cycles. Despite this, CC N-779 still gave very accurate results in the nozzle, predicting an average N_f of 99 for SCLs 7-9, which is equivalent to that predicted from elastic-plastic FEA. As shown by Figure 102 (d), Ranganath's method produced conservative values of N_f for all assessment locations in the FE model. However, like CC N-779, it also predicted a different fatigue limiting location to elastic-plastic FEA, with the highest fatigue damage expected at SCL 4, which permits only 27 cycles. SCL 4 is situated in the transition region between the vessel nozzle and attached piping, close to the juncture. This is similar to the situation observed for the PWR auxiliary piping nozzles, where Ranganth's method was also found to predict the highest damage in the nozzle-to-piping transition region.

Figure 103 shows the contour plot of $K_e^{FEA} \geq 1.0$ at nozzle-to-pipe juncture region of the FE model. As shown, K_e^{FEA} on the internal surface is relatively uniform, and increases proportionally for both the nozzle and pipe sections with increasing severity of thermal transient. On the outside surface, at the local discontinuity induced by the tapered transition between the nozzle and piping, K_e^{FEA} is close to unity for the less severe design transients but increases as the through-thickness thermal gradient becomes high enough to induce local plasticity on the outside surface. However, since

the bulk of the section thickness exhibits strict shakedown, strain concentration at the outer surface of the discontinuity is modest, and is not as severe as the internal surface. Due to the high thermal resistance of both the nozzle and piping, high local thermal stresses meant that K_e^{FEA} on the surface was always greater than 1.0 even for the less severe transients. Figure 104 shows the variation in the ASME III elastic stress parameters calculated for the tapered nozzle-in-vessel. The maximum S_n/S_m occurs at the pipe juncture (SCL 3), and is mainly due to the large bending stresses induced by mismatch in the radial displacements of the nozzle and pipe sections. The maximum S_p/S_m however occurs in the nozzle region (SCL 7) due to the much higher combination of S_n and $S_{p,lt}$. The performance of the ASME III K_e factors were evaluated at each assessment location and the results are summarised in Figure 105.

As shown by Figure 105 (b), $K_e^{XIII-3450}$ was generally found to be conservative by a factor of 2.2x to 2.8x; this is consistent with the results obtained for the PWR auxiliary piping nozzles. Similarly, only in cases where $S_n < 3S_m$ was $K_e^{XIII-3450}$ found to be modestly non-conservative, up to a maximum of 15%.

Figure 105 (c) shows the relative performance of CC N-779 at each assessment location. The results indicate that CC N-779 performs reasonably well for both the attached piping region (SCLs 1-3) and the nozzle region (SCLs 7-10), producing results that are within 5-10% of K_e^{FEA}, albeit slightly on the non-conservative side. CC N-779 was most conservative at SCL 3 by up to a factor of 1.15x, explaining why CC N-779 predicts the lowest N_f at this location. The reason for this is that $S_{p,lt}$ is relatively low compared with S_{n-tb}, which results in a higher weighting being applied to the more conservative K_e^{N-779} factor (which is equivalent to $K_e^{XIII-3450}$). However, CC N-779 does not perform as well for the tapered transition region (SCLs 4-6), potentially under predicting K_e^{FEA} by up to 17%. This is because the contribution of S_{n-tb} decreases relative to $S_{p,lt}$ along the transition length towards the nozzle, which increases the weighting applied to K_v^{N-779} compared to K_e^{N-779}, resulting in a lower overall correction.

As shown by Figure 105 (d), Ranganath's K_e^R was found to be conservative in all cases where $S_n > 3S_m$. K_e^R was found to be conservative by a factor of 1.2x to 1.6x for the nozzle and pipe sections, and by a factor of 1.4x to 2.0x for the tapered transition

region. The higher conservativism of K_e^R and N_f in the tapered transition region follows closely the variation in *R*, which was found to be especially high in this region, with $S_{n\text{-}tb}$ accounting for between 25-40% of S_n. The higher value of *R* is expected for this region of thickness transition where a large axial thermal gradient develops, since the time to cool-down and warm-up is much longer for the nozzle than for the pipe. The magnitude of $S_{n\text{-}tb}$ is therefore likely to be higher in this situation. Thus, it may be concluded that K_e^R will be more conservative at locations at or near transitions in section thickness under thermal shock conditions. *Ceteris paribus*, the conservativism of K_e^R is expected to increase in proportion to the difference in section thickness between two connected structures, since this controls the severity of the resulting axial thermal gradient and consequently the magnitude of $S_{n\text{-}tb}$.

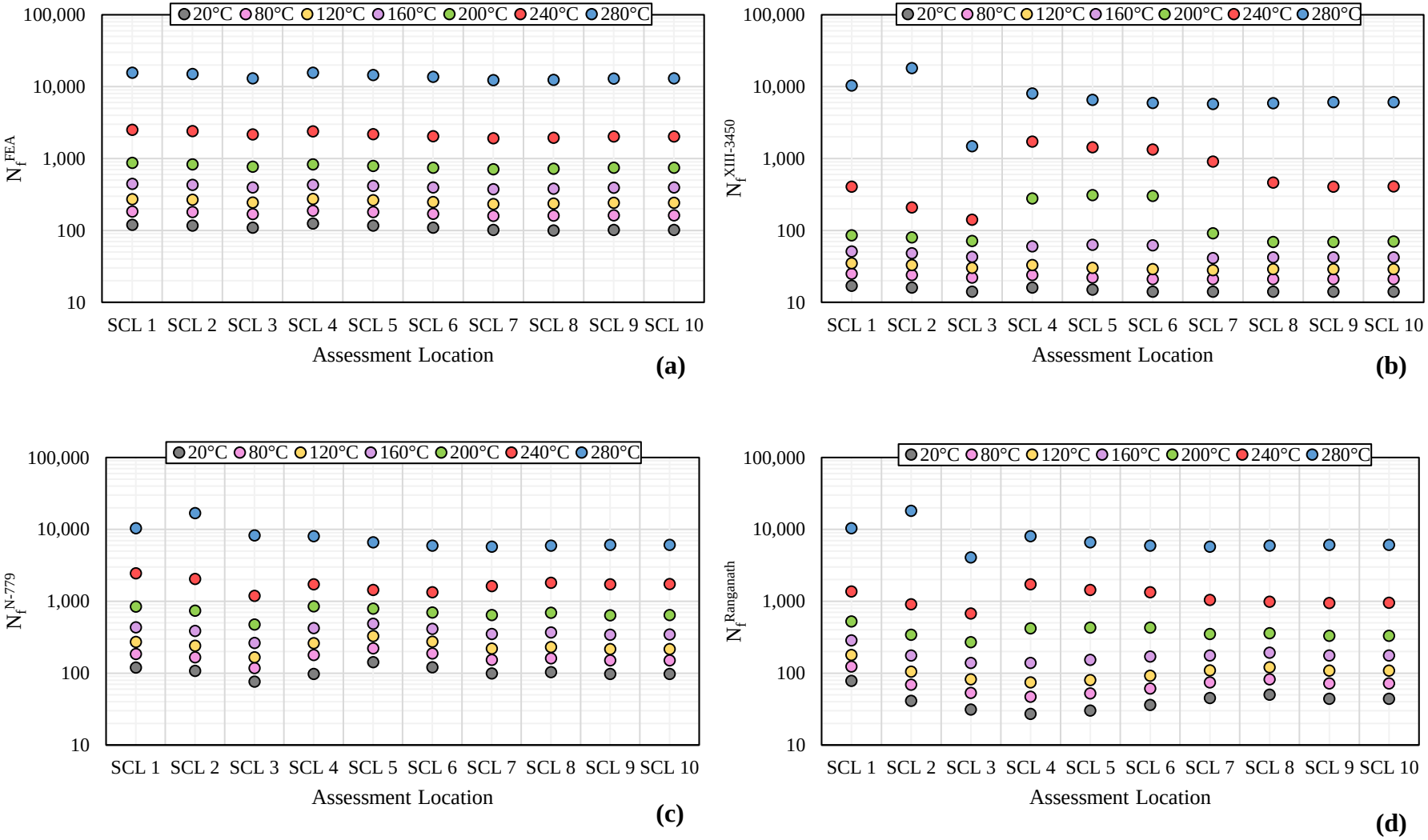

Figure 102. Allowable cycles, N_f, for tapered nozzle-in-vessel.

(a) Elastic-plastic FEA; (b) Appendix XIII-3450; (c) CC N-779; (d) Ranganath's method

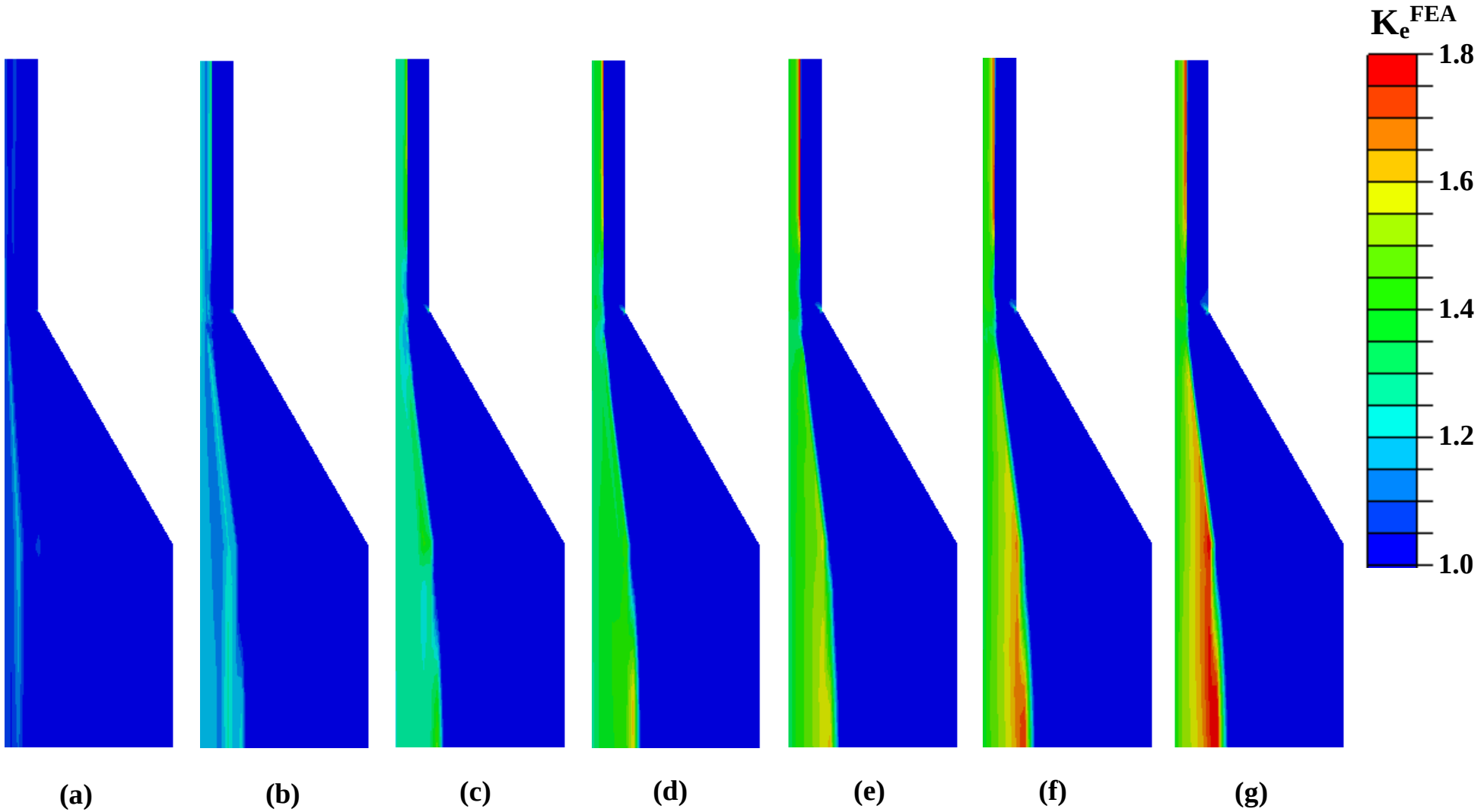

Figure 103. Contour plot of $K_e^{FEA} \geq 1.0$ for tapered nozzle-in-vessel FE model by minimum design transient fluid temperature.

(a) 280°C; (b) 240°C; (c) 200°C; (d) 160°C; (e) 120°C; (f) 80°C; (g) 20°C

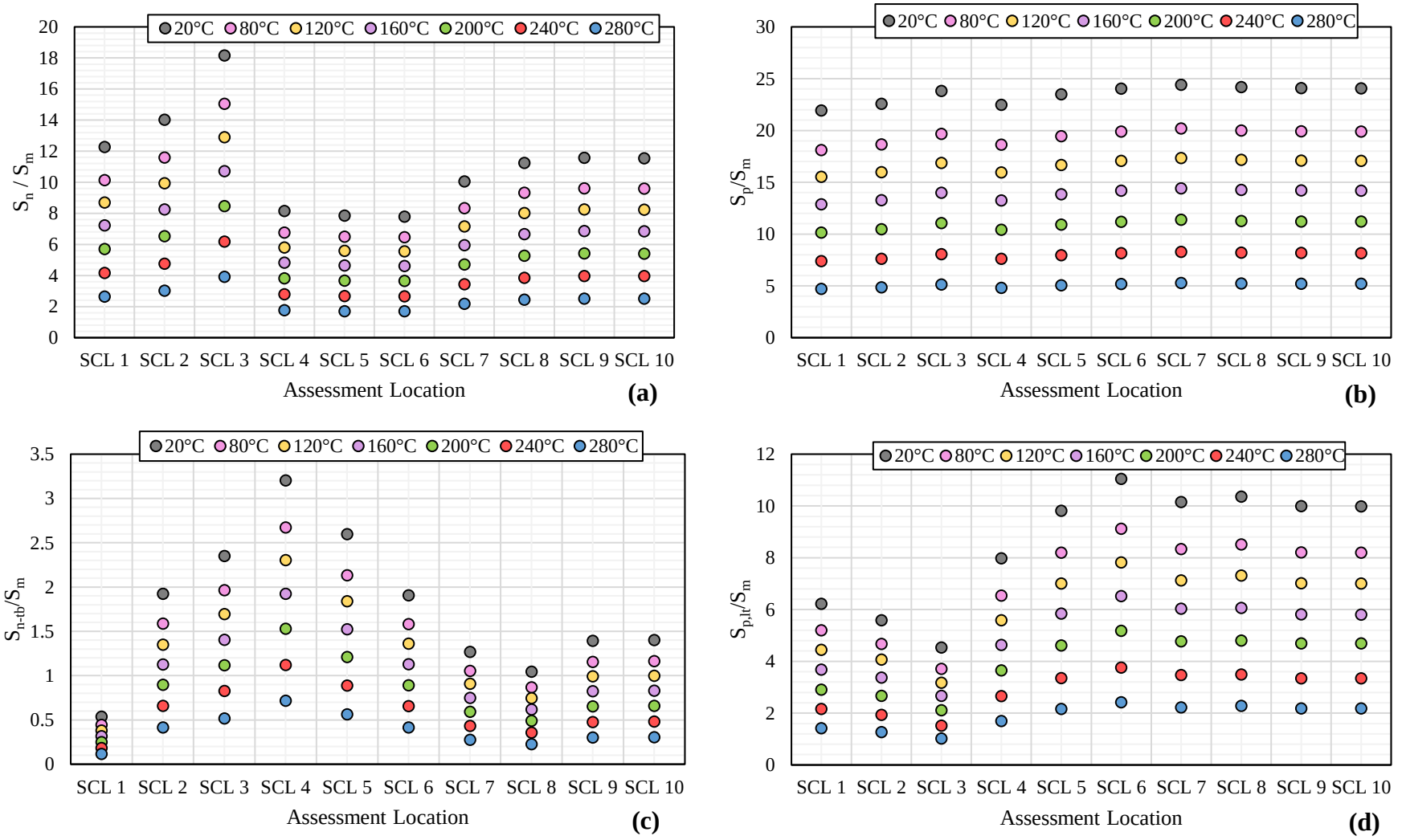

Figure 104. ASME III elastic stress parameters calculated for tapered nozzle-in-vessel.

(a) S_n/S_m (b) S_p/S_m (c) $S_{n\text{-}tb}/S_m$ (d) $S_{p,lt}/S_m$

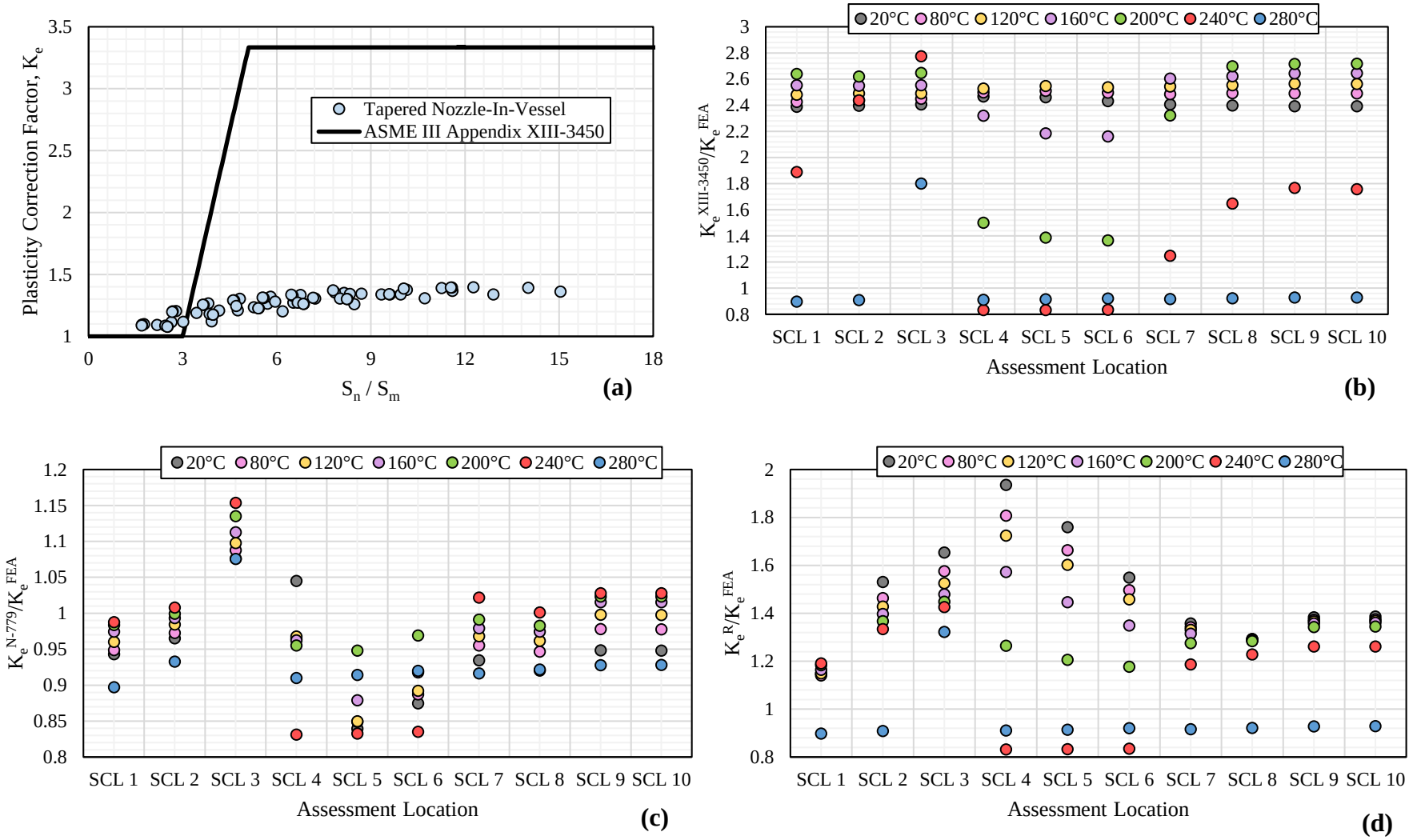

Figure 105. Performance of ASME III K_e factors for tapered nozzle-in-vessel.

(a) K_e^{FEA} vs. S_n/S_m (b) Appendix XIII-3450 vs. E-P FEA ($K_e^{XIII-3450}/K_e^{FEA}$) (c) CC N-779 vs. E-P FEA (K_e^{N-779}/K_e^{FEA}) (d) Ranganath's method vs. E-P FEA (K_e^{R}/K_e^{FEA})

7.5. PWR Nozzle with Thermal Sleeve

This section presents the results obtained from fatigue analysis of the PWR nozzle with attached thermal sleeve as described in Hubel [175].

The number of allowable cycles calculated at each assessment location using the Appendix I DFC is shown in Figure 106. N_f calculated by elastic-plastic FEA is shown by Figure 106 (a). Infinite life was predicted for SCLs 1 and 2 situated in the attached piping. This is attributed to the small wall thickness of 8mm, which minimised the thermal resistance of the pipe. The N_f predicted at SCLs 8-11 situated in the nozzle were over two orders of magnitude higher than at the thermal sleeve attachment point. This is due to the compact nature of the nozzle being of only 43mm thickness and the additional protection afforded by the thermal sleeve and stagnant fluid. The rapid cooling of the nozzle due to the injection of cold fluid caused the thermal sleeve to shrink, resulting in a tensile stress on the inside surface and a compressive stress on the surface in contact with the stagnant fluid. This caused large bending action at the sleeve attachment point. As can be seen, the critical location is SCL 7 situated at the notch root induced by the thermal sleeve attachment point, which permits 790 cycles of the most severe design transient. SCLs 5 and 6 were also found to exhibit high damage, permitting 1071 and 1258 cycles, respectively. SCL 4 at the nozzle-to-pipe juncture was found to be of lesser concern. As shown by Figure 106 (b), ASME III Appendix XIII-3450 shows the fatigue limiting location to be at SCL 5, situated slightly above the thermal sleeve attachment point, permitting only 65 cycles. On the other hand, Figure 106 (c) and (d) show that both CC N-779 and Ranganath's method predict the fatigue limiting location to be at SCL 6, which is between the nozzle surface and sleeve thickness slightly below the attachment point. CC N-779 and Ranganath's method both permit only 112 and 69 cycles respectively at this location. Both approaches are significantly more conservative in this case compared with the previously discussed FE models.

The contour plot of $K_e^{FEA} \geq 1.0$ at the critical nozzle-to-sleeve juncture region is shown in Figure 107. K_e^{FEA} is shown to be most significant at the locations of highest $S_p/3S_m$ observed in Figure 84, thus affirming that elastic stress contours appear to be a good predictor of high strain concentration in this case where peak plasticity is dominant.

The magnitude of K_e^{FEA} is highest at the nozzle surface slightly above the sleeve attachment point (SCL 5, or Point B in Figure 84) and at the notch induced by the nozzle-to-sleeve juncture (SCL 7, or Point C in Figure 84). Nonetheless, the magnitude of K_e^{FEA} on the internal surface of each assessment location is still very low, varying up to a maximum of approximately 1.27. Cyclic plasticity did not extend significantly into the thickness of the nozzle region. This was attributed to the stagnant fluid contained by the sleeve, which significantly reduced the heat transfer to the nozzle region, and thus the severity of the surface (local) thermal stresses. This also restricted the severity of any radial thermal gradient developed in the nozzle region, so limiting thermal bending stresses. However, whilst radial heat transfer in the nozzle region is attenuated, this also results in amplification of the axial thermal gradient developed between the nozzle and much thinner attached piping.

Figure 108 shows the variation in the ASME III elastic stress parameters calculated for the PWR nozzle with thermal sleeve. It is clear that SCLs 5-7 experience the highest S_p, but each show very different behaviour in their resultant stress range. In particular, SCL 6 experiences only a very small $S_{p,lt}$ superimposed on top of very high $S_{n\text{-}tb}$, indicating that sectional plasticity is prevalent in the sleeve just below the attachment point. This is also confirmed by the contours of Figure 107, which shows that for the more severe transients, K_e^{FEA} is greater than unity across the entire sleeve thickness. Additionally, thermal membrane stresses, $S_{n\text{-}tb}$, account for over 60% of S_n at SCL 6, due to the large axial thermal gradient formed between the sleeve and the nozzle during the heat-up and cool-down periods. Consequently, SCL 6 does not satisfy the requirements of ASME III Appendix XIII-3450 (a); nevertheless, plastic shakedown was still achieved, and so the Code K_e factors were still examined at this location to compare with K_e^{FEA}. The trend in K_e^{FEA} vs. S_n/S_m and the performance of the ASME III K_e factors by assessment location are shown in Figure 109.

In Figure 109 (b), $K_e^{XIII\text{-}3450}$ was generally found to be very conservative, potentially by up to a factor of 3.4x. $K_e^{XIII\text{-}3450}$ was found to be particularly conservative at SCL 6, even for the less severe transients, owing to the very high S_n/S_m at this location. In contrast, $K_e^{XIII\text{-}3450}$ was found to be much lower at the notch (SCL 7), as S_n only modestly exceeded $3S_m$. Thus, $K_e^{XIII\text{-}3450}$ was slightly non-conservative at this location. The magnitude of $K_e^{XIII\text{-}3450}$ at SCL 7 is quite sensitive to the orientation of the SCL.

If the SCL is instead positioned to span horizontally from the notch surface, the magnitude of S_n is higher and $K_e^{XIII-3450}$ produces a more conservative correction. However, this particular nozzle geometry is quite complex and the application of SCLs in this situation can be difficult for assessing fatigue. In particular, it is not always possible to ensure that the SCL orientation is perpendicular to the stress flow. Guidelines for this type of geometry are not covered in WRC-429 or ASME VIII-2 Annex 5A.

In Figure 109 (c), CC N-779 was found to be moderately conservative for SCLs 4 and 5, where the influence of the less conservative K_v^{N-779} factor was more dominant. CC N-779 was also found to be very conservative at SCL 6, due to the very large contribution of S_{n-tb} to S_n, which results in a greater weighting applied to the more conservative K_e^{N-779} rather than K_v^{N-779}.

In Figure 109 (d), Ranganath's K_e^R shows a generally similar trend to that of CC N-779, but is much more conservative for SCLs 4 and 5. This is due to the conservative assumption of K_{th}^R equal to 1.4 in the K_e^R methodology. At SCL 6, the magnitude of K_e^R is the same as $K_e^{XIII-3450}$, and both are equally conservative when compared to K_e^{FEA}. This is due to the high value of R = 0.65 at this location, leading Ranganath's method to become equal to Appendix XIII-3450 for S_n exceeding $7.7S_m$. It is therefore expected that both corrections should perform similarly in cases where S_n is high and is dominated by S_{n-tb}.

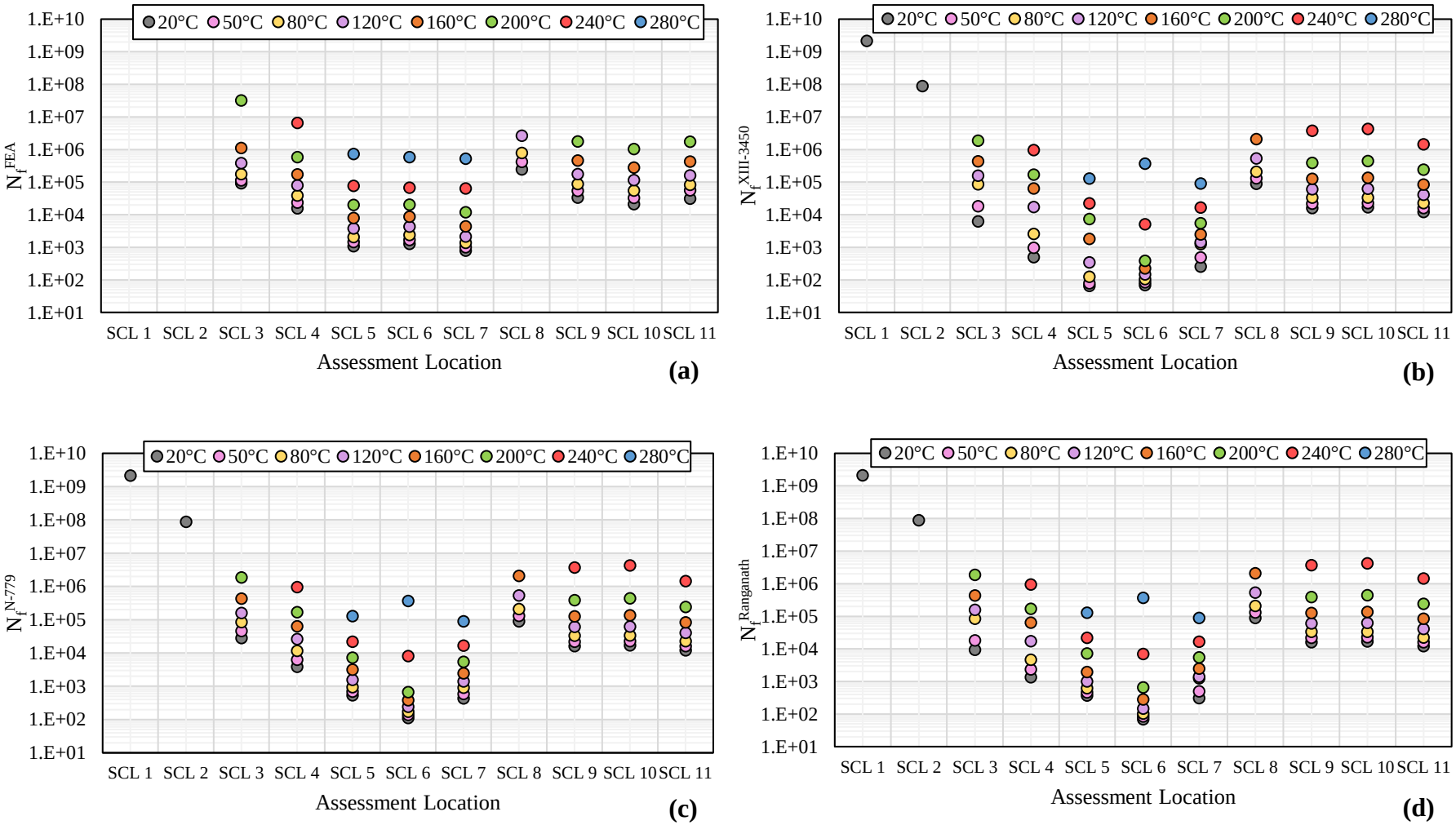

Figure 106. Allowable cycles, N_f, for PWR nozzle with thermal sleeve.

(a) Elastic-plastic FEA; (b) Appendix XIII-3450; (c) CC N-779; (d) Ranganath's method

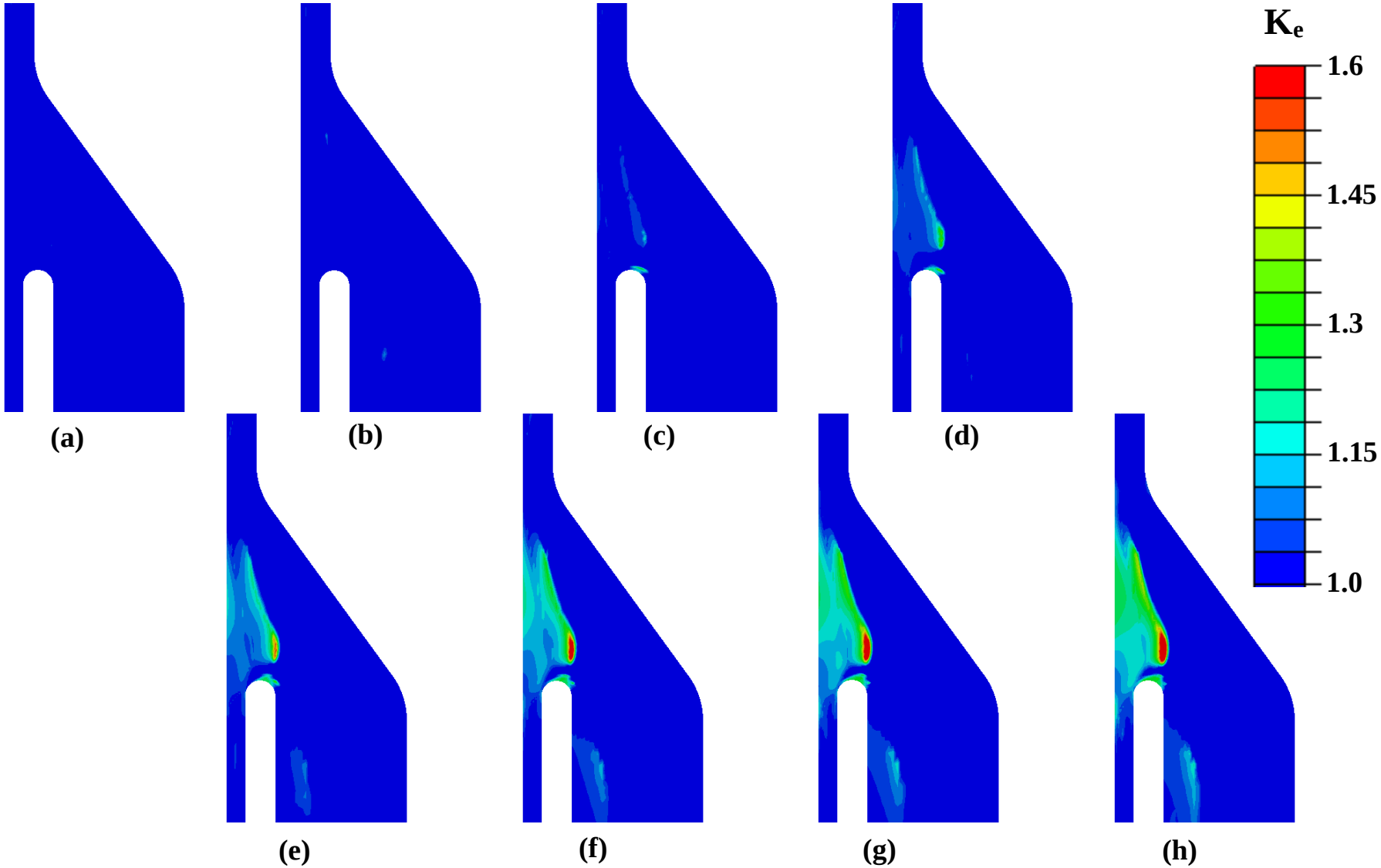

Figure 107. Contour plot of $K_e^{FEA} \geq 1.0$ for PWR nozzle thermal sleeve by design transient minimum fluid temperature.

(a) 280°C; (b) 240°C; (c) 200°C; (d) 160°C; (e) 120°C; (f) 80°C; (g) 50°C; (h) 20°C

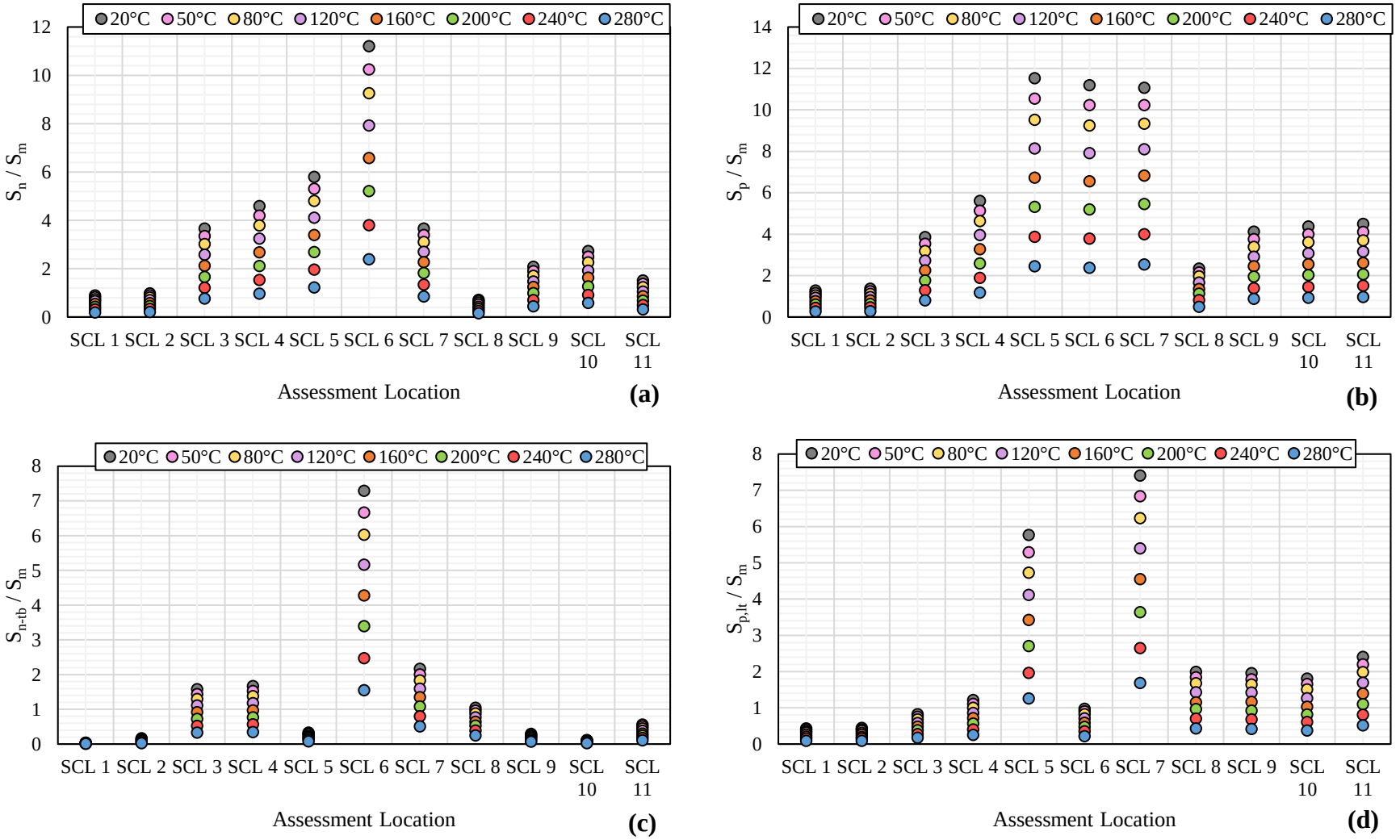

Figure 108. ASME III elastic stress parameters calculated for PWR nozzle with thermal sleeve

(a) S_n/S_m (b) S_p/S_m (c) $S_{n\text{-}tb}/S_m$ (d) $S_{p,lt}/S_m$

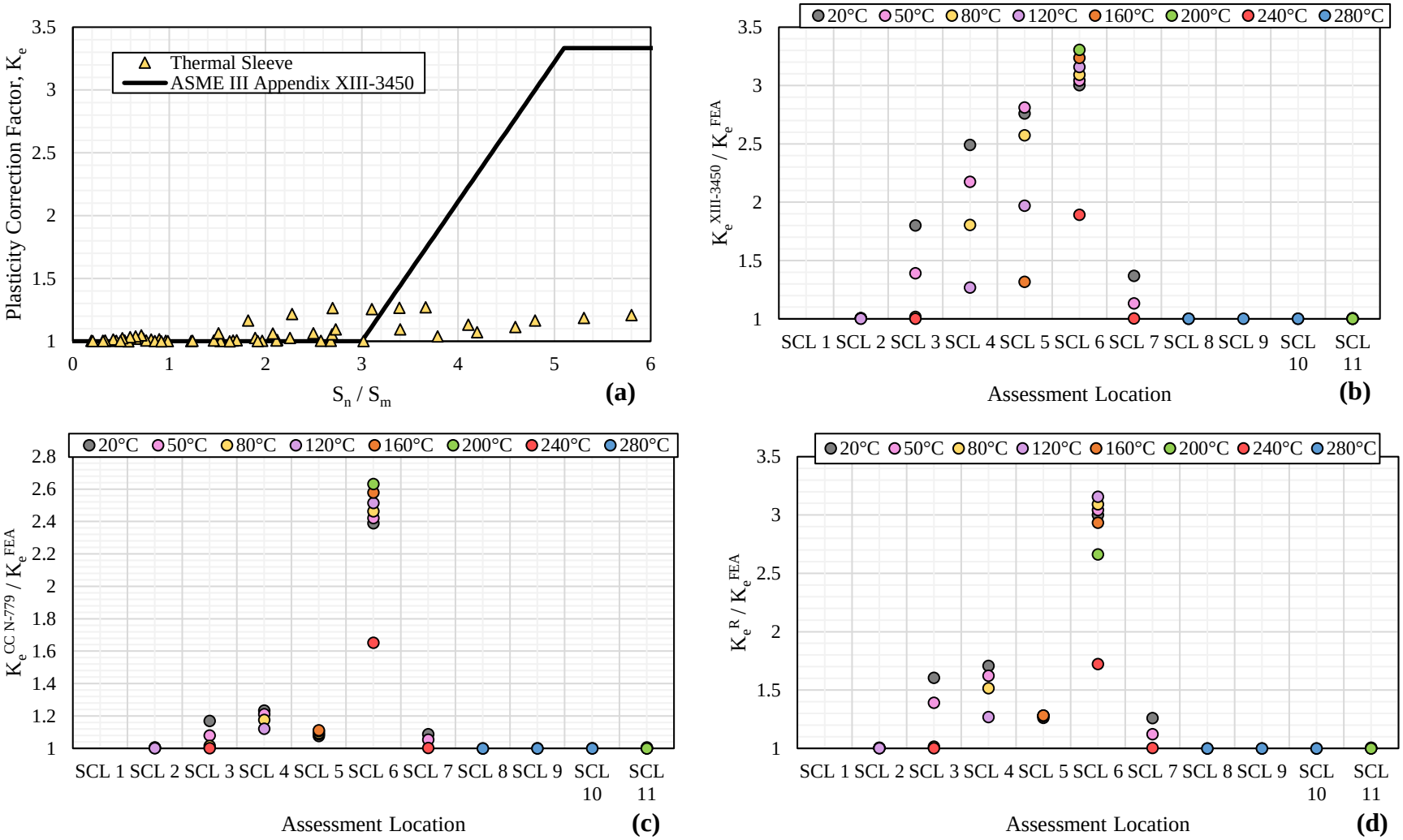

Figure 109. Performance of ASME III K_e factors for PWR nozzle with thermal sleeve.

(a) K_e^{FEA} vs. S_n/S_m (b) Appendix XIII-3450 vs. E-P FEA (c) CC N-779 vs. E-P FEA (d) Ranganath's method vs. E-P FEA

7.6. Nuclear Vessel Skirt Support (Y-Piece)

This section summarises the results obtained from fatigue analysis of the Y-Piece skirt support described in Kasahara [176].

The results obtained for the Y-Piece are summarised in Figure 110. The number of allowable cycles calculated at the skirt juncture using the Appendix I DFC is shown in Figure 110 (a). As can be seen, elastic-plastic FEA permits 247 cycles at the skirt juncture for the most severe design transient. Both ASME III Appendix XIII-3450 and Ranganath's method conservatively permit only 42 cycles under these conditions. CC N-779 was also found to be similarly conservative in this case, permitting only 99 cycles.

The K_e^{FEA} factors were calculated at every node in the Y-Piece FE model and plotted to examine the contours of K_e^{FEA} at the skirt-to-vessel juncture, which showed very high $S_p/3S_m$ in the initial fatigue scoping calculations (Figure 89). Figure 111 shows the contour plot of $K_e^{FEA} \geq 1.0$ at the skirt-to-vessel juncture for each design transient. As the thermal gradient between the vessel and support skirt increases, cyclic plasticity begins to spread in the thickness of the skirt, close to the attachment point with the supported vessel. Since the thermal gradient acts uniformly along the longitudinal axis of the skirt, this produces a large K_e^{FEA} across the entirety of the skirt thickness. Gross plastic cycling is apparent, wherein the skirt acts as a plastic hinge, resulting in a ratchet mechanism at the juncture. However, since the difference in the hysteresis loop tip-to-tip strain range between cycles was found to be negligible, the K_e^{FEA} values calculated for the final (10^{th}) cycle of the elastic-plastic fatigue evaluation were still deemed valid for purposes of this study.

Figure 110 (b) shows the variation in the ASME III elastic stress parameters calculated at the assessment location. In this case, S_p is characterised by a modest local thermal stress range, $S_{p,lt}$, superimposed with a high membrane-plus-bending stress range, S_n. Additionally, $S_{n\text{-}tb}$ accounts for over one-half of S_n, which led to difficulties in satisfying the requirements of ASME III Appendix XIII-3450 (a) for this particular geometry. The criterion of $S_{n\text{-}tb} \leq 3S_m$ (Eq. (64)) was violated for vessel warm-up temperatures exceeding 250°C. Despite this, the Code K_e factors were still calculated to determine their conservatism relative to K_e^{FEA}. The variation of K_e^{FEA} vs. S_n/S_m at

the skirt juncture is shown by Figure 110 (c). Whilst Figure 111 shows the skirt juncture exhibits cyclic plasticity through-thickness, on the internal surface where fatigue cracking is of most significance, K_e^{FEA} was found to be quite modest, tending to a maximum of 1.54. Initially, K_e^{FEA} was found to vary linearly with increasing S_n/S_m, though does appear to relent somewhat as S_n exceeds $8S_m$.

The performance of the ASME III K_e factors relative to K_e^{FEA} is shown by Figure 110 (d). The performance of $K_e^{XIII-3450}$ for the Y-Piece FE model was found to be very conservative, achieving the maximum $K_e^{XIII-3450}$ of $1/n$ for vessel warm-up temperatures exceeding 225°C. Since the cyclic response at the skirt juncture is dominated by sectional plasticity, peak strain concentration was also found not to occur for $S_n < 3S_m$, and thus $K_e^{XIII-3450}$ was conservative across the entire range of S_n/S_m. CC N-779 was found to be quite conservative for the Y-Piece FE model. This was due to the dominant contribution of S_{n-tb} to S_n, leading to a significant weighting applied to $K_e^{XIII-3450}$, with the less conservative K_v^{N-779} applying only to the much smaller contribution of $S_{p,lt}$. Similarly, Ranganath's method was also found to be quite conservative, falling between Appendix XIII-3450 and CC N-779. Due to the large fraction of S_n attributed to S_{n-tb}, this results in a high value of R in Ranganath's K_e^R formulation, which applies a greater weighting to $K_e^{XIII-3450}$ and controls the threshold value of S_n/S_m beyond which K_e^R becomes equal to $K_e^{XIII-3450}$. Since the weightings applied to $K_e^{XIII-3450}$ in CC N-779 and Ranganath's method are mathematically equivalent, the higher conservatism of K_e^R in the range of $3S_m<S_n\leq 3mS_m$ is due to the definition of K_{th}^R, which applies to $S_{n,tb}$. The fact that K_{th}^R is more pessimistic than K_v^{N-779} and $S_{n,tb}$ is larger than $S_{p,lt}$ in this case leads to somewhat higher conservatism in K_e^R. It should be emphasised however that all three approaches produce rather conservative results for this geometry and loading condition, despite the Appendix XIII-3450 (a) criterion being violated.

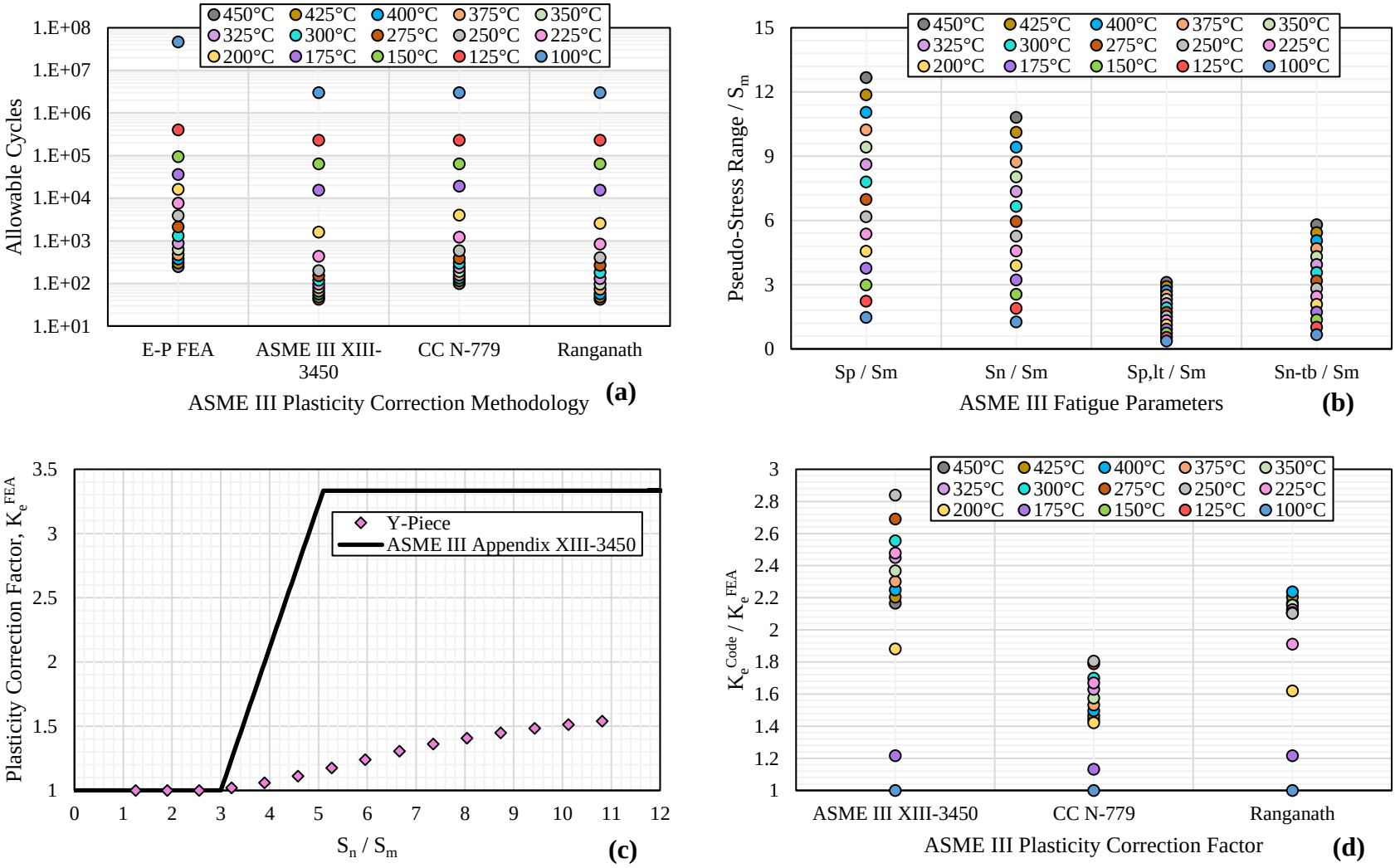

Figure 110. Summary of results obtained for Y-Piece FE model.

(a) Allowable cycles, N_f; (b) ASME III elastic stress parameters; (c) K_e^{FEA} vs. S_n/S_m; (d) Performance of ASME III K_e factors

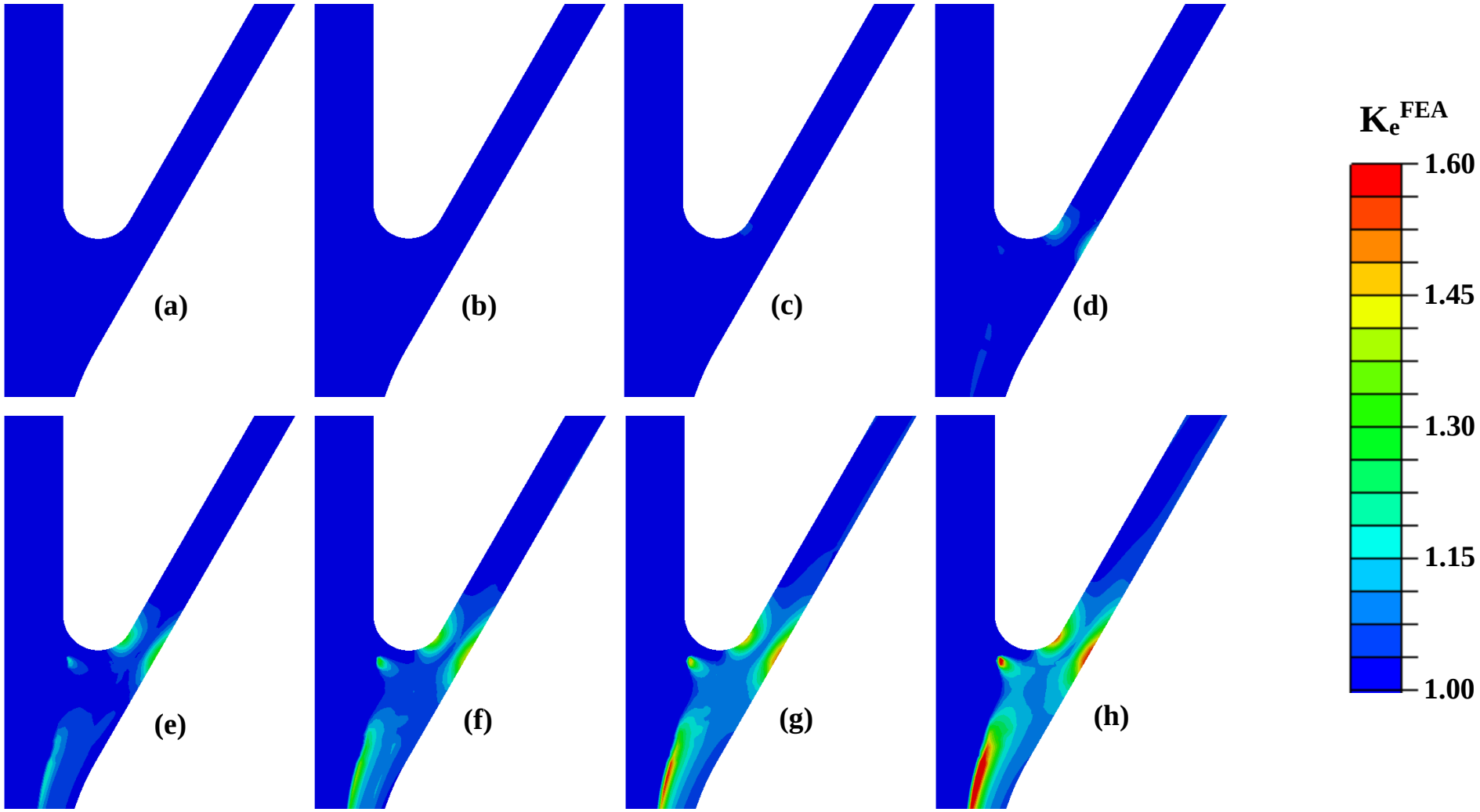

Figure 111. Contour plot of $K_e^{FEA} \geq 1.0$ for Y-Piece FE model by maximum vessel temperature.

(a) 100°C; (b) 150°C; (c) 200°C; (d) 250°C; (e) 300°C; (f) 350°C; (g) 400°C; (h) 450°C

7.7. Notched Cylinder

This section summarises the results obtained from fatigue analyses conducted on the notched cylinder FE models described in Section 6.7.

The number of allowable cycles, N_f, calculated as a function of ρ for the axial, radial linear, and radial parabolic thermal gradients using the Appendix I DFC are respectively shown in Figure 112, Figure 113, and Figure 114. As shown by Figure 112 (a) and Figure 114 (a), N_f^{FEA} decreases with decreasing ρ in the case of the axial thermal and radial parabolic thermal gradients, but actually increases with decreasing ρ for the case of the radial linear thermal gradient shown in Figure 113 (a). For the thermal loading conditions considered, the radial parabolic thermal gradient was found to be the most damaging. The allowable cycles predicted by Appendix XIII-3450, $N_f^{XIII\text{-}3450}$, are shown by Figure 112-Figure 114 (b) for the axial, radial linear, and radial parabolic thermal gradients, respectively. In general, $N_f^{XIII\text{-}3450}$ was found to be an order of magnitude lower than N_f^{FEA}. In particular, for the radial parabolic thermal gradient, $N_f^{XIII\text{-}3450}$ was found to be below the range of tabulated values specified for the Appendix III DFC. In contrast, as shown from Figure 112-Figure 114 (c), the allowable cycles predicted by CC N-779, $N_f^{N\text{-}779}$, was found to be consistently higher than N_f^{FEA} for the radial linear and radial parabolic thermal gradients, irrespective of ρ. As shown from Figure 112-Figure 114 (d), the allowable cycles permitted by Ranganath's method, N_f^{R}, were generally found to be lower than N_f^{FEA} for the radial parabolic thermal gradient, but coincided more closely with N_f^{FEA} in the case of the axial and radial linear thermal gradients. The reason for these differences was further examined by considering the variation in K_e^{FEA} for comparison with the Code K_e factors.

The K_e^{FEA} factors were calculated at every node in the FE model for each combination of loading type and notch root radius of curvature, ρ. Figure 115, Figure 116, and Figure 117 show the contour plots of $K_e^{FEA} \geq 1.0$ calculated in the vicinity of the notch tip for the axial, radial linear, and radial parabolic thermal gradient load cases, respectively. For the sake of brevity, only the resulting K_e^{FEA} contours for the case of ρ=2.5 mm is shown. As can be seen from Figure 115, strain concentration at the notch tip is relatively modest for the case of the axial thermal gradient, varying up to a

maximum 1.27 for ρ=2.5 mm. Furthermore, the region for which $K_e^{FEA} \geq 1.0$ is limited to the notch tip and the immediately surrounding material, and is therefore indicative of highly localised plasticity. On the other hand, Figure 116 and Figure 117 show that strain concentration at the notch tip is much more severe in the case of the radial linear and radial parabolic thermal gradients. Furthermore, the region for which $K_e^{FEA} \geq 1.0$ extends beyond the local material surrounding the notch, indicating plasticity is prevalent both through-thickness and along the length of the cylinder.

Figure 118, Figure 119, and Figure 120 shows the variation in the ASME III elastic stress parameters, whilst Figure 121, Figure 122, and Figure 123 show the performance of the ASME III K_e factors for the notched cylinder considering the axial, radial linear, and radial parabolic thermal gradients, respectively. The FE-derived K_e^{FEA} vs. S_n/S_m obtained for the notched cylinder FE models are also respectively shown in Figure 121 (a), Figure 122 (a), and Figure 123 (a) for the axial, radial linear, and radial parabolic thermal gradient load cases. The trend in K_e^{FEA} vs. S_n/S_m varies both with notch size (ρ) and loading type.

In the case of the axial thermal gradient, K_e^{FEA} exhibits an approximately linear trend with S_n/S_m and shows no sign of relenting. This is attributed to large elastic follow-up, owing to the fact that the thermal load acts over a sufficiently long range that localised relaxation and redistribution near the notch has no effect on the magnitude of the remote stresses; thus, the secondary thermal stress in this case acts more like a primary stress than a secondary stress. The effect of ρ is two-fold. First, decreasing ρ increases the sharpness of the notch and so increasing the severity of peak strain concentration at the notch tip. Secondly, decreasing ρ also increases the effective load-bearing cross section of the cylinder at the notch. This reduces the magnitude of S_n attained at the notch tip. However, the relationship between ρ and S_n diminishes as $\rho \rightarrow 0$, as little difference in S_n was observed for the three sharpest notch geometries, which each formed only 12.5%, 6.25%, and 3.125% of the nominal thickness of the cylinder.

For the case of a linear thermal gradient acting through-thickness (i.e. radially), K_e^{FEA} calculated at the notch tip exhibits asymptotic behaviour with increasing S_n/S_m. As shown by Figure 122 (a), the largest notch size of ρ=5mm initially exhibits the smallest K_e^{FEA} for S_n/S_m up to approximately 10 S_m, following which it exhibits the higher

K_e^{FEA}. As was highlighted in Figure 116, the magnitude of K_e^{FEA} remains highest at the notch tip, but is also significantly elevated in the thickness of the notched section. The thermal bending stresses that arise induces plasticity at the inner and outer surfaces, which then extends inward as the magnitude of the linear through-thickness thermal gradient is increased. Consequently, only a small region of the notched section remains elastic for the most severe loading conditions. As shown by Figure 119, a much higher magnitude of S_n/S_m was observed here compared to the case of the axial thermal gradient, with the thermal bending stresses, $S_{n,tb}$ providing the majority contribution to S_n. It is noteworthy that the maximum S_p is observed for the largest notch (ρ=5mm), which contrasts with that observed for axial thermal gradient case. The relationship between S_n and ρ is also more pronounced, with S_n decreasing by a factor of 2 between the largest and smallest notch sizes; for large ρ, S_p is dominated by S_n, and for small ρ, S_p is dominated by $S_{p,lt}$. For the largest notch (ρ=5mm), K_e^{FEA} did not exceed 1.0 for $S_n < 3S_m$, in contrast to the smaller notch sizes, which showed significant peak strain concentration. The effect of decreasing ρ can therefore be seen to shift the dependence of K_e^{FEA} from net-section plasticity to local plasticity at the notch tip under these loading conditions.

As observed in Figure 123 (a), K_e^{FEA} also appears to exhibit asymptotic behaviour with increasing S_n/S_m for the case of a parabolic (shock) thermal gradient acting through-thickness. The magnitude of K_e^{FEA} was found to vary inversely with ρ, with smaller ρ showing the highest K_e^{FEA} as a function of S_n/S_m. However, as shown in Figure 120 (c), it was found that the ASME III Appendix XIII-3450 (a) requirement that $S_{n\text{-}tb}$ remain below $3S_m$ was not satisfied in the case of the largest notch (ρ=5mm) for maximum surface temperatures exceeding 200°C. The reason for this is due to increasing mismatch in thermal resistance introduced between the notched section and remaining length of the cylinder as ρ is increased. Initially, the sharp change in temperature induces high local thermal stresses on the entire cylinder surface. As the transient progresses, thermal bending stresses begin to develop through-thickness, which lag the initial peak stress attained on the surface. However, heat conduction occurs at a faster rate in the notched section, which has a lower thermal resistance due to the reduction in cross-section. This also causes an axial thermal gradient to develop between the notched section and remaining length of the cylinder, producing elevated

thermal membrane stresses at the notch tip. This therefore poses problems in satisfying the Appendix XIII-3450 (a) limit. As ρ is decreased, the severity of the axial thermal gradient is reduced, leading to a reduction in $S_{n\text{-}tb}$ as shown by Figure 120 (c). However, as shown by Figure 120 (a), the relationship between S_n and ρ is less clear, and does not show a decreasing trend as was observed for the other thermal load cases. Overall, the thermal shock gradient is more representative of plant conditions, and shows characteristics common to both the pure axial and radial linear thermal gradient cases.

In general, $K_e^{XIII\text{-}3450}$ showed reasonable conservatism for the notched cylinder FE models, but did show the potential to be non-conservative depending on ρ and the severity of the thermal transient. As shown by Figure 121 (b), in the case of the axial thermal gradient, $K_e^{XIII\text{-}3450}$ was generally equal to unity, since S_n was modest and did not exceed $3S_m$ for all but the most severe loading. As a result, $K_e^{XIII\text{-}3450}$ was found to be potentially non-conservative by up to 10% for ρ=5mm and by up to 25% for ρ=0.3125mm due to peak strain concentration at the notch tip. It was also observed that for $3S_m<S_n<3.4S_m$, $K_e^{XIII\text{-}3450}$ was found to still be slightly non-conservative in this region. However, for $S_n>3.4S_m$, $K_e^{XIII\text{-}3450}$ was found to be conservative for all notch sizes considered. $K_e^{XIII\text{-}3450}$ was most conservative for ρ=5mm due to a combination of the higher S_n/S_m, resulting in a higher $K_e^{XIII\text{-}3450}$, and the lower value of K_e^{FEA} observed at the notch tip. As shown by Figure 122 (b), in the case of the radial linear thermal gradient, $K_e^{XIII\text{-}3450}$ was also found to be non-conservative by up to 25% for $S_n < 3S_m$. One exception was for ρ=5mm, which did not exhibit peak strain concentration and $K_e^{XIII\text{-}3450}$ was conservative for all transients considered. Where S_n greatly exceeded $3S_m$, $K_e^{XIII\text{-}3450}$ was found to be show similar levels of conservatism for all ρ, varying between a factor of 1.6x and 2.4x. As shown in Figure 123 (b), for the case of the radial parabolic thermal gradient, $K_e^{XIII\text{-}3450}$ was found to be potentially non-conservative by up to 40% for $S_n < 3S_m$. At high S_n/S_m, $K_e^{XIII\text{-}3450}$ showed similar conservativism between a factor of 1.8x and 2.4x for all ρ.

CC N-779 was found to perform poorly for the notched cylinder FE models, routinely under predicting the elastic-plastic strain range at the notch tip. In the case of the axial thermal gradient, $K_e^{N\text{-}779}$ was found to be increasingly non-conservative with decreasing notch root radius, ρ. As shown by Figure 121 (c), $K_e^{N\text{-}779}$ is shown to be

non-conservative by up to 6% for ρ=5mm, and by up to 28% for ρ=0.3125mm. For the radial linear thermal gradient, $K_e^{N\text{-}779}$ performed particularly badly as shown by Figure 122 (c), producing non-conservative predictions for all notch sizes, ρ. The performance of $K_e^{N\text{-}779}$ was worse for increasing notch size (ρ), and was found to be non-conservative by up to 35% for ρ=5mm, and by up to 26% for ρ=0.3125mm. $K_e^{N\text{-}779}$ is dominated by the Poisson's ratio correction, $K_v^{N\text{-}779}$ in this case, which is concluded to be inadequate. For the radial parabolic thermal gradient, $K_e^{N\text{-}779}$ also performed badly, and observed to be non-conservative by up to around 30% as shown by Figure 123 (c). The difference in performance of $K_e^{N\text{-}779}$ by notch size was not remarkable. Overall, the poor performance of CC N-779 is attributed mainly to the Poisson's ratio correction factor, $K_v^{N\text{-}779}$, which is the dominant correction factor in each situation. Whilst $K_v^{N\text{-}779}$ may be suitable to account for thermal-plastic strain concentration in plane unnotched sections, it is concluded to be inadequate at geometric discontinuities such as notches where it cannot sufficiently account for the additional peak strain present at such locations. Based on this evidence, an alternative approach is hereby proposed for applying Code Case N-779 in the assessment of thermal-plastic notch effects. It is recommended that the geometry of the notch be excluded from the FE model, and instead be accounted for separately by the notch plasticity adjustment factor, $K_n^{N\text{-}779}$. To account for plastic strain redistribution at the notch, K_T is instead to be substituted in place of $S_{p\text{-}lt}/S_n$ in Eq. (87). The magnitude of K_T may be obtained either numerically or through handbook solutions for the notch geometry in question. The combined effect of both $K_v^{N\text{-}779}$ and $K_n^{N\text{-}779}$ will lead to a significantly higher plasticity correction, thereby improving the accuracy of CC N-779 the procedure in these situations.

Ranganath's method was found to perform reasonably well for the notch cylinder FE models, and offered significantly improved accuracy compared to Appendix XIII-3450 and CC N-779. Whilst the predictions of K_e^R were generally found to be conservative, there were a few situations where K_e^R produced slightly non-conservative results that warrant some further inquiry. In the case of the axial thermal gradient, K_e^R was found to be conservative in most cases where S_n exceeded $3S_m$. As shown from Figure 121 (d), K_e^R was found to be most conservative up to a factor of 1.48x for the largest notch size, ρ=5mm. This is because the largest notch produced a

lower K_e^{FEA} due to its reduced sharpness, whilst S_n was also higher leading to a higher value of K_e^R. However, despite exhibiting the highest magnitude of $S_{n\text{-}tb}$, the largest notch actually produced the smallest values of *R*, since $S_{n\text{-}tb}$ only comprised approximately 30% of S_n; this is in contrast to the smallest notch, where $S_{n\text{-}tb}$ accounted for 40% of S_n, therefore resulting in higher *R*. K_e^R showed an approximately linear decrease in conservatism with decreasing ρ, and was found to be non-conservative by up to 20% and 24% for the two smallest notch sizes (ρ=0.625 and ρ=0.3125) respectively, for S_n slightly greater than $3S_m$. As shown by Figure 122 (d), for the radial linear thermal gradient, K_e^R was found to predict quite closely the actual value of K_e^{FEA} for $S_n>3S_m$. Considering the largest notch size (ρ=5mm), K_e^R was found to produce results that were increasingly conservative by up to 14% for the most severe thermal gradient. In this case, whilst the largest notch experiences the highest combination of S_p and S_n, $S_{n\text{-}tb}$ only forms 12% of S_n, and thus K_e^R is dominated by K_{th}^R due to the smaller value of *R*. Despite this, K_e^R is sufficiently conservative to account for the higher K_e^{FEA} observed at the largest notch. K_e^R also performed well for ρ=2.5mm and ρ=1.25mm, respectively producing results that were conservative by up to 17% and 10% compared to K_e^{FEA}. However, for the two smallest notch sizes (ρ=0.625mm and ρ=0.3125mm), K_e^R produced slightly non-conservative results up to 13%. This was attributed to the lower calculated value of *R* for these notch sizes, where $S_{n\text{-}tb}$ only accounted for 8% and 5% of S_n, respectively. As shown by Figure 123 (d), in the case of the radial parabolic thermal gradient, K_e^R performed similarly to that of the radial linear thermal gradient, albeit with slightly higher conservatism. For the largest notch size (ρ=5mm) which exhibited the smallest K_e^{FEA}, K_e^R produced results that were conservative between a factor of 1.3x and 1.9x for $S_n>3S_m$. This was attributed to the large contribution of $S_{n\text{-}tb}$, which in this case accounts for 40% of S_n. This resulted in a larger value of *R* and therefore higher K_e^R. The smaller notch sizes all shown a similar range of S_n/S_m due to the insensitivity of S_n to the notch geometry. However, the contribution of $S_{n\text{-}tb}$ to S_n did vary considerably, which influenced the conservatism of K_e^R. For the notch sizes ρ=2.5mm and ρ=1.25mm, K_e^R coincided more closely with K_e^{FEA}, producing results that were between a factor of 1.06x and 1.44x conservative for $S_n>3S_m$. $S_{n\text{-}tb}$ only accounted for 19% and 18% of S_n for ρ=2.5mm and ρ=1.25mm respectively, and thus *R* is less than one-half of that calculated for ρ=5mm. For the two

smallest notches ρ=0.625mm and ρ=0.3125mm, K_e^R was found to be non-conservative by up to 5% and 15%, respectively for $S_n > 3mS_m$. In this case, $S_{n\text{-}tb}$ only accounted for 11% and 6% of S_n for ρ=0.625mm and ρ=0.3125mm respectively, leading to a lower value of K_e^R.

As discussed in Section 4.5.1, the final form of K_e^R proposed in Record 17-225 includes a Neuber notch correction factor, K_n^R, which is equivalent to the notch factor, $K_n^{WRC\text{-}361}$, specified in WRC-361 [110]. The intended purpose of K_n^R is to account for plastic strain redistribution in the presence of a local discontinuity and is to be applied over and above K_T [131]. As the notch geometry is sufficiently detailed in the FE model, K_T is already accounted for in the calculation of S_p. For the previous FE case studies, K_e^R has been calculated without consideration of K_n^R and has been shown to perform sufficiently well alone. However, K_n^R is evidently applicable for this case study and it was decided to investigate the effect of including K_n^R for each of the loading and geometries considered.

To consider the effect of the Neuber notch correction factor, a new factor K_e^{R+} is defined to represent K_e^R, which explicitly includes K_n^R. In this evaluation, K_T is calculated simply as the S_p/S_n ratio for each load case. Figure 124 shows the ratio of K_e^{R+} vs. K_e^R for each of the notched cylinder FE models. As shown, K_e^{R+} is considerably higher than K_e^R for $S_n>3mS_m$. K_e^{R+} was generally found to be up to 1.1x higher for the axial thermal gradient (Figure 124 (a)), between a factor of 1.1x to 1.53x higher for the radial linear thermal gradient (Figure 124 (b)), and between a factor of 1.4x and 1.78x higher for the radial parabolic thermal gradient (Figure 124 (c)). Figure 125 shows the performance of K_e^{R+} relative to K_e^{FEA} with varying notch size (ρ) for each loading condition considered. Overall, K_e^{R+} was determined to be conservative to K_e^{FEA} for all cases where S_n exceeded $3S_m$. The greatest difference in performance between the K_e^R and K_e^{R+} approaches was found to be for the radial parabolic thermal gradient (Figure 125 (c)), where K_e^{R+} was found to be conservative between a factor of 1.4x – 1.66x, whilst K_e^R was found to be non-conservative for the two smallest notches sizes (ρ=0.625 and 0.3125 mm). Nonetheless, K_n^R does not address the potential non-conservativism inherent to each of the ASME III K_e factors where peak strain concentration occurs for $S_n<3S_m$. As K_n^R is only applicable for $S_n>3S_m$, K_e^{R+}

remains equal to unity for $S_n<3S_m$ and therefore can still under predict the localised elastic-plastic strain range.

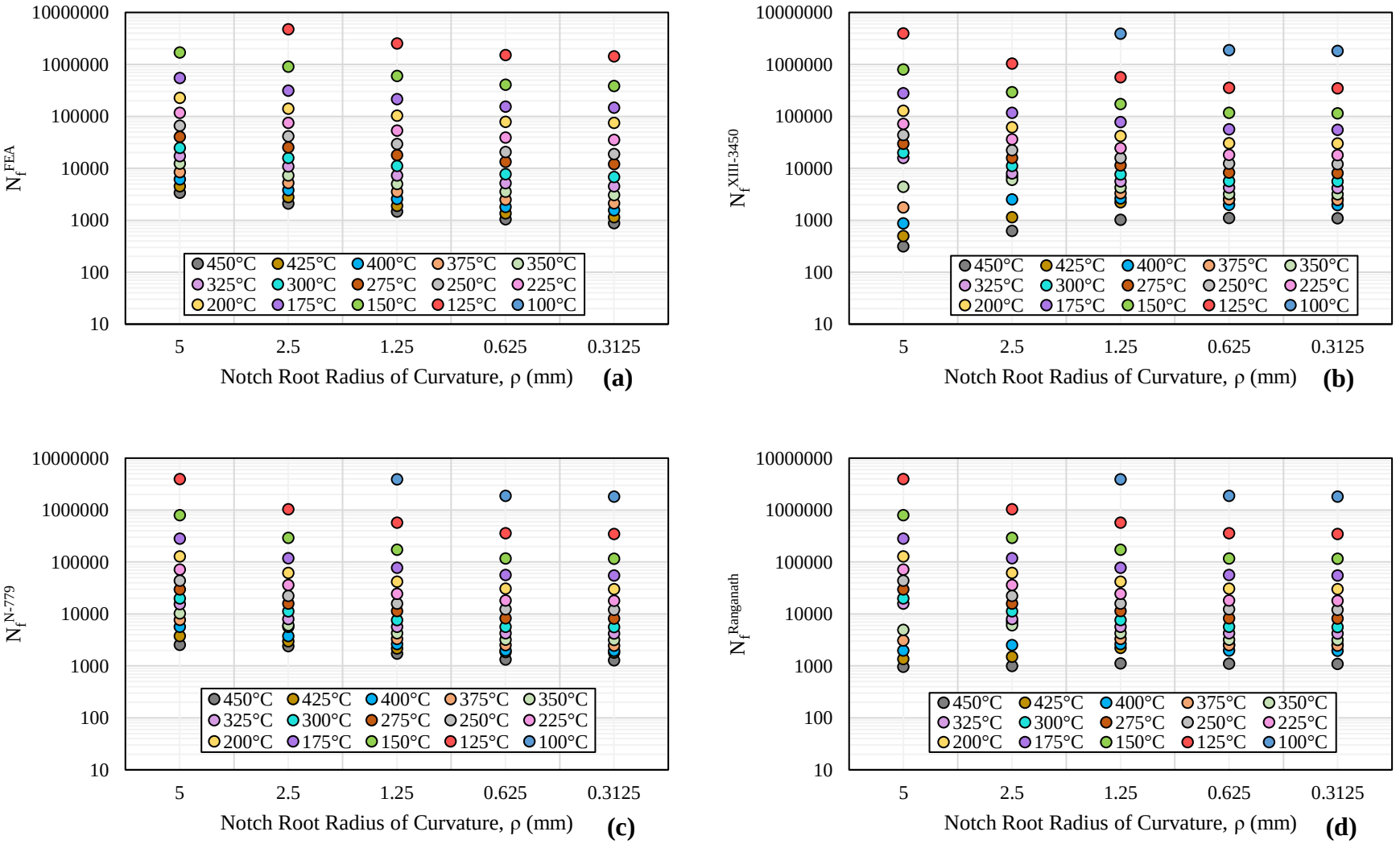

Figure 112. Allowable cycles, N_f, for notched cylinder subjected to axial thermal gradient.

(a) Elastic-plastic FEA; (b) Appendix XIII-3450; (c) CC N-779; (d) Ranganath's method

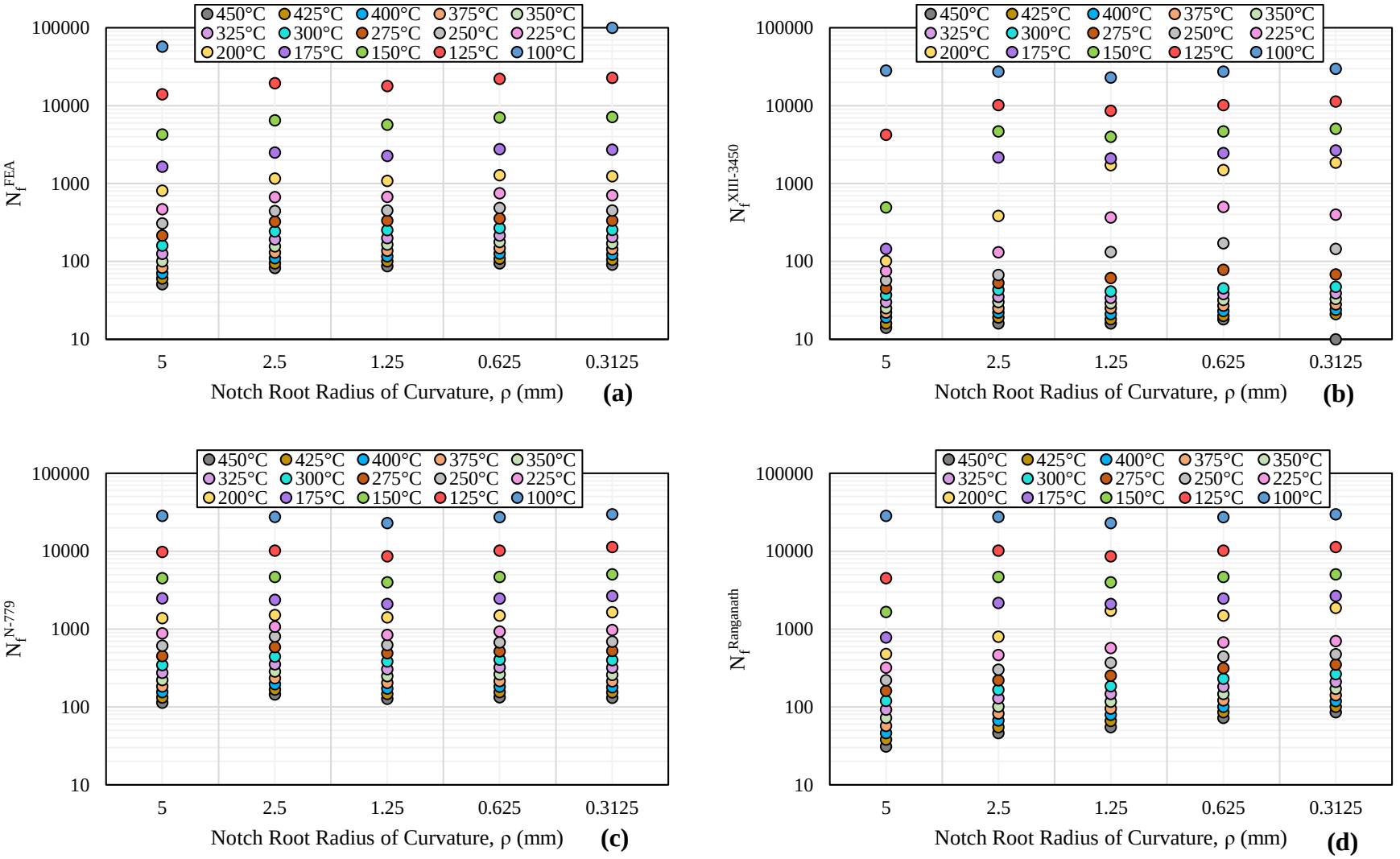

Figure 113. Allowable cycles, N_f, for notched cylinder subjected to radial linear thermal gradient.

(a) Elastic-plastic FEA; (b) Appendix XIII-3450; (c) CC N-779; (d) Ranganath's method

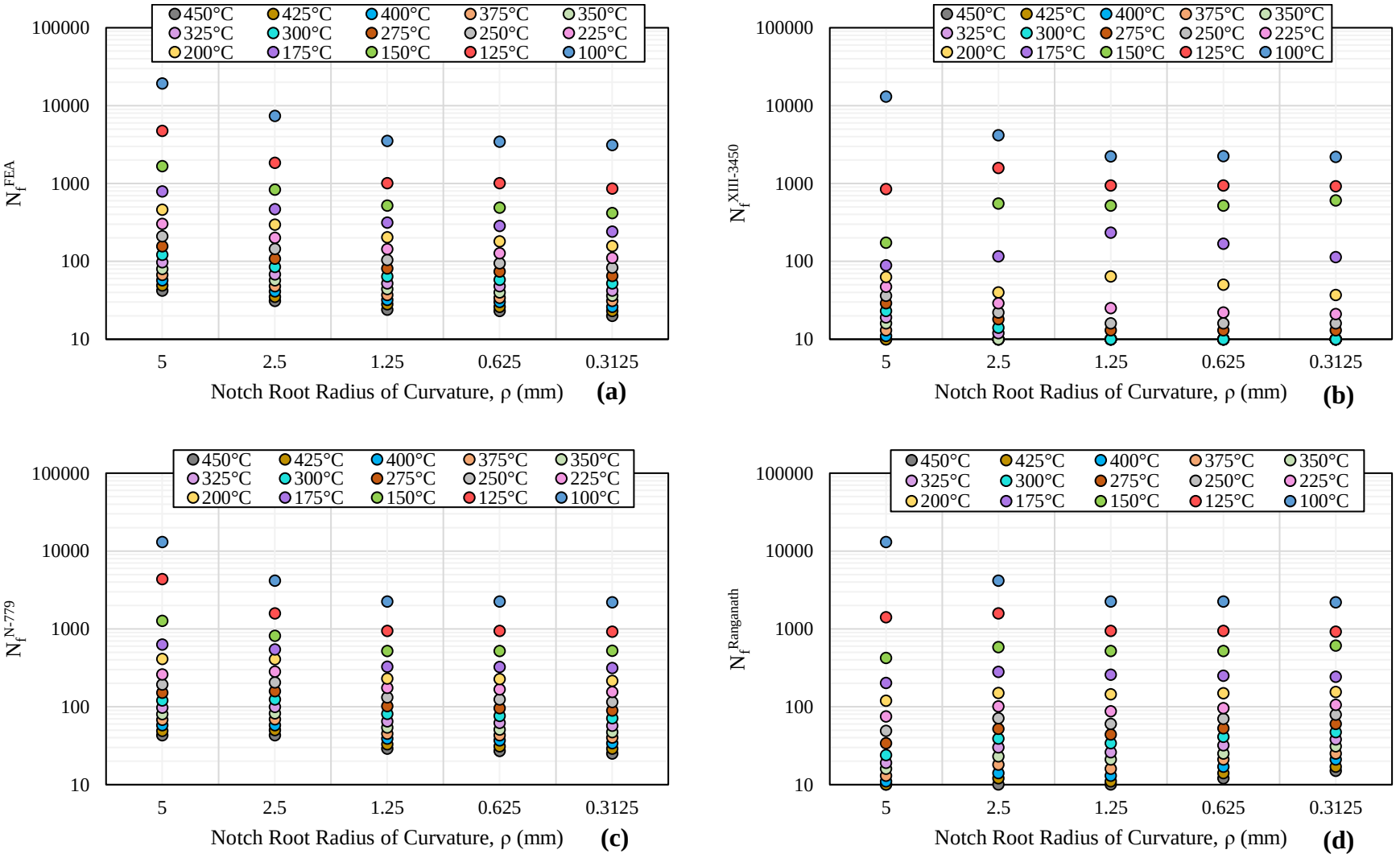

Figure 114. Allowable cycles, N_f, for notched cylinder subjected to radial parabolic thermal gradient.

(a) Elastic-plastic FEA; (b) Appendix XIII-3450; (c) CC N-779; (d) Ranganath's method

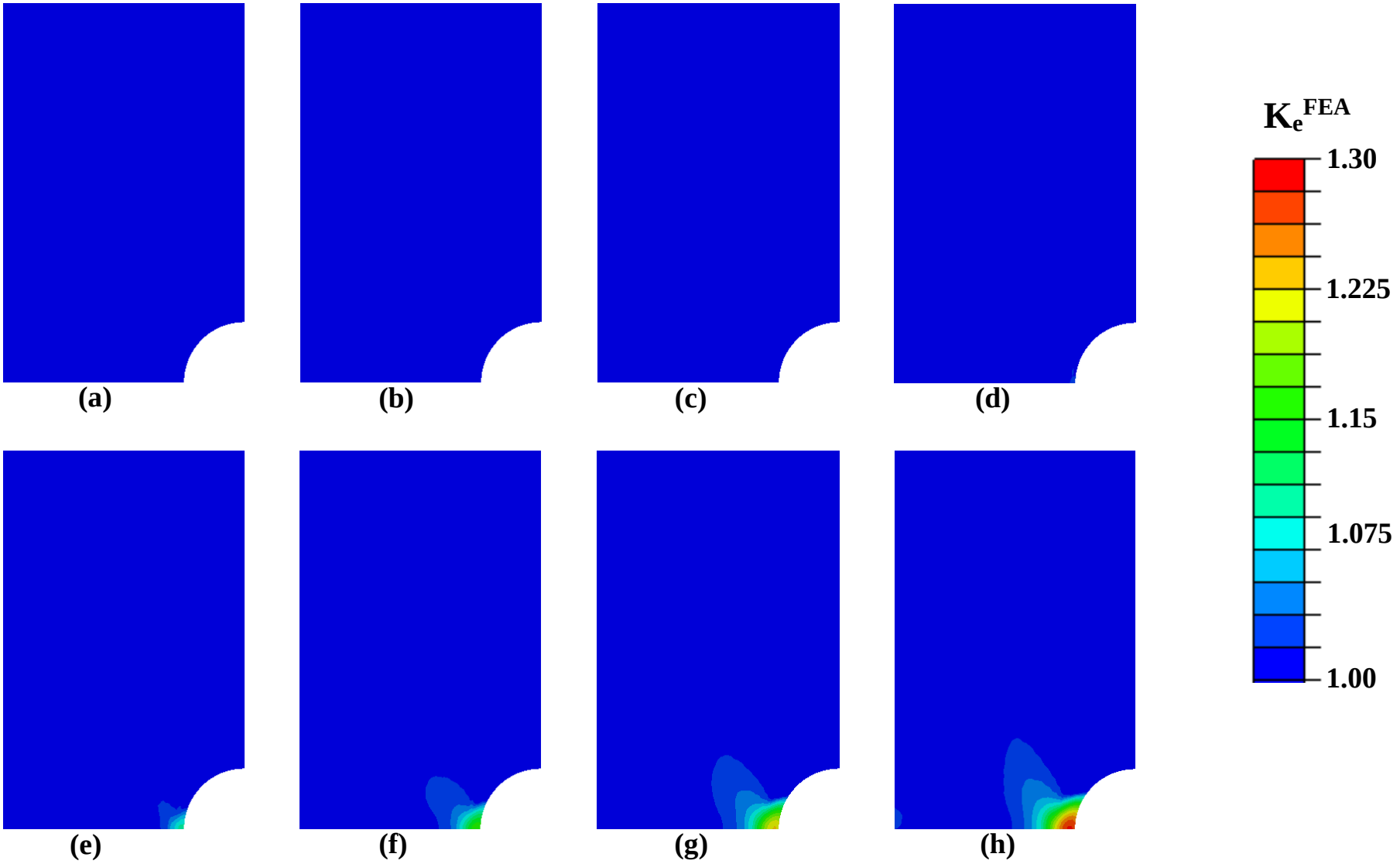

Figure 115. Contour plot of $K_e^{FEA} \geq 1.0$ for notched cylinder (ρ=2.5 mm) subjected to axial thermal gradient by maximum surface temperature.

(a) 100°C; (b) 150°C; (c) 200°C; (d) 250°C; (e) 300°C; (f) 350°C; (g) 400°C; (h) 450°C

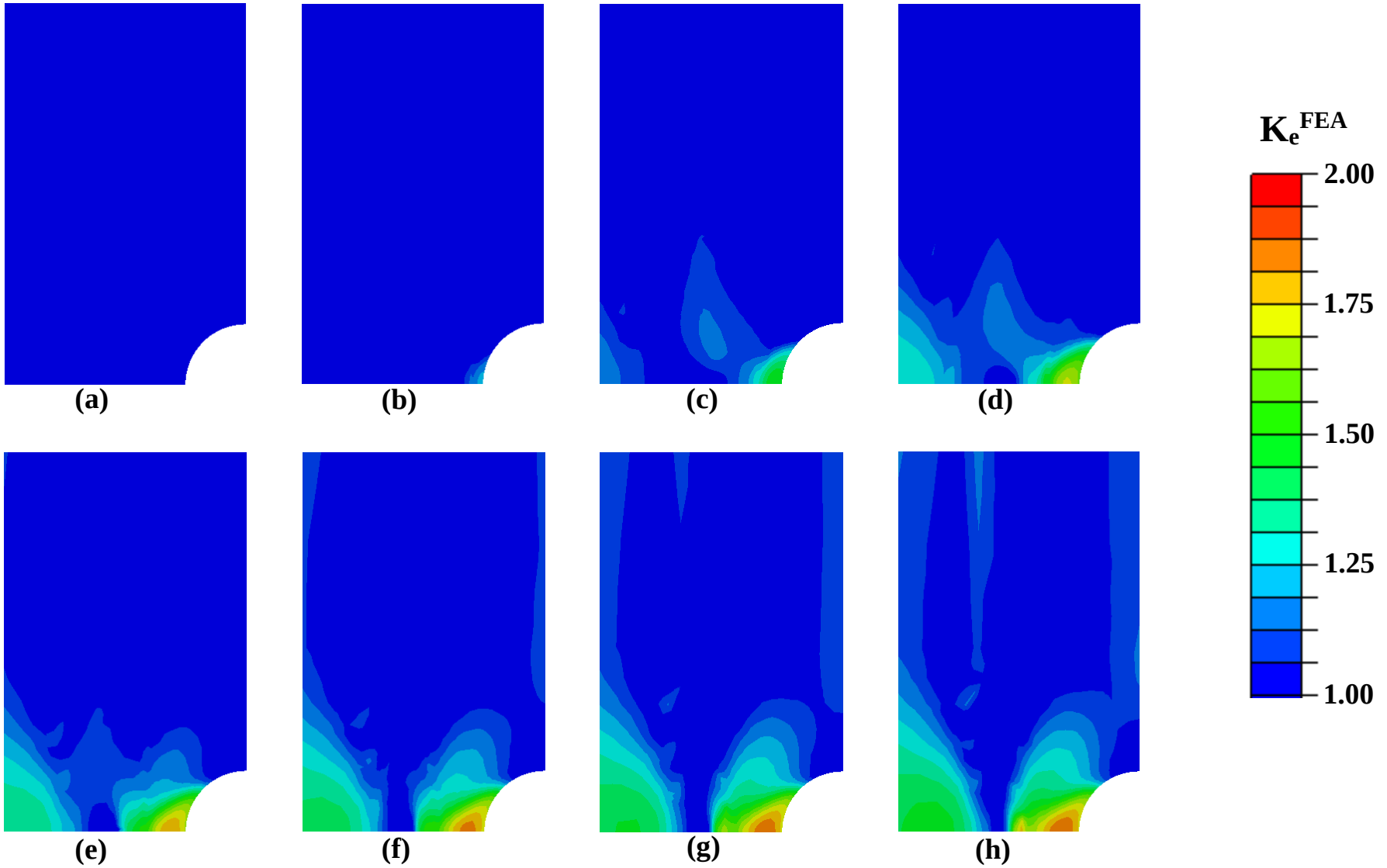

Figure 116. Contour plot of $K_e^{FEA} \geq 1.0$ for notched cylinder (ρ=2.5 mm) subjected to radial linear thermal gradient by maximum surface temperature.

(a) 100°C; (b) 150°C; (c) 200°C; (d) 250°C; (e) 300°C; (f) 350°C; (g) 400°C; (h) 450°C

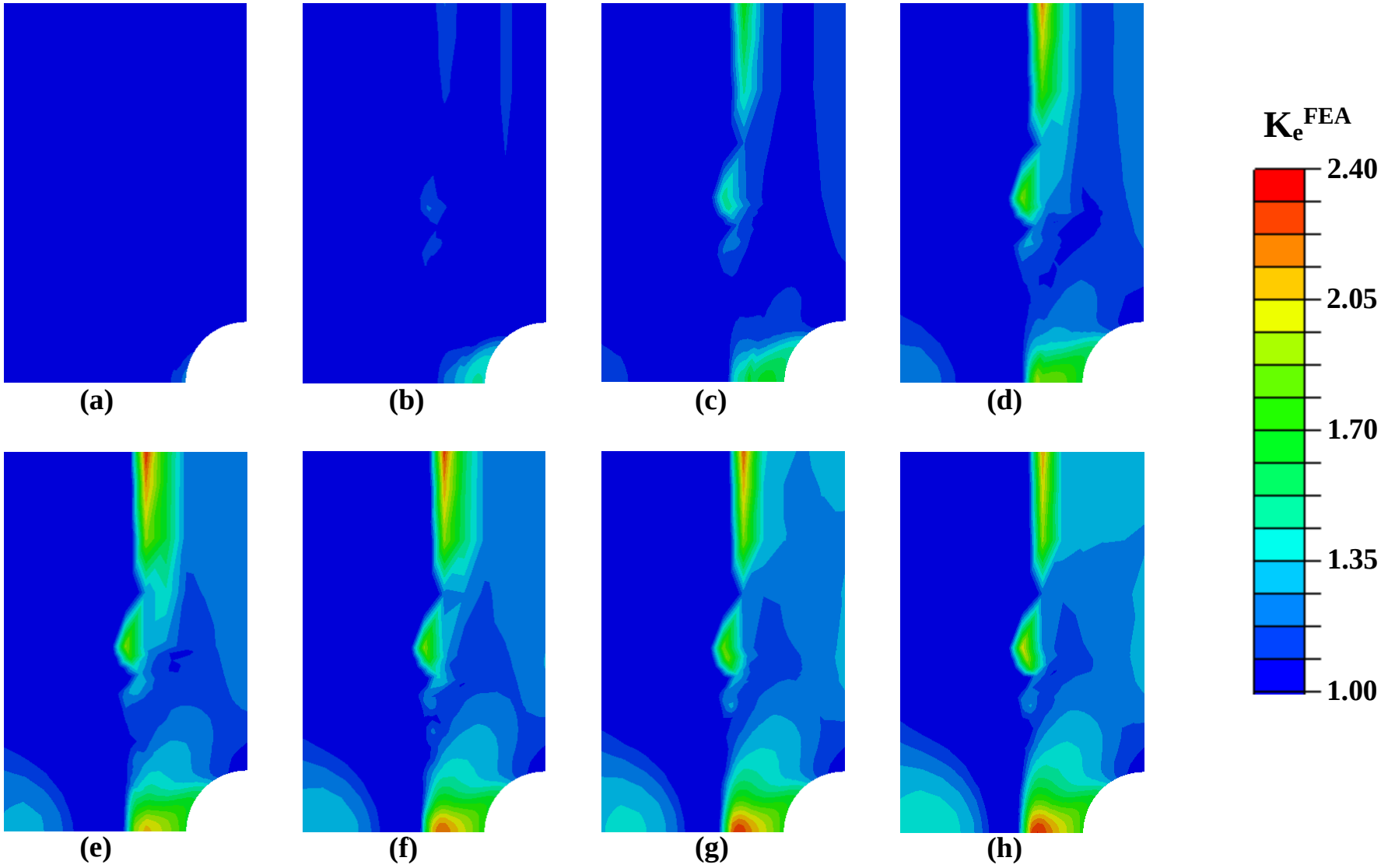

Figure 117. Contour plot of $K_e^{FEA} \geq 1.0$ for notched cylinder (ρ=2.5 mm) subjected to radial parabolic thermal gradient by maximum surface temperature.

(a) 100°C; (b) 150°C; (c) 200°C; (d) 250°C; (e) 300°C; (f) 350°C; (g) 400°C; (h) 450°C

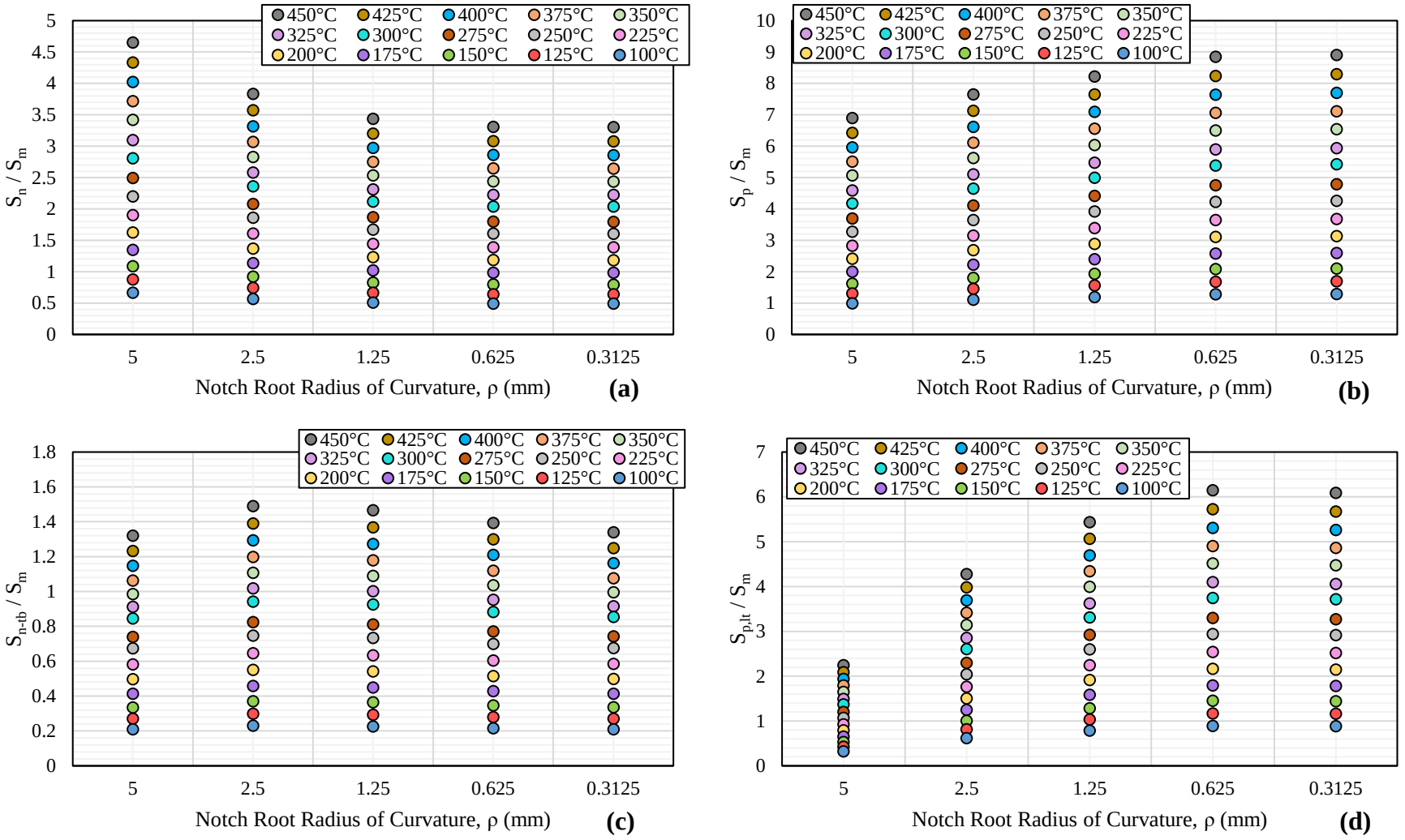

Figure 118. ASME III elastic stress parameters calculated for notched cylinder subjected to axial thermal gradient.

(a) S_n/S_m (b) S_p/S_m (c) $S_{n\text{-}tb}/S_m$ (d) $S_{p,lt}/S_m$

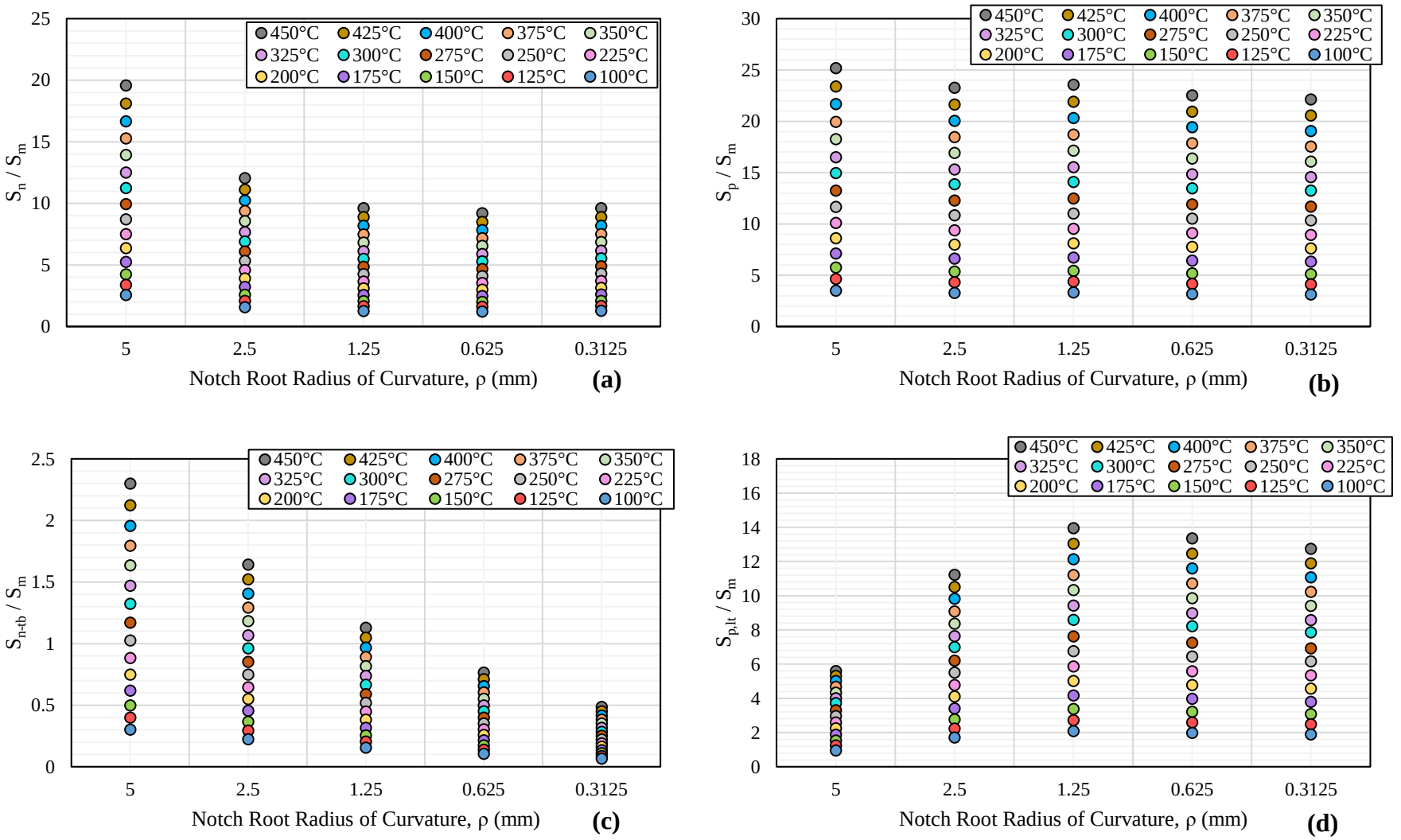

Figure 119. ASME III elastic stress parameters calculated for notched cylinder subjected to radial linear thermal gradient.

(a) S_n/S_m (b) S_p/S_m (c) $S_{n\text{-}tb}/S_m$ (d) $S_{p,lt}/S_m$

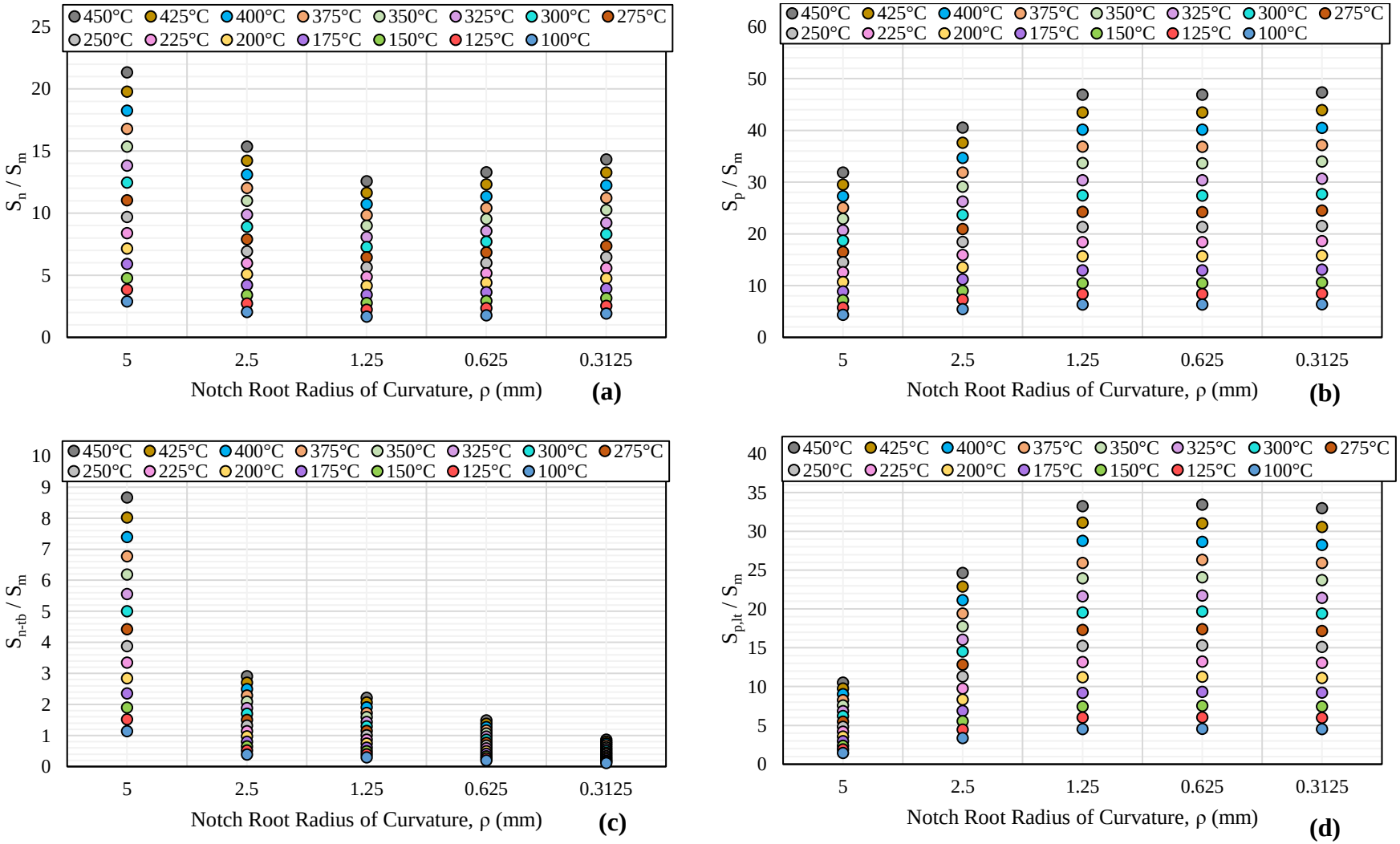

Figure 120. ASME III elastic stress parameters calculated for notched cylinder subjected to radial parabolic thermal gradient.

(a) S_n/S_m (b) S_p/S_m (c) $S_{n\text{-}tb}/S_m$ (d) $S_{p,lt}/S_m$

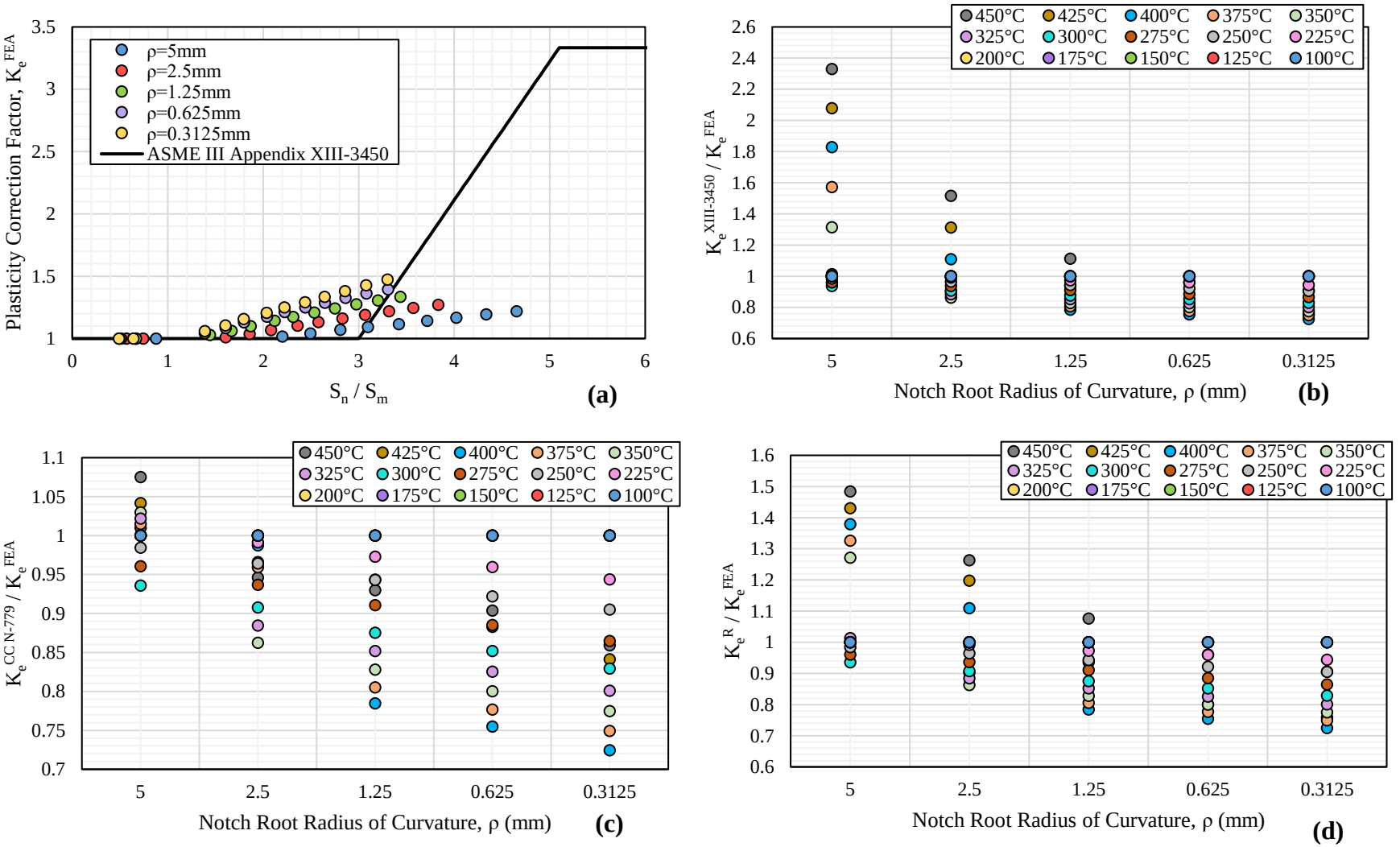

Figure 121. Performance of ASME III K_e factors for notched cylinder subjected to axial thermal gradient.

(a) K_e^{FEA} vs. S_n/S_m (b) Appendix XIII-3450 vs. E-P FEA (c) CC N-779 vs. E-P FEA (d) Ranganath's method vs. E-P FEA

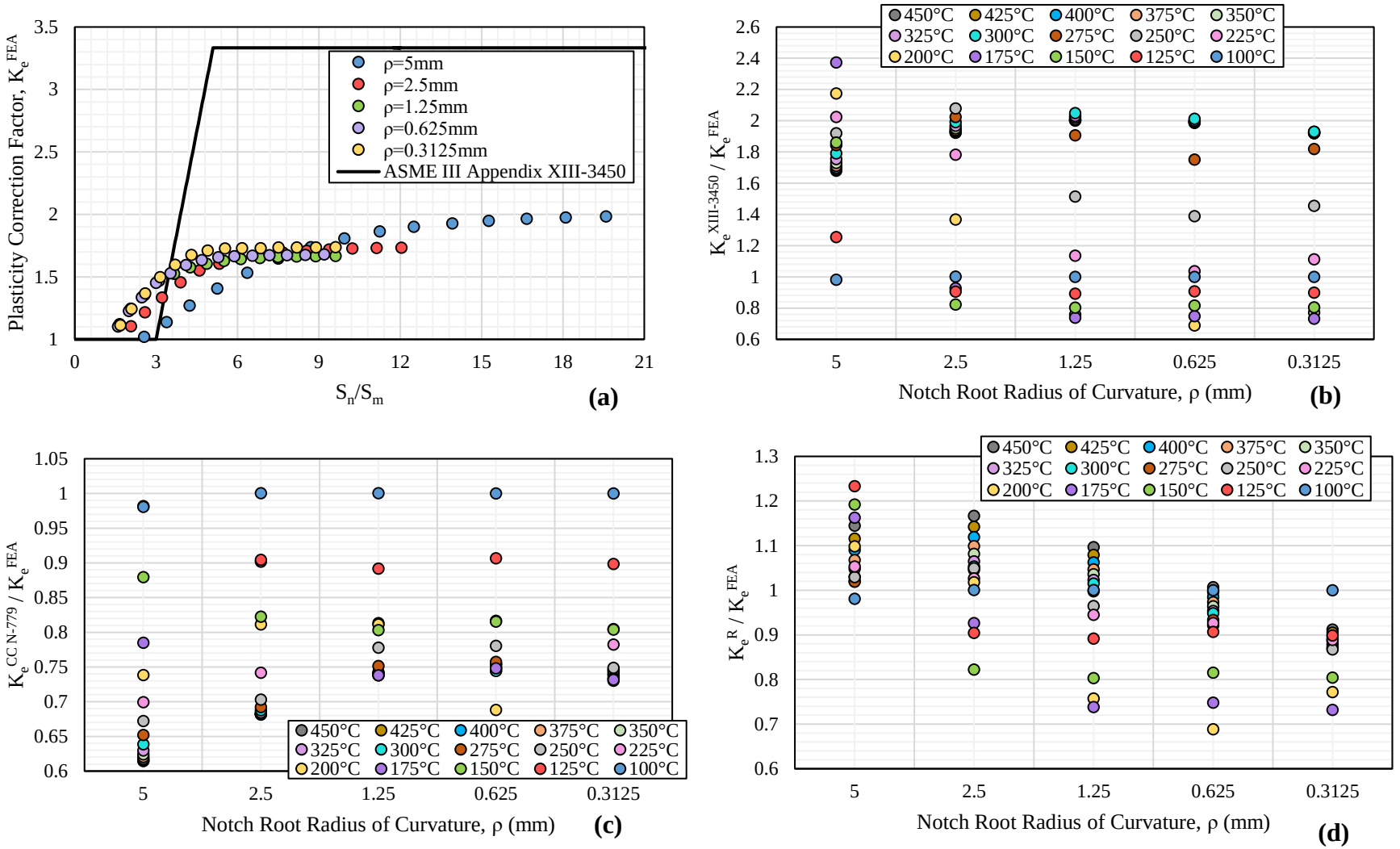

Figure 122. Performance of ASME III K_e factors for notched cylinder subjected to radial linear thermal gradient.

(a) K_e^{FEA} vs. S_n/S_m (b) Appendix XIII-3450 vs. E-P FEA (c) CC N-779 vs. E-P FEA (d) Ranganath's method vs. E-P FEA

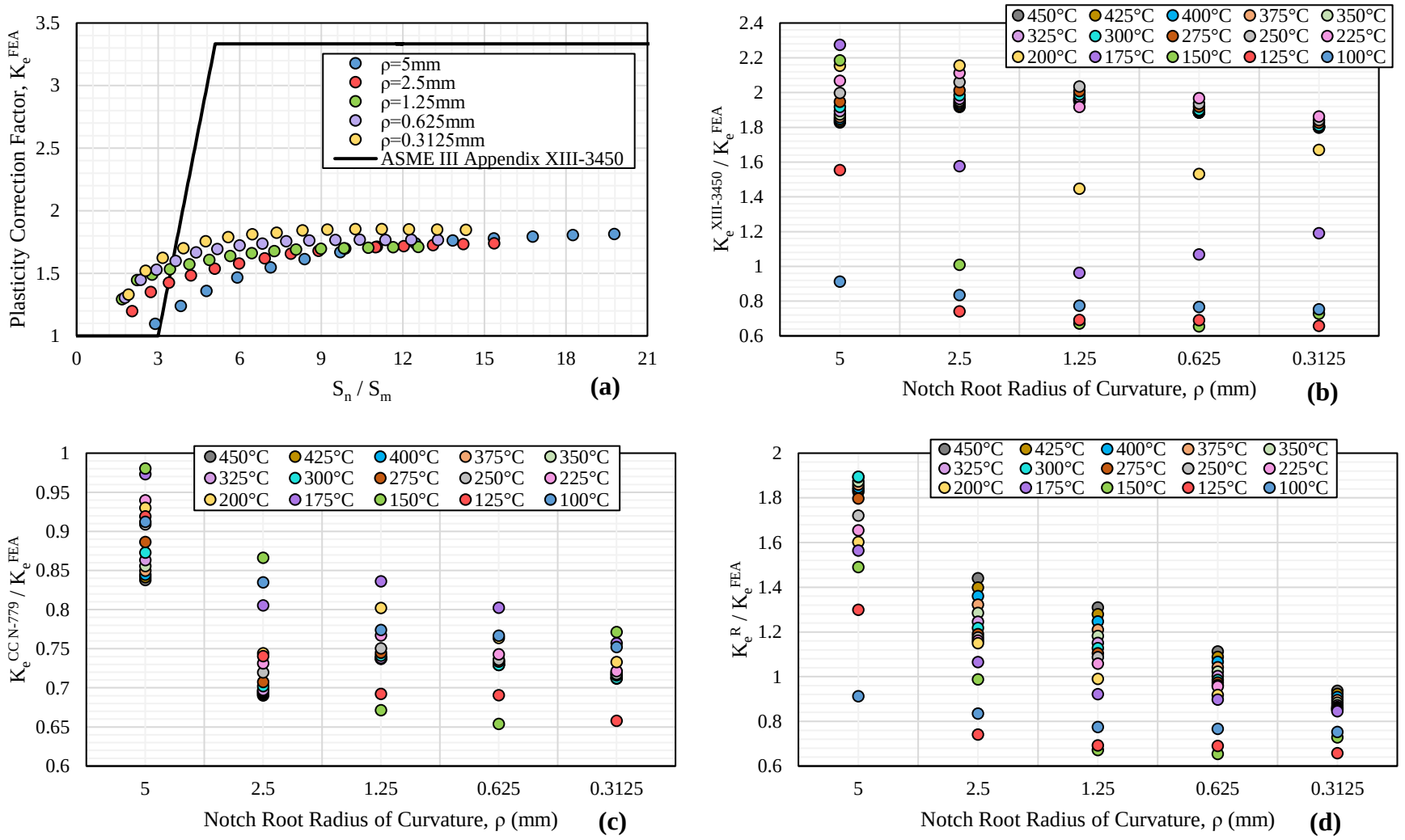

Figure 123. Performance of ASME III K_e factors for notched cylinder subjected to radial parabolic thermal gradient.

(a) K_e^{FEA} vs. S_n/S_m (b) Appendix XIII-3450 vs. E-P FEA (c) CC N-779 vs. E-P FEA (d) Ranganath's method vs. E-P FEA

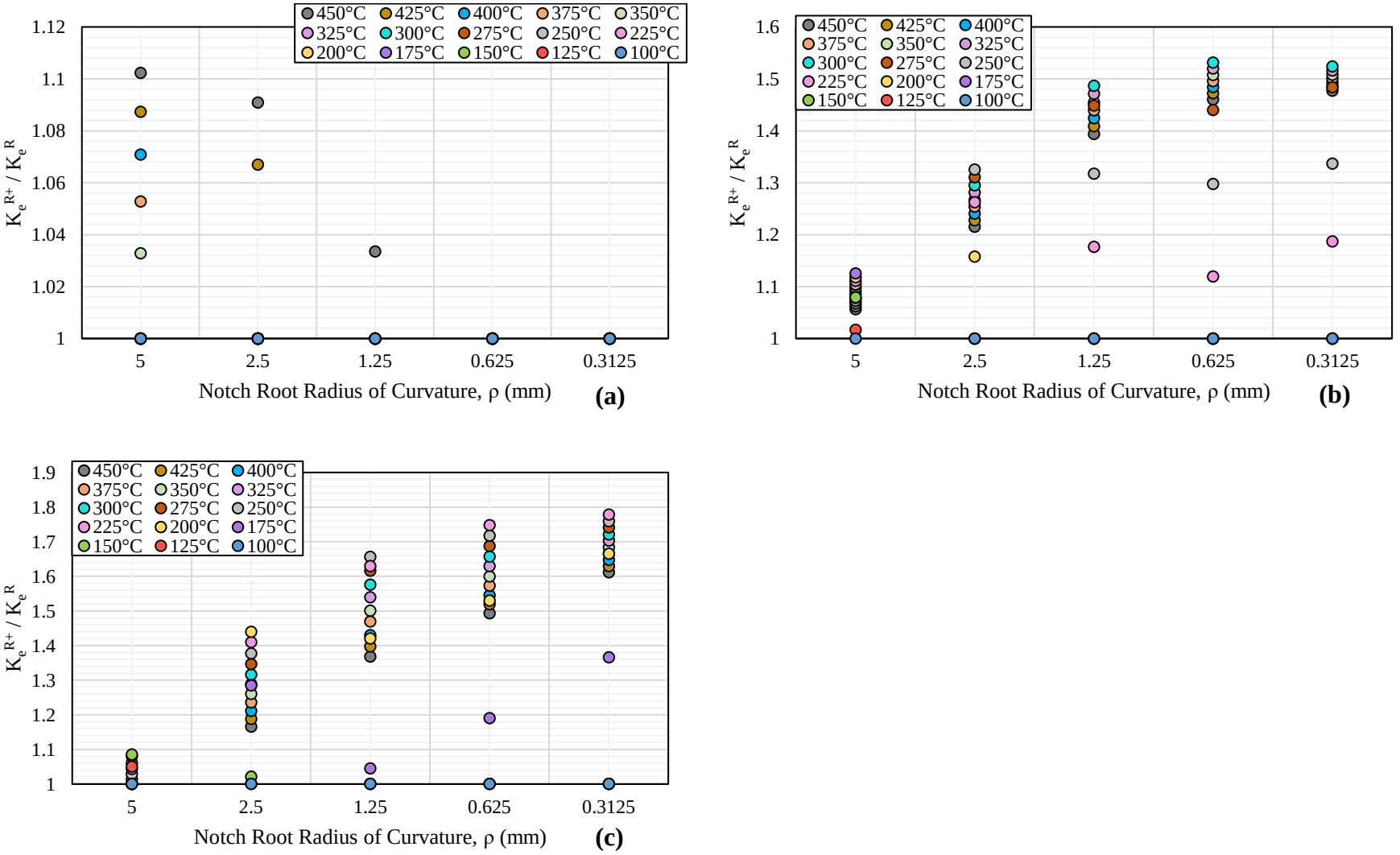

Figure 124. Comparison of Ranganath's method with- (K_e^{R+}) and without (K_e^R) proposed notch factor, K_n^R.

(a) Axial thermal gradient; (b) Radial linear thermal gradient; (c) Radial parabolic thermal gradient.

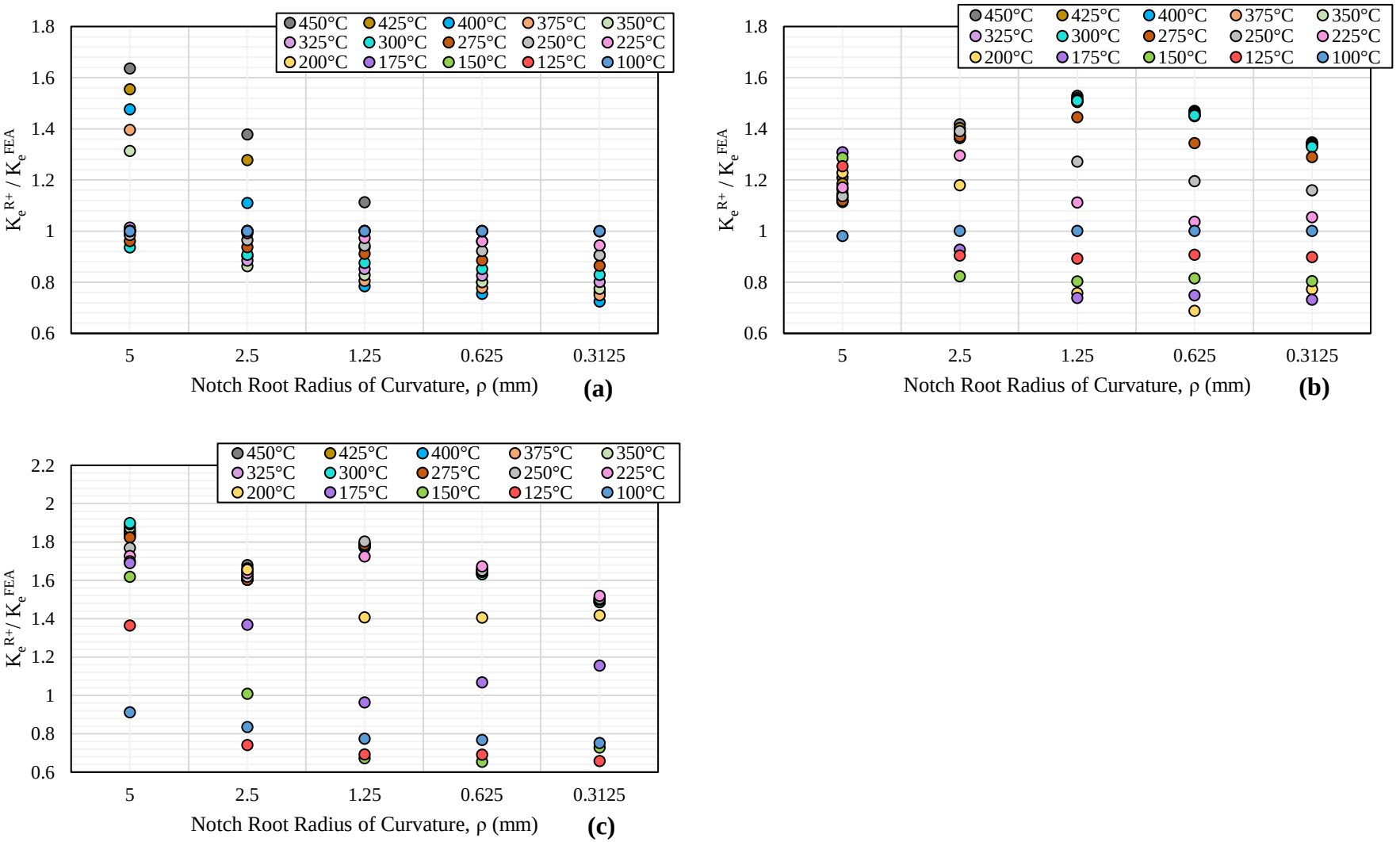

Figure 125. Performance of Ranganath's K_e^{R+} vs. notch root radius (ρ) for notched cylinder FE models

(a) Axial thermal gradient; (b) Radial linear thermal gradient; (c) radial parabolic (shock) thermal gradient

7.8. Relative Performance of Code K_e Factors

To compare the performance of the Code K_e methods for each FE model, the Code K_e factors are plotted against the FE-derived correction factors as shown in Figure 126-Figure 134. The black line represents the condition where the Code K_e factor is equal to the FE-derived K_e factor. Points situated below this line indicate that the Code K_e correction underpredicts the strain range determined from elastic-plastic FE analysis. The red line denotes the ASME Code limit of $3S_m$, which represents the threshold beyond which the Code plasticity correction is applied. The accuracy and practicality of each method is summarised below, considering the general performance achieved across all FE models.

7.8.1. ASME III Appendix XIII-3450

An inherent assumption in the ASME III Code methodology is that peak strain concentration cannot occur for $S_n < 3S_m$. Whilst this assumption is legitimate for the simple configurations considered by Langer [104], it is not strictly true when extending to more complex structures and loading conditions. Even in situations where a plastic zone is limited in its extent, as in the case of a thermal shock or local discontinuity, K_e will still be greater than 1.0 based on Langer's original definition. Consequently, the Appendix XIII-3450 $K_e^{XIII\text{-}3450}$ factor was found to be moderately non-conservative for S_n slightly above the $3S_m$ limit. Naturally, it is also non-conservative below the $3S_m$ limit, however in this situation the XIII-2500 Poisson's ratio correction would apply, which could potentially produce an overall conservative result. In particular, in this work it was found that in the presence of a notch, the ASME XIII-3450 K_e factor can under predict the elastic-plastic strain range by up to 35%.

In contrast, as S_n increases beyond $3S_m$, $K_e^{XIII\text{-}3450}$ quickly becomes very conservative. For unnotched sections subjected to thermal shock conditions, the $K_e^{XIII\text{-}3450}$ maximum value of 3.33 was generally found to be a factor of 2.2x to 3.0x larger than the corresponding value of K_e^{FEA}. For the notched cylinder, $K_e^{XIII\text{-}3450}$ was still found to be overconservative by a factor of 1.8x to 2.4x.

Whilst the Appendix XIII-3450 $K_e^{XIII\text{-}3450}$ is straightforward to apply, its practicality is significantly outweighed by its aforementioned conservatism. Due to the non-linearity of the design fatigue curves in the low-cycle regime, the use of the $K_e^{XIII\text{-}3450}$ factor can

very easily produce a cumulative usage factor (CUF) over an order of magnitude higher than elastic-plastic FEA, which could be unacceptable in the current industry climate.

7.8.2. ASME Code Case N-779

CC N-779 was found to perform well for the stepped pipe FE model (Figure 127), predicting modestly conservative corrections for $S_n \leq 5.5S_m$. For higher S_n, CC N-779 was slightly non-conservative up to a maximum of 14%. This aligned closely with the results obtained independently by Emslie et al [133]. In general, CC N-779 did not perform as well for the PWR nozzle FE models (Figure 128 and Figure 129), producing under predictions of 10-25% for $S_n \leq 10S_m$. This was observed particularly for the crotch corner and pipe-to-nozzle juncture. For the thermal sleeve and Y-piece FE models (Figure 130 and Figure 131), CC N-779 produced more conservative results. This was attributed to the higher value of $S_{n,tm}$ due to the presence of a larger axial thermal gradient, which results in a greater weighting being applied to the more conservative Appendix XIII-3450 $K_e^{XIII-3450}$ factor. In the case of the notched cylinder FE model subjected to a radial parabolic thermal gradient (Figure 134), CC N-779 was found to produce non-conservative results up to around 30% across all notch sizes. Since the notched cylinder FE model included discretisation of the notch region, K_n^{N-779} is equal to unity, with only the Poisson's ratio correction factor, K_v^{N-779} being applicable. However, K_v^{N-779} was found to be insufficient to account for the additional concentration of peak strain at the notch root. The modification to K_v^{N-779} proposed by Lang et al [181] was also considered and was typically found to increase the conservatism of CC N-779 by up to 10%.

Whilst CC N-779 is not as straightforward to apply as Appendix XIII-3450, it can still be reliably automated using programming methods, minimising the additional effort involved. Nonetheless, the lack of consistency and non-conservatism in the results calculated by CC N-779 for several FE models is concerning, especially in the case of notched geometries. Accordingly, it is concluded that CC N-779 does not constitute a viable alternative to Appendix XIII-3450, and cannot be recommended for application to austenitic stainless steels based on the evidence presented in this work.

7.8.3. Ranganath's Method

Ranganth's method was found to produce conservative results for almost all cases considered. For the stepped pipe FE model (Figure 127), K_e^R was generally found to be 10-30% conservative for $S_n > 3S_m$, showing a decreasing trend which aligned closely with the RCC-M thermal-plastic correction factor, K_e^{ther}. This is to be expected since both approaches share the same technical basis outlined in WRC-361 [110]. For the PWR nozzle FE models (Figure 128 and Figure 129), K_e^R showed somewhat greater conservatism compared to the stepped pipe, albeit with higher scatter depending on the relative proportions of $S_{n,tb}$ and $S_{n,tm}$ at the assessment location. Similarly to CC N-779, K_e^R also showed greater conservatism for the Y-piece model (Figure 131) since $S_{n,tm}$ accounted for a larger proportion of S_n, thereby producing a larger value of *R*.

The value of K_e^R calculated for all FE models initially did not consider the Neuber notch correction factor, K_n^R. For the notched cylinder FE models, K_e^R was calculated with and without K_n^R to examine further the observations of Reinhardt [130] under more realistic loading conditions. For the case of the notched cylinder subjected to a radial parabolic thermal gradient (Figure 134), K_e^R appears to be reasonably conservative compared with the results obtained from elastic-plastic FE analysis when K_n^R is excluded. For $S_n > 3mS_m$, K_e^R was found to produce results that were conservative by up to 90%, 44%, 31% respectively for the three largest notch sizes considered in this study (ρ = 5, 2.5, 1.25 mm). K_e^R was however found to produce slightly non-conservative results up to 5% and 15% for the two smallest notch sizes (ρ = 0.625, 0.3125 mm). This was mainly attributed to the fact that S_n is not well suited as a characteristic parameter when assessing local discontinuities. S_p increases significantly at the notch root for decreasing ρ, while the value of S_n remains almost constant. In addition, it was found that the magnitude of $S_{n,tm}$ also decreased with decreasing ρ. This is especially significant as this resulted in lower values of *R*, and consequently a decreasing trend in K_e^R despite an increase in K_e^{FEA} at the notch root. Overall, without considering K_n^R, the higher conservatism of Ranganath's Method compared to CC N-779 is partly due to its use of the maximum Poisson's ratio correction factor of 1.4, which produced more reasonable results. When K_n^R described by Eq. (121) is included, the conservatism of Ranganath's method relative to the

results of elastic-plastic FE analysis increases considerably. For $S_n>3S_m$, K_e^R is conservative by a factor of 1.3x to 1.9x for all notch sizes when K_n^R is included.

It has been highlighted [182] that there also exists the potential for some ambiguity in the final value of K_e^R, depending on the subtraction methodology employed to calculate $S_{n\text{-}tb}$. As highlighted by Reinhardt [130], performing this subtraction on a component basis and forming the stress intensity of the result often produces different results when compared to subtracting stress intensities. This was found to be important, since, as shown in Figure 135 for the stepped pipe FE model, adopting the latter approach can produce up to a 25% reduction in the value of K_e^R, which can make the difference between a conservative and non-conservative prediction. This may warrant further engineering judgement for plants undergoing license extension, since existing fatigue tables often only present ranges in terms of stress intensities for a given load pair. For application to new designs, it is recommended to perform this subtraction on a component basis to eliminate possible ambiguity in the results.

7.8.4. RCC-M B-3234.6

The results presented in this paper considered only cyclic thermal transients, and thus only the RCC-M thermal plastic correction factor, K_e^{ther}, was applicable. K_e^{ther} showed a very similar to trend to Ranganath's K_e^R, for the stepped pipe FE model, producing results that were 1.1x to 1.4x conservative. K_e^R was however found to be significantly more conservative than K_e^{ther} for the PWR nozzle FE models (Figure 127-Figure 129) and the Y-piece FE model (Figure 131). The reason for this is that K_e^{ther} does not distinguish between membrane, bending, and peak stresses arising due to thermal effects, and implicitly assumes they behave as secondary stresses. In contrast, K_e^R assumes $S_{n,tm}$ to act as a primary stress, thereby requiring a larger correction. Thus, both approaches can be expected to deviate with increasing $S_{n,tm}/S_n$. Whilst RCC-M did exhibit slight non-conservativism for the notched cylinder FE models (Figure 132-Figure 134), this was very slight and not of serious concern. Overall, the RCC-M method was concluded to be the best performing S_n-based method, producing consistently conservative corrections for most FE models whilst being straightforward to apply. The simple formulation of the RCC-M is therefore very useful and merits further examination.

7.8.5. JSME

As discussed by Asada and Nakamura [122], the JSME K_e^{JSME} was derived based on a series of elastic-plastic FE analyses conducted on representative components using simplified monotonic analysis with an elastic perfectly-plastic (EPP) material model. From the results, it is clear that K_e^{JSME} is quite conservative for all models, which is largely attributed to its being derived based on EPP material properties. In contrast to other S_n-based K_e factors, K_e^{JSME} actually becomes more conservative with increasing S_n. Whilst K_e^{JSME} is much less pessimistic than $K_e^{XIII\text{-}3450}$, it is still judged to be too conservative for unnotched assessment locations. However, for the case of notched geometries, K_e^{JSME} appears to be quite useful, predicting conservative corrections in all cases, but only modestly so. In this case, K_e^{JSME} was found to be conservative by a factor of 1.6x at most, though was more typically between 1.2x and 1.5x conservative. Therefore, despite being based on S_n, K_e^{JSME} is concluded to be a good option for notched geometries.

7.8.6. JSME Code Case NC-CC-005

The JSME Code Case NC-CC-005 $K_e^{JSME\ CC}$, which is a function of S_p only, was derived based on the same set of bounding EPP FE analysis results used to derive K_e^{JSME}, but does not require stress linearisation. As shown by the results, $K_e^{JSME\ CC}$ is always more conservative than K_e^{JSME}, and also applies for $S_n < 3S_m$ if $S_p \geq 3S_m$. $K_e^{JSME\ CC}$ was generally found to be between a factor of 1.8x to 2.6x conservative relative to K_e^{FEA}, and is judged to be much too pessimistic for the assessment of austenitic stainless steel components.

7.8.7. PNAE-G7-086-002

The PNAE G-7-086-002 correction factor, K_e^{PNAEG}, appeared to fall between the JSME K_e^{JSME} and $K_e^{JSME\ CC}$ in terms of conservatism for each of the FE models considered. However, in some cases, particularly for very high S_p, it was found that the conservatism of K_e^{PNAEG} was similar to that of $K_e^{XIII\text{-}3450}$. It was also found that K_e^{PNAEG} can actually be more conservative than $K_e^{XIII\text{-}3450}$, though the requirement that S_n does not exceed four times the cyclic proportional limit stress per Eq. (100) would normally be violated in such a scenario. Nonetheless, K_e^{PNAEG} is very conservative for austenitic stainless steels, which limits its usefulness.

7.8.8. R5 V2/3

The R5 Neuber methodology was found to be excessively conservative at unnotched assessment locations, in overall agreement with the conclusions drawn by other authors that Neuber's rule is not well suited to thermal loading [181]. In general, the Neuber methodology was found to be conservative between a factor of 1.6x to 2.2x for this situation. Neuber's rule was however found to predict more reasonable results for notched assessment locations, predicting corrections that were generally conservative by a factor of 1.2x to 1.8x. On the other hand, applying the R5 K_v factor but excluding the Neuber correction produced very reasonable results. This approach was generally conservative up to a maximum of 25% for unnotched assessment locations. Overall, the R5 Appendix A7 methodology is quite useful from a practical standpoint as it does not involve stress linearisation, and only requires that the intersection of the Neuber hyperbola with the cyclic SSC be determined *a priori*.

7.8.9. ASME VIII-2, Section 5.5.3

The ASME VIII-2, Section 5.5.3 $K_e^{VIII\text{-}2}$ factor is essentially equivalent to the ASME III, Appendix XIII-3450 K_e factor, with the only difference being that the former is based on von Mises theory, with the latter being based on Tresca. Thus, $K_e^{VIII\text{-}2}$ produced results identical to $K_e^{XIII\text{-}3450}$ with the exception of the transition region of $3S_m < S_n < 3mS_m$, where $K_e^{VIII\text{-}2}$ was found to be slightly less conservative due to the lower value of S_n calculated by von Mises theory.

7.8.10. ASME VIII-2, Annex 5-C

The ASME VIII-2, Annex 5-C K_e^{5C} factor has a very similar form to CC N-779. However, as highlighted in Section 4.6.1.2, the former approach does possess a more conservative Poisson's ratio correction factor, K_v^{5C}, which tends to a maximum value of 1.6, compared to 1.4 for $K_v^{N\text{-}779}$. Overall, ASME VIII-2, Annex 5-C was found to be more accurate than CC N-779 for unnotched assessment locations, predicting corrections that were generally between 1.0x and 1.3x conservative, which is very promising. However, despite the more conservative formulation of K_v^{5C}, Annex 5-C was still found to be non-conservative for notched locations by up to around 25%.

7.8.11. EN-13445 Annex 18

The EN-13445 Annex 18 thermal-plastic correction factor, K_v^{EN}, which is a function of linearised S_n, was found to produce the least conservative results of the different factors considered. K_v^{EN} generally produced non-conservative corrections for unnotched locations, potentially under predicting K_e^{FEA} by up to 20%. K_v^{EN} is therefore concluded to be insufficient to account for strain concentration due to Poisson's ratio effects. For notched locations, K_v^{EN} produced similar results to CC N-779, and was typically non-conservative by 20-35%.

7.8.12. AD 2000-Merkblatt

The correction described in AD 2000-Merkblatt S2, K_v^{MB}, is a function of S_p only and therefore does not require stress linearisation. K_v^{MB} was found to be both straightforward to apply and reasonably accurate, generally within 10%, for unnotched assessment locations, albeit slightly on the non-conservative side. K_v^{MB} was found to be non-conservative by 20-30% at notched locations; however, K_v^{MB} still performed better than other more complex K_e factors such as CC N-779 in this situation, with significantly less effort involved.

7.8.13. Rolls-Royce (F_u)

The Rolls-Royce Unified Correction Factor, F_u, was found to perform very well for most of the FE models considered. For the stepped pipe (Figure 127), F_u predicted corrections that were conservative between a factor of 1.05x and 1.15x. In the case of PWR nozzles (Figure 128 and Figure 129), F_u was generally conservative between a factor of 1.1x and 1.25x. For the Y-Piece (Figure 131), F_u coincided almost exactly with K_e^{FEA}. Considering the notch cylinder FE models (Figure 132-Figure 134), F_u was also found to perform reasonably well, coinciding very closely with K_e^{FEA} for $S_n >> 3S_m$. There is the potential for F_u to be slightly non-conservative in the range of $3S_m<3S_n<6S_m$ for the notched cylinder, though this is limited to around 15% at most. Overall F_u was found to perform the best out of the complex methods (E.g. CC N-779, Annex 5-C) considered here, which involve more than one correction factor.

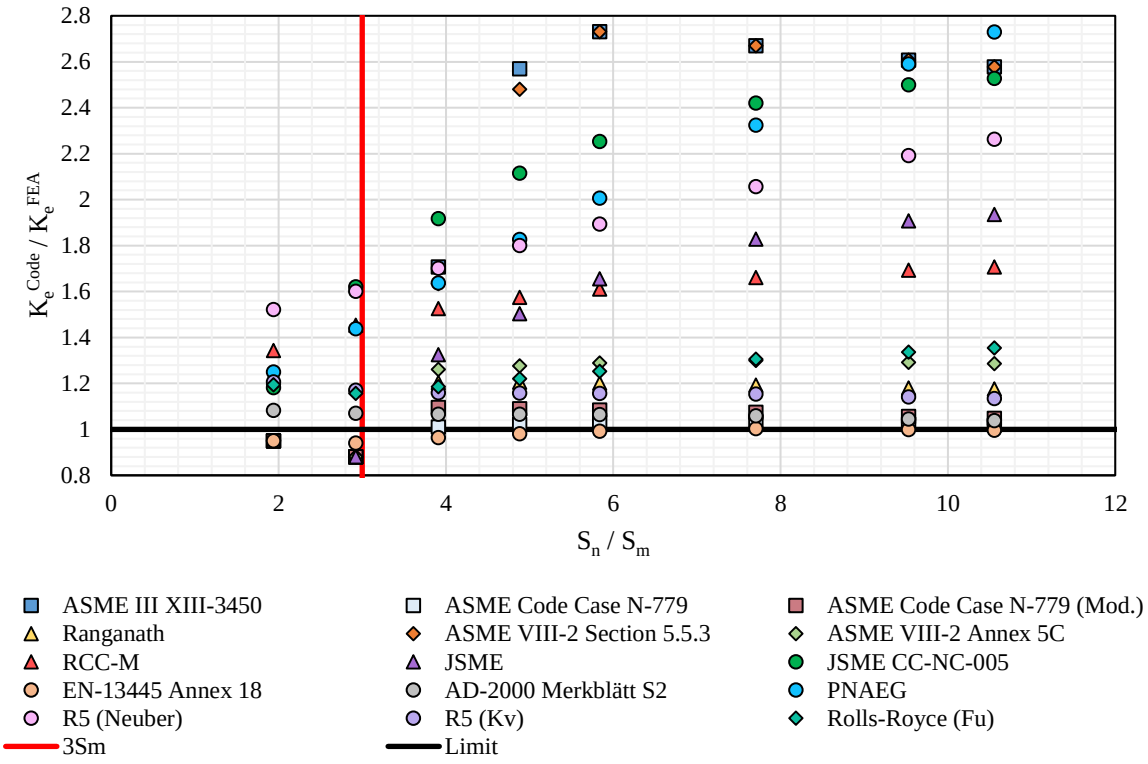

Figure 126. Relative performance of Code K_e factors for thick-walled cylinder FE model.

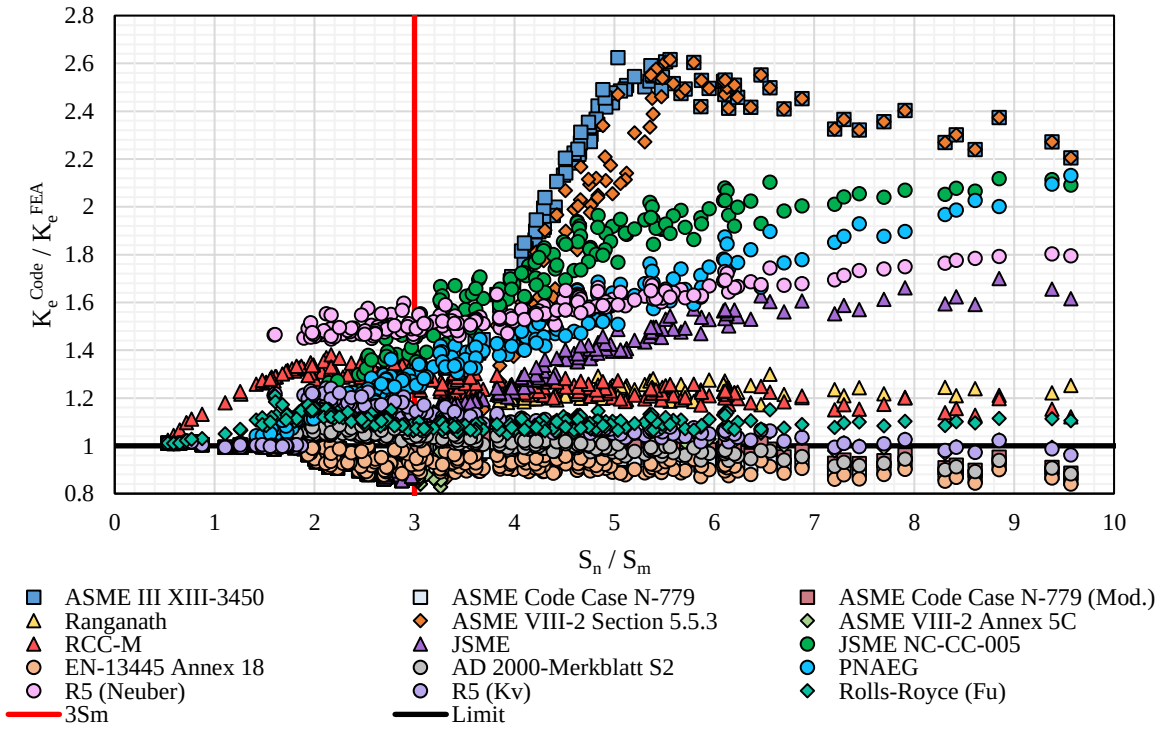

Figure 127. Relative performance of Code K_e factors for the Stepped Pipe FE model

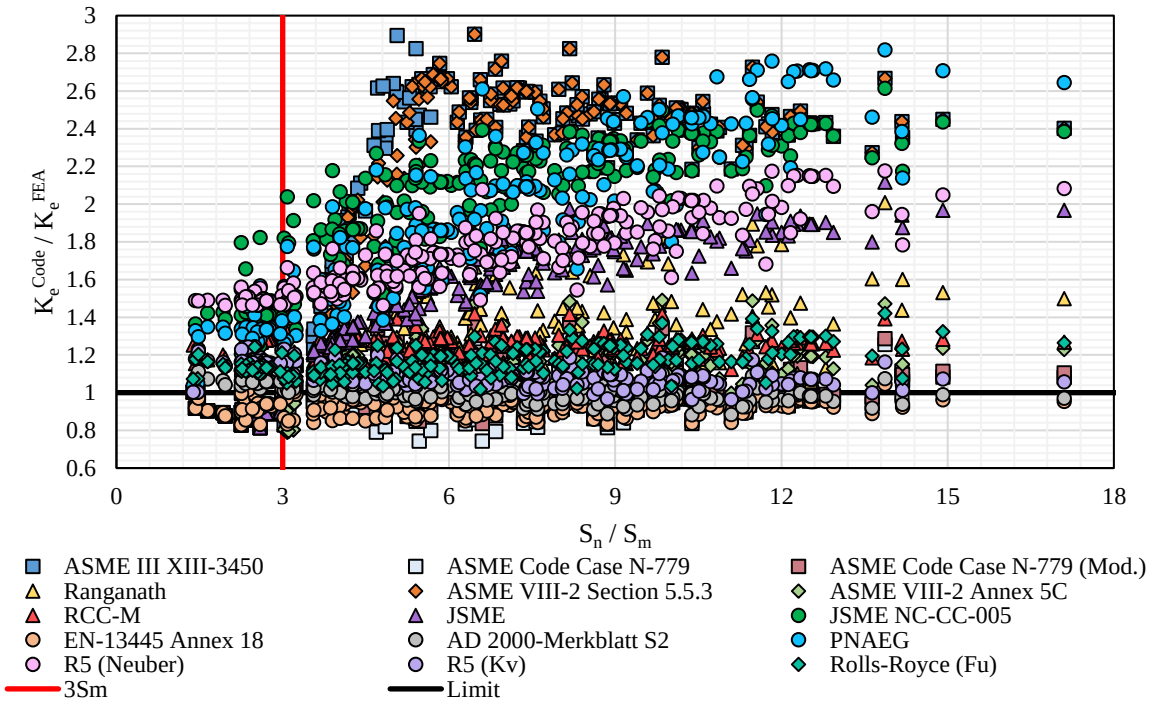

Figure 128. Relative performance of Code K_e factors for PWR auxiliary piping nozzle FE models.

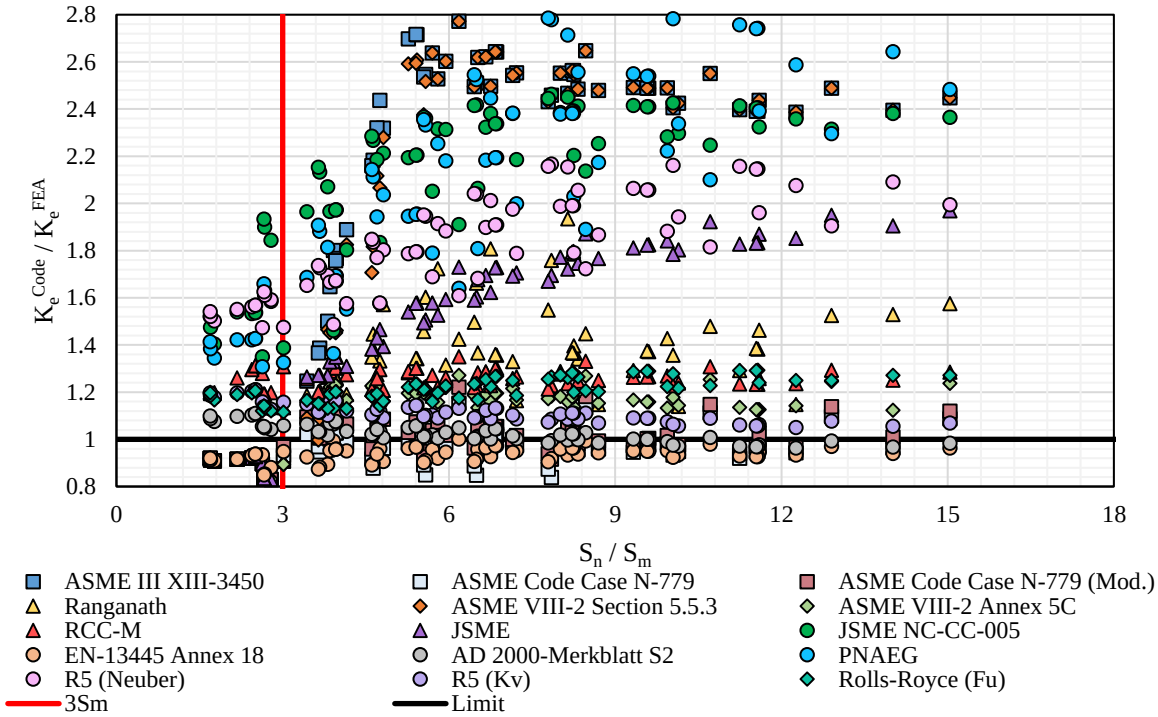

Figure 129. Relative performance of Code K_e factors for tapered nozzle-in-vessel FE model

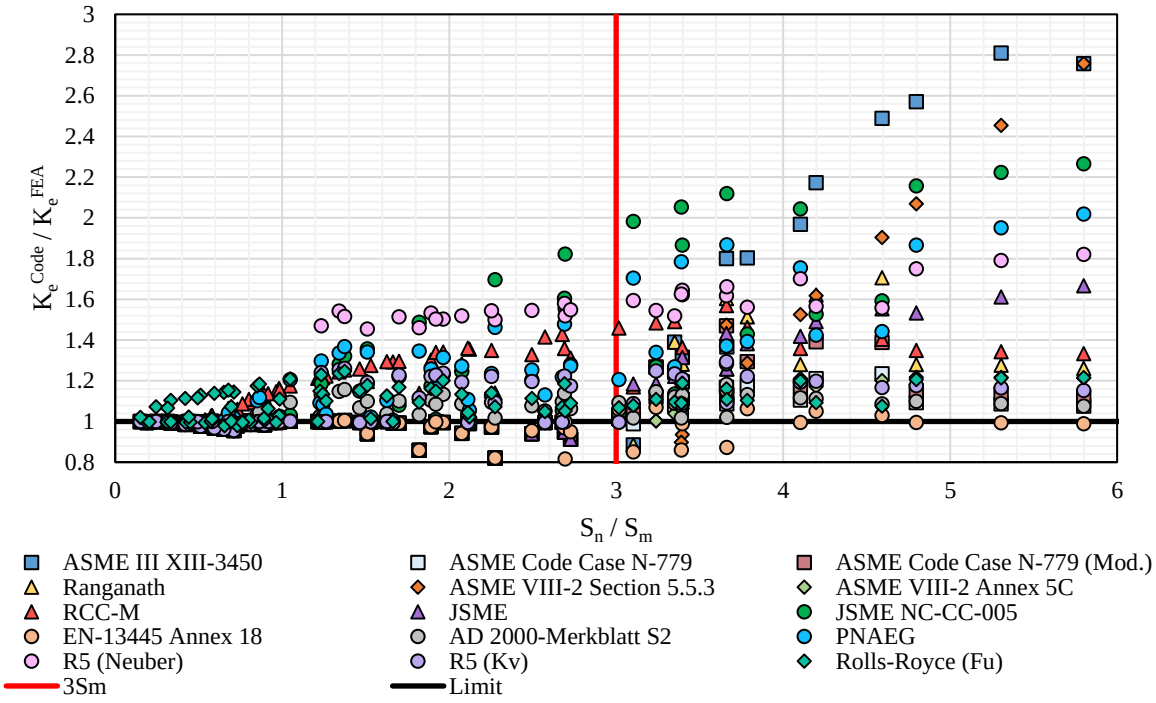

Figure 130. Relative performance of Code K_e factors for PWR thermal sleeve FE model

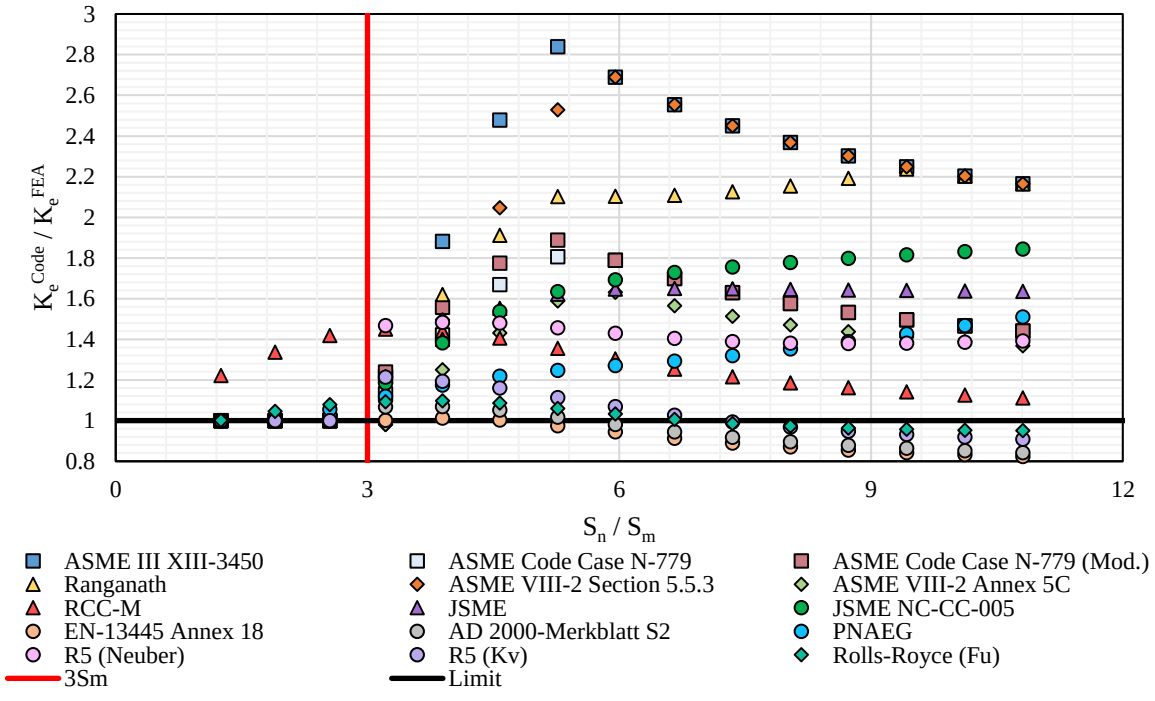

Figure 131. Relative performance of Code K_e factors for Y-Piece FE model

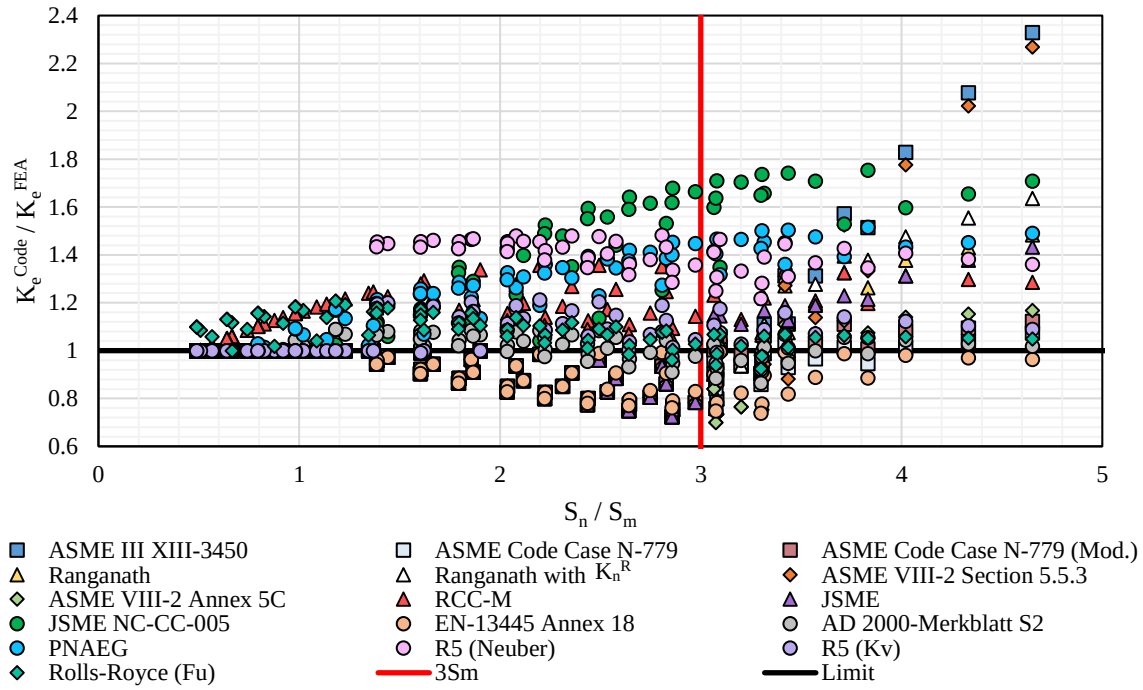

Figure 132. Relative performance of Code K_e factors for notched cylinder subjected to axial thermal gradient.

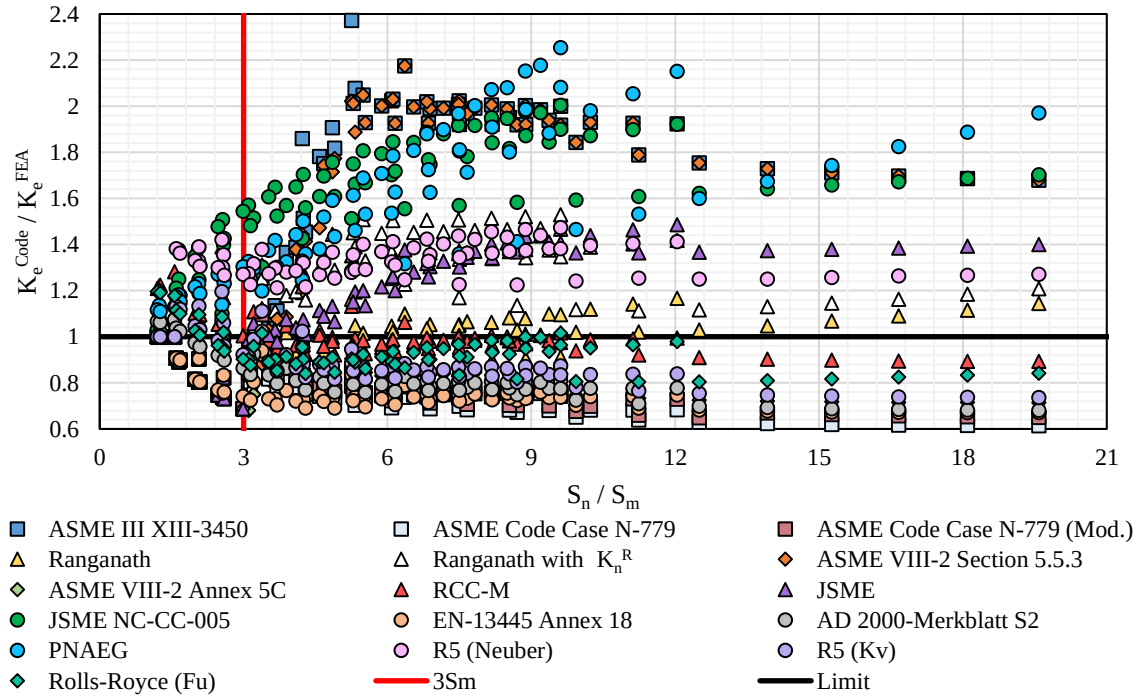

Figure 133. Relative performance of Code K_e factors for notched cylinder subjected to radial linear thermal gradient

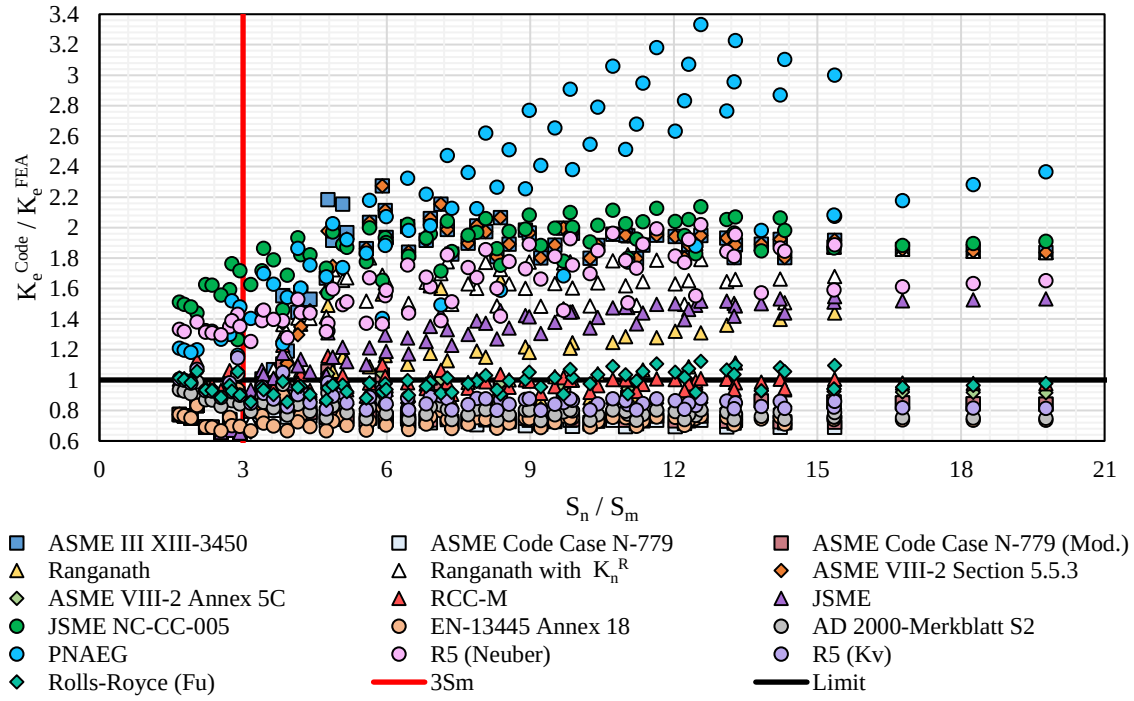

Figure 134. Relative performance of Code K_e factors for notched cylinder subjected to radial parabolic thermal gradient.

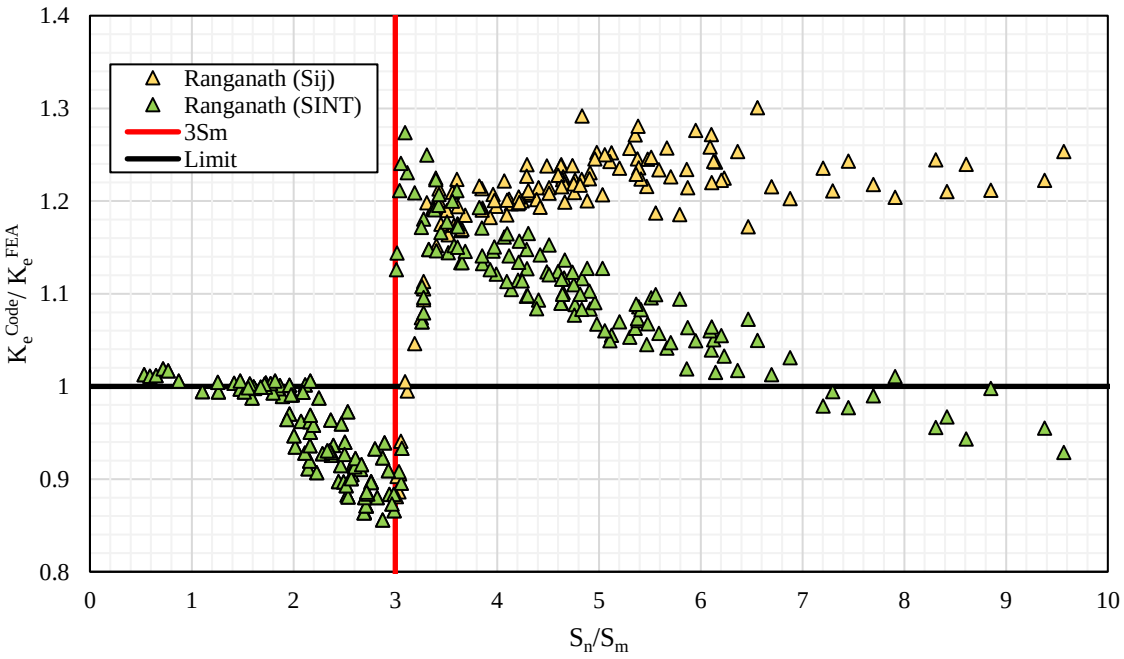

Figure 135. Illustration of potential ambiguity in Ranganath's K_e^R factor for stepped pipe FE model.

7.9. Discussion

Comparison of the FE-derived K_e^{FEA} factors presented in this section highlights clearly the excessive conservatism of the existing Appendix XIII-3450 K_e factor for austenitic stainless steels, often over 200%. Such levels of conservatism may not be tolerable for longer plant life design and the potential for load-following plant operation. The adoption of a less conservative option for simplified elastic-plastic analysis within ASME III is therefore necessary to meet future industry objectives.

7.9.1. Consideration of Ranganath's Method

Based on the results presented in this work, Ranganath's proposed K_e^R factor has been shown to represent a considerable improvement over the current Appendix XIII-3450 K_e factor. It was also found to be easier to apply and produced more consistent results than CC N-779. One could however argue that the basis for inclusion or otherwise of the notch factor, K_n^R, is a matter of Code interpretation of the intent of K_e. One interpretation is that the role of K_e is to preclude the initiation of surface cracks at local hot spots, though this seems unrealistic. In the author's interpretation, the intention of the Code K_e is to preclude the formation of structurally significant cracks arising due to gross section plastic cycling. This is consistent with Langer's original definition of K_e (Section 4.1.1). The additional application of K_n^R could therefore be seen as excessively pessimistic for local discontinuities, which typically exhibit a steep strain gradient. The argument here is that even if crack nucleation were conceded on the surface, this could very well be offset by the sharp decay in the crack driving force with increasing crack penetration. Nonetheless, even when K_n^R was included, the resulting value of K_e^R was still considerably less pessimistic than the Appendix XIII-3450 K_e factor.

It is concluded that the application of K_e^R excluding K_n^R is sufficiently conservative for all but the most severe stress concentrations. It is therefore recommended that greater flexibility should be afforded to the analyst in determining whether the application of K_n^R is appropriate or not on a case-by-case basis. For the assessment of very sharp notches and/or crack-like discontinuities where peak strain concentration is likely to be most severe, the application of FSRFs or adopting a fracture mechanics approach is likely to be more appropriate.

7.9.2. Margin Considerations

The overall process for determination of K_e^{FEA}, as well as the judgement of Code K_e described in this Chapter has necessarily involved a number of engineering assumptions, which can have a direct effect on the margin inherent in both calculations. As discussed by Emslie et al [133], the judgements made on the choice of stress analysis techniques and input material properties are therefore crucially important to understanding the conservatisms 'built-in' to the final value of K_e^{FEA}. In this work, the decision was taken to adopt material properties that were nominally mean and therefore K_e^{FEA} may be interpreted as representative of the average level of strain concentration experienced by the structure. It is important to recognise however that the margin inherent in K_e^{FEA} cannot be interpreted without knowing the underlying assumptions that underpin its calculation. This further highlights the importance of adopting a consistent framework for both the elastic and elastic-plastic analyses.

8. Proposal of Alternative Plasticity Correction Methods

This section describes the development of two alternative plasticity correction methods, derived based on the results presented in Chapter 7, for application to austenitic stainless steel components. Firstly, the preliminary considerations relevant to both proposals are discussed. Then, a general plasticity correction method referred to as the *Global Plasticity Correction Factor* (F_g) approach is proposed and discussed. An alternative method referred to as the *Stress-Modified Neuber* (SMN) approach is then proposed, following a brief overview of its technical basis. Both methods are shown to be fully compatible with state-of-the-art approaches for evaluating the environmental effect (F_{en}) of complex strain and temperature waveforms on fatigue damage. To demonstrate the usefulness of each method, their performance is demonstrated using a representative case study on an LWR plant component subjected to multiple complex operating transients. Finally, the potential industry use cases and limits to the applicability of each method are summarised.

8.1. Preliminary Considerations

The role of a plasticity correction factor is to provide a reasonable approximation of the local elastic-plastic response whilst being straightforward to apply. A good balance of accuracy and practicality is therefore needed. The compiled K_e^{FEA} results vs. S_n/S_m and S_p/S_m obtained for all FE models are summarised in Figure 136 and Figure 137. As it is more representative of power plant loading, only the K_e^{FEA} results obtained for the notched cylinder subjected to the radial parabolic thermal gradient are shown. In total, this represented 696 individual data points. The trend in the K_e^{FEA} results clearly shows that a great variety of LWR plant structures exhibit a similar elastic-plastic response under cyclic thermal loading. Based on a brief examination of the elastic-plastic FE results presented in this work, it was desirable to explore alternative approaches to performing the plasticity correction for application to ASME III type fatigue assessments.

As highlighted in the FE results comparison of Section 7, the Appendix XIII-3450 $K_e^{XIII\text{-}3450}$ factor is non-conservative in the region of $S_n = 3S_m$, which defines the

boundary between surface and sectional plasticity in ASME III. It would be desirable to eliminate this discontinuity in behavior, and to account for both surface and sectional plasticity effects within a single correction. This is in common with the approaches adopted by RCC-M B 3234.6 and the Unified Correction Factor proposed by Emslie et al [133], which were both found to perform very well. In ASME III, surface plasticity arising due to Poisson's ratio effects is treated in Appendix XIII-2500. However, the Poisson's ratio correction of $S_{p,lt}$ according to Appendix XIII-2500 need not be applied if $K_e^{XIII-3450}$ is required. Since $S_{p,lt}$ forms part of S_p, and is therefore multiplied by $K_e^{XIII-3450}$, it is thought that the Code authors deemed this sufficiently conservative not to warrant a further correction. *Chapter 6, Subsection NB – Class 1 Components, Section 6.7.5* of the Companion Guide to the ASME BPVC states the following regarding Appendix XIII-2500:

"…The foregoing procedure was developed assuming that discontinuity or interaction analyses were the methods of choice. With today's use of FEA, the current approach adds difficulty to the normal process. For this reason, and because of unnecessary conservatism, various groups within the Code are suggesting methods for use with FEA. The fundamental and accurate step is to apply the Poisson's ratio adjustment to that part of the total stress range exceeding the yield strength, while at the same time demonstrating that this above yield stress can be related to local thermal stresses"

Therefore, whilst industry demand exists to replace Appendix XIII-2500, any alternative methods must be capable of covering for Poisson's ratio effects whilst being more straightforward to apply. Surface plasticity due to notch effects also require consideration.

The proposed requirements for any alternative approach are as follows. First, it must have general applicability to arbitrary plant structures including vessel components (NB-3200), support structures (NF-3000), and piping components (NB-3600). It must be appropriately conservative compared to elastic-plastic FEA results (i.e. bound the dataset), and be expressed in a simple format. Ideally, it must at most require knowledge of only the two basic stress quantities, S_p and S_n. This is useful since S_p and S_n are readily available without the need to separate mechanical and thermal stress

contributions. This also eliminates the aforementioned potential for error arising from subtracting stress ranges.

It is also important to highlight that in Section 7 the elastic-plastic FE comparisons were presented incorporating two important considerations; first, in the elastic fatigue evaluations, the stress intensities were calculated based on the Tresca theory of failure; and secondly, the design stress intensity, S_m, was calculated based on the maximum temperature of the cycle. However, it is recognised that ASME III XIII-3420 permits S_m to be calculated from the average of the maximum and minimum temperature values for the thermal transients considered in this work. Additionally, there has been notable industry demand for the adoption of von Mises theory within the elastic DBA procedures of various nuclear design codes, including ASME Section III [162]. These assumptions can affect the relationship between S_n and K_e^{FEA}. As an example, Figure 138 shows the relationship between S_n and K_e^{FEA} depending on the assumed failure theory and choice of S_m value. As can be seen, the trend in K_e^{FEA} does show some variation, and whilst relatively minor, it would be desirable to account for this behaviour if necessary. Therefore, to enable general applicability, any alternative method should be compatible with the use of either Tresca or von Mises theory in the elastic stress analysis, and the choice of different assumed values of S_m.

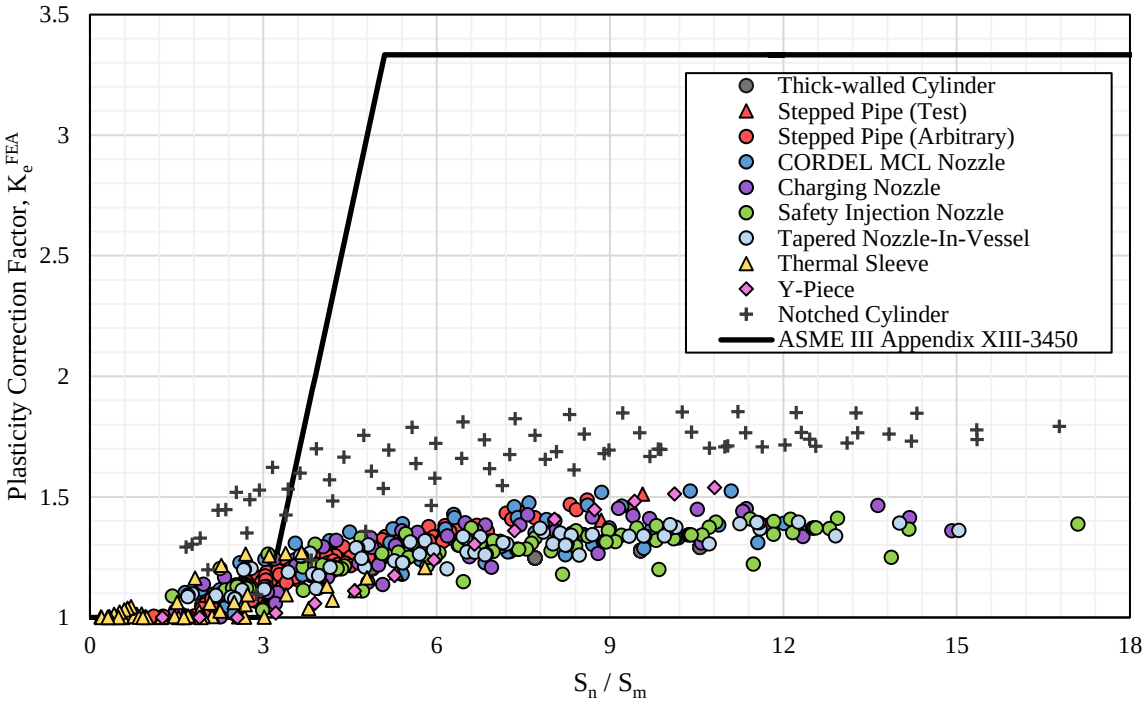

Figure 136. Summary of FE-derived plasticity correction factors, K_e^{FEA} vs. S_n/S_m, obtained for all FE models.

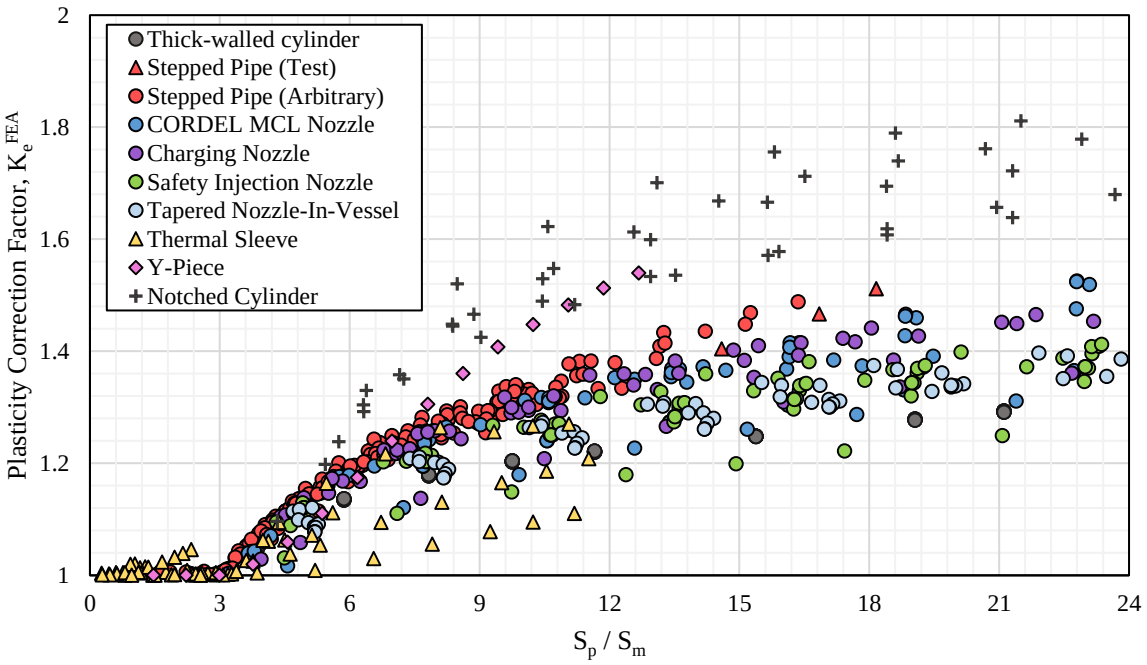

Figure 137. Summary of FE-derived plasticity correction factors, K_e^{FEA} vs. S_p/S_m, obtained for all FE models

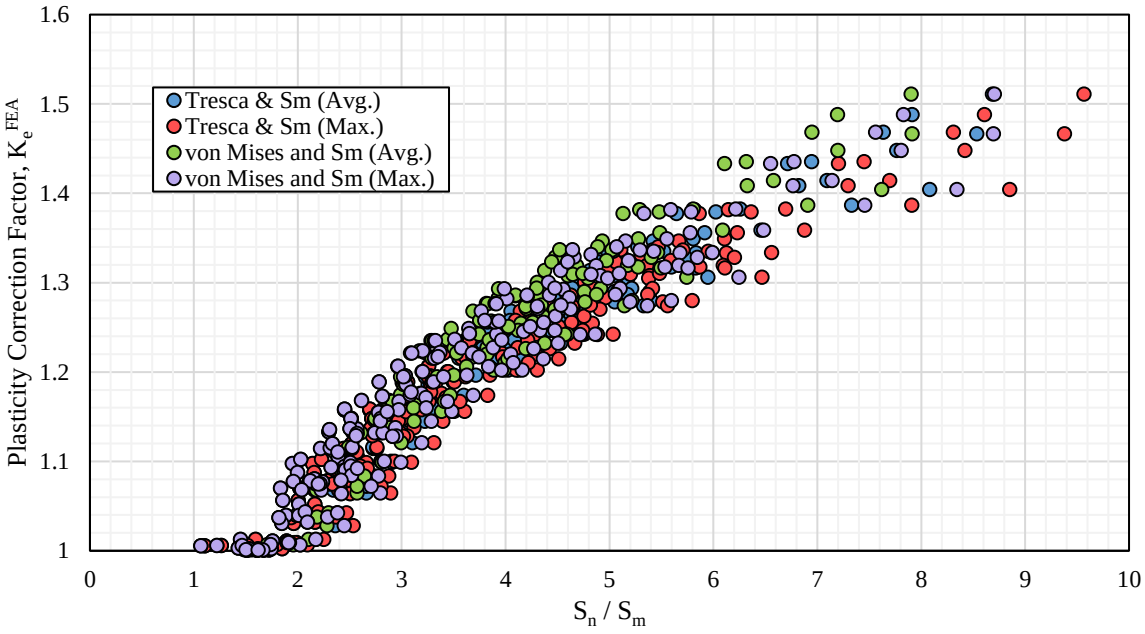

Figure 138. Variation of FE-derived K_e^{FEA} vs. S_n/S_m for stepped pipe depending on failure theory and definition of S_m adopted in elastic analysis.

8.2. Global Plasticity Correction Factor (F_g)

This section outlines a generalised plasticity correction method, applicable to any arbitrary geometry, intended as a simple but conservative option. This approach aims to provide an upper bound estimate of the elastic-plastic strain range expected from equivalent elastic-plastic analysis. In an industry context, this approach might be useful for performing initial scoping calculations in parallel with an applicable design code approach (e.g. ASME III Appendix XIII-3450), to obtain a margin comparison. It might also serve as a screening method, which, if showing acceptable results, no further work need be undertaken. Otherwise, the results may be further refined by undertaking detailed elastic-plastic analysis.

The proposed approach is described in terms of a global plasticity correction factor, F_g, which is itself a function of two other correction factors, F_p, and F_e. F_p is a surface plasticity correction factor, described by Eq. (168) and shown in Figure 139; F_p is based on a power-law fit to S_p/S_m, which accounts for enhancement of strain due to Poisson's ratio effects and strain redistribution at local discontinuities. F_e is a sectional plasticity correction factor, described by Eq. (169) and shown in Figure 140; F_e is

based on a plateau curve fit to S_n/S_m, which accounts for strain concentration under net section plasticity, and fulfills the intended role of the original ASME Code K_e factor. F_g is calculated by Eq. (170) as the maximum value of either F_p or F_e, and is used to correct the alternating stress amplitude, S_a, for input to the fatigue design curve. Whilst F_e is strictly applicable for S_n exceeding $3S_m$, F_p is applicable whenever yielding on the surface of the component is conceded, irrespective of the magnitude of S_n. In this way, F_p ensures that peak strain concentration is covered for both $S_n < 3S_m$, and at the transition where S_n is equal to, or slightly exceeds $3S_m$. The model parameters, A, B, C, and D, were determined by establishing fits to F_p and F_e that bounded 95% of the observations across all FE models. This ensured that F_g will always give conservative corrections in comparison to the elastic-plastic FE results. The bounding model parameters did not vary significantly for Tresca vs. von Mises stress intensity or the choice of S_m value. Therefore, average values of A = 0.708, B = 0.318, C = 2.344, and D = 3.304 are proposed for general application. The variation of F_g as a function of S_p/S_m and S_n/S_m is shown from the heat-map of Figure 141.

$$F_p = \begin{cases} 1.0 \;\; if \; S_p < 3S_m \\ A \cdot \left(\dfrac{S_p}{S_m}\right)^B \quad if \; S_p \geq 3S_m \end{cases} \tag{168}$$

$$F_e = \begin{cases} 1.0 \;\; if \; S_n < 3S_m \\ \dfrac{C \cdot S_n/S_m}{D + S_n/S_m} \quad if \; S_n \geq 3S_m \end{cases} \tag{169}$$

$$F_g = max\left[F_p, F_e\right] \tag{170}$$

As the results for the notched cylinder FE model exhibited the most pessimistic trend, one could argue that it is excessively conservative to base both corrections on this FE model, especially when assessing plane unnotched sections. After all, it is important to acknowledge that this FE model considered notch geometries that were particularly severe ($K_T > 3.5$), which can often be eliminated in pressure vessels by adopting good design practice. However, the level of conservatism is commensurate with the intent

of F_g, which is to function as a simple, geometry-independent correction. It is also confirmed that F_g is able to account for many realistic structural discontinuities in the FE models considered, which included nozzle crotch corners, nozzle-to-pipe transitions, skirt-to-vessel junctures, etc. The performance of the proposed F_g factor is shown by Figure 142, and is shown to produce consistently conservative corrections across all FE models considered in this work. This conservatism was generally limited at most to 40% and 50% for notched and unnotched sections, respectively. Thus, F_g is expected to be conservative for the vast majority of realistic cases, though not unreasonably so on the basis of the results presented in Figure 142.

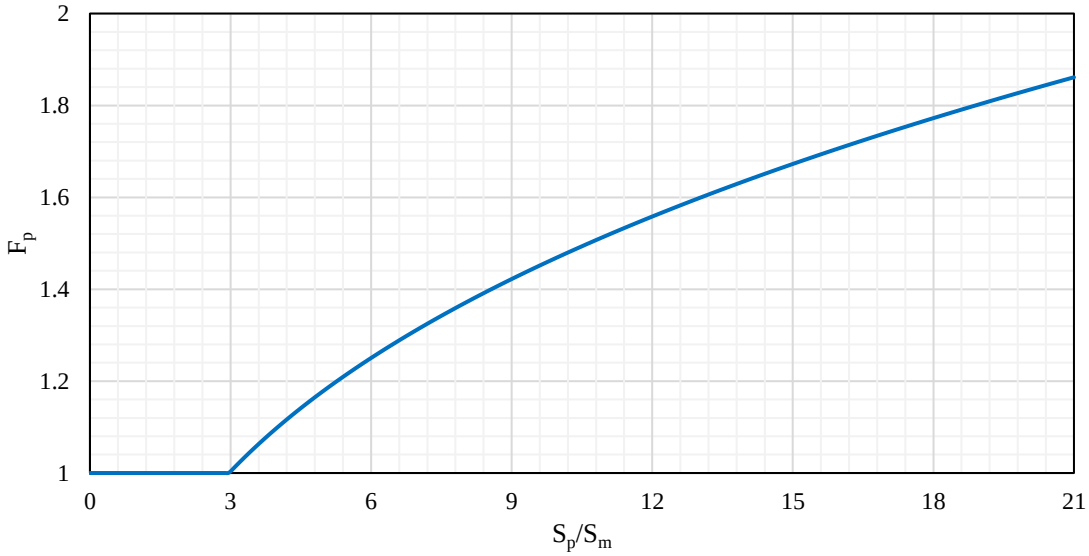

Figure 139. Proposed surface plasticity correction factor, F_p

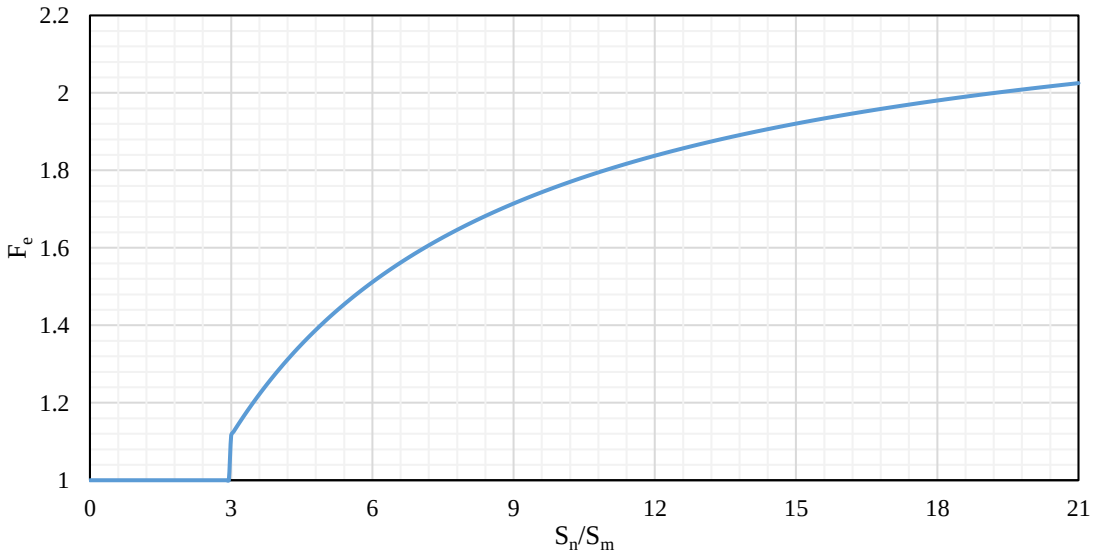

Figure 140. Proposed sectional plasticity correction factor, F_e

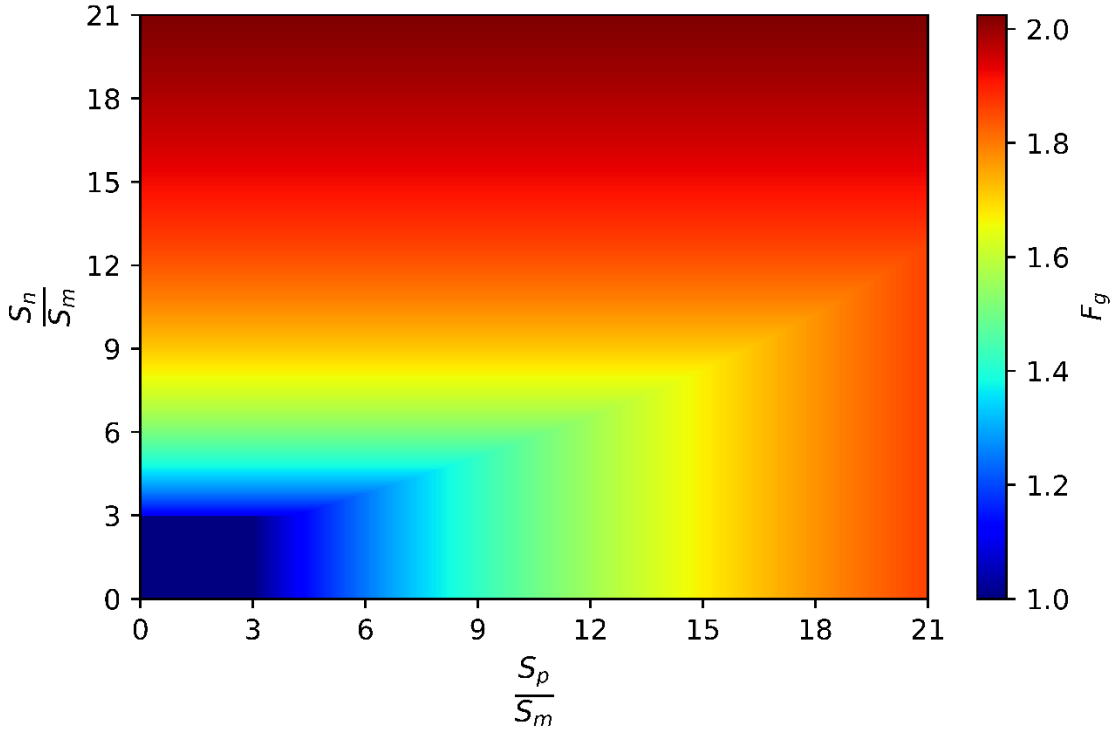

Figure 141. Variation of global plasticity correction factor, F_g, as a function of F_p and F_e

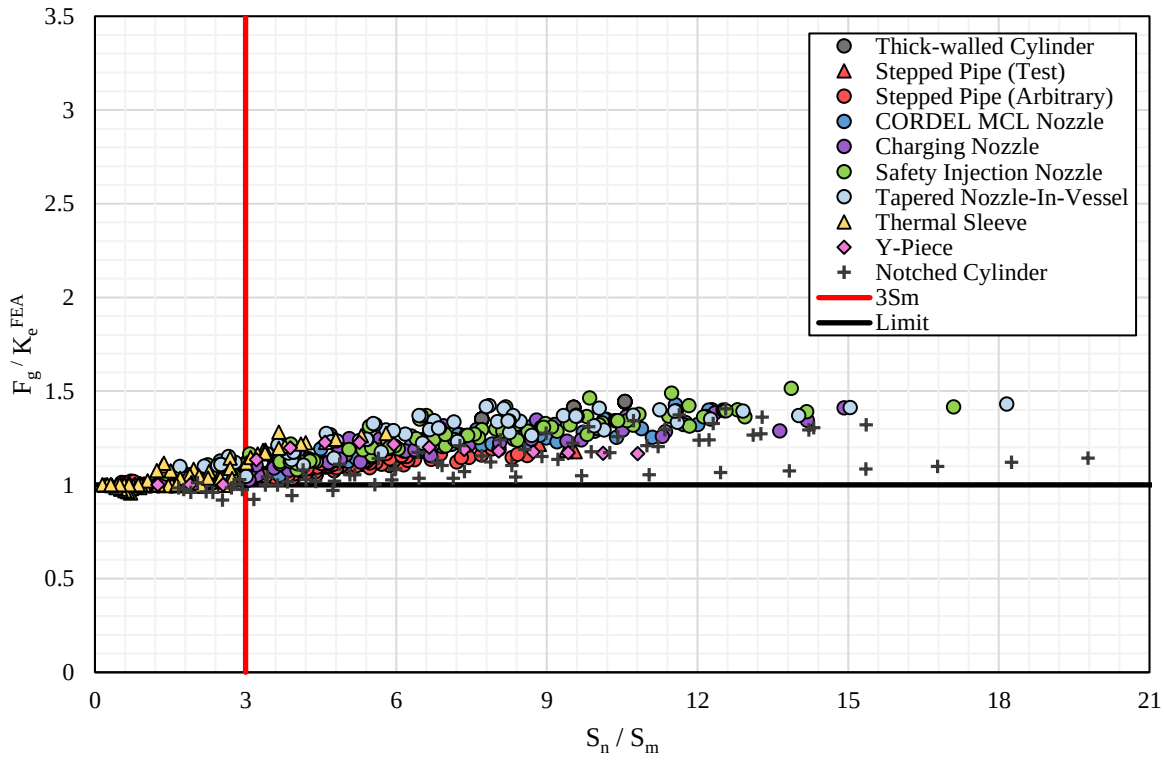

Figure 142. Performance of proposed global plasticity correction factor, F_g, for all FE models.

8.3. Stress-Modified Neuber (SMN) Methodology

One disadvantage of the F_g approach is its reliance on traditional elastic stress analysis techniques, most notably the use of stress linearisation to determine the magnitude of S_n. Thus, in common with other code methods that are predominantly based on S_n, an intimate knowledge of the time history of the through-wall stresses is still required to apply this approach. This carries some notable drawbacks. First, whilst fictitious elastic stresses can be obtained with relatively little effort, the calculation is necessarily more time-consuming due to the need to linearise non-linear elastic stress distributions through-thickness at every time-step. This can be time-consuming, especially when assessing several cross-sections in a structure for many different transients. Secondly, there is the aforementioned potential for S_p to vary out-of-phase with S_n, particularly for thick-walled sections subjected to thermal shocks. This can introduce additional ambiguity into the selection of appropriate time points for definition of fatigue load pairs. The location of maximum S_p is also not necessarily identical to the location of the maximum K_e factor, nor to the location of maximum S_{alt}. Therefore, an approach that can be performed without the necessity of stress linearisation is also desirable.

This section proposes an alternative plasticity correction method, termed the *Stress-Modified Neuber* (SMN) method, which is a function of S_p only. The proposed approach considers the elastic follow-up behaviour of the structure. A brief overview of the technical background to this approach is first provided, following which a simple design criterion is proposed.

8.3.1. Elastic Follow-Up Basis for Strain Concentration

To elaborate the basis for this approach, it is necessary to introduce a new parameter, denoted K_σ, and expressed by Eq. (171).

$$K_\sigma = \frac{\Delta\sigma_{eq}^{ep}}{\Delta\sigma_{eq}^{e}} \tag{171}$$

where $\Delta\sigma_{eq}{}^{e}$ and $\Delta\sigma_{eq}{}^{ep}$ are the equivalent stress ranges calculated by elastic and elastic-plastic analysis, respectively. K_σ is defined here as the *stress redistribution factor* and denotes the fractional reduction in equivalent stress range due to plasticity. K_σ is useful as it provides a stress corollary to how K_e is determined by elastic-plastic FEA and provides insight into how much stress redistribution is allowed to occur at the location

being assessed for a given amount of strain concentration, K_e. Both K_e and K_σ are non-dimensional parameters, and elastic follow-up behaviour can be expressed by forming a non-dimensional stress-strain diagram with both quantities. This is illustrated by Figure 143. The elastic follow-up behaviour is quantified by the elastic follow-up factor, *q*, defined by Eq. (172), which expresses the ratio of the elastic follow-up strain to the elastically calculated strain; here, the elastic follow-up strain is assumed to arise due to plasticity only.

$$\mathrm{q} = \frac{K_e - K_\sigma}{1 - K_\sigma} \tag{172}$$

When plotted in normalised stress-strain space, *q* traces out a straight line between the elastic and inelastic solutions. A value of unity implies a constant strain and corresponds to a purely displacement controlled condition, whilst a value of infinity denotes pure load control wherein the strain tends to infinity under constant load.

In design codes such as the structural design code for the Japanese prototype FBR *'Monju'* [183], an elastic follow-up factor of q = 3 is assumed and is based partially on the series two-bar model described in Kasahara [184], illustrated by Figure 144. The value of *q* = 3 corresponds to the case where both bars possess the same material and cross-section properties, and Bar 2, which remains elastic, is twice the length of Bar 1, which experiences plasticity. For this special case, it has also been shown that *q* becomes independent of the applied displacement and the constitutive model so long as it is sufficient to introduce plasticity into Bar 1, and is only affected by the level of constraint provided by Bar 2 [184]. In other words, in the case of rate-independent plasticity, *q* is dependent only on the geometry for this configuration.

The two-bar problem is simplistic in that the elastic and plastic regions remain fixed and therefore the compliance of the system is constant and the capacity for stress redistribution is limited. In real structures, the compliance is a function of both the geometry and the magnitude of applied loading. As the severity of loading increases, the relative portions of the structure remaining either elastic or plastic evolves continuously, and therefore so too must the magnitude of *q*.

A more realistic analogue of the two-bar model examined briefly here is that of a thick-walled cylinder subjected to a thermal shock at its internal surface. The bulk of the

cylinder wall thickness in this case is analogous to the stiffer bar of the series two-bar problem.

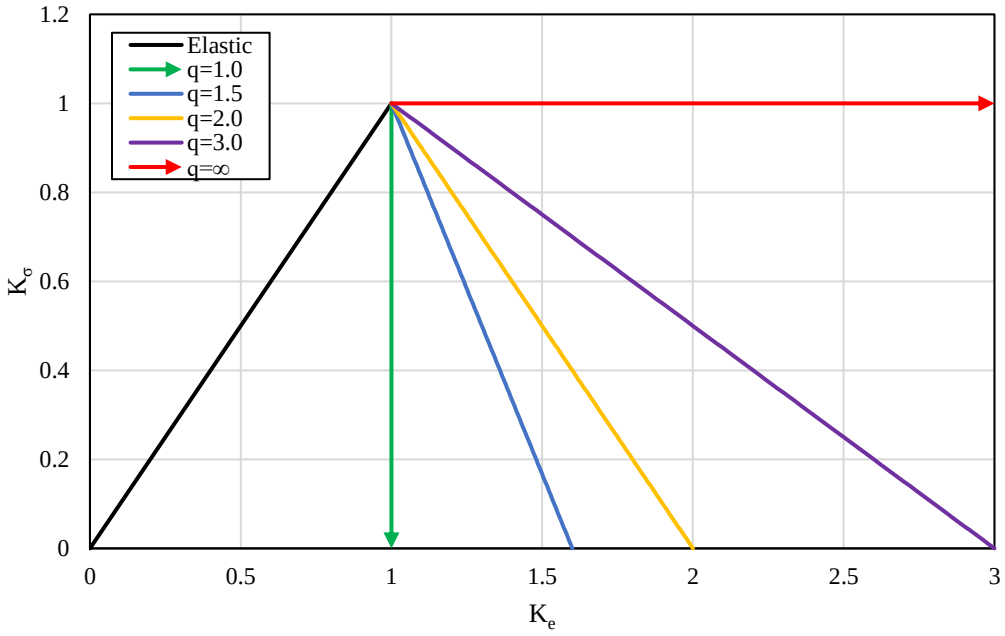

Figure 143. Non-dimensional elastic follow-up diagram.

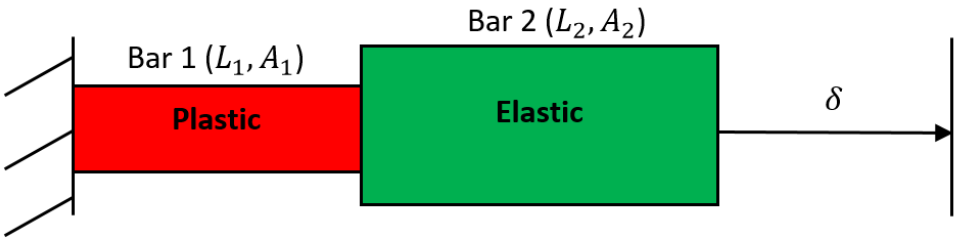

Figure 144. Series two-bar model described by Kasahara [184].

8.3.1.1. Thick-walled Cylinder Under Thermal Shock

The temperature change at the internal surface during the ramp period is 300°C. Constant elevated temperature material properties for stainless steel were chosen for this study: elastic modulus, E = 159 MPa, and yield strength, σ_y = 111 MPa. In the elastic-plastic analysis, a bilinear kinematic rule is assumed for simplicity with the tangent modulus, E_T, as the controlled variable. For a thermal shock acting on a thick walled pipe, plastic deformation is generally limited to a small region close to the internal surface, with the bulk of the pipe wall remaining elastic. The size of the elastic

region (or ‘core’) is therefore very large compared to the small plastic zone at the surface. The relative size of the elastic and plastic zones depends on both the loading level and the elastic-plastic material behaviour. As the load level was fixed, different hardening moduli were instead considered ranging from the case of purely elastic (E_T = E) to elastic perfectly plastic (E_T = 0). The elastic-plastic solutions obtained for each case is normalised by the solution obtained for elastic behaviour and presented in Figure 145. Rather than showing a straight line as in the case of the two-bar model, the observed behaviour is a hyperbola. The hyperbola exhibits an initially steep slope followed by a much gentler slope at lower levels of tangent modulus (i.e. greater plastic deformation near the inner surface). This corroborates observations by Kasahara [176], [184] and Sato et al [185] in studies of elastic-plastic-creep deformations in high temperature components. This has previously been referred to as the *Stress Redistribution Locus (SRL)* and this terminology is adopted here. In the case of elastic-plastic deformations, the behaviour of the SRL is explained by the fact that the compliance of the pipe varies as ratio of plastic zone to the elastic core varies with E_T, and thus *q* also changes. To validate this explanation, the case of a pipe with a fixed elastic core was also investigated.

8.3.1.1. Thick-walled Cylinder with Fixed Elastic Core

In the pipe model with fixed elastic core, different fractions of the pipe are defined to follow bilinear kinematic hardening behaviour, whilst the remainder observed Hooke’s law. The same loading is considered as for the basic pipe model. At each ratio of elastic core, a series of elastic-plastic FE analyses were conducted for each level of tangent modulus and the case of EPP behaviour. Elastic core ratios investigated were 95%, 90%, 85%, 80%, 75%, 70%; no further reduction was considered as a fundamental requirement of ASME III Subsection NB is that gross vessel behaviour should remain elastic under design loading, and therefore that would violate this requirement. The results obtained for the fixed core pipe model are shown in Figure 146 alongside the SRL derived for the standard model for comparison. As shown, elastic-plastic behaviour is found to be highly dependent on the ratio of the elastic core, with each case having a fixed follow-up factor. Smaller differences in the elastic follow-up lines were observed between the 70-80% elastic core ratios as through-wall plasticity arising from the thermal shock only penetrated modestly into this region.

The SRL is found to intersect each of the follow-up lines at varying levels of E_T. This confirms the hypothesis that the elastic core plays a crucial role in the shape of the SRL, as the SRL essentially represents a series of follow-up lines that would be observed at discrete intervals in a period of continuous loading. As the elastic core shrinks, the magnitude of q is increasing irrespective of the magnitude of E_T, though the trend for the case of EPP behaviour was found to be far more pessimistic than for when hardening is included. This variation of elastic follow-up factor with ratio of elastic core is shown by Figure 147.

8.3.1.1. Influence of Constitutive Law and Temperature

Both the simple and fixed elastic core pipe models considered a bilinear kinematic hardening rule with temperature independent properties. It is hypothesised that since the SRL is derived based on normalised stress-strain relationship, then the SRL for a given geometry subjected to predominantly strain-controlled loading should coincide irrespective of the constitutive relation and magnitude of the applied loading.

One possible situation where differences could be expected to occur is where the influence of temperature on mechanical properties is included in the analysis. The reason for this is that the yield strength of austenitic stainless steels can vary considerably depending on temperature. Therefore, the temperature distribution prevailing in the pipe following the thermal shock can have a controlling influence on the size of the elastic core. For instance, if elevated temperature material properties were to be used instead of temperature-dependent properties, then at first glance it would be expected that the plastic zone size would be larger in the case of the former for the same level of applied loading. However, both the elastic modulus and thermal expansion coefficient also vary with temperature. In the case of austenitic stainless steels, the use of temperature-dependent properties normally results in higher elastic stresses and strains compared with the use of fixed elevated temperature properties. Therefore, both of these phenomena could potentially be self-balancing with little to no difference observed between SRLs for both cases. The above parameters were briefly examined for the same pipe model.

For each condition, a series of elastic-plastic FE analysis were conducted for different thermal shocks. The results are summarised in Figure 148, which shows the SRL

derived based on both the temperature-dependent and temperature-independent solutions. The SRL derived previously based on the temperature-independent bilinear rule is also shown for comparison. As shown, the SRLs coincide closely irrespective of temperature, constitutive relation, or loading level. It is therefore concluded that the shape of the SRL of a realistic structure experiencing predominantly thermal loads is relatively insensitive to the choice of constitutive model, temperature, and magnitude of applied loading.

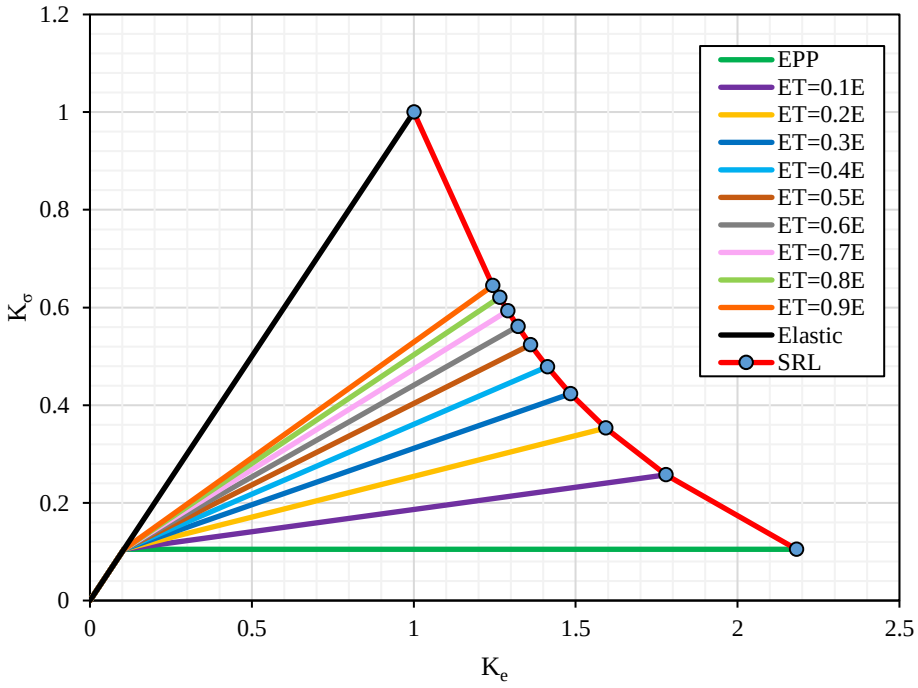

Figure 145. SRL for thick-walled pipe under thermal shock

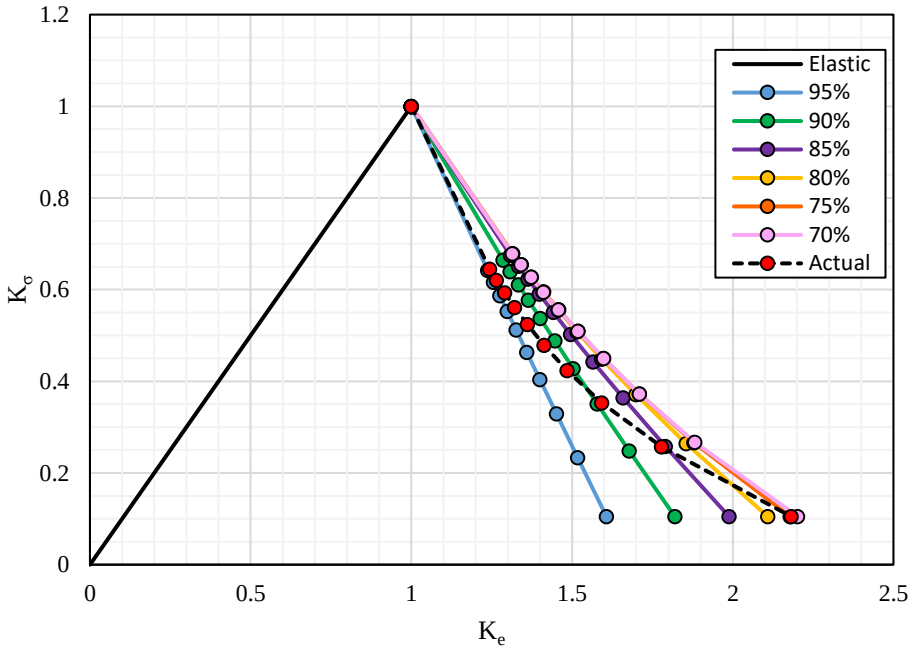

Figure 146. SRLs of thick-walled pipe with fixed elastic core.

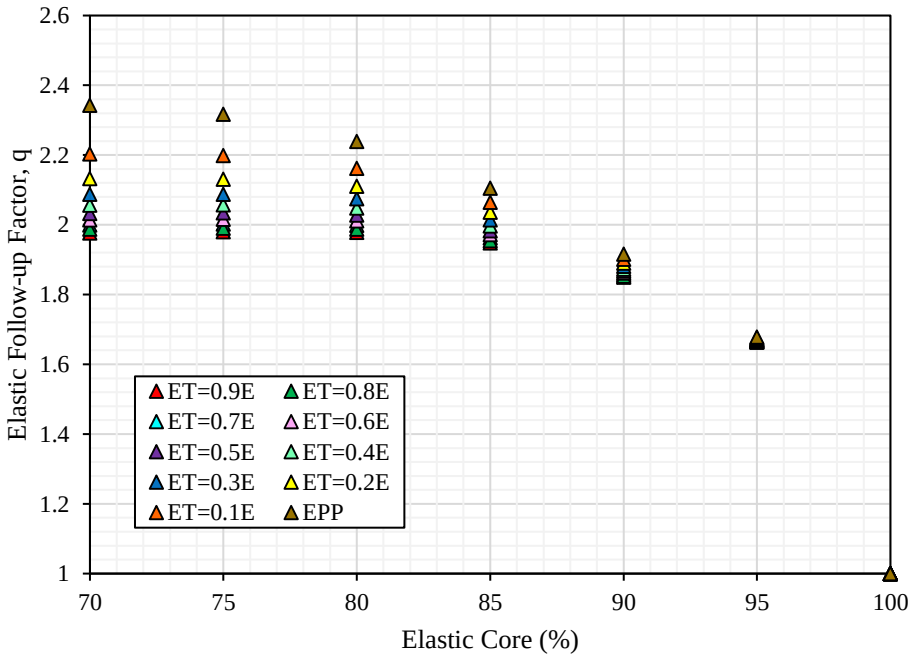

Figure 147. Variation of elastic follow-up factor, q, for thick-walled pipe with fixed elastic core.

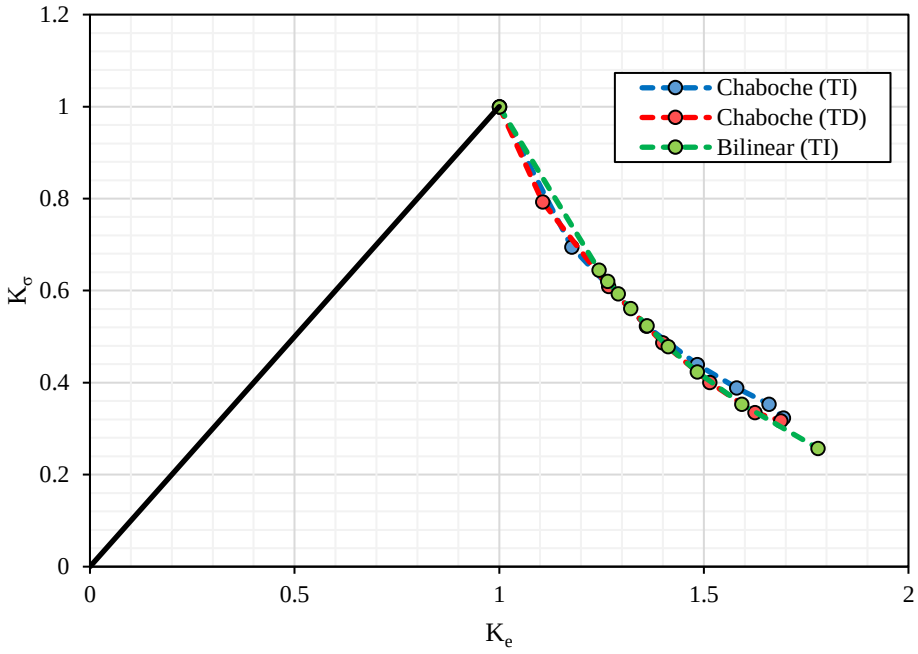

Figure 148. Effect of constitutive model and temperature-dependence on SRL for thick-walled pipe.

8.3.2. Stress Redistribution Locus (SRL) of LWR Components

The SRL is potentially useful for predicting how a structure is likely to behave plastically since it indicates the magnitude of elastic follow-up strain expected for an arbitrary loading condition. This allows for differentiation of certain classes of structure based on their tendency to exhibit low or high elastic follow-up; the former are considered inelastically stable whilst the latter are not. Figure 149 shows the difference in the SRL for a structure with low elastic follow-up and one with high elastic follow-up. Even under conditions of very high local stresses, strain concentration in a structure with low elastic follow-up is self-limiting as stress redistribution is able to progress uninhibited. The elastic portion of the structure is therefore able to constrain the plastic region strongly and achieve stability. The SRL behaviour of LWR plant representative components is closely examined here.

The compiled K_σ vs. K_e data obtained for each of the elastic-plastic FE models is shown in Figure 150. Each data point represents a specific loading condition analysed at each assessment location within the component. For each structure, the difference in behaviour at each assessment location was found not to be especially significant.

The trend in the K_σ vs. K_e results traces out the trajectory of the SRL for each component.

The SRL plot for the thick-walled cylinder and stepped pipe are shown by Figure 150 (a). The SRL for the thick-walled cylinder is steeper than that of the stepped pipe, and follows roughly a straight line corresponding to an elastic follow-up factor of q = 1.3. Different behaviour may be expected for the case of a linear thermal gradient, as this loading condition would limit stress redistribution. For the stepped pipe, data points are plotted for each of the four stepped thicknesses; the trends in the results coincide irrespective of section thickness. The stepped pipe exhibits larger elastic follow-up than the thick-walled cylinder due to the difference in stiffness between each section. The SRL for the stepped pipe also follows a straight line initially corresponding to an elastic follow-up factor of q = 1.4, but then exhibits slight curvature with increasing load.

The SRL plot for the PWR RCS piping nozzles is shown by Figure 150 (b). A similar overall trend in SRL behaviour is observed for the different piping nozzle geometries. The safety injection nozzle shows a trend of slightly greater steepness for larger load levels; this may be expected since the safety injection nozzle is somewhat thicker than the other two configurations and larger elastic core is present. Some variations were observed for the SRL data points obtained between different assessment locations. In particular, the trend for the shell juncture and shell body is slightly steeper than that of the nozzle body and nozzle crotch. This is consistent with design practice wherein nozzles are assumed to present the greater risk of elastic follow-up due to the expansion stresses from attached piping. As shown by Figure 150 (c), very similar results are also observed for the Tapered Nozzle-in-Vessel. This indicates that the SRLs for the piping nozzles also equally represent the behaviour of much thicker vessel nozzles connected to large bore piping. The SRL plot for the PWR Nozzle with attached thermal sleeve is shown by Figure 150 (d). The SRLs show a very high steepness corresponding to an elastic follow-up factor of q < 1.3, with the highest elastic follow-up experienced by the thermal sleeve near the juncture. The nozzle has a much-improved capacity to redistribute high local stresses, and overall exhibits very low elastic follow-up relative to other nozzles that forego the thermal sleeve attachment.

The SRL plot for the Y-Piece is shown by Figure 150 (e). The Y-Piece is unique to the other structures considered since it experiences predominantly a large axial thermal gradient due to the thermal gradient developed between the skirt and supported vessel. This results in very high stresses acting over the entire thickness of the skirt juncture. As a result, the structure has a very limited capacity to redistribute these high uniform stresses due to its lower compliance. The SRL for the Y-Piece shows much greater curvature as an example of a structure that exhibits moderate-to-high elastic follow-up. The SRL does however appear to become linear for $K_\sigma < 0.6$, corresponding approximately to an elastic follow-up factor of $q = 2.0$.

Figure 150 (f) shows the SRL plot obtained for the notched cylinder subjected to thermal shock loading. The notched cylinder shows an entirely different SRL shape to the other components considered. Initially, the SRLs for the various notch sizes appear to follow a straight line corresponding to relatively high elastic follow-up factor of $q = 2.0 – 2.5$. However, as the loading becomes more severe, the SRLs appear to increase sharply in steepness and eventually become vertical; this indicates characteristics of a displacement-controlled structure, wherein any increase in loading produces the same level of strain concentration. The notched cylinder therefore appears to exhibit mixed behaviour of initially high elastic follow-up, where localised plasticity at the notch tip is enhanced by elastic-follow up of the surrounding elastic region, but then exhibits low elastic follow-up under globalised plasticity. This behaviour appears to show a similarity to that observed for crack-like defects, wherein high thermal stresses can enhance the crack driving force under small-scale yielding, but have little to no influence under gross plasticity [186]. Analogously, as thermal stresses acting remotely become sufficient high to induce global yielding, this essentially ‘washes out’ the initially large elastic follow-up effect. The effect of notch size also did not show any discernible trend, with both $\rho = 5$ mm and $\rho = 0.3125$ mm showing very similar behaviour.

Overall, the SRLs of the various LWR plant representative components considered show generally similar behaviour, with all structures exhibiting inelastic stability.

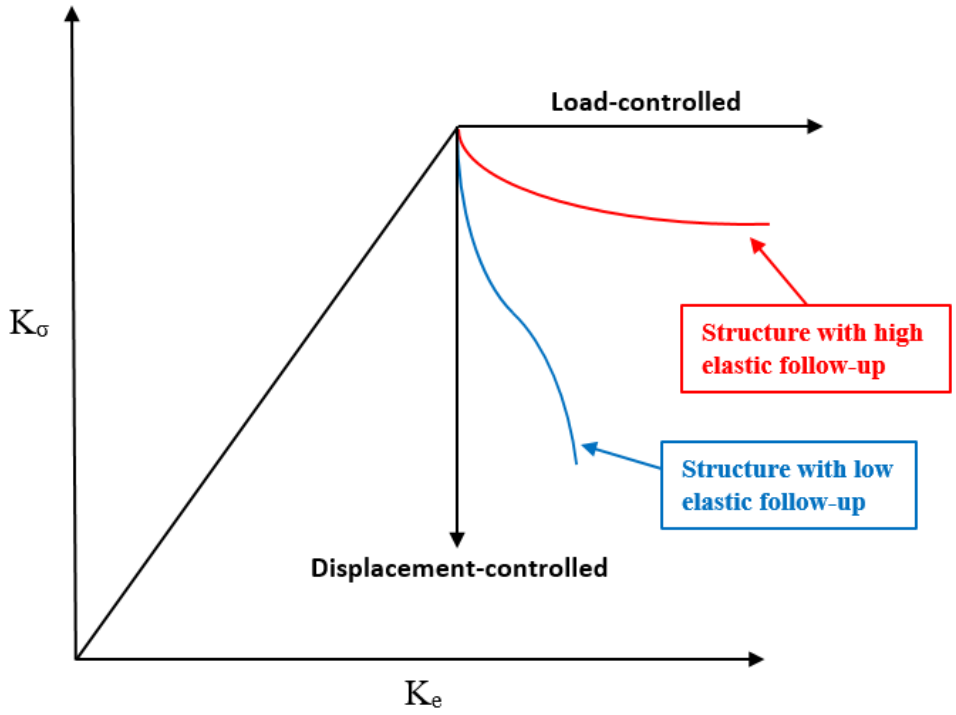

Figure 149. Illustration of stable and unstable inelastic responses of structures.

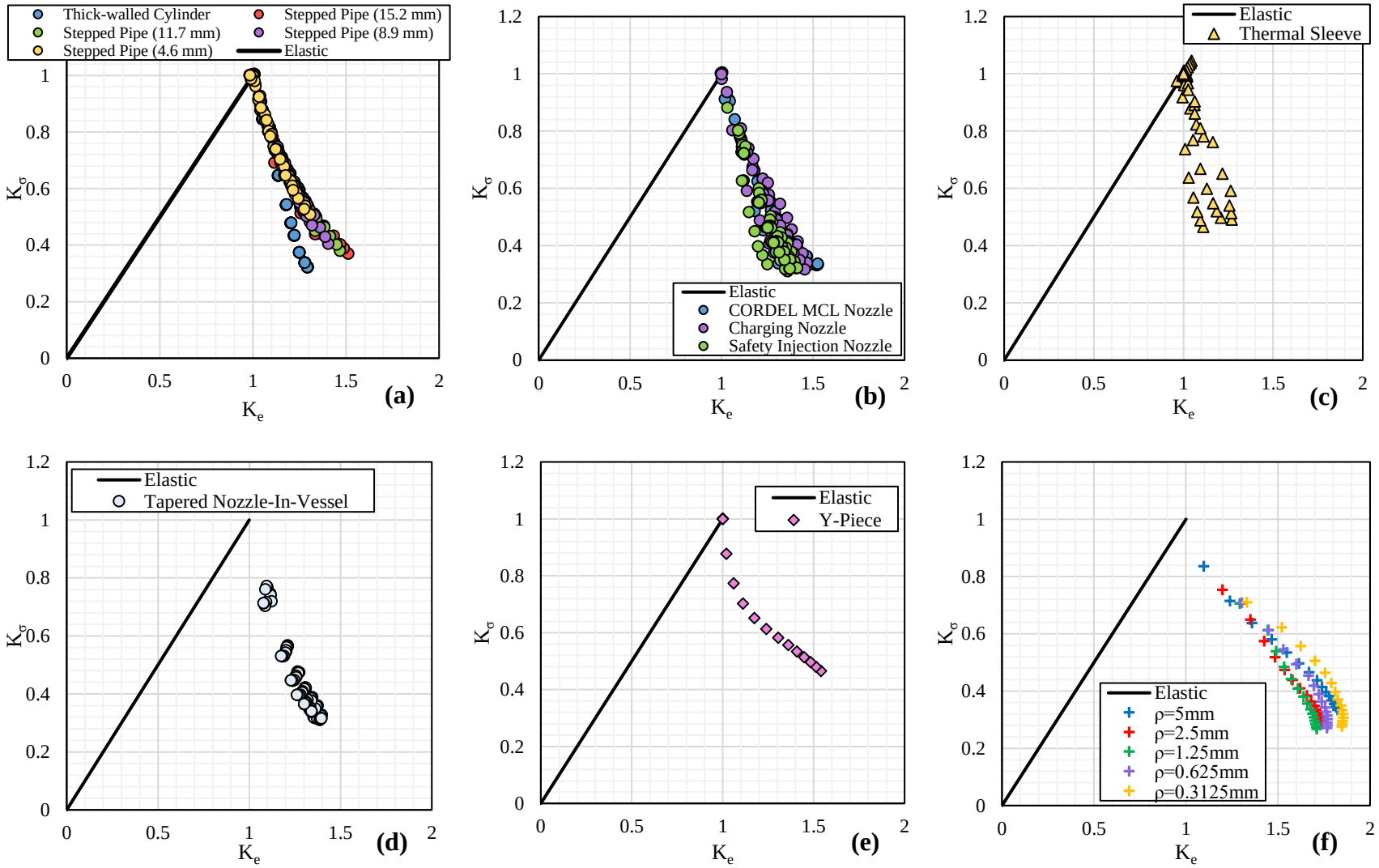

Figure 150. Stress redistribution loci of LWR plant representative components.

8.3.3. Approximation by Modified Neuber Construction

Based on the results presented in Figure 150, potentially more practical plasticity correction methods that may be able to predict closely the actual SRL behaviour of LWR components with knowledge of only the surface elastic stresses were investigated.

A proposed method to accomplish this is to adopt an approach similar to the *Generalised Neuber Methodology* described in R5 V2/3 Appendix A7 [127]. The Neuber framework is very practical and lends itself well to implementation within software. The hyperbolic approximation of Neuber also shows a reasonable resemblance to the shape of the SRL for many structures. However, as highlighted by the results presented in Section 7.8, Neuber's rule has the potential to be very conservative for LWR components subjected to thermal loading. The reason for this is that Neuber's rule implicitly involves an assumption regarding the level of elastic follow-up due to plasticity. The Neuber correction is equivalent to an elastic follow-up factor of

$$q = \frac{2 - K_\sigma}{1 - K_\sigma} \tag{173}$$

The implication of Eq. (173) is that whilst q is approximately equal to 2 for modest levels of plasticity, it becomes unboundedly high for more severe loading. Thus, Neuber's rule assumes a large amount of elastic follow-up, or put differently, it assumes the structure is inelastically unstable (load-controlled). As can be seen by Figure 151, the LWR plant representative components assessed in this thesis do not behave as per the Neuber construction. In his original derivation of the rule, Neuber considered the case of a blunted crack under small-scale yielding conditions subjected to out-of-plane shear loading [187]. It therefore also may not be particularly accurate if the geometry being assessed is not notch-like. To approximate the response of high temperature FBR components due to combined creep and fatigue, Shimakawa et al [188] proposed the following adjustment (Eq. (174)) to the Neuber's hyperbola by inclusion of a modification factor, formalised by the symbol kappa (κ) in [189].

$$K_e = \frac{1}{\kappa}\left[\frac{1}{K_\sigma} + (\kappa - 1)K_\sigma\right] \tag{174}$$

The modification factor, κ, which controls the slope of the Neuber hyperbola, is expressed by Eq. (175):

$$\kappa = \frac{\frac{1}{K_\sigma} - K_\sigma}{K_e - K_\sigma} \tag{175}$$

The effect of κ is illustrated graphically in Figure 151. A value of κ = 1.0 reduces to the case of Neuber's rule. Values of κ > 1.0 result in a steeper hyperbola with lower strain concentration experienced for an assumed level of stress redistribution compared to the Neuber's rule. Shimakawa et al [188] proposed a value of κ = 1.6 as a conservatively bounding approximation of the SRL behaviour of FBR plant representative components and has been verified extensively with FEA [190]. As shown in Figure 151, the SRL curve corresponding to κ=1.6 also conservatively approximates the behaviour of most LWR components reasonably well. It can be seen that the SRL curve follows very closely the SRL of the Y-Piece, which exhibited the highest elastic follow-up of the LWR components considered.

However, the response of the Y-Piece is not representative of most LWR components that are susceptible to fatigue. As shown, the use of the SRL curve with κ=1.6 appears to be excessively conservative for components which exhibit relatively low elastic follow-up such as nozzles and piping. Therefore, it would be desirable to propose a different correction for structures exhibiting modest elastic follow-up, which is more typical, but whilst retaining Neuber's simple graphical interpretation. Irrespective of the value of κ, the hyperbolic relation of Neuber implies that the structure will always tend to inelastic instability under severe loading; varying the value of κ does however control the point at which this shift from a low to high follow-up response occurs. Nonetheless, adopting a modified Neuber relation with a fixed value of κ is not sufficient for low follow-up structures since, as highlighted in Figure 151, the actual SRL behaviour does not always resemble a hyperbola. Adopting a single hyperbola is therefore unable to reflect the true behaviour over the entire range of possible loadings. However, for a given load state (i.e. a single point on the K_σ-K_e diagram), there must be some particular hyperbola, described by a single value of κ, that will coincide exactly with the true inelastic response.

It is possible to obtain a more accurate result by considering a range of different hyperbolae, which can match the SRL behaviour for an arbitrary state of loading. In this approach, κ is no longer fixed but is instead dependent on severity of loading. Figure 152 shows the variation of κ as a function of S_p/S_m for each of the LWR plant representative components considered. As can be seen, for the typical structures exhibiting low-to-moderate elastic follow-up, the value of κ deviates significantly above 1.6. Thus, it was possible to establish a relationship between κ and S_p/S_m that was modestly bounding, which could be used to evaluate these structures with greater accuracy. The second order polynomial described by Eq. (176) was used to establish a lower-bound fit to the κ vs. S_p/S_m data, as illustrated in Figure 152.

$$\kappa = -0.00145\left(\frac{S_p}{S_m}\right)^2 + 0.0758\left(\frac{S_p}{S_m}\right) + 1.2225 \qquad (176)$$

Figure 153 shows the performance of the SMN correction based on Eq. (176) compared with the K_e^{FEA} results presented in Section 7 for the plant representative FE models. In this case, the value of κ was calculated based on the average of the tabulated S_m values corresponding to the metal temperatures at the peak and valley of each cycle (per Appendix XIII-3420), whilst the modified Neuber correction was performed based on average of these two metal temperature. This introduces slightly higher conservatism than implied by Figure 152, owing to simplified assumption that the entire cycle may be characterised by average temperature values of E, K^c, and n^c when applying the modified Neuber correction. Nonetheless, this approach resulted in predictions that were conservative between a factor of 1.04x and 1.36x for the applicable low-to-moderate elastic follow-up structures, and in most cases was 10-30% conservative to elastic-plastic FEA. It was found that the use of Eq. (176) to determine κ reduced excess conservatism by between a factor of 1.5x and 2.0x for these structures compared with adopting κ = 1.6. Eq. (176) may therefore be utilised in situations of local plasticity (i.e. where $S_p > 3S_m$) to generate a modified Neuber hyperbola that will give more realistic results for structures exhibiting modest elastic follow-up. For structures which pose a risk of high elastic follow-up or whose inelastic response is not well defined, the use of κ = 1.6 appears to be more appropriate.

Concerning the assessment of notches that are explicitly included in the FE model, a similar approach might be adopted, though, as previously noted for the notched cylinder studied in Section 7.7, the level of elastic follow-up exhibited is very much dependent on whether plasticity is localised to the notch tip. Under these circumstances, the original form of Neuber's rule actually gives quite good predictions of the local strain, being conservative by a factor of 1.4x to 1.6x, which is reasonable. On the other hand, if plasticity is globalised, then Neuber's rule can be very pessimistic, and the modification $\kappa = 1.6$ is likely to give more reasonable predictions. For sharp discontinuities such as closure or fillet welds, which are not typically modelled by FEA, it is instead recommended to use a FSRF or adopt a fracture mechanics methodology when assessing such features.

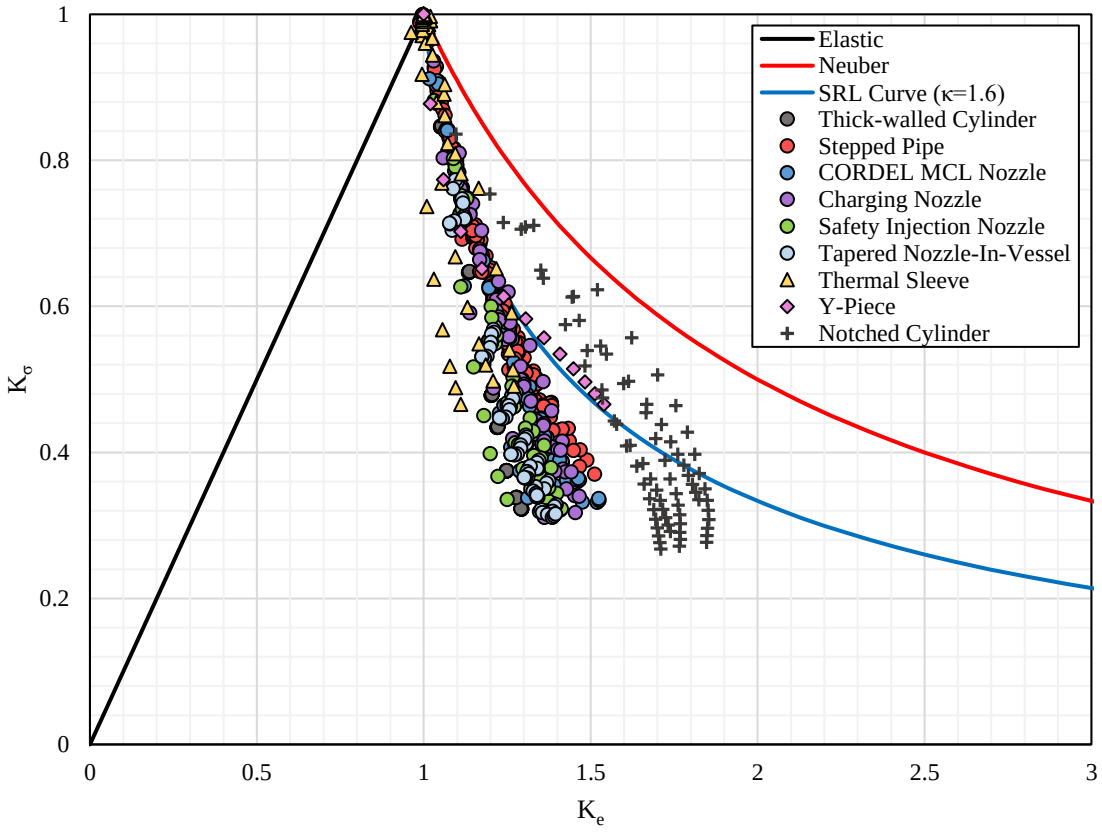

Figure 151. SRL behaviour of LWR plant representative components.

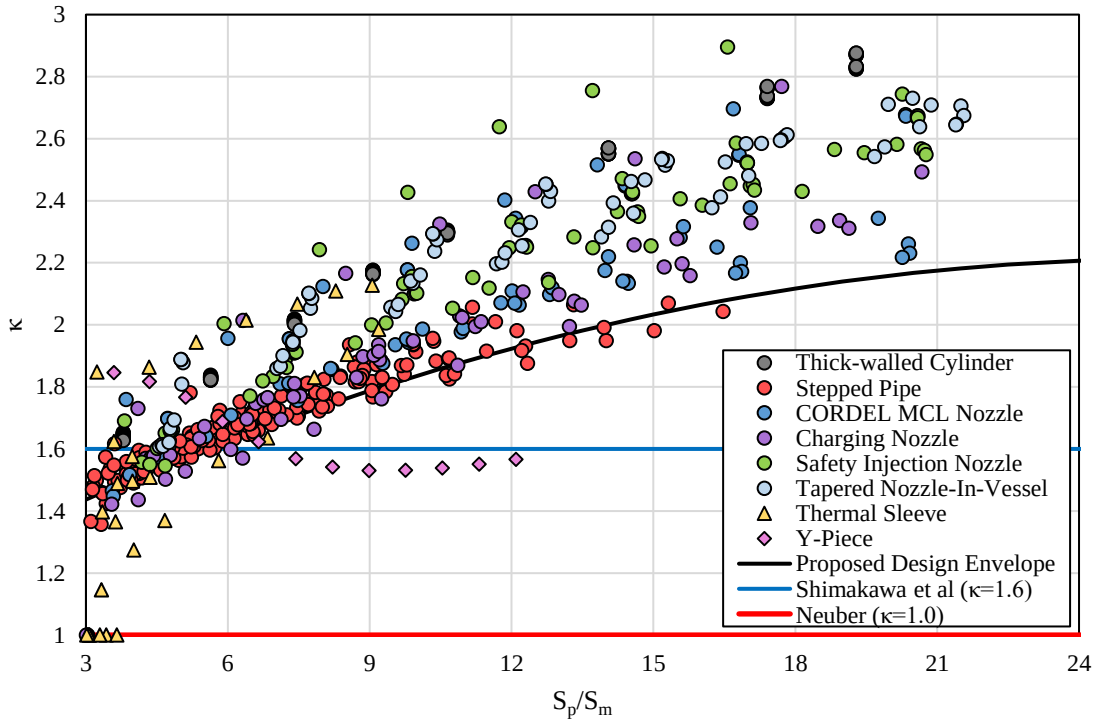

Figure 152. Proposed κ vs. S_p/S_m design envelope for LWR plant components.

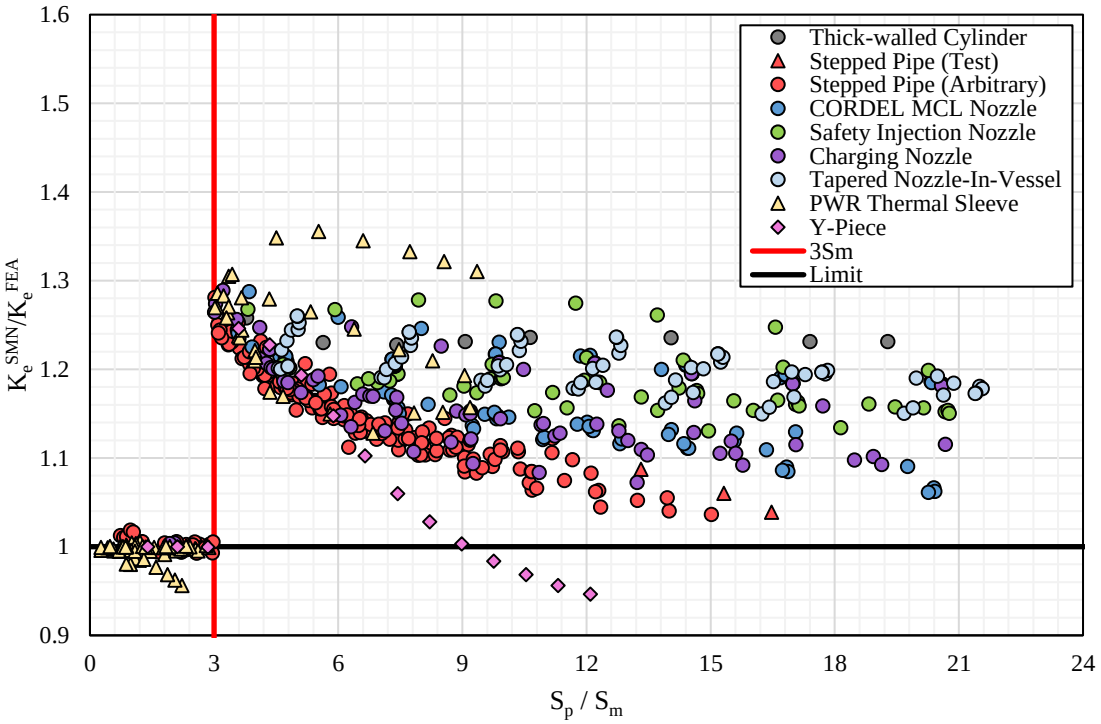

Figure 153. Performance of SMN correction for elastic-plastic FE models.

8.3.4. Proposed Design Procedure

Based on the observations highlighted in the Sections 8.3.2 and 8.3.3, this section proposes a possible procedure for application to ASME III type fatigue assessments without the need to perform stress linearisation. Figure 154 gives a high-level overview of the proposed approach. Prior to commencing the procedure, elastic FEA is first conducted for all applicable design transients and the fatigue load pairs are identified using the EVP cycle counting approach described in 3.3.3 and stored in order of decreasing S_p. The fatigue evaluation procedure is iterative and is described by the following steps. In the first iteration of the procedure, for each cycle, the value of S_p is examined and if S_p is less than or equal to $3S_m$, then no plasticity correction is needed and S_p may be used as is to determine S_{alt}. Otherwise, the SMN correction is applied, adopting an appropriate value for κ. The corrected strain range, $\Delta\varepsilon$, is then multiplied by half the reference modulus, E_c, to determine S_{alt}. This process is performed for all counted cycles and the CUF is calculated. If the CUF is less than unity, then this satisfies the requirement of ASME III Appendix XIII-3520 (e) and no further work is needed. Otherwise, the analyst may opt to refine the analysis assumptions in order to reduce input conservatism and achieve an acceptable value of CUF. If the CUF is still found to be unacceptable, then the fatigue check is not satisfied, and other options must be explored to achieve a satisfactory result.

One important distinction between the SMN method adopted here and many of the Code K_e methods is that it requires the solution of a system of two non-linear simultaneous equations – namely the Neuber relation and one of either the cyclic R-O or Masing relations – containing two unknowns. Numerical iteration is therefore necessary for inversion of the R-O or Masing equations and achieving an inelastic solution. The Newton-Raphson (NR) algorithm is commonly used to determine the roots of non-linear systems of equations, as it exhibits quadratic convergence if the initial guess of the roots of the system is reasonably close to the exact solution. However, one drawback of the NR algorithm is that convergence is conditional on the accuracy of the initial estimate of the roots. If the initial guess is not sufficiently close, solution divergence occurs. The plasticity correction must be repeatedly applied during the fatigue assessment. The number of times this is done equals the number of assessment locations times the number of transient load pairs at each location requiring

a plasticity correction. If this is applied at every node in a finite element model, this product can easily exceed 10^4-10^5. Consequently, it is crucial that the plasticity correction be implemented efficiently and remains numerically stable.

One such algorithm that fulfils both these conditions is the algorithm described by Navarro [191] and henceforth referred to as the *Navarro Algorithm* (NA). The NA is based on fixed-point iteration, and was demonstrated in [191] to be unconditionally convergent. Navarro demonstrated the efficiency of the algorithm in determining the intersection between Neuber's hyperbola and Molski-Glinka's strain energy density equation with the R-O cyclic SSC. A modification to the Navarro algorithm is proposed here to converge on the solution corresponding to the intersection point of the modified Neuber hyperbola and cyclic SSC. The modified algorithm introduces two parameters, ϕ and κ. ϕ is introduced to readily alternate between the use of the cyclic R-O relation and Masing's relation, whilst κ is as described by Eq. (176) and is introduced to adjust Neuber's hyperbola such that it coincides more closely with the SRL of the component. A flowchart of the modified Navarro algorithm is shown by Figure 155.

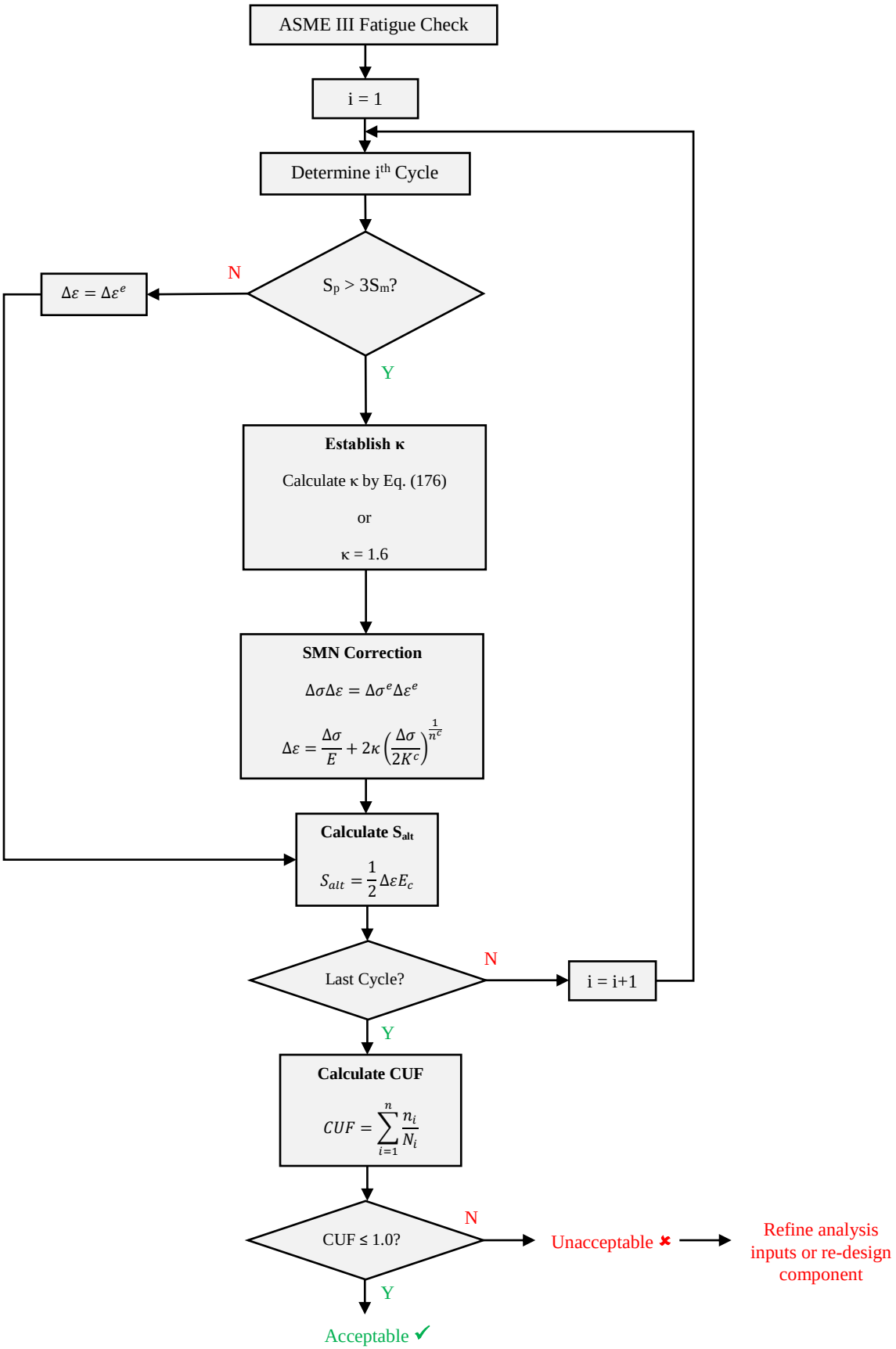

Figure 154. High-level overview of proposed SMN methodology.

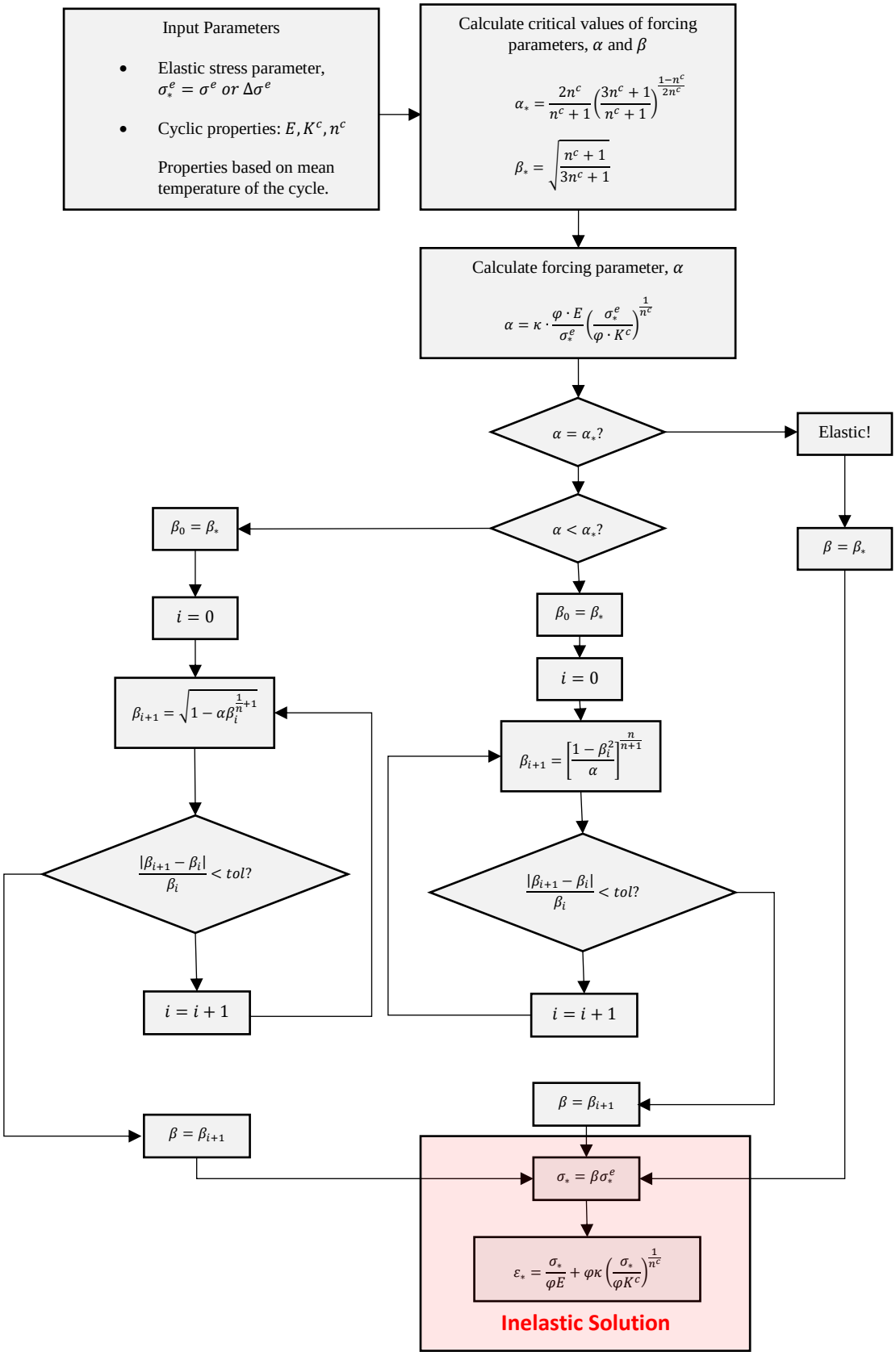

Figure 155. Flowchart of proposed modified Navarro algorithm.

8.4. Consideration of Environmental Fatigue (F_{en}) Effects

An important consideration for both the proposed F_g and SMN methods is the ability to incorporate environmental fatigue penalty (F_{en}) factors when applying these approaches to component fatigue assessments. As discussed in Section 3.4.1, individual F_{en} factors must be determined for each cycle considered in the fatigue assessment for those locations in contact with the hot reactor coolant environment; the partial usage factor for each cycle is multiplied by the associated F_{en}; the corrected partial usage factors are then summed to determine the environmentally corrected CUF, U_{en}. For austenitic stainless steels in the PWR environment, F_{en} depends on strain rate and temperature, which vary continuously during plant transient loading and therefore the significance of F_{en} also varies depending on the position within the cycle. This differs from the isothermal, constant strain rate test conditions upon which the F_{en} correlations were developed, and accordingly a number of detailed calculations methods have been proposed for establishing an effective F_{en} value, $F_{en,eff}$, for more complex plant transient loading. One such method is the *Modified Rate Approach* (MRA) outlined in [72], which involves dividing the rising portion of the cycle stress-time history into small piecewise linear segments, calculation partial F_{en} values for each increment per Eq. (177), and then numerically integrating over the full cycle strain range per Eq. (178) to obtain $F_{en,\,eff}$.

$$F_{en} = exp(T'O'\dot{\varepsilon}') \tag{177}$$

where T', O', and $\dot{\varepsilon}'$ are defined in [72] as functions of temperature, water dissolved oxygen content and strain rate, respectively.

$$F_{en,eff} = \sum_{k=1}^{n} F_{en,k}(\dot{\varepsilon}_k, T_k)\frac{\Delta\varepsilon_k}{\varepsilon_{max} - \varepsilon_{min}} \tag{178}$$

The MRA numerical integration method is illustrated by Figure 156. The MRA method is endorsed in RG 1.207, Rev.1 [77] as an acceptable approach for determining F_{en} values for complex plant transients.

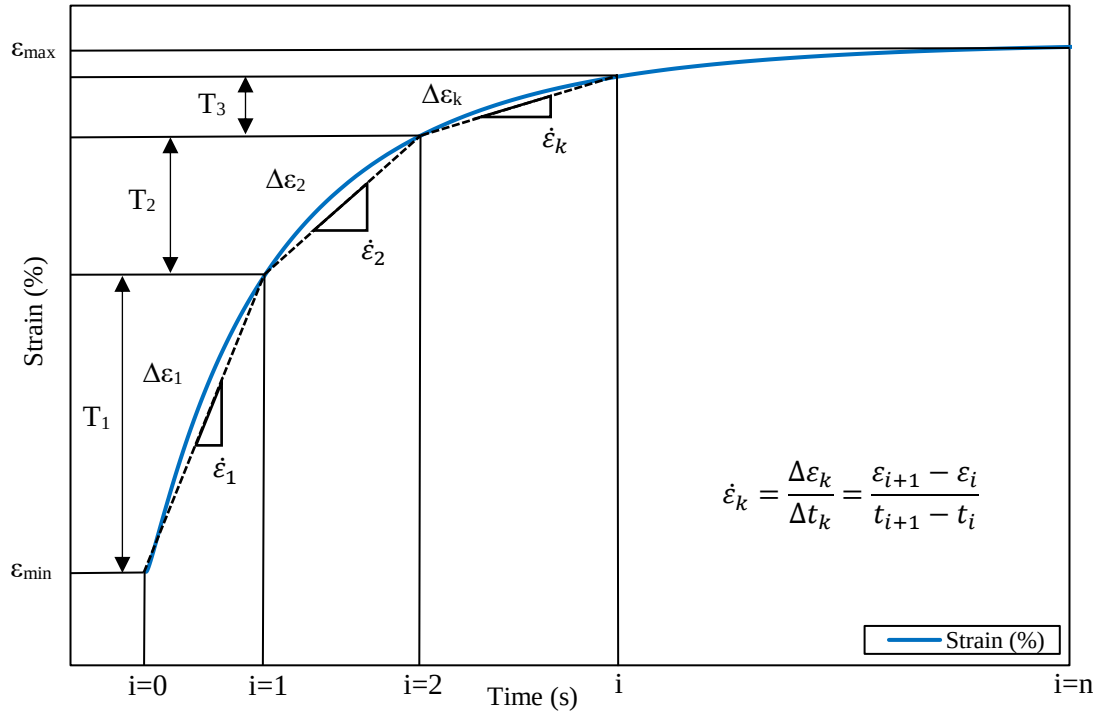

Figure 156. Numerical integration of F_{en} over rising portion of strain cycle.

More recently, a substantial and growing body of testing data has emerged for which the MRA does not perform well in predicting the observed difference in life for complex loading conditions where temperature and strain exhibit a phase difference, or where slow strain rate conditions are prevalent at the bottom of the strain waveform. To address this issue, Currie et al [192] examined alternative models for integrating the F_{en} through the cycle, including approaches which weight F_{en} increments depending on the position within the strain cycle. Currie et al proposed an alternative F_{en} integration approach termed the *Strain-life Weighted* (SNW) method, and demonstrated the improved accuracy of the approach compared to MRA based on additional validation test data [193]. The SNW method weights the F_{en} through the rising part of the loading cycle based on the instantaneous fatigue damage inferred from the strain-life curve for that part of the cycle. Thus, relative damage over the entire cycle is assumed proportional to the instantaneous fatigue life meaning that F_{en} conditions at the peak of the cycle are more significant than at the bottom, which is consistent with the power-law form of the strain-life curve. The general form of the SNW method utilises the Langer model described by Eq. (5), adopting the ANL mean model parameters reported in [72] with values of A, B, and C of 6.891, 1.92, and 0.112

respectively. This is equivalent to the transformed pseudo-stress-life model described by Eq. (32). Per Currie et al [193], the final form of the SNW weighting factor, *w*, is defined by Eq. (179) as the ratio of the fatigue life, N, corresponding to the cycle strain range, $\varepsilon_{max} - \varepsilon_{min} = \Delta\varepsilon = 2\varepsilon_a$, to the instantaneous fatigue life, N_{inst}, corresponding to the current strain range, $\varepsilon - \varepsilon_{min}$, within the rising portion of the cycle.

$$w = \frac{N}{N_{inst}} = exp\left(B \cdot ln\left(\frac{(\varepsilon - \varepsilon_{min}) - C}{(\varepsilon_{max} - \varepsilon_{min}) - C}\right)\right) \tag{179}$$

Thus, the effective $F_{en,eff}$ for the SNW method is obtained from Eq. (180) by numerical integration of the rising strain cycle (Figure 156) for the conditions stipulated below:

$$F_{en,eff} = \sum_{i=0}^{n-1} F_{en,i\rightarrow i+1} \cdot (w_{i+1} - w_i) \tag{180}$$

For $\varepsilon_i > (\varepsilon_{min} + C)$ and $(\varepsilon_{max} - \varepsilon_{min}) > C$:

$$w_i = exp\left(1.92 \cdot ln\left(\frac{(\varepsilon_i - \varepsilon_{min}) - 0.112}{(\varepsilon_{max} - \varepsilon_{min}) - 0.112}\right)\right) \tag{181}$$

For $\varepsilon_i \leq (\varepsilon_{min} + C)$ and $(\varepsilon_{max} - \varepsilon_{min}) > C$:

$$w_i = 0 \tag{182}$$

For $(\varepsilon_{max} - \varepsilon_{min}) \leq C$:

$$w_i = \frac{\varepsilon_i - \varepsilon_{min}}{\varepsilon_{max} - \varepsilon_{min}} \tag{183}$$

Figure 157 shows the shape of the SNW F_{en} weighting curve at various strain amplitudes compared to the MRA weighting curve, which gives equal weighting to all positions within the rising strain cycle.

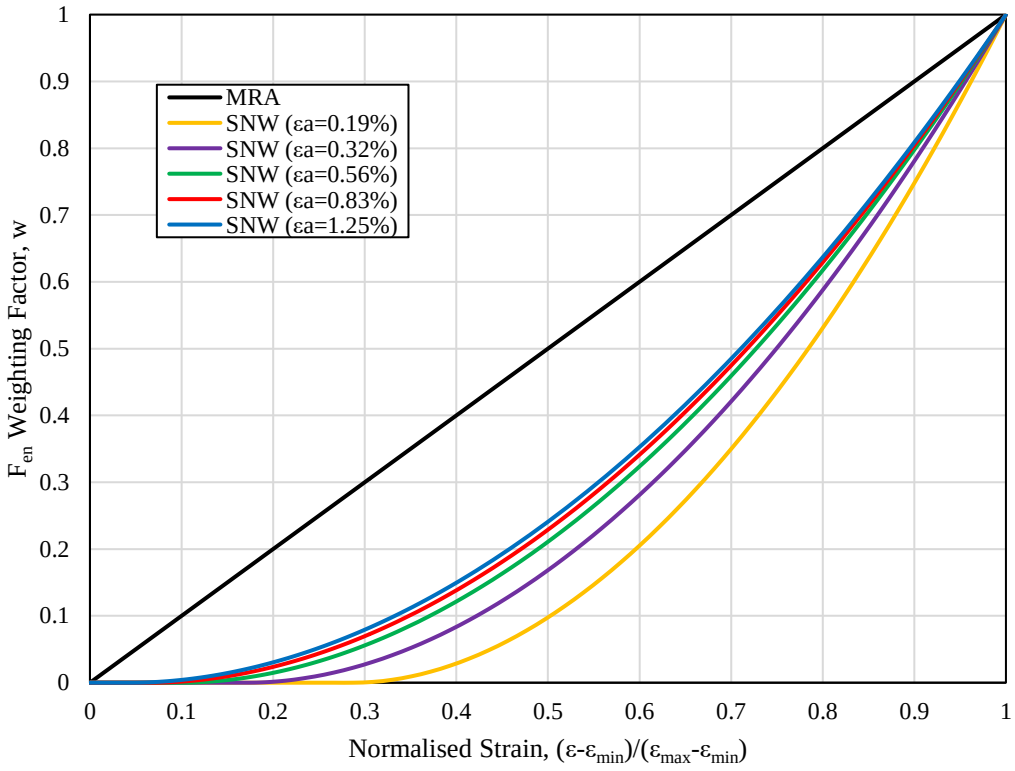

Figure 157. Comparison of MRA and SNW F_{en} weighting curves.

Note that in the final form of the SNW method shown above, the SNW weighting curve adopts a value of C reduced by a factor of two compared to ANL mean model, as this showed improved prediction accuracy for available test data. Thus, the implication is that for strain amplitudes less than 0.056%, the SNW method reduces to the MRA method. Whilst this is conservative, such low strain amplitudes are expected to contribute negligibly to total damage. The SNW method has since been formally proposed to the ASME WGEFEM as a draft Code Case (Record 19-702 [194]) which also includes guidelines on the post-processing of stress and temperature histories to facilitate its application.

To apply either the MRA or SNW approaches described above in a consistent fashion, a continuous, monotonically increasing strain history must be derived for each cycle. This strain history must be fully defined over the entire range from the transient minimum to the maximum and the range of this strain history must be equivalent to the pseudo-stress (or strain) range calculated for the cycle, after correcting for plasticity effects. However, it should be noted that two transient segments are

associated with each counted cycle: one associated with the time history values (stress, temperature, etc.) of the valley and the other is associated with the values of the peak. These can be portions of the time history of the same transient in the case of inside pairs, or of two different transients in the case of outside pairs. In the case of outside pairs, this can frequently give rise to situations where the history between the minimum and maximum is not fully defined due to a time discontinuity between the two transient segments (usually a gap or sub cycle/overlap). In such situations, a *Transient Linking* method must be employed to combine both segments into a single continuous history to determine strain rate and the related F_{en}. Recommended best practices for transient linking including the treatment of gaps and sub cycles are provided in the SNW draft Code Case [194].

Both the proposed F_g and SMN methods are fully compatible with the MRA and SNW F_{en} approaches, and the required strain history may be derived from the elastic stress history in the following steps:

1. The alternating stress intensity, S_{alt}, for the cycle is divided by the reference elastic modulus of the DFC to obtain the strain amplitude, ε_a. (Note that ε_a is the 'corrected' strain amplitude after accounting for plasticity).
2. The dominant stress component that most closely represents the loading history during the cycle is selected. Normally, this will be the hoop stress. However, if no single stress component is dominant, then signed stress intensity may also be used provided care is taken to smooth out oscillations in the stress history that may arise if the sign changes suddenly.
3. At each time point during the cycle, the selected stress value is divided by the elastic modulus corresponding to the instantaneous wetted surface temperature.
4. The total strain range, $\Delta\varepsilon$, is determined by the difference between the strain values at the start and end of the cycle.
5. At each time point in the cycle, the elastic strain history obtained in Step 3 is multiplied by twice ε_a, and divided by $\Delta\varepsilon$. The purpose of this final step is to correct the elastic strain history for plasticity to be consistent with the value of S_{alt} determined for the cycle. In this way, the difference between the maximum and minimum values within the strain history, $\varepsilon_{max} - \varepsilon_{min}$, is guaranteed to be exactly equal to $[(2 \cdot S_{alt}) / E_c] = 2\varepsilon_a$.

The above procedure is actually applicable irrespective of the plasticity correction method employed in the assessment, so long as it is capable of providing a single scalar value of S_{alt} in an equivalent manner to traditional ASME Code K_e factors. Both the F_g and SMN methods satisfy this requirement, and therefore their applicability to environmental fatigue assessments is confirmed.

8.5. Application to a Chemical & Volume Control System (CVCS) Nozzle

To demonstrate the potential improvements that may be achieved by adopting the proposed plasticity correction methods, this section presents a fatigue assessment using an example of a real world PWR plant. The component under consideration is a highly loaded nozzle from the Chemical and Volume Control System (CVCS) described by Rudolph et al [195].

8.5.1. Problem Description

The geometry of the CVCS nozzle is shown in Figure 158. The nozzle is fabricated from austenitic stainless steel SA 351 CF8A, which is the cast equivalent of Type 304 (18Cr-8Ni). The temperature-dependent thermal and mechanical properties for Type 304 defined in ASME Section II, Part D were adopted for this problem.

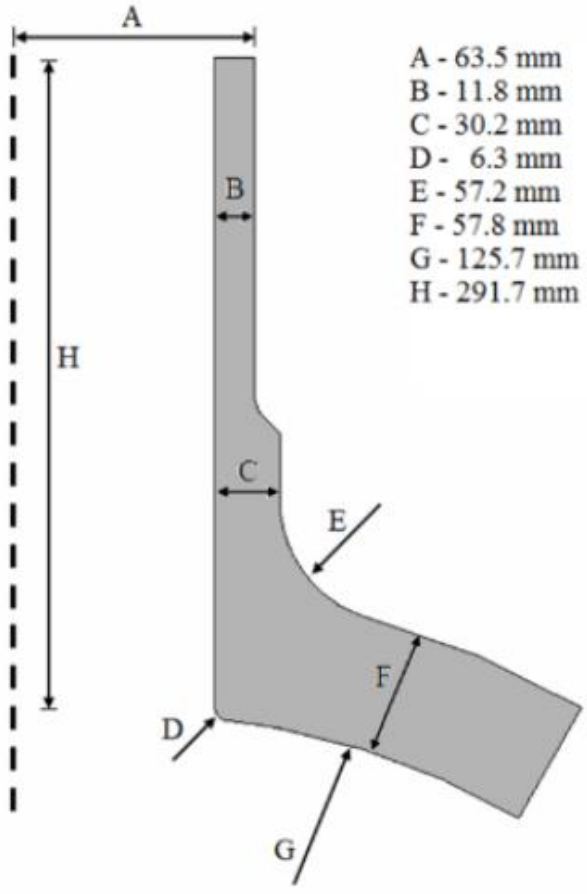

Figure 158. CVCS nozzle geometry (taken from PVP2015-45668 [195]*).*

A total of six design transients described in [195] were considered and are summarised in Figure 159. Four of the transients (T1D, T2D, T3D, and T5D) are characterised by sharp thermal shocks and are expected to occur infrequently (Service Level B). The other two transients (T6D and T7D) represent modest variations in temperature and arise due to daily changes in the power state of the plant (Service Level A). As discussed in [195], the stresses arising due to fluctuating pressure are not significant, and therefore transient variations in pressure are neglected herein. A constant HTC equal to 12kW/m^{2}K was adopted for the thermal analyses of all transients.

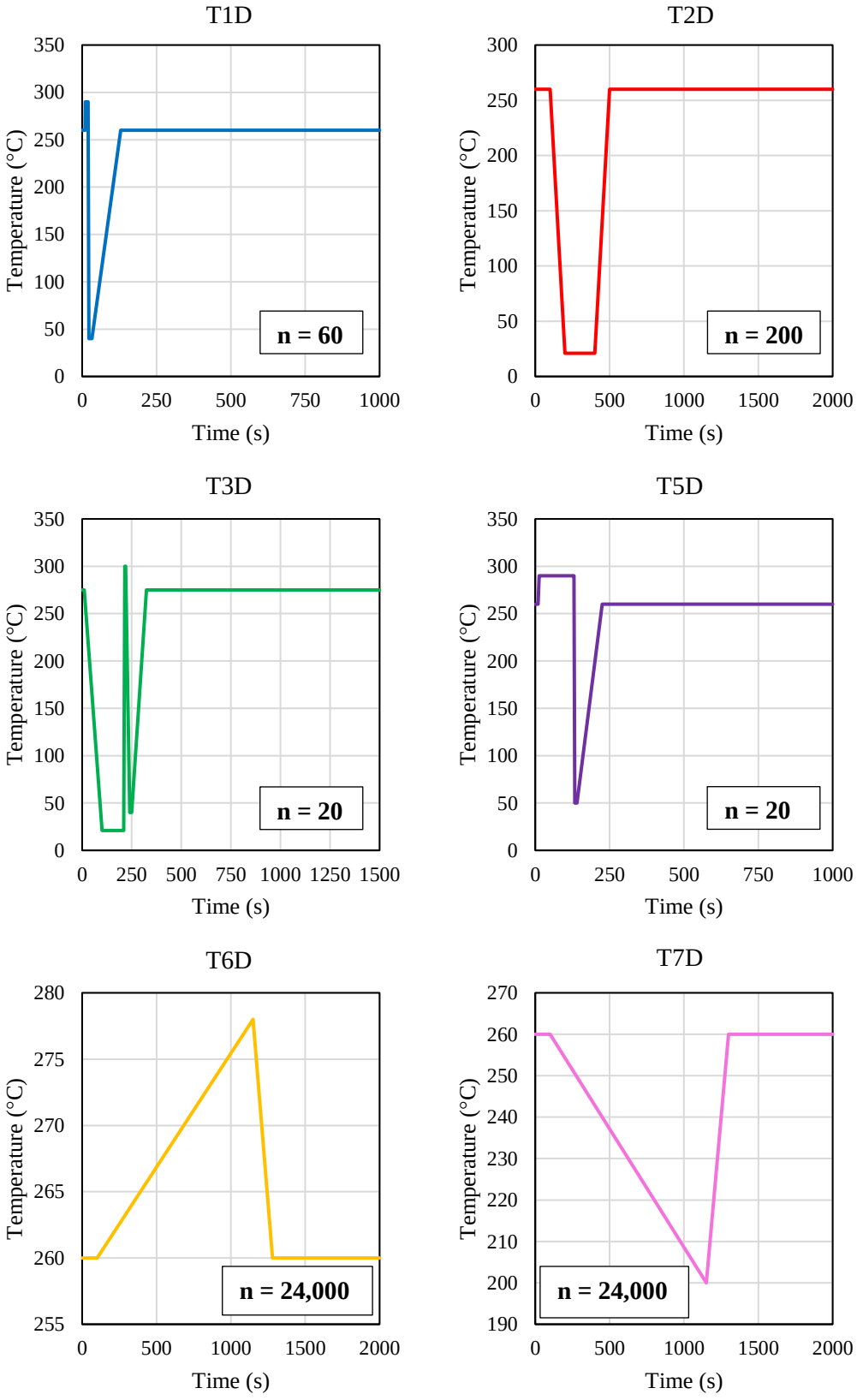

Figure 159. Design transients considered for CVCS nozzle.

8.5.2. Initial Appendix XIII-3520 Fatigue Evaluation

Initial Appendix XIII-3520 elastic fatigue analyses were conducted using the Appendix XIII-3450 K_e factor for the design transients specified in Figure 159. To establish the limiting locations for fatigue at which to position the SCLs, an initial scoping calculation was performed to determine the maximum value of $S_p/3S_m$ at every point in the nozzle, considering all design transients. The contours of $S_p/3S_m$ are shown by Figure 160. As can be seen, the maximum $S_p/3S_m$ occurs on the internal surface of the pipe and nozzle, and is particularly concentrated in the crotch region.

Figure 161 shows the final mesh adopted for the thermal and structural analyses of the nozzle. The mesh contained a total of 1764 quadratic, quadrilateral elements and 5525 unique nodal points. Twenty elements were adopted through-thickness of every section with element bias towards the internal surface to ensure that the surface stresses were accurately captured. In Figure 161, SCLs 1-5 represent the fatigue assessment locations identified based on the contours of $S_p/3S_m$ in Figure 160. The stresses extracted at these locations were used in the fatigue analysis.

Two calculation approaches were adopted for the Appendix XIII-3520 fatigue evaluation. The first assessment (Option 1) considered using conservative values of S_m and E_a, respectively calculated per Eqs. (52) and (53) based on the maximum temperature of the fatigue load pair. A subsequent assessment (Option 2) adopted less pessimistic values of S_m and E_a, which is permitted per Appendix XIII-3420 as secondary stresses arise only due to thermal loads in this problem. The stress differences were calculated according to Appendix XIII-2420. The stress intensity determined relative to the global extreme attained across all design transients was calculated and is shown in Figure 162 for SCL 3, which was found to be the fatigue limiting location.

To identify the peaks and valleys in the relative stress intensity history, a filtering algorithm was applied to eliminate any data that did not represent a turning point (Figure 163). The fatigue load pairs were then established by rearranging the peaks and valleys in order of decreasing S_p as shown by Figure 164. For each load pair, a conservative value of S_n was determined based on the methodology adopted in Section 3.3.3.3. Table 9 summarises the Appendix XIII-3520 fatigue assessment results

obtained at SCL 3 based on worst-case values of S_m and E_a. As can be seen, the CUF limit of unity is considerably exceeded and is attributed to the attainment of very high $K_e^{XIII-3450}$ values for the majority of fatigue load pairs considered. With some refinement in the analysis input assumptions, it is possible to reduce the CUF somewhat. Figure 165 summarises the CUF values calculated at each location based on Option 1 and Option 2 defined above. Adopting less pessimistic values of S_m and E_a enables a reduction in the maximum CUF by around 11% from 3.63 to 3.23. Other refinements are possible, such as adopting less pessimistic HTCs, though these are still unlikely to reduce the CUF sufficiently to achieve an acceptable result, which may therefore necessitate extensive and costly use of elastic-plastic FEA or a potential redesign of the nozzle. This emphasises the crucial need for an improved plasticity correction method for application to new designs.

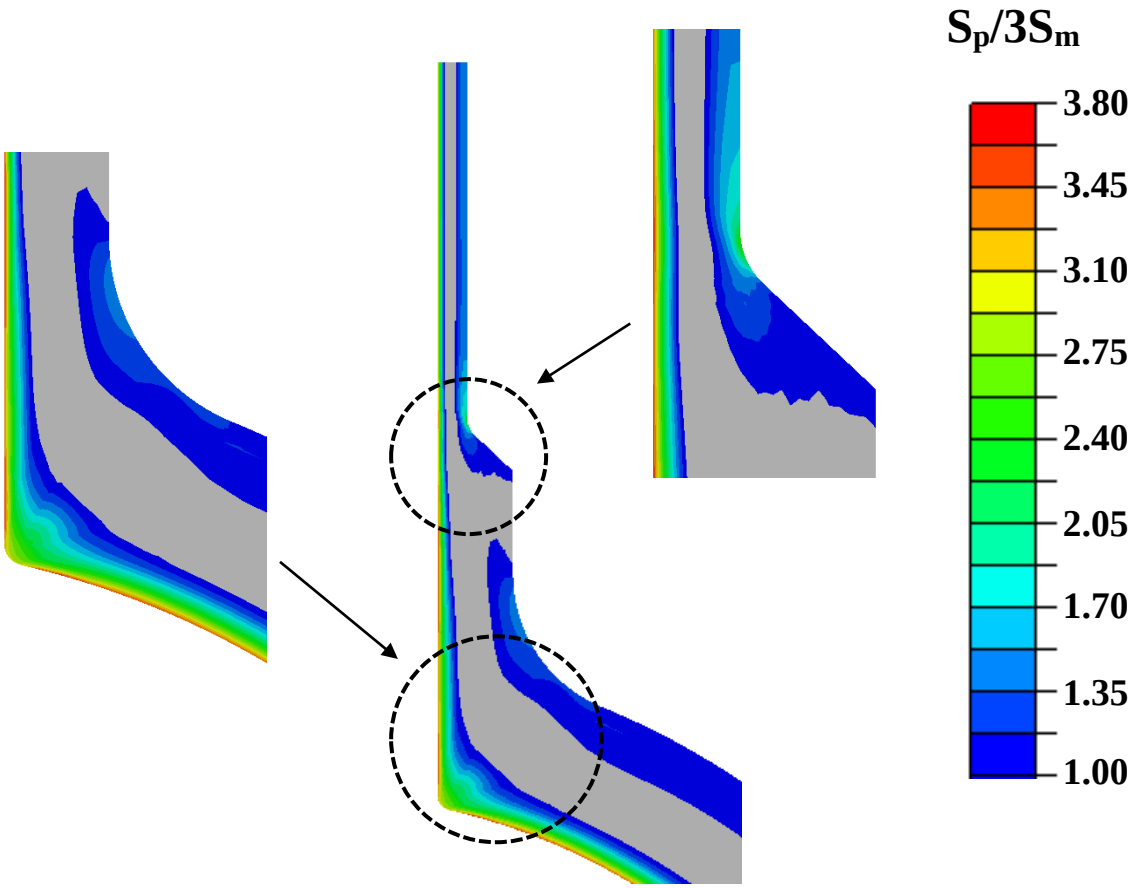

Figure 160. Contours of maximum $S_p/3S_m$ for CVCS nozzle.

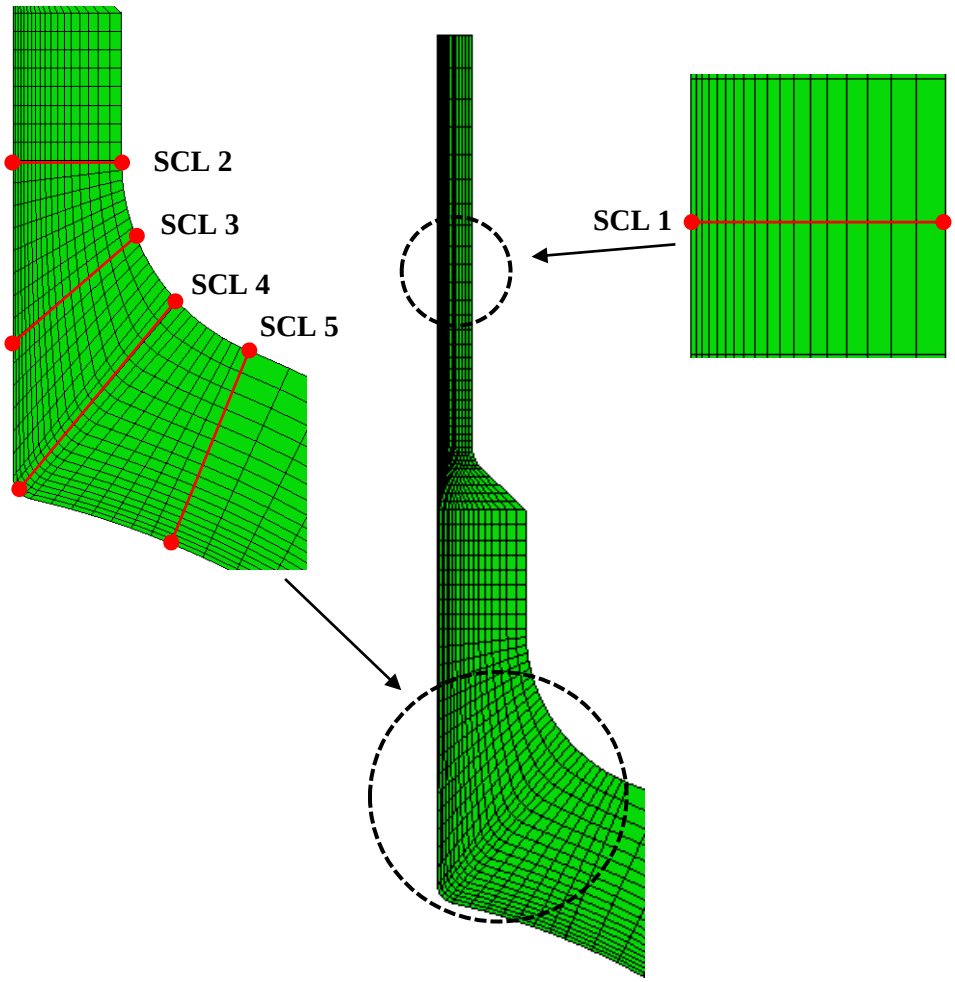

Figure 161. Finite element mesh of CVCS nozzle

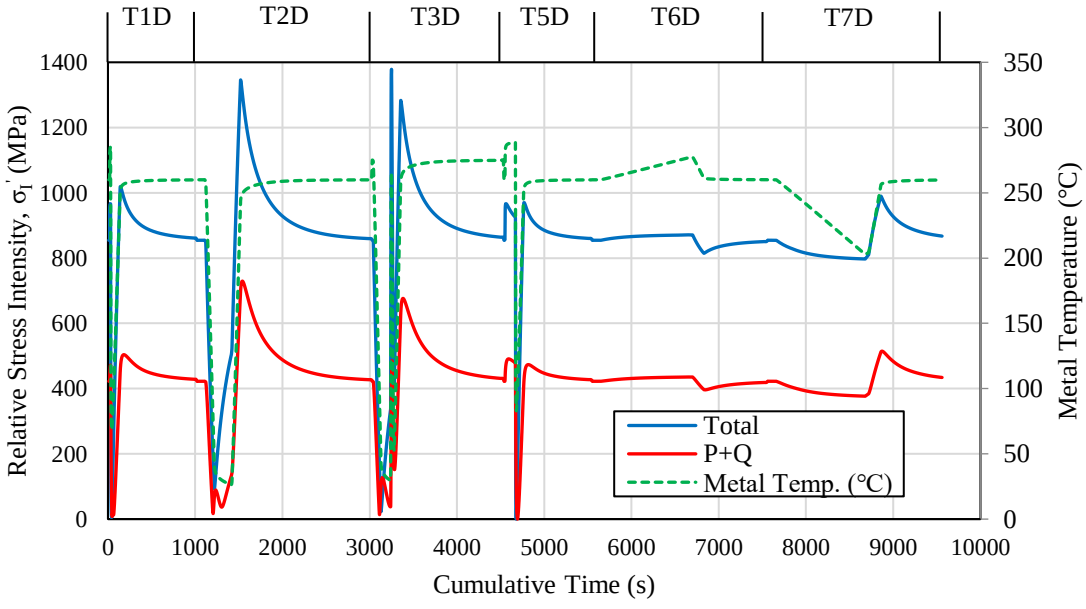

Figure 162. Relative stress intensity and metal temperature at SCL 3.

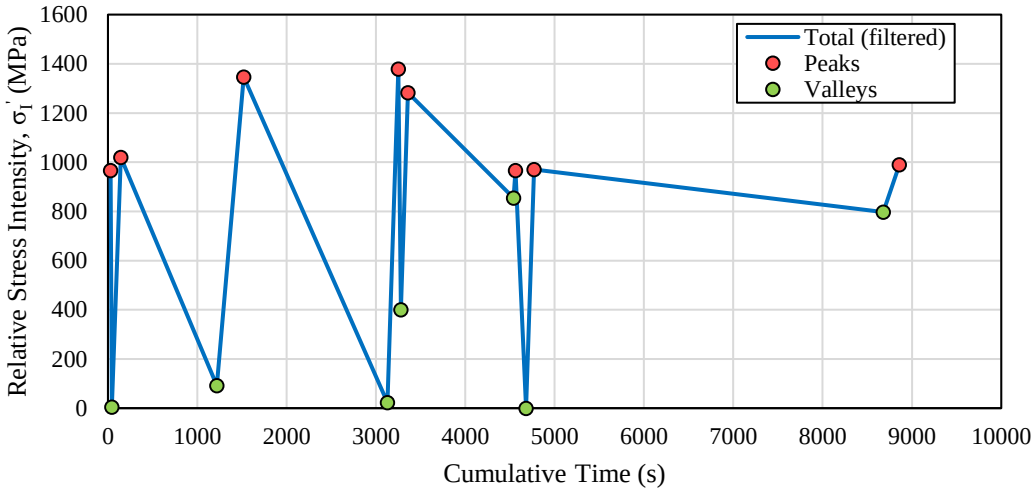

Figure 163. Relative stress intensity for SCL 3 after filtering and peak-valley identification.

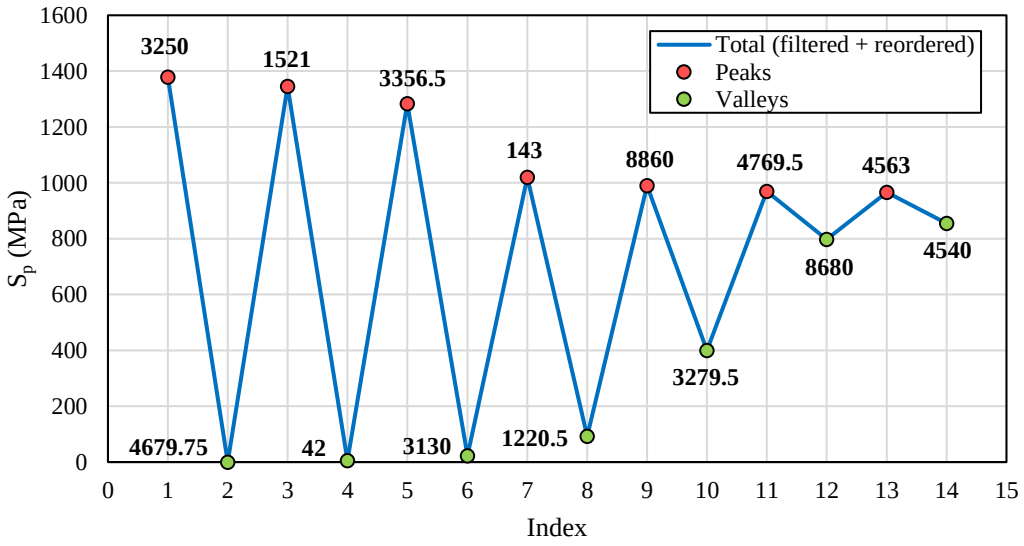

Figure 164. Reordered fatigue load pairs for SCL 3 with time points within real stress history labelled.

Table 9. Summary of Appendix XIII-3520 fatigue assessment results for SCL 3.

	$Tran^A$	$Time^A$	n^A	$Tran^B$	$Time^B$	n^B	S_p	S_n	S_m	K_e	S_{alt}	n^P	CUF
1	T3D^x	3250^x	20	T5D^x	4680^x	20	1379	485	120	2.155	1626	20	0.130
2	T2D	1521	200	T1D^x	42^x	60	1341	727	123	3.333	2428	60	1.055
3	T2D	1521	140	T3D^x	3130^x	20	1323	730	123	3.333	2396	20	1.355
4	T2D^x	1521^x	120	T2D	1221	200	1254	730	123	3.333	2271	120	2.960
5	T3D^x	3357^x	20	T2D	1221	80	1191	676	121	3.333	2170	20	3.203
6	T1D^x	143^x	60	T2D^x	1221^x	60	927	613	122	3.264	1650	60	3.607
7	T7D	8860	24000	T3D^x	3279^x	20	590	469	121	1.961	631	20	3.619
8	T7D^x	8860^x	23980	T7D	8680	24000	193	138	121	1.000	112	23980	3.630

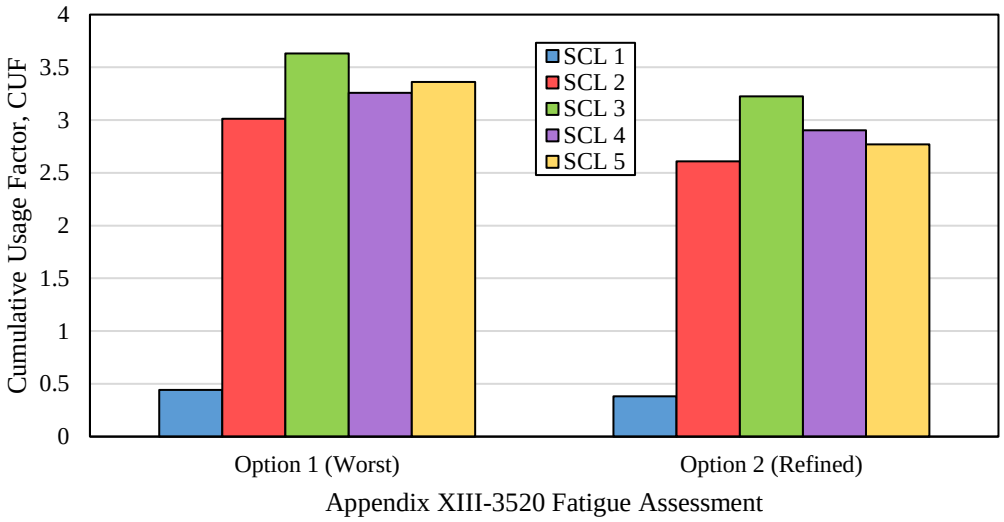

Figure 165. Summary of baseline CUFs calculated per Appendix XIII-3520 depending on calculation option.

8.5.3. Refinement of Plasticity Corrections

The initial Appendix XIII-3520 fatigue assessment yielded a best-case CUF of 3.23 after adoption of realistic material properties. A further refinement was therefore performed using the F_g and SMN methods proposed in Sections 8.2 and 8.3, respectively. In performing the calculation based on SMN, κ was calculated according to Eq. (176); the fixed value of κ=1.6 proposed by Shimakawa [188] was also adopted for comparison. The proposed plasticity correction methods were applied based on von Mises theory.

The PCFs calculated at each location for all applicable fatigue pairs are summarised in Figure 166 with respect to S_n/S_m. The proposed approaches are significantly less pessimistic than $K_e^{XIII\text{-}3450}$. In this case, the F_g and SMN proposals produce similar results in the range of $S_n < 5S_m$, beyond which F_g exhibits greater conservatism due to the formulation of F_e. It can be seen that in some situations the SMN predicts a K_e factor of 1.0 despite $S_n > 3S_m$; it is possible for S_n to be greater than S_p in situations where the stresses reverse rapidly. Thus, F_g predicts plasticity in such cases, despite S_p actually being less than $3S_m$. Nevertheless, this highlights a potential consequence of the EVP cycle counting adopted by the Code, and the conservativism inherent in the approach used to calculate S_n.

The SMN approach adopting κ=1.6 produced corrections that were either slightly more, or less, conservative than those obtained from realistic calculation of κ per Eq. (176), depending on the severity of S_p. The differences between both approaches are illustrated in Figure 167, which shows the predicted SRL points for each fatigue load pair. Adopting the more realistic value of κ gives slightly higher corrections for modest S_p, whilst predicting lower corrections at higher S_p. This represents a more accurate description of the true elastic-plastic response of the CVCS nozzle than adopting κ=1.6, which assumes large elastic follow-up.

The CUFs calculated at each location are summarised in Figure 168 for each calculation approach. As shown, the adoption of the advanced F_g and SMN plasticity correction methods in the refined calculations results in a dramatic reduction in the CUFs. The maximum CUFs calculated for the F_g, SMN (variable κ), and SMN (κ=1.6) were found to be 0.570, 0.567, and 0.660, respectively. This represents an approximately five-fold reduction in conservatism compared to the initial assessment performed using the Appendix XIII-3450 K_e factor. All however predict the critical location to be at SCL 5, on the shell side of the nozzle crotch, whose fatigue load pairs experienced higher values of S_p on average. Thus, peak strain concentration was deemed the limiting factor for fatigue rather than sectional plasticity implied by Appendix XIII-3450. The CUFs determined based on F_g and SMN (κ=1.6) were found to be very similar, with the exception of the nozzle crotch corner, where the SMN method predicts a CUF that is 22% lower than F_g. The F_g approach predicts higher damage at this location since it is controlled by F_e, which is a function of S_n and is found to be much higher at this location. However, as previously highlighted from the elastic-plastic FEA results presented in Sections 5.4 and 7.3, strain concentration at the nozzle crotch corner is attributed mainly to peak stresses and is lower than other locations. Thus, the CUFs calculated by the SMN approach are more consistent with the observations from elastic-plastic FEA. In general, the SMN approach is expected to yield better accuracy, especially in situations of peak strain concentration, where traditional S_n-based methods may struggle to reflect the actual elastic-plastic response of the material. It is therefore expected to be well suited to assessing complex geometries including 3D FE models, where traditional approaches relying on stress linearisation may encounter difficulty. Overall, the F_g and SMN methods enable a

more appropriate evaluation of the CUF, whilst retaining a reasonable level of conservatism compared to elastic-plastic FEA.

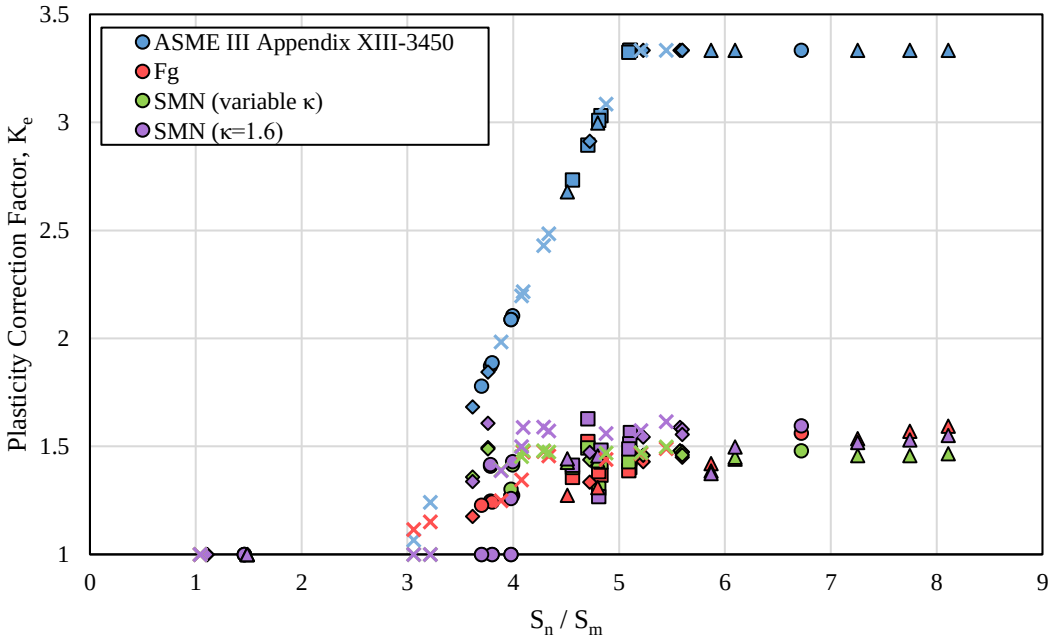

Figure 166. Comparison of K_e factors calculated for CVCS nozzle considering all fatigue load pairs.

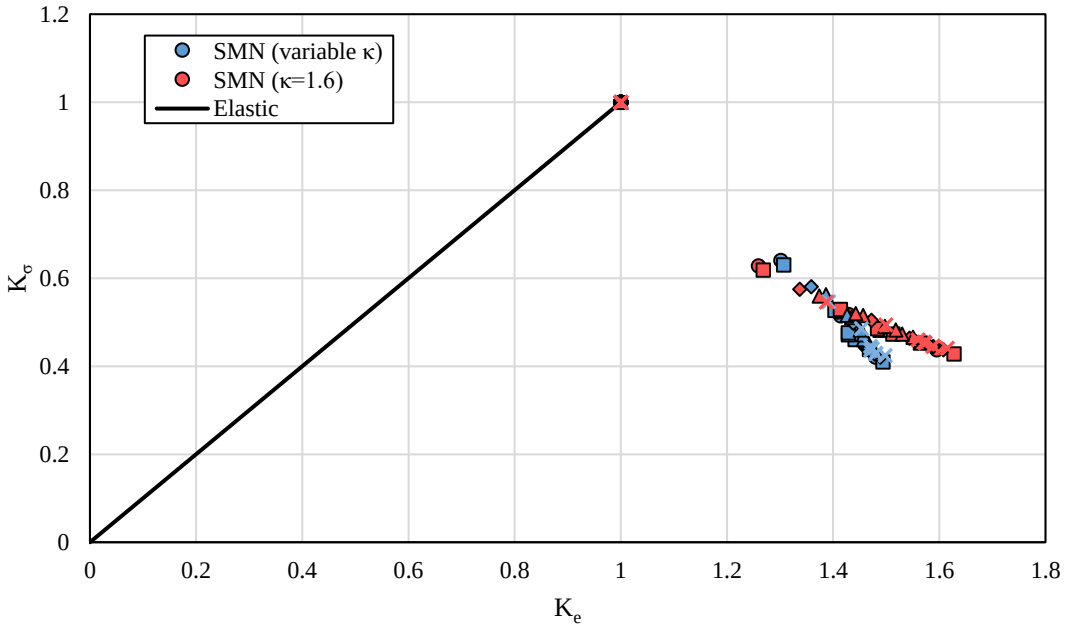

Figure 167. Comparison of the SMN plasticity corrections obtained for the CVCS nozzle.

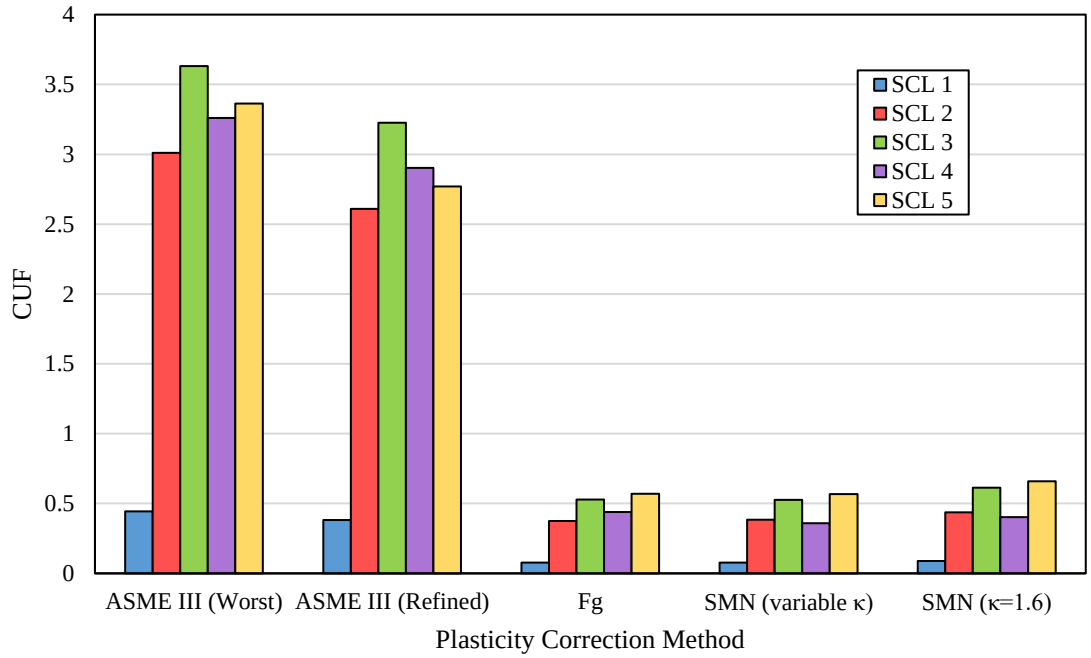

Figure 168. Summary of CUFs after refinement of plasticity corrections.

8.5.4. Environmental Fatigue Assessment

The final calculation of environmentally assisted fatigue usage (CUF_{en}) was performed considering both the existing ASME III Appendix XIII-3450 K_e methodology and the proposed F_g and SMN plasticity correction methods. The assessment adopted the F_{en} correlations defined in NUREG/CR-6909 Rev. 1 for austenitic stainless steels. The strain history for each fatigue load pair was derived based on the dominant stress component for each fatigue load pair using the approach described in Section 8.4. Discontinuous transient segments associated with outside fatigue pairs were post-processed in accordance with the guidance provided in [194]. To enable a suitably refined integration of F_{en} for each fatigue load pair, linear interpolation and insertion of additional points was performed to restrict the temperature difference between successive time points to be ≤ 5°C.

Whilst it is acknowledged that the location of highest CUF might not necessarily correspond to the location of CUF_{en}, this represents a very small minority of cases since K_e generally has a much more significant effect on cumulative fatigue damage than does F_{en} [196]. In this case, SCL 3 was also found to be the location of highest

CUF_{en}, when considering the $K_e^{XIII-3450}$ and adopting worst-case values of S_m and E_a. Therefore, for the sake of brevity, only the results obtained at SCL 3 are discussed here.

Figure 169 (a) and (b) shows the effective environmental fatigue penalty ($F_{en,eff}$) factors calculated respectively for each fatigue load pair using the MRA and SNW approaches, with consideration of the adopted plasticity correction method. Generally, the MRA method was found to produce $F_{en,\,eff}$ values that were between 20-60% higher than the SNW method, irrespective of the plasticity correction method employed. The use of a less conservative plasticity correction method results in a corrected strain history with a lower average strain rate for which numerical integration of F_{en} is to be performed. Consequently, applying the MRA method in conjunction with the proposed F_g and SMN methods always results in a higher $F_{en,\,eff}$ up to a maximum of 13% compared with the use of the more conservative $K_e^{XIII-3450}$. On the other hand, the differences in $F_{en,eff}$ for the most severe fatigue load pairs are generally much smaller (within 5%) when applying the SNW approach, and it is not necessarily the case that the F_g or SMN plasticity corrections will result in a higher $F_{en,eff}$. In particular, for situations where a significant portion of the corrected strain history derived using the F_g or SMN methods fell below (ε_{min} + 0.112%), and was therefore associated with a SNW weighting factor of zero ($w_i = 0$), this yielded a lower $F_{en,eff}$ compared to the use of the $K_e^{XIII-3450}$. The effect of the plasticity correction method on $F_{en,eff}$ calculated using the SNW approach is therefore very much dependent on the characteristics of stress and temperature history.

The final CUF_{en} calculated at SCL 3 is summarised in Figure 170 for each plasticity correction and F_{en} integration approach. The calculation using $K_e^{XIII-3450}$ in conjunction with the MRA F_{en} method yields very pessimistic CUF_{en} values of 10.10 or 9.08 depending on whether worst-case or refined values of S_m and E_a are adopted. The CUF_{en} calculated for the F_g, SMN (variable κ), and SMN (κ=1.6) were found to be 1.615, 1.612, and 1.859, respectively when utilising the MRA F_{en} method. Applying the SNW method instead of MRA was found to reduce the CUF_{en} significantly, by approximately 39% in the case of the traditional ASME III approach using $K_e^{XIII-3450}$, and between 47-50% for the F_g, SMN (variable κ), and SMN (κ=1.6) methods. This

suggests that greater benefits may be achieved from the use of improved plasticity correction methods in combination with the more realistic SNW F_{en} approach, owing to their observed synergy for this problem case; this however remains subject to further validation considering a wider range of plant representative transients. When applying the SNW method, the final CUF_{en} calculated for the F_g, SMN (variable κ), and SMN (κ=1.6) were found to be 1.084, 1.080, and 1.256, respectively. This represents a six- to seven-fold reduction in CUF_{en} between compared to the use of $K_e^{XIII-3450}$.

Whilst CUF_{en} still very slightly exceeds the Appendix XIII-3520 (e) limit of unity using the proposed F_g and SMN methods in this case, the expectation is that only very minor analysis refinements would be necessary to yield acceptable results. One possibility is to establish more realistic HTCs and/or thermal ramp times for the most severe transient(s). Another option is to remove some of the conservatism associated with PTP cycle counting, in which sub-cycles are allowed to cross-combine between transients (i.e. outside fatigue pairs). One method of achieving this has been proposed by Rawson and Rice [197] and involves performing rainflow cycle counting for all possible transient pairings, and combining these pairings on an order of decreasing contribution to fatigue usage. Thus, the potentially time-consuming exercise of performing multiple elastic-plastic FEA to further refine individual fatigue load pairs is no longer necessary. The results of the refined calculations presented herein therefore demonstrate the considerable benefit in both accuracy and efficiency that may be achieved through the adoption of more realistic plasticity correction methods for austenitic stainless steel components.

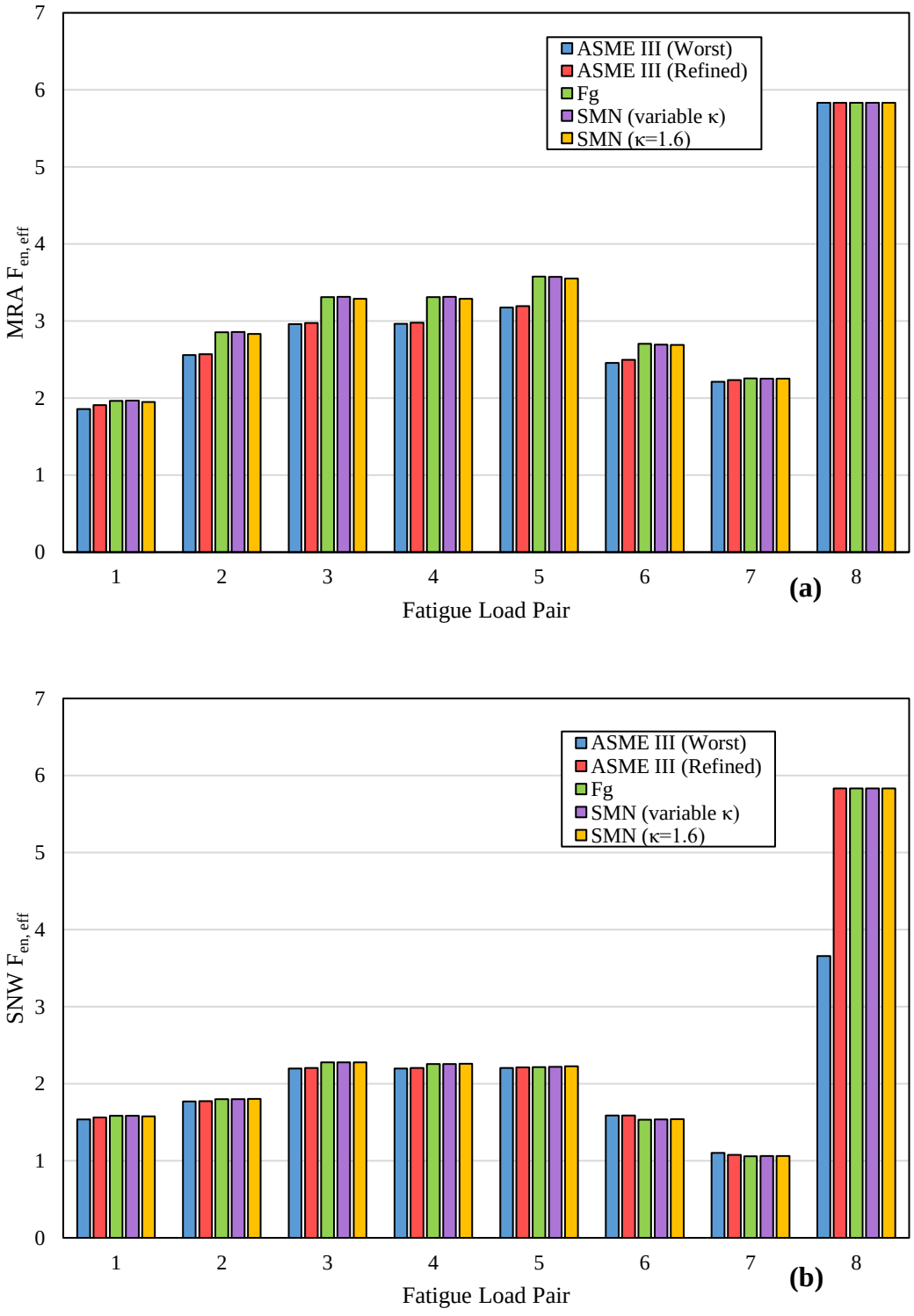

Figure 169. Comparison of $F_{en,\,eff}$ calculated at SCL 3 for all fatigue load pairs. (a) MRA; (b) SNW

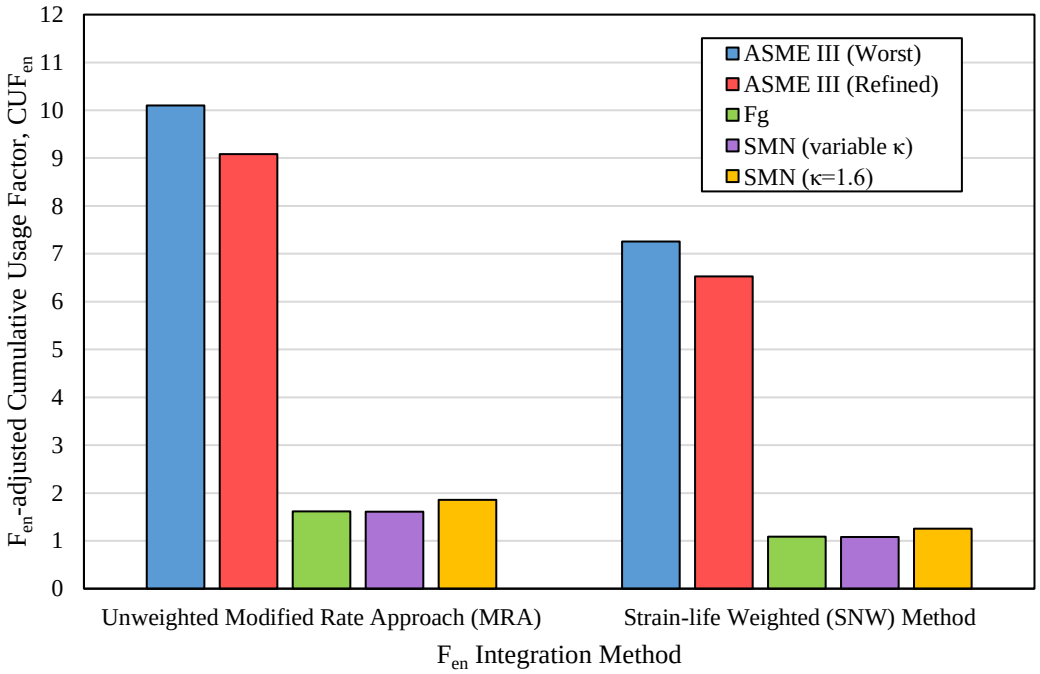

Figure 170. Final CUF_{en} calculated at SCL 3 considering F_{en} integration method.

8.6. Discussion

A brief discussion of further important considerations pertinent to the proposed plasticity correction methods is provided here.

8.6.1. Industry Application

Both the F_g and SMN approaches have been demonstrated to be practical tools for Code fatigue assessment, with the ability to incorporate environmental effects. The question of which approach to adopt will ultimately dictated by the problem statement, work schedule, and the quality of information available to the analyst. The F_g approach is likely to be more appropriate for routine design calculations as it does not require any additional information beyond that required in ASME III; elastic-plastic material properties are not needed. Thus, it may be easily substituted in place of $K_e^{XIII\text{-}3450}$ when performing traditional ASME III-type design fatigue calculations.

The SMN method does however possess some distinct advantages over the F_g approach which may extend its usefulness to other applications beyond traditional Code fatigue assessments. First, the SMN method is considerably more efficient to

apply than the F_g method (and ASME III K_e), as it does not require stress linearisation. Linearisation of stresses at every time step constitutes a major computational expense associated with the traditional ASME III approach, and consequently the analysis time savings achievable from using the SMN method are very significant, by at least one to two orders of magnitude when performing calculations using a programming language such as Python. Furthermore, the relative savings on analysis time from using the SMN method increase with the size of the problem; for instance, where many SCLs must be assessed and/or there are a very high number of fatigue-relevant transients. The SMN method therefore has the potential to reduce analysis conservatism in these situations, as it may obviate the need to conservatively group transients due to the overall analysis costs being far more manageable.

Secondly, as it does not require linearised stresses, the SMN approach can be applied without the need for SCLs. This approach therefore offers the potential of a fatigue assessment of an entire component to be undertaken, often referred to as an *SCL-free fatigue assessment*, producing values of CUF_{en} at every surface node of an FE model. These contours of CUF_{en} would provide a greater awareness of locations of high environmental fatigue damage, eliminating analyst judgement in determining suitable SCL locations *a priori*. Additionally, this approach could yield useful information to be utilised in the crack growth stage of a total life assessment. An important input to the crack growth assessment is the crack aspect ratio at initiation. This could potentially be estimated by examining contours of CUF_{en} on the surface of the FE model, where $CUF_{en} > 1.0$ may equate to an initiated crack of known depth consistent with the adopted strain-life curve (e.g. 250 μm). The contours may be used to visualise the extent of damage at a critical location to estimate an aspect ratio with the initiation crack depth for input to a subsequent crack growth assessment.

Finally, owing to its aforementioned computational efficiency, the SMN approach could also be well suited to probabilistic treatment of surrogate models (e.g. response surfaces fitted to structural FE models) for fatigue initiation assessment using the Monte Carlo method. A Design of Experiments approach may be adopted whereby an optimal matrix of input parameters (e.g. geometric dimensions, loads, HTCs, material properties, etc.) can be established for the relevant structural FE model or sub-

structure. The data generated from the matrix of FE runs yields information on the relative influence of the various input parameters on the response parameters of interest (e.g. stress, strain, temperature, etc.) which can then be used to define a response surface representation of the FE model. The response surface can then be rapidly solved for a large number of trials each with randomly sampled input variables to converge on the probability of fatigue crack initiation for a given component.

However, whilst the potential industrial applications are promising, some limitations of the proposed methods must first be addressed through further validation studies. To conclude, the current limitations that are necessary to address in future are briefly summarised.

8.6.2. Limits to Applicability

As discussed in Section 8.1, the F_g and SMN methods proposed in this work are intended to be applicable to austenitic stainless steel material used in Section III, Division 1, Class 1 Vessels (NB-3200), Supports (NF-3000), and Piping (NB-3600). However, they are not applicable to austenitic stainless steel bolting. The S_m values for bolting materials used in Class 1 construction are provided in ASME II, Part D, Table 4, and their variation with temperature differs considerably to those of Table 2A. Therefore, the application of these methods to bolting materials could be potentially non-conservative and will require further validation.

The elastic-plastic FE analysis results underpinning the F_g and SMN methods were obtained exclusively from 2D axisymmetric FE models. Therefore, the validity of both approaches has currently only been demonstrated for application to 2D axisymmetric analysis. Due to advances in computing power and storage capabilities, it is now more practical to undertake FE stress analysis of complex 3D models. Further validation is however required to confirm that both approaches remain reliable when applied to 3D FE models. In the case of the F_g approach in particular, the assessment of 3D geometries introduces some additional challenges due to its reliance on stress linearisation. The application of stress linearisation to elastic FE stress results from complex 3D models is not straightforward, and can be subjective in certain situations. The assessment of 3D structural discontinuities (e.g. nozzle crotch region) can be particularly challenging using these techniques. It is therefore expected that the SMN

method would be better suited to the assessment of complex 3D geometries, being that it only relies on the stress state at a discrete point and has been found to characterise peak strain concentration more accurately for the 2D structures considered in this work.

It should also be noted that the FE case studies analysed in this work considered predominantly thermal transient loading. Whilst mechanical stresses do fluctuate in LWR components, for example due to variations in the primary circuit internal pressure, these stresses are often very small compared to the thermal stresses. Furthermore, with the exception of plant heatup/cooldown and hydrotest transients, pressure-induced stresses are not expected to vary significantly for the majority of Level A and B transients. Therefore, it is concluded that the F_g and SMN methods would remain applicable to the assessment of combined thermal-mechanical loading cycles that might realistically be experienced in LWR plant components.

9. Conclusions

The outcomes of the research programme presented in this thesis include:

1. A comprehensive survey of simplified elastic-plastic analysis methods based on elastic DBA has been conducted, considering both ASME Section III and other nuclear and non-nuclear design and construction codes. The technical basis for each approach has been evaluated and key differences in design philosophy identified.
2. A framework for determination of PCFs, K_e^{FEA}, from elastic-plastic fatigue analysis has been proposed for austenitic stainless steels. Due consideration was paid to the choice of cyclic stress-strain data, cyclic plasticity model, and effective multiaxial strain measure.
3. An extensive programme of elastic-plastic finite element fatigue analyses has been performed for a selection of LWR plant representative austenitic stainless steel components to derive realistic PCFs, K_e^{FEA}. The FE-derived K_e^{FEA} data was used to benchmark the predictive capability of existing Code methods based on elastic DBA.
4. Two new approaches, the *Global Plasticity Correction Factor* (F_g) and *Stress-Modified Neuber* (SMN) methods have been proposed. Both methods have been demonstrated to give a more appropriate evaluation of component fatigue usage compared to ASME III Appendix XIII-3450.

The following conclusions are drawn from the research findings:

1. The investigation of simplified elastic-plastic analysis methods show that there are considerable differences in the methodology and technical basis underpinning the various Code K_e factors. The main findings concerning austenitic stainless steels are:
    a. The ASME III Appendix XIII-3450 K_e factor is considerably more conservative than other code K_e factors.
    b. ASME Code Case N-779, which is currently the only alternative to Appendix XIII-3450, is complicated to apply and requires additional parameters, which have thus far limited its applicability.

c. The approach originally proposed by Ranganath [128], which has recently been approved for publication as an ASME Section III Code Case (Record 17-225), is identified as more practical alternative to Code Case N-779. The final form of Ranganath's method proposed in Record 17-225 [132] incorporates an additional notch factor, K_n^R, which was identified as a possible source of unnecessary conservatism. Further validation of K_n^R was adopted as one objective within this thesis.

d. The formulation of the Poisson's ratio correction factor, K_v, adopted within different Codes, is found to be inconsistent. It has been shown that K_v tends to a theoretical maximum of 1.4, irrespective of the yield theory adopted. Some C&S such as RCC-M and ASME VIII-2 Div. 2, Annex 5-C, have been found to adopt a more pessimistic interpretation of K_v, derived based on the proposal by Moulin and Roche [112]. This interpretation is however not physically correct, as it does not adopt a consistent definition of the effective Poisson's ratio.

e. Most methods demand S_n and therefore necessitate stress linearisation. Some methods such as R5 and AD 2000-Merkblatt demand only S_p and are concluded to be more practical for fatigue analysis.

2. The proposed framework for direct calculation of K_e^{FEA} for austenitic stainless steel components by elastic-plastic fatigue analysis considered three important factors. First, the derivation of a cyclic SSC from suitable data available for austenitic stainless steels; secondly, the definition and calibration of a cyclic plasticity model for implementation within FE software; finally, the choice of a suitable effective strain measure for characterisation of fatigue damage under multiaxial loading. The main features incorporated within the proposed framework are as follows:

   a. A large database of publically available cyclic stress-strain data for austenitic stainless steels obtained from the technical literature has been compiled and evaluated. The cyclic SSCs proposed in NUREG/CR-5704 for Type 304 material were examined and validated against a larger body of data available for Type 304 in the annealed condition at

test temperatures below 430°C and 95% confidence limits were established based on K^c. The NUREG/CR-5704 Type 304 cyclic SSCs were concluded to be suitable for general elastic-plastic fatigue analysis. The use of the mean cyclic SSCs, rather than 5% lower bound, has been found to be reasonable since it is consistent with the fatigue design philosophy of the Code.

b. A comparison has been performed between the mean NUREG/CR-5704 Type 304 cyclic SSCs and those prescribed in ASME VIII, Div. 2 and RCC-MR codes and the cyclic SSCs predicted from MMUS. The NUREG/CR-5704 cyclic SSCs were shown to be more conservative than the other cyclic SSCs. Additionally, the other cyclic SSCs were shown to reflect poorly the hardening rate exhibited under uniaxial strain cycling tests. The design code cyclic SSCs are concluded to be potentially non-conservative and therefore inappropriate for evaluation of K_e^{FEA}.

c. The constitutive model of Chaboche has been adopted for elastic-plastic FE implementation owing to its ability to simulate kinematic hardening accurately. The calibration and optimisation of the model parameters has been demonstrated and validated by elastic-plastic FEA of a single element incremental step test.

d. The most appropriate choice of effective multiaxial strain measure for fatigue analysis was investigated by survey of the technical literature and a numerical case study on a PWR auxiliary piping nozzle. The effective octahedral shear strain range (EOSR) has been shown to be the most accurate and practical of the strain measures considered in this study for calculation of K_e^{FEA} and proposed for general application.

3. A series of elastic-plastic FEA analyses of LWR plant representative components subjected to representative design thermal transients were performed to establish accurate K_e^{FEA} factors for austenitic stainless steels. The performance of the various code-based K_e factors calculated based on elastic DBA were evaluated relative to the actual K_e^{FEA} factors to establish the advantages and limitations of each approach. The conclusions of this study are:

a. The actual K_e^{FEA} factors established by elastic-plastic analysis have been shown to be significantly less pessimistic than implied by the ASME III Appendix XIII-3450 K_e equations. Considering all elastic-plastic FE models, the K_e^{FEA} factors were shown to vary up to maxima of 1.54 and 1.85 for unnotched and notched assessment locations, respectively.
b. In situations where S_n exceeded $3S_m$, $K_e^{XIII-3450}$ has been shown to be conservative between a factor of 2.2x and 3.0x for unnotched locations, and 1.8x and 2.4x for notched locations. Where S_n is slightly less than $3S_m$, $K_e^{XIII-3450}$ could potentially under predict the elastic-plastic strain range by up to 35%.
c. CC N-779 has been shown to produce slightly non-conservative results for unnotched assessment locations, up to around 20%. CC N-779 was found to exhibit very poor performance for assessing notched geometries, producing results that were consistently non-conservative by around 30%. CC N-779 was concluded to be generally inadequate and is not recommended.
d. Ranganath's method was shown to perform reasonably well in most situations involving unnotched assessment locations, producing results that were generally conservative between a factor of 1.1x and 1.6x for S_n exceeding $3S_m$. Ranganath's method was however shown to produce slightly non-conservative results for sharp notches in absence of an additional notch correction. Following inclusion of the notch factor, K_n^R, Ranganath's method was shown to be conservative between a factor of 1.3x and 1.9x for all notch sizes. It was recommended that greater flexibility should be afforded to the analyst in determining the applicability of K_n^R to limit unnecessary conservatism in the approach. A potential ambiguity within Ranganath's approach was identified and a recommended calculation approach was justified to avoid this possibility. The final form of Ranganath's method proposed in Record 17-225 is concluded to be appropriate and the results presented in this

thesis strongly support its application as a less conservative alternative to the existing Appendix XIII-3450 methodology.

e. The performance of K_e factors adopted by other C&S and proposed by industry were also evaluated. It was shown that the corrections based wholly or partially on S_p generally produced more accurate results, of which the AD 2000-Merkblatt, R5 K_v, and Rolls-Royce F_u methods were found to be the most consistently accurate. Out of the approaches based on S_n only, the RCC-M B-3234.6 methodology was concluded to be the best method, producing results that were consistently conservative by between a factor of 1.1x and 1.4x. The JSME method was found to be excessively conservative for plane unnotched sections, but was concluded to be a very viable approach for the assessment of notched sections.

4. The two alternative plasticity correction approaches proposed in this thesis, the F_g and SMN methods, have been validated based on the compiled K_e^{FEA} data obtained from all elastic-plastic FE analyses performed in this work. Both approaches have been shown to be compatible with basic ASME III stress quantities and straightforward to implement. The basic features of each approach are:

    a. The F_g approach is based on both S_p and S_n and is defined so as to bound the K_e^{FEA} factors obtained across all FE models. The F_g approach is considerably less conservative than the existing Appendix XIII-3450 K_e approach. The F_g approach is applicable to both unnotched and notched geometries. The conservatism of the F_g approach has been shown to be limited to a maximum of 40% and 50% for unnotched and notched geometries, respectively.

    b. The SMN approach depends on S_p only and therefore does not require stress linearisation. The SMN approach does however require knowledge of cyclic stress-strain properties. The SMN approach is based on the SRL concept and aims to replicate the SRL behaviour of the component via a modification to the Neuber hyperbola. This modification is implemented using an adjustment factor, κ, applied to

the plastic term of the cyclic R-O relation, which has been shown to vary as a function of the load level. For typical structures known to exhibit low to moderate elastic follow-up, this behaviour has been represented by a conservative relation between κ and S_p/S_m, appropriate for design applications. For structures exhibiting large elastic follow-up, $\kappa = 1.6$ is concluded to be more appropriate and has been shown to modestly bound the elastic-plastic FEA results for all component FE models. An algorithm for implementing the SMN approach has been shown to be both very efficient and unconditionally convergent.

c. The potential benefits of the F_g and SMN approaches were demonstrated by considering a realistic case study of a CVCS nozzle subjected to multiple complex thermal transients. The initial Appendix XIII-3520 fatigue assessment utilising the existing Appendix XIII-3450 K_e approach was shown to be excessively conservative, yielding worst- and best-case CUFs of 3.63 and 3.23. Refined calculations adopting the F_g and SMN methods were shown to produce significantly lower maximum CUFs of 0.570 and 0.567, respectively. When incorporating environmental effects, the use of the Appendix XIII-3450 K_e approach yielded worst- and best-case CUF_{en} of 10.10 and 9.08 when adopting the MRA F_{en} approach. The use of the SNW F_{en} method reduced the CUF_{en} slightly, to 7.26 and 6.52 respectively for both cases. At the same location, the F_g and SMN methods applied in combination with the SNW F_{en} method reduced the CUF_{en} significantly to 1.084 and 1.080, respectively. By adopting the proposed plasticity correction methods, design justification of the CVCS nozzle is made possible with only minor additional analysis refinements.

d. The applicability of both the F_g and SMN methods has only been reliably demonstrated for Class 1 vessels, supports, and piping represented using 2D axisymmetric FE models. Further validation is required to confirm their suitability for application to complex 3D FE models and bolting materials.

10. Further Work

The work presented in this thesis addresses shortcomings in the existing ASME Section III criteria for simplified elastic-plastic fatigue analysis and proposes alternative approaches that more accurately predict the cyclic elastic-plastic response of nuclear pressure vessels and piping components. Further to this work, the following topics are identified as requiring future consideration:

1. **Further Validation of the Proposed F_g and SMN Methods**

   Whilst a considerable amount of realistic K_e^{FEA} data has been established in Section 7, it is important to further validate the F_g and SMN methods with additional sources of data. As a first step, the applicability of both approaches to complex 3D FE models must be confirmed to provide greater confidence in their predictive capabilities. In future, it may be possible to establish K_e^{FEA} values based on direct strain measurements obtained from component features testing, which would serve as a valuable supplement to the existing FEA data. An additional goal is to establish the validity of F_g for other high alloy steels including nickel-based alloys, thereby extending its practical application to other commonly used nuclear component steels.

2. **SCL-Free Fatigue Assessment**

   The SMN method proposed in 8.3 does not require stress linearisation, and therefore SCLs are not necessary to apply this approach to an Appendix XIII-3520 type fatigue assessment. This approach therefore offers the potential of a fatigue assessment of an entire component to be undertaken producing a CUF at every node of a finite element model. However, satisfaction of the Appendix XIII-3430 thermal stress ratchet criteria, which does require stress linearisation, is a prerequisite for the fatigue assessment and therefore limits the potential benefits of the SMN and other SCL-free methods. It is therefore recommended that further investigation be performed into determining suitable elastic DBA criteria for evaluating thermal stress ratchet, which do not rely on stress linearisation. Prior work undertaken in this area by the JSME Code Committees in the early 2000s should serve as a useful starting point for further inquiry.

3. Probabilistic Assessment of Fatigue Initiation

The adoption of a total life approach based on probabilistic methods using target reliability as a quantified margin will require improved accuracy of fatigue initiation predictions at low computational cost. The proposed F_g and SMN methods could therefore potentially serve as useful tools for the initiation stage of a probabilistic total life assessment. Further investigation should focus on assessing the performance of the proposed methods for rapid development and probabilistic treatment of finite element response surfaces using the Monte Carlo approach.

11. References

[1] American Society of Mechanical Engineers, “ASME Boiler and Pressure Vessel Code, Section III, Division 1.” ASME, 2017.

[2] Ministry of Transport and Civil Aviation, “Civil Aircraft Accident Report, Report of the Court of Inquiry into the Accidents to Comet G-ALYP and Comet G-ALYY,” London, UK, 1955.

[3] D. E. Matthews, R. S. Hill, and C. W. Bruny, “PVP2018-84031: 2025 NuclearCode: The Vision for the Future of ASME Nuclear Codes and Standards,” in *ASME 2018 Pressure Vessels and Piping Conference*, 2018.

[4] ASTM, “ASTM E446 - Standard Practice for Conducting Force Controlled Constant Amplitude Axial Fatigue Tests of Metallic Materials,” 2002.

[5] ASTM, “Standard Test Method for Strain-Controlled Fatigue Testing,” *E606/E606M-12*, vol. 96, no. 2004, pp. 1–16, 2004.

[6] O. H. Basquin, “The Exponential Law of Endurance Tests,” *Proc. ASTM*, vol. 10, no. 2, p. 625, 1910.

[7] L. F. Coffin Jr, “A Study on the Effects of Cyclic Thermal Stresses on a Ductile Material,” *Trans. Am. Soc. Mech. Eng.*, vol. 76, pp. 931–950, 1954.

[8] S. S. Manson, “Behaviour of Materials under Conditions of Thermal Stress,” 1954.

[9] S. S. Manson, *Thermal Stresses and Low-Cycle Fatigue*, 1st ed. New York: McGraw-Hill, 1966.

[10] B. Langer, “Design of Pressure Vessels for Low-Cycle Fatigue,” *J. Basic Eng.*, vol. 84, no. 3, pp. 389–399, 1962.

[11] J. A. Bannantine, J. J. Comer, and J. L. Handrock, *Fundamentals of Metal Fatigue Analysis*. Englewood Cliffs, NJ (USA): Prentice Hall, 1990.

[12] United States Department of Commerce - Office of Technical Services, “Tentative Structural Design Basis for Reactor Pressure Vessels and Directly Associated Components (Pressurized, Water-Cooled Systems),” 1958.

[13] R. W. Smith, M. H. Hirschberg, and S. S. Manson, “Fatigue Behavior of Materials Under Strain Cycling in Low and Intermediate Life Range,” Cleveland, OH, 1963.

[14] A. Nachtigall, “Strain-Cycling Fatigue Behavior of Ten Structural Metals Tested in Liquid Helium, Liquid Nitrogen, and Ambient Air,” *Prop. Mater. Liq. Nat. Gas Tankage*, pp. 378-378–19, 1974.

[15] J. Colin, A. Fatemi, and S. Taheri, “Fatigue behavior of stainless steel 304L including strain hardening, prestraining, and mean stress effects,” *J. Eng. Mater. Technol. Trans. ASME*, vol. 132, no. 2, pp. 0210081–02100813, 2010.

[16] J. Le Roux, D. Matériaux, J. Colin, and A. Fatemi, “PVP2008-61789,” pp. 1–

10, 2017.

[17] M. Botshekan, “Comportement mécanique et stabilité microstructurale d’un acier inoxydable austénitique type AISI 316LN sous forte plasticité monotone et cyclique à 77K et 300K,” Ecole Centrale de Lille, 1980.

[18] S. T. Utz, “Thermische Ermüdung in Kraftwerkskomponenten: Experimentelle und numerische Untersuchungen,” University of Stuttgart, 2015.

[19] B. Reicherter, “Untersuchung der werkstoffmechanischen Vorgänge zur verbesserten Lebensdauervorhersage im Low Cycle Fatigue Bereich,” University of Stuttgart, 2011.

[20] M. T. Medhurst, “Zyklisches Verhalten metastabiler austenitischer Feinbleche in Abhängigkeit des Umformgrades,” Technischen Universität Clausthal, 2014.

[21] J. Solin, “Fatigue of Stabilized SS and 316NG in PWR Environment,” in *ASME 2006 Pressure Vessels and Piping Conference*, 2006.

[22] J. Solin, S. Reese, and W. Mayinger, “PVP2012-78721, Fatigue Performance of Stainless Steels in NPP Service Conditions,” *Am. Soc. Mech. Eng. Press. Vessel. Pip. Div. PVP*, vol. 1, pp. 173–181, 2012.

[23] J. Solin, S. Reese, and W. Mayinger, “Discussion on fatigue design curves for stainless steels,” *Am. Soc. Mech. Eng. Press. Vessel. Pip. Div. PVP*, vol. 1, pp. 267–272, 2011.

[24] O. K. Chopra, “NUREG/CR-5704: Effects of LWR Coolant Environment on Fatigue Design Curves of Austenitic Stainless Steels,” Argonne, Illinois, 1999.

[25] J. B. Vogt, S. Degallaix, and J. Foct, “Low cycle fatigue life enhancement of 316 L stainless steel by nitrogen alloying,” vol. 4, no. 4, pp. 211–215, 1984.

[26] National Research Institute for Metals (Japan), “NRIM Fatigue Data Sheet No. 15,” Tokyo, Japan, 1979.

[27] National Research Institute for Metals (Japan), “NRIM Fatigue Data Sheet No. 49,” 1985.

[28] National Research Institute for Metals (Japan), “NRIM Fatigue Data Sheet No. 65,” Tokyo, Japan, 1990.

[29] National Research Institute for Metals (Japan), “NRIM Fatigue Data Sheet No. 100,” Tokyo, Japan, 2006.

[30] S. Bradai, “Study of the Effect of Equibiaxial Loading on the Fatigue Lifetime of Austenitic Stainless Steel (In French),” Ecole Polytechnique, 2014.

[31] L. De Baglion and J. Mendez, “Low cycle fatigue behavior of a type 304L austenitic stainless steel in air or in vacuum, at 20°C or at 300°C: Relative effect of strain rate and environment,” *Procedia Eng.*, vol. 2, no. 1, pp. 2171–2179, 2010.

[32] A. Le Pécheur, “Fatigue thermique d’ un acier inoxydable austénitique : influence de l’état de surface par une approche multi-échelles,” 2008.

[33] L. De Baglion, “Comportement et Endommagement en fatigue oligocyclique d’un acier inoxydable austénitique 304L en fonction de l’environnement (Vide, Air, Eau primaire REP) à 300°C,” *Sci. Ingénierie en Matériaux, Mécanique, Energétique Aéronautique*, p. 306, 2011.

[34] N. Huin, “Environmental effect on cracking of a 304L austenitic stainless steel in PWR primary environment under cyclic loading,” Institut Pprime (France), 2011.

[35] N. Miura and Y. Takahashi, “High-cycle fatigue behavior of type 316 stainless steel at 288 °C including mean stress effect,” *Int. J. Fatigue*, vol. 28, no. 11, pp. 1618–1625, 2006.

[36] H. D. Solomon, C. Amzallag, and R. E. DeLair, “Comparison of the Fatigue Life of Type 304L SS as measured in Load and Strain controlled Tests,” in *12th International Conference on Environmental Degradation of Materials in Nuclear Power System - Water Reactors*, 2005, pp. 1101–1110.

[37] J. B. Conway, R. H. Stentz, and J. T. Berling, “WRC 539: The Fatigue, Tensile, and Relaxation Behaviour of Stainless Steels.”

[38] D. L. Keller, “Progress on LMFBR Cladding, Structural, and Component Materials Studies During July, 1970, Through June 1971. Report: National Technical Information Service (U. S. Atomic Energy Commission), BMI-1914.,” 1971.

[39] R. W. Weeks, D. R. Diercks, and C. F. Cheng, “ANL Low-Cycle Fatigue Studies -- Program, Results, and Analysis, ANL-8009,” 1973.

[40] H. Bernstein and C. Loeby, “Low Cycle Corrosion Fatigue of Three Engineering Alloys in Salt Water,” *J. Eng. Mater. Technol.*, vol. 110, no. 3, pp. 234–239, 1988.

[41] V. S. Srinivasan, R. Sandhya, M. Valsan, K. B. S. Rao, and S. L. Mannan, “Comparative evaluation of strain controlled low cycle fatigue behaviour of solution annealed and prior cold worked 316L(N) stainless steel,” *Int. J. Fatigue*, vol. 26, no. 12, pp. 1295–1302, 2004.

[42] R. Sandhya, A. Veeramani, K. Bhanu Sankara Rao, and S. L. Mannan, “On specimen geometry effects in strain-controlled low-cycle fatigue,” *Int. J. Fatigue*, vol. 16, no. 3, pp. 202–208, 1994.

[43] H. D. Solomon, C. Amzallag, and R. E. DeLair, “Cycle Fatigue Limit of Type 304L SS in Air and PWR Water, at 150°C and 300°C,” in *12th International Conference on Environmental Degradation of Materials in Nuclear Power System - Water Reactors*, 2005, pp. 1083–1089.

[44] W. Ramberg and W. R. Osgood, “Description of Stress-Strain Curves by Three Parameters;,” Washington, DC (USA), 1943.

[45] J. Bauschinger, “Ueber die Veranderung der Elasticitatsgrenze und

elastcitatsmodul verschiedener," *Met. Civil. N.F.*, vol. 27, pp. 289–348, 1881.

[46] W. Gerber, "Bestimmung der zulossigen Spannungen in Eisen Constructionen," *Z. Bay. Arch. Ing. Ver.*, vol. 6, p. 101, 1874.

[47] C. R. Soderberg, "Factor of safety and working stress," *Trans. Am. Soc. Mech. Eng.*, vol. 52, pp. 13–28, 1930.

[48] J. Goodman, "Mechanics Applied to Engineering," *Mech. Appl. to Eng.*, pp. 631–636, 1899.

[49] J. Morrow, "Fatigue properties of metals," in *Fatigue Design Handbook*, Warrendale, PA: SAE, 1968.

[50] R. E. Peterson, *Stress Concentration Factors*. Wiley, 1974.

[51] K. Wellinger and H. Dietmann, *Festigkeitsberechnung - Grundlagen und technische Anwendung*. Alfred Kroener Verlag, 1976.

[52] T. H. Smith, K. N., Watson, P. and Topper, "A stress-strain function for the fatigue of materials," *J. Mater*, vol. 5, pp. 767–778, 1970.

[53] G. L. Wire, T. R. Leax, and J. T. Kandra, "Mean Stress and Environmental Effects on Fatigue in Type 304 Stainless Steel," 1999.

[54] P. Soo and J. G. Y. Chow, "The Effects of Mean Tensile Stresses on High-Cycle Fatigue Life and Strain Accumulation in Some Reactor Materials, BNL-NUREG-50654," 1977.

[55] M. J. Manjoine and R. E. Tome, "Proposed Design Criteria for High Cycle Fatigue of Stainless Steels," in *International Conference on Advances in Life Prediction Methods*, 1983, pp. 51–57.

[56] S. Asada, T. Ogawa, M. Higuchi, H. Kanasaki, and Y. Takada, "PVP2016-63796, Study on Mean Stress Effects for Design Fatigue Curves," 2019, pp. 5–10.

[57] D. L. DuQuesnay, T. H. Topper, M. T. Yu, and M. A. Pompetzki, "The effective stress range as a mean stress parameter," *Int. J. Fatigue*, vol. 14, no. 1, pp. 45–50, 1992.

[58] A. G. Palmgren, "Die Lebensdauer von Kugellagern (Life Length of Roller Bearings or Durability of Ball Bearings)," *Zeitschrift des Vereines Dtsch. Ingenieure*, vol. 14, pp. 339–341, 1924.

[59] M. A. Miner, "Cumulative damage in fatigue," *Am. Soc. Mech. Eng. - J. Appl. Mech.*, vol. 12, pp. 159–164, 1945.

[60] M. Kamaya and M. Kawakubo, "Loading sequence effect on fatigue life of Type 316 stainless steel," *Int. J. Fatigue*, vol. 81, pp. 10–20, 2015.

[61] W. E. Cooper, "The Initial Scope and Intent of the Section III Fatigue Design Procedure," in *Workshop on Cyclic Life and Environmental Effect in Nuclear Applications*, 1992.

[62] The American Society of Mechanical Engineers, “Criteria of Section III of the ASME Boiler and Pressure Vessel Code for Nuclear Vessels,” New York, USA, 1964.

[63] ASME, “Chapter 40: History, Philosophy, & Background of Section III, & Development of ASME Code Rules for Nuclear Vessels,” in *Companion Guide to ASME III*, ASME.

[64] J. F. Tavernelli and L. F. Coffin Jr., “Experimental Support for Generalized Fatigue Equation Predicting Low-Cycle Fatigue, Memo Report No. ME-83,” 1959.

[65] A. Johannson, “Fatigue of Steels at Constant Strain Amplitude and Elevated Temperature,” in *Proceedings Colloqium on Fatigue*, 1955.

[66] E. E. Baldwin, G. J. Sokol, and L. F. Coffin Jr., “Cyclic strain fatigue studies on AISI type 347 stainless steel,” *Proc. Amer. Soc. Test. Mater.*, vol. 57, pp. 567–586, 1957.

[67] L. F. Coffin Jr. and J. F. Tavernelli, “The Cyclic Straining and Fatigue of Metals,” *Trans. Metall. Soc. AIME*, vol. 215, pp. 794–807, 1959.

[68] A. G. Pickett and S. C. Grigory, “Welding Research Council Bulletin 135: Cyclic Pressure Tests of Full Sized Pressure Vessels,” San Antonio, TX, 1968.

[69] J. Spence and W. B. Carlson, “A Study of Nozzles in Pressure Vessels Under Pressure Fatigue Loading,” *Proc. Inst. Mech. Eng.*, vol. 182, no. 31, pp. 657–684.

[70] C. E. Jaske and W. J. O’Donnell, “Fatigue Design Criteria for Pressure Vessel Alloys,” *J. Press. Vessel Technol.*, vol. 99, no. 4, pp. 584–592, 1977.

[71] U.S. Nuclear Regulatory Commission, “NUREG/CR-6909 - Effects of Light Water Reactor Coolant Environments on the Fatigue Life of Reactor Materials,” Washington, DC, 2007.

[72] U.S. Nuclear Regulatory Commission, “NUREG/CR-6909 - Effects of Light Water Reactor Coolant Environments on the Fatigue Life of Reactor Materials, Revision 1,” Washington, DC, 2014.

[73] American Society of Mechanical Engineers, “ASME BPVC Section II, Part D,” 2015.

[74] D. R. Miller, “Thermal-Stress Ratchet Mechanism in Pressure Vessels,” *J. Basic Eng.*, vol. 81, no. 2, pp. 190–194, 1959.

[75] ASME, “Boiler and Pressure Vessel Code, Section XI, Rules for Inservice Inspection of Nuclear Power Plant Components,” 2017.

[76] K. Wright, “A Total Life Assessment Approach with Quantified Margins with LWRs,” in *IAEA Technical Meeting on Fatigue Assessment in Light Water Reactors for Long Term Operation: Good Practices and Lessons Learned*, 2016, no. July.

[77] U.S. Nuclear Regulatory Commission, “Regulatory Guide 1.207, Revision 1: Guidelines for Evaluating the Effects of Light-Water Reactor Water Environments in Fatigue Analysis of Metal Components,” 2018.

[78] ASME, “Record 18-257: Proposed Code Case N-XXX, Code Case for Fatigue Thickness and Gradient Factors for ASME Section III Class 1 Piping Components,” 2018.

[79] S. R. Gosselin, D. Nunez, T. Esselman, and J. Cluever, “Development of Fatigue Usage Life and Gradient Factors,” 2018.

[80] Python Software Foundation, “Python 2.7.3.” 2012.

[81] T. Oliphant, “Numerical Python (NumPy).” 2006.

[82] Dassault Systèmes Simulia, “ABAQUS Version 6.14-5.” .

[83] F. W. Dittus and L. M. . Boelter, “Heat Transfer in Automobile Radiators of the Tubular Type,” *Univ Calif Publ Eng 2443-461. Repr. Int Commun Heat Mass Transf*, vol. 12, pp. 3–22, 1985.

[84] E. N. Sieder and G. E. Tate, “Heat Transfer and Pressure Drop of Liquids in Tubes,” *Ind. Energy Chem. Res.*, vol. 28, pp. 1429–1435, 1936.

[85] V. Gnielinski, “New Equations for Heat and Mass Transfer in Turbulent Pipe and Channel Flow,” *Int. J. Chem. Eng.*, vol. 16, pp. 359–368, 1976.

[86] J. L. Hechmer and G. L. Hollinger, “WRC Bulletin 429 - 3D Stress Criteria Guidelines For Application,” Cleveland, OH, 1998.

[87] D. Gilmartin, D. Mackenzie, and C. D. Bell, “Limitations of Stress Linearisation in Elastic Design By Analysis of Thick Walled Components,” in *Proceedings of the Interntational Conference on Nuclear Engineering (ICONE) 2019*, 2019.

[88] American Society for Testing and Materials (ASTM), “E1049-85, Standard Practices for Cycle Counting in Fatigue Analysis,” West Conshohocken, PA (USA).

[89] T. L. Meikle V, E. Lyles Cranford III, and M. A. Gray, “PVP2010-25891, Method for Selecting Stress States for Use in an NB-3200 Fatigue Analysis,” in *ASME 2010 Pressure Vessels and Piping Conference*, 2010.

[90] T. Gilman, “Stress Based Fatigue Monitoring: Methodology for Fatigue Monitoring of Class 1 Nuclear Components in a Reactor Water Environment, EPRI Technical Report 1022876,” 2011.

[91] F. M. S. Costa, J. L. F. Freire, J. Rudolph, and J. E. Maneschy, “PVP2016-63931, A Proposal to Consider Cycle Counting Methods for Fatigue Analysis of Nuclear and Conventional Power Plant Components,” in *ASME 2016 Pressure Vessels and Piping Conference*, 2016.

[92] S. R. Gosselin, F. A. Simonen, P. G. Heasler, and S. R. Doctor, “NUREG/CR-6934: Fatigue Crack Tolerance in Nuclear Power Plant Piping, A Basis for

Improvements to ASME Code Section XI Appendix L," Richland, WA (USA), 2007.

[93] E. Blondet and C. Faidy, "ICONE10-22762: High Cycle Thermal Fatigue in French PWR," in *Proceedings of the 2002 International Conference on Nuclear Engineering (ICONE)*, 2002, pp. 429–436.

[94] J. Alain *et al.*, "PVP2011-57951: High Cycle Thermal Fatigue Issues in RHRS Mixing Tees and Thermal Fatgue Test on a Representative 304L Mixing Zone," in *ASME 2011 Pressure Vessels and Piping Conference*, 2011.

[95] P. Hirschberg, A. F. Deardorff, and J. Carey, "Operating Experience Regarding Thermal Fatigue of Non-Isolable Piping Connected to PWR Reactor Coolant Systems," in *International Conference on Fatigue of Reactor Components*, 2000.

[96] C. Basavaraju, K. A. Manoly, M. C. Murphy, and W. T. Jessup, "PVP2013-97218: BWR Steam Dryer Issues and Lessons Learned Related to Flow Induced Vibration," in *ASME 2013 Pressure Vessels & Piping Conference*, 2013.

[97] K. Iida, "A review of fatigue failures in LWR plants in Japan," *Nucl. Eng. Des.*, vol. 138, no. 3, pp. 297–312, 1992.

[98] C. L. Atwood, V. K. Shah, and W. J. Galyean, "Analysis of Pressurized Water Reactor Primary Coolant Leak Events Caused by Thermal Fatigue," Idaho Falls, ID (USA), 1999.

[99] J. Economou, Y. Thebault, and P. Costes, "PVP2011-57893: Small Bore Pipe Branch Connections Fatigue," in *ASME 2011 Pressure Vessels and Piping Conference*, 2011, vol. C, pp. 3–7.

[100] P. Y. Chen, P. Sekerak, T. Scarbrough, and C. L. Wu, "Potential Adverse Flow Effects at Nuclear Power Plants," in *International Conference on Nuclear Engineering (ICONE)*, 2008, vol. 4, pp. 271–276.

[101] L. L. Da Silva, T. R. Mansur, and C. A. Cimini Junior, "Thermal fatigue damage evaluation of a PWR NPP steam generator injection nozzle model subjected to thermal stratification phenomenon," *Nucl. Eng. Des.*, vol. 241, no. 3, pp. 672–680, 2011.

[102] C. Currie, J. Mann, P. Gill, D. Leary, and K. Wright, "PVP2019-93855, Extension of the Weighted Stress Intensity Factor Rate (WKR) Method to Characterisation of Varying Temperature and Loading Rate in Plant Realistic Waveform Fatigue Crack Growth Calculations," in *ASME 2019 Pressure Vessels and Piping Conference*, 2019.

[103] K. Wright, "Developments in Environmentally Assisted Fatigue Methodologies," in *Trans. SMiRT-24*, 2017.

[104] B. F. Langer, "Design-Stress Basis for Pressure Vessels," in *The William M. Murray Lecture*, 1970.

[105] American Society of Mechanical Engineers, "Criteria of the ASME Boiler and

Pressure Vessel Code for Design by Analysis in Sections III and VIII, Division 2," New York, 1969.

[106] M. Radomski and D. J. White, "Some theoretical considerations relating to strain concentration in elastic-plastic bending of beams," *J. Strain Anal. Eng. Des.*, vol. 3, no. 4, pp. 304–312, 1968.

[107] D. J. White and M. Radomski, "Strain concentration in beams under cyclic plastic straining," *J. Strain Anal. Eng. Des.*, vol. 3, no. 4, pp. 313–324, 1968.

[108] B. F. Langer, "Fatigue Evaluation for Primary-Plus-Secondary Stresses which Exceed 3Sm, ASME Code Committee Correspondence," 1969.

[109] S. W. J. Tagart, "Plastic Fatigue Analysis of Pressure Components," in *ASME Paper 68-PVP-3, Presented at the Joint Petroleum / PVP Conference*, 1968.

[110] J. M. Grandemange, J. Heliot, J. Vagner, A. Morel, and C. Faidy, "WRC 361: Part 1, Improvements on Fatigue Analysis Methods for the Design of Nuclear Components Subjected to the French RCC-M Code," Shaker Heights, OH (USA), 1991.

[111] A. Nadai, *Theory of Flow and Fracture of Solids*, 2nd Editio. McGraw-Hill, 1950.

[112] D. Moulin and R. L. Roche, "Correction of the Poisson effect in the elastic analysis of low-cycle fatigue," *Int. J. Press. Vessel. Pip.*, vol. 19, no. 3, pp. 213–233, 1985.

[113] American Society of Mechanical Engineers (ASME), "Code Case N-779: Alternative Rules for Simplified Elastic-Plastic Analysis, Class 1 Section III, Division 1," Washington, DC (USA), 2009.

[114] S. Adams, "An Alternative Simplified Elastic-Plastic Analysis Method Technical Support Document, ASME Code Correspondence," 2007.

[115] Nuclear Regulatory Commision, "NRC Regulatory Guide 1.193 - ASME Code Cases Not Approved for Use," 2007.

[116] AFCEN, "RCC-M: Rules for Design and Construction of Nuclear Components from PWR Nuclear Islands," 2014.

[117] C. Faidy, "Tutorial on C&S ASME," in *ASME 2006 Pressure Vessels and Piping Conference*, 2006.

[118] Japanese Society of Mechanical Engineers, *Rules on Design and Construction for Nuclear Power Plants, Division 1: Light Water Reactors*. Japanese Society of Mechanical Engineers (JSME), 2015.

[119] "MITI Notification 501, Technical Standards for the Construction of Nuclear Power Plant Components (in Japanese)."

[120] Thermal and Nuclear Power Engineering Society (TENPES), "Final Report: Committee on Stress Compensated (Ke) Factor for Simplified Elastic-Plastic Analysis, (in Japanese), (2000-6)."

[121] K. Iida, Y. Asada, K. Okabayashi, and T. Nagata, “Simplified Analysis and Design for Elevated Temperature Components of Monju,” *J. Nucl. Eng. Des.*, vol. 98, pp. 305–317, 1987.

[122] S. Asada and T. Nakamura, “Simplified Elastic-Plastic Analysis Methods in the JSME Rules on Design and Construction,” *J. Environ. Eng.*, vol. 6, no. 4, pp. 753–764, 2011.

[123] Japanese Society of Mechanical Engineers (JSME), “Code Case NC-CC-005: Alternative Structural Evaluation Criteria for Class 1 Vessels Based on Elastic-Plastic Finite Element Analysis (in Japanese),” 2008.

[124] GOST, “PNAE G-7-002-86: Rules of Strength Calculation for Equipment and Pipelines of Nuclear Power Plants,” Moscow, Russia, 1987.

[125] K. Molski and G. Glinka, “A Method of Elastic-Plastic Stress and Strain Calculation at a Notch Root,” *Mater. Sci. Eng.*, vol. 50, no. 1, pp. 93–100, 1981.

[126] EDF Energy Nuclear Generation, “R5, Assessment Procedures for the High Temperature Response of Structures, Revision 4,” 2014.

[127] EDF Energy Nuclear Generation Ltd., “R5 V2/3 Appendix A7, Enhancement of Strain Range due to Plasticity and Creep,” Barnwood, Cheshire, UK, 2003.

[128] S. Ranganath and N. A. Palm, “PVP2017-66240: Alternative Approaches for ASME Code Simplified Elastic-Plastic Analysis,” in *ASME 2017 Pressure Vessels and Piping Conference*, 2017.

[129] S. Ranganath and N. Palm, “Alternative Approaches for ASME Code Simplified Elastic-Plastic Analysis,” in *NRC Public Meeting on Fatigue Research and Related ASME Activities*, 2016.

[130] W. Reinhardt and S. Ranganath, “PVP2018-85146: Comparison of New Proposal for Simplified Elastic-Plastic Analysis and Code Case N-779,” in *ASME 2018 Pressure Vessels and Piping Conference*, 2018.

[131] S. Ranganath and N. Palm, “Alternative Approaches for ASME Code Simplified Elastic-Plastic Analysis,” in *NRC Public Meeting on EAF Research and Related ASME Activities*, 2018.

[132] ASME, “Record 17-225: Proposed Code Case N-XXX, Alternative Rules for Simplified Elastic-Plastic Analysis in Section III,” 2020.

[133] J. Emslie, C. Watson, and K. Wright, “PVP2014-28633: ASME III Fatigue Assessment Plasticity Correction Factors for Austenitic Stainless Steels,” in *ASME 2014 Pressure Vessels and Piping Conference*, 2014.

[134] D. P. Jones, J. E. Holliday, T. R. Leax, and J. L. Gordon, “PVP2004-2748: Analysis of a Thermal Fatigue Test of a Stepped Pipe,” in *ASME 2004 Pressure Vessels and Piping Conference*, 2004, pp. 67–77.

[135] American Society of Mechanical Engineers, *ASME BPVC, Section VIII, Division 2: Alternative Rules*, 2015th ed. American Society of Mechanical

Engineers, 2015.

[136] G. Baylac and D. Koplewicz, “EN 13445: Unfired pressure Vessels, Background to the rules in Part 3 Design,” 2004.

[137] American Society of Mechanical Engineers (ASME), “ASME VIII-2, Annex 5-C: Alternative Plasticity Adjustment Factors and Effective Alternating Stress for Elastic Fatigue Analysis,” 2007.

[138] “CEN/TC 54; EN 13445-3:2014/prA3:2015; 2015-10. Clause 18: "Detailed assessment of fatigue life“, Annex NA: "Instructions for determining structural hotspot stress by finite element analysis using shell and brick elements“.”

[139] G. Han and S. Guzey, “Structural Stress Determination at a Hot-Spot,” *J. Press. Vessel Technol.*, vol. 142, no. 4, 2020.

[140] Arbeitsgemeinschaft Druckbehälter (AD), “AD 2000-Merkblatt, Special Cases, S2: Analysis for Cyclic Loading,” 2004.

[141] I. Saito and T. Shimakawa, “PVP2004-2690, Outline of the JSME (Japan Society of Mechanical Engineers) Rules on Design and Construction of Nuclear Power Plants.,” in *ASME 2004 Pressure Vessels and Piping Conference*, 2004, vol. 480.

[142] S. Asada, T. Hirano, T. Nagata, and N. Kasahara, “PVP2010-25525, Overview of Code Case on Alternative Design Methodology by Using Elastic-Plastic Finite Element Analysis for Class 1 Vessels in the JSME Rules on Design and Construction,” in *ASME 2010 Pressure Vessels and Piping Conference*, 2010.

[143] R. Hales, S. R. Holdsworth, M. P. O’Donnell, I. J. Perrin, and R. P. Skelton, “A code of practice for the determination of cyclic stress-strain data,” *Mater. High Temp.*, vol. 19, no. 4, pp. 165–185, 2002.

[144] ASME, “Chapter 6: Subsection NB - Class 1 Components,” in *Companion Guide to ASME III*, 1998th ed., ASME, 2014.

[145] D. A. OSAGE and J. C. SOWINSKI, “ASME Section VIII - Division 2 - Criteria and Commentary,” 2014.

[146] C. Baumel and T. Seeger, *Materials Data for Cyclic Loading: Supplement 1*, 2nd ed. Amsterdam, The Netherlands: Elsevier Science Publishers, 1990.

[147] U. Muralidharan and S. S. Manson, “A Modified Universal Slopes Equation for Estimation of Fatigue Characteristics of Metals,” *J. Eng. Mater. Technol.*, vol. 110, no. 1, pp. 55–58, 1988.

[148] M. A. Meggiolaro and J. T. P. Castro, “Statistical evaluation of strain-life fatigue crack initiation predictions,” *Int. J. Fatigue*, vol. 26, no. 5, pp. 463–476, 2004.

[149] AFCEN, *RCC-MRx: Design and Construction Rules for Mechanical Components in High-Temperature Structures, Experimental Reactors and Fusion Reactors*, 2018th ed. Paris, France: AFCEN, 2018.

[150] ITER, “Structural Design Criteria for ITER In-Vessel Components (SDC-IC), Appendix A, Materials Design Limit Data,” 2013.

[151] American Iron and Steel Institute (AISI), “High-Temperature Characteristics of Stainless Steels, A Designers’ Handbook Series, No. 9004.”

[152] J. L. Chaboche and D. Nouailhas, “Constitutive Modeling Of Ratchetting Effects—Part I: Experimental Facts And Properties Of The Classical Models,” *J. Eng. Mater. Technol.*, vol. 111, no. 4, pp. 384–392, 1989.

[153] J. L. Chaboche and D. Nouailhas, “Constitutive Modeling Of Ratchetting Effects—Part II: Possibilities Of Some Additional Kinematic Rules,” *J. Eng. Mater. Technol.*, vol. 111, no. 4, pp. 409–416, 1989.

[154] P. J. Armstrong and C. O. Frederick, “Report RD/B/N731A: A Mathematical Representation of the Multiaxial Bauschinger Effect,” Berkeley, UK, 1966.

[155] J. L. Chaboche, “A review of some plasticity and viscoplasticity constitutive theories,” *Int. J. Plast.*, vol. 24, no. 10, pp. 1642–1693, 2008.

[156] A. Kalnins, J. Rudolph, and A. Willuweit, “PVP2013-98150, Using the Nonlinear Kinematic Hardening Material Model of Chaboche for Elastic-Plastic Ratcheting Analysis,” in *ASME 2013 Pressure Vessels & Piping Conference*, 2013.

[157] K. Levenberg, “A Method for the Solution of Certain Non-Linear Problems in Least Squares,” *Q. Appl. Math.*, vol. 2, no. 2, pp. 431–441, 1944.

[158] D. Marquardt, “An Algorithm for Least-Squares Estimation of Non-Linear Parameters,” *SIAM J. Appl. Mathet.*, vol. 11, no. 2, pp. 431–441, 1963.

[159] N. E. Dowling, *Mechanical Behavior of Materials: Engineering Methods for Deformation, Fracture, and Fatigue*, 4th Editio. Pearson, 2012.

[160] J. Miller, “Low-Cycle Fatigue Under Biaxial Strain-Controlled Conditions,” *J. Mater.*, vol. 7, no. 3, pp. 307–314, 1971.

[161] A. Fatemi and D. F. Socie, “A Critical Plane Approach To Multiaxial Fatigue Damage Including Out of Phase Loading,” *Fatigue & Fracture of Engineering Materials & Structures*, vol. 11, no. 3. pp. 149–165, 1988.

[162] T. Gilman and F. Ku, “PVP2016-63861: Environmentally-Assisted Fatigue Analysis Using a Strain-Based Approach,” in *ASME 2016 Pressure Vessels and Piping Conference*, 2016.

[163] T. Damiani, “ASME III Working Group on Fatigue Strength (WGFS) Committee Correspondance, Revision to Elastic-Plastic Strain Basis Proposal (Ballot 17-3555),” Las Vegas (NV), USA, 2018.

[164] W. Reinhardt, “Strain Measures for Fatigue Assessment Using Elastic-Plastic FEA,” in *ASME 2005 Pressure Vessels and Piping Conference*, 2005.

[165] J. Draper, *Modern Metal Fatigue Analysis*. The UK Forum for Engineering Structural Integrity (FESI), 2008.

[166] T. Itoh, M. Sakane, M. Ohnami, and D. F. Socie, “Nonproportional Low Cycle Fatigue Criterion for Type 304 Stainless Steel,” *J. Eng. Mater. Technol.*, vol. 117, no. 3, pp. 285–292, 1995.

[167] D. F. Socie and G. Marquis, *Multiaxial Fatigue*. SAE International, 2000.

[168] CORDEL Mechanical Codes and Standards Task Force (MCSTF), “Non-Linear Analysis Design Rules, Part 2a: Specification of Benchmarks on Nozzles under Pressure, Thermal, and Piping Loads,” 2019.

[169] T. Gilman, B. Weitze, J. Rudolph, A. Willuweit, and A. Kalnins, “Using Nonlinear Kinematic Hardening Material Models For Elastic-Plastic Ratcheting Analysis,” *ASME 2015 Press. Vessel. Pip. Conf.*, vol. 137, no. June, pp. 1–10, 2015.

[170] D. Leary, C. Currie, and K. Wright, “PVP2019-93849: Critical Review of Strain Measures for Characterisation of Fatigue Damage in ASME Section III Fatigue Assessments,” in *ASME 2019 Pressure Vessels and Piping Conference*, 2019.

[171] Z. Y. Yu, S. P. Zhu, Q. Liu, and Y. Liu, “Multiaxial fatigue damage parameter and life prediction without any additional material constants,” *Materials (Basel).*, vol. 10, no. 8, 2017.

[172] J. Batten, C. Currie, K. Wright, and J. Mann, “Scaling of SN curves for varying ‘initiation’ crack definitions from striation counted environmental fatigue specimens: A 250 micron austenitic stainless steel Sn curve and associated fen factors,” in *American Society of Mechanical Engineers, Pressure Vessels and Piping Division (Publication) PVP*, 2019, vol. 1, pp. 1–11.

[173] M. E. Nitzel, A. G. Ware, and D. K. Morton, “Comparison of ASME Code NB-3200 and NB-3600 Results for Fatigue Analysis of B31.1 Branch Nozzles,” Idaho Falls, Idaho, 1996.

[174] K. Kobayashi and J. Yamada, “Estimation of Inelastic Behavior for a Tapered Nozzle in Vessel due to Thermal Transient Load using Stress Redistribution Locus Method,” *J. Solid Mech. Mater. Eng.*, vol. 6, no. 4, pp. 278–287, 2012.

[175] H. Hubel, *Simplified Theory of Plastic Zones Based on Zarka’s Method*. Springer, 2017.

[176] N. Kasahara, “Strain Concentration at Structural Discontinuities its Prediction based on Characteristics of Compliance Change in Structures,” *JSME Int. J.*, vol. 44, no. 3, pp. 354–361, 2001.

[177] Eastop and McConkey, *Applied Thermodynamics for Engineering Technologists*, 5th Editio. .

[178] T. Fujioka, “Elastic-Route Estimation of Strain Range in Notched Components Under Thermal Loading Without Performing Stress Linearization,” *J. Press. Vessel Technol.*, vol. 137, no. April 2015, pp. 1–6, 2017.

[179] J. Mann, M. Twite, and M. G. Burke, “PVP2016-63238, Analysis of Fatigue Crack Growth in Standard Endurance Test Specimens in Support of Total Life Approaches to Fatigue Assessment,” in *ASME 2016 Pressure Vessels and Piping Conference*, 2016.

[180] K. Wright, D. Leary, and J. Batten, “Probabilistic Fatigue Analysis: Assessment of an Environmental Fatigue Thermal Shock Test to Quantify Deterministic Code Margin,” in *3rd International Seminar on Probabilistic Methodologies for Nuclear Applications*, 2019.

[181] H. Lang, J. Rudolph, and R. Ziegler, “Performance study of Ke factors in simplified elastic plastic fatigue analyses with emphasis on thermal cyclic loading,” *Int. J. Press. Vessel. Pip.*, vol. 88, no. 8–9, pp. 330–347, 2011.

[182] D. Clarkson, D. Mackenzie, and C. Bell, “Performance Study of Design Code Rules for Simplified Elastic-Plastic Fatigue Analysis of Nuclear Power Plant Pressure Vessels,” in *ESIA15 & ISSI-2019 Joint Conference on Engineering Structural Integrity Assessment*, 2019.

[183] N. Kasahara, T. Nagata, K. Iwata, and H. Negishi, “Advanced creep-fatigue evaluation rule for fast breeder reactor components: generalization of elastic follow-up model,” *Nucl. Eng. Des.*, vol. 155, no. 3, pp. 499–518, 1995.

[184] N. Kasahara, “Strain Concentration Mechanism during Stress Relaxation Process and its Prediction,” in *Proceedings of CREEP7*, 2001.

[185] M. Sato, H. Kikuchi, and N. Kasahara, “PVP2011-57552: Study on Mechanism of Stress-Strain Redistribution Under Elastic-Plastic-Creep Deformations,” in *ASME 2011 Pressure Vessels and Piping Conference*, 2011.

[186] P. James, “Calculation of KJ under secondary loads in isolation for R6,” in *ASME 2015 Pressure Vessels and Piping Conference*, 2015, vol. 6A-2015.

[187] H. Neuber, “Theory of Stress Concentration for Shear-Strained Prismatical Bodies With Arbitrary Nonlinear Stress-Strain Law,” *J. Appl. Mech.*, vol. 28, no. 4, pp. 544–550, 1961.

[188] T. Shimakawa, O. Watanabe, N. Kasahara, K. Kobayashi, Y. Takizawa, and S. Asada, “Creep-Fatigue Life Evaluation based on Stress Redistribution Locus (SRL) Method, PVRC/EPERC/JPVRC Joint Workshop,” 2002.

[189] T. Teremae, “The Strain Estimation of Statically Determinate Structures Subjected to Forced Displacement by Reference Stress Method,” *Trans. Japan Soc. Mech. Eng.*, vol. 74, no. 740, pp. 592–597, 2008.

[190] O. Watanabe, K. Kobayashi, and K. Nakamura, “PVP2013-97865: Development of Guideline for Prediction of Inelastic Strain for Creep-Fatigue Evaluation,” in *ASME 2013 Pressure Vessels & Piping Conference*, 2013.

[191] A. Navarro, “An unconditionally convergent iterative algorithm for the intersection of Neuber’s and Molski-Glinka’s rules with the Ramberg-Osgood stress-strain relationship,” *Theor. Appl. Fract. Mech.*, vol. 69, pp. 53–62, 2014.

[192] C. Currie, N. Platts, A. Morley, M. Twite, and K. Wright, “PVP2017-66030: Models for Calculating The Effect of Environment on Fatigue Life (Fen) For Complex Waveforms and/or Non-Isothermal Conditions,” 2017, pp. 1–12.

[193] C. Currie, A. Morley, D. Leary, N. Platts, M. Twite, and K. Wright, “PVP2018-84879: Further Validation of the Strain-Life Weighted (SNW) Fen Method for Plant Realistic Strain and Temperature Waveforms,” in *ASME 2018 Pressure Vessels and Piping Conference*, 2018.

[194] ASME, “Record 19-702: Proposed Code Case N-XXX, Alternative Fen Integration Method,” 2019.

[195] J. Rudolph *et al.*, “PVP2015-45668, Load Data Evaluation, Stress Analysis and Cycle Counting for the Qualified Thermal Fatigue Assessment of a NPP Component,” in *ASME 2015 Pressure Vessels and Piping Conference*, 2015, pp. 1–10.

[196] J. Emslie and C. Watson, “PVP2013-97230, A Parametric Study Into the Competing Effects of Stress and Strain Rate in Environmental Fatigue Usage Calculations,” in *ASME 2013 Pressure Vessels & Piping Conference*, 2013.

[197] L. Rawson and D. Rice, “PVP2012-78296: Strain-Based Fatigue Methods Using Modern Finite Element Analysis for the Assessment of Pressure Vessels Equivalent to the ASME III Code,” in *Volume 1: Codes and Standards*, 2012, p. 841.